IN
(1720)

A Reproduced Copy

OF

PB86-139169

(NASA-CR-176721) PROCEEDINGS OF THE FIRST NATIONAL WORKSHOP ON THE GLOBAL WEATHER EXPERIMENT: CURRENT ACHIEVEMENTS AND FUTURE DIRECTIONS, VOLUME 2, PART 1 Final Report (National Academy of Sciences - National

N86-24121
THRU
N86-24141
Unclas
G3/47 09046

Reproduced for NASA

by the

NASA Scientific and Technical Information Facility

FFNo 672 Aug 65

PB86-139169

Proceedings of the National Workshop on the Global Weather Experiment (1st) Current Achievements and Future Directions Volume 2. Part 1

National Research Council, Washington, DC

Prepared for

National Science Foundation, Washington, DC

Oct 85

50772-101

REPORT DOCUMENTATION PAGE	1. REPORT NO.	2.	3. Recipient's Accession No. PB86 139169/AS

4. Title and Subtitle
Proceedings of the First National Workshop on the Global Weather Experiment: Current Achievements and Future Directions
Volume Two, Part 1 of 2

5. Report Date
October 1985

6.

7. Author(s)

8. Performing Organization Rept. No.

9. Performing Organization Name and Address
National Research Council
Commission on Physical Sciences, Mathematics, and Resources
2101 Constitution Avenue, N.W.
Washington, D.C. 20418

10. Project/Task/Work Unit No.

11. Contract(C) or Grant(G) No.
(C)
(G) NSF ATM-8025329

12. Sponsoring Organization Name and Address
National Science Foundation
National Oceanic and Atmospheric Administration
National Aeronautics and Space Administration

13. Type of Report & Period Covered
Final

14.

15. Supplementary Notes
Proceedings of a workshop held at Woods Hole, Massachusetts, July 9-20, 1984

16. Abstract (Limit: 200 words)

An assessment of the status of research using Global Weather Experiment (GWE) data and of the progress in meeting the objectives of the GWE, i.e., better knowledge and understanding of the atmosphere in order to provide more useful weather prediction services.

Volume Two of the report consists of a compilation of the papers presented during the workshop. These cover studies that addressed GWE research objectives and utilized GWE information. The titles in Part 1 of this volume include Data Systems and Quality, Analysis and Assimilation Techniques, Impacts on Forecasts, Tropical Forecasts, Analysis Intercomparisons, Improvements in Predictability, and Heat Sources and Sinks.

17. Document Analysis a. Descriptors
meteorology, atmospheric sciences, weather prediction, global circulation, numeric modeling and prediction, objective analysis and assimilation, satellite observing systems, tropical meteorology, oceanography, monsoons, heat sources and sinks, cumulus parameterization

b. Identifiers/Open-Ended Terms
Global Atmospheric Research Program (GARP), Global Weather Experiment (GWE), First GARP Global Experiment (FGGE), Monsoon Experiment (MONEX), Observing Systems Simulation Experiments (OSSE)

c. COSATI Field/Group

18. Availability Statement
Distribution is unlimited.

19. Security Class (This Report)
unclassified

21. No. of Pages
397

20. Security Class (This Page)
unclassified

22. Price

(See ANSI-Z39.18) See Instructions on Reverse OPTIONAL FORM 272 (4-77)
(Formerly NTIS-35)

Proceedings of the First National Workshop on the Global Weather Experiment

Current Achievements and Future Directions

Volume Two, Part One

Proceedings of the First National Workshop on the Global Weather Experiment:

Current Achievements and Future Directions

Volume Two, Part I

Woods Hole, Massachusetts
July 9–20, 1984

First GARP Global Experiment (FGGE) Advisory Panel
U.S. Committee for the Global Atmospheric Research Program
Board on Atmospheric Sciences and Climate
Commission on Physical Sciences, Mathematics, and Resources
National Research Council

NATIONAL ACADEMY PRESS
Washington, D.C. 1985

NOTICE The project that is the subject of this report was approved by the Governing Board of the National Research Council, whose members are drawn from the councils of the National Academy of Sciences, the National Academy of Engineering, and the Institute of Medicine. The members of the committee responsible for the report were chosen for their special competences and with regard for appropriate balance.

The National Research Council was established by the National Academy of Sciences in 1916 to associate the broad community of science and technology with the Academy's purposes of furthering knowledge and of advising the federal government. The Council operates in accordance with general policies determined by the Academy under the authority of its congressional charter of 1863, which establishes the Academy as a private, nonprofit, self-governing membership corporation. The Council has become the principal operating agency of both the National Academy of Sciences and the National Academy of Engineering in the conduct of their services to the government, the public, and the scientific and engineering communities. It is administered jointly by both Academies and the Institute of Medicine. The National Academy of Engineering and the Institute of Medicine were established in 1964 and 1970, respectively, under the charter of the National Academy of Sciences.

This material is based upon work supported jointly by the National Science Foundation, the National Oceanic and Atmospheric Administration and the National Aeronautics and Space Administration under Grant Number ATM-8025329.

U.S. COMMITTEE FOR THE GLOBAL ATMOSPHERIC RESEARCH PROGRAM (GARP)

Verner E. Suomi, University of Wisconsin, Madison, Chairman
Joseph Smagorinsky, Princeton University, Vice Chairman
Julia N. Paegle, University of Utah
Ronald B. Smith, Yale University
John A. Young, University of Wisconsin, Madison

FIRST GARP GLOBAL EXPERIMENT (FGGE) ADVISORY PANEL

Julia N. Paegle, University of Utah, Chairman
John H. E. Clark, Pennsylvania State University
Roger W. Daley, National Center for Atmospheric Research
Donald R. Johnson, University of Wisconsin
Eugenia Kalnay, National Aeronautics and Space Administration

FGGE WORKSHOP ORGANIZING COMMITTEE

Donald R. Johnson, University of Wisconsin, Madison, Chairman
John H. E. Clark, Pennsylvania State University
Roger Daley, National Center for Atmospheric Research
Jay S. Fein, National Science Foundation
Rex J. Fleming, National Oceanic and Atmospheric Administration
Paul Julian, Dalhousie University
Eugenia Kalnay, National Aeronautics and Space Administration
T. N. Krishnamurti, Florida State University
Julia N. Paegle, University of Utah
Norman A. Phillips, National Oceanic and Atmospheric Administration
Richard J. Reed, University of Washington
Pamela L. Stephens, National Science Foundation

STAFF

Thomas O'Neill, National Research Council, Executive Secretary

BOARD ON ATMOSPHERIC SCIENCES AND CLIMATE

Charles L. Hosler, Jr., Pennsylvania State University, Chairman
Ferdinand Baer, University of Maryland
Louis J. Battan, University of Arizona
William C. Clark, International Institute for Applied Systems Analysis
Robert A. Duce, University of Rhode Island
John A. Eddy, National Center for Atmospheric Research
Francis S. Johnson, University of Texas, Dallas
Michael B. McElroy, Harvard University
James C. McWilliams, National Center for Atmospheric Research
Volker A. Mohnen, State University of New York, Albany
Andrew F. Nagy, University of Michigan
Roger R. Revelle, University of California, San Diego
Juan G. Roederer, University of Alaska
Norman J. Rosenberg, University of Nebraska
Stephen H. Schneider, National Center for Atmospheric Research
John W. Townsend, Fairchild Space & Electronics Company

EX-OFFICIO MEMBERS

Werner A. Baum, Florida State University
Devrie Intriligator, Carmel Research Center
Joseph Smagorinsky, Princeton University
Verner E. Suomi, University of Wisconsin, Madison

STAFF

John S. Perry, Staff Director
Fred D. White, Staff Officer
Thomas O'Neill, Staff Officer

COMMISSION ON PHYSICAL SCIENCES, MATHEMATICS, AND RESOURCES

FOREWORD

After more than a decade of international and national planning, the Global Weather Experiment (GWE), formerly known as the First GARP Global Experiment (FGGE), was undertaken in December 1978 and continued through November 1979. This unprecedented and audacious venture was the work of many nations. Routine operational weather observing systems were thrown into high gear and were augmented on a massive scale by many special systems--satellites, aircraft, buoys, and ships. The year's effort culminated in a gathering of global observational data detailing the behavior of the atmosphere and ocean worldwide.

The primary motivation for the experiment was to explore the possibilities for greatly extended prediction of the atmosphere's behavior through the use of advanced observing techniques, computer capabilities, and numerical models, and on the basis of this experience, to design a global atmospheric observing system of the future.

Since completion of the observational phase, the global data sets have been in use by many research scientists, particularly to distinguish between prediction errors due to failures in observations and those due to failures in modeling and understanding. Their ultimate goal is to acquire better knowledge and understanding of the atmosphere so that better and more useful weather prediction services may be provided to the world.

The FGGE Advisory Panel of the U.S. Committee for the Global Atmospheric Research Program felt that a detailed assessment should be undertaken of the status of GWE research and the progress in meeting the previously established objectives of GWE. A two-week workshop was held at the National Academy of Sciences Study Center in Woods Hole, Massachusetts, in July 1984. Two reports have resulted from the workshop--one compiling the papers that were presented during the first seven days and one summarizing the proceedings. These reports are intended to inform researchers worldwide on what has been done and to present recommendations on what more should be done.

On behalf of the U.S. Committee for the Global Atmospheric Research Program, I wish to express our gratitude to Julia N. Paegle, Chairman of the FGGE Advisory Panel, to Donald R. Johnson, Chairman of the FGGE Workshop Organizing Committee, and to all those who continue to add to GWE's success.

Verner E. Suomi, Chairman
U.S. Committee for the Global
Atmospheric Research Program

PREFACE

The scientific results of the First National Workshop on the Global Weather Experiment (GWE) are presented in two volumes. The first volume presents the findings and a summary of the symposium presentations and discussions, while the second contains the papers given by participants. The objectives of the workshop were to (1) summarize research progress in meeting the GWE objectives, (2) identify future research needed to achieve these objectives, and (3) estimate the time and resources that will be needed in the future to fulfill the objectives. Two early international workshops sponsored by the World Meteorological Organization had been held shortly after the year of the Global Weather Experiment--one in Bergen, Norway, June 1980; the other in Tallahassee, Florida, January 1981. The results presented at these workshops were of a preliminary nature, since the Level III data sets just being prepared by the two major centers--the European Medium Range Forecast Center (ECMWF) and the Geophysical Fluid Dynamics Laboratory (GFDL)--were not yet available to the scientific community.

The objectives of the GWE, while determined through international efforts, are set forth for the U.S. scientific community in The Global Weather Experiment--Perspectives on its Implementation and Exploitation, a report of the FGGE Advisory Panel to the U.S. Committee for the Global Atmospheric Research Program, National Research Council, National Academy of Sciences.

Readers will recognize that the main body of the report of the workshop addresses five subject areas that reflect the stated scientific objectives of the GWE. Figure 1 portrays the interrelationship among the five areas. The observational system formed the basis for the unique experiment, data analysis and assimilation utilized the observations to construct the global structure of the atmosphere, the research thrusts of prediction experiments, and diagnostic and phenomenological studies follow from the data and analyses, and the final area of design of the future global observing system ultimately depends on all of the above. In the Executive Summary, however, these five subject areas have been combined under three headings dealing with the GWE observing system and future designs, analyses and predictions, and diagnostics and phenomenological studies.

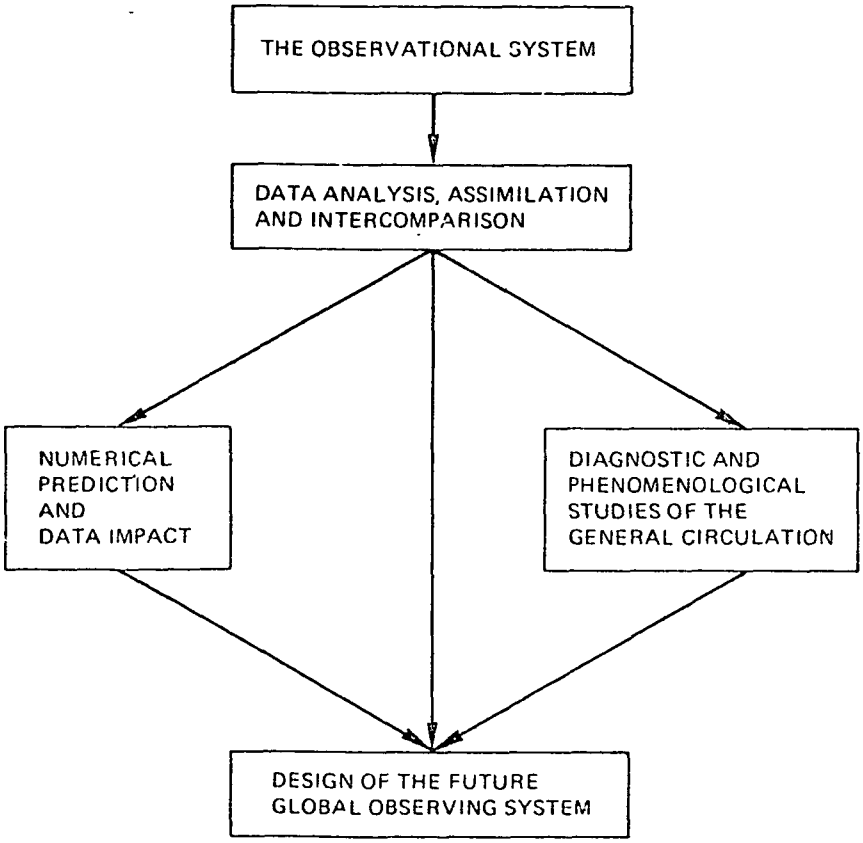
THE OBSERVATIONAL SYSTEM
DATA ANALYSIS, ASSIMILATION AND INTERCOMPARISON
NUMERICAL PREDICTION AND DATA IMPACT
DIAGNOSTIC AND PHENOMENOLOGICAL STUDIES OF THE GENERAL CIRCULATION
DESIGN OF THE FUTURE GLOBAL OBSERVING SYSTEM

FIGURE 1

Now, five years after the experiment, the results stemming from analyses and prediction for the GWE are comprehensive but not yet finalized since all the utility of the information gathered from the most extensive global weather observing system has not been realized. The overall assessment of the participants was that important advances were made in observing, analyses, prediction, and diagnostics of the global atmosphere circulation through the GWE. Insight into the design of a future global observing system has been gained, but much remains to be accomplished. Tasks to pursue which further the GWE objectives by identifying future research needed to achieve the objectives were outlined admirably. However, definitive estimates of time and resources needed in the future to fulfill these objectives remain elusive due largely to the iterative nature of analyses and prediction experiments as well as the open-ended nature of improvements in observational technology and model development. A primary purpose of the two volumes is to document the basis of this assessment.

In order to make this assessment and prepare findings, the FGGE Workshop Organizing Committee felt that a workshop format was essential in order to allow substantial time for discussion and exchange of ideas among the observationalists, analysts, theoreticians, and numerical modelers. Thus the seminar was organized by topical areas that covered the broad range of scientific efforts that were the foundation of the GWE. Session organizers for each topical area were assigned responsibilities to invite key speakers and enlist session chairmen and rapporteurs. With 20 sessions, the attendance at the workshop was limited primarily to active participants. Unfortunately, the size of the Academy's summer study facilities at Woods Hole and the need to prepare general findings that covered a broad range of scientific specialities limited attendance. In order to provide an opportunity for exchange among the larger community of scientists engaged in GWE research, the U.S. FGGE Committee has called for a national conference on the scientific results of the GWE to be held in conjunction with the 1986 annual meeting of the American Meteorological Society.

The first volume contains three summaries: the first, an executive summary that highlights the most important findings stemming from the GWE; the second, a supplementary scientific summary that covers additional key results and recommendations; and a third, a comprehensive summary of the presentations and discussion within each topical area. Detailed achievements, unresolved problems, and recommendations are included in each of the comprehensive summaries. These summaries were prepared by the workshop participants who were responsible for their respective areas.

The second volume contains the papers presented at the Workshop. Key speakers were invited to prepare and present a scientific summary of results within each topical area with the guideline that the summaries were to cover studies that addressed GWE research objectives and utilized GWE information.

It is hoped that the summaries, findings, and research thrusts reported in these two volumes will be informative to the general scientific community as future research is addressed to the GWE

objective of both improving large-scale weather prediction and laying the foundation for a dynamical basis for climate.

The FGGE Workshop Organizing Committee expresses appreciation to all who contributed to the success of the workshop: To the organizers who arranged the sessions and prepared session summaries; to the speakers who prepared and presented papers; to the rapporteurs for recording the highlights of the discussions; to the participants who engaged in lively discussion and debate; to Thomas H. R. O'Neill of the NRC staff for the planning, implementation, and documentation of the meeting; and to Vicki Allaback of the University of Wisconsin and Doris Bouadjemi of the NRC staff for their secretarial assistance during the course of the workshop. We also express our appreciation to all scientists at large who contributed to the success of the GWE. Finally, we express our appreciation to the individuals, organizations, and government activities of all nations that have provided support for the GWE.

Donald R. Johnson, Chairman
FGGE Workshop Organizing Committee

CONTENTS

PART I

1. DATA SYSTEMS AND QUALITY

Organizer	Rex J. Fleming
Session Chairman	Thomas H. Vonder Haar
Speakers	William L. Smith Ronald D. McPherson Rex J. Fleming Paul R. Julian
Rapporteur	Pamela L. Stephens

SATELLITE OBSERVED THERMODYNAMICS DURING FGGE

William L. Smith
University of Wisconsin

ABSTRACT

During the First GARP Global Experiment (FGGE), determinations of temperature and moisture were made from TIROS-N and NOAA-6 satellite infrared and microwave sounding radiance measurements. The data were processed by two methods differing principally in their horizontal resolution. At the National Earth Satellite Service* (NESS) in Washington, D.C., the data were produced operationally with a horizontal resolution of 250 km for inclusion in the FGGE Level IIb data sets for application to large-scale numerical analysis and prediction models. High horizontal resolution (75 km) sounding data sets were produced using man-machine interactive methods for the "Special Observing Periods" of FGGE at the NASA/Goddard Space Flight Center and archived as supplementary Level IIb. The procedures used for sounding retrieval and the characteristics and quality of these thermodynamic observations are given in this report.

INTRODUCTION

The TIROS-N satellite was the first of a new series of operational polar orbiting satellites launched into orbit on October 13, 1978, just prior to the beginning of FGGE. The second spacecraft in the series, NOAA-6, was launched into orbit on June 27, 1979, midway through the FGGE year. The complement of infrared and microwave instruments aboard each of the polar orbiting spacecraft provided a complete global coverage of vertical temperature and moisture profile data every 12 hours. With the two spacecraft, complete coverage was achieved every six hours. Table 1 provides the characteristics and purpose of the radiance observations provided by the various spectral channels of each of the three sounding instruments: (1) the High-Resolution Infrared Radiation Sounder (HIRS), (2) the Microwave Sounding Unit (MSU), and (3) the Stratospheric Sounding Unit (SSU). The spatial resolution and

*Now known as the National Environmental Satellite, Data, and Information Service (NESDIS).

TABLE 1 Characteristics of TOV Sounding Channels

	Channel number	Channel central wavenumber	Central wavelength (μm)	Principal absorbing constituent	Level of peak energy contribution (mb)
HIRS	1	668	15 00	CO_2	30
	2	679	14 70	CO_2	60
	3	691	14.50	CO_2	100
	4	704	14 20	CO_2	400
	5	716	14 00	CO_2	600
	6	732	13 70	CO_2/H_2O	800
	7	748	13 40	CO_2/H_2O	900
	8	898	11 10	Window	Surface
	9	1028	9 70	O_3	25
	10	1217	8 30	H_2O	900
	11	1364	7 30	H_2O	700
	12	1484	6 70	H_2O	500
	13	2190	4 57	N_2O	1000
	14	2213	4 52	N_2O	950
	15	2240	4 46	CO_2/H_2O	700
	16	2276	4 40	CO_2/H_2O	400
	17	2361	4 24	CO_2	5
	18	2512	4 00	Window	Surface
	19	2671	3 70	Window	Surface
	20	14367	0.70	Window	Cloud
		Frequency (GHz)			
MSU	21	50 31		Window	Surface
	22	53 73		O_2	700
	23	54 96		O_2	300
	24	57 95		O_2	90
		Wavelength (μm)			
SSU	25	15 0		CO_2	15 0
	26	15 0		CO_2	4 0
	27	15 0		CO_2	1 5

scan geometry are different for each instrument, but it suffices to state that nearly complete coverage of sounding radiance data is achieved in a swath that below the spacecraft is 2250 km wide. The meteorological soundings that were produced globally have a horizontal resolution and spacing of 250 km. Higher horizontal resolution of 75 km is achieved for limited geographical regions during special observation periods using man-machine interactive processing methods (Greaves et al., 1979).

The purpose of this paper is to summarize the data processing techniques and describe the characteristics and quality of the TIROS Operational Vertical Sounder (TOVS) soundings as produced for the FGGE. For a more complete description of the TIROS-N sounding instruments and their associated data processing techniques, the reader is referred to papers by Smith et al. (1976, 1979, 1981) and McMillin et al. (1982, 1983).

GLOBAL OPERATIONAL SOUNDINGS

A global coverage of vertical temperature and moisture soundings were produced with 250 km spatial resolution by NESS operations. The

operational data processing system, originally developed by Smith and Woolf (1976), had undergone continuous refinement during FGGE. These refinements dealt principally with safeguarding the output against erroneous soundings produced by cloud attenuated microwave observations (Phillips, 1980) and minimizing horizontal discontinuities resulting from the geographical stratifications of the statistical data used in the profile retrieval process. Since the FGGE, significant improvements in the operational system for handling cloud influences have been implemented (McMillin et al., 1982, 1983).

Processing Characteristics

The details of the operational processing system are presented by Smith et al. (1979), Broderick et al. (1981), and McMillin and Dean (1982). The two polar orbiting satellites operating during FGGE, TIROS-N and NOAA-6 respectively, possessed an equator crossing time (local) of 1500 and 1900 when northbound and approximately 0300 and 0700 when southbound. Each satellite completed 14 orbits per day with a westward shift of about 25.5° longitude between adjacent orbits. The scan width of the sounding instruments resulted in overlapping views poleward of 38°. Each HIRS measurement (scan spot) resolves a circular area that is 25 km diameter at the subsatellite point, whereas the MSU resolves a circular area of 110 km diameter at the satellite subpoint. The fields of view enlarge and become elliptical as the instruments scan away from the satellite subpoint. Fifty-six HIRS spots are contained within each scan line covering a linear distance of about 2250 km. The MSU instrument has 11 fields of view along its swath having the same linear extent. A sounding is made for every array of seven HIRS scan lines and scan spots, resulting in 5 x 6 array of profiles for each 40 x 56 array of scan spots. The nominal horizontal resolution of soundings from TOVS is about 250 km.

The conversion of measured radiances to temperature and moisture profiles requires several adjustments to produce the final radiances from which temperatures and dewpoints are produced using linear regression coefficients. These include adjustments for the changing scan angle, surface emissivity, and clouds. (There was no account for terrain elevation in the operational system so their results are unreliable in mountainous regions.)

The operational method of processing the TOVS sounding data during FGGE was developed by Smith and Woolf (1976). Temperature and water vapor profiles were produced from "clear radiances" that have been corrected for any clouds that are inferred to be present. The processing program that produces clear radiances first attempts to identify scan spots that are completely clear. Failing in this, the program then attempts to extract clear radiances from scan spots that are only partly covered with clouds. If this too fails, it attempts to produce temperatures from the four microwave channels and the four stratospheric HIRS channels, since the latter measurements are not as significantly affected by clouds as are the tropospheric HIRS channels. These are in essence the three retrieval paths that are

identified as clear, partly cloudy, and overcast, respectively. In the clear and partly cloudy paths, retrievals use radiances from all 24 HIRS and MSU channels, and identical coefficients are used to convert from radiance to temperature and dewpoint. However the overcast path retrievals utilize a different set of coefficients, since only stratospheric HIRS radiances and MSU radiances are used.

One would expect clear retrievals to be more accurate than partly cloudy retrievals because of certain assumptions regarding cloud height uniformity involved in the partly cloudy method. However the difference between the overcast retrievals and either the clear or partly cloudy retrievals is much greater than the difference between clear and partly cloudy retrievals. In addition, the relative accuracies of the three types are sensitive to limits in tests used to accept or reject the attempted retrievals. For example, inclusion of some partly cloudy measurements in the ones selected as clear will decrease the accuracy of this group of soundings. Also, the decision about the retrieval method selected involves tests that are only indirectly related to cloud amounts. These tests involve comparisons between measured and expected albedo and surface temperatures, and between a measured microwave radiance and a microwave radiance predicted from those infrared radiances that are subject to cloud contamination.

The second important feature of the processing procedure is the regression for atmospheric temperature and water vapor mixing ratio alluded to above. Regression coefficients for a given latitude zone are updated weekly using collocated radiosonde and satellite data uniformly distributed over the preceding two weeks. Coefficients are then used for the following week. This procedure results in an average time lag ranging from one and one-half weeks in a data-rich region (e.g., 30-60°N) to two and one-half weeks in a data sparse region (e.g., 30-60°S). Separate regression coefficients are calculated for each of five latitude zones: 90°N-60°N, 60°N-30°N, 30°N-30°S, 30°S-60°S, and 60°S-90°S.

To eliminate temperature discontinuities that would otherwise occur at 30° and 60°, the coefficients used for a retrieval are interpolated from those for the five zones. In the interpolation, the highest probing microwave channel (57.95 GHz), which senses the lower stratosphere, is used as the interpolating variable. The instrumentation and the processing of the radiances from the sounders on the two satellites were essentially the same, with the notable exception that the MSU channel 3 on NOAA-6 was not used after early December 1979 because it was considered too noisy.

An example coverage of operational TIROS-N retrievals are shown in Figure 1. The symbols indicate the type of retrieval path used; open circles for clear, solid circles for overcast cloud, and stars for partly cloudy. During the FGGE, generally 80 percent of the soundings were produced according to either the clear or partly cloudy path, with the remaining 20 percent produced according to the infrared channel deficient overcast path.

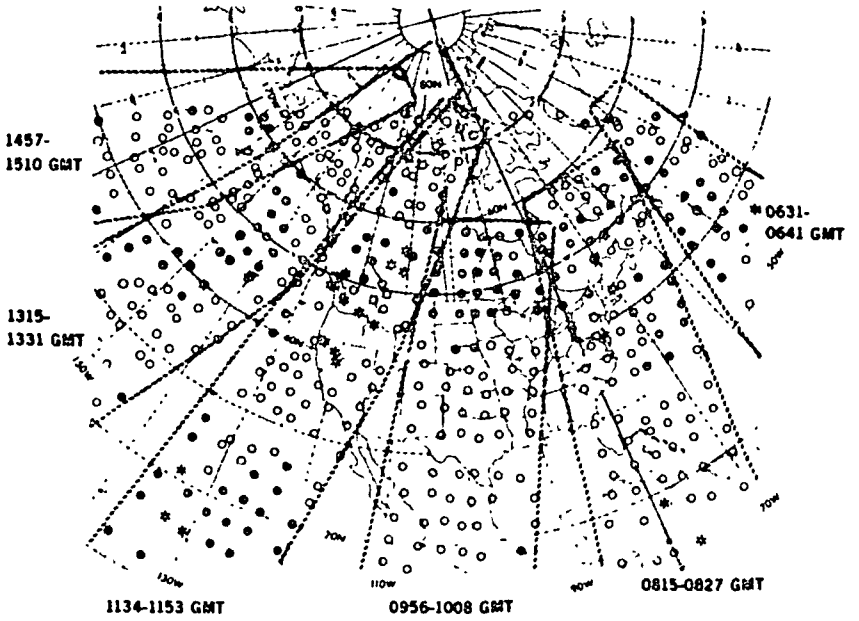

FIGURE 1 TIROS-N retrieval locations for April 6, 1979. Broken lines delineate orbital swaths with times as indicated. Open circles indicate clear path, stars indicate partly cloudy path, and solid circles indicate cloudy path retrievals (after Broderick et al., 1981).

Radiosonde Temperature Comparisons

When evaluating satellite retrievals, radiosondes are often used as a comparison. The comparisons given here were computed by a program at the National Meteorological Center that was designed by A. Desmarais. Comparisons are calculataed from radiosondes within ± 3 hours and within 3^{o} of great circle arc from the satellite observation. These time and space discrepancies limited the utility of these comparisons for error assessments. In addition, the comparisons are mainly representative of the northern hemisphere even though the data are global. This bias toward the northern hemisphere is a consequence of the large number of radiosondes and, thus, comparisons in that area. The comparisons in this study include both land and sea areas. However, radiosondes are more numerous over land, thus the land cases dominate. Because there is no method to account for terrain elevation in the operational retrieval method, the radiosonde comparison statistics exaggerate the retrieval errors in the lower troposphere.

The number of comparisons also varies with the satellite (i.e., TIROS-N or NOAA-6) and the type of retrieval. However, comparisons for a single satellite for a month typically total over 2000 for cloudy

TABLE 2 RMS Differences (^{o}K) Between Satellite Retrievals and Radiosondes During FGGE

Layer (mb)	Clear	Partly Cloudy	Overcast Cloud
100--70	2.2	2.2	2.2
200-100	2.1	2.2	2.3
300-200	2.3	2.5	2.8
400-300	2.3	2.4	3.0
500-400	2.3	2.4	3.0
700-500	2.0	2.1	2.7
850-700	2.4	2.7	3.4
1000-850	2.8	3.1	3.8

soundings, 7000 for partly cloudy soundings, and over 10,000 for clear soundings.

Table 2 shows the RMS difference between NESS operational temperature soundings and radiosondes for the FGGE year. This statistic was obtained from more than 150,000 clear sounding comparisons, 100,000 partly cloud comparisons and 35,000 overcast cloud comparisons. Similar statistics have been provided elsewhere by Smith (1979, 1981), Phillips et al. (1979), Schlatter (1980), Broderick et al. (1981), Gruber and Watkins (1982), and Koehler et al. (1983). The main point to be made from all these statistics is that clear and partly cloudy retrievals are of similar accuracy and overcast cloud retrievals are of greatly reduced accuracy throughout the troposphere. The reduced accuracy of the overcast retrievals is due to the limited number of tropospheric sounding microwave channels and their deficient vertical resolution in the low troposphere due to non-unity surface emissivity.

It should be remembered that the error implied in Table 2 is due mainly to the poor vertical resolution of the TOVS. Consequently much of the error is a synoptic scale systematic error. Consequently errors in horizontal temperature gradients are much smaller, generally 1^{o}C or less depending on the depth of the atmospheric layer (Schlatter, 1980).

Geopotential Thickness Comparisons

Figure 2 presents analyses of TOVS derived 1000-500 mb geopotential thickness for a 12 hour time period (Figure 2a) on April 29-30, 1979. Shown for comparison is the National Meteorological Center (NMC) analysis (Figure 2b), devoid of TOVS data, for 0000 GMT on April 30. The NMC analysis is of historical significance in that it is the last analysis performed without the inclusion of TIROS-N data (i.e., the 1200 GMT analysis on April 30 included TIROS-N soundings). (TIROS-N sounding data was included in operational analyses on March 6, but only over water south of 10^{o}S. On April 30, all oceanic soundings were introduced in the analysis at all latitudes.) The correspondence

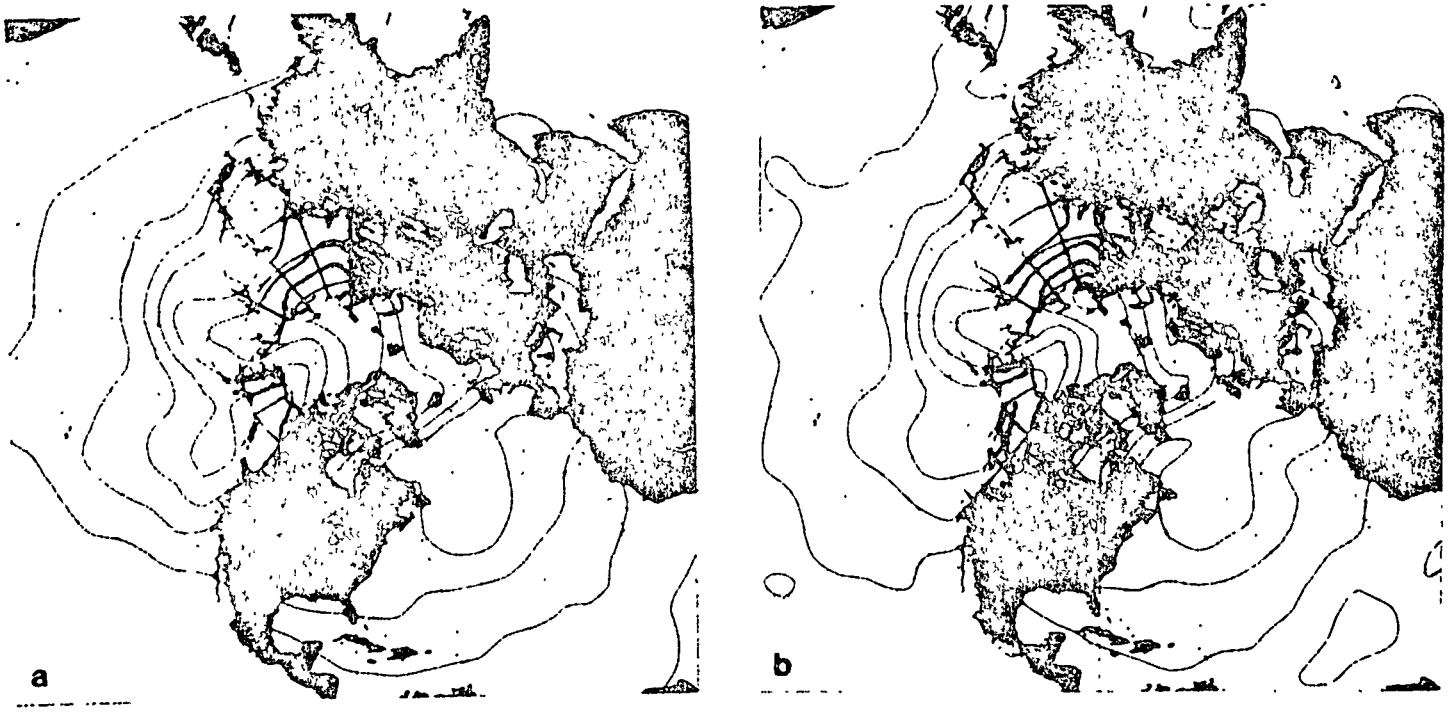

FIGURE 2 Comparison of 1000-500 mb thickness charts obtained solely from TIROS-N sounding data (a) and from conventional data (b). (a) TIROS-N, 29 April, 1800 GMT-30 April, 0600 GMT, (b) NMC, 30 April, 0000 GMT (after Smith et al., 1981).

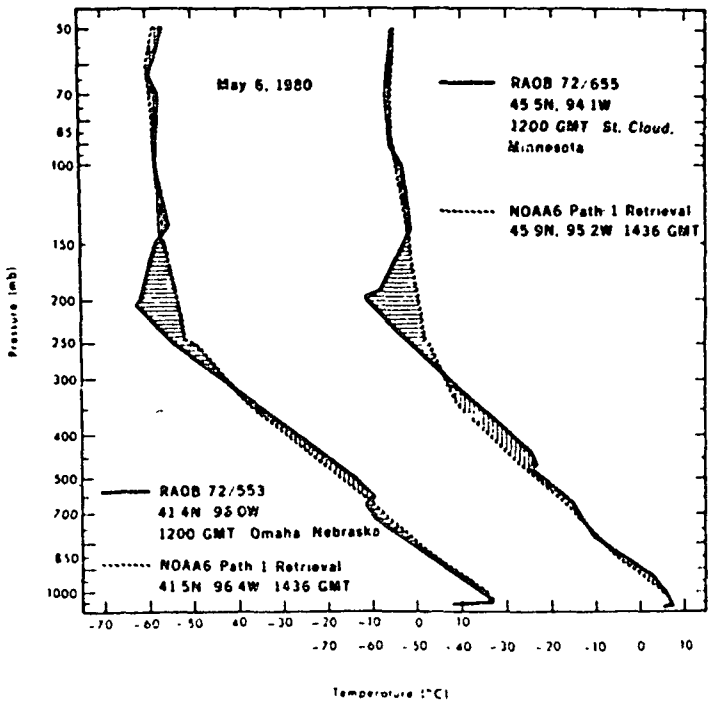

FIGURE 3 Radiosonde (1200 GMT) and NOAA-6 retrieval (1436 GMT) pairs for 6 May 1980. Radiosonde temperatures in solid line and retrievals in broken line (after Broderick et al., 1981).

between the "pure" satellite analyses and the NMC analysis, which did not incorporate the TOVS data at this time, is striking. The agreement over the continents validates the TOVS data. The agreement over the oceanic regions pays tribute to the NMC analysis-forecast system since the analyses in these regions are largely constructed from surface and aircraft observations with a 12 hour forecast used as a first guess in the analysis cycle. The most notable differences between the TIROS and conventional analyses are in the low pressure areas over the northeastern Pacific and eastern Europe, both of which are more intense in the TIROS analysis.

Vertical Temperature Structure

Figure 3 is given to illustrate the vertical resolution of the TOVS soundings produced during FGGE. Two of the NOAA-6 soundings are collocated with the Omaha, Nebraska, and St. Cloud, Minnesota, radiosondes. These two pairs of soundings, shown in Figure 3, illustrate graphically the fact that horizontal gradients tend to be weakened due to inadequate vertical resolution. The base of an upper

level front can be seen in the radiosondes sloping from near 600 mb at Omaha up to 475 mb at St. Cloud. The surface inversion at Omaha is probably evidence of the slightly cooler and drier air mass, although it is difficult to distinguish it from a normal nocturnal inversion. At St. Cloud this cooler air mass may be associated with the slightly stable layer just above 700 mb up to 570 mb. The intrusion of Arctic air may be evidenced by the lower stable portion of the radiosonde profile. At Omaha, the NOAA-6 retrieval is clearly somewhat warmer in the lower portion of the troposphere up to the upper frontal inversion and then colder above up to nearly 300 mb. This structure shows how the satellite sounding depict a more nearly vertical frontal zone by being warmer in the cold air below the frontal surface and colder above. The retrieval profile is definitely warmer than the raob in the tropopause region. Near St. Cloud the satellite retrieval, being deeper into the colder air than Omaha, agrees with the radiosonde up to just above 500 mb. Above this level up to 300 mb the retrieval is colder, with once again the warmer tropopause region above 300 mb. This set of retrieval comparisons shows how significant vertical temperature gradients tend to be underestimated due to the deficient vertical resolution of the TOVS sounding system.

The deficient vertical resolution of TOVS soundings is responsible for the reduced horizontal variance and horizontal error correlation of the satellite temperature profiles noted by Phillips et al. (1979), Phillips (1980), Schlatter (1981), and McMillin and Dean (1982). The fact that empirical regression coefficients are used for the retrieval also greatly contributes to horizontal smoothing and error correlation because of the inherent space and time colocation noise in the regression sample. Also, Le Marshall and Schreiner (1984) have shown that much of the horizontal variance loss by the operational regression retrieval method is due to the manner in which the radiance data is corrected for view angle. Physical methods of retrieval that do not require limb corrected data have proven to be superior in accuracy to the empirical regression method used during FGGE.

Water Vapor Retrievals

Unfortunately there has been very little evaluation of the TIROS-N/NOAA-6 water vapor retrievals during FGGE. This is in part due to the very difficult task of evaluating water vapor estimates using radiosonde comparisons because of the large space and time variability of atmospheric moisture. Theoretical expectations of the water vapor profile retrieval performance have been given by Smith and Woolf (1976).

The most extensive use of the operational water vapor retrievals during FGGE has been to define the precipitable water over the Indian Ocean during the 1979 summer monsoon (Cadet, 1983). In this application, water vapor bogus was used in disturbed cloudy areas since no operational TOVS water vapor retrievals are provided. The cloud bogus is based on TOVS overcast path temperature soundings and the assumption of a relative humidity of 90 percent between the surface and 700 mb, 80 percent between 700 and 400 mb, and 70 percent above.

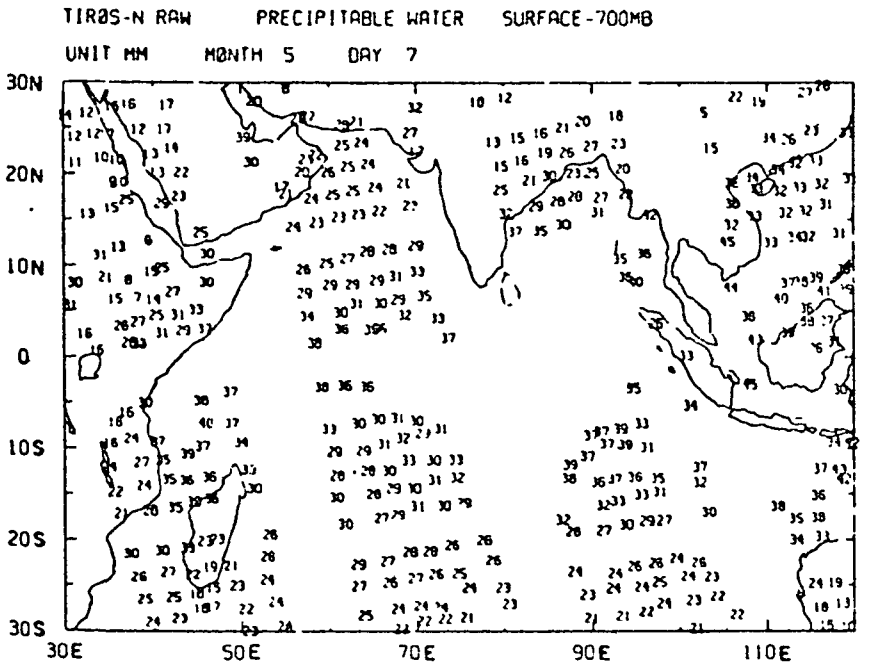

FIGURE 4a TIROS-N soundings obtained around 1030 GMT over the Indian Ocean on 7 May 1979. Precipitable water within the layer surface-700 mb (after Cadet, 1983).

Figure 4a shows a typical coverage of operational TIROS-N water vapor soundings over the Indian Ocean. The data void areas are due to overcast cloud where temperature but no water vapor profiles are retrieved. Figure 4b shows an analysis of precipitable water for the lower troposphere (surface to 700 mb) based on the TIROS-N water vapor retrievals and cloud bogus data. The detail is noteworthy. Cadet (1983) has verified these analyses using aircraft dropsonde data and shows that the accuracy for the surface to 700 mb, 700 to 500 mb, and 500 to 300 mb layers is better than 10 to 20 percent, depending on atmospheric layer.

"SPECIAL EFFORT" HIGH RESOLUTION SOUNDINGS

The special effort (Greaves et al., 1979; Atlas, 1981) was conducted for the special observing periods of FGGE (January-March and May-July 1979) as a joint project between NASA, NOAA, and the University of Wisconsin. Man-computer Interactive Data Access System (McIDAS) videographic terminals developed by the Space Science and Engineering Center (SSEC) of the University of Wisconsin were utilized by experienced meteorologists at the National Meteorological Center (NMC) for data evaluation and quality assessment, and at the Goddard

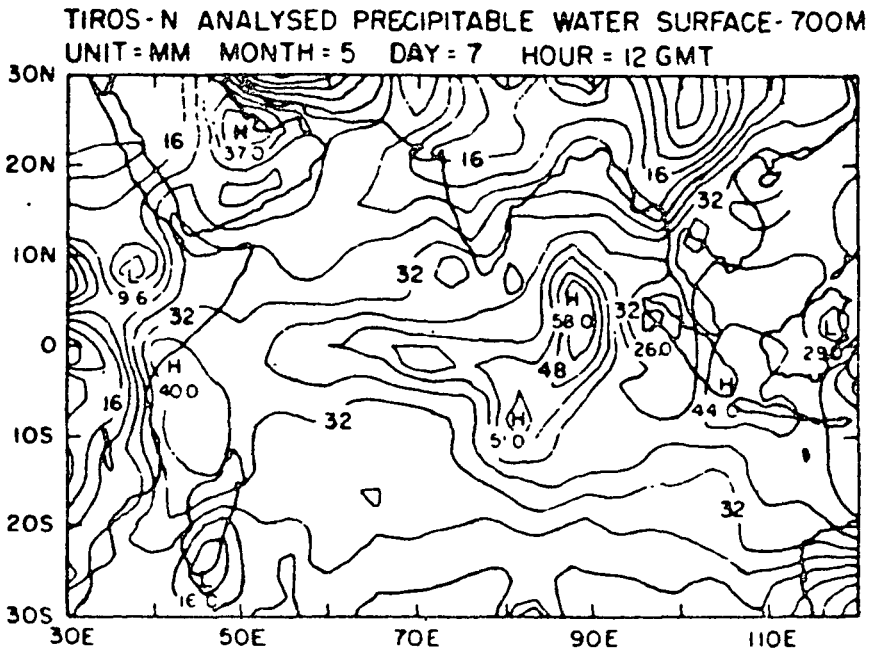

FIGURE 4b Analyzed field of precipitable water for layer surface-700 mb on 7 May 1979 from TIROS-N water vapor retrievals and bogus data (after Cadet, 1983).

Laboratory for Atmospheric Sciences (GLAS) for satellite data enhancements. The interactive programs for this purpose were developed by the National Environmental Satellite Service Development Laboratory at the University of Wisconsin and the SSEC (Smith et al., 1978, 1979, 1981).

For each synoptic period there was an initial editing of FGGE data by NMC. At this stage, quality indicators were assigned to temperature soundings. The determination of data quality was made on the basis of synoptic considerations, including horizontal, vertical and temporal consistency. Regions where data deficiencies exist or where higher resolution data were needed to adequately represent the atmospheric thermal structure were then selected for enhancement. The eastern North Pacific was routinely enhanced because of the importance of this region to forecasting for North America. In addition, cases of blocking, cut off low development, cyclogenesis, and tropical circulations were preselected for enhancement by an ad hoc international committee of participating scientists.

The sounding data enhancement was aimed at supplementing the operational satellite sounding data set with higher resolution soundings in meteorologically active regions, and with new soundings where data voids or soundings of questionable quality exist. The algorithm for retrieving temperature profiles from the TIROS-N

observations of radiance displayed on McIDAS was the same regression algorithm used by NESS for the objective generation of operational temperature and water vapor profiles. The operational profiles have a horizontal resolution of 250 km, whereas special effort profiles can be retrieved at the resolution of the measurements (25 km for HIRS and 150 km for MSU) but is nominally 75 km.

The sounding enhancement process at GLAS was performed as follows: once an area had been selected, the McIDAS operator began by displaying the locations of all available conventional and special FGGE data for that area, the Level III analysis, and visible, infrared, and microwave images from TIROS-N. At this stage, the operator noted where data deficiencies exist, and from the TIROS-N images determines the extent of cloudiness and where the most intense atmospheric thermal gradients were located. High resolution temperature retrievals were then generated for the area. This was followed by a manual editing of the retrievals to remove small-scale discontinuities due to cloud-induced noise while retaining significant meteorological structures. Enhanced microwave retrievals, consistent with neighboring infrared retrievals, were then generated in cloudy areas.

After the entire enhancement process is completed, a final editing and quality assessment of the enhanced data was performed at NMC. The data was then archived as supplementary Level IIb.

Subjective comparisons of enhanced soundings and radiosonde reports were performed after the enhancement process was completed. These comparisons showed that the enhanced and operational retrievals tended to be similar in cloud free areas. However, large differences occasionally occur. The differences are accentuated in and around cloudy areas where the interactive processing at high resolution allows for the generation of substantially more infrared retrievals, and where the microwave retrievals show greater internal consistency than the operational retrievals.

An example illustrating some of the effects of the sounding data enhancement is presented in Figure 5. In Figure 5, 1000 to 300 mb thickness analyses of operational (solid line) and special effort retrievals (dashed lines), and plotted radiosonde reports are shown for a section of the North Pacific at 0000 GMT January 7, 1979. Large differences in the orientation, gradient, and absolute value of the enhanced and operational thickness contours are evident. In addition, the errors relative to the colocated radiosondes have been reduced in this case by 30 to 80 geopotential meters.

Finally, Figure 6 shows the coverage and an analysis of high spatial resolution total precipitable water estimates derived from TOVS data during the MONEX using a physical as oppposed to a statistical algorithm (Smith et al,. 1983). In the physical algorithm, the resulting temperature and moisture profile are obtained by numerical solution of the radiative transfer equation. Water vapor profiles are achieved to the earth's surface under cloudy conditions utilizing the microwave temperature profile and relative humidity profile obtained by interpolation between cloud level and the surface. Comparisons between physical retrievals and those achieved using operational empirical regression coefficients reveal that the gradient accuracy and

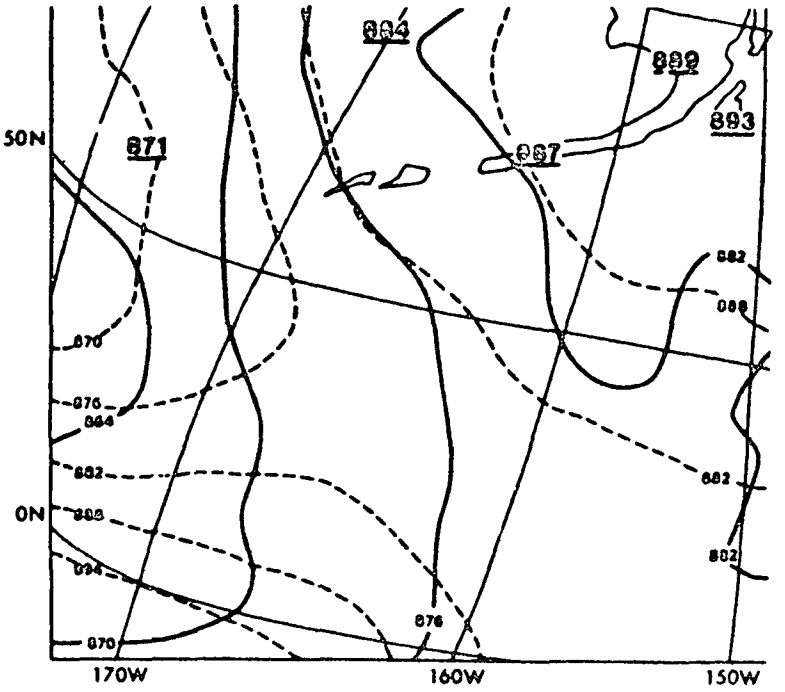

FIGURE 5 1000-300 mb thickness analyses of operational soundings (solid lines) and special effort soundings (dashed lines) for 0100 GMT 7 January 1979. Radiosonde observations of 1000-300 mb thickness in decameters are plotted as large numbers (after Atlas, 1981).

horizontal variance is much improved in the physical solutions (Menzel, 1984). Note the much greater density and improved coverage of the physical high resolution retrievals shown in Figure 6 as compared to the operational TOVS soundings shown in Figure 4a.

SUMMARY

The thermodynamic observations from satellites during FGGE consisted of globally produced temperature and water vapor soundings at 250 km resolution and limited area special effort soundings at 75 km resolution. The accuracy of the temperature profiles is better than 2.5°C, depending on level, as judged from comparisons with radiosondes. The accuracy of the layer mean precipitable water retrievals is 10-20 percent as judged from comparisons with aircraft dropsondes. The higher resolution special effort enhanced soundings tend to improve the accuracy and occasionally intensify the temperature and water vapor gradients in a realistic manner. Also, the interactive special effort soundings fill in major gaps in the operational coverage. The main deficiencies of the FGGE satellite sounding data are:

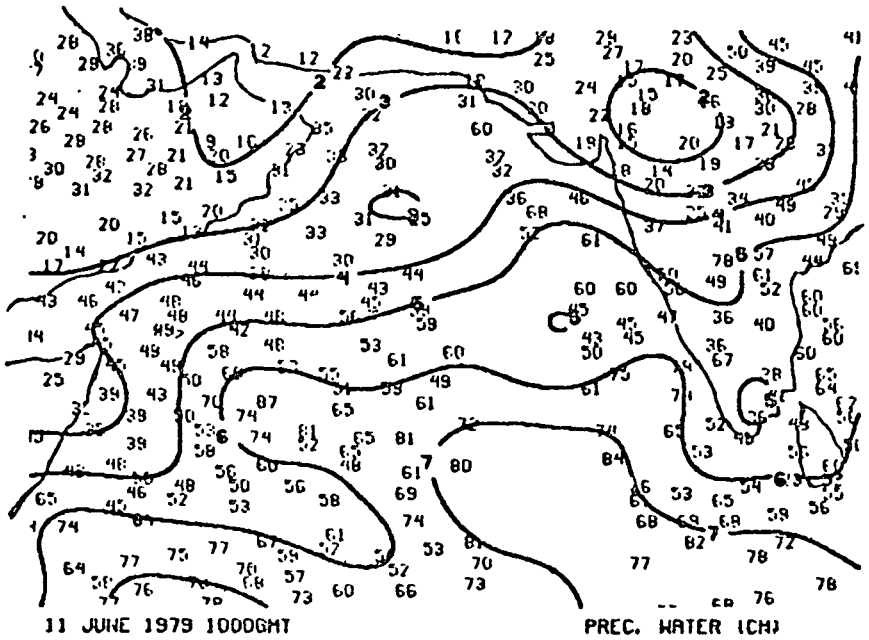

FIGURE 6 Total precipitable water values (mm) and a contour analysis (cm) for 11 June 1979 in the MONEX special observation region. This example is taken from an extensive set of soundings derived during Summer MONEX by A. J. Schreiner at the University of Wisconsin.

1. Deficient accuracy in overcast cloud areas,
2. Deficient horizontal gradient definition due to the TOVS inherently low vertical resolution (approximately 5 km),
3. Lack of globally produced moisture profiles in overcast cloud regions,
4. Inability of the operational regression method to account for variable terrain conditions, thereby yielding unreliable results in mountainous regions,
5. Poor accuracy near the earth's surface due to the lack of utilization of conventional surface observations in the sounding retrieval process.

It should be noted that many of the FGGE time period sounding deficiencies have been alleviated through improved processing procedures, in particular, methods for handling clouds and the use of physical solutions rather than empirical regression procedures (McMillin et al., 1983; Smith et al., 1983). Because of the unique coverage of in situ observations (e.g., buoy and aircraft observations) during the FGGE, it may be worthwhile at some future time to reprocess the TOVS observations during the FGGE time period in order to take advantage of the processing algorithm improvements.

REFERENCES

Brodrick, H., C. Watkins, and A. Gruber (1981). Statistical and synoptic evaluations of TIROS-N and NOAA-6 retrievals. NOAA Technical Report NESS 86, Washington, D.C., 48 pp.

Cadet, D. L. (1983). Mean fields of precipitable water over the Indian Ocean during the 1979 summer monsoon from TIROS-N soundings and FGGE data. Tellus 35B, 329-345.

Greaves, J. R., G. DiMego, W. L. Smith, and V. E. Suomi (1979). A special effort to provide improved sounding and cloud motion wind data for FGGE. Bull. Amer. Meteor. Soc. 60, 124-127.

Gruber, A., and C. D. Watkins (1982. Statistical assessment of the quality of TIROS-N and NOAA-6 satellite soundings. Mon. Wea. Rev. 110, 867-876.

Koehler, T. L., J. C. Derber, B. D. Schmidt, and L. H. Horn (1983). An evaluation of soundings, analyses, and model forecasts derived from TIROS-N and NOAA-6 satellite data. Mon. Wea. Rev. 111, 562-571.

Le Marshall, J. F., and A. J. Schreiner (1984). Limb effects in satellite temperature sounding. Submitted to J. Clim. Appl. Meteorol.

McMillin, L. M., and C. Dean (1982). Evaluation of a new operational technique for producing clear radiances. J. Appl. Meteorol. 21, 1005-1014.

McMillin, L. M., and C. A. Dean (1982). Variance ratios, loss of energy and regression in satellite temperature retrievals. Mon. Wea. Rev. 110, 296-299.

McMillin, L. M., D. G. Gray, H. F. Drahos, M. W. Chalfant, and C. S. Novak (1983). Improvements in the accuracy of operational satellite soundings. J. Clim. Appl. Meteorol. 22, 1948-1955.

Menzel, W. P. (ed.) (1983). Technical Proceedings of the First International TOVS Study Conference. A report from the Cooperative Institute for Meteorological Satellite Studies, 1225 West Dayton Street, Madison, Wisconsin, 53706.

Phillips, N. (1980). Two examples of satellite temperature retrievals in the North Pacific. Bull. Amer. Meteorol. Soc. 61, 712-717.

Phillips, N., L. McMillin, A. Gruber, and D. Wark (1979). An evaluation of early operational temperature soundings from TIROS-N. Bull. Amer. Meteorol. Soc. 60, 1188-1197.

Schlatter, T. W. (1981). An assessment of operational TIROS-N temperature retrievals over the United States. Mon. Wea. Rev. 109, 110-119.

Smith, W. L., and H. M. Woolf (1976). The use of eigenvectors of statistical covariance matrices for interpreting satellite sounding radiometer observations. J. Atmos. Sci. 33, 1127-1140.

Smith, W. L., C. M. Hayden, H. M. Woolf, H. B. Howell, and F. W. Nagle (1978). Interactive processing of TIROS-N sounding data. Preprints, AMS Conference on Weather Forecasting and Analysis and Aviation Meteorology, Silver Spring, Maryland, 16-19 October 1978, pp. 390-395. Published by the American Meteorological Society, Boston, Massachusetts.

Smith, W. L., H. M. Woolf, C. M. Hayden, D. Q. Wark, and L. M. McMillin (1979). The TIROS-N operational vertical sounder. Bull. Amer. Meteorol, Soc. 60, 1177-1187.

Smith, W. L., F. W. Nagle, C. M. Hayden, and H. M. Woolf (1981). Vertical mass and moisture structure from TIROS-N. Bull. Amer. Meteorol. Soc. 62, 388-393.

Smith, W. L., H. M. Woolf, C. M. Hayden, A. J. Schreiner, and J. F. Le Marshall (1983). The physical retrieval TOVS export package. In W. P. Menzel (ed.), Technical Proceedings of the First International TOVS Study Conference. A report from the Cooperative Institute for Meteorological Satellite Studies, 1225 West Dayton Street, Madison, Wisconsin, 53706.

D2

CLOUD-DRIFT WIND ESTIMATES DURING FGGE

Ronald D. McPherson
National Meteorological Center

INTRODUCTION

During the FGGE year of 1979, five meteorological satellites were positioned in geostationary orbit at intervals of approximately 70° longitude. Imagery from these satellites was used to produce estimates of wind by tracking identifiable cloud targets through a sequence of images. This generated a set of wind observations covering most of the area equatorward of about 45° latitude. Figure 1 illustrates the configuration of the geostationary satellite system during 1979. Data from the Japanese Geostationary Meteorological Satellite (GMS), stationed at 140°E, were processed by the Japanese Meteorological Satellite Center (JMSC) in real time twice daily and were transmitted via the Global Telecommunications System (GTS). The two U.S. satellites (GOES West, 135°W, and GOES East, 75°W) produced data that were processed in real time by the U.S. National Environmental Satellite Service (NESS)*, but thrice daily, and transmitted on the GTS. METEOSAT, at the Greenwich meridian, was operated by the European Space Agency (ESA) until November 25, 1979. These data were also processed in real time and made available through the GTS.

Imagery from the Indian Ocean satellite--actually an older GOES that was reactivated and moved to 59°E--was processed post facto by ESA and by the Space Science and Engineering Center of the University of Wisconsin (UW/SSEC). The latter also reprocessed portions of the real time data generated by the three operational centers. Somewhat different techniques were used at the processing centers. Nevertheless, the total result of these activities is a data set of unparalleled magnitude, providing meteorologists with a nearly global view of the wind field, with special emphasis on the tropics.

This paper reviews the procedures and techniques used by data producers to generate data that are widely used by the research community, and to summarize the experience thus far with respect to their quality and utility. The impact of cloud-drift winds on forecast models is not addressed. In the next section, the process of

*Now the National Environmental Satellite and Data Information Service (NESDIS).

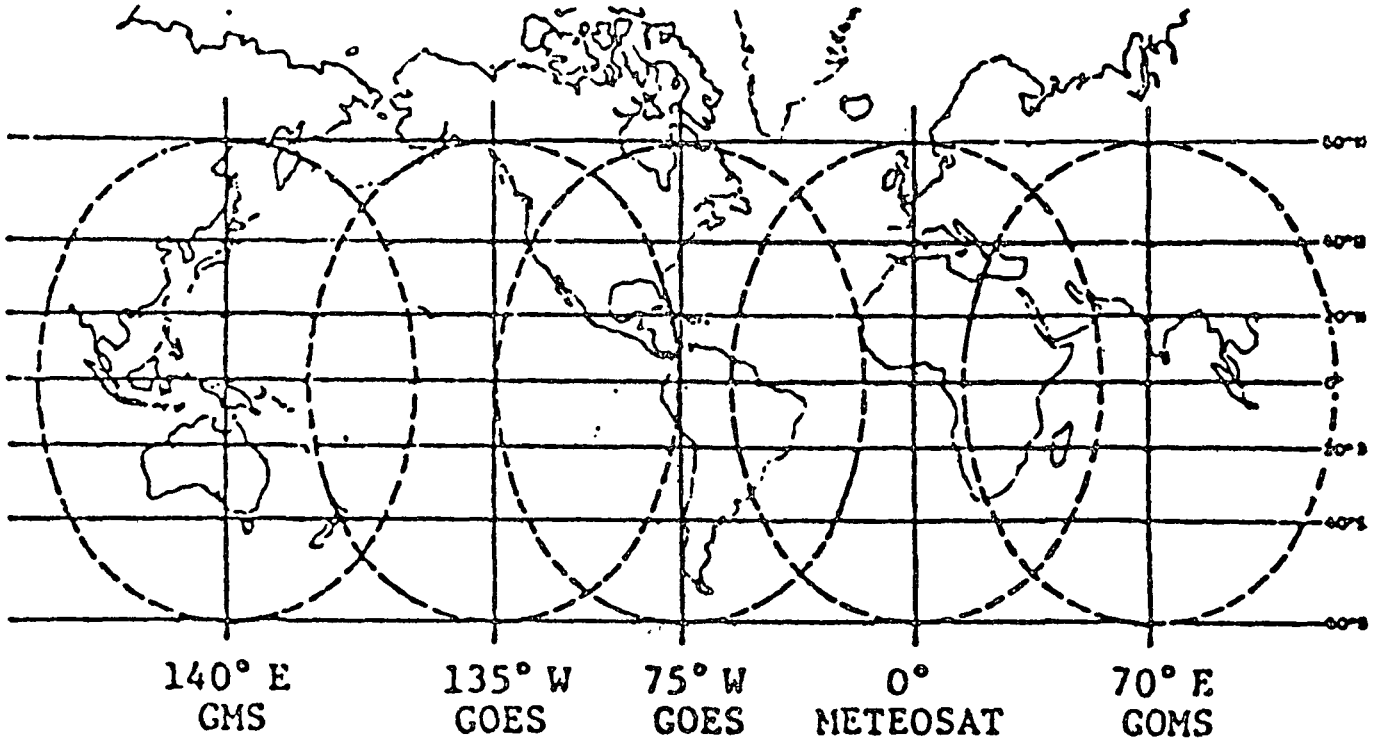

FIGURE 1 Fields of view of five geostationary satellites in which winds can be derived. During 1979 a backup GOES was operated at 59° in place of GOMS as shown at 70°E. Outlined areas represent a 60° geocentric angle about each satellite subpoint. After Hubert (1979).

transforming image data to wind vectors is discussed first in general terms, followed by a more detailed exposition of the practices at each center. Emphasis is placed on the differences between the processing techniques used in each system. An assessment of the quality of the data is given in the third section. The vehicles for assessment are collocation of the cloud-drift winds with other kinds of wind reports, quality control procedures including a special effort conducted in the United States to edit the FGGE data through subjective evaluation by skilled synoptic meteorologists, and finally the treatment of the data by analysis systems. The fourth section reviews the use of the cloud-drift wind data by global data assimilation systems, including quality control and relative weighting. Problems encountered in using the data are also discussed. A summary concludes the note.

PRODUCTION OF FGGE CLOUD-DRIFT WIND DATA SETS*

General

A set of cloud-drift wind vectors is produced as a result of five activities:

1. Registration. Cloud images from the satellites must be adjusted so that the relationship of a cloud target to earth locations is known to considerable accuracy. This enables the displacements between successive images to be calculated accurately. The U.S. procedure is to compute approximate registration from the orbital and scan parameters of the spacecraft, and then adjust these by matching a set of known landmarks, e.g., White Sands, New Mexico.
2. Selection. To be a suitable target, a cloud must persist in recognizable form through at least two, and preferably three, sequential images. It must also be advected by the wind, as opposed to moving with a wave or appearing to move as a result of development. Typically, suitable targets tend to be found in the lower troposphere, where cumulus clouds tend to move with the wind near the cloudbase, and in the upper troposphere, where cirrus elements may be tracked. Relatively few targets can be selected in the middle troposphere.
3. Tracking. The displacement of the selected target is calculated over the sequence of images. A wind vector is then determined from the displacement divided by the time interval between images.
4. Altitude Assignments. The wind vector is then assigned to an altitude most representative of the observed motion.
5. Quality Control. Because all the above steps are vulnerable to errors of various types, it is necessary to remove unrepresentative vectors, or at least identify them, before transmitting them to users.

*Most of the material in this section has been liberally extracted from Hubert (1979), Kodaira et al. (1981), and Mosher (1979).

Two general approaches to selection and tracking have been used. the first is automatic and relies on pattern correlation techniques for matching cloud patterns between successive images. The second is essentially manual: an analyst is presented with an animated (either photographically, e.g., movie loop, or electronically) sequence of images and selects suitable targets based on knowledge of atmospheric motions and experience. These are used in varying degrees of mixture at the several centers.

Altitude assignment techniques can also be described in two broad categories. One relies on climatology: the wind vectors are assigned to the height most commonly associated with the type of cloud target. The other makes use of the cloud brightness temperature, matching it with the latest estimate of the temperature in the area. The altitude at which the best match occurs is assumed to be the altitude of the cloud. As in selection and tracing, these two are used in varying degrees at the processing centers.

Quality control techniques used for editing cloud vectors generally use a mixture of automatic and manual procedures. Typically, a vector will be compared with some a priori estimate of the wind at that location (from a forecast or the most recent analysis), with neighboring cloud-drift winds, or with neighboring winds from other sources. Vectors identified as suspicious are referred to an analyst for final judgment.

Data sets produced by these procedures have certain unique characteristics. The vectors, especially those produced by the United States, generally tend to be at two levels--low and high--corresponding to the two basic types of targets--cumulus and cirrus clouds. Low-level and high-level winds tend not to overlap. If low-level targets are visible, it is because there are no high-level targets to obscure them. Areas of thin cirrus occasionally allow tracking of both low- and high-level targets, but this accounts for no more than 10 percent of the total area. Most of the high-level targets come from thicker cirrus, which obscures lower targets. Middle clouds are most often found underneath cirrus shields and are frequently amorphous and difficult to track; consequently, few vectors are obtained in the middle troposphere. The tracking procedures used by ESA and JMSC during FGGE generated more middle cloud vectors and more overlap between high and low vectors than were generated by NESS.

Coverage afforded by cloud-drift vectors is generally confined to the area equatorward of 45° latitude, although large displacements can be measured with acceptable accuracy as much as 50° from the satellite subpoint. There is some deterioration of accuracy with distance away from the subpoint, but it is not serious except near the extreme limits.

The principal sources of observational errors in cloud-drift vectors are the selection of suitable targets and the assignment of the vectors to the proper altitude. Of these, the latter is probably the most serious.

The next paragraphs summarize the details of cloud-drift vector processing at the several centers during the FGGE year.

United States (NESS)

Low-level winds from the two U.S. satellites were generated operationally during 1979 using an automatic pattern recognition technique. It continues in use today. Areas covering 125 x 125 km with less than 70 percent coverage by high or middle clouds are examined for suitable low cloud clusters. The areas are positioned on a staggered grid--at the corners and centers of 5° latitude squares. Tracking is accomplished at each gridpoint by searching a prescribed section of successive images and correlating all pairs of coincident picture elements at each successive lag location. The location of maximum correlation indicates the displacement of the cloud cluster between the two images. Vectors thus determined are assigned to the points of staggered grid. Climatological altitude assignment is used; all U.S. NESS low-level vectors are assigned to 900 mb. A quality indicator or confidence factor is assigned to each vector depending on the level of agreement with its neighbors and on the degree of peakedness of the correlation field: strongly peaked correlations suggest relatively high confidence. Quality control is performed by comparing each wind to an analysis of the combined 850 mb first guess and derived winds. Deviations that are too large or that unduly disturb the vorticity field cause the offending vector to be removed.

NESS high-level winds were produced manually during FGGE using movie-loop techniques. These have changed since 1979 in significant ways, but this paragraph summarizes only the practices used during the FGGE year. A sequence of images was projected on an electronic digitizing board. The operator, examining both motion and brightness temperatures, selected targets and measured their displacements by marking their initial position (latitude and longitude) and final position on the digitizing board. These positions were automatically entered onto computer cards so that displacements could be calculated. Altitude assignment was done by matching the brightness temperature of the cloud target with the temperature profile of the latest analysis. Because the selection and tracking process required the analyst to use judgment, quality control procedures at this point consisted of simply displaying the calculated vectors for gross errors.

Japan (Meteorological Satellite Center)

Japanese low-level winds were obtained during FGGE using a mixture of manual and automatic methods. Images were presented to an operator on a video display device. The operator selected the targets to be tracked. A search was then made of the next image (0.5 h interval) using cross-correlation calculations to locate the target. This was done first with a coarse resolution image to obtain a first estimate of the displacement. Then it was repeated with a higher resolution image to obtain a final value. Three successive images were used, but the final vector came only from the last two. Because the operator selected targets of opportunity, no grid array was used. Altitude

assignment matched the cloudtop temperature and a recent analysis or forecast. Later studies showed that low-level clouds move with the wind near their base rather than their top, so this was a source of error.

High-level winds were obtained using a movie-loop technique similar to that described in the previous section. The altitude assignment differed from the U.S. practice however in that high-level vectors were assigned to the climatological tropopause. This proved to be a serious deficiency, as will be illustrated later in this paper, and was subsequently changed in December 1982.

Quality control for all winds used a combination of objective and subjective methods. For each vector, correlations between successive images, variations of cloud temperature from picture to picture, and calculated accelerations were required to be within prespecified limits. Failure resulted in deletion from the data set. The surviving vectors were displayed on a video device for the operator's judgment and, where possible, were compared with nearby radiosonde winds. Synoptic reasonableness and consistency were principal criteria for retention.

Europe (European Space Agency)

Cloud-drift wind vectors from METEOSAT-1 imagery were produced by ESA at Darmstadt, Federal Republic of Germany. Operations during the FGGE year were somewhat limited, being terminated by satellite failure on November 25, 1979. METEOSAT-2 winds again became available in May 1982 once per day (noon, Greenwich), and twice per day in September 1982. The wind determination technique used by ESA during FGGE depended on pattern recognition at all levels and was highly automated. Correlation among three successive images was done in two steps, first using infrared then visible imagery. In the infrared search a segment of 32 x 32 elements from the middle image searches for the best correlation position with a 96 x 96 array in both the first and last pictures. With this estimate, the vector is fine tuned using only the first and last images--56 x 56 array from one searcher within a 64 x 64 array of the other. Altitude assignment was done by matching the brightness temperature of the target cloud with the closest temperature profile obtained from a recent analysis or forecast. Quality control was performed principally by subjective methods by a meteorologist with the aid of computer-interactive graphics displays.

United States (University of Wisconsin/SSEC)

The University of Wisconsin/SSEC cloud-drift wind processing system for FGGE was both manual and automatic. It relied on skilled analysts and computer interactive graphics as in the ESA quality control system, but allowed the analyst a much larger role as in the Japanese and U.S./NESS systems. Mosher (1979) notes that target selection is best

done by people, for judgment is required, while tracking and other activities involving calculation is best done by computer.

The UW/SSEC system displayed image data on a video device. The operator selected the target; and the computer tracked it via correlation techniques, calculated the wind vector, and displayed it for the analyst's approval. This system was used for all targets, regardless of type or level of cloud heights assigned by the cloud temperature/nearby profile matching technique. A correction was applied to allow for the fact that clouds sometimes appear warmer than they actually are, because clouds are not black-body radiators. The correction makes use of visible data, and so is not available at night.

Three images separated by 0.5 h were used to generate vectors. Each target thus produced two vectors, which were used in quality control. Pairs differing by more than 5 m/s in either component were rejected. Surviving pairs were averaged to produce the final vector. A neighbor check was also used.

ASSESSMENT OF CLOUD-DRIFT WIND DATA QUALITY

Any set of observations of the atmosphere is beset with errors. In the absence of an absolute standard of truth, assessing the quality of a particular set consists of applying a number of different tests, none of which are entirely satisfactory. Judgment thus rests on the sum of fragmentary and occasionally contradictory evidence and is rarely either conclusive or absolute.

This section presents three such fragments. First, comparisons between approximately coincident cloud-drift vectors and other winds are discussed. Second, results of quality control procedures illustrate the number of "rogue" observations present in a data set. Finally, the relative compatibility with data assimilation systems of several kinds of wind data is considered.

Collocations

Collocation comparisons consist in matching a cloud-drift wind vector with a nearby vector from some other source, where "nearby" is defined as a prespecified window in three-dimensional space and time. Obviously, the atmosphere has some variability over such a window. This acts to inflate the difference between the wind vectors to some extent.

This discussion will consider two categories of collocations: Type 1, where cloud-drift wind vectors from two adjacent satellites are collocated in the area of overlap, and Type 2, where cloud-drift wind vectors are matched with rawinsondes and aircraft. The former are a measure of the uncertainty in cloud-drift vectors. The latter contain errors both of the cloud-drift wind and the other observation, as well as the natural variability across the collocation window.

Two sources of information are used here: a collocation program carried out by the United States (NESS) under the auspices of a working

group called Coordination for Geostationary Meteorological Satellites (CGMS) and an independent program conducted by the U.S. National Meteorological Center. The NESS program uses an elliptical space window oriented along the direction of the wind, and $\pm$ 3 h in time. Type 1 vectors are considered collocated in the vertical if they are in the same category: low (surface to 700 mb), midlevel (699 to 400 mb), or high (<400 mb). Type 2 vectors are matched if the vertical window is 500 m or less. A description of the NESS collocation program may be found in Whitney (1983) and several working papers for the CGMS made available through personal communication with L. F. Whitney.

The NMC program matches reports within 3^{o} latitude and 1 h. No Type 1 collocations are done, however Type 2 matches included both rawinsonde and aircraft, separately.

Table 1 presents comparisons between adjacent satellites in the areas of overlap for the period May 10, 1979 through June 5, 1979, during the second Special Observing Period, taken from the NESS collocation program. The numbers are quite uniform, with only the METEOSAT-GOES/E high-level comparison exhibiting less agreement. Note especially that the GOES/E-GOES/W comparison, where winds are produced using identical equipment, procedures, and personnel, are the lowest of all, but not by much. This suggests that the uncertainty in cloud-drift winds is not due to differences in techniques used at the various processing centers.

Table 2 gives the Type 2 NESS comparison against rawinsondes for the same period only for the operational vectors. Indian Ocean vectors, or GOES vectors reprocessed by UW/SSEC, are not included. The numbers are generally larger for Type 2 comparisons but agree well among themselves, except for the GMS high-level winds. This is a consequence of the JMSC climatological altitude assignment referred to earlier. Operational data assimilation systems typically assume rawinsonde RMS vector errors ranging from 3 to 8 m/s (e.g., Bengtsson et al., 1982, Table 1). Assuming that cloud wind errors and radiosonde wind errors are uncorrelated, and thus their contributions add as squares, the numbers in Table 2 can be adjusted to range from about 5 m/s to 14 m/s.

Figures 2 and 3 illustrate the comparison of the NESS collocation statistics during the FGGE year with those of subsequent years. Type 1 comparisons are shown in Figure 2. Significant changes have occurred

TABLE 1 Room-Mean-Square Vector Difference (m/s) between Collocated Cloud-Drift Wind Vectors Produced by Two Adjacent Satellites, for the Period 5/10/79 thru 6/5/79

Satellites	Low (sfc - 700 mb)	High (<400 mb)
METEOSAT - GOES/E	4.5	12.0
GOES/E - GOES/W	4.1	8.0
GMS - GOES/W	5.6	9.4
GOES/E/W - UW/SSEC	4.4	8.5
METEOSAT - UW/SSEC (Indian Ocean)	4.9	8.3

TABLE 2 Root-Mean-Square Differences (m/s) Between Cloud-Drift Vectors and Collocated Rawinsonde Vectors, for the Period 5/10/79 thu 6/5/79

Satellite	Low	Mid	High
GOES/E-W	5.6	8.7	13.0
GMS	6.0	9.4	15.8
METEOSAT	6.0	9.1	12.9

since 1979 mostly in the high-level winds: GOES/W-GOES /E differences have steadily declined, presumably as a result of experience and standardization of practices at NESDIS. GOES/W-GMS differences declined remarkably in the summer of 1981. These figures show considerable variation with time in the high-level winds. Users of this data base should consider incorporating this fact in their data assimilation systems.

Figures 4 and 5, from the NMC collocation program, display the variations with time in Type 2 collocations for all operational geostationary satellites (high level only) for the period October 1978 through May 1980. Collocations of Aircraft-to-Satellite Data Relay (ASDAR) and radiosonde winds are included for comparison. The RMS vector error is shown in Figure 4; part (a) compares GOES/W and GMS with the ASDAR collocation, and part (b) compares GOES/E and METEOSAT with the ASDAR collocation.

Clearly, the GMS-radiosonde collocations are much larger than any of the others, especially in the northern hemisphere winter. The ASDAR-radiosonde trace is relatively constant with time, and generally below 12 m/s; the average over 1979 is 11.7 m/s. Both GMS and GOES/W show large seasonal variations, especially in the former. There is considerable month-to-month variation in the GOES/E-radiosonde collocation, with particularly large maxima in August and December. METEOSAT also shows temporal variations, but with much smaller magnitude.

Averaged over 1979 (through October for METEOSAT), the various systems yield errors of 16.8 m/s for GMS, 14.1 m/s for GOES/E, 13.4 m/s for GOES/W, and 13.5 m/s for METEOSAT. These numbers are slightly higher than the NESDIS collocations in Table 2, but the relative scores agree well.

Monthly averaged mean speed difference for this period are given in Figure 5. Very large temporal variations are apparent, especially for GMS winds. GOES/W winds were faster than their matched radiosonde counterparts during all of 1979. GOES/E winds began the year with a positive mean difference. METEOSAT mean speed differences were negative throughout the year.

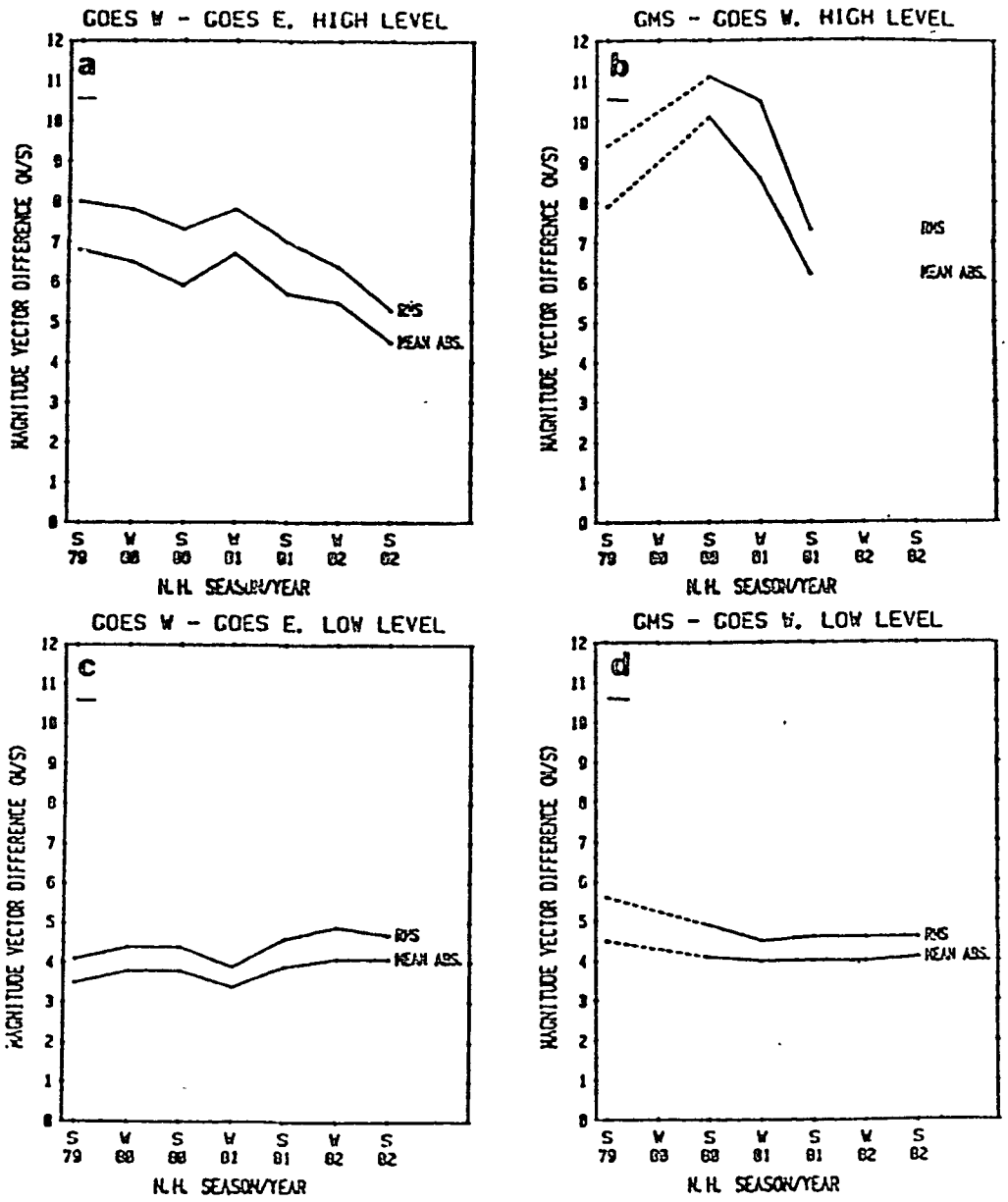

FIGURE 2 Statistical comparison of collocated cloud-drift winds from a) GOES-E and GOES-W above 400 mb; b) GMS and GOES-W above 400 mb; c) GOES and GOES-W below 700 mb; d) GMS and GOES-W below 700 mb. Taken from CGMS-VII Working Paper, Agenda Item G.1, 4/25/83. Courtesy of L. Whitney, NESDIS.

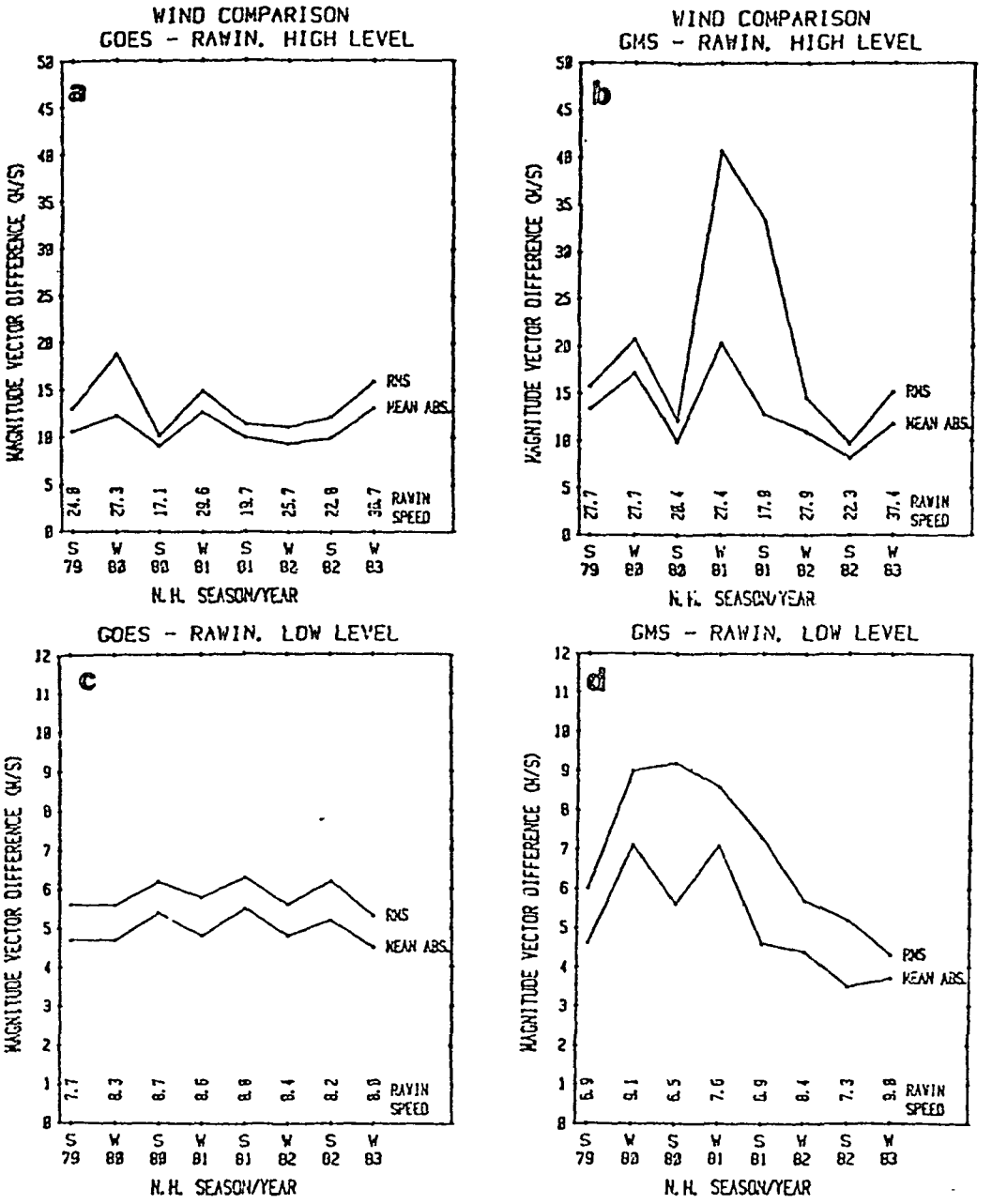

FIGURE 3 Statistical comparison of collocated cloud-drift winds and rawinsondes: a) GOES above 400 mb; b) GMS above 400 mb; c) GOES below 700 mb; d) GMS below 700 mb. Taken from CGMS-VII Working Paper, Agenda Item G.1, 4/25/83. Courtesy of L. Whitney, NESDIS.

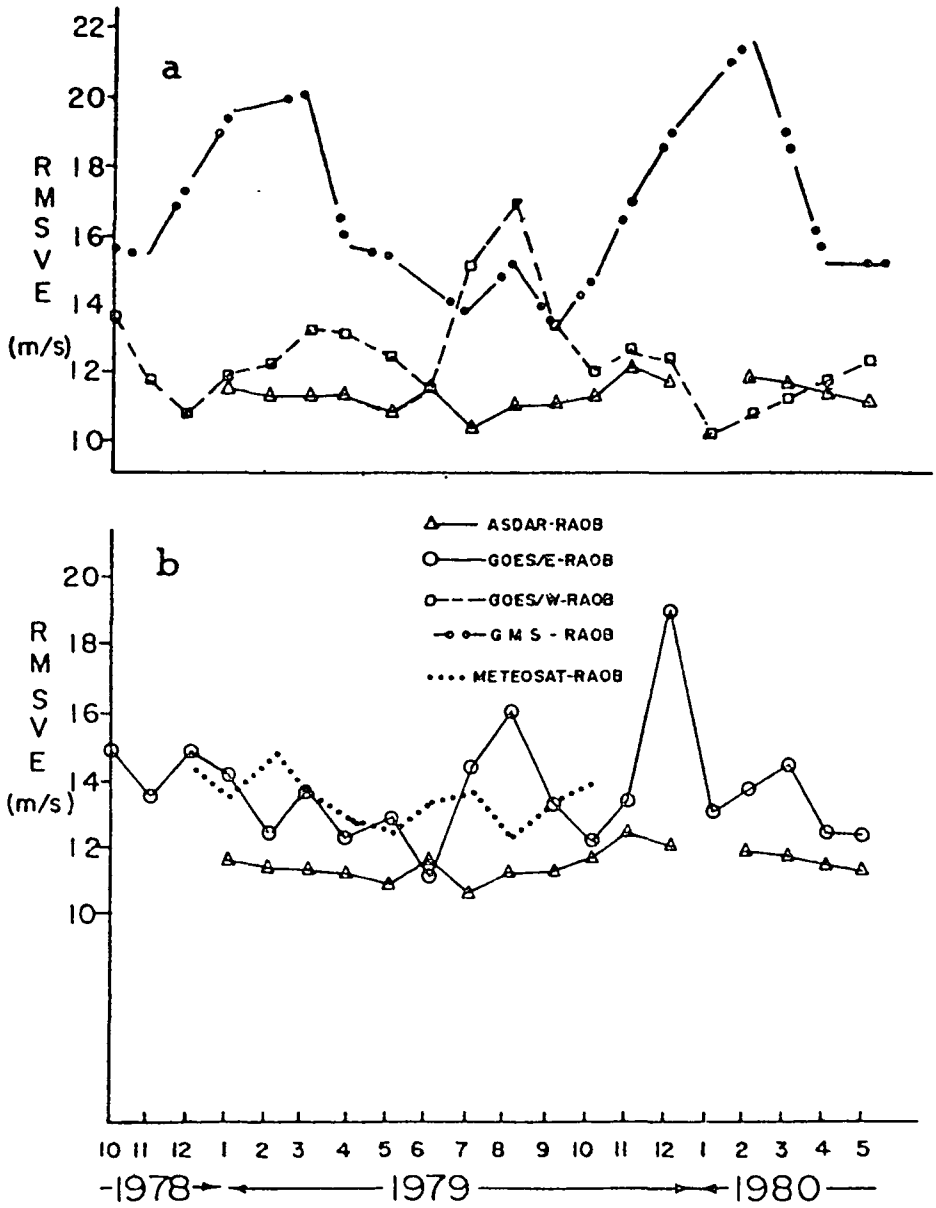

FIGURE 4 RMS vector differences between wind sensing systems and nearby radiosondes during FGGE, using the NMC collocation program. Collocation window is three degrees latitude and one hour. Part (a) includes GOES-W and GMS comparisons, while part (b) shows GOES-E and METEOSAT. ASDAR versus radiosonde is included in both.

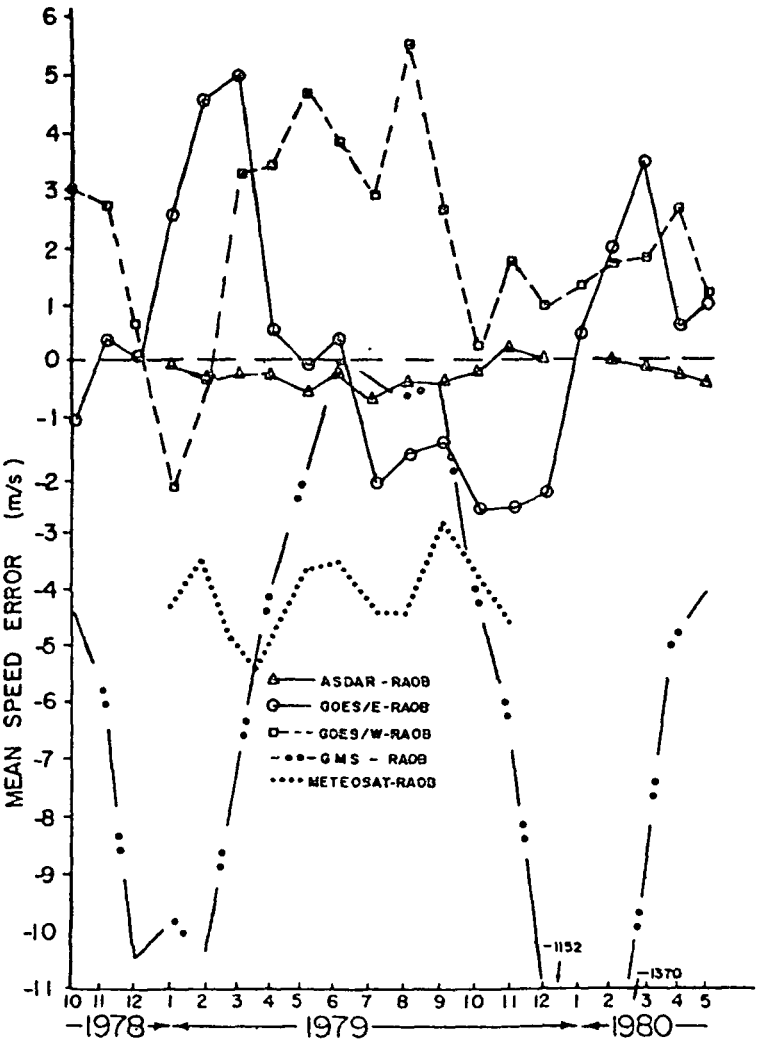

FIGURE 5 Mean speed differences between various wind sensing systems during FGGE, using the NMC collocation program.

Analysis of Quality Control Results

The United States mounted a "Special Effort" to examine the FGGE data base and edit at least parts of it to ensure a high quality data set. This effort has been discussed by Greaves et al. (1979). It involved subjective evaluation of certain data sets, especially satellite derived soundings and cloud-drift winds, by skilled analysts using computer interactive graphics and all other available information. Suspect observations were flagged.

Partial results were presented by DiMego et al. (1981). Table 3 has been extracted from that source. Of the vectors edited, about 4 percent of NESS-produced winds were judged incorrect, while slightly over 20 percent of the JMSC vectors were so judged. This probably reflects the altitude assignment problems referred to earlier. The remaining producers fall in between. Overall, about 13 percent of the vectors edited were flagged as incorrect.

These results suggest that the likelihood of encountering "rogue" reports is uncomfortably large in some of the cloud-drift wind data sets.

Compatibility with Data Assimilation Systems

This tends to be confirmed by the experience of users who ingest the cloud-drift wind data into data assimilation systems. Although all such systems incorporate automated quality control procedures that screen much of the incorrect data, some inevitably survive to affect the assimilation. A larger percentage of "rogue" reports will contribute to a looser "fit" of that data set by the assimilation system. Other factors may also contribute.

Figure 6, taken from a paper by Halem et al. (1982), depicts RMS differences between analyses produced by the Goddard Laboratory for Atmospheric Sciences' (GLAS) global data assimilation system and selected FGGE data sets. In Figure 6a, the fit of the GLAS analysis to

TABLE 3 Summary of Cloud-Drift Wind Vector Editing by the U.S. 'Special Effort' Team, For the Period 1/5/79 thru 1/30/79

Producer	Total Vectors	Vectors Edited	Vectors Flagged
NESS(GOES/E-W)	34239	7267	292 (4%)
UW/SSEC (GOES/E-W)	76345	6837	803 (12%)
UW/SSEC (GMS, IO)	60526	5927	1161 (19%)
ESA (METEOSAT)	19855	4487	679 (15%)
JMSC (GMS-1)	16093	5700	1127 (20%)
TOTAL	207058	30218	4062 (13%)

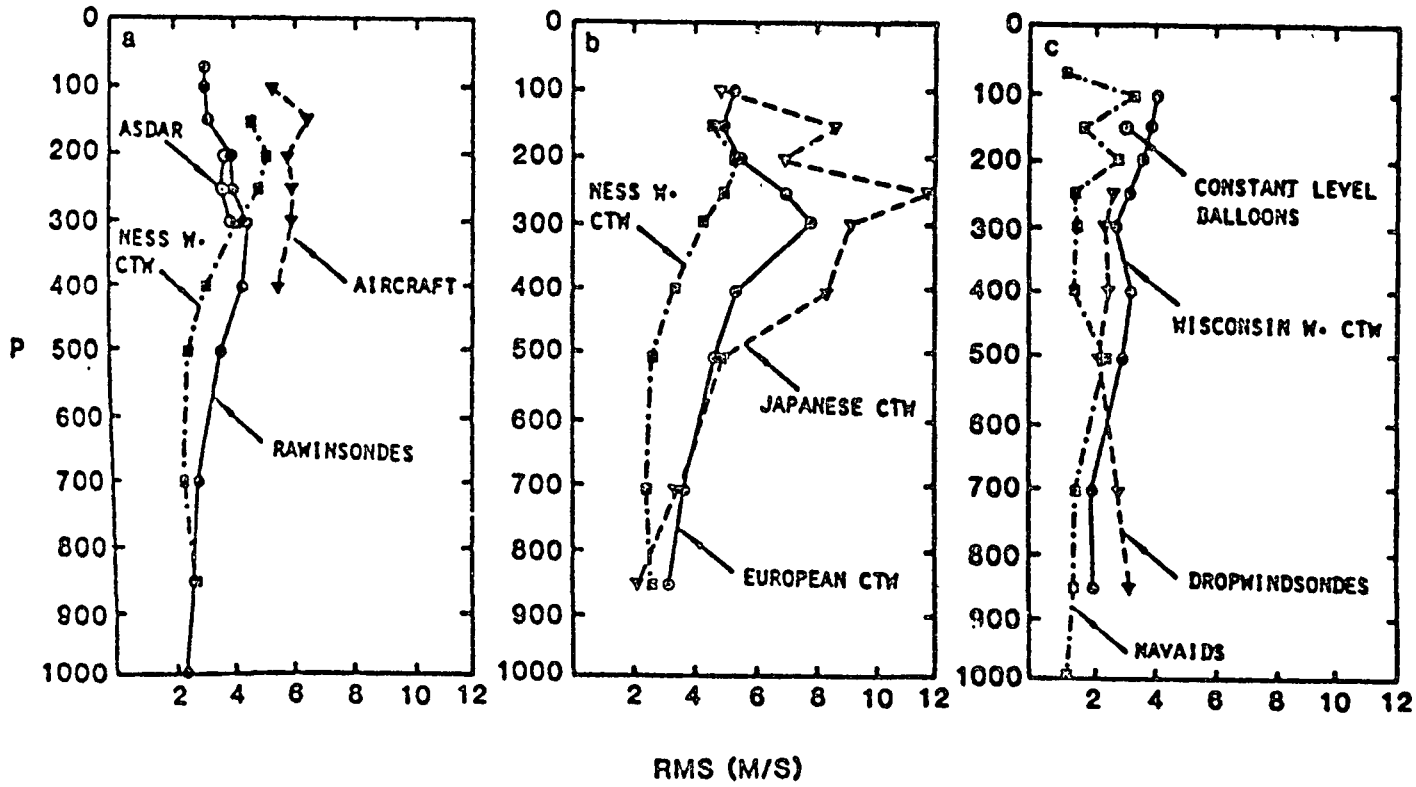

FIGURE 6 Vertical profile of rms differences between the FGGE wind analysis and data from different wind observing systems in meters per second. CTW is an acronym for cloud-track winds. a) NESS West cloud-track winds compared with three other wind observing systems. b) Three different cloud-track wind systems compared. c) RMS differences for tropical wind observing systems. After Halem, et al. (1982).

four different types of wind information is presented. the range among them is about 2 to 3 m/s at low levels and 3 to 6 m/s above 400 mb. A much greater range appears in Figure 6b, comparing the fit of the GLAS analysis to three sets of cloud-drift winds. The analysis thus experiences greater difficulty in fitting the METEOSAT and GMS winds than the NESS winds or any of the other sources. This is consistent with Table 3, where METEOSAT and GMS winds were identified as incorrect much more frequently than the NESS winds.

COMMENTS ON THE UTILITY OF CLOUD-DRIFT WIND VECTORS

The preceding assessment of the quality of the cloud-drift winds is reflected in the way data assimilation systems treat the vectors relative to other sources of wind information. Table 4, extracted from Bengtsson et al. (1982), gives the estimated RMS observational errors assigned to various types of wind observations in the ECMWF assimilation system. The numbers in the table are for each component of the wind rather than an RMS vector error estimate. Overall, rawinsonde and aircraft are considered the most accurate wind reports, followed by NESS/SSEC cloud-drift winds, and then ESA and JMSC winds.

In spite of these relatively larger error estimates and the problems of coverage and quality control that have been mentioned previously, cloud-drift wind data are regarded by users as very important, especially over vast areas otherwise devoid of wind reports.

The principal problem encountered is that of quality control. Vectors that have improper altitude assignment and still elude data checks cause considerable difficulties in data assimilation systems. As Bengtsson et al. (1982) noted, "...fleets of cloud-drift winds are sometimes assigned to completely erroneous heights." In such circumstances, the winds may confuse automated quality control, which is based on spatial consistency between neighboring reports. Several nearby erroneous winds will support each other and may be admitted into the analysis. When this occurs, havoc may result. Hollingsworth et al. (1984) present an example of analysis error resulting from suspect cloud-drift winds over the Mediterranean.

TABLE 4 Estimated Observational Errors Assigned to Different Wind Observing Systems in the ECMWF Data Assimilation System in m/s. (Component rather than vector error is presented.)

Pressure	Observing System			
	Radiosonde/Aircraft	NESS/UWSSEC	ESA	JMSC
300 mb and above	6	8	8	13
400	5	7	8	10
500	4	7	8	10
700	3	5	8	6
850	2	4	7	6
1000	2	4	7	6

SUMMARY

Cloud-drift winds constitute an important component of the FGGE data base. They were generated by four different centers, using somewhat different procedures. Some of those differences had a major impact on the quality and utility of the data. The most prominent example is the JMSC procedure for altitude assignment.

There are limitations of the data that users should be aware of. Coverage is limited to equatorward of 45° latitude and tends to be at a single level, high or low, depending on whether the target clouds are cirrus or cumulus. Sources of error include nonadvective cloud motions and assignment of the vectors to an altitude unrepresentative of the motion. The latter is by far the most serious.

UW/SSEC and NESS high-level winds were produced by systems that allow human judgment a role in target selection. Their data sets have been found to be the most accurate and reliable. Winds produced by ESA are less highly regarded, perhaps because their more automated system allowed a larger number of incorrect vectors from poor target selections. The JMSC high-level winds during FGGE are subject to serious errors because of the practice of assigning them to the height of the climatological tropopause.

Data users are still learning how to use these data in combination with other types of information. The major obstacle is the automatic removal of groups of erroneous cloud-drift winds.

ACKNOWLEDGEMENTS

The author wishes to express his appreciation to L. F. Whitney of NESDIS for generously sharing his time, knowledge, and material for the preparation of this paper. T. Hamada of JMSC also contributed much material, as did C. Vlcek of NMC. T. Hamrick of NMC assisted in the compilation of the NMC collocation statistics. The manuscript was typed by M. Chapman. Two of the figures were drafted by C. Burley.

REFERENCES

Bengtsson, L., M. Kanamitsu, P. Kallberg, and S. Uppala (1982). FGGE 4-dimensional data assimilation at ECMWF. Bull. Amer. Meteorol. Soc. 63, 29-43.

DiMego, G., C. McCalla, J. Badner, D. Mannarano, and H. Carney (1981). The United States "Special Effort:" Results of data editing for the first special observing period. Paper presented at the International Conference on Early Results of FGGE and Large-Scale Aspects of its Monsoon Experiments, January 12-17, 1981, Tallahassee, Fl.

Greaves, J., G. DiMego, W. Smith, and V. Suomi (1979). A "Special Effort" to provide improved sounding and cloud motion wind data for FGGE. Bull. Amer. Meteorol. Soc. 60, 124-127.

Halem, M., E. Kalnay, W. Baker, and R. Atlas (1982). An assessment of the FGGE satellite observing system during SOP-1. Bull. Amer. Meteorol. Soc. 63, 407-426.

Hamada, T. (1982). New procedure of height assignment to GMS satellite winds. Japanese Meteorological Satellite Center Tech. Note No. 5, pp. 91-95.

Hollingsworth, A., A. Lorenc, S. Tracton, K. Arpe, G. Cats, S. Uppala, and P. Kallberg (1984). The response of numerical weather prediction system to FGGE IIb data, Part I: Analyses. Submitted to Quart. J. Roy. Meteorol. Soc.

Hubert, L. (1979). Wind derivation from geostationary satellites. Chapter 2 of WMO Tech. Note 166, Quantitative Meteorological Data from Satellites, J. Winston, ed., 33-59.

Kodaira, N., K. Kato, and T. Hamada (1981). Man-machine interactive processing for extracting meteorological information, real time, in Parallel Computing--Image Analysis, M. Onoe, K. Preston, and A. Rosenfeld, eds., Plenum Press, New York, 297-323.

Mosher, F. (1979). Cloud-drift winds from geostationary satellites. Atmospheric Technology 10, 53-60.

Whitney, L. (1983). International comparison of satellite winds--an update. Adv. Space Res. 2, 73-77.

BUOY SYSTEMS DURING THE FGGE

Rex J. Fleming
Office of Climatic and Atmospheric Research
National Oceanic and Atmospheric Administration

ABSTRACT

This paper discusses the data quality, impact, and application of various buoy systems deployed during the FGGE. Three general categories of buoy systems provided critical coverage of environmental phenomena in the Arctic Ocean basin, the tropical oceans, and the southern hemisphere. Results of the added pressure information in the Arctic are presented. The impacts of the southern hemisphere buoy systems on pressure fields, SST fields, and ocean circulation are provided. Those findings from the tropical drifters, relevant to the FGGE time scales, are indicated. All three types of buoy systems, each uniquely engineered for application in different regions of our planet, contributed to the broad objective of advancing weather and climate predictions in several special ways. Comments are provided about the role of buoys in a future observing system, and a consortium of interested countries is strongly advocated in order to accelerate this role.

INTRODUCTION

This paper is one of several discussing the First GARP Global Experiment (FGGE) data systems. Subjects addressed here include the data quality of the buoy systems, the application and impact of these buoy systems relevant to FGGE objectives, and comments on the future role of drifters as part of an optimal observing system for the future.

There were three general categories of new buoy systems that were deployed during the Global Weather Experiment. These buoys provided critical coverage of environmental phenomena in the Arctic Ocean basin, the tropical oceans, and the southern hemisphere. Each buoy system transmitted data to the National Oceanic and Atmospheric Administration (NOAA) polar-orbiting satellite system, and the buoy positions were computed from the Doppler shift of the transmission as received by the satellite. All three types of buoy systems, each uniquely engineered for applications in different regions of our planet, contributed to the broad objective of advancing weather and climate predictions in several special ways.

ARCTIC BASIN BUOYS

The Arctic Basin Buoy Program began as a modest effort during the FGGE, primarily to provide a uniform coverage of the pressure field in the otherwise data-sparse region of the Arctic. The Arctic Ocean is covered by a layer of sea ice, which averages 3 to 4 m in thickness. Initially, 20 ice buoys were air-dropped in an approximate 400 km grid covering the Arctic basin. The buoy hulls measured 62 cm in diameter, weighed 38 kg, and were parachuted to the ice below. The buoys were powered by small lithium cells, communicated their data over 25 times per day, and were located to within 500 m by the French-supplied ARGOS location system onboard the U.S. satellites.

Results and Impact on Synoptic-Scale Weather Forecasting

Prior to FGGE there were very few data to analyze weather systems over the vast Arctic Ocean. As a result of this lack of knowledge, weather events were often not forecast properly in the high-impact coastal marine areas that ring the Arctic basin. Arctic ice buoys in FGGE helped to remedy this problem.

The pressure values from the buoys were transmitted in real time and were found to be of high quality. Several countries (e.g., Canada, Norway, United States) reported improved analyses and forecasts resulting from the availability of this surface pressure information. The improvements have been noted in cases ranging from detecting intense mesoscale systems to improving the shape and intensity of polar high pressure domes. An example of the impact of the Arctic basin buoys on northern hemisphere surface pressure analyses and forecasts is provided by the severe blizzard to hit the Alaskan coast on February 12, 1982. Similar cases were observed in 1979, but this situation is used here because of the graphics provided by Fathauer (1982). This was one of several severe winter blizzards to affect Alaska in the 1981-1982 season.

Preliminary analyses for the Arctic region are prepared by the forecast office in Anchorage. These are transmitted by facsimile to about 40 locations in Alaska. Fairbanks, Alaska, (responsible for forecasts in the northwest region of Alaska) reanalyze surface analyses for late data or prepare their own analyses when a quick look is needed. A comparison of the analyses at 1800 GMT February 11, 1982 of Anchorage (Figure 1 with no buoy data) with that of Fairbanks (Figure 2 with buoy data) shows that considerably more accurate assessments of the locations and intensities of pressure systems and fronts is possible when these buoy data are present.

The fast-developing low in the northern Chukchi Sea was identified and subsequently tracked by the buoy data. As a result, a blizzard warning for the Arctic coast of Alaska was issued four hours before total white-out conditions occurred as forecast. In this, and in many similar cases, the polar-orbiting satellite data did not show the cold front and low pressure center that caused the blizzard conditions (with

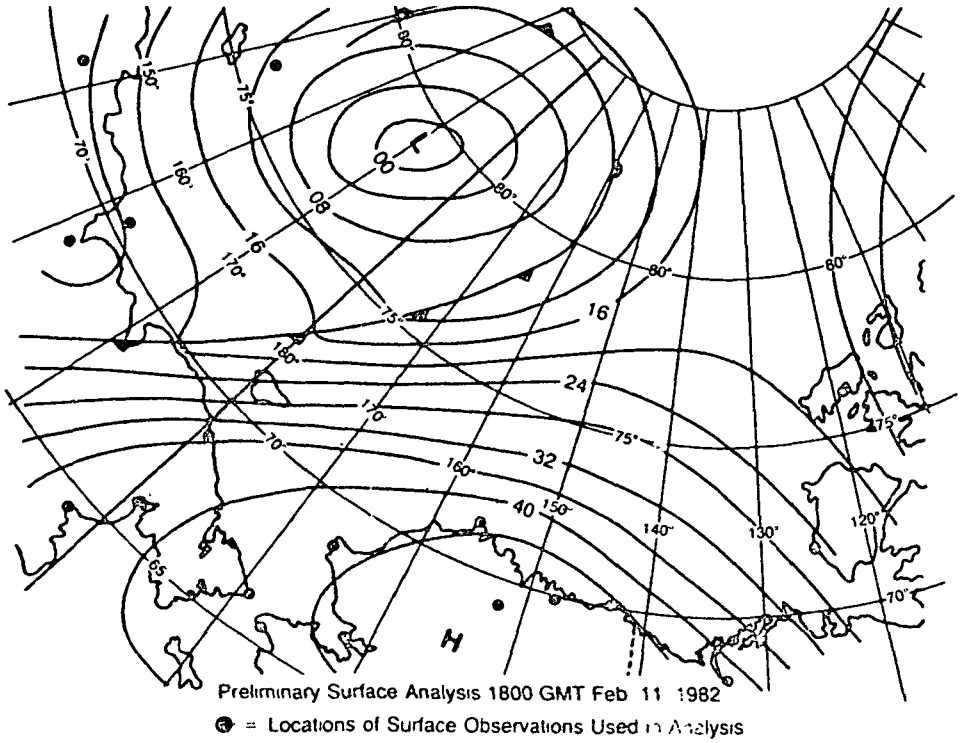

FIGURE 1 Preliminary surface analysis 1800 GMT February 11, 1982. Dots are locations of surface observations used in analysis.

clear definition) until the storm had already been in progress several hours.

The above example concerned subjective forecasts. What about numerical prediction in the Arctic? In the past, there has been insufficient data to properly evaluate numerical models. The FGGE data finally provide significant data with which to check the accuracy of the models in this region. Moritz (1983) has evaluated numerical forecasts in the Arctic by comparing geostrophic winds derived from the analyzed and forecast pressure fields. Among his findings, Moritz shows that NMC's 1000 mb height forecasts produce geostrophic winds that better persistence only out to 3 days, and that despite the higher persistence of the wind field in the Arctic, compared to midlatitudes, the forecast skill is smaller in the Arctic than in midlatitudes.

The Arctic continues to grow in importance for natural resources, transportation, and defense. More accurate surface winds would be extremely valuable. Improved surface data coverage by buoys is possible. More satellite soundings over the Arctic could be processed (many are not processed because of so many satellite passes over the region). However, in trying to bring the Arctic forecast skill up to levels of the midlatitudes, the question is: What combination of

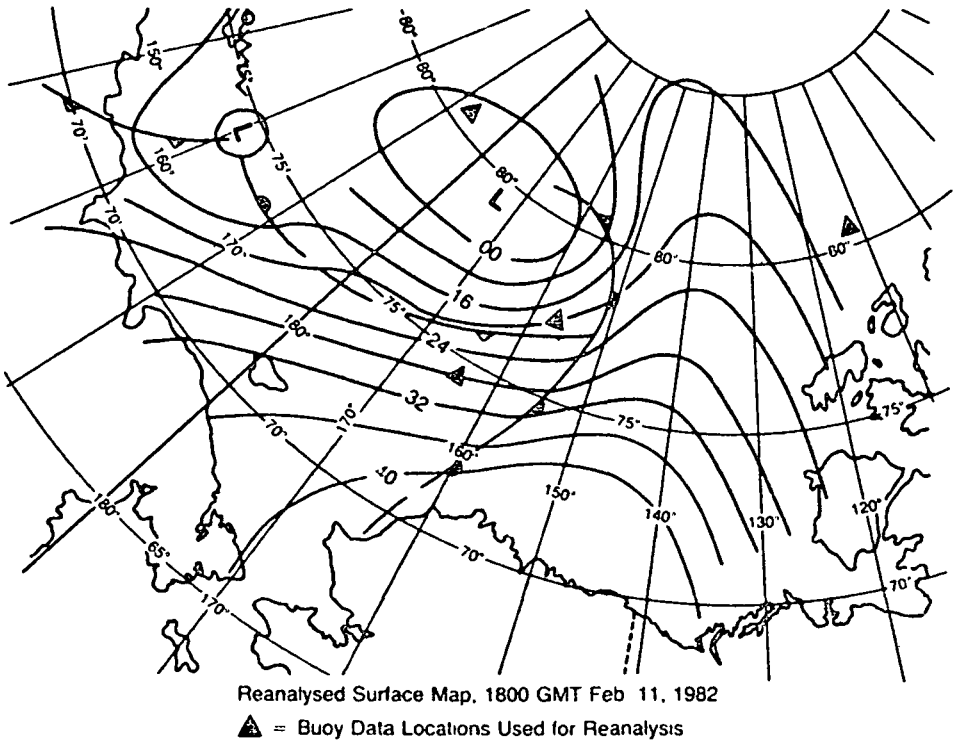

FIGURE 2 Reanalyzed map of Figure 1. Triangles mark buoy locations used for reanalysis.

increased data and further model improvements would be required? Further research on the numerical forecast accuracy in the Arctic region is necessary.

Results for Climate Modeling

The Arctic basin buoys have been continued for an additional five years in order to obtain a valuable time series of factors that affect the flow of ice in the region. Since the time scale goes beyond the FGGE period of interest, only a brief mention of these results are provided for completeness.

Untersteiner and Thorndike (1982) have provided the following results, which are based on the actual observed ice motion (known from the positions of the ice buoys) and the geostrophic wind forcing (computed from the pressure field primarily derived from the buoy measured pressures). With these two fields in hand, the long-term average ocean current is estimated by subtracting the share of the ice motion due to the wind from the actual ice motion. It is found that for time scales of days to a few months, the ice motion is dominated

(80 percent) by the synoptic-scale weather systems. For longer time scales (several months and beyond), one half of the long-term ice drift is due to the mean seasonal geostrophic wind and the other half is a consequence of the mean ocean circulation. These approximate ratios apply to the central Arctic basin. Near the shore and in winter, ice stresses propagating out from the coastline substantially alter the ratios.

An estimate of the mean ice motion over many years (including the buoy data from the Arctic Basin Buoy Program begun during the FGGE) was made by Colony and Thorndike (1982). They describe the mean ice drift as a combination of the anticyclonic motion in the Amerasia basin and the linear motion often referred to as the Transpolar Drift Stream (see Figure 3). These are motions forced by the mean atmospheric surface pressure field and the geometry of the basin (see Figure 4). The authors found that the interpolated mean vorticity of the ice motion was -5×10^{-8} s^{-1}, which corresponds to a rotation of about 45^{o} per year.

THE SOUTHERN HEMISPHERE BUOY PROGRAM

The details of the southern hemisphere buoy program have been documented in several national and international documents, and only a few highlights of operations are required to introduce the subject here. The 318 buoys that were deployed during the FGGE year were provided by 8 different countries. The deployment was shared by 14 countries and was achieved by parachuting buoys from aircraft and by launching them from a variety of vessels--research ships, Antarctic supply vessels, military vessels, commercial ships, and even a longboat from Pitcairn Island.

The southern hemisphere buoys measured pressure, sea-surface temperature (SST), and air temperature. Their contribution to the objectives of FGGE was primarily to provide for the first time an accurate synoptic coverage of the southern hemisphere surface pressure fields--both for its intrinsic value and as a reference level for the satellite soundings so that the reconstructed atmospheric mass field would be independent of any model assumptions or first guess. A secondary value of the buoys was the SST information that provides an important boundary forcing field for the atmosphere over time periods covered by extended range forecasts. Another, though limited, value of the buoys was their drift characteristics. Each of these uses of the southern hemisphere buoys will be briefly summarized in the following sections.

The accuracy and resolution of the instruments pertinent to these applications are expressed in terms of U.S. test results. These results may be better or worse than other countries buoy systems but can be considered representative. The buoys were equipped with a quartz oscillator pressure sensor--a very stable device designed to minimize "drift" in the pressure measurement to less than 1 mb per year. The digital resolution (one count) was 0.15 mb. In field operations, special tests, and low-level overflights by aircraft, buoy

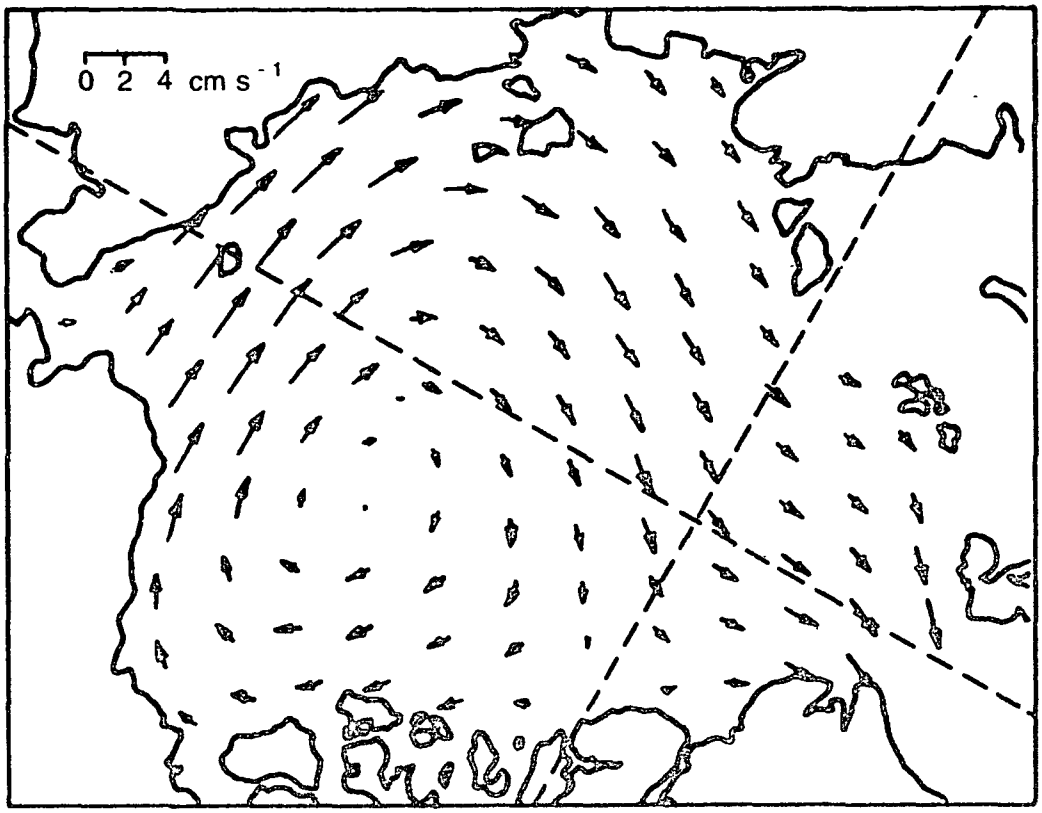

FIGURE 3 Field of interpolated mean ice motion. The vectors originate at the center of the boxes. The interpolated motion in data-sparse regions should be regarded with caution.

pressure sensors were found to remain stable to within 1 mb. The buoy water temperature sensors were thermistors with a specified accuracy of $\pm 1^{\circ}C$ with a range of -5° to $+35^{\circ}C$. The digital resolution (one count) was $0.16^{\circ}C$. Laboratory and field tests indicated that these sensors performed as expected. With rare exceptions, when a buoy instrument failed during the Experiment, it was obvious that it had done so. The location accuracy of the Argos system was checked by many groups. From a controlled test of fixed platforms, the United States found mean radial errors for all position fixes from actual locations to be 0.26 km.

Concerning the lifetime of the U.S. buoys relative to all possible failure modes (sensor, transmitter, batteries, biofouling), piracy, and so on), Kerut (1981) determined that the average time to failure was 319 days. The average time to failure was defined as the total buoy network operating time divided by the number of failed buoys.

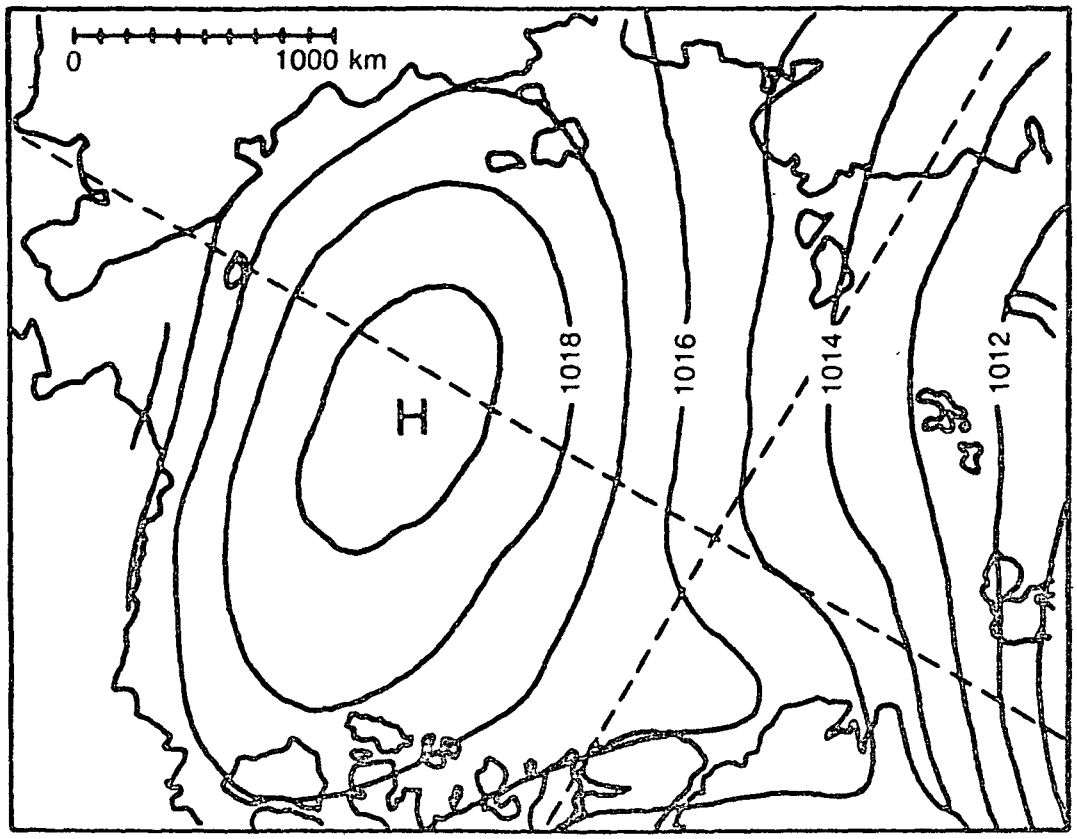

FIGURE 4 Mean surface atmospheric pressure (1979-1982) taken from Thorndike et al. (1983). The isobars are in millibars.

The deployment of the buoys in the southern hemisphere was a remarkable example of international cooperation. Over certain months, the surface pressure coverage was better over the southern hemisphere oceans than the northern hemisphere oceans. Figure 5 from Fleming et al. (1979) shows the coverage on May 30, 1979. Garrett (1983) points out that 70 percent of the ocean between 20°S and 65°S was within 500 km of a working buoy from April until September of 1979.

Pressure Information

In speaking about the impact of the FGGE systems on operational synoptic analysis, Zillman (1983) stated that "Without doubt, the most outstanding contribution was made by the drifting buoy system. By providing an extensive network of regular pressure observations over the previously data-sparse ocean areas, the buoy system essentially

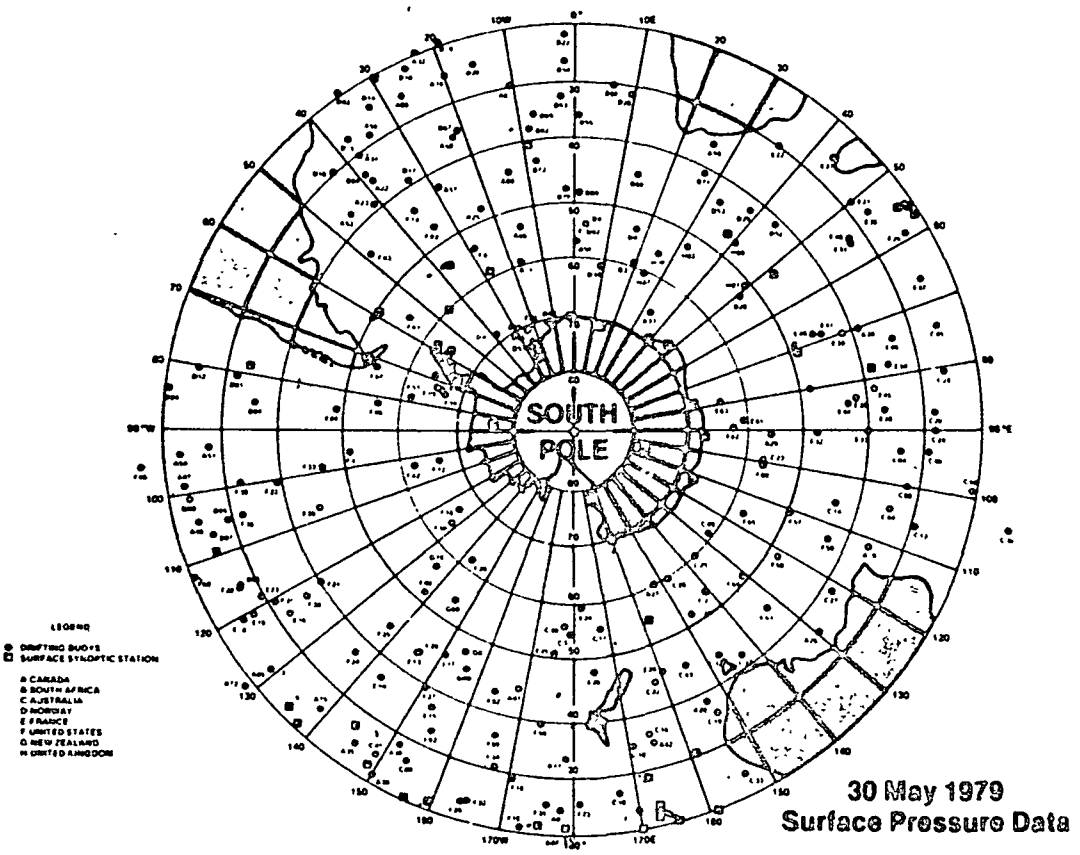

FIGURE 5 Real-time surface pressure observation points from drifting buoys and land stations over the southern hemisphere oceans and Antarctica on May 30, 1979.

removed, for the first time, the major hurdle that had stood in the way of reliable routine surface-pressure analysis over the entire hemisphere." Zillman gave concrete examples of the value of the improved pressure field in operational numerical prognosis (see other papers of this FGGE Workshop) and in regional and local forecasting. An example of a typical analyses is given in Figure 6.

The quality of the pressure information from buoys can be extremely high--contributing to a spectrum of interests ranging from detailed daily analyses to more meaningful climatological statistics. However, as with any fully automated system, careful checks need to be added (either manual or automatic) to maintain this consistent quality. For example, prior to the FGGE (but after the mid-1960s), visual and infrared imagery from polar-orbiting satellites were used by the Australian Weather Bureau to help locate major synoptic systems. While various semi-quantitative imagery interpretation techniques had been

FIGURE 6 MSL pressure analysis for 12 GMT July 26, 1979 from the archives of WMC, Melbourne (* = FGGE buoys, o = ships, 0 = synops).

devised for ascribing numerical values to pressure fields (e.g., Guymer, 1978), it was not possible to produce confident detailed surface pressure analyses.

Pressure information from the FGGE buoys showed more confident specification of the centers of highs and lows, the variations in the position and intensity of the circumpolar trough, the oscillations in the strength of the subtropical highs, the central pressures of the high-latitude cyclones to be quite often 20 mb deeper than would have otherwise been estimated, and that the westerly flow south of Australia was considerably stronger than otherwise would have been identified. From these results, Guymer and LeMarshall (1981) concluded that

pre-FGGE analysis procedures may have led to systematic underestimation of synoptic systems over the high-latitude oceans. Among the many examples to support this, the authors stated that in June 1978 only about 25 depressions were analyzed as being below 960 mb. In June of the FGGE year, there were 118 lows analyzed as being below 960 mb (more than 30 of these were occurring north of 60°S compared with 6 on the June 1978 analyses).

The above results were obtained and are believable because a manual analysis process provided the opportunity for careful quality control of the buoy pressure data and the elimination of unrepresentative observations. Zillman (1983) points out that at the end of SOP-1, of the 156 buoys operating, 135 were considered by the Melbourne analysts to be producing reliable data and 21 were not. He also points out that the buoy pressure observations were found to be generally compatible with relevant island and ship observations and spurious readings from faulty buoys were generally obvious. Thus, it is a relatively trivial, but important, matter to build in appropriate quality control procedures to the future global observing system which will most certainly include buoy systems in significant numbers.

SST and Ocean Circulation Information

Since the cessation of whaling in the southern oceans, there have been virtually no sources of conventional SST observations south of about 40°S. The limited data that have been available have been quite inadequate as a basis for spatial analysis of five-day, or even monthly, means (Zillman, 1983). This situation changed during the FGGE year when the World Meteorological Center, Melbourne, began operational production of five-day and monthly SST maps for the entire southern hemisphere. The FGGE systems that made this possible were the drifting buoys, the TIROS-N satellite system, and the geostationary satellites.

Zillman (1983) reports that in a typical month of some 20,000 SST observations available from the buoys, about 13,000 were considered acceptable (compared with 5000 to 6000 ship observations). A slight bias towards buoy temperatures being lower than ship temperatures was found (T(B) - T(S) being -0.3°C). Since the FGGE, there have been improvements in SST information from buoys and from satellite algorithms. Strong (1984) has summarized the improvements in satellite techniques and indicates how important the buoy SSTs are in maintaining a consistent satellite product.

Obtaining ocean circulation information from drifting buoys (drogued or not) is still an inexact science. There have been recent improvements in drogue technology and in the interpretation of the Lagrangian drift. However, most of the southern hemisphere FGGE buoys were not drogued. Coupled with the fact that the effects of the wind on the buoy motions were only partially known (different countries having different buoy designs), the circulation information was only qualitative.

Garrett (1983) has summarized these results as follows: Maps of mean buoy drift velocities averaged over 300 km cells resemble

established ideas of the general southern ocean circulation and show significant correlation with surface currents computed from dynamic heights. Maps of mesoscale variability of buoy motions show maxima associated with the return flow of western boundary currents and places where the Antarctic Circumpolar Current crosses meridional ridges. This distribution of variability agrees reasonably well with maps of "eddy kinetic energy" obtained from ship drifts and satellite altimetry. Keeley and Taylor (1982) have produced an atlas of FGGE drifting buoy tracks.

BUOYS IN THE TROPICAL OCEANS

Oceanographic drifting buoys were located in all three tropical oceans during the FGGE. These were primarily supporting scientific research directed to climate applications and do not require attention in this paper. However, two results are reported here: one related to atmospheric forcing in the tropics (SST), and one of general interest (Legeckis waves in the equatorial ocean).

Results from 62 satellite tracked drifting buoys deployed from February 1979 to December 1980 are described by Patzert and McNally (1981). While the results show the value of the buoys in monitoring the coherent character of the tropical current systems, the result of most interest to FGGE was the very accurate SST measurements that are obtainable from these tropical oceanographic drifters--even diurnal SST variability was discernible (rms values at 1 m depth were 0.3°C). This accuracy is important. Future systems must be able to monitor small but important SST anomalies that can affect long range weather forecasts.

Legeckis (1977) first reported the appearance of a cusp-shaped wave pattern along the Equatorial Front (cold water primarily caused by equatorial upwelling separated from warm water just north of the equator) in infrared photographs made from geostationary satellite data. The waves were typically about 1000 km long, extending between 95°W and 130°W. The waves have been identified during the summer months of each year since 1975, except 1976 and 1982, both of which were El Nino years. The waves were identified in May 1979 between 95°W and 110°W and extended between 85°W and 128°W during the time of their maximum development in July and August. Hanson and Paul (1984) have described the results of their 20 drogued buoys, which were in the near-equatorial Pacific during the FGGE. Figure 7 illustrates the energetic mesoscale circulation patterns associated with the frontal wave pattern as deduced from the buoy motions. Each of the troughs contain an anticyclonic eddy that moves westward with the Legeckis wave phase, and a smaller cyclonic eddy resides below the cusp-like wave crests. The larger eddies are the better documented, having been sampled by several drifters continuously during the four months when the waves were visible.

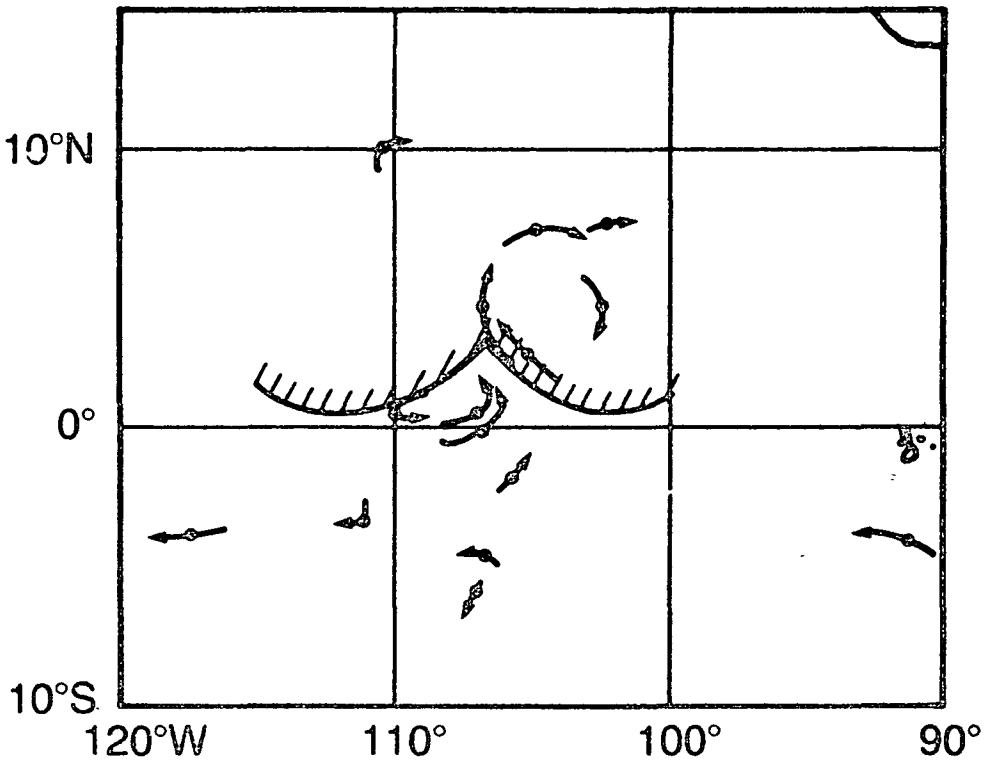

FIGURE 7 Drifting buoy trajectories in relation to cusp-shaped SST front. Hachured line shows location of SST front, and round dots show buoy location, both on June 23, 1979. Trajectory segments show buoy movements during preceding and succeeding four-day intervals.

DESIGN OF A FUTURE BUOY OBSERVING SYSTEM

Considerable progress has been made in all aspects of buoy systems, and the stage is set for their use as a major component of a composite atmospheric and oceanic observing system that will serve both the operational and research interests of weather, climate, and marine applications. New and better sensors have become available, procedures for accessing data locally and virtually instantaneously are in being, and an international mechanism for sharing in and reducing the costs of the Argos system exists. The only remaining element that is missing is an international mechanism to optimize the deployment of buoy networks for regional and global applications. It is hoped that the 10-year Tropical Ocean and Global Atmosphere (TOGA) Program will provide the stimulus to complete this last needed component.

In designing an observing system of the future tailored to the time scales of GARP, one should be aware of some recent technological advances. A brief discussion of a few of these will conclude this paper.

High quality sensors for pressure and temperature already exist. An important advance is a low-cost pressure sensor that maintains its calibration over long periods of time. New sensors measuring new variables are in various stages of development. These include wind speed, wind direction, precipitation, and radiation. New lower cost oceanographic buoys are being developed to measure temperature as a function of depth and to provide better indications of currents near the surface and at various depths. New advances are being made in smaller, lighter hulls, in low profile antenna, and in simplified drogues for air deployment. Finally, one of the most exciting developments is the miniature solar-powered PTT (weighing less than 200 g), which will open the door to significant numbers of new low-cost platforms in many application areas.

Virtually all the elements of an international buoy system are available, and only loose ends remain to be neatly bound. A consortium of interested user countries with buoy resources or deployment capabilities can blend and mold a working global observing system to help achieve the observational requirements of those operational programs of the World Meteorological Organization and the International Oceanographic Commission, and also help meet the goals of the major international research programs that are emerging from the World Climate Research Program. The time to establish this International Buoy Consortium is now!

REFERENCES

Colony, R., and A. S. Thorndike (1982). Sea ice motion in response to geostrophic wind. J. Geophys. Res. 87, 5845-5852.

Fathauer, T. (1982). The use of Arctic Basin buoys in northern Alaska weather forecasts. Presentation at Arctic Basin Buoy Program Meeting, Seattle, Wash., March 16-17.

Fleming, R. J., T. M. Kaneshige, W. E. McGovern, and T. E. Bryan (1979). The Global Weather Experiment II. The second special observing period. Bull. Amer. Meteorol. Soc. 60, 1316-1322.

Garrett, J. (1983). FGGE buoys: 5 years later. EOS Trans. 64, 962.

Guymer, L. B. (1978). Operational application of satellite imagery. Tech. Rep. 29, Bureau of Meteorology, Melbourne.

Guymer, L. B., and J. F. LeMarshall (1981). Impact of FGGE buoy data on southern hemisphere analyses. Bull. Amer. Meteorol. Soc. 62, 38-47.

Hanson, D. V., and C. A. Paul (1984). Genesis and effects of long waves in the equatorial Pacific. Submitted to J. Geophys. Res.

Keeley, J. R., and J. D. Taylor (1982). FGGE atlas of sea-surface temperature and drifting buoy tracks. Deep Sea Res. 29A, 659-661.

Kerut, E. (1981). Southern hemisphere drifting buoys. The Global Weather Experiment--Final Report of U.S. Operations, R. J. Fleming, ed., Department of Commerce, Rockville, Md., 41-60.

Legeckis, R. (1977). Long waves in the eastern equatorial Pacific Ocean. Science 197, 1179-1181.

Moritz, R. E. (1983). Accuracy of surface geostrophic wind forecasts in the central Arctic. Mon. Wea. Rev. 111, 1746-1758.

Patzert, W. C., and G. J. McNally (1982). Surface current variability in the tropical Pacific during 1979 and 1980 using drifting buoys. Recent Progress in Equatorial Oceanography: A Report of the Final Meeting of SCOR WG 47. University/N.Y., I.T. Press, Fort Lauderdale, Fla., 151-156.

Strong, A. E. (1984). Use of drifting buoys to improve accuracy of satellite sea-surface temperature measurements. Tropical Ocean-Atmosphere Newsletter, No. 25, 16-18.

Untersteiner, N., and A. S. Thorndike (1982). Arctic data buoy program. Polar Record 21, 127-135.

Zillman, J. W. (1983). The impact of the Global Weather Experiment, in The Results of the Global Weather Experiment, WMO Document No. 610, 41-134.

THE TROPICAL SPECIAL OBSERVING SYSTEM

Paul R. Julian
National Center for Atmospheric Research

The planning for FGGE that involved the establishing of observational requirements for the tropics was an especially difficult job. Not only did those responsible for the planning and requirements not know exactly how to formulate the latter, the job of how to fulfill them with the resources available looked formidable indeed. From a strict scientific viewpoint and using what was learned from GATE, it was thought that an observing system capable of resolving the transient westward moving disturbances of the tropics was needed. If that job could be accomplished, then the more energetic tropical storms as well as the planetary-scale flow components could be captured. It is well to recall that, at the time, only sketchy ideas were had concerning the role of the tropics for extended-range prediction in midlatitudes. It is also necessary to recall that an objective of the FGGE (and GARP) was to attempt to determine that role.

The requirements that were finally established are set out in Table 1 together with a very brief summary of how the actual Tropical Observing System (TOS) performed in SOP-1. The evaluation of the overall TOS in fulfilling these requirements may be said to have been marginal. However, the responsibility now is to evaluate the performance of the TOS, not with respect to the requirements but with respect to the stated goals of FGGE.

The task of assessing the performance of the TOS toward fulfilling the goals of FGGE is a very broad, encompassing task because it must consider aspects ranging from observing system accuracy to observing system impact studies. Furthermore, quantitative summaries over the FGGE year or even over the SOPs are time consuming and expensive to obtain, and it is not at all clear what quantitative information is appropriate.

Here some of the performance summaries of the components of the Tropical Observing System will be briefly covered, some of the more important points concerning the quality of the data from each of the observing systems will be emphasized, and examples of the assimilation of the IIb data by the ECMWF and GFDL IIIb schemes will be shown. Table 2 summarizes very briefly the content of the TOS data base for the Special Observing Periods. More extensive statistical summaries may be found in the FGGE Operations Report (GARP, WMO) (1980) and The Final Report of U.S.Operations in FGGE (1980).

TABLE 1 Wind Requirements--Equatorial Tropics--SOPs

All winds to ∓ 2 mps

	Horizontal Resolution	Vertical Resolution	Soundings Per Day
Stratosphere	4000 km	3 levels	1
Troposphere, Active Regions	350 km or 500 km	5 levels	1 or 2
Troposphere, Inactive Regions	500 km or 700 km	5 levels	1 or 2

TROPICAL CONSTANT LEVEL BALLOON SYSTEM (TCLBS)

System

The TCLBS was instituted to fill a gap in the vertical coverage of the wind observation program in the tropics owing to the limited operational altitude of the Aircraft Dropwindsonde aircraft. Experience gained at NCAR during a previous constant level balloon experiment (TWERLE) provided the confidence that a similar system could be deployed in FGGE. The TCLBS, as a part of the Special Observing System, consisted of 153 (and 157) platforms launched from two (three) sites within the tropics during SOP-1 (SOP-2). Because of air safety considerations the float altitude was chosen to be above commercial airspace, at 135 to 140 mb. Thus in the tropics the balloon platforms were in the upper troposphere and subject to the vicissitudes provided by convection; when floating in the extratropics the balloon platforms were in the lower stratosphere. Political and air safety considerations dictated that two cutdown systems be integrated into the TCLBS: one to destroy the platform should it be forced downward to a pressure greater than that at the top of commercial airspace (143 mb); and a second to destroy the platform were it to drift northward of an arbitrary geomagnetic latitude. A sizeable fraction of platform loss was accounted for by these cutdown mechanisms (Figure 1). The platform tracking was done by the ARGOS on board the NOAA-NESS satellites, and the location and data collection system performed in a very satisfactory fashion. Level IIb data were prepared at NCAR by employing an interactive graphics system that allowed the platform file obtained from Service ARGOS to be edited (Figure 2). The position and

TABLE 2 Tropical Observing System Summary

	Intensive Observing Periods, I, II	
TWOS	60-80 wind soundings per day (TWOS-radar soundings increase this some)	[65]
ACDWS	25-110 wind soundings per day	[68]
TCLBS	4 x (100-150) wind vectors per day	[500]
WWW	125 wind soundings per day	
Cloud-drift	2250 wind vectors per day	
Aircraft	250-300 wind vectors per day	

position/velocity observations remaining were analyzed by a quantitative polynomial fit so that position and velocity could be interpolated at the standard six-hour synoptic times. Quantitative uncertainties in the wind vectors calculated by such a procedure depend on the tracking accuracy and the trajectory determination and have been found to be less than 2.0 mps (vector RMS) for 90 percent of the vectors produced. This figure is less than the uncertainty in any other wind observing system and is the direct result of the tracking accuracy and quasi-Lagrangian nature of the system.

Assimilation

Owing to the IIb data editing and the low vector uncertainties, which enter a data assimilation system as observation error, the TCLBS data should have been accommodated with a relatively high degree of accuracy by the IIIb analyses. A sample of the ECMWF IIIb fit to the IIb TCLBS gives, for the tropics, an RMS difference of 3.5 mps. The principal problem encountered in assimilating the TCLBS data in the ECMWF scheme was that of accounting for the vertical variation in the forecast (guess)-observation wind components and the vertical extent of the local optimum interpolation analysis volume. Both of these made the data selection portion of the scheme occasionally reject a TCLBS vector when, at least from an educated subjective synoptic viewpoint, it should not have done so. The major data competitor in the tropical upper troposphere was cirrus-drift satellite winds, which have a much larger uncertainty: since these were nearly always in the same vertical slab at the TCLBS vectors, the optimum interpolation scheme melded the vectors in the analysis volume together, but with relative weights favoring the TCLBS. Strong vertical shears in the tropical upper troposphere (e.g., Madden and Zipser, 1970) are real, and data selection criteria and vertical structure functions in the optimum interpolation simply cannot cope with these situations. Cases may be presented which indicate flow reversal of nearly 180° between 150 and

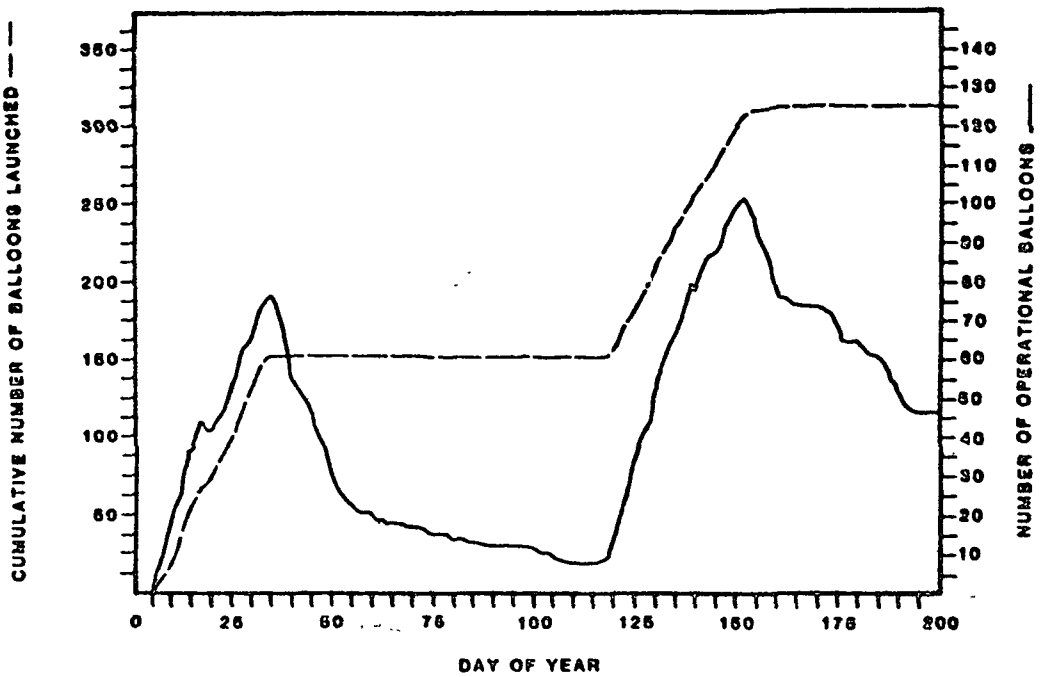

FIGURE 1 TCLBS launch profile, all launch sites (Canton Island, Ascension Island, and Guam).

135 mb. Madden and Zipser (1970) found 24 percent of soundings taken in the Line Island Experiment had 150 mb vertical shears exceeding 15 m/s km^{-}.

Case Study, January 27, 200-150 mb

This example was chosen because it includes many of the problems encountered in assimilating wind data in the tropics. A sequence of 150 mb data plots (Figures 3-6) indicates a group of TCLBS platforms moving from Central Africa (1900 GMT, January 26) to Lake Victoria (24 hours later). Wind data from conventional rawin systems (150 mb) agree with the TCLBS vectors (130 mb). However at 1200 GMT, January 27, cloud motion vectors from 200 to 150 mb and the 200 mb winds from the rawin at Nairobi, specify flow from nearly the opposite direction. Intersystem and intrasystem agreement is good, and any analysis system, objective or subjective, is faced with the problem of accommodating all the data--there appears to be no valid reason to reject any of them. A check of satellite imagery in this case can suggest if large-scale deep convection is involved in the situation. The infrared TIROS-N imagery for passes on January 27 show moderately deep convection (equivalent black-body temperatures in the range 230°K) in the vicinity of Lakes

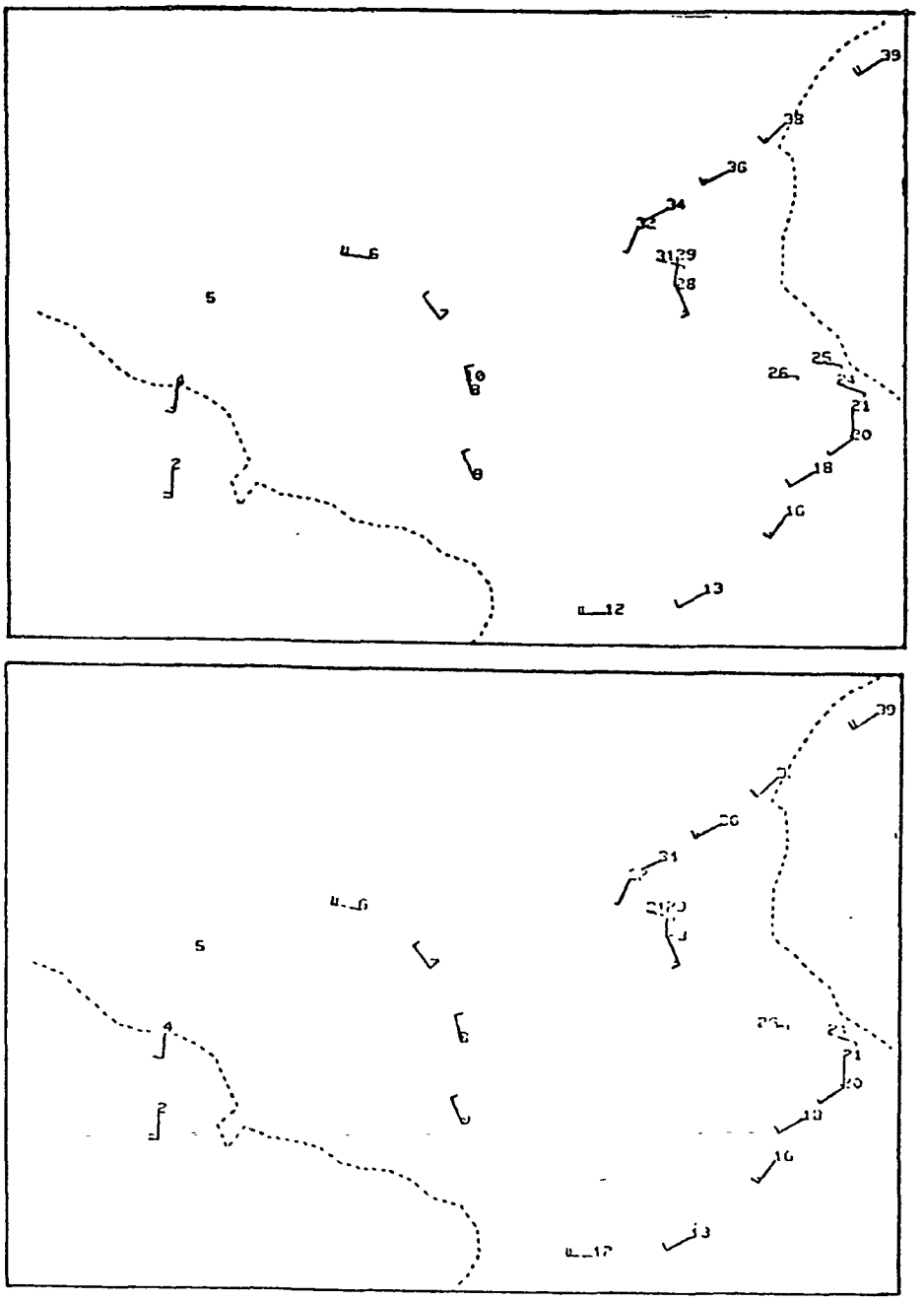

FIGURE 2 Example of interactive editing of TCLBS trajectory files. Unedited screen, above; and edited, below. Numbers are serial file numbers.

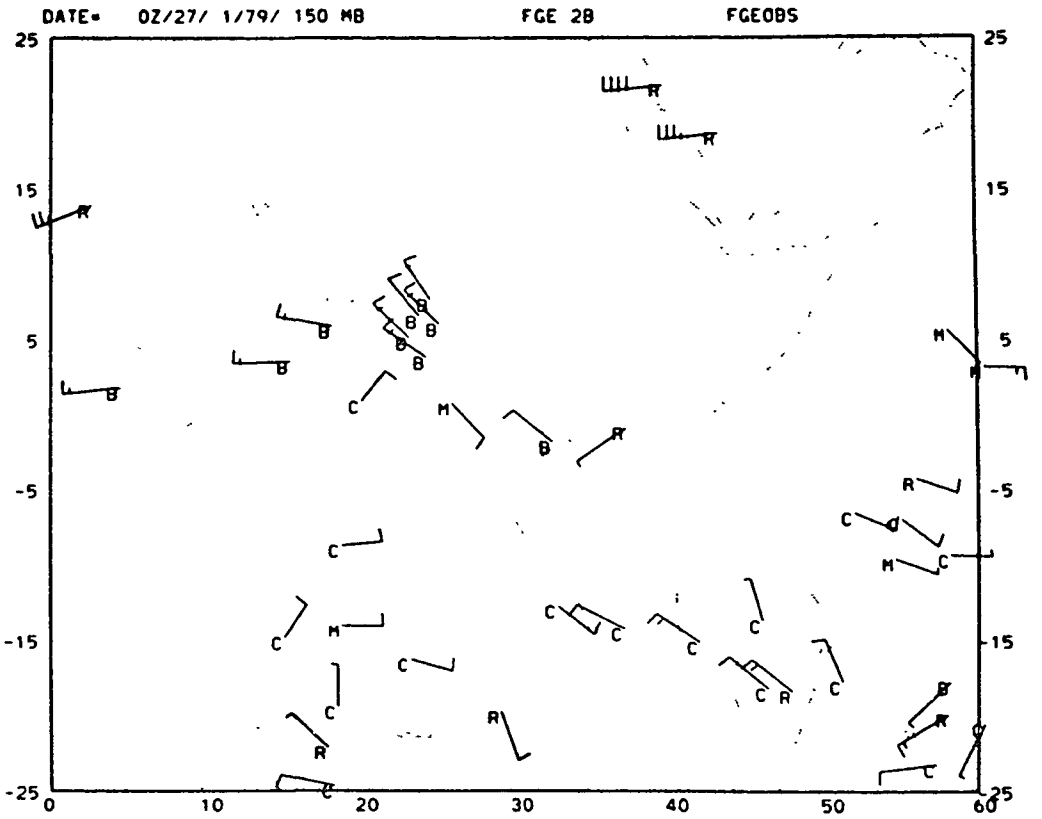

FIGURE 3 150 mb data for 0000 GMT for January 27 during SOP-1. R indicates rawin; C, cloud motion vector; M, super-ob cloud motion vector; and B, constant level balloon.

Nyasa and Tanganyika, but, quantitatively, these infrared fluxes are neither characteristic of convection reaching the tropopause (ebbs about 210°K) nor are they very widespread. Thus a possible solution to the situation is that flow at 250 to 200 mb is associated with this convection, but that the northwest flow above 200 mb is not. The resulting vertical shear is then strong with nearly a 180° direction change between 200 and 150 mb. A synoptic analyst interested in depicting what is actually going on in the tropical upper troposphere would then, presumably, require that no datum in this situation be rejected by the data selection portion of an objective analysis scheme, and that the respective analyses at 200 and 150 mb be faithful to the data. But the construction of an analysis to be presented to a numerical forecast model may require a different solution to the problem. If the analysis is to represent a tropical flow field close to the slow manifold of the forecast model, then it is not clear what the analysis scheme should produce here. More will be said on this

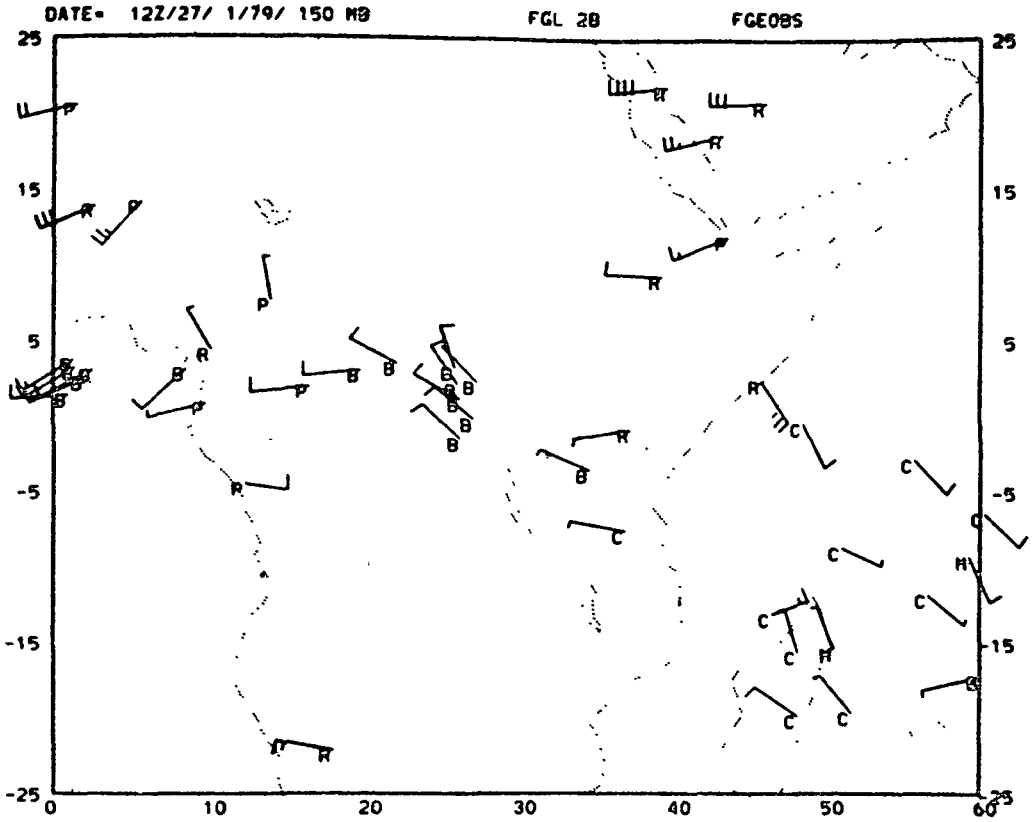

FIGURE 4 150 mb data for 1200 GMT for January 27 during SOP-1. R indicates rawin; C, cloud motion vector; M, super-ob cloud motion vector; and B, constant level balloon.

point in the contribution on analysis comparisons in the tropics--the point here is to focus on the joint subjects of observing system performance and assimilation system behavior.

Science

Examination of the trajectories of the TCLBS platforms has revealed more than a few instances of quasi-Lagrangian motion that exhibits an apparent dominant inertial component. Many instances of anticyclonic loops (Figures 7 and 8) in the tropics may be found. While not fulfilling all the kinematic requirements of inertial motion, such examples do suggest upper troposphere flow is occasionally dominantly inertial in character. Figure 9 shows a remarkable trajectory of a TCLBS platform spanning 70° of longitude that fulfills (to within a few percent) all the kinematic requirements for pure inertial motion.

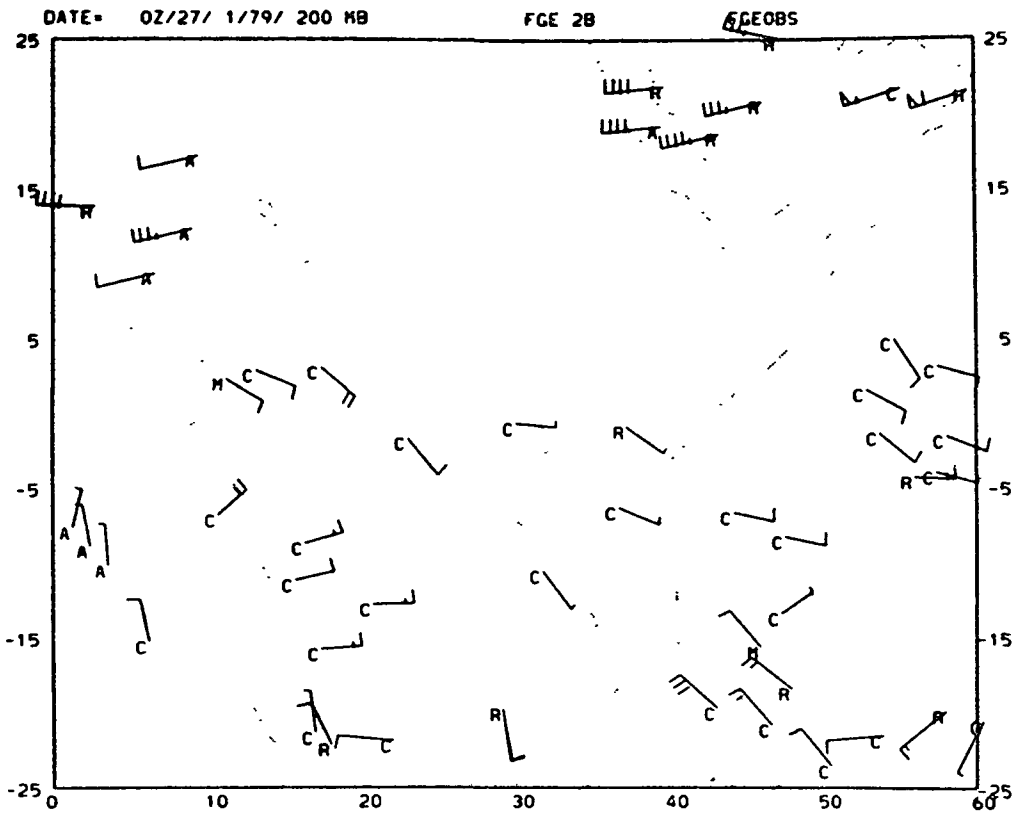

FIGURE 5 200 mb data for 0000 GMT for January 27 during SOP-1. R indicates rawin; C, cloud motion vector; M, super-ob cloud motion vector; and A, aircraft data.

Evaluation: Past and Future

Evaluations appearing during and immediately after FGGE used the words "disappointing" or "did not meet requirements," or ignored the system altogether. In the ensuing years, it has been concluded that such evaluations, besides being hardly objective, were based on:

1. The misconception that the TCLBS was not an expendable system. NCAR had acquired knowledge and expertise in the maintenance of CLB platforms in the tropics, and the system design and costs were as those of an expendable system. The higher than expected loss of platforms in the first week of life (infant mortality) was almost certainly due to the combination of launching in convectively active regions coupled with the pressure cutdown device. Nonetheless, to evaluate the system performance against such rigid standards as "150 platforms in the tropics per each SOP" certainly does not take into account the

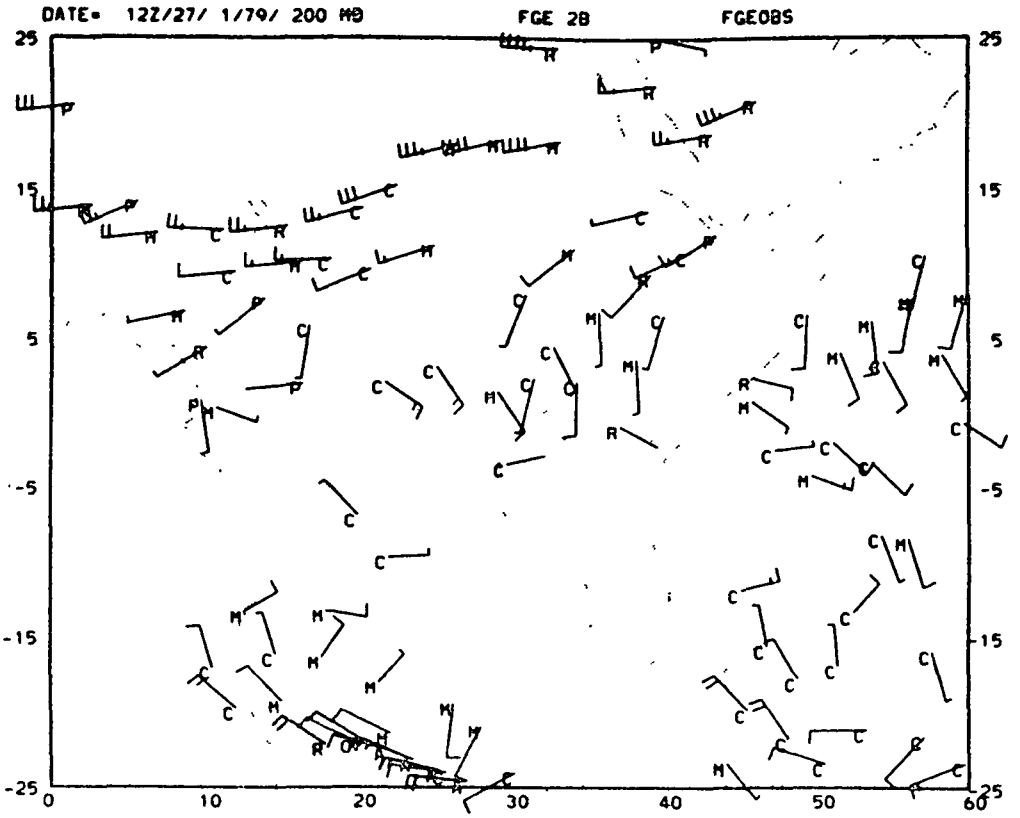

FIGURE 6 200 mb data for 1200 GMT for January 27 during SOP-1. R indicates rawin; C, cloud motion vector; M, super-ob cloud motion vector; and A, aircraft data.

characteristics of the system in the tropical atmosphere nor does it view the system as expendable.

2. The misconception that the TCLBS was solely a tropical wind observing system. Although the justification for mounting the TCLBS was to fill an important gap in the tropical troposphere, it was recognized from the start that the platforms would not remain in the tropics and that trajectories in the extratropics of the southern hemisphere would constitute a valuable addition to the data base. (Recall that in the early days of FGGE planning, there was to be a southern hemisphere constant level balloon system!) I found statements to the effect that "the TCLBS did not remain long in the tropics," as a consequence, very unfortunate.

3. From the following points of view I consider the TCLBS to have been a success. First, from a phenomenological standpoint, the detection of strong upper tropical tropospheric convergence lines (areas), the intensity of cross-equatorial flow, and the semi-inertial

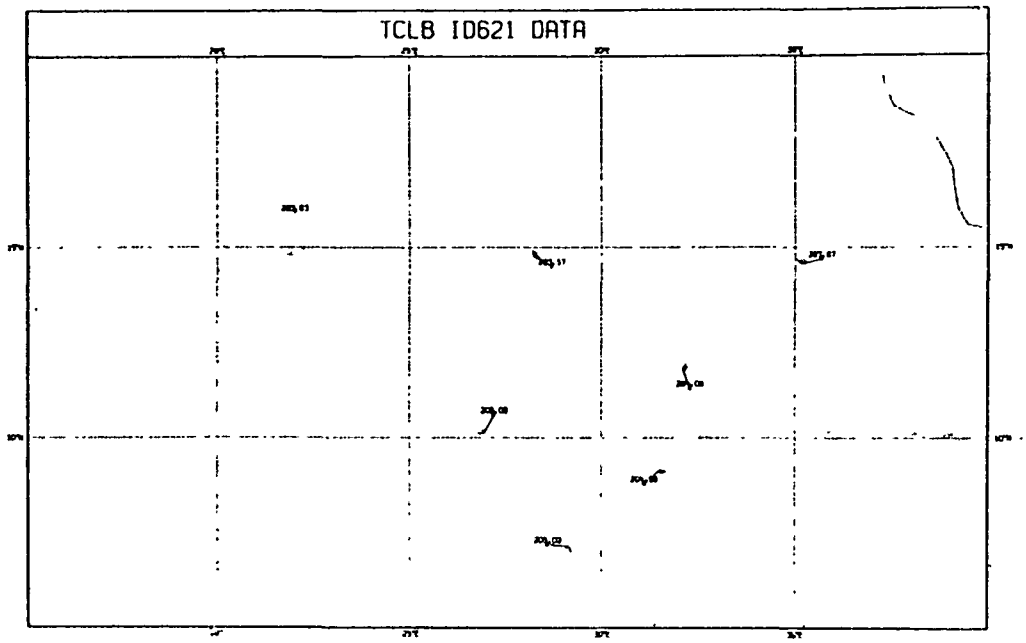

FIGURE 7 Example of inertial (?) loop by TCLBS platform. Notation 203.57, February 3, 0.57 (times 24) is GMT.

behavior of the platform trajectories are major contributions. Second, no other observing system has the proven potential of being able to delineate the southern hemisphere subtropical jet stream (and higher latitude lower stratospheric flow) with the accuracy of 2 mps.

Finally, even as an expendable system, it is a cost effective system: In 1978 dollars each wind vector cost about $16. Today, that cost in 1984 dollars would be reduced to approximately $4 using similar platform lifetimes. Elimination of the pressure cutdown device could, in a future system, significantly extend tropical lifetimes making a further reduction in cost per observation.

AIRCRAFT DROPWINDSONDE SYSTEM (ACDWS)

The ACDWS was the most logistically and technically complicated system deployed during FGGE. The deployment of that system aboard a fleet of aircraft of three different makes, operating from four remote bases, was a major accomplishment of the U.S. FGGE Project Office and the U.S. program. It should be pointed out that, like the Drifting Buoy System, the ACDWS hardware had received only limited testing before the Experiment. The IIb software system used to process the drops was virtually untested at the commencement of SOP-1 operations. A summary of the numbers of sorties flown, number of sondes dropped, logistic

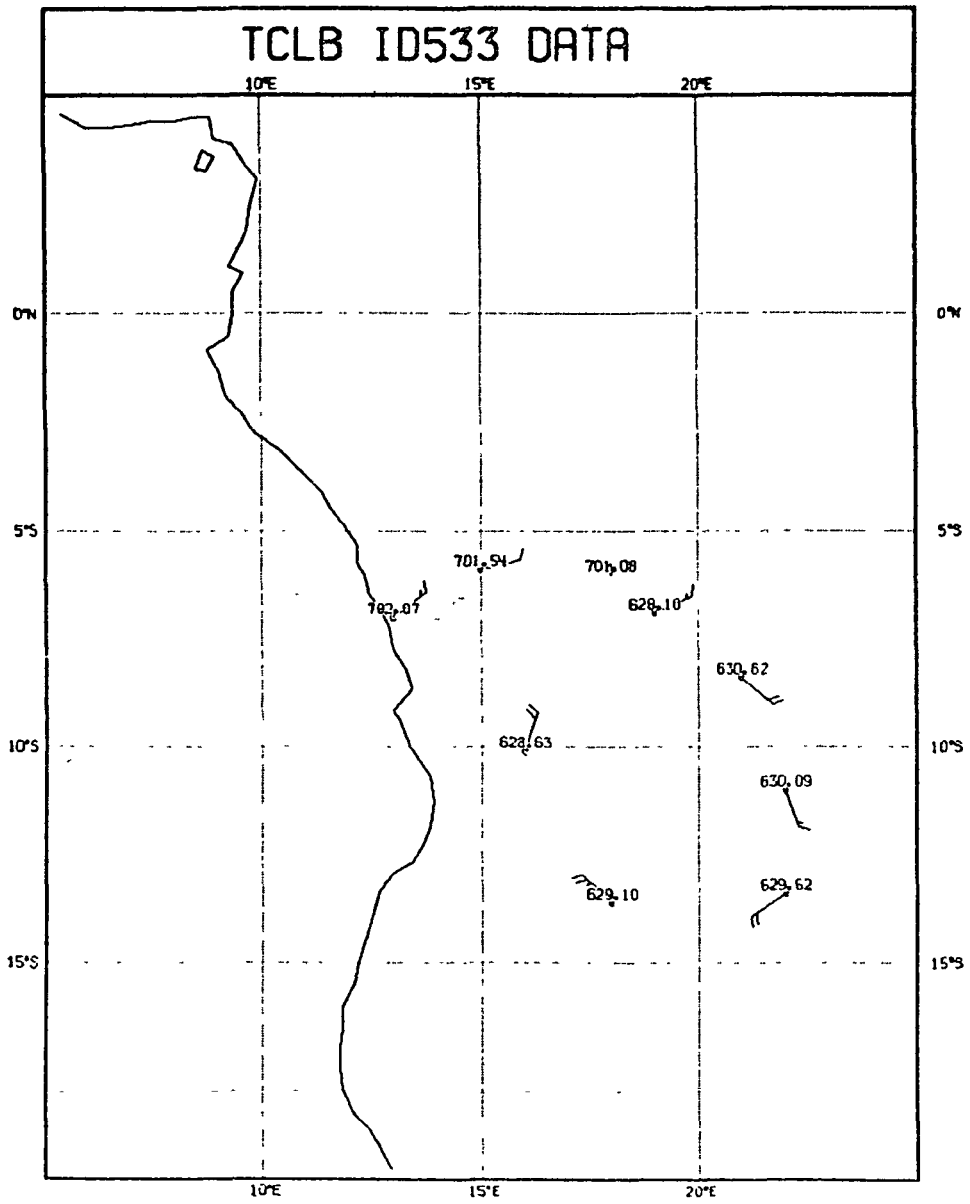

FIGURE 8 Same as Figure 7.

difficulties and successes may be found in The Global Weather Experiment, Final Report of U.S. Operations. A summary of the data processing and ACDWS omega windfinding may be found in Julian (1982).

In this contribution, I will concentrate on two particular features of the ACDWS winds: First, the quality of the Main versus the Final

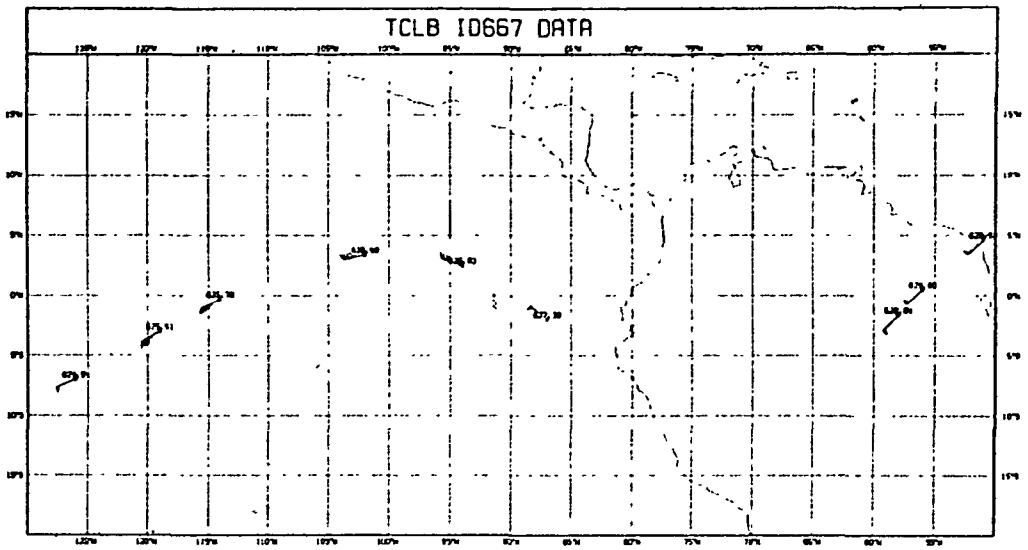

FIGURE 9 Portion of TCLB platform 667 showing possible pure inertial trajectory. Code same as Figure 8.

IIb data sets and, second, the assimilation of the Main (Final) IIb data by the ECMWF (GFDL) IIIb schemes.

Very briefly, omega windfinding is a relatively complex process compared with radar or radio-direction finding techniques, and the assessment of quality or uncertainty, while quantitative, is more involved. Sources of uncertainty may be divided into those external to the system, mainly ascribable to various kinds of unsteadiness in the omega navigation net, and those internal to the system, mainly electronic and antenna noise. The latter may be quantified so that a minimum uncertainty or error can be attached to each wind vector. The former source of error is quite small save two important instances. One of these, the occurrence of sudden ionospheric disturbances caused by solar activity, was significant but could be (and was) easily monitored. In spite of some apprehensions about deploying a sensitive system during sunspot maximum, only 10 drops out of nearly 5000 processed had to be eliminated because of the sudden ionospheric disturbances.

The other sources of external error however proved to be unsuspected, difficult to monitor, and much more serious on its impact on the Main Level IIb data set. Normal VLF propagation involves a standing wave mode propagating between the earth's surface and the ionosphere, and normally dissipation of the electromagnetic wave is such that received signals from a great-circle least distance path predominate at any locality--that is, the direct wave signal strength is much greater than the wave propagating through the antipodal point (e.g., Figure 10). Enough was known or predicted by waveguide theory

FIGURE 10 True azimuthal plot of sonde-omega transmitter geometry for representative drop in the Arabian Sea. Great circle least-distance paths for all eight omega stations are shown. The circle represents the solar terminator at about 1300 LST.

in 1978 to stipulate that eastward daytime propagation was favored over westward propagation. As a result, the data processing algorithm used to derive the Main IIb set did not use omega signals from stations occurring at a great circle distance greater than 140°E of the drop. However, quick feedback from MONEX dropwindsonde users at Florida State University pointed to some serious problems with vectors from drops in the Indian Ocean. Subsequent examination of these drops and detailed recalculations elicited the fact that, on occasion, the eastward

propagating signals instead of being dominant over 220° of arc (as above) were dominant over as much as 250°. (For the example shown in Figure 10, Hawaii propagates anomalously instead of as shown.) This longpath or anomalous propagation, as it is termed, is especially problematic because, save by recalculating the winds with and without a suspect signal, it cannot be detected uniquely by the ACDWS system itself. (This is not the case in the TWOS-Navaid system because of the availability in that system of direct (local) omega recorded by the ship itself). A survey of the magnitude of the problem was undertaken by the ACDWS data processing group at NCAR with the results given in Table 3. A number of solutions were investigated, and ultimately all drops for the Final Level IIb were recalculated with an algorithm that uniformly eliminated certain omega stations for each of the sortie routes flown. This solution accepted maximum impact of degraded omega geometry and was necessary because of the impossibility of detecting the anomalous propagation uniquely for each drop. Thus it should be emphasized that ECMWF IIIb, utilizing Main IIb, was assimilating less accurate data than GFDL (and GLAS) IIIb, which used the recalculated data.

TABLE 3 Summary of Vector Differences, Original (Main IIb) and Reprocessed (Final IIb) Solutions

SOP1

Region	Total # Drops	# Reprocessed (percent)	% with vector difference 2 mps	4 mps
Arabian Sea 20-73 E	300	221 (42)	56	32
Bay of Bengal 73-106E	391	103 (26)	20	10
Hawaii, central Pacific 140E - 120W	943	264 (28)	25	19
E. Pacific 120-190	303	170 (56)	42	18
W. Atlantic 90-20W	113	80 (71)	18	3
E. Atlantic 20W-20E	66	56 (85)	53	12
	2125	894 (42)	31	18

Assimilation

An assessment of the fit to the Level IIb ACDWS data by the Level IIIb analyses is made difficult because of the varying uncertainties of the ACDWS vectors. At least in the ECMWF system, the coded uncertainties were used as specific observation errors by the optimum interpolation formulation. Thus to do a thorough job of quantitative assessment, the observed minus analyzed vectors should be stratified by the uncertainties of the observed vectors, and this has not been done. Qualitative and some quantitative assessment suggests that ACDWS data was accommodated in the ECMWF assimilation scheme less "tightly" than conventional rawin- or radar-determined winds. This should be the case because of the errors introduced by the longpath anomalous propagation phenomenon. However, a case study can be shown that serves to illustrate some points of the Level IIIb assimilation of ACDWS data.

The case selected is for February 2, 0600 GMT, for the section 60° to 120°E. This case was chosen because the maximum difference between the ACDWS wind vectors, Main and Final IIb, occurs in the Indian Ocean. Figure 11a shows the Main IIb, and Figure 11b the reprocessed Final IIb. In this case, all the vectors eastward at 80°E are different, and although the speeds are small, rather significant changes in the observed directions occur, particularly in the complex 0 to 10°S, 60 to 70°E.

Evaluation: Past and Future

A thorough evaluation of the ACDWS cannot be made at present mainly because complete assimilation of the reprocessed (Final IIb) data has not been accomplished. Together with the TWOS, the aircraft dropwindsonde system provided a rigorous field test for omega windfinding. This test provided the experience and basis for the design of a shipboard omega balloon-sonde system presently being tested in high latitudes of the northern hemisphere. In the future, there is the possibility of deploying these sounding systems from ships of opportunity in the tropics as well as in the higher latitudes. It is not practical to consider aircraft dropwindsondes as an operational system, but the system is, and will be, used in tropical storm and hurricane reconnaissance.

TROPICAL WIND OBSERVING SHIPS (TWOS)

Two different wind measuring systems were used for the TWOS component of the TOS. One, referred to in FGGE jargon as TWOS-Navaid, employed a standard balloon-borne sonde with the omega windfinding system used to track the balloon. The principles of calculating winds are identical to the Aircraft Dropwindsonde System, although different algorithms were used. Since the sondes were launched from slow moving or stationary ships, the TWOS-Navaid system recorded local, or direct, omega signals together with sonde-retransmitted omega. This

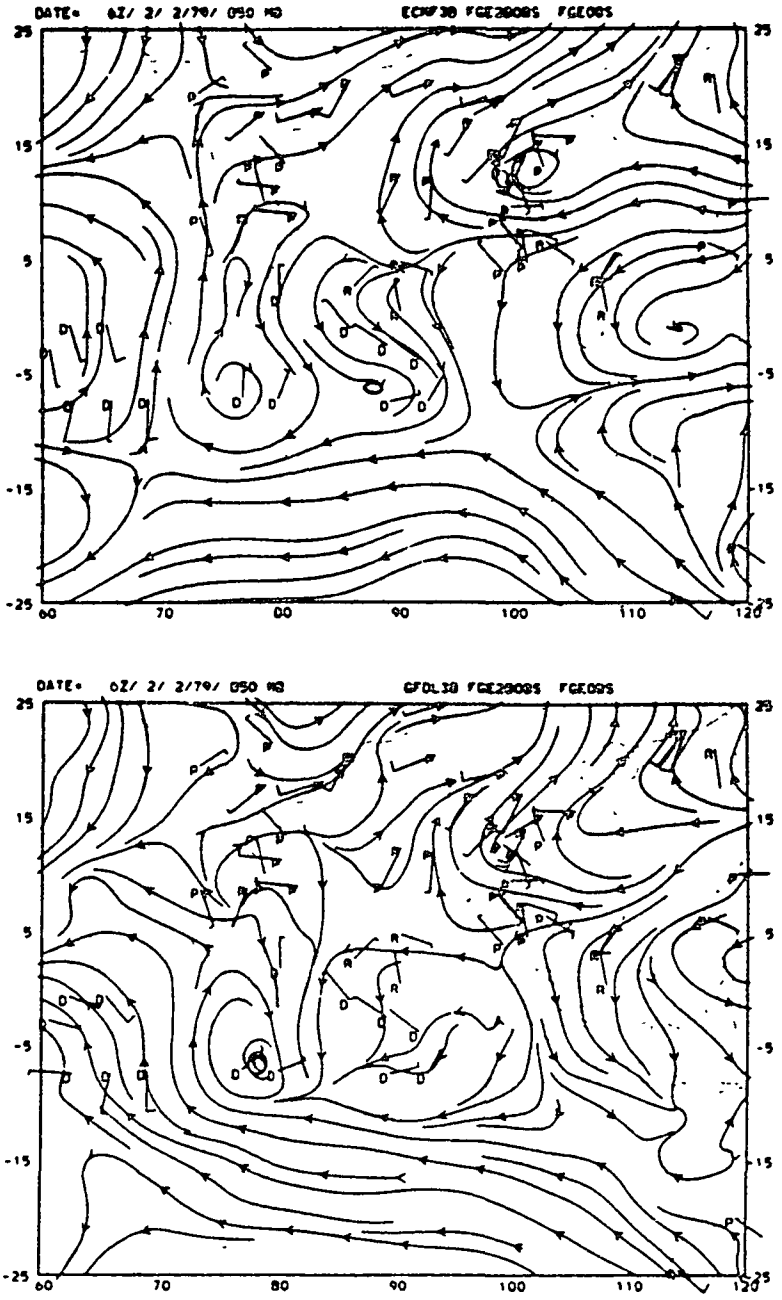

FIGURE 11 (a) Main IIb dropwindsonde data (D), rawin (R), and Pibal (P) observations for February 2, 0600 GMT, 850 mb. Superimposed is the ECMWF IIIb streamline analysis. (b) Same as (a) but for reprocessed dropwindsonde data (Final IIb) and GFDL streamline analysis.

significant difference made the selection of omega signals for wind calculation much more straightforward than in the dropsonde system. The large aircraft velocities precluded using local omega for this purpose.

The ships contributed by the Soviet Union to the TOS carried a radar-tracking wind measurement system, presumably comparable to that used in GATE. Little is known about the quality of these TWOS-radar observations. Subjective comparison with wind vectors obtained by other observing systems suggests that no major difficulties occurred. The agreement in such comparisons is generally good.

CONCLUSIONS

The Tropical Observing System provided unprecedented coverage of the tropics by employing a variety of observing systems and techniques. Evaluation of the data base produced by the mix of systems reveals that the inter-system compatibility is good to excellent. Problems center on the correct height assignment of satellite-observed cloud motion vectors, and on uncertain wind vectors from the aircraft dropwindsonde system. The TOS produced large numbers of observations of single-level wind vectors in the upper and lower troposphere. Evaluation of these data together with wind profiles reveals two characteristics of the tropical troposphere which present special problems for four-dimensional assimilation schemes. The first of these is the existence in the tropical upper troposphere of circulation systems with a very small apparent vertical depth. The resulting wind shears are not represented correctly by single-level wind vectors, and, in most instances, assimilation produces an aliasing to deeper vertical scales. Coupled with this representational problem is the problem of determining what modes in the tropics should be analyzed for numerical prediction purposes. The second characteristic of the tropics presenting a problem for four-dimensional assimilation is the existence of area of significant convergence/divergence (on scales that are resolved by global numerical models) associated with deep convection. Some recent progress in modifying assimilation schemes to handle these situations has been made.

ACKNOWLEDGMENT

The National Center for Atmospheric Research is sponsored by the National Science Foundation.

REFERENCES

Joint Planning Staff for GARP (1980). FGGE Operations Report, Volume No. 1, Observing System Operations, 1 December 1978 - 30 June 1979. Global Atmospheric Research Programme. World Meteorological Organization, Geneva, 78 pp.

Julian, P. R. (1982). The aircraft dropwindsonde system in the Global Weather Experiment. Bull. Amer. Meteorol. Soc. 73, 619-627.

Madden, R. A., and E. J. Zipser (1970). Multi-layered structure of the wind over the equatorial Pacific during the Line Islands Experiment. J. Atmos. Sci. 27, 336-342.

U.S. FGGE Office (1980). Final Report of U.S. Operations. National Oceanic and Atmospheric Administration, Washington, D.C.

OMIT

2. ANALYSIS AND ASSIMILATION TECHNIQUES

Organizer	Roger W. Daley
Session Chairman	Paul R. Julian
Speaker	Roger W. Daley
Rapporteur	David Baumhefner

OBJECTIVE ANALYSIS AND ASSIMILATION TECHNIQUES USED FOR THE PRODUCTION OF FGGE IIIb ANALYSES

R. Daley,[1] A. Hollingsworth,[2] J. Ploshay,[3]
K. Miyakoda,[3] W. Baker,[4] E. Kalnay,[4] C. Dey,[5]
T. Krishnamurti,[6] and E. Barker[7]

ABSTRACT

A set of tables has been prepared that allows side-by-side comparison of the characteristics of six data assimilation systems (ECMWF, GFDL, GLAS, NMC, FSU, and NEPRF) used to produce FGGE IIIb analyses.

INTRODUCTION

The main[8] FGGE IIIb analyses were produced by two institutions--the European Centre for Medium Range Weather Forecasts (ECMWF) and the Geophysical Fluid Dynamics Laboratory (GFDL). Both these analysis sets are complete and cover the whole FGGE year. In addition, partial FGGE IIIb analysis sets have been produced in the United States by four other institutions--the Goddard Laboratory for Atmospheric Science (GLAS), the National Meteorological Center (NMC), Florida State University (FSU), and the Naval Environmental Prediction Research Facility (NEPREF).

Analysis and assimilation schemes are highly complex and, in general, not as well-documented as they should be. This is an attempt to summarize compactly the most important features of the six FGGE IIIb assimilation schemes. A system of seven tables, which cover analysis archiving, observation types, quality control, data assimilation

---

[1]National Center for Atmospheric Research (NCAR)
[2]European Centre for Medium Range Weather Forecasts (ECMWF)
[3]Geophysical Fluid Dynamics Laboratory (GFDL)
[4]Goddard Laboratory for Atmospheric Science (GLAS)
[5]National Meteorological Center (NMC) Camp Springs, Md.
[6]Florida State University (FSU) Tallahassee
[7]Naval Environmental Prediction Research Facility (NEPRF) Monterey, Calif
[8]Both ECMWF and GFDL have announced their intention of partially re-analyzing the FGGE data base, but this article is not concerned with this re-analysis.

cycles, assimilating models, initialization, and analysis technique, has been adopted. This format allows side-by-side comparison of each analysis and assimilation system.

It is intended that these tables serve as a quick and ready guide to the basic properties of each analysis scheme. If more details are required, a table of references is also appended.

TABLE 1 Analysis Archives

Institution	Grid	Pressure Levels	Variables	Time Period(s)	Format	Frequency	Availability
ECMWF	Standard	Standard + 70,30,20 P_{msl}(3)	Standard (RH,ω,T from initialized analyses)	Standard	Standard	Standard	Standard
GFDL	Standard	Standard + 950,900,800 30,5,2,.4	Standard + mixing ratio, surface wind stress	Standard	Standard	Standard	Standard
GLAS	4° × 5° lat/long	Standard +70 missing 10	Standard + diabatic heating	SOP1 SOP2 July 1979	GLAS IIIb	00, 06, 12, 18	GLAS
NMC	2.5°×2.5° lat/long	Standard	Standard ω through 100 mb	14-20 Nov 1979 plans for SOP1 & SOP2	NMC Office Note 84	Standard	NMC
FSU	Standard 2°lat/long 1°lat/long	Standard to 200 850 750 200 surface	Standard u, v precipitation	(1) May 1 - July 31	Standard (2)	12Z 12Z	FSU FSU NCAR
Navy (NEPRF)	2.5°×2.5° lat/long	Standard	Standard missing RH and ω	Selected cases	Standard	00, 06, 12, 18	NEPRF (not yet completed)

Standard grid - 1.875° latitude/longitude
Standard pressure levels - 1000, 850, 700, 500, 400, 300, 250, 200, 150, 100, 50, 10
Standard variables - u, v (ms^{-1}), Φ(m), RH(%) - below 300, T(°K), ω(mb s^{-1})
Standard period - December 1, 1978 - November 30, 1979
Standard format - FGGE level 3b format
Standard availability - National Climate Center and NCAR
Standard frequency - 00Z and 12Z plus 06Z and 18Z during SOP's
(1) - June 11-20, 1979, and July 1-10, 1979
(2) - Buffered binary
(3) - P_{msl} - mean sea level pressure

TABLE 2(a) Observation Types

Institution	Surface Land Ship	Rawind Pilot Balloon	Aircraft ASDAR AIDS AIREPS	TWOS NAVAIDS	Aircraft Dropwind	Constant Level Balloon	Drifting Buoys	VTPR
ECMWF	✓	✓	✓	✓	✓	✓	✓	only Dec 78 So.Hem.
GFDL	✓ + supplementary data from UK, USA + ships	✓	✓	✓	✓ reprocessed	✓	+ ✓ Antarctic buoys	✓
GLAS	✓	✓ thermister corrected above 100 mb	✓	✓	✓	✓	✓	✓ Only SOP1
NMC	✓	✓	✓	✓	✓	✓	✓	
FSU	✓	✓	✓ (1)	✓ (1)	✓ (1)	✓	✓	✓
Navy (NEPRF)	✓	✓	✓	✓	✓	✓	✓	✓

✓ Main FGGE I-b data set - Sweden
(1) delayed MONEX
ASDAR - Aircraft to satellite data relay
AIDS - Aircraft integrated data system
AIREPS - Aircraft report
TWOS - Tropical wind observing ship
VTPR - Vertical temperature profile radiometer

TABLE 2(b) Observation Types

Institution	LIMS	TIROS-N microwave infrared	Satellite Cloud Track Winds (2)	Other	Data Cut-Off	Comments
ECMWF		✓ (1)	(4)		3 months	No MONEX or WAMEX data
GFDL	No data inserted at top 2 levels	✓ + US special effort	✓ some reprocessed by Wisconsin	PAOBS	(3)	
GLAS		✓ (1c)	No LMD, HIMAWARI winds reprocessed Wisconsin			
NMC		✓ (1a,b)	✓		✓	
FSU	✓	✓ (1)	✓	IIc + satellite precip estimates		No WAMEX
Navy (NEPRF)		✓	✓		1 year	

✓ Main FGGE II-b data set
(1) Microwave not used (a) over land, (b) 20°N - 20°S, (c) over ocean in heavy precipitation.
(2) NESS, Wisconsin, LMD, METEOSAT, HIMAWARI
Main FGGE II-b data set
(3) Includes UK and US supplemental data sets; US special effort data; Japanese-Wisconsin satellite winds; summer MONEX (FSU)
(4) GOES-Indian Ocean winds processed by DFVLR, (FRG) at 06 GMT and 18 GMT, eliminated after 15 January, 1979. All other cloud wind vectors from main FGGE IIb data set were used.
LIMS - Limb infrared monitor of the stratosphere
NESS - National Environmental Satellite Service
LMD - Laboratoire de Météorologie Dynamique (Paris)
PAOBS - Synthetic (bogus) southern hemisphere data provided by Australia

TABLE 3 Quality Control

Institution	Preassigned quality indication (1)	Preliminary checks				First guess check (2)	Buddy check (3)	Other
		Location duplicates format	Time	Climatology (gross)	Vertical consistency			
ECMWF	✓	✓(6)	✓(4)	✓	✓	✓	✓(5)	Check datum against analysis performed without that datum
GFDL	✓	✓		✓	✓	✓	✓	Checks data against previous analyses at 00Z - 12Z
GLAS	✓	✓			✓ height only	✓	✓	Additional drifting buoy checks (P. Julian)
NMC	✓	✓				✓	✓	
FSU	✓	✓	✓ (4)	✓	✓	✓	✓	
Navy (NEPRF)	✓	✓	✓		✓	✓	✓	Check datum against analysis performed without that datum

(1) Preassigned quality indications are already attached to the FGGE II-b data set.
(2) First guess check - check of observation against forecast.
(3) Buddy check - comparison of a datum with nearby observations.
(4) Corrections are made to off-time data.
(5) Redundant observations are "super-obbed."
(6) Corrects incorrectly located stations, eliminates ships over land and erroneous buoys.

TABLE 4(a) Assimilating Model Basic Information

Institution	Horizontal Discretization	Vertical Discretization	Time Discretization	Model Variables	Topography	Horizontal Dissipation
ECMWF (1)	Second order Arakawa C grid 1.875°	Sigma 15 levels .996-.025	Semi-implicit Δt = 15 min filter = .05	T,u,v,p_s q	Moderately smoothed	$k\nabla^4$ $k=9\times10^{15}m^4s^{-1}$
GFDL	Spectral R30	Sigma 18 levels .998-.0022	Semi-implicit 8min$\leq\Delta t\leq$25min	T,ζ,D, p_s, q	Spectrally truncated	$k\nabla^2$ $k=4.96\times10^4m^2s^{-1}$
GLAS	Fourth order 4° x 5°	Sigma 9 levels .945-.065	Matsuno Δt = 10 min.	T,u,v,p_s, q	Smoothed with 8th order digital filter	16th order digital filter (Shapiro)
NMC	Spectral R30	Sigma 12 layers with mid-points .962 - .021	Semi-implicit Δt = 17 min. filter = 0.04	T,ζ,D, q,P_s	Spectrally truncated R30	$k\nabla^4$ $k=6\times10^{15}m^4s^{-1}$
FSU	Not applicable					
Navy (NEPRF)	Spectral T40 and fourth order 2.4° x 3°	Sigma 12 levels 1. - .01	Semi-implicit Δt = 10 min.	T,ζ,D,p_s,q —— T,u,v,p_s,q	Envelope orography	Non-linear Smagorinsky

T (temperature), ζ (vorticity), D (divergence), p_s (surface pressure), q (mixing ratio), u, v (wind components)

(1) at 10, 20, 30 mb the first guess was climatology from 1 December 78 to 10 January 79. Thereafter persistent wind shear and thickness were added to model's 50 mb (ϕ, v) to obtain first guess.

TABLE 4(b) Assimilating Model Physical Parameterization

Institution	Boundary Layer Flux	Sea Surface Temperature	Land Surface Temperature	Convective Parameterization	Radiation	Vertical Dissipation
ECMWF	Monin-Obukhov	Specified from Climatology	Predicted land surface temperature	Kuo scheme	Fully interactive clouds, no diurnal cycle	Mixing length function of Ri
GFDL	Monin-Obukhov	Specified from Climatology	Surface heat balance, diurnal cycle	Moist convective adjustment	Climatological clouds, diurnal cycle	Mixing length
GLAS	Bulk aerodynamic	Specified from Climatology	Surface heat balance, diurnal cycle	Arakawa scheme	Fully interactive clouds, diurnal cycle	Very weak linear diffusion
NMC	Bulk aerodynamic	Specified from climatology	No land surface heat or moisture flux	Kuo scheme	None	None
FSU	Not applicable					
Navy (NEPRF)	Bulk aerodynamic	Analyzed	Surface heat balance	Arakawa scheme	Fully interactive clouds diurnal cycle	Linear diffusion

Ri (Richardson number)

TABLE 5 Initialization

Institution	Procedure
ECMWF	NNMI - adiabatic Machenhauer - 2 iterations 5 of 15 vertical modes adjusted
GFDL	NNMI - adiabatic Machenhauer - 4 iterations 7 of 18 vertical modes adjusted 6 hour frequency cut-off
GLAS	None (Matsuno time differencing does damp out gravity modes during model integration)
NMC	NNMI - adiabatic Machenhauer, 2 iterations 4 of 12 vertical modes adjusted
FSU	Not applicable
Navy (NEPRF)	NNMI - Baer-Tribbia

NNMI - nonlinear normal mode initialization

TABLE 6(a) Analysis Technique

Institution	Basic Technique	Coordinate System Horizontal + Vertical	Imposed Dynamic Constraints on analysis increments	Method of Data Insertion See Fig. 1	Number of iterations at each insertion	Time window
ECMWF	3-dimensional multivariate OI of OMFD	Local pressure	Non-divergence, geostrophy in extratropics	discrete	1	6 hours (corrected for off time)
GFDL	Horizontal and vertical univariate OI of OMFD	Local pressure	None	continuous	1	2 hours
GLAS	Horizontal univariate SCM of OMFD	Local Pressure	Geostrophic correction of first guesss wind field in extratropics	discrete	3	6 hours
NMC	3-dimensional multivariate OI of OMFD	Local pressure	Non-divergence, geostrophy in extratropics	discrete	1	6 hours
FSU	(1)	Local pressure	None	discrete	1	6 hours (corrected for off time)
Navy (NEPRF)	3-dimensional multivariate OI of OMFD	Local pressure	Non-divergence, geostrophy in extratropics	discrete	1	6 hours

OI - optimal interpolation
SCM - successive correction method
OMFD - observation minus forecast differences
analysis increments - analysis minus forecast differences
(1) - first guess obtained from ECMWF IIIb analyses and univariate SCM used on MONEX observations minus first guess

TABLE 6(b) Analysis Technique

Institution	Functional dependence of analysis weights	Horizontal dimensions of local analysis "bin"	Vertical dimension of "bin"	Maximum number of observations per "bin" + max. search radius	Interpolation of analysis back to model coordinates	Miscellaneous
ECMWF	ABCD	660 × 660 km	whole column unless more than 192 observations	192 obs ≈ 2000 km	interpolation of analysis values (full field)	analysis increments in each "bin" are averaged to produce global analysis
GFDL	ABC	1 gridpoint	distance between 3 consecutive pressure levels	8 obs 250 km	interpolation of analysis increments	no insertion above σ =.052
GLAS	AB	1 gridpoint	adjacent pressure levels	no limit 800 km	interpolation of analysis increments	search radius is data-density dependent
NMC	ABCD	1 gridpoint	4 mandatory pressure levels above and below analysis level	20 obs 1500 km	interpolation of analysis increments	no data inserted in top σ layer (midpoint = σ .021)
FSU	AB	1 gridpoint	Procedure is strictly horizontal	> 100 obs 2 grid intervals	not applicable	
Navy (NEPRF)	ABCD	1 gridpoint	Whole column unless more than 200 observations	200 obs 900 km	interpolation of analysis increments	

bin - the local three-dimensional volume in which the analysis is performed
A - assumed data quality
B - distance between observation point and analysis point
C - distance to adjacent observations and their quality
D - assumed accuracy of forecast

TABLE 7 Reference and Addresses

Institution	Contact person	References
ECMWF	Dr. A. Hollingsworth ECMWF Shinfield Park Reading, Berks. RG2 9AX England	Lorenc, A., 1981; A global 3-dimensional multivariate statistical interpolation scheme. Mon. Wea. Rev., 109, 701-721. Bengtsson, L., M. Kanamitsu, P. Kallberg and S. Uppala, 1982: FGGE 4-dimensional data assimilation at ECMWF. BAMS, 63, 29-43. Louis, J., 1981: ECMWF forecast model documentation
GFDL	Mr. J. Ploshay or Dr. K. Miyakoda GFDL Princeton University P.O. Box 308 Princeton, NJ 08542	Ploshay, J., R. White and K. Miyakoda, 1983: FGGE III-b daily global analyses - Part I. NOAA Data Report, ERL GFDL-1, GFDL, Princeton, New Jersey
GLAS	Dr. W. Baker Laboratory for Atmos. Sciences Goddard Space Flight Center Code 911 Greenbelt, MD 20771	Baker, W., 1983: Objective analysis and assimilation of observational data from FGGE. Mon. Wea. Rev., 111, 328-342.
NMC	Dr. C. Dey NOAA Nat.Meteor.Center W/NMC 22 World Weather Bldg. Room 204 Washington, DC 20233	Dey, C. and L. Morone, 1984: Evolution and performance of the National Meteorological Center Global Data Assimilation Scheme: January-December, 1982. (Submitted to Mon. Wea. Rev.)
FSU	Prof. T. Krishnamurti Dept. of Meteorology and Oceanography Florida State Univ. Tallahassee, FL 32306	Krishnamurti, T., R. Pasch, H. Pan, S. Chu, and K. Ingles, 1983: Details of low latitude medium range numerical weather prediction using a global spectral mode, 1: Formation of a monsoon depression. J. Meteor. Soc. Japan, 61, 188-206.
Navy (NEPRF)	Dr. E. Barker Naval Environmental Prediction Research Facility Monterey, CA 93940	Barker, E., 1982: A comparison of two initialization methods in data assimilation. Naval Environmental Prediction Research Facility. Tech. Report 80-06.

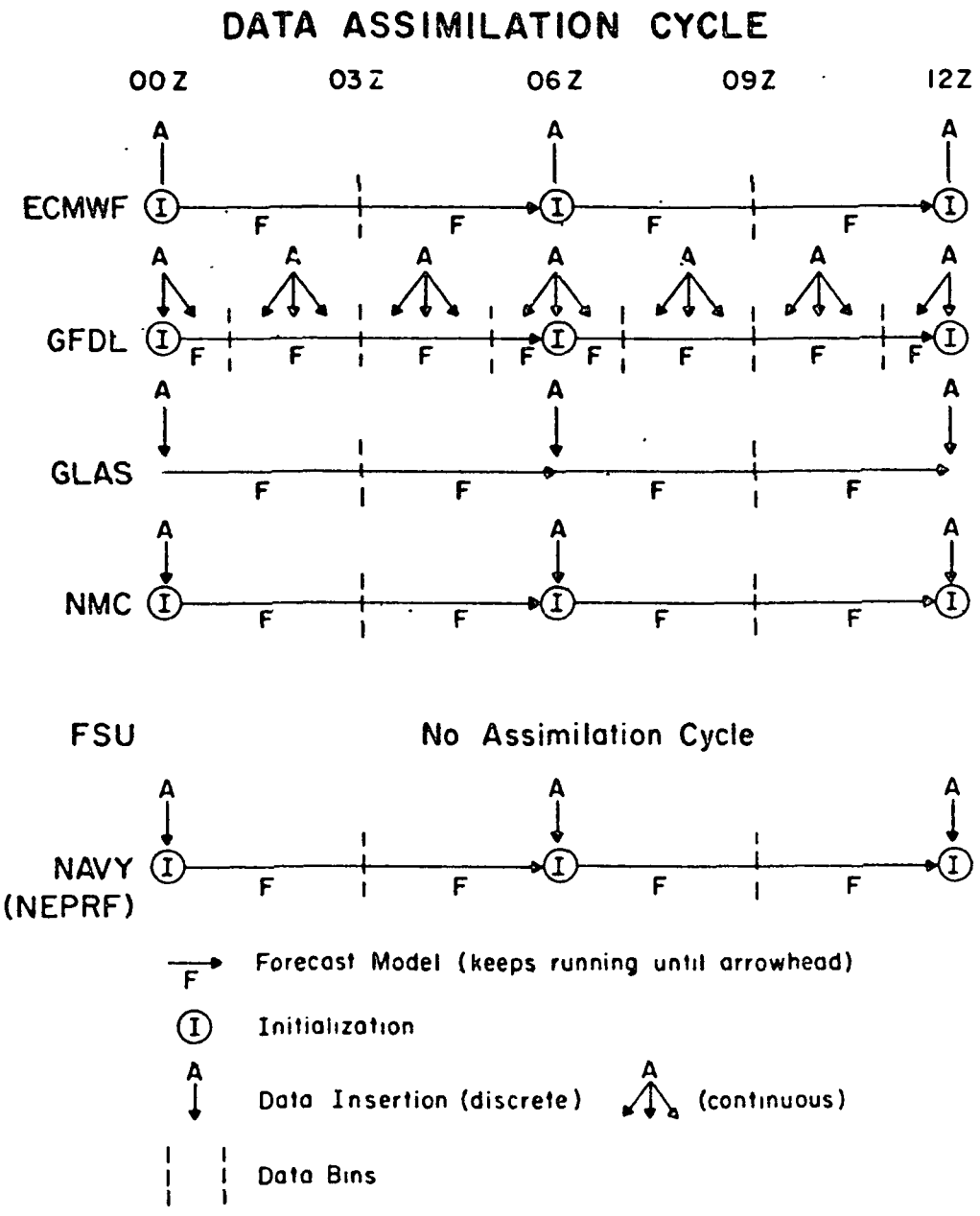

FIGURE 1 The data assimilation cycle for the six data assimilation schemes. A single 12-hour segment is shown. In a given data bin all the data for a 2-hour period (GFDL) or a 6-hour period (all other schemes) will be assimilated into the analyses.

omit

3. IMPACTS ON FORECASTS (ECMWF)

Organizer	Eugenia Kalnay
Session Chairman	Lennart Bengtsson
Speaker	Anthony Hollingsworth
Rapporteur	Ronald D. McPherson

D6

RESULTS FROM TWO RECENT OBSERVING SYSTEM EXPERIMENTS

S. Uppala, P. Kallberg, A. Hollingsworth, and S. Tibaldi
European Centre for Medium Range Weather Forecasts

ABSTRACT

Two Observing System Experiments have been carried out at ECMWF. The impact of various observing systems have been examined for two periods during the FGGE year: November 8-9, 1979 (OSE-1) and February 22 to March 7, 1979 (OSE-II). Attempts have been made to understand the effect of the observing systems on both the analyses and the quality of the short- and medium-range forecasts.

The results confirm that the impact of a particular observing system (e.g., SATEM) is dependent on the level of synoptic activity present in the areas where this particular observing system is the main source of meteorological information. SATOB data are also shown to be important for the analyses of tropical regions, whereas SATEM data are of paramount importance for the extratropical analyses over ocean areas. Aircraft data, where available, are an invaluable addition to the global observational data base. These results therefore demonstrate clearly the value of each of the observing systems. The fact that, in particular circumstances, there may be some redundancy between the systems is a strength rather than a weakness of the composite global observing system.

INTRODUCTION

The purpose of the Observing System Studies carried out at ECMWF is to estimate the information content of individual components of the Global Observing System as to their impact on objective analyses, short-range and medium-range numerical weather products, and ultimately to contribute to the design of a "best-mix" system for operational use in the coming decade. Observing system studies fall into two broad categories--Observing System Experiments (OSEs) and Observing System Simulation Experiments (OSSEs).

At ECMWF an OSSE has been initiated in collaboration with several European and non-European institutions in order to evaluate the usefulness and reliability of OSSEs. However the main emphasis at ECMWF has recently been on completing two OSEs using FGGE data. The first of these, OSE-I, covers the period November 8 to 18, 1979, and

the results from the experiments were presented last year and described in ECMWF/SAC(83)5. The second set, OSE-II, consisted of similar experiments but for the period February 22 to March 7, 1979. This paper will concentrate on OSE-II, although results from OSE-I will be used throughout to evaluate the experiment.

Our OSE work can be divided into two broad categories:

1. The study of the effect of the addition of a single observing system to a minimum system which is taken as the conventional data distributed on the GTS--SYNOP, SHIP, TEMP, PILOT, and DRIBU. The systems to be added to this minimum system are SATEM or SATOB or AIREP/AIDS/ASDAR.
2. "Best-mix" studies where a single observing system is withdrawn from the maximum composite observing system.

Initially, studies of the second category were undertaken. However, the results of these studies indicated that a full understanding required consideration of the simple single-system problems that fall in the first category. This report will be mainly devoted to such studies.

OSE work is difficult because the results may depend on the assimilation and forecast system used, the synoptic situation, and possibly on the redundancies in the data in certain regions. We shall refer to examples of these difficulties later in this paper.

Another major difficulty, characteristic of OSE-type studies, is that when one is studying the effect of moderate changes in the accuracy of the analyses, the signal in the verification of the forecasts against the true atmospheric state is sometimes weak after the first two days. This is because the model errors grow so rapidly that they can swamp the signal from the analysis error. Figure 1 shows an estimate for the relative contributions to total mean square forecast error of the model error and the analysis error in analysis comparison experiments (Arpe et al., 1984). The analysis error is a relatively large contributor to total forecast error in the short-range forecasts (day 0 to 1.5) and in the late medium-range forecasts (after day 5). In the intervening period the approximately linear growth of model error is so rapid that it can mask the effect of the roughly exponential growth of analysis error in the verifications against reality. For this reason, statistics on the forecast divergences are a useful tool in studies of data impact. This also has as a consequence that a true appreciation of the significance of analysis differences and data impact can only be had by a combination of detailed synoptic investigation and the application of available objective tools.

THE SYNOPTIC SITUATION, DATA COVERAGE, AND EXPERIMENTAL SCENARIOS

The selection of the period for OSE-I, November 8 to 19, 1979, was based on good data coverage (there were two polar orbiting satellites) and the marked activity over the Pacific for the FGGE winter. Figure 2 shows the mean circulation at the surface and 500 mb during this

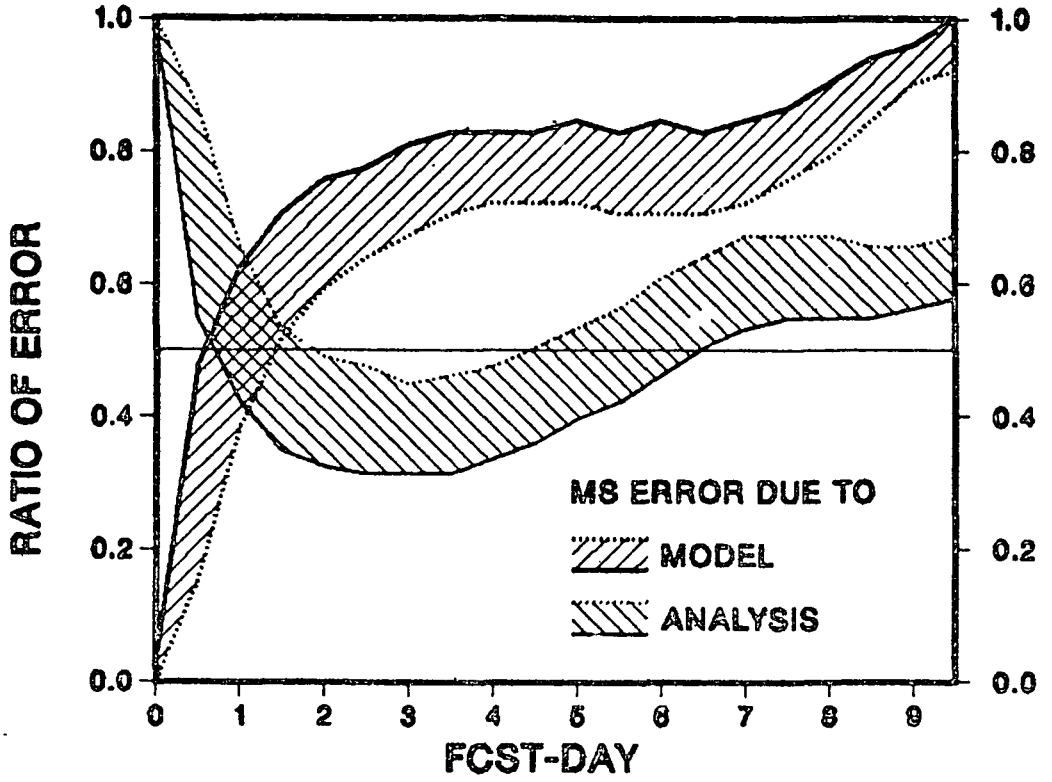

FIGURE 1 Relative contribution of analysis error and model error to the forecast error as a function of forecast time.

period. The intense activity over the Pacific is connected with the movement of the deep trough toward North America. However over the North Atlantic, the flow is relatively blocked; further east there is a deep trough extending to the Mediterranean.

A second set of experiments, OSE-II, was performed in order to see if the conclusions based on OSE-I are valid for an independent period. The period used, February 22 to March 7, 1979, was chosen because of its relatively high activity for the FGGE winter over the eastern North Atlantic and western Europe. Another reason is that it had different observational characteristics since it belonged to the Special Observing Period I, and thus contains data from special platforms that were mainly in the tropics. Also, there was only one polar orbiting satellite. Figure 3 shows the mean PMSL and 500 mb height fields for the period. Note that at the surface the Aleutian and Icelandic lows are very distinctive. At 500 mb the mean flow over the Pacific and Atlantic is relatively zonal, and this indicates that during OSE-II there is generally less activity than during OSE-I. This is confirmed by Figure 4 which shows the variability of the 500 mb height during OSE-I and OSE-II. In the northern hemisphere it is clear that there is

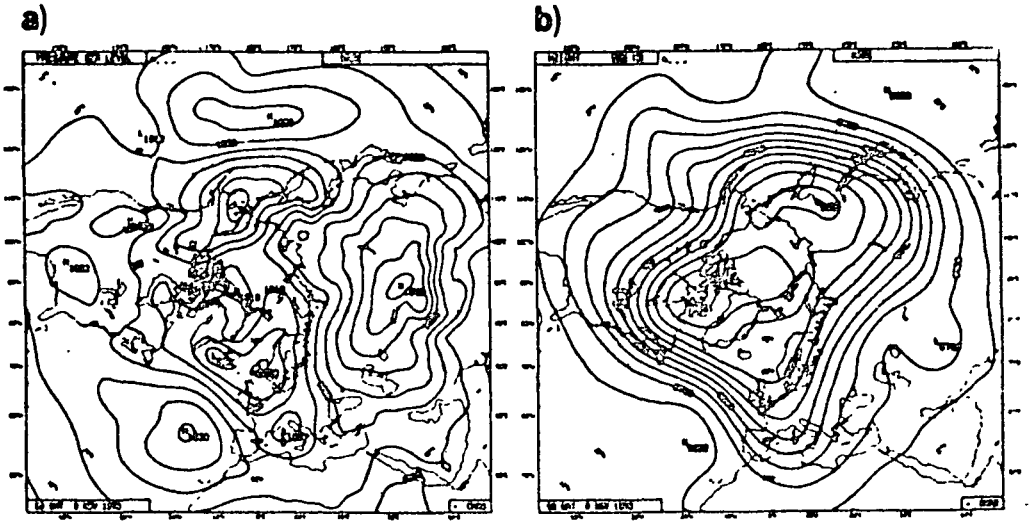

FIGURE 2 Time averaged mean sea level pressure (a, left) and 500 mb height (b, right) for OSE-I, for the northern hemisphere.

much more activity over the oceans in OSE-I than in OSE-II. This is particularly true over the eastern and western Pacific, and over the North Atlantic. It is also worth mentioning that preceding OSE-II there was a strong stratospheric warming that split the polar vortex.

The difference in the activity between the two OSE periods will, as can be seen later, be reflected in the quality of the forecasts using different observational scenarios. The space-based observations--SATEMs, SATOBs, and aircraft data--will be of greater importance when the main activity occurs in areas where they are the main source of observations.

As will be shown later, neither SATEM nor SATOB data greatly influenced forecast quality during OSE-II. The reason may be associated with the gap in the SATEM data over the eastern Pacific, which is apparent in the data used for the 0000 GMT analyses during this period (all forecasts were run from 0000 GMT analyses). The gap is clearly illustrated in Figure 5c, and comparison with Figure 4 shows that it coincides with a particularly active region. Examination of the sounding around the gap reveals that many of them are microwave soundings which are given a low weight in the analysis scheme. As a comparison, a typical 1200 GMT SATEM coverage is also shown in the same figure. During OSE-I, forecasts were run from both 0000 and 1200 GMT analyses, and Figures 5a and 5b also show typical SATEM coverages at these hours. Clearly, the Pacific is well covered at both times, while sometimes the Atlantic has only a few SATEMs.

During OSE-I, 10-day forecasts were run from selected dates and times: November 1000 GMT, 1100 GMT, 1200 GMT, 1300 GMT, 1400 GMT, 1600 GMT, and 1800 GMT. In all, there are seven forecasts.

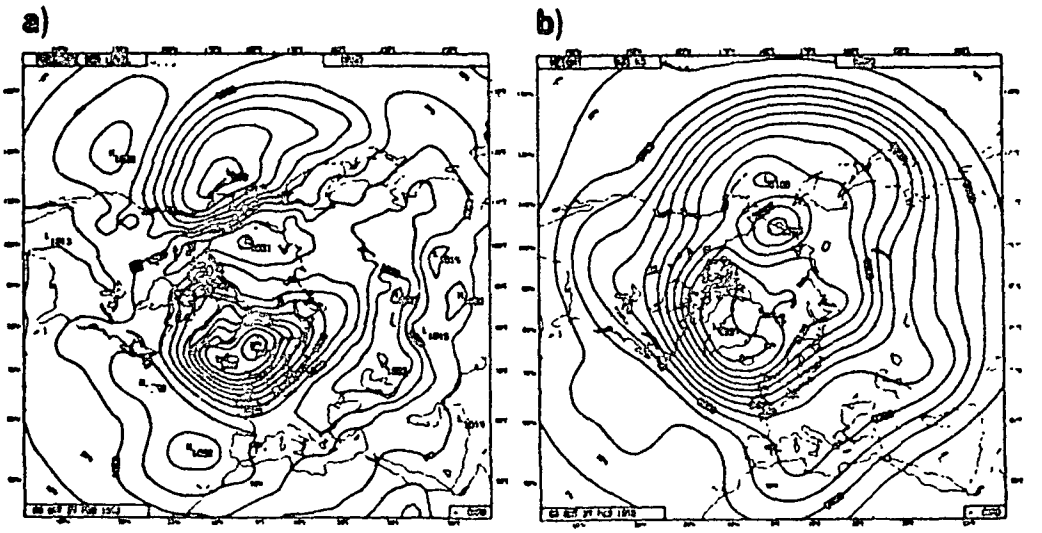

FIGURE 3 Time averaged mean sea level pressure (a, left) and 500 mb height (b, right) for OSE-II, for the northern hemisphere.

For OSE-II, 10-day forecasts were run from 0000 GMT data from 9 consecutive days between February 27 and March 7.

Table 1 gives a list of all experimental configurations run for both OSEs and their characteristics.

IMPACT OF THE DATA ON THE ANALYSES

We now show examples of the impact of each observing system (aircraft data--denoted by ACFTs, SATOBs, and SATEMs) on the analyses. Figures 6 and 7 show the effect on the mean 250 mb wind field of (1) all three space-based platforms together, (2) ACFTs alone, (3) SATOBS alone, and (4) SATEMs alone, when they are added to the minimum system for both OSE-I and OSE-II. The ACFT data support the SATOB data in the tropics, and all three support each other in the subtropical regions. The smaller impact of SATEMs compared with SATOBs in OSE-I is reversed in OSE-II; this illustrates the degree of sensitivity to the synoptic situation, since data coverage alone suggests the opposite behavior (two polar orbiting satellites in OSE-I and only one in OSE-II).

Figures 8 and 9 show a similar set of mean charts for the northern hemisphere 500 mb height. During OSE-I the largest impact of the space-based observations is over the North Pacific, with SATEMs (and to a lesser extent ACFTs) having a major role in providing information. The situation during OSE-II is very different--SATOBs now play an important role and the main area of influence is now over Europe with a somewhat reduced activity over the North Pacific. The apparent influence of single level data on the 500 mb analysis (PMSL analyses

a) OSE-I

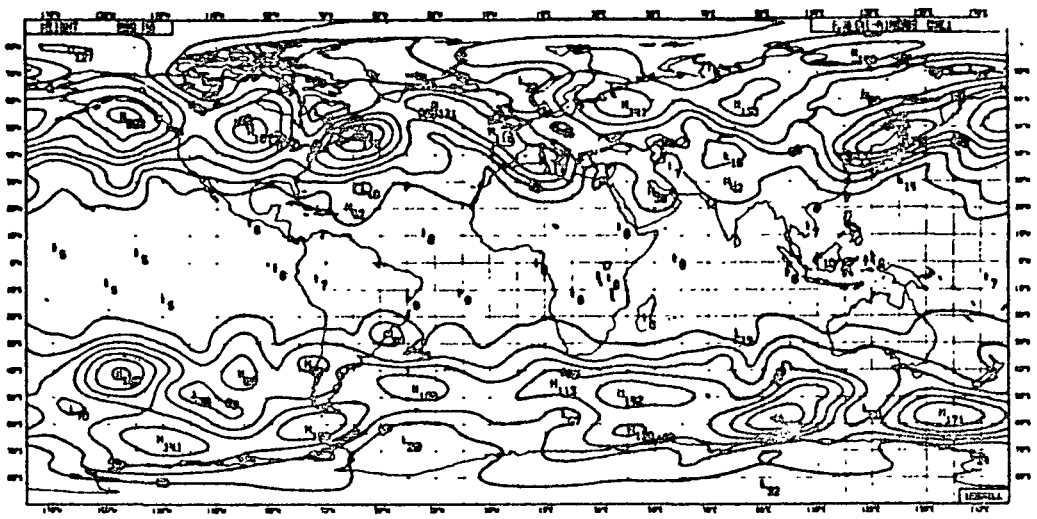

b) OSE-II

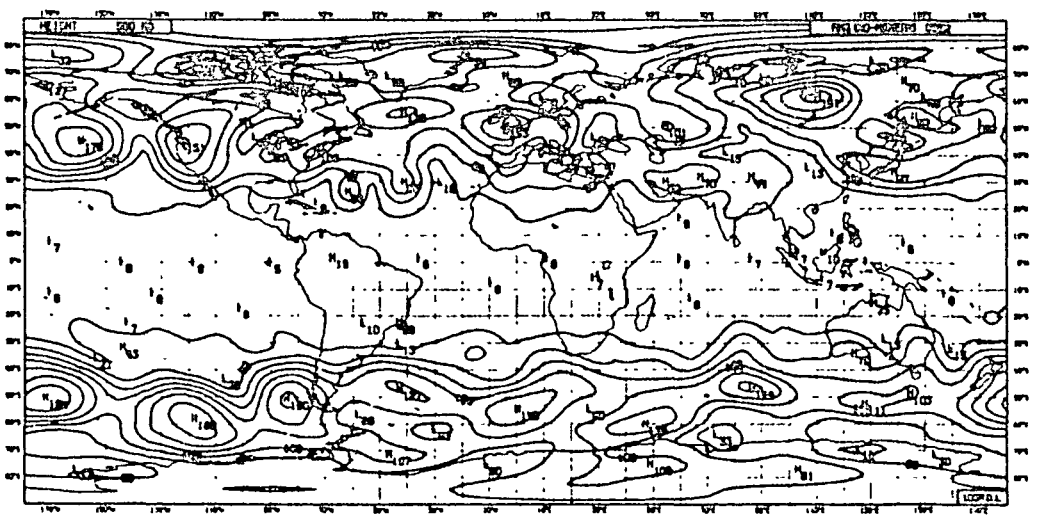

FIGURE 4 Time variability (RMS z-mean) of 500 mb height field during November 10-19, 1979 (OSE-I, a) and during February 27 to March 7, 1979 (OSE-II, b).

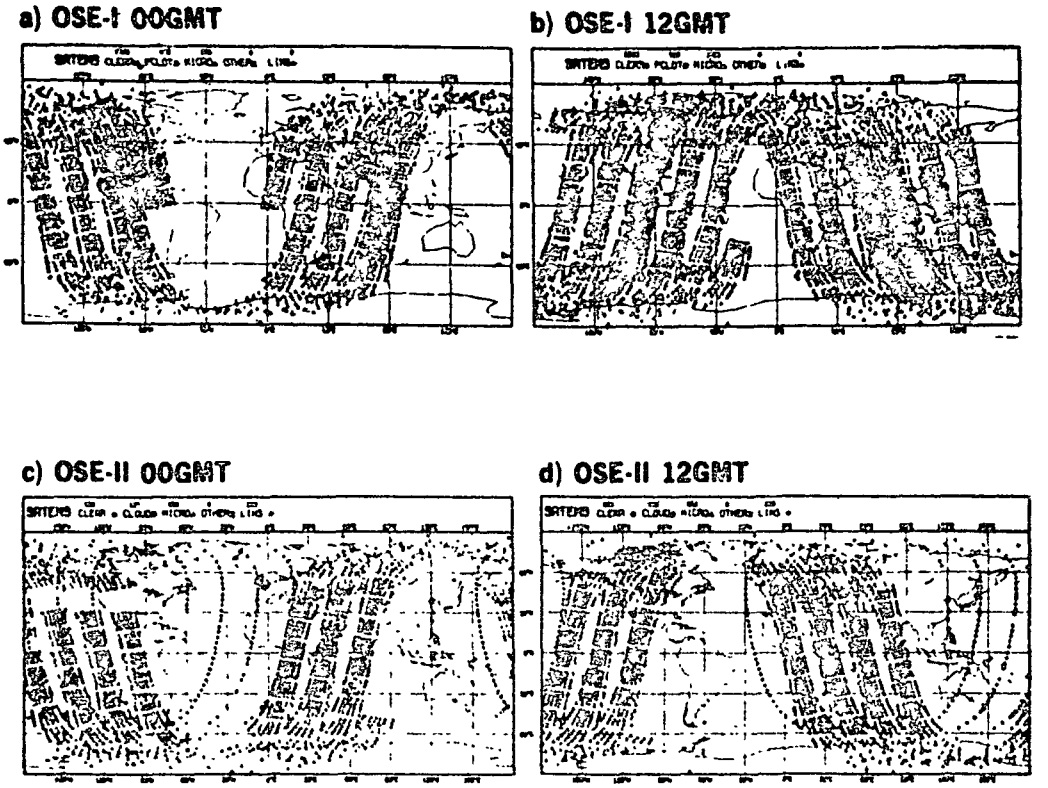

FIGURE 5 Representative SATEM coverage examples during OSE-I: (a) at 0000 GMT November 13, 1979, (b) at 1200 GMT November 11, 1979. The same during OSE-II: (c) at 0000 GMT February 7, 1979, (d) at 1200 GMT February 7, 1979.

showed no appreciable differences) confirms that the ECMWF Data Assimilation System is capable of successfully extracting tropospheric mass field information from single level platforms.

Figure 10 shows RMS analyses differences between the CONTROL and Minimum System (surface-based observations only) for both OSE-I and OSE-II. This, together with Figure 4, confirms that the coverage of the ocean areas by space-based platforms during OSE-I coincided with large atmospheric activity in the same areas (West and North Atlantic, and East and North Pacific). The situation was different during OSE-II, with reduced activity over the ocean areas. This effect superimposed with the above-mentioned intermittent data void areas over the North Pacific gives a reduced impact of the space-based platforms.

Figure 11 attempts to partition the collective impact of the space-based platforms between SATEMs and SATOBs in OSE-I. It confirms the dominant role of SATEMs over SATOBs in defining the midlatitude mass field in the northern hemispehre. In the southern hemisphere

TABLE 1 List of Acronyms Identifying the Scenarios for Data Assimilated for OSE-1 (November 7 to 18, 1979; Seven Forecasts--Six from 0000 GMT and One from 1200 GMT) and OSE-II (February 22 to March 7, 1979; Nine Forecasts--All from 0000 GMT).

Maximum System (CONTROL)	AI
Minimum System (SURFACE based) = Maximum System minus SATEMs SATOBs and ACFTs	SO
SATEM System = Minimum System + SATEMs	SM
SATOB System = Minimum System + SATOBs	SB
ACFT System = Minimum System + ACFTs	SX
SPACE based System = Maximum System minus TEMPs, PILOTs and SYNOP winds	SP
1 Polar orbiting satellite only As SM (SATEM System), but with 1 satellite instead of 2 (OSE-I only)	N1

SATOBs also seem to play an important role, probably due to the paucity of data.

IMPACT OF THE DATA ON THE SHORT-RANGE FORECAST FIELDS

This section deals with the impact of the different observing systems on the quality of the six-hour forecasts used as a first guess in the data assimilation cycle. A useful tool in evaluating the efficiency of an assimilation is to compare the relative magnitudes of the changes made by the forecast step, analysis step, and initialization step in the assimilation system (Hollingsworth and Arpe, 1982; ECMWF/SAC(84)5). If F, A, and I are measures of the RMS amplitudes of these changes, then in a good data assimilation cycle one should find that F > A > I. This, in turn, means that most of the changes from one analysis to the next are accomplished by the six-hour forecast. In doing so a small amount of noise or undesirable imbalances (gravity modes) are brought into the analyzed fields, but this is eliminated by the initialization step that should bring about even smaller changes.

a) AI-SO

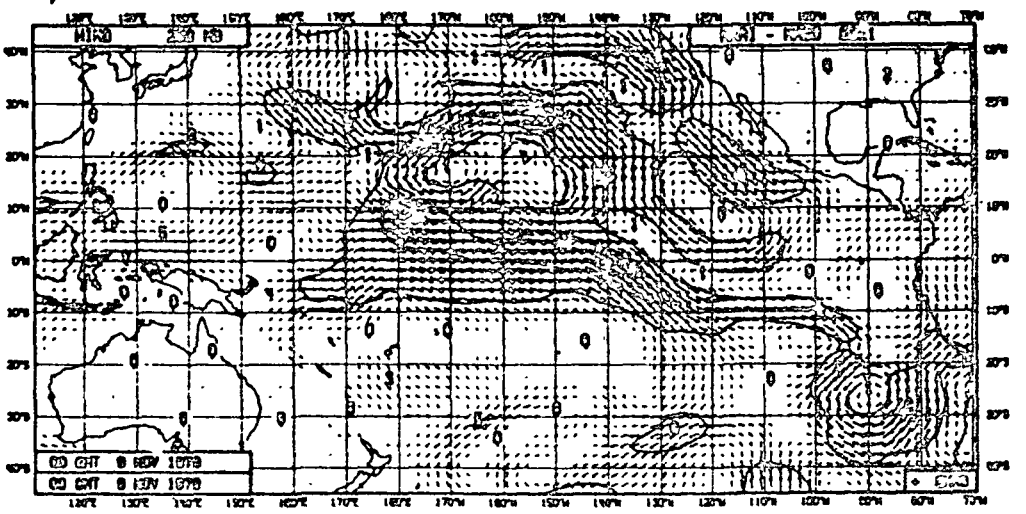

b) SX-SO

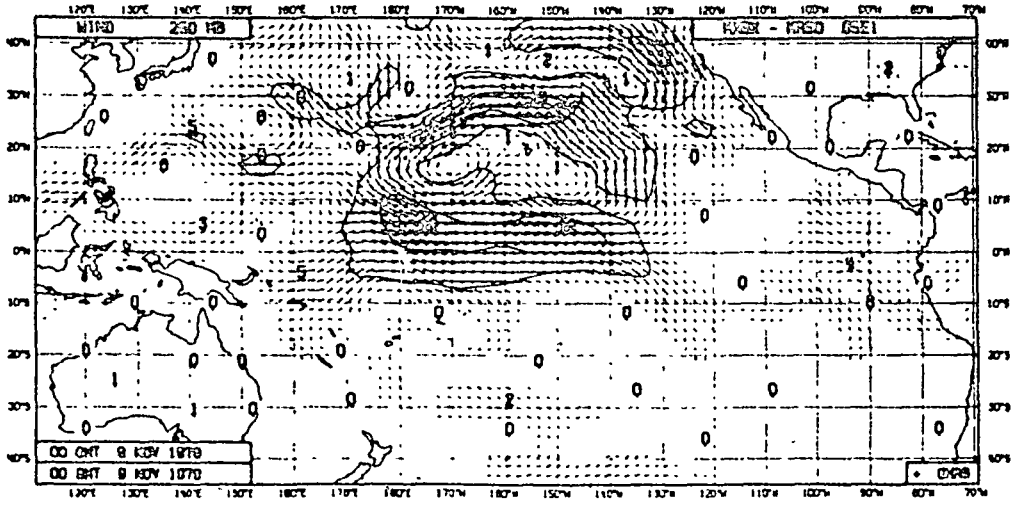

FIGURE 6 Differences of the mean wind at 250 mb over the tropical Pacific during OSE-I: (a) CONTROL ACFT minus SURFACE, (b) SURFACE + ACFT minus SURFACE, (c) SURFACE + SATOB minus SURFACE, and (d) SURFACE + SATEM minus SURFACE.

c) SB-SO

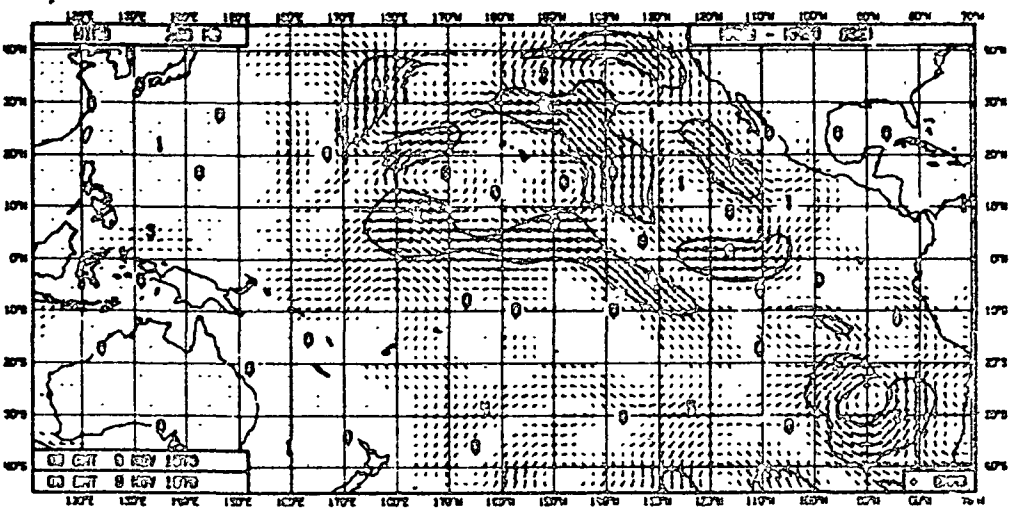

d) SM-SO

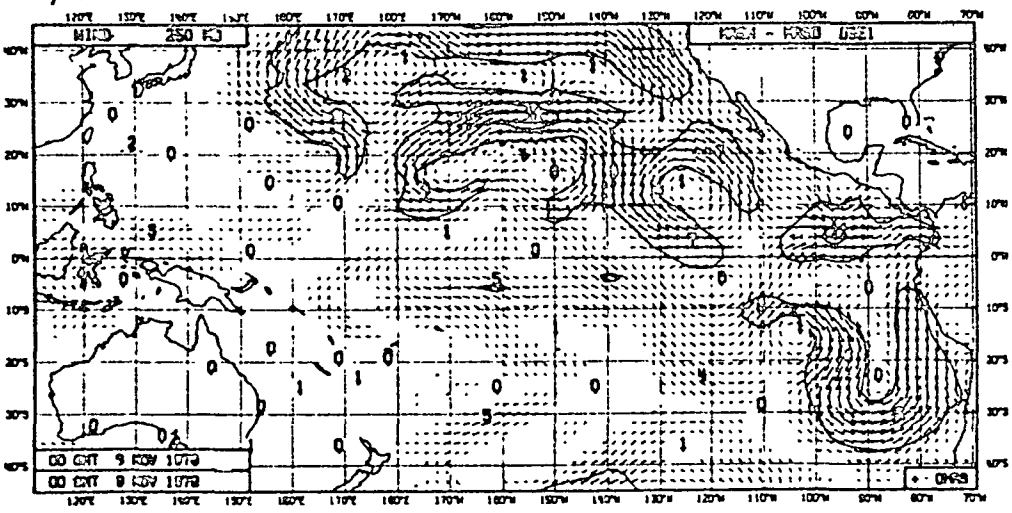

FIGURE 6 continued

a) AI-SO

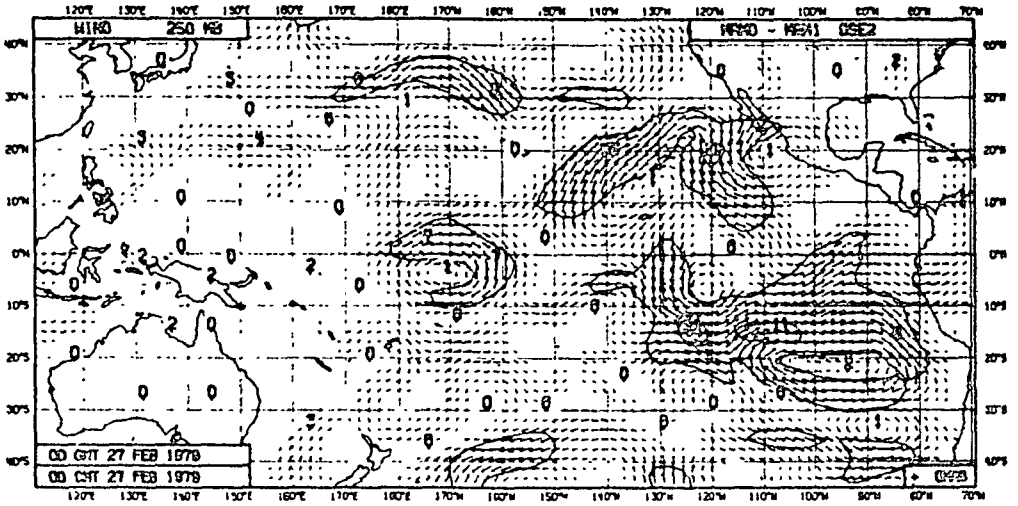

b) SX-SO

Not available

FIGURE 7 Differences of the mean wind at 250 mb over the tropical Pacific during OSE-II: (a) CONTROL minus SURFACE, (c) SURFACE + SATOB minus SURFACE, and (d) SURFACE + SATEM minus SURFACE.

c) SB-SO

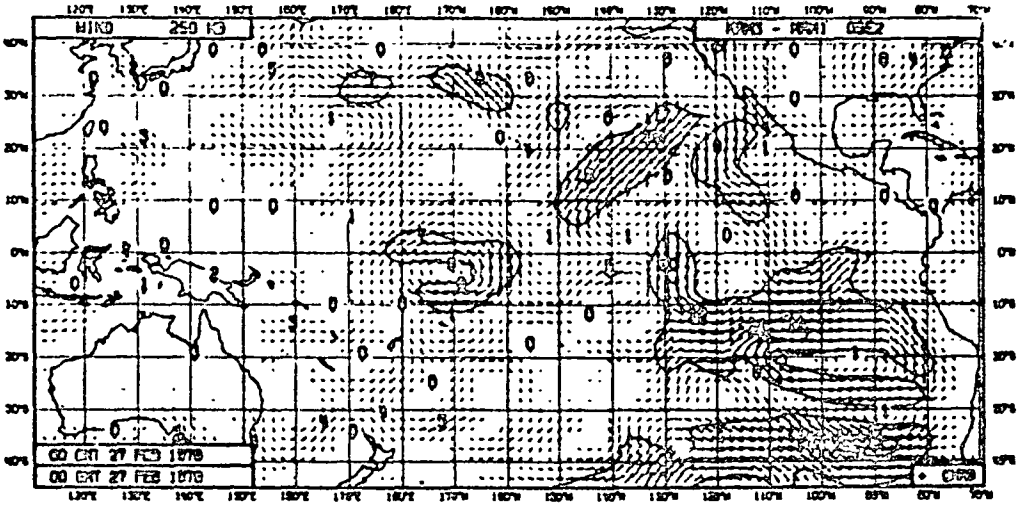

d) SM-SO

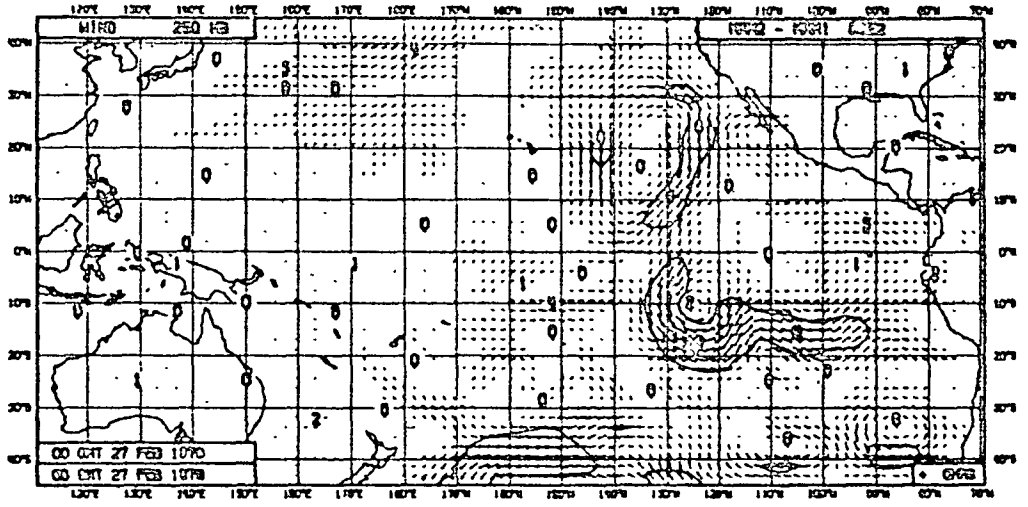

FIGURE 7 continued

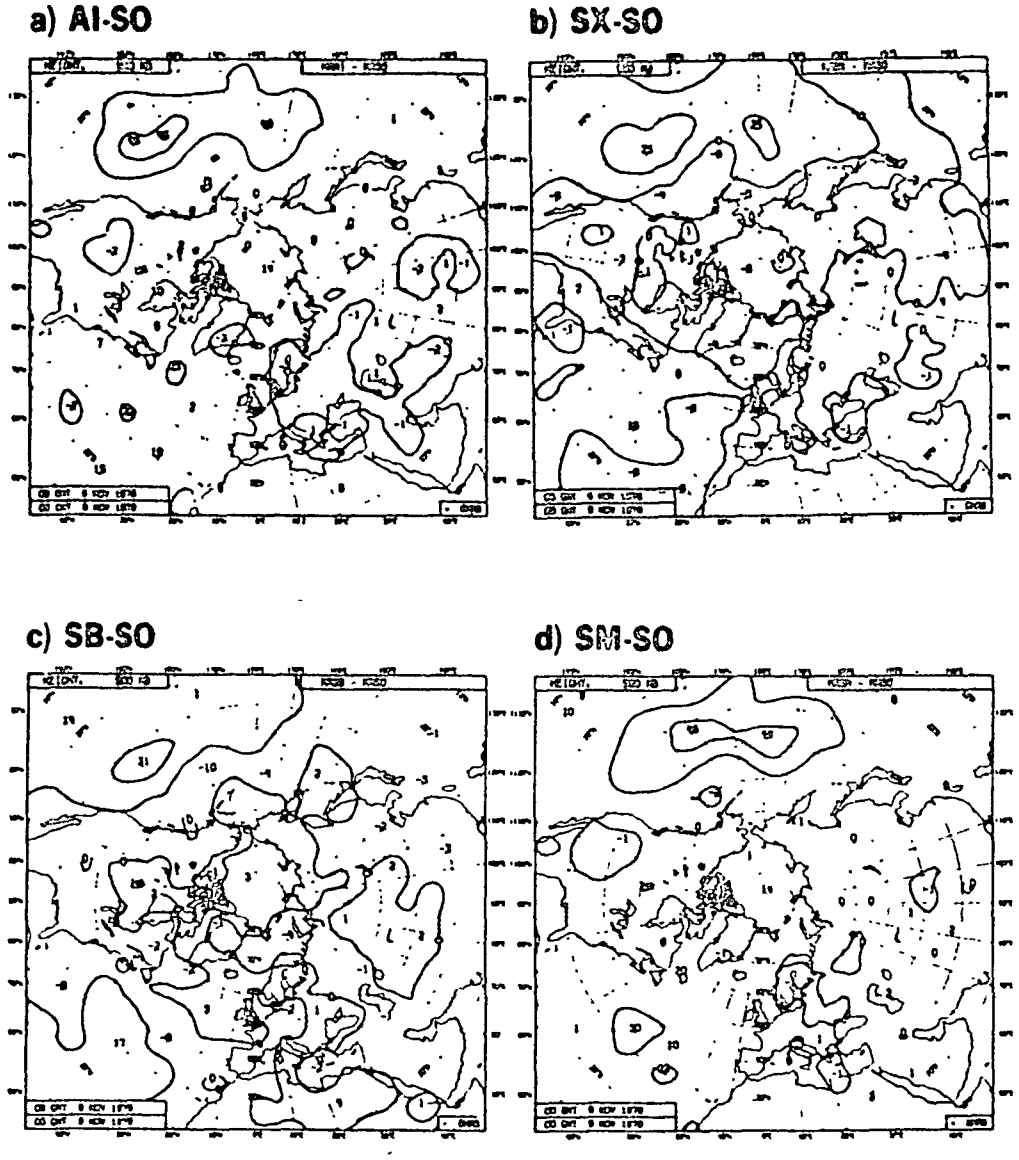

FIGURE 8 Differences of the mean 500 mb height over the northern hemisphere during OSE-I: (a) CONTROL minus SURFACE, (b) SURFACE + ACFT minus SURFACE, (c) SURFACE + SATOB minus SURFACE, and (d) SURFACE + SATEM minus SURFACE.

a) AI-SO

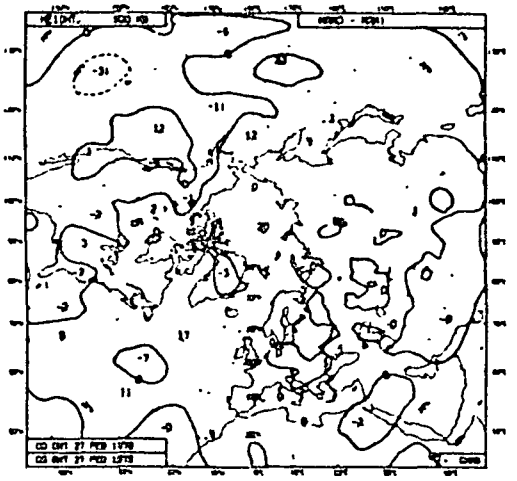

b) SX-SO

Not available

c) SB-SO

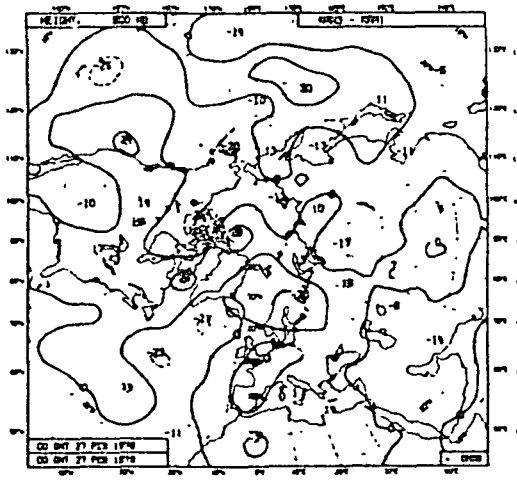

d) SM-SO

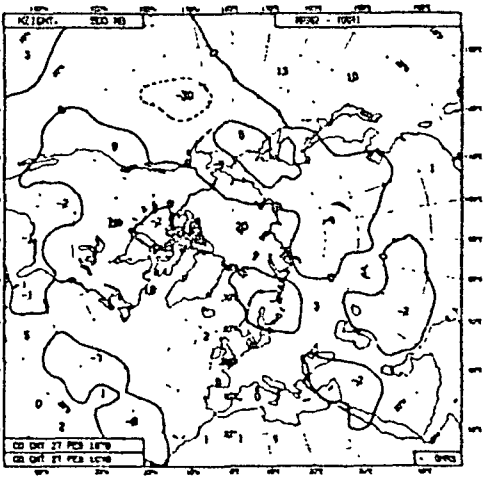

FIGURE 9 Differences of the mean 500 mb height over the northern hemisphere during OSE-II: (a) CONTROL minus SURFACE, (c) SURFACE + SATOB minus SURFACE, and (d) SURFACE + SATEM minus SURFACE.

a) OSE-I

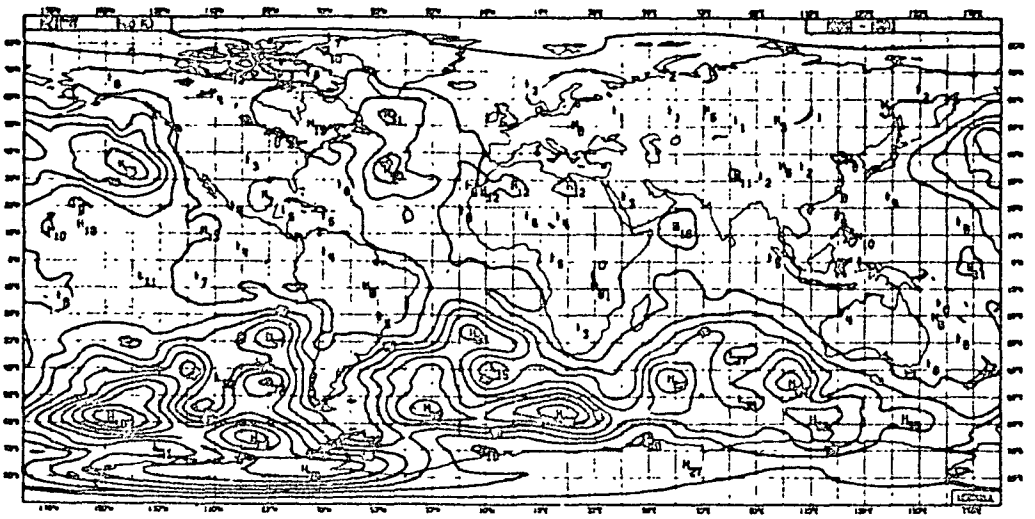

b) OSE-II

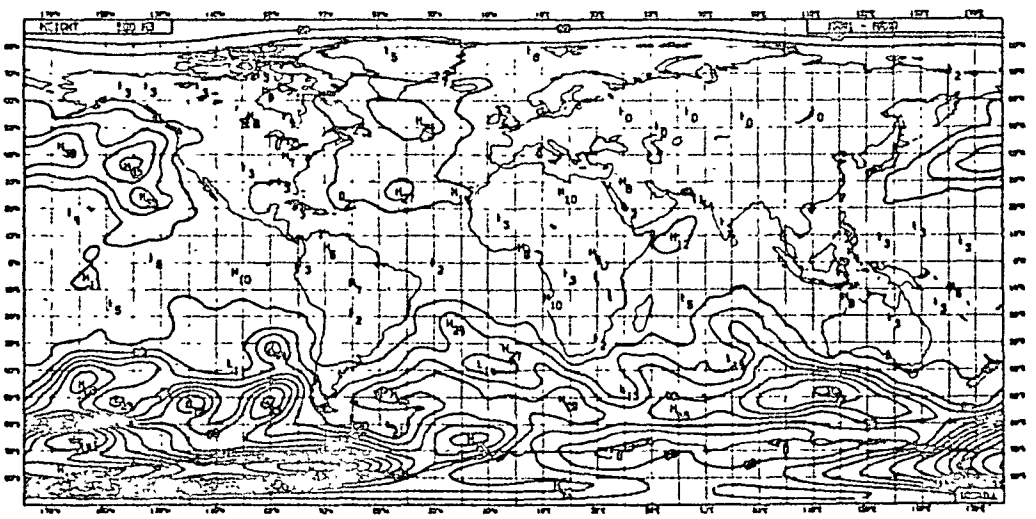

FIGURE 10 RMS of the difference between CONTROL and SURFACE 500 mb height analyses during OSE-I (a, top) and OSE-II (b, bottom).

a) SO-SB

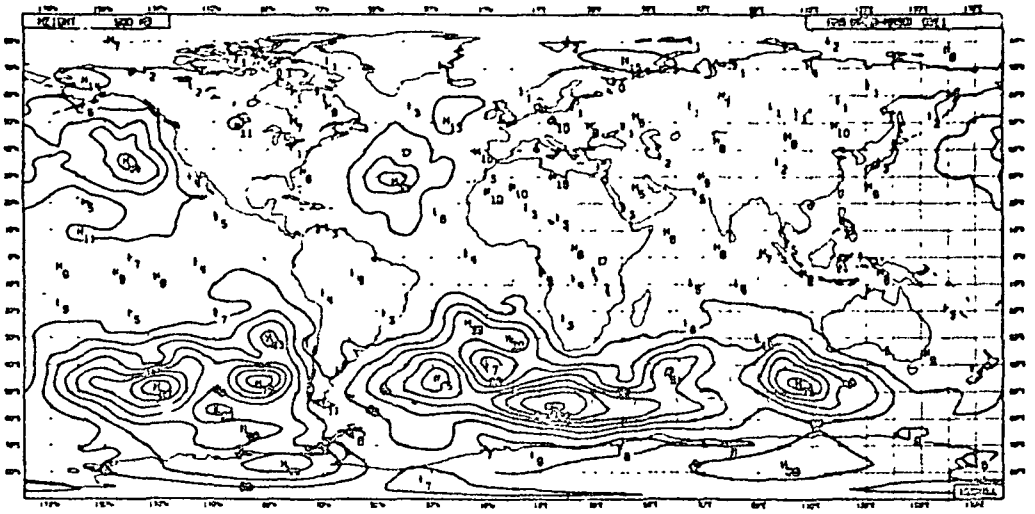

b) SO-SM

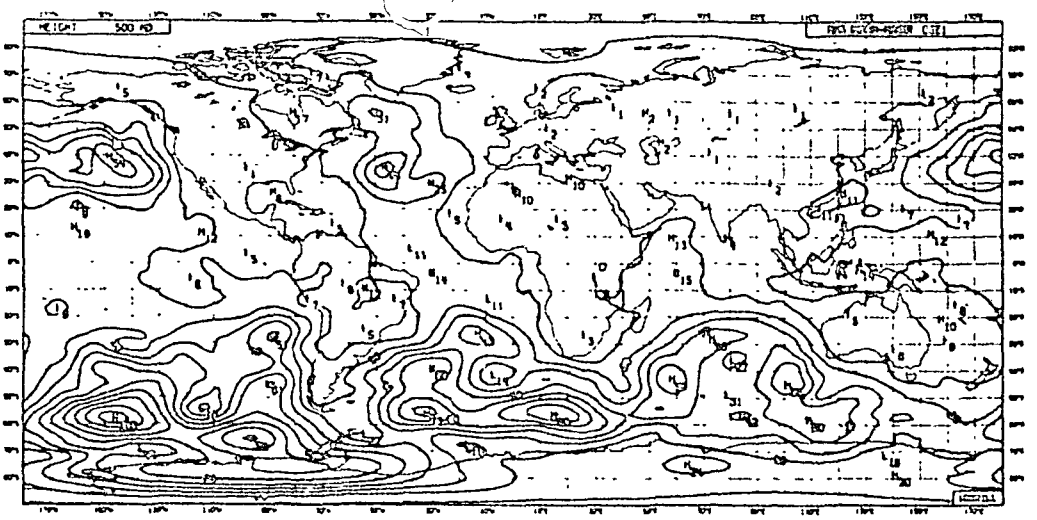

FIGURE 11 RMS of the difference between SURFACE analyses and SURFACE plus SATOB analyses (a, top) and SURFACE plus SATEM analyses (b, bottom) for 500 mb height during OSE-I.

Figure 12 maps the magnitude of P for both OSE-I and OSE-II for the two control assimilations. The blocked flow in the North Atlantic is clearly evident in both periods, with most of the activity forced to take place north of the blocked ridge. This is even more evident during OSE-II. The level of activity in the six-hour forecasts is roughly similar in the two periods in the eastern Pacific. The western Pacific however has its markedly larger meteorological activity during OSE-I confirmed by these short-range forecast changes.

Figure 13 shows the OSE-I RMS differences between the six-hour forecast in the AI, SX, SB, and SM assimilations (for the meaning of the acronyms, see Table 1) and the verifying AI (CONTROL) analyses that are our best estimates of the true state of the atmosphere. The panel labeled AI (Figure 13a) also represents the RMS analysis changes (the quantity A defined above) for the AI (CONTROL) assimilation of OSE-I. A comparison between Figures 12a and 13a confirms that in the control assimilation, with all available data included, the relationship F > A is well satisfied.

Comparison of the four panels of Figure 13 shows a number of important features. The dominant information source for the southern hemisphere are the SATEMs. The SATOBs also contribute to the accuracy of the assimilating forecast well to the south of 45°S. It is gratifying to note that the two data sources together give a noticeably more accurate forecast in the southern hemisphere than either system alone. Aircraft data were extremely sparse in the southern hemisphere. In the northern hemisphere subtropics, both the SATEM and SATOB data lead to more accurate short-range forecasts, while poleward of 45°N the SATEM data have the larger effect.

These maps of short-range forecast error are probably the most accurate estimates available for the accuracy of the analyses (and therefore for the impact of the data) in the different assimilations. It is clear that the SO (surface-based) system has large errors over the northern hemisphere oceans. These are much larger over the Pacific than the Atlantic in this period because of the synoptic situation. It should be noted that all Ocean Weather Ship data are included in the Minimum System.

Figure 14 shows the corresponding results for OSE-II. The main results in the southern hemisphere are just as they were in OSE-I. The SATEMs are essential for the high midlatitudes, while the SATOBs are essential for the tropics (wind data not shown however), and both systems complement each other in the subtropics.

In the northern hemisphere, the results for OSE-I and OSE-II are not similar. It should be remembered that only one satellite was available during OSE-II. Although the short-range forecast errors are smaller in the SM assimilation than in the SO assimilation over both oceans of the northern hemisphere, the differences are modest, and the patterns are very similar. This similarity prompted a thorough perusal of all data coverage maps, which showed that there were many missing swaths in the eastern Pacific for the 0000 GMT analyses from which all the forecasts were run. Every swath but one in the ten-day period had a gap between about 50°N and 30°N, and many partial swaths terminated at 50°N or began at 30°N. There was little SATEM cover in the eastern Pacific between 30°N and 50°N for the 0000 GMT analyses of OSE-II.

a) OSE I

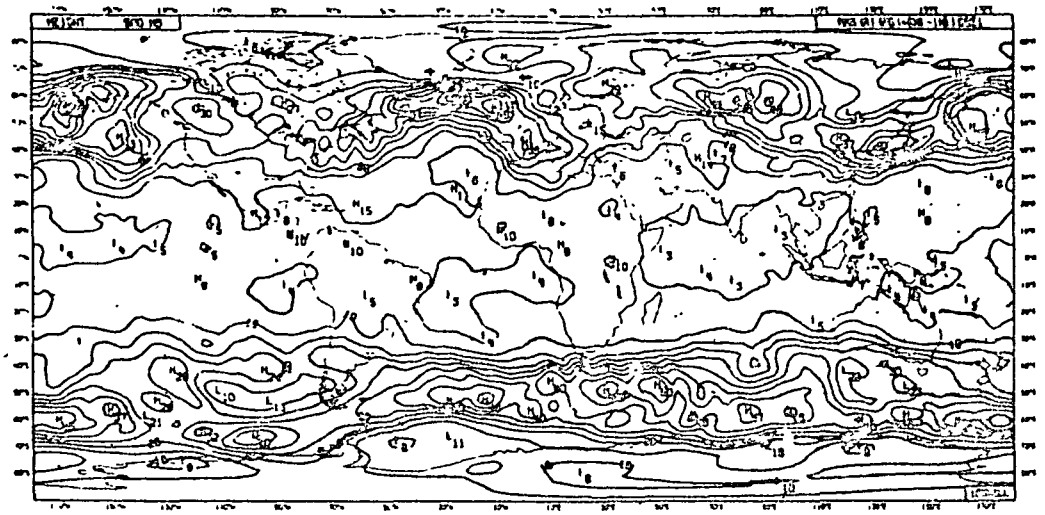

b) OSE II

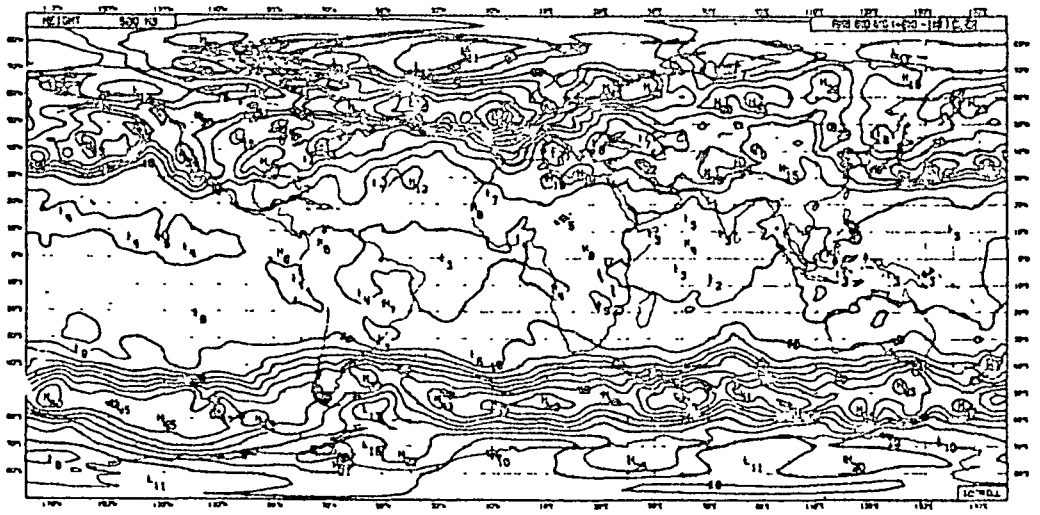

FIGURE 12 The meteorological activity in the six-hour forecast measured as RMS of six-hour forecast minus initial state in OSE-I (top panel) and in OSE-II (lower panel) for 500 mb height.

a) AI

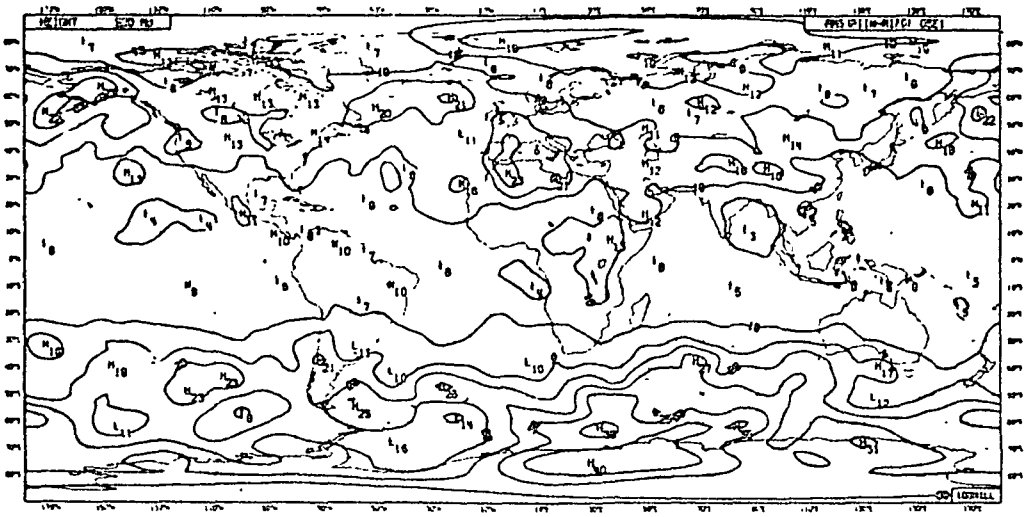

b) SO

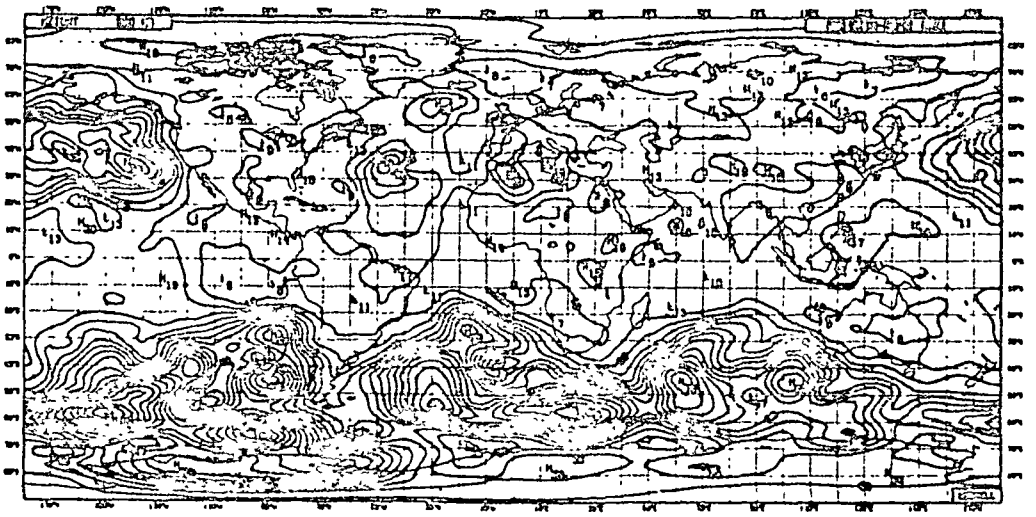

FIGURE 13 RMS of the six-hour forecast error for 500 mb height in OSE-I when verified against control initialized analyses: (a) CONTROL, (b) SURFACE, (c) SURFACE + SATOB, and (d) SURFACE + SATEM.

c) SB

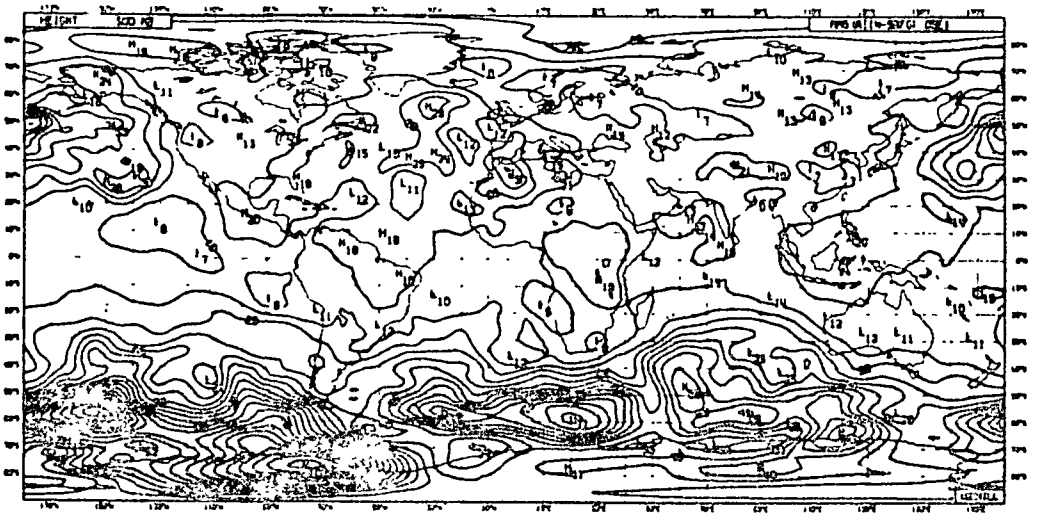

d) SM

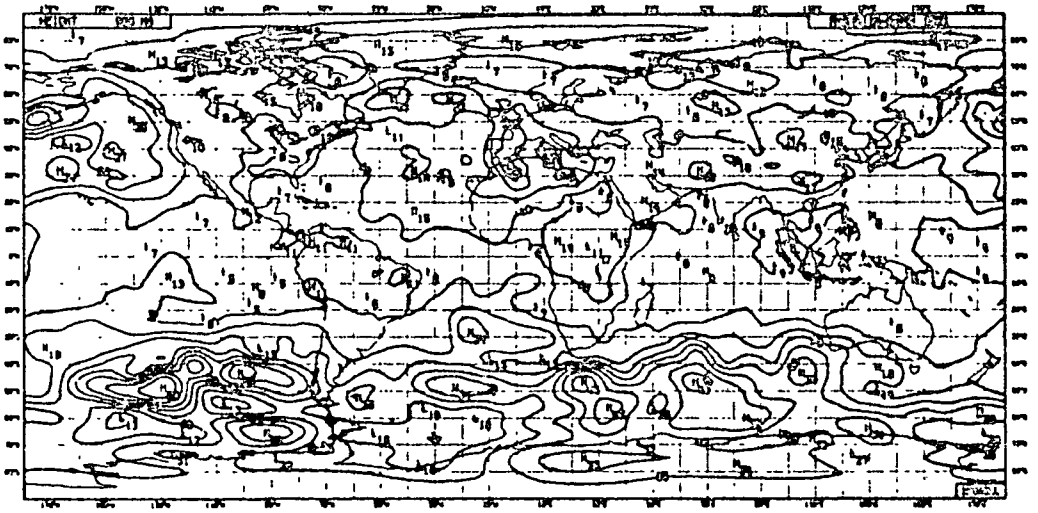

FIGURE 13 continued

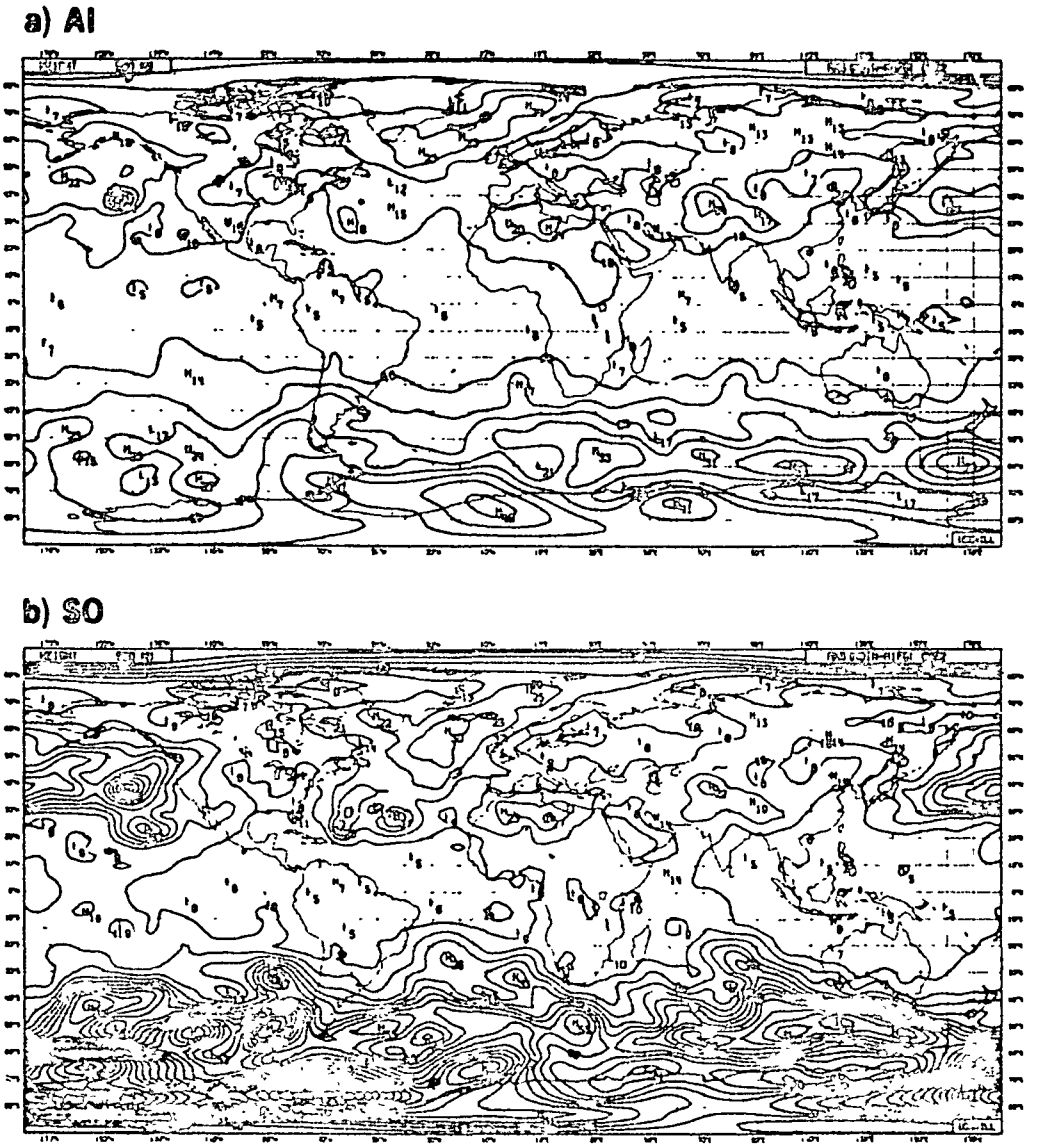

FIGURE 14 RMS of the six-hour forecast error for 500 mb height in OSE-II when verified against control initialized analyses: (a) CONTROL, (b) SURFACE, (c) SURFACE + SATOB, and (d) SURFACE + SATEM.

c) SB

d) SM

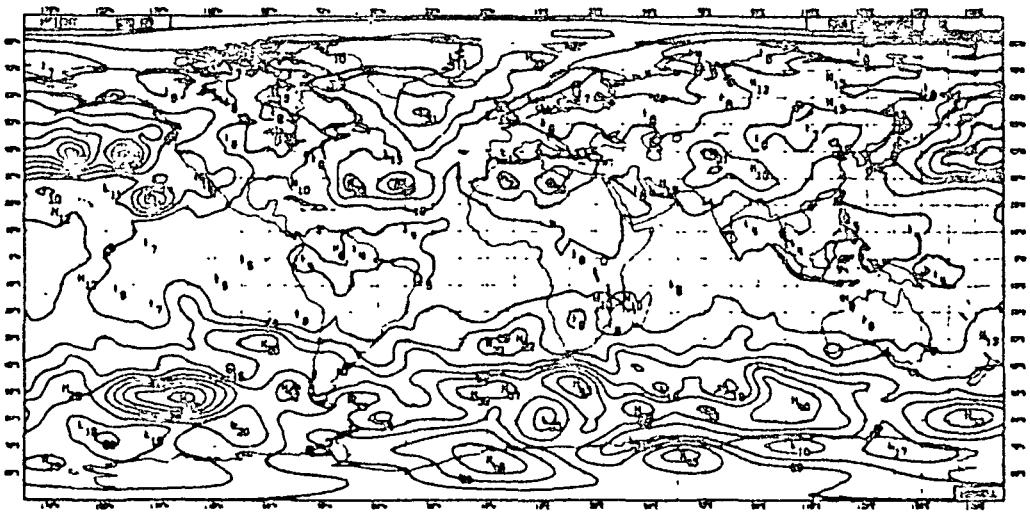

FIGURE 14 continued

We conclude that the missing SATEM data during OSE-II contributed substantially (together with the reduced activity over the northern hemisphere oceans) to the reduced impact of this observing system, compared to the one observed during OSE-I.

IMPACT OF THE INDIVIDUAL SYSTEMS IN OSE-I and OSE-II

This section deals with the impact of the individual systems on the assimilations through a study of the divergence of the forecasts of the SM, SB, SX systems from the SO system.

As already anticipated in the introduction, a difficulty common to most OSE-type studies is that, by the time the analysis differences caused by different observing system configurations have had the opportunity to produce suitable forecast differences, the model-generated errors have reached such a dominating level that they tend to mask any other effect (see Figure 1). An alternative approach is to analyze the forecast differences from a given configuration (in our case the Minimum System, SO). In such a case, one is able to attribute all detectable differences to the differences in initial conditions, arising from the differences in observing system.

The divergences of the forecasts from each other give no indication of their absolute quality. This question will be addressed in the next section. For the moment it can be taken for granted that in OSE-I the addition of data to the Minimum System improved the forecast, while this is not so obviously true in OSE-II. However, the addition of data to the assimilation did not degrade the forecasts.

Synoptic Examples of Forecast Divergence

Two examples were chosen from the OSE-I and OSE-II periods. For each example we show the impact of a single data system on an analysis and forecast by presenting difference maps between the forecast based on the Minimum System (SO) and the forecasts based on the Minimum System plus SATEMs (SM), or the Minimum System plus SATOBs (SB), or the Minimum System plus ACFTs (SX). The results from the latter have only been analyzed for OSE-I.

The sequence of forecasts from 1200 GMT on November 11, Figures 15 to 17, show remarkable similarities in the impact of each individual system. The SATEM and ACFT data show extraordinary similarity out to day 7, while all three data systems have similar impact out to day 4. The analysis system was therefore capable of using any one system, or all three systems, very effectively.

The corresponding charts for an equivalent experiment in OSE-II (Figures 18 to 20) show dramatically different results. This case was chosen because it had the most complete 0000 GMT SATEM coverage in the Pacific for the whole period. The important activity in the Pacific was associated with a jet near 20°N, 120°W. The impacts of the SATOB and SATEM data on the forecast are quite different with essentially zero impact from the SATEM data out to day 5.

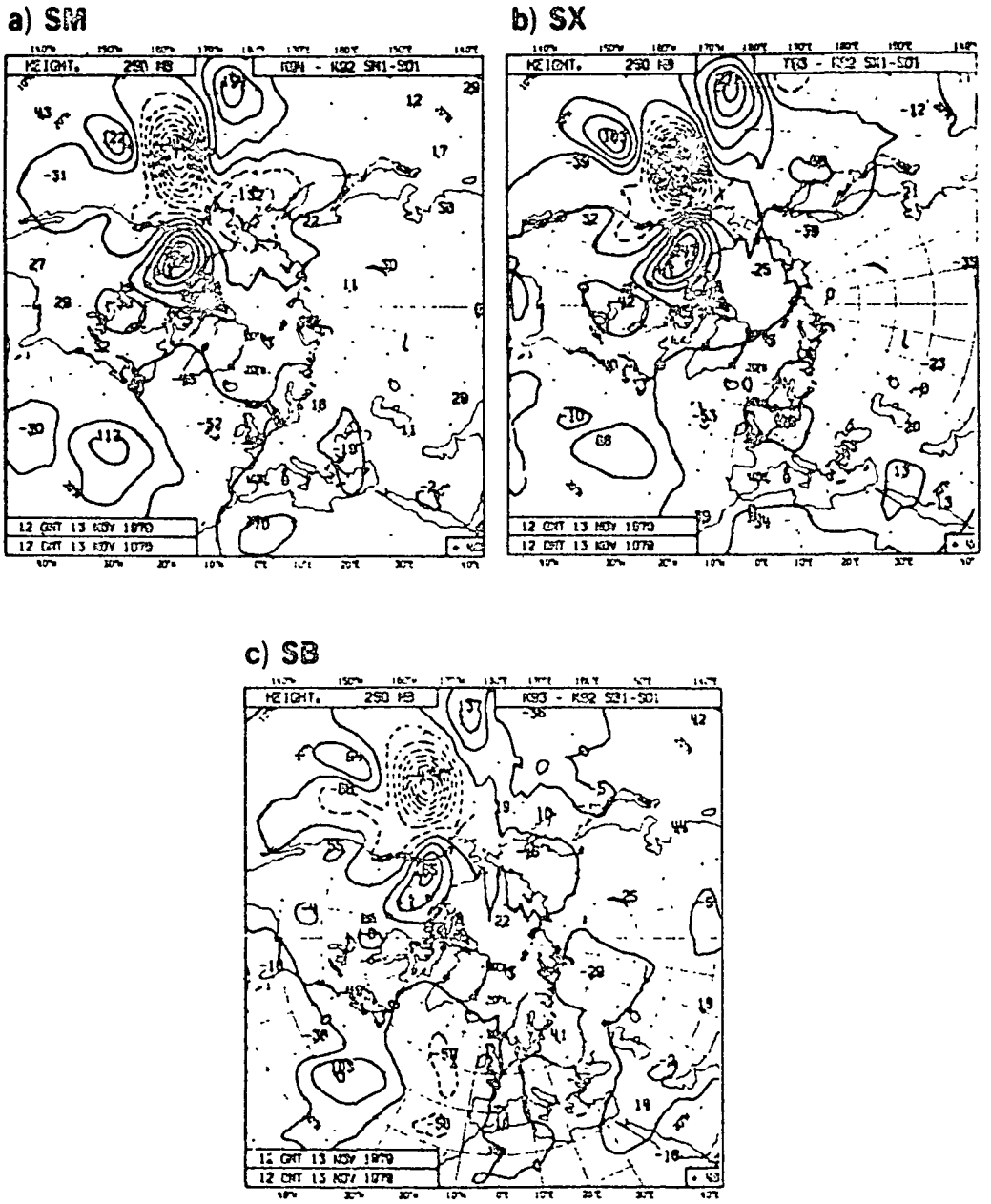

FIGURE 15 Day two (+48 hour) forecast divergences from the SURFACE forecast started from November 11, 1979, 1200 GMT/OSE-I at 250 mb level for (a) SURFACE + SATFM (top left), (b) SURFACE + ACFT (top right), and (c) SURFACE + SATOB (lower panel).

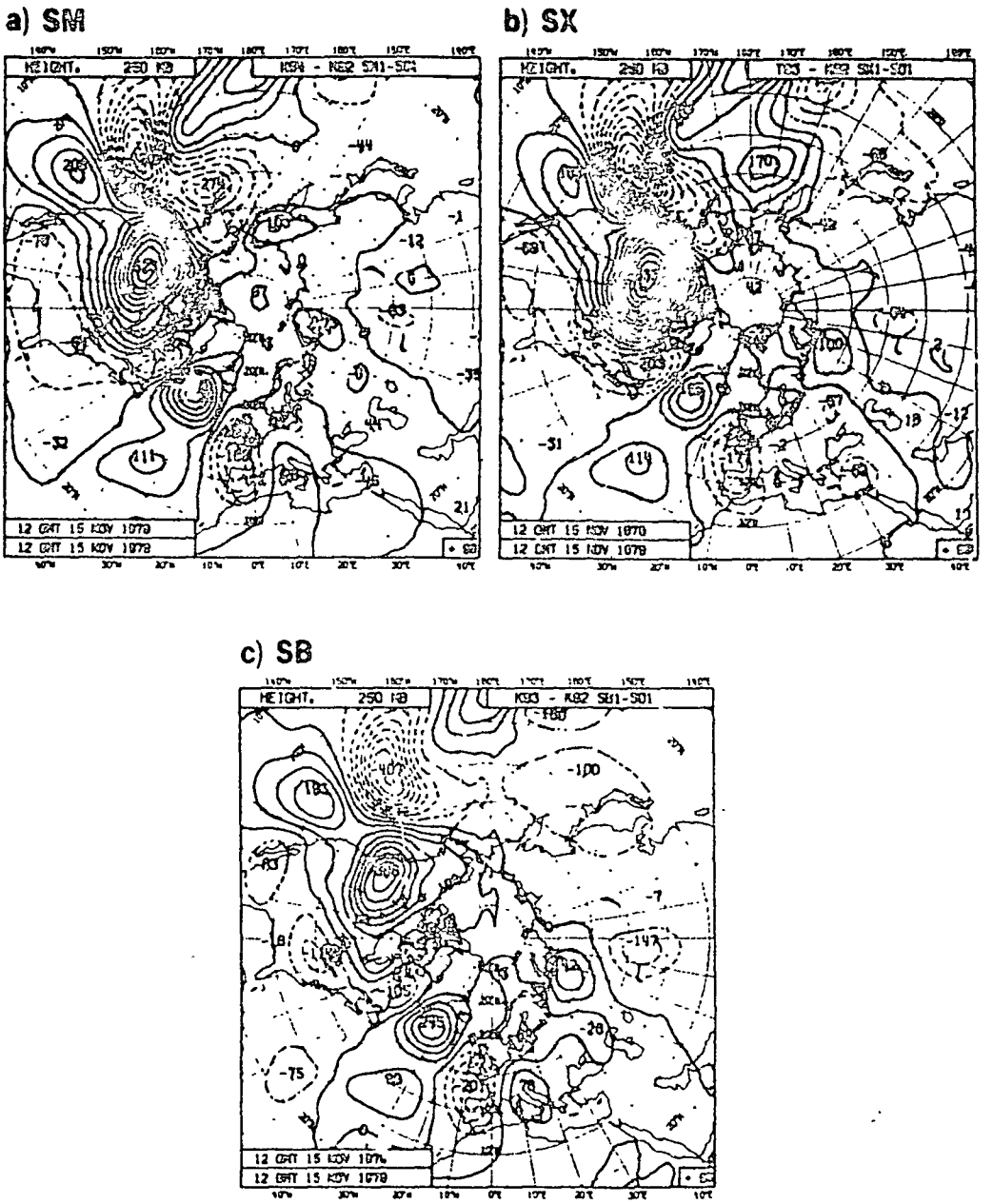

FIGURE 16 Day four (+96 hour) forecast divergences from the SURFACE forecast started from November 11, 1979, 1200 GMT/OSE-I at 250 mb level for (a) SURFACE + SATEM (top left), (b) SURFACE + ACFT (top right), and (c) SURFACE + SATOB (lower panel).

a) SM

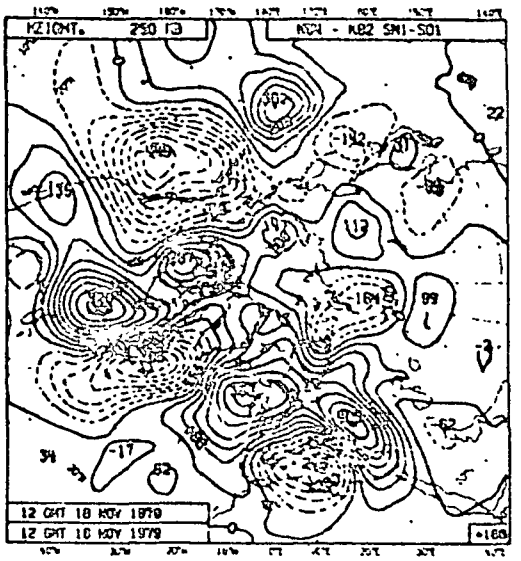

b) SX

c) SB

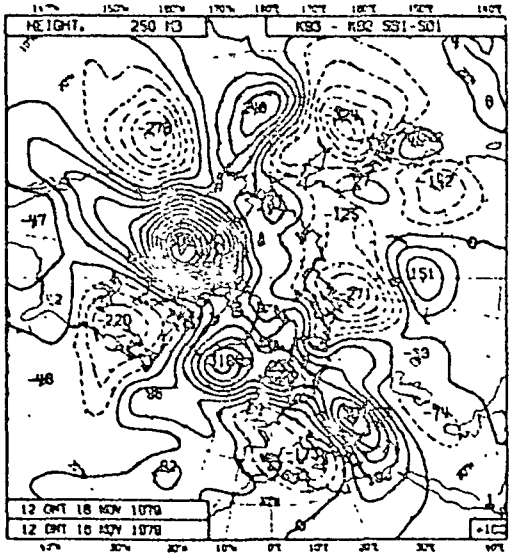

FIGURE 17 Day seven (+168 hour) forecast divergences from the SURFACE forecast started from November 22, 1979, 1200 GMT/OSE-I at 250 mb level for (a) SURFACE + SATEM (top left), (b) SURFACE + ACFT (top right), and (c) SURFACE + SATOB (lower panel).

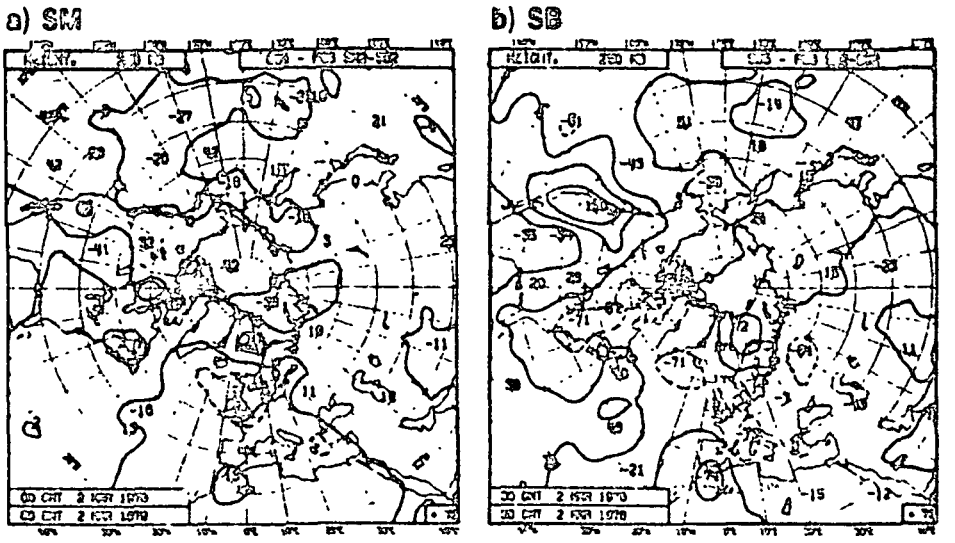

FIGURE 18 Day three (+72 hour) forecast divergences from the SURFACE forecast started from February 27, 1979, 0000 GMT/OSE-II at 250 mb level for (a) SURFACE + SATEM (left), and (b) SURFACE + SATOB (right).

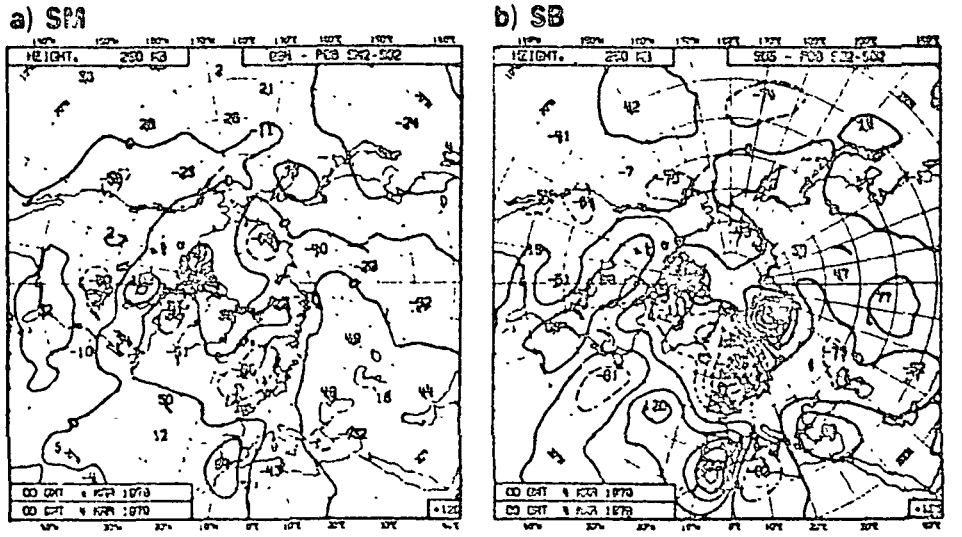

FIGURE 19 Day five (+120 hour) forecast divergences from the SURFACE forecast started from February 27, 1979, 0000 GMT/OSE-II at 250 mb level for (a) SURFACE + SATEM (left), and (b) SURFACE + SATOB (right).

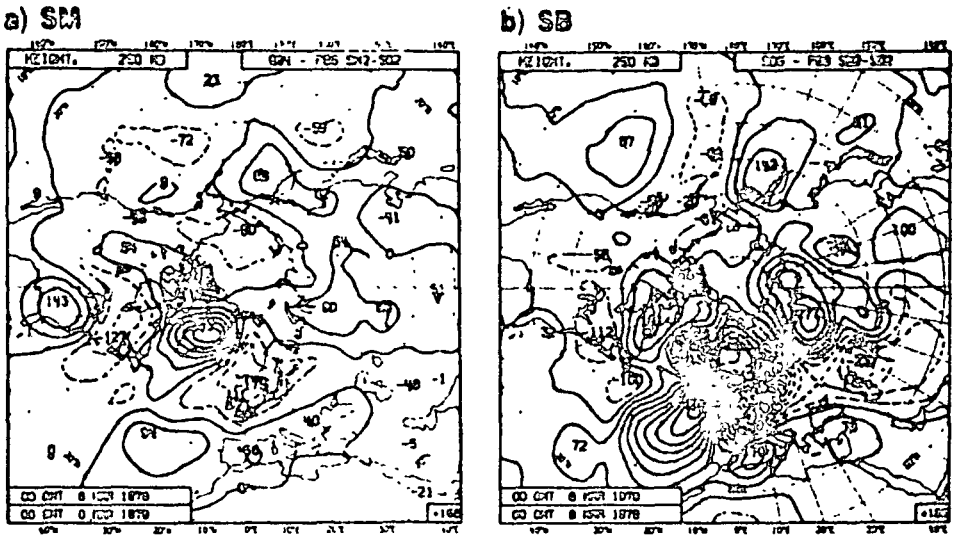

FIGURE 20 Day seven (+168 hour) forecast divergences from the SURFACE forecast started from February 27, 1979, 0000 GMT/OSE-II at 250 mb level for (a) SURFACE + SATEM (left), and (b) SURFACE + SATOB (right).

Statistics of Forecast Divergences

The examples above show that there can be much or little redundancy among the observing systems depending on the synoptic situation. Statistics of forecast divergence are a useful way to quantify the impact of the data. For this purpose, the forecasts from the AI system are used as a reference. Figure 21 shows the divergences in 500 mb geopotential as measured by anomaly correlations for the two hemispheres poleward of latitude 20°, and for both OSE periods.

The divergence of the forecasts from the CONTROL system happens much faster in OSE-I than in OSE-II. The SATEM experiments are closest to the CONTROL in the southern hemisphere, as expected, with the SATOB data showing a considerable effect in the southern hemisphere also.

In the northern hemisphere, SM and SX are closest to AI in OSE-I, with SB lying between SM and SO. In OSE-II, the relative positions of SM and SX are reversed, with SX closest to AI. This is consistent with the last synoptic case study and the considerations laid out earlier.

IMPACT OF DATA ON FORECAST SKILL

Figure 22 shows the forecast anomaly correlation of 500 mb geopotential height for the OSE-I and OSE-II experiments for AI, SM, SB, and SO. The most dramatic difference between the two periods is in the impact of the special data in OSE-I, the lack of impact of these data in OSE-II, and the remarkably good performance of the SO system in

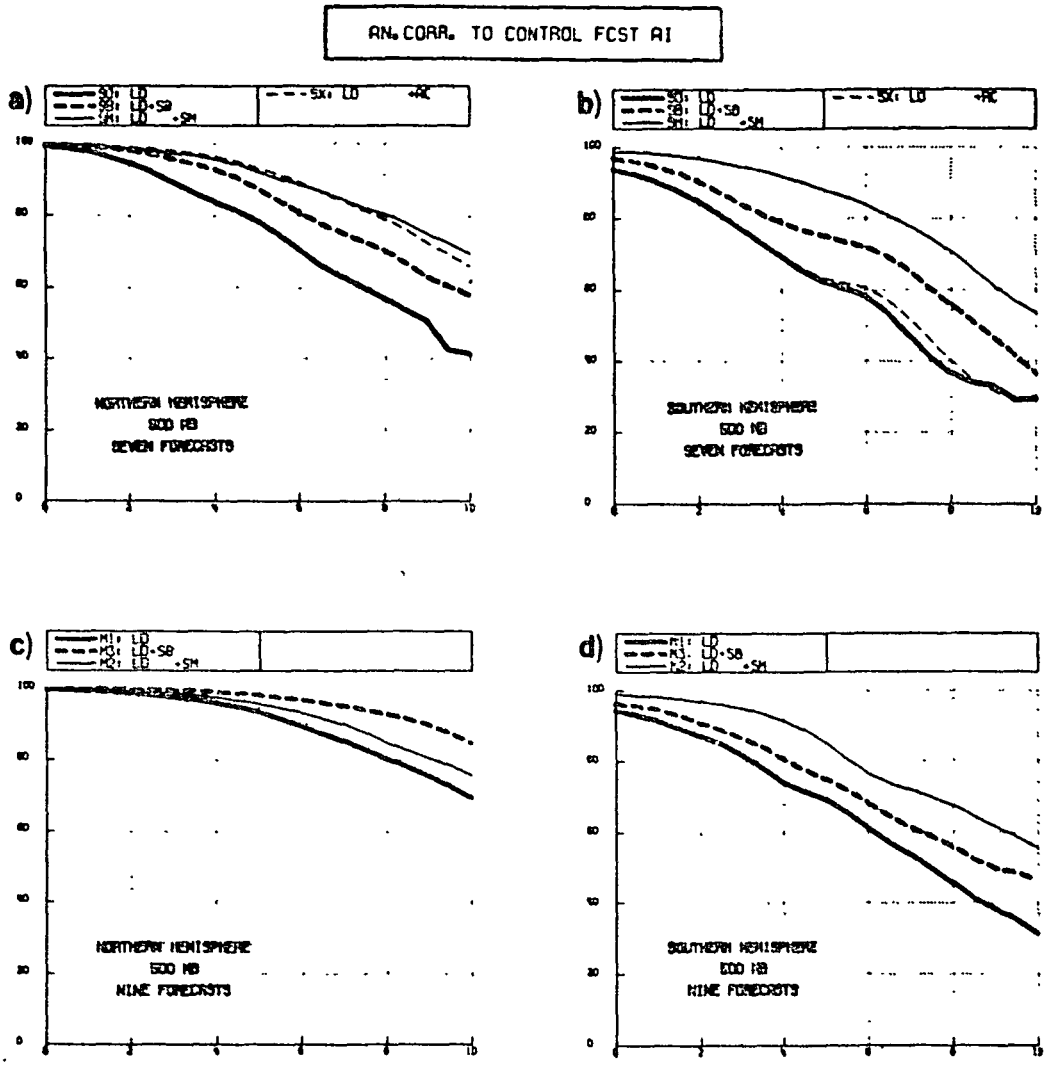

FIGURE 21 Mean anomaly correlations of tropospheric geopotential height for the experiment forecasts when verified against control forecasts. OSE-I, upper panels; OSE-II, lower panels. Left panels, northern hemisphere; right panels, southern hemisphere. (Continuous thick: SO: SURFACE; dashed thick: SB: SURFACE + SATOB; continuous thin: SM: SURFACE SATEM; dashed thin: SX: SURFACE + ACFT.

OSE-II. These results are all consistent with the differences in synoptic situation and data coverage noted earlier. In the southern hemisphere, the importance of the SATEM data is confirmed in bot! OSE-I and OSE-II.

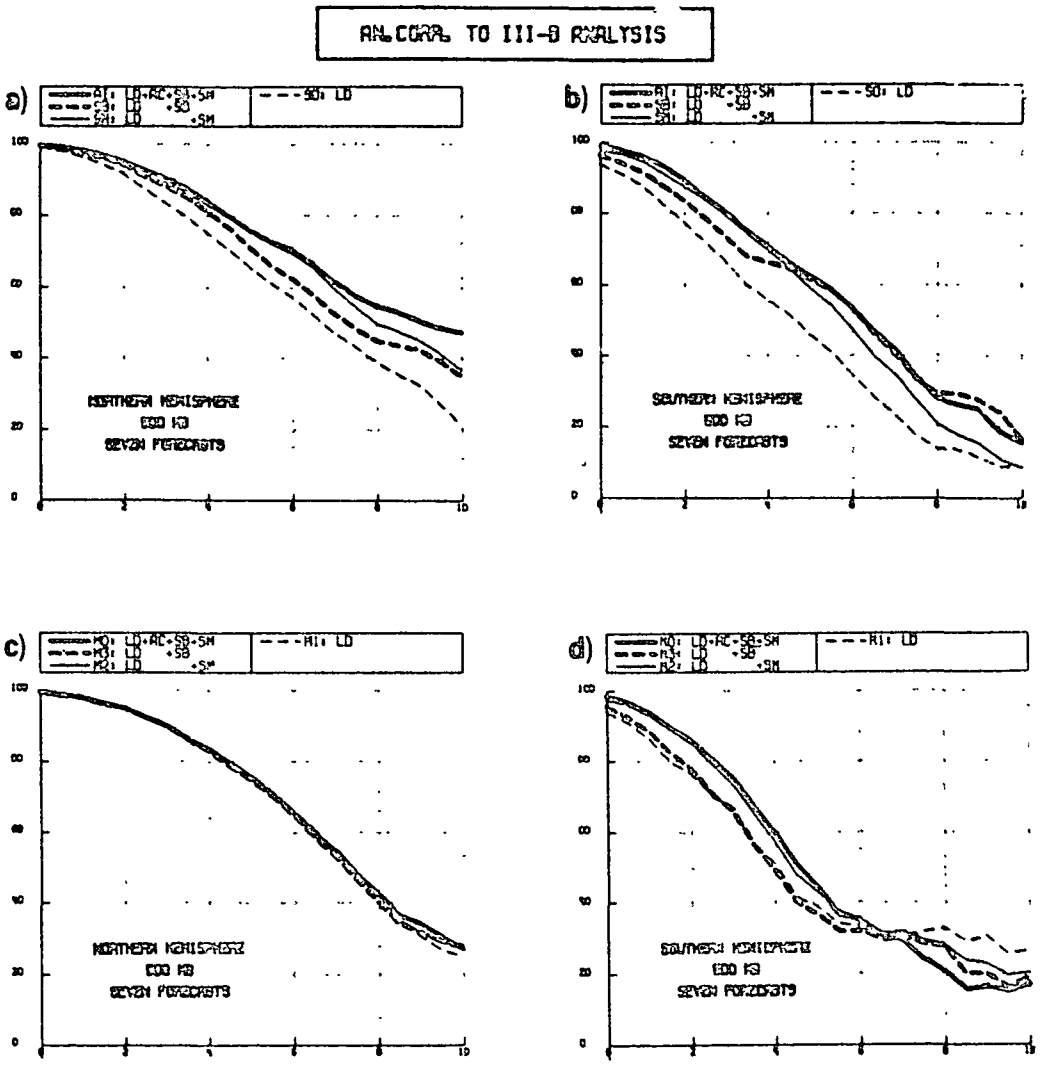

FIGURE 22 Mean anomaly correlation of tropospheric geopotential height verified against CONTROL analyses. OSE-I, upper panels; OSE-II, lower panels. Left panels, northern hemisphere; right panels, southern hemisphere. (Continuous thick: AI: CONTROL; dashed thick: SB: SURFACE + SATOB; continuous thin: SM: SURFACE + SATEM; dashed thin: SX: LAND + ACFT.

Finally, Figure 23 shows forecast results for AI, SO, and for yet another set of experiments SP, which attempts to probe the "best-mix" problem and which consisted of data that could in principle be collected from space (surface pressure, ACFT, SATEM, SATOB, but not TEMP). These results, consistently with the single system experiment

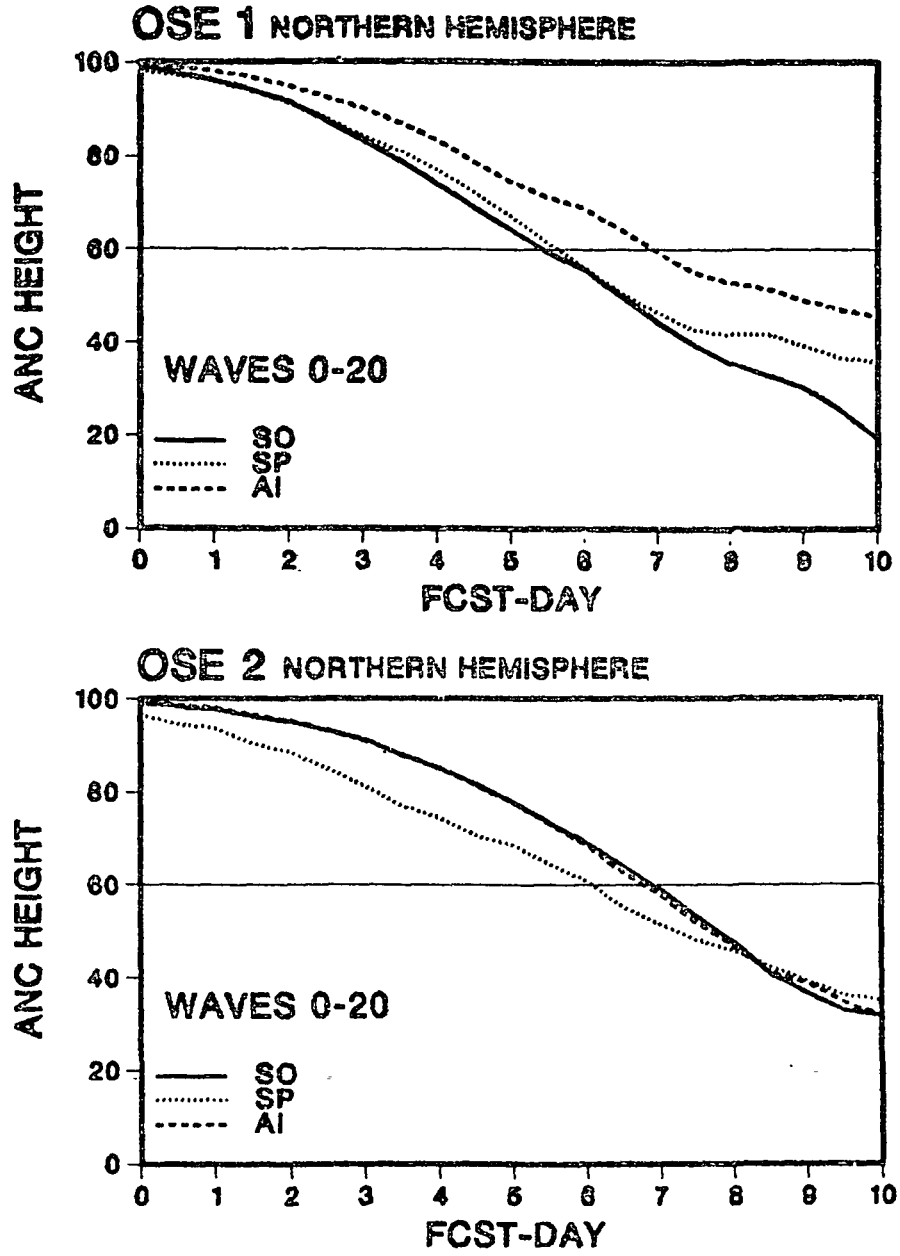

FIGURE 23 Mean anomaly correlations of tropospheric geopotential height for surface-based system (SO), space-based system (SP), and control (AI) forecasts in the northern hemisphere for OSE-I (top) and OSE-II (bottom).

results, confirm that the space-based system alone is equivalent to the surface-based system alone only during the OSE-I period. During OSE-II however, because of the reasons exposed above, the performance of the space-based platforms is considerably poorer.

The difficulties inherent to the "best-mix" problem are well illustrated by the aircraft impact studies of Baede (1983) and Barwell and Lorenc (1984). Their results showed that the deletion of ACFT data from the complete system had little effect on the forecast skill after two days. This is consistent with the results of Hollingsworth and Arpe (1982) and Arpe et al. (1984) that show that, provided the analyses are of good quality, model error is the dominant source of forecast error in the range between 2 and 5 days (Figure 1).

CONCLUSIONS

The combined results of the two OSEs show that the SATOB data are crucial for the tropical analyses, that the SATEM data are important for the extratropical analyses over oceans, and that aircraft data, where available, are an invaluable addition to the observation data base.

In the first of our experimental periods, OSE-I, the crucial analysis area for forecast success (area of highest synoptic activity) lay in the central Pacific midlatitudes and subtropics, in an area where there was an abundance of all three types of data. The results below indicate that in this case any one of the observing systems was able to provide the essential information.

In the second of our experimental periods, OSE-II, there was much less activity over the oceans than in the first period. Only the SATEM and SATOB data were studied in detail for this second period, but neither of them show much effect on forecast quality. Further detailed investigation showed that there was a gap in the potentially available SATEM data over the eastern Pacific that could well have affected the results. We conclude that the much reduced activity over the oceans, coupled with the absence of SATEM data, led to the negligible impact of the SATEM and SATOB data on forecast skill in this second period.

The results demonstrate clearly the value of each of the observing systems. The fact that in certain situations there may be redundancy between the systems is a strength rather than a weakness of the composite system. Aircraft data, particularly from wide-bodied jets, can be much more accurate at a single level than either of the other two systems. The SATEMs and SATOBs complement each other in providing global coverage, while the aircraft data complement the rather inaccurate microwave retrievals in cloudy areas of the extratropics and complement the SATOB data in cloud-free areas of the tropics.

REFERENCES

Arpe, K., A. Hollingsworth, A. P. Lorenc, M. S. Tracton, G. Cats, and P. Kallberg (1984). The response of numerical weather prediction systems to FGGE IIb data, Part II: Forecasts. (in preparation).

Baede, A. P. M. (1983). Impact of aircraft wind data on ECMWF analyses and forecasts during the FGGE period, November 8-19, 1979. Preprints, Sixth Conference on Numerical Weather Prediction, June 6-9, 1983, Omaha, Nebraska. American Meteorological Society, Boston, Mass.

Barwell, B. R., and A. Lorenc (1984). A study of the impact of aircraft wind observation on a large-scale analysis and numerical weather prediction system. Manuscript

Hollingsworth, A., and K. Arpe (1982). Biases in the ECMWF data assimilation system. ECMWF Tech. Memo No. 46.

omit

4. IMPACTS ON FORECASTS (GLAS)

Organizer	Eugenia Kalnay
Session Chairman	Milton Halem
Speakers	Eugenia Kalnay Kamal Puri
Rapporteur	Wayman E. Baker

D7

GLAS EXPERIMENTS ON THE IMPACT OF FGGE SATELLITE DATA ON NUMERICAL WEATHER PREDICTION

E. Kalnay, R. Atlas, W. Baker, and J. Susskind
Laboratory for Atmospheric Sciences
NASA/Goddard Space Flight Center

INTRODUCTION

The lack of adequate observational data has long been recognized as a major factor limiting both meteorological research and weather forecasting. Numerical weather prediction (NWP) models require the complete specification of the initial value of the forecast variables, yet only a fraction of the required initial data are available at any given time. The required data consist of the three-dimensional fields of temperature, humidity, and horizontal velocity at locations comparable in spatial density with the gridpoints of the model used for NWP.

The conventional data obtained by ground-based methods available at synoptic times (0000, 0600, 1200, and 1800 GMT) are concentrated over land areas primarily in the northern hemisphere and fall far short of being sufficient in number or coverage. Thus the use of space-based measurements offers an effective way to supplement the conventional synoptic network by providing observations not only in the traditionally data poor regions of the oceans, the southern hemisphere, and the stratosphere, but also at higher horizontal resolution than is available from conventional observations. However, since space-based measurements of temperature and wind have had larger error levels than those of rawinsonde observations, it has been argued that they could actually degrade analyses that incorporate them. In addition, polar orbiting satellites provide asynoptic data whereas numerical forecasts are performed at operational centers every day from 0000 and/or 1200 GMT initial conditions. Thus appropriate four-dimensional data assimilation schemes are required in order to improve NWP using both conventional and satellite observations.

In this paper, simulation studies and pre-FGGE data impact studies are briefly reviewed (Section 2). The rest of the paper is devoted to recent FGGE forecast impact studies, many of them performed at the Goddard Laboratory for Atmospheric Sciences (GLAS). Other experiments, such as those performed at the European Centre for Medium Range Weather Forecasts (ECMWF) and the British Meteorological Office, are reviewed elsewhere in this report. Section 3 is devoted to an early study of the first FGGE Special Observing Period (SOP-1), and Section 4 contains more recent results for SOP-1 and SOP-2. The forecast impact of the

drifting buoys is discussed in Section 5, and Section 6 presents some results obtained using GLAS temperature retrievals instead of operational soundings. Finally, some case studies are reviewed in Section 7.

REVIEW OF PREVIOUS SIMULATION AND PRE-FGGE IMPACT STUDIES

Since the advent of meteorological satellites in the 1960s, a considerable research effort has been directed toward the design of spaceborne meteorological sensors, the development of optimal methods for the utilization of satellite soundings and winds in global-scale models, and an assessment of the influence of existing satellite data and the potential influence of future satellite data on numerical weather prediction. Observing system simulation experiments have played an important role in this research and in the planning of Data Systems Tests (DSTs) and the First GARP Global Experiment (FGGE). Such studies have aided in the design of the global observing system, the testing of different methods of assimilating satellite data, and in assessing the potential impact of satellite data on weather forecasting.

Simulation studies conducted by Charney et al. (1969), Halem and Jastrow (1970), Jastrow and Halem (1973), Kasahara (1972), Gordon et al. (1972), and others indicated that all three primary meteorological variables--wind, pressure, and temperature--could be approximately determined if a continuous time history of any one of these variables were assimilated into a general circulation model. In addition, these studies provided an analysis of the GARP data requirements, the "useful" range of predictability, the need for reference level data, and the relative usefulness of asynoptic versus synoptic measurements and analysis. From the results, it was concluded that the assimilation of satellite-derived temperature profiles meeting the GARP data specifications, i.e., accuracies of $\pm$ 3 m/s in winds, $\pm$ 1°C in temperature, and $\pm$ 3 mb in pressure, should yield a substantial improvement to the accuracy of numerical weather forecasts.

However, an examination of the underlying rationale for these studies, as well as a comparison of their results with the results of subsequent real data impact tests, indicates several important limitations. The most important weakness stems from the fact that the same numerical model was used both to generate the simulated observations and to test the effectiveness of these observations (identical twin experiments). Other weaknesses relate to the model dependence of the studies and the specification of observational errors as random that result in an underestimation of their effect.

Early real data experiments using vertical temperature profile radiometer (VTPR) satellite temperature soundings showed very little forecast impact (Atkins and Jones, 1975; Bonner et al., 1976; Druyan et al., 1978). Bonner et al. (1976) attributed at least part of the smallness of the impact to the lack of retrieved temperatures in the meteorologically active baroclinic zones, where extensive cloud cover is usually present. In such areas the VTPR instrument was not capable of providing temperature information below the clouds.

In the DSTs conducted in preparation for FGGE by the National Aeronautics and Space Administration (NASA) and the National Oceanic and Atmospheric Administration (NOAA), data from two satellite observing systems were used: the High Resolution Infrared Sounder (HIRS) and Scanning Microwave Spectrometer (SCAMS) data from the Nimbus-6 satellite as well as VTPR data from the NOAA-4 satellite. These two satellite systems provided many more temperature profiles per day, and the profiles derived from Nimbus-6 were somewhat more accurate than the VTPR profiles, which had been used exclusively before. In addition, the SCAMS instrument was theoretically capable of sounding the atmosphere under cloudy conditions, thereby increasing the yield in and around baroclinic zones.

Ghil et al. (1979) utilized the GLAS general circulation model with second-order accuracy and a horizontal resolution of 4^{o} latitude by 5^{o} longitude to test different methods for the assimilation of the DST data. Their evaluation of 11 SAT and NOSAT forecasts, generated during the January to March 1976 (DST-6) period, showed that satellite-derived temperature data can have a modest but statistically significant positive impact on numerical weather forecasts in the 48 to 72 h range, as verified over the northern hemisphere, and this impact depends on the quantity of satellite data available and on the method of satellite data assimilation.

Tracton et al. (1980) using the National Meteorological Center (NMC) 6-level primitive equation model found a much smaller influence of DST-6 satellite sounding data. In their discussion of the differences between the GLAS and NMC impact results, Tracton et al. argued that the degree of influence of satellite sounding data decreases with the skill of the analysis system and that of the forecast model used for the impact testing. However, Atlas et al. (1982)conducted experiments showing that increased model resolution enhanced the forecast impact of satellite data.

AN ASSESSMENT OF THE FGGE SATELLITE OBSERVING SYSTEM DURING SOP-1

At the Goddard Laboratory for Atmospheric Sciences, a series of assimilation/forecast experiments (described in detail by Halem et al., 1982; and Kalnay et al., 1983) were conducted to assess the prognostic impact of the complete FGGE special observing system as well as its individual components, including temperature sounding data derived from the TIROS-N polar-orbiting satellite, cloud track winds determined from geostationary satellite observations, and drifting buoy data that were collected by satellite during FGGE. These experiments utilized the GLAS analysis/forecast system, which consists of an objective analysis scheme that uses the continuity provided by a model first-guess 6-hour forecast, integrated from a previous analysis. The analysis, a modified successive correction method that includes the effect of variable data density and quality (Baker, 1983), uses data collected in a $\pm$ 3-hour window about the analysis time. Both the analysis and the forecasts are still performed on the rather coarse 4^{o} latitude by

5° longitude grid, but the model utilized is the GLAS general circulation model with fourth-order accuracy (Kalnay-Rivas et al., 1977, 1979). During the analysis cycle, a Matsuno time scheme is used to eliminate high frequency gravity waves, in a procedure analogous to dynamic initialization with physical processes included.

Three experiments to assess the influence of the FGGE observing systems on the global analysis were performed for the period January 5 through March 5, 1979. The acronyms for the different experiments are FGGE, NOSAT, and NORAOB, after the data sets used. FGGE differs from NOSAT by the addition of satellite systems and special observing systems such as constant-level balloons, dropwindsondes, and certain aircraft reports collected by satellites (ASDAR). Similarly, NORAOB contains no rawinsonde data except for the NAVAIDS.

A measure of the influence of the observational data on an analysis cycle can be obtained by calculating the rms difference between the 6-hour forecast first guess and the completed analysis. Figures 1a and 1b present the rms difference fields between the 300 mb 6 h forecast (the first-guess field) of geopotential height and the final analysis for NOSAT and FGGE, respectively, for the period January 5 through January 21, 1979. The shaded areas in these figures indicate regions where the average difference during the 16-day period is small (less than 20 m); diagonal hatching indicates large corrections with an average greater than 60 m; blank areas correspond to intermediate values between 20 and 60 m.

Figure 1a shows that the rms difference between the 6 h NOSAT forecast and the NOSAT analysis over the vast oceanic regions in both hemispheres is less than 20 m, while the difference over regions with dense rawinsonde observations can be greater than 60 m. The observed structure in the 6 h forecast difference can be explained by the fact that the 6 h forecast itself defines the atmosphere in data-sparse regions, which leads to lower "errors." These small corrections are just an indication of the serious data gaps of the conventional network. Large 6 h differences are present in local regions in the southern hemisphere and in the tropics. By comparing Figure 1a with Figure 2a, which shows the distribution of rawinsondes, it may be seen that corrections as large as 120 m occur in data-sparse regions at isolated ocean and island stations. It is interesting to note that the maximum 6 h forecast error of 60 to 80 m occurs along the full length of the western boundary of the North American continent, as well as over other continental regions downstream of data-sparse areas. Along the northwest coast of Europe, this sharp error gradient does not appear because of the presence of ship rawinsondes in the Atlantic.

Figure 1b depicts the FGGE 6 h forecast rms error in the 300 mb height field. Comparison with Figure 1a reveals that the large 6 h forecast differences have been reduced significantly, especially along coastal boundaries and at isolated oceanic stations. On the other hand, a large increase of rms differences is observed in data-sparse regions such as the northern Pacific. This indicates that satellite and other FGGE observing systems have eliminated most of the data gaps in the NOSAT system and are introducing substantial changes in the 6 h forecast fields used in the FGGE analysis. Moreover, the closer

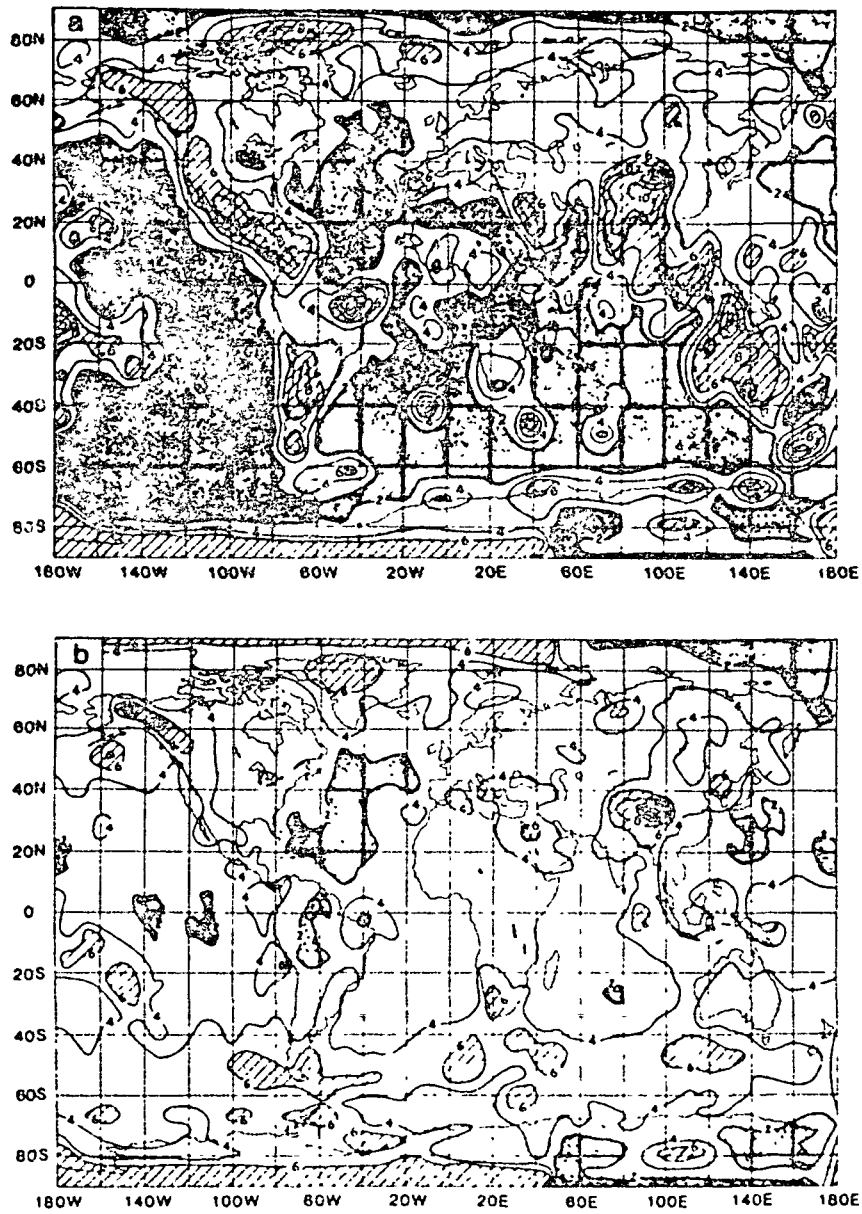

FIGURE 1 The rms difference between the 6 h forecast of the 300 mb geopotential height field and the analysis for the period January 5 to 21, 1979. Contour interval is 20 m. (a) RMS difference between the NOSAT analysis and forecast. (b) RMS difference between the FGGE analysis and forecast.

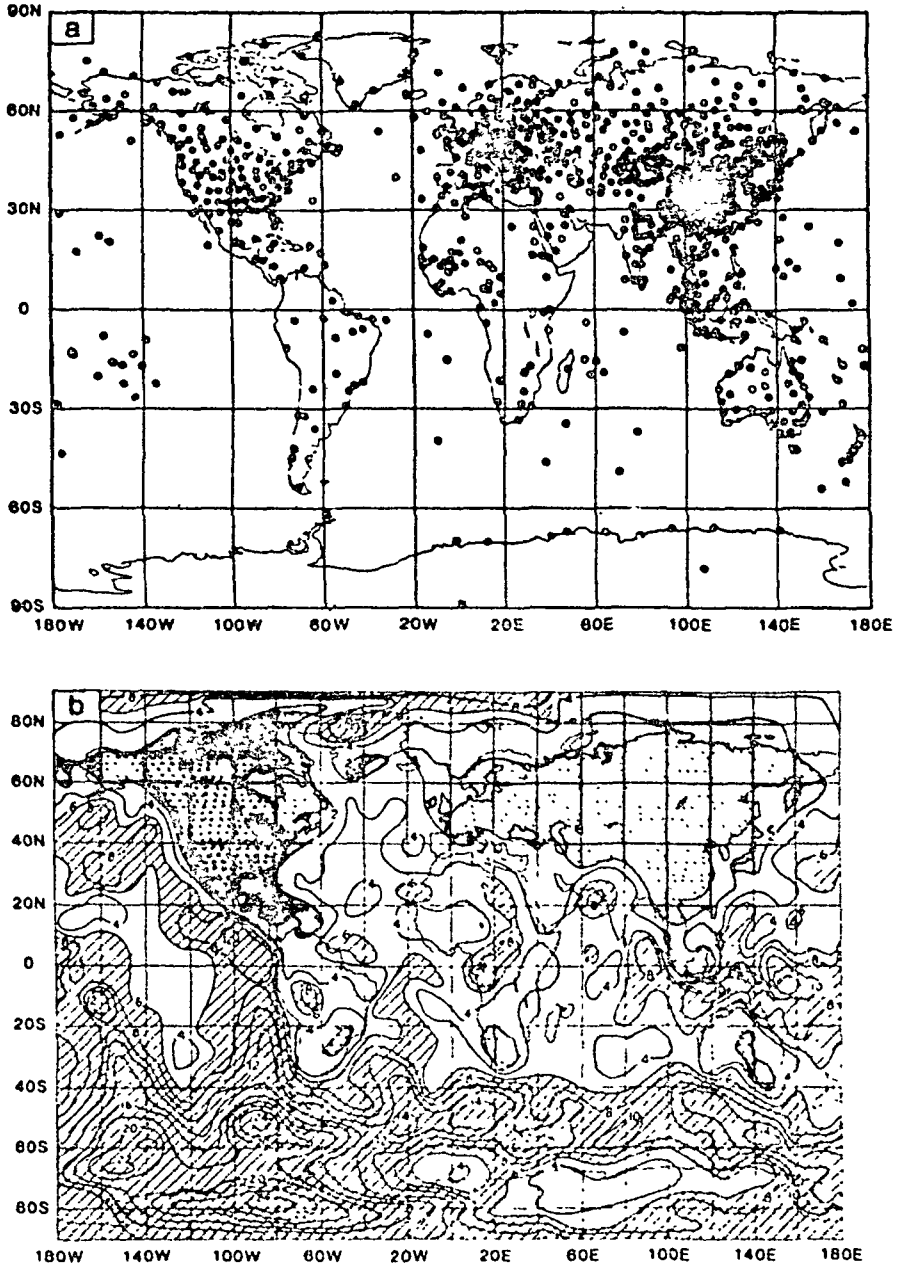

FIGURE 2 (a) Reporting rawinsonde stations at 0000 GMT January 9, 1979. (b) As in Figure 1, except the rms difference between the FGGE and NOSAT analyses.

agreement of the rawinsonde heights to the 6 h forecast in FGGE suggests that the satellite data over the oceans have produced a more accurate initial state.*

The rms difference between the FGGE and NOSAT analyses is shown in Figure 2b. In the data-sparse regions, the difference ranges from 80 m over the Pacific to more than 200 m in the southern hemisphere. The differences in the tropics and oceanic regions of the southern hemisphere are about as large as those between randomly chosen synoptic situations. Only over the North American and Eurasian continents is the difference between the analyses smaller than 20 m.

A series of five-day forecasts were made from initial conditions taken every fourth day from January 9 through March 2, 1979 from each of the three analysis cycles. Figures 3a and 3b show the S_1 skill-score impact results of three-day forecasts evaluated relative to the NMC analysis over North America, Europe, and Australia for the sea level pressure and 500 mb geopotential height fields. The improvement over Australia with the FGGE data is more consistent and significant in the sea level pressure and 500 mb geopotential height than over the northern hemisphere. A smaller positive impact occurs over Europe. The sea level pressure impact over North America is negligible, while at 500 mb the impact is less consistent than over Europe but still positive.

COMPARISONS OF SOP-1 and SOP-2 FORECAST IMPACTS

Recently, forecast impact experiments have been performed with an analysis/forecast system that has a number of improvements on the system utilized by Halem et al. (1982). Several modifications were made in the analysis scheme, the most important being the interpolation of the analysis minus 6 h forecast deviations rather than of the analyzed fields themselves. The analysis scheme with the present modifications is described in detail in Baker (1983). The forecast model is still the 4° latitude, 5° longitude, and 9 vertical levels GLAS fourth-order general circulation model with several minor corrections implemented in the physics and numerics.

The improved vertical interpolation in the analysis resulted in better assimilation of rawinsonde data, which has more vertical structure than satellite data. As a result, there was an improvement of the forecasts derived from conventional data only and, consequently, a small reduction of the positive impact of satellite data from that obtained by Halem et al. (1982).

Although the experiments are not yet complete, the following preliminary figures summarize the number of cases of positive and

---

*The large rms 6 h differences over the Himalayas in Figure 1a, which remain in Figure 1b, are due to the vertical interpolation from the model first-guess in σ coordinates to the analysis in pressure coordinates.

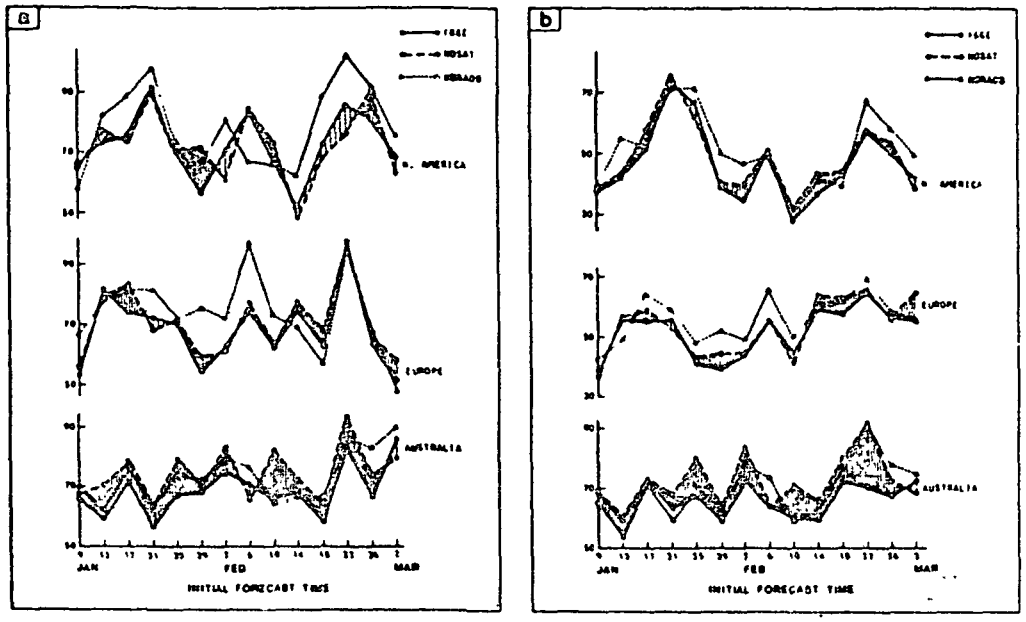

FIGURE 3 S_1 skill scores for 72 h forecasts from the FGGE, NOSAT, and NORAOB systems over North America, Europe, and Australia from 0000 GMT of the indicated initial days during SOP-1. All forecasts verified against the NMC analysis. (a) Sea level pressure forecasts. (b) 500 mb forecasts.

negative forecast impacts verified so far separately over two regions in the northern hemisphere (covering approximately North America and Europe) and the southern hemisphere (Australia and South America). Two forecasts are considered to be different if their S_1 skill scores, verified with the ECMWF analysis, differ by more than 2 points. Only those forecasts for which at least one of the forecasts retains useful skill (defined as $S1 \leq 80$ for sea level pressure and ≤ 60 for 500 mb heights) are counted.

Figures 4 and 5 present the results corresponding for SOP-1 and SOP-2. In the northern hemisphere, the forecast impact of the FGGE special observing system is positive and somewhat larger in winter than in summer. In the southern hemisphere, the impact is much larger both in winter and in summer.

FORECAST IMPACT OF DRIFTING BUOYS

Two recent papers (Bourke et al., 1982; Kalnay et al., 1983) have presented results of studies of the impact of the FGGE observing system in the southern hemisphere. While both papers concluded that the TIROS-N satellite temperature soundings had a large positive impact,

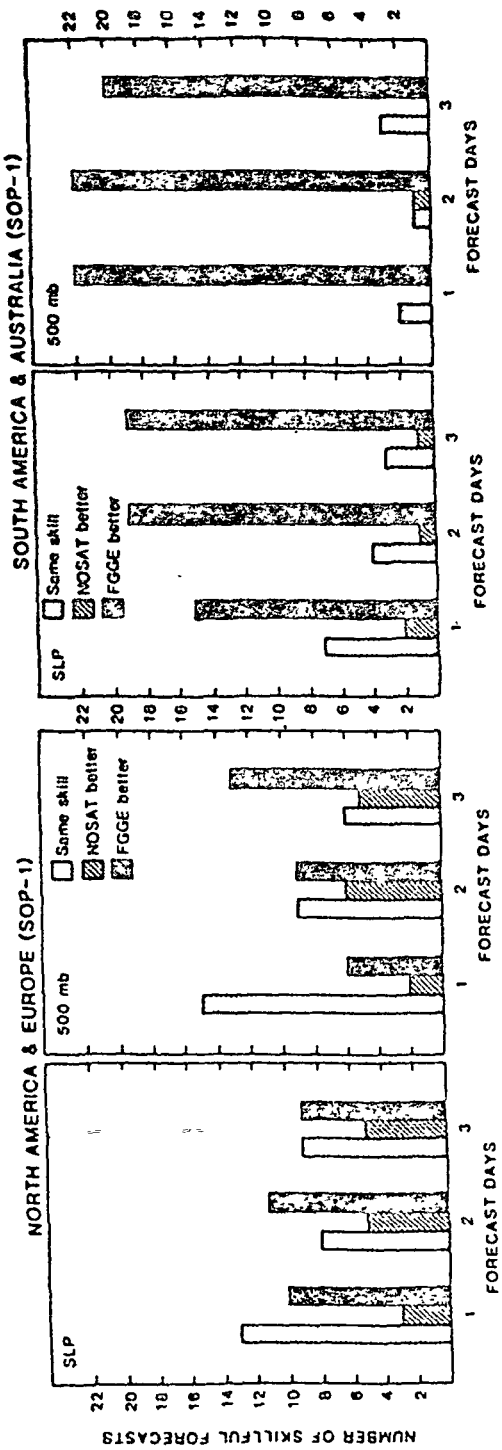

FIGURE 4 Number of cases of positive and negative forecast impacts from the FGGE special observing system during SOP-1.

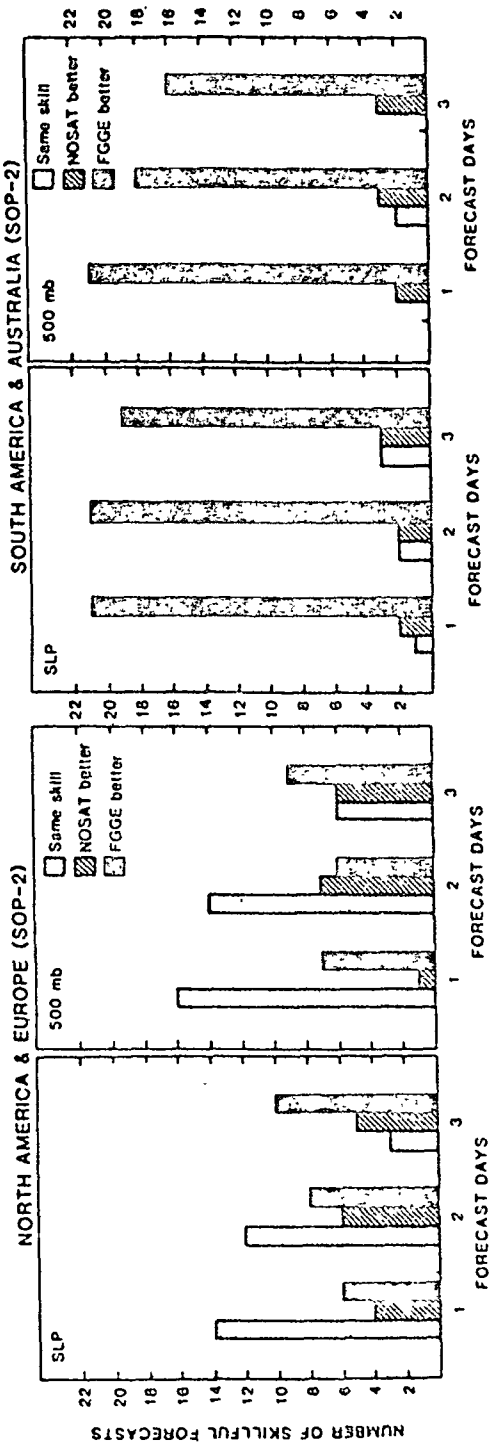

FIGURE 5 Number of cases of positive and negative forecast impacts from the FGGE special observing system during SOP-2.

the conclusions were significantly different with respect to the impact of the drifting buoys.

The Bourke et al. (1982) study was based on the comparison of assimilation cycles covering the period May 17 to May 26, 1979 using the ANMRC analysis/forecast system. Three assimilation cycles were performed: a control assimilation cycle including all FGGE data, a cycle without buoys (NB), and a cycle without satellite temperature soundings (NT). Only three forecasts from May 20, May 22, and May 24, 1979 were performed from each cycle. The results indicated that over the Australian region, the buoys had a significant positive impact. In hemispheric verifications the impact of the buoys was much smaller than that of satellite soundings, except on 12 h sea level pressure forecasts.

Kalnay et al. (1983) performed a study covering the FGGE SOP-1 period (January 5 to March 5, 1979). Four assimilation cycles were conducted: a "FGGE" cycle that used all FGGE data, a "NOSAT" cycle that used only conventional data (surface observations by land stations and ships, rawinsondes, and aircraft reports), a "NOSAT plus BUOYS" cycle in which the buoy data was added to the conventional data base, and a "FGGE minus BUOYS" cycle in which drifting buoys were subtracted from the FGGE data. About 14 forecasts from initial conditions every four days in the cycle were performed for each cycle. The results verified over the South American region indicated that the buoys had a substantial positive impact when added to the NOSAT system, but on the average a negligible impact when deleted from the full FGGE four-dimensional assimilation.

There are several possible causes for these different results:

1. The two studies used different seasons, southern hemisphere summer in the Kalnay et al. (1983) paper and early winter in the Bourke et al. (1982) paper. This introduces significant differences in the atmospheric circulation, and hence possible data impact differences.
2. The number of buoys, which started to be deployed during the early FGGE period, increased considerably during the SOP-2.
3. There is a possible sampling problem in comparing about a dozen forecasts covering two months with three forecasts corresponding to one week.
4. The results were verified in different regions, and the data impact may depend on this factor.
5. The two analysis/forecast systems may show different sensitivity to the data.

It is of great practical importance to determine the factors that may have influenced these results. For this purpose Kalnay et al. (1984) extended the study to FGGE SOP-2 (May and June 1979) and performed similar buoy data impact studies. This study included the three forecast cases previously performed by Bourke et al. (1982), and verifications over the same regional areas.

The results of Kalnay et al. (1984) are summarized as follows: As indicated in Figures 6 and 7, the addition of buoys has little effect in the northern hemisphere both in winter and in summer. In the

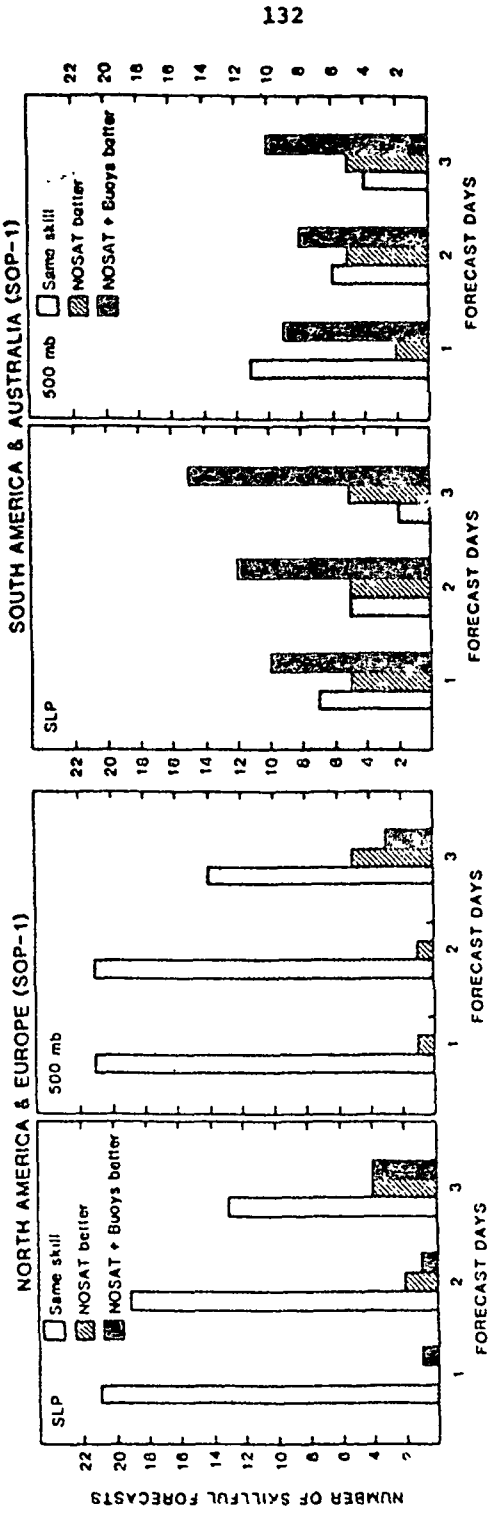

FIGURE 6 Number of cases of positive and negative forecast impacts resulting from adding drifting buoy data to the NOSAT system during SOP-1.

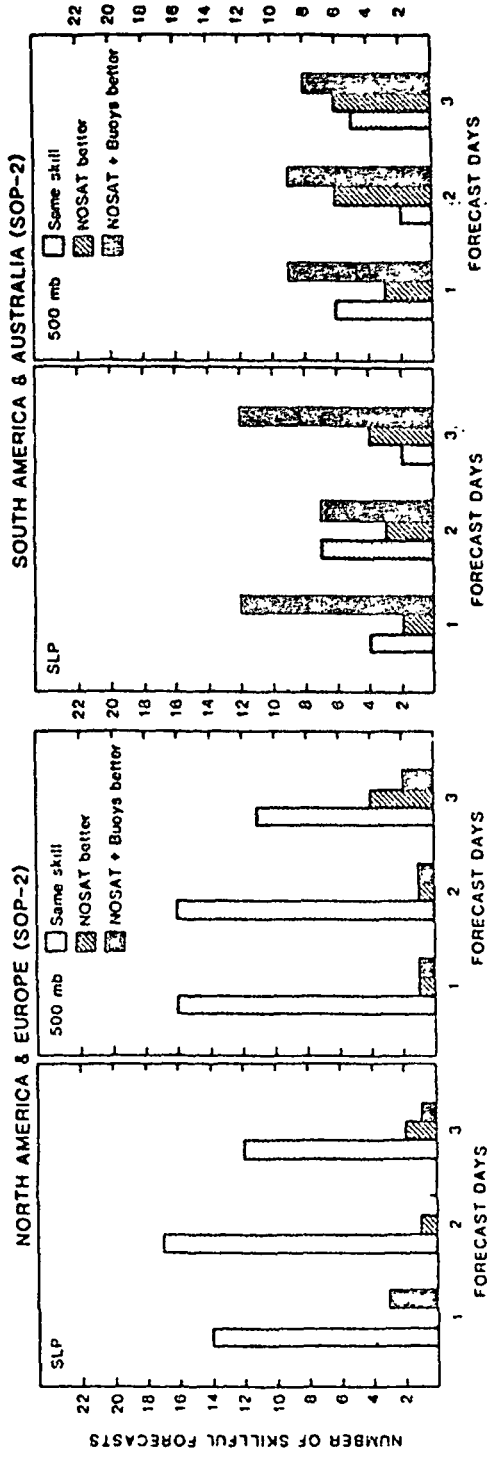

FIGURE 7 Number of cases of positive and negative forecast impacts resulting from adding drifting buoy data to the NOSAT system during SOP-2.

southern hemisphere, the addition of buoy data to the conventional observing system has a clear positive impact, especially on the sea level pressure forecast in both seasons.

The result of deleting the buoy data from the complete FGGE system is shown in Figures 8 and 9. In agreement with Kalnay et al. (1983), the impact from deleting the buoys is negligible during SOP-1 both in the southern and northern hemispheres. During SOP-2 the impact is somewhat larger, especially during the first two days of the southern hemisphere forecasts. The buoy information is therefore less redundant during SOP-2 than SOP-1, which helps to explain the difference in the results obtained by Kalnay et al. (1983) and Bourke et al. (1982).

As an example of the different impacts in the southern hemisphere, 72 h sea level pressure forecasts from 0000 GMT May 20, 1979 are presented. Figures 10a and 10b show the 72 h NOSAT and FGGE prognoses, while Figures 10c and 10d show the corresponding forecasts from the NOSAT plus buoy data and FGGE minus buoy data experiments, respectively. The verifying ECMWF analysis at 0000 GMT May 23, 1979 is shown in Figure 10e.

Comparison of Figures 10a and 10b with the analysis shows that when all FGGE data are included, there is a large improvement over southern South America and much of the southern hemisphere extratropical oceans. In particular, the intensity and location of several cyclones are better predicted in the FGGE forecast. Over Australia the differences are smaller. Neither the NOSAT nor FGGE experiments predict the cyclone south of the Great Australian Bight.

The addition of buoy data to the NOSAT assimilation (Figure 10c) produces a large improvement over South America and portions of the extratropical oceans. This effect is in general smaller than that for the complete FGGE data set. Removal of the buoys from the FGGE system (Figure 10d) has a smaller effect over most areas, although examples of large degradation are evident. In particular, the cyclone near 60°S, 80°E is significantly better forecast when buoy data are included with other FGGE data sets.

IMPACT OF GLAS TEMPERATURE SOUNDINGS AND CLOUD TRACKED WINDS

Susskind et al. (1984) have developed a temperature retrieval system based on the inversion of the physical radiative transfer equation using simultaneously infrared and microwave channels. As a result, the system not only produces atmospheric temperature soundings (GLAS retrievals) but also a number of important climate and weather parameters (ice and snow cover, cloud heights and amounts, day and night land and sea-surface temperatures, and others that are discussed elsewhere in this report).

In Figure 11 a preliminary comparison of the forecast skill using the FGGE system is presented, in one case with the GLAS temperature retrievals, and in the other the NESS retrievals operational during FGGE SOP-1. In the northern hemisphere, the use of the GLAS soundings produces a significant improvement in the sea level pressure forecasts. Most of the improvements are as large as 5 S_1 points or

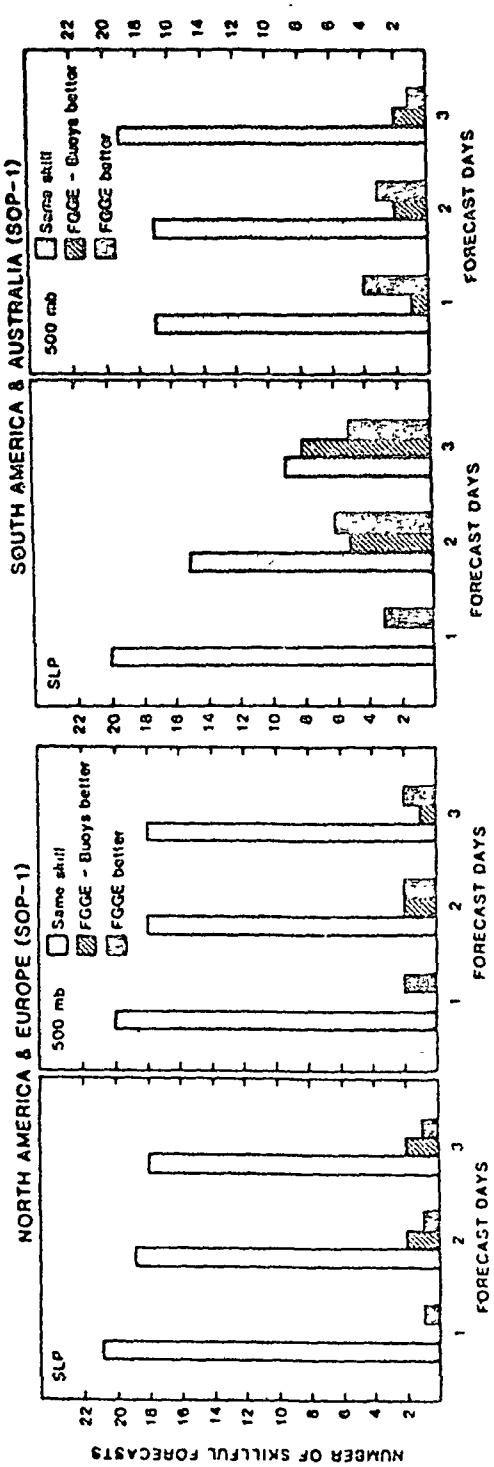

FIGURE 8 Number of cases of positive and negative forecast impacts resulting from deleting drifting buoy data from the FGGE system during SOP-1.

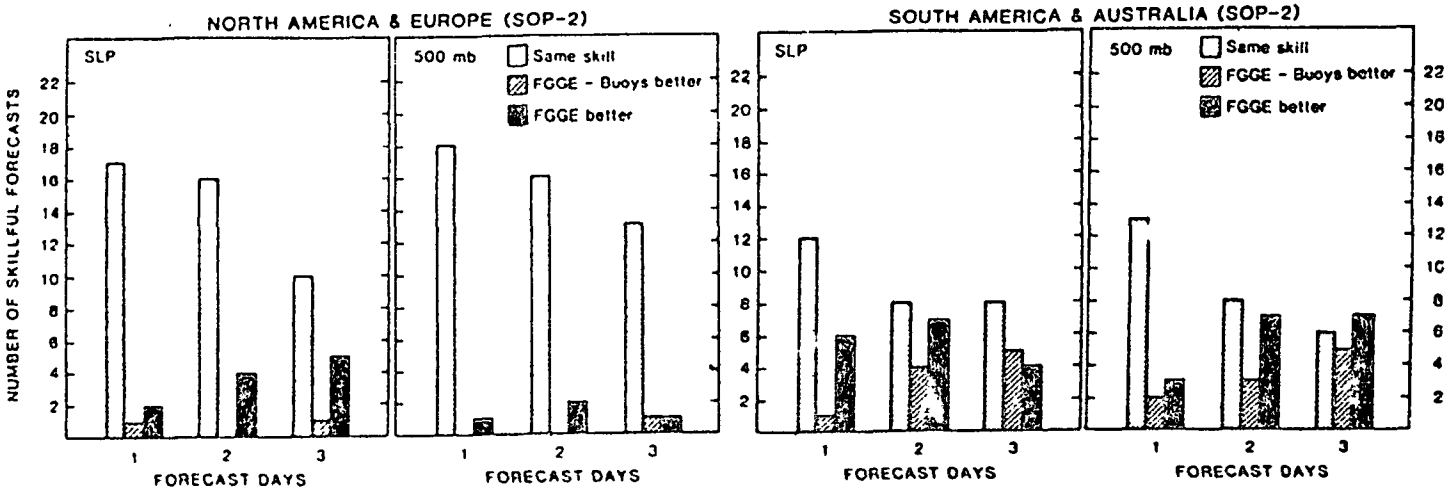

FIGURE 9 Number of cases of positive and negative forecast impacts resulting from deleting drifting buoy data from the FGGE system during SOP-2.

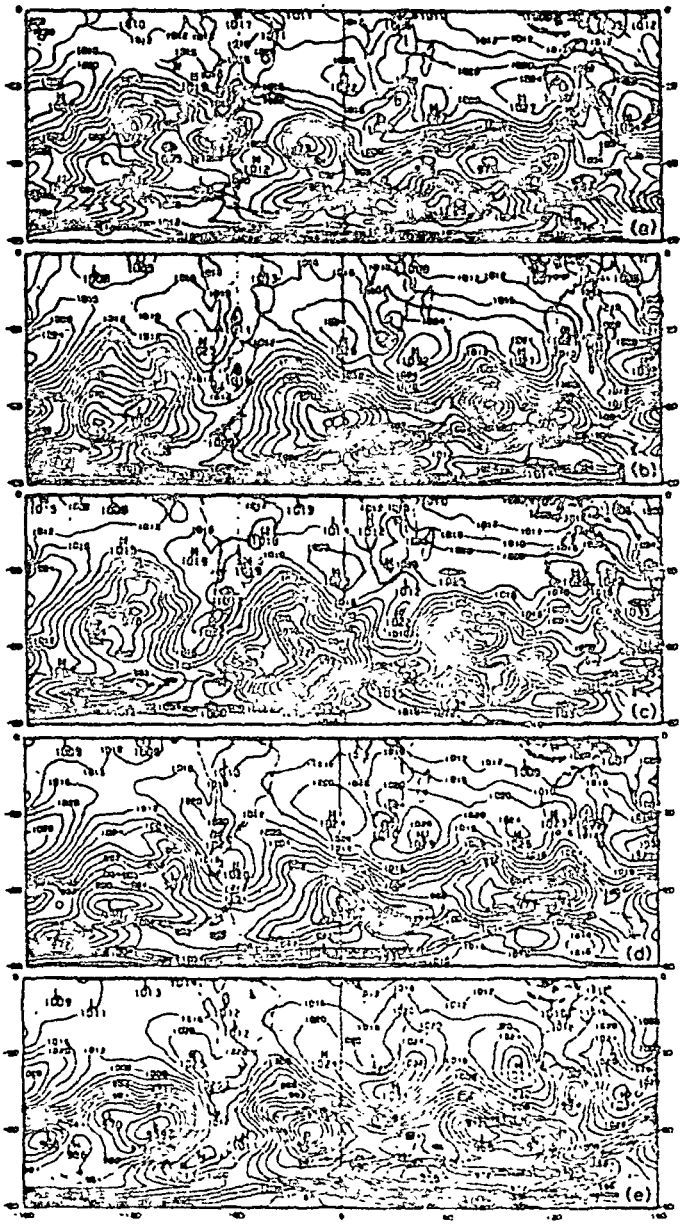

FIGURE 10 Southern hemisphere sea level pressure fields for 0000 GMT May 23, 1979. (a) The 3-day NOSAT forecast. (b) The FGGE forecast. (c) The NOSAT plus buoy forecast. (d) The FGGE minus buoy forecast. (e) The verifying analysis.

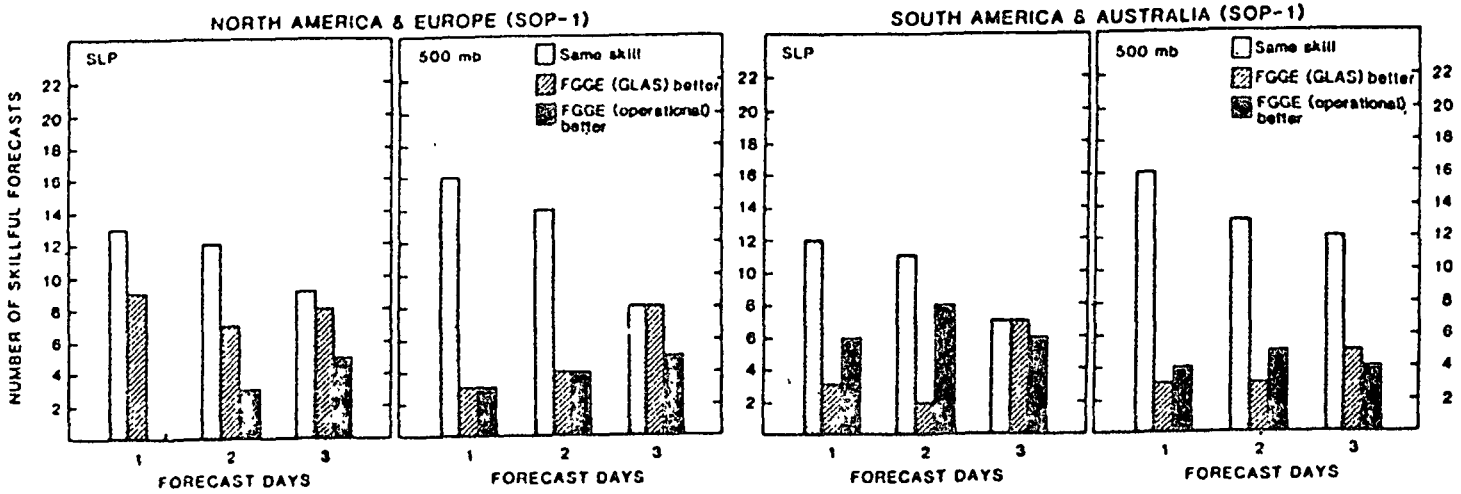

FIGURE 11 Number of cases of positive and negative forecast impacts from replacing the operational TIROS-N soundings with GLAS temperature soundings during SOP-1.

more, and almost all occur over North America, virtually eliminating the cases of negative impacts when compared with NOSAT forecasts. This suggests that the GLAS retrievals are superior to the FGGE operational retrievals in the Pacific Ocean. This may be partly due to the data gap present in the operational retrievals off the west coast of North America at 00 GMT (see Figure 1a of Halem et al., 1982). Furthermore, the accuracy of the GLAS retrievals is much less affected by cloudiness than that of the operational retrievals (Susskind et al., 1984), which may have been an advantage in generating temperature soundings in the Pacific storm track region. In the southern hemisphere, on the other hand, the use of the GLAS retrievals produces for the first two days slightly worse forecasts than the operational retrievals, although both systems are vastly superior to the NOSAT forecasts.

In Figure 12 a preliminary comparison is made of the forecasts using conventional data, with GLAS soundings, and the full FGGE system, also with GLAS soundings. It is clear that the additional components of the FGGE system (and in particular cloud-track winds, which constitute the largest component) have made a significant contribution to the forecast skill in the southern hemisphere. Even in the northern hemisphere their contribution is important especially in the 3-day forecast.

In the previous comparisons, verifications were limited to land areas where there are enough conventional observations, avoiding a possible bias toward satellite data that constitute most of the oceanic observations. In Figures 13 and 14 we now present the ensemble of about 8-10 hemispheric verifications (S_1 skill scores) against the ECMWF analysis of SOP-2. Figure 13a shows that the FGGE satellite data improved the forecast in the northern hemisphere by about six hours, indicated schematically by the dotted lines. In the southern hemisphere, the improvement is much larger, about 48 to 60 hours.

Figure 14a indicates that when the buoys are added to the sparse conventional (NOSAT) system in the southern hemisphere, they improve the forecast skill by about 24 hours. In the presence of the satellite observing system, however, they contribute only about 12 hours (Figure 14b). Figure 14c demonstrates that the rest of the satellite temperature retrievals and cloud-track winds added to the NOSAT system contribute 24 to 36 hours more to the forecast skill than buoys.

OTHER STUDIES

In a joint study by the Israel Meteorological Service (IMS) and NOAA/NESDIS, data impact experiments were also performed (Thomasell et al., 1983; Wolfson et al., 1983). The 5-layer subhemispheric primitive equation model of the IMS, which has realistic orography but no physics except for surface friction, was utilized. The analysis scheme used is a successive correction method, but with a first guess provided by the 12-hour old final analysis. They ran experiments with and without satellite temperature soundings for three periods (January 1 to 12, 1980, January 15 to 23, 1979, and December 20 to 26, 1979) and performed 2-day forecasts every 12 GMT. They found that in this system, the satellite data generally reduced systematic forecast errors

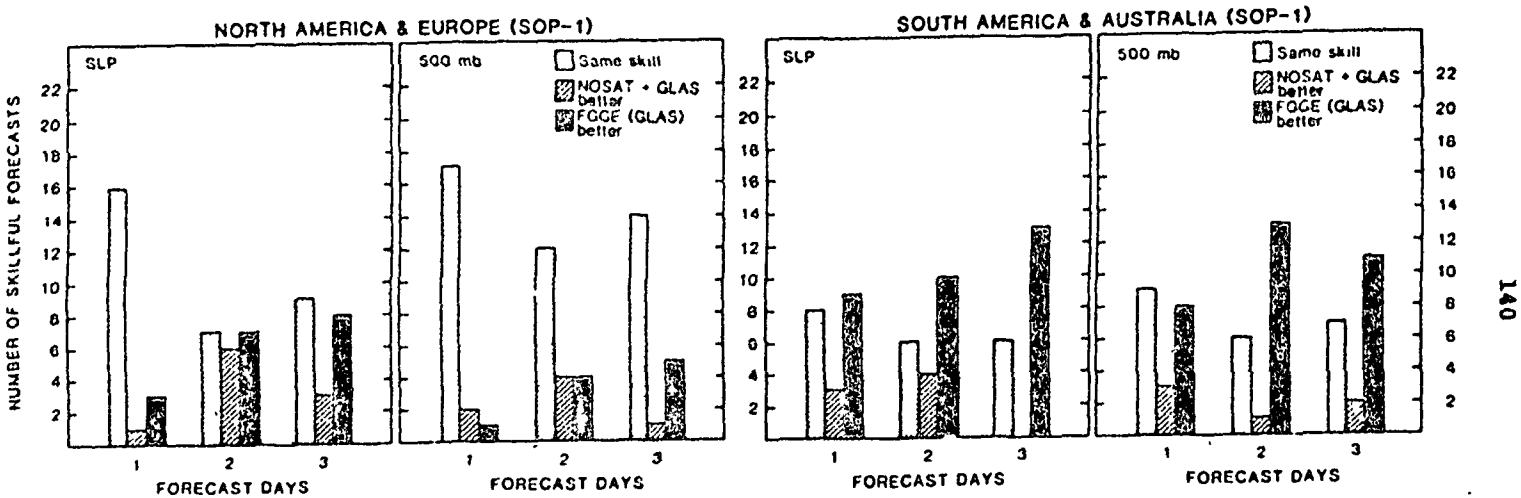

FIGURE 12 Number of cases of positive and negative forecast impacts from deleting the FGGE special observing system except for the GLAS temperature soundings (SOP-1).

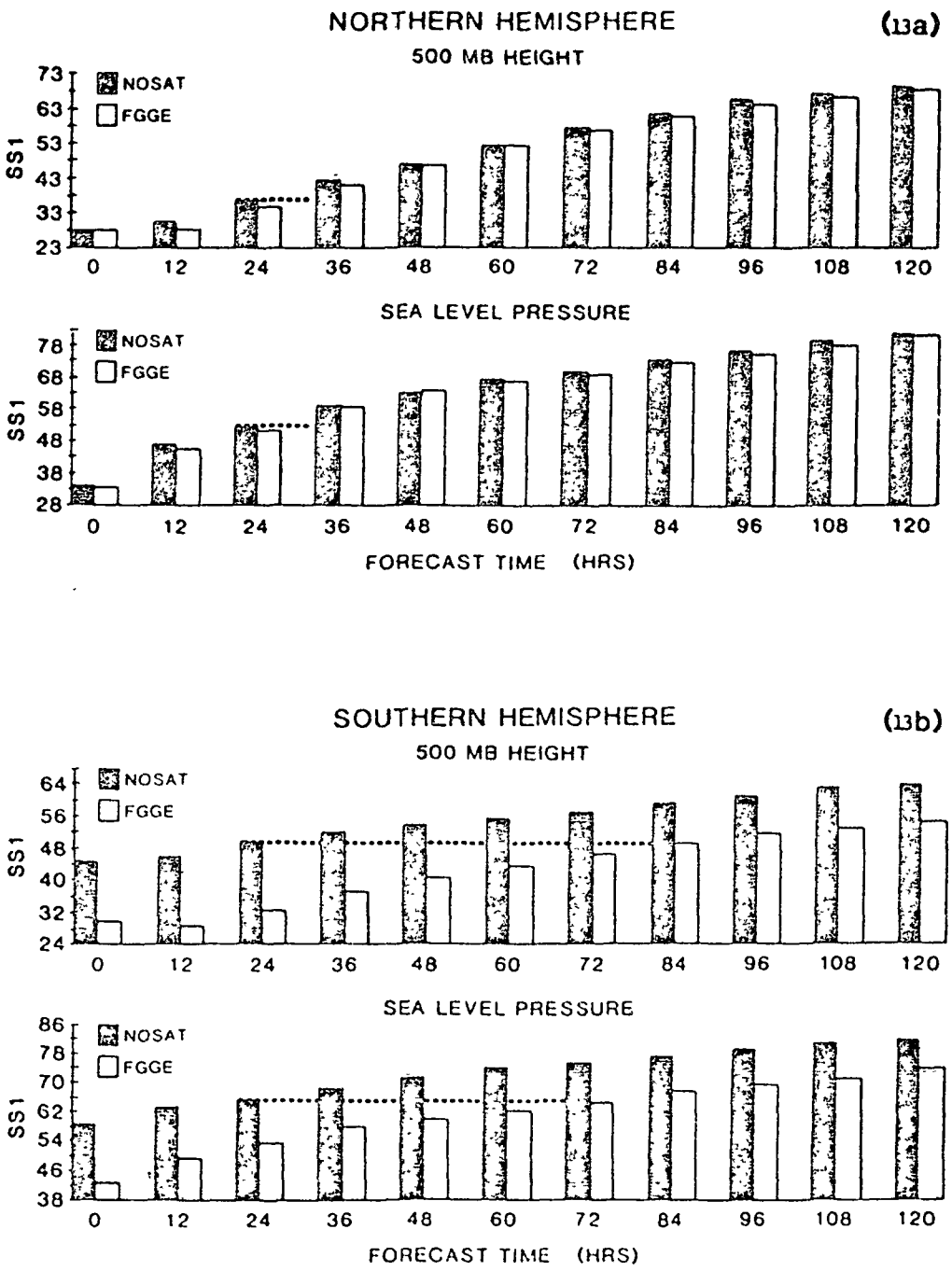

FIGURE 13 Improvement in skill from the FGGE satellite data for an ensemble of forecasts verified against the ECMWF analysis.

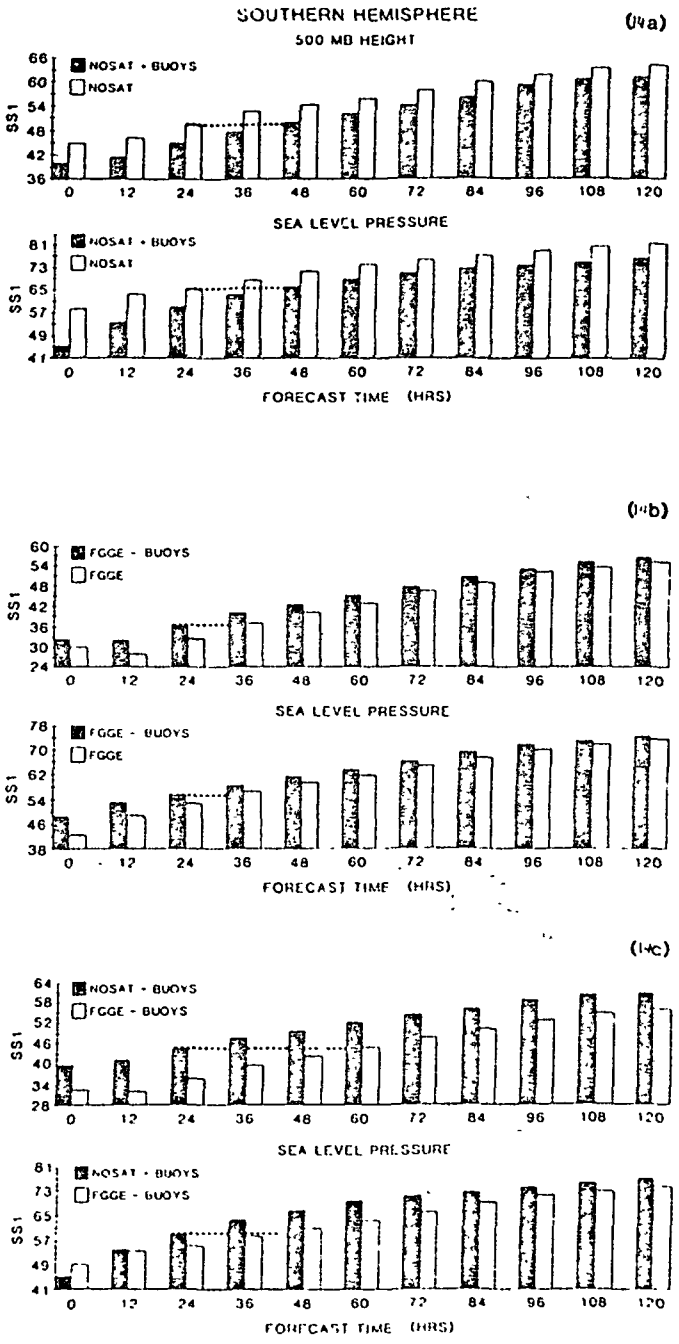

FIGURE 14 Impact of the drifting buoys in the southern hemisphere for an ensemble of forecasts verified against the EMCWF analysis.

as well as rms forecast errors especially over regions where the satellite data had been introduced. Since no satellite data were used over Eurasia, no significant impacts were found there. This system was found to be prone to errors along the line of time discontinuity of satellite data. Both this effect and the rather large positive forecast impact in the northern hemisphere obtained with this system may be the result of the type of analysis cycle utilized. Unlike the four-dimensional analysis/forecast cycles performed at operational centers, at GLAS, and at GFDL, the IMS system does not allow the information from data-rich regions to be transported to data-sparse regions.

Finally, we mention a case study performed by Baker et al. (1984) utilizing different FGGE data bases to produce analyses from January 18 to 21, 1979. Three-day forecasts starting on January 21 from the different analyses were then produced and compared. This day was chosen because it resulted in the largest negative impact over North America of the FGGE observing system with respect to the NOSAT system. It was found that the use of GLAS temperature retrievals eliminated this negative impact. An interactive analysis/forecast/retrieval system, in which the 6 h forecast was also used as a first guess for the GLAS temperature retrievals, produced a further improvement of the forecast.

The accuracy of satellite temperature soundings depends on the vertical structure of atmospheric columns associated with different types of air masses. We plan to perform further experiments to test whether the use of "interactive" systems, in which the temperature retrieval algorithm benefits from the latest available information about the atmospheric structure, results in significant improvements over a longer period.

ACKNOWLEDGEMENT

The work reported here is the result of several years of effort that would not have been possible without the strong support of the National Aeronautics and Space Administration and the Goddard Space Flight Center management.

REFERENCES

Atkins, M. J., and M. V. Jones (1975). An experiment to determine the value of satellite infrared spectrometer (SIRS) data in numerical forecasting. Meteorol. Mag. 104, 125-142.

Atlas, R., M. Halem, and M. Ghil (1982). The effect of model resolution and satellite sounding data on GLAS model forecasts. Mon. Wea. Rev. 100, 662-682.

Baker, W. E. (1983). Objective analysis and assimilation of observational data from FGGE. Mon. Wea. Rev. 111, 328-342.

Baker, W. E., R. Atlas, M. Halem, and J. Susskind (1984). A case study of forecast sensitivity to data and data analysis techniques. Mon. Wea. Rev. 112, 1544-1561.

Bonner, W., P. Lemar, R. van Haaren, A. Desmarais, and H. O'Neil (1976). A test of the impact of NOAA-2 VTPR soundings on operational analyses and forecasts. NOAA Tech. Memo. NWS-57, NMC, Washington, D.C., 43 pp. (NTIS PB-256075).

Bourke, W., K. Puri, and R. Seaman (1982). Numerical weather studies from the FGGE southern hemisphere data base. Mon. Wea. Rev. 110, 1787-1800.

Charney, J., M. Halem, and R. Jastrow (1969). Use of incomplete historical data to infer the present state of the atmosphere. J. Atmos. Sci. 26, 1160-1163.

Druyan, L. M., T. Ben-Amram, Z. Alperson, and G. Ohring (1978). The impact of VTPR data on numerical forecasts of the Israel Meteorological Service. Mon. Wea. Rev. 106, 859-869.

Ghil, M., M. Halem, and R. Atlas (1979). Time-continuous assimilation of remote-sounding data and its effect on weather forecasting. Mon. Wea. Rev. 107, 140-171.

Gordon, C. T., L. Umscheid, Jr., and K. Miyakoda (1972). Simulation experiments for determining wind data requirements in the tropics. J. Atmos. Sci. 29, 1064-1075.

Halem, M., and R. Jastrow (1970). Analysis of GARP data requirements. J. Atmos. Sci. 27, 177.

Halem, M., E. Kalnay, W. E. Baker, and R. Atlas (1982). An assessment of the FGGE satellite observing system during SOP-1. Bull. Amer. Meteorol. Soc. 63, 407-426.

Jastrow, R., and M. Halem (1973). Simulation studies and the design of the First GARP Global Experiment. Bull. Amer. Meteorol. Soc. 54, 13-21.

Kalnay, E., R. Atlas, W. Baker, and M. Halem (1983). FGGE forecast impact studies in the southern hemisphere. Proceedings of the First International Conference on Southern Hemisphere Meteorology, July 31-August 6, pp. 180-183.

Kalnay, E., R. Atlas, and M. Halem (1984). Forecast skill of drifting buoys in the southern hemisphere. Proceedings of the Tenth Conference on Weather Forecasting and Analysis, June 25-29, Clearwater Beach, Florida.

Kalnay-Rivas, E., A. Bayliss, and J. Storch (1977). The fourth-order GISS model of the global atmosphere. Beitr. Phys. Atmos. 50, 299-311.

Kalnay-Rivas, E., and D. Hoitsma (1979). The effect of accuracy, conservation, and filtering on numerical weather forecasting. Preprints, Fourth Conference on Numerical Weather Prediction, Silver Spring, Md. American Meteorological Society, Boston, pp. 302-312.

Kasahara, A. (1972). Simulation experiments for meteorological observing systems for GARP. Bull. Amer. Meteorol. Soc. 53, 252-264.

Susskind, J., J. Rosenfield, D. Reuter, and M. T. Chahine (1984). Remote sensing of weather and climate parameters from HIRS2/MSU on TIROS-N. J. Geophys. Res., 89D, 4677-4694.

Thomasell, A., J. T. Chang, N. Wolfson, A. Gruber, and G. Ohring (1983). The impact of satellite soundings and their distribution on forecast accuracy. Proceedings of the Sixth Conference on Numerical Weather Prediction, Omaha, Nebraska, pp. 237-242.

Tracton, M. S., A. J. Desmarais, R. D. McPherson, and R. J. van Haaren (1980). The impact of satellite soundings upon the National Meteorological Center's analysis and forecast system--the data systems tests results. Mon. Wea. Rev. 108, 543-586.

Wolfson, N., A. Thomasell, G. Ohring, H. Gruber, H. Broderick, and Y. T. Chang (1983). The impact of satellite data on the systematic error of a NWP model. Proceedings of the Sixth Conference on Numerical Weather Prediction, Omaha, Nebraska, pp. 237-242.

omit

5. TROPICAL FORECASTS

Organizer	Eugenia Kalnay
Session Chairman	Paul R. Julian
Speakers	T.N. Krishnamurti William A. Heckley
Rapporteur	Jagadish Shukla

THE IMPACT OF THE FGGE OBSERVING SYSTEMS IN THE SOUTHERN HEMISPHERE

K. Puri, W. Bourke, R. Seaman
Australian Numerical Meteorology Research Centre

ABSTRACT

Results of studies carried out at the Australian Numerical Meteorology Research Centre (ANMRC) and the Australian Bureau of Meteorology to assess the impact of FGGE on numerical weather prediction in the southern hemisphere are presented. These studies indicate that the FGGE data base had a significant impact on analysis and numerical weather prediction. From the operational standpoint, the most outstanding contribution was made by the drifting buoy data that enabled reliable routine surface pressure analyses to be made over the entire hemisphere. The results of a limited study using the ANMRC data assimilation scheme show that the quality of prediction to 48 hours hinges crucially on both the buoy pressure data and satellite temperature soundings with single level satellite winds having a small impact.

INTRODUCTION

The purpose of this paper is to provide an assessment of the impact of FGGE on numerical weather prediction (NWP) in the southern hemisphere. From the earliest stages of the planning of the experiment, it was realized that it would be the southern hemisphere that would pose the most formidable problems to the implementation of a global observing system and that it would be the southern hemisphere that would stand to gain most from a successful experiment. The magnitude of problems caused by the inadequate data base is evident from Figure 1 (taken from Zillman, 1983), which is a map of the Regional Basic Synoptic Network of upper air observing stations of the World Weather Watch. Although the situation is not too different in the northern and southern tropics, it can be seen that south of 30°S the southern hemisphere networks are extremely sparse with an entire 90° segment in the south Pacific completely devoid of upper air stations of any kind. The coverage of surface pressure data is similarly very poor. An indication of the improvement in coverage during FGGE is shown in Figure 2, which clearly shows the role of drifting buoys in filling up the great data voids of the oceans.

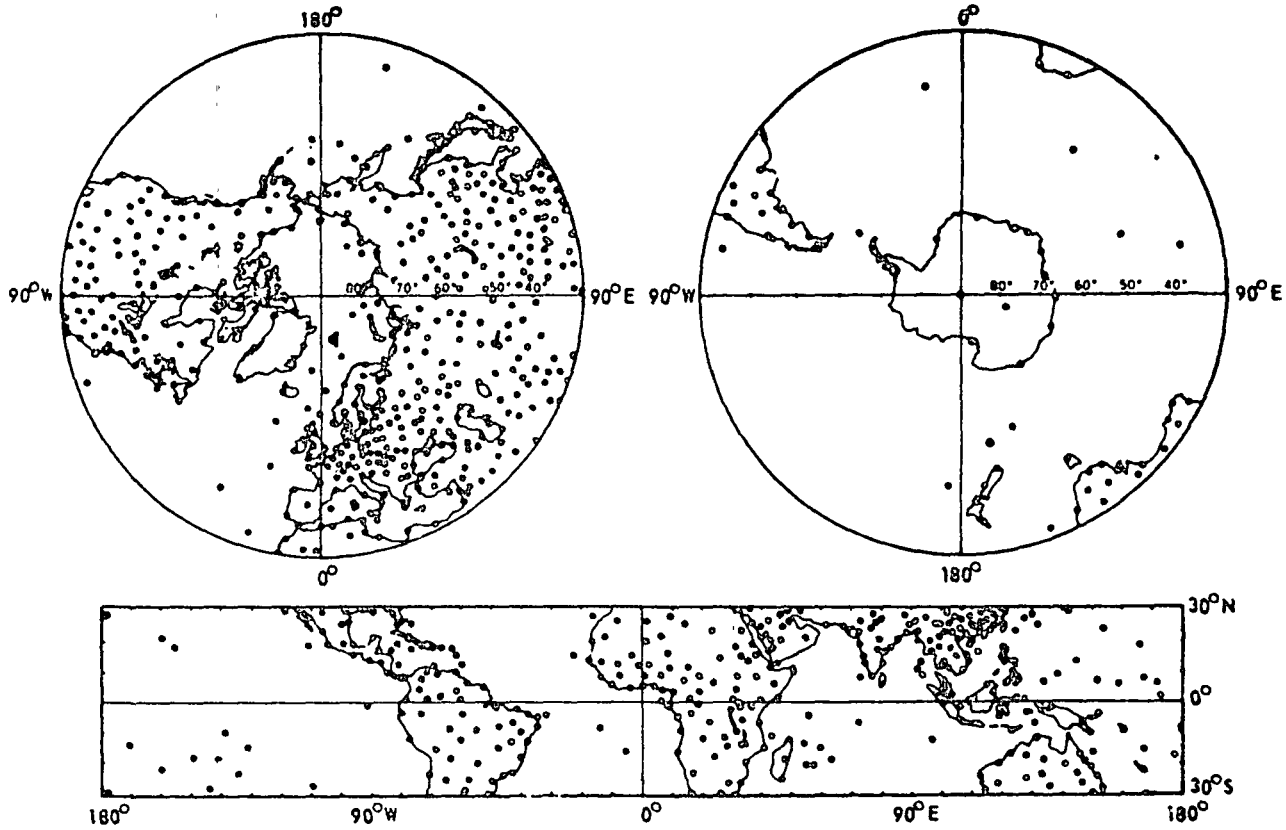

FIGURE 1 Coverage of upper air observing stations included in the Regional Basic Synoptic Network of the WWW Global Observing System. Each dot represents a station providing one or more conventional (balloon) upper air soundings of wind and/or temperature daily.

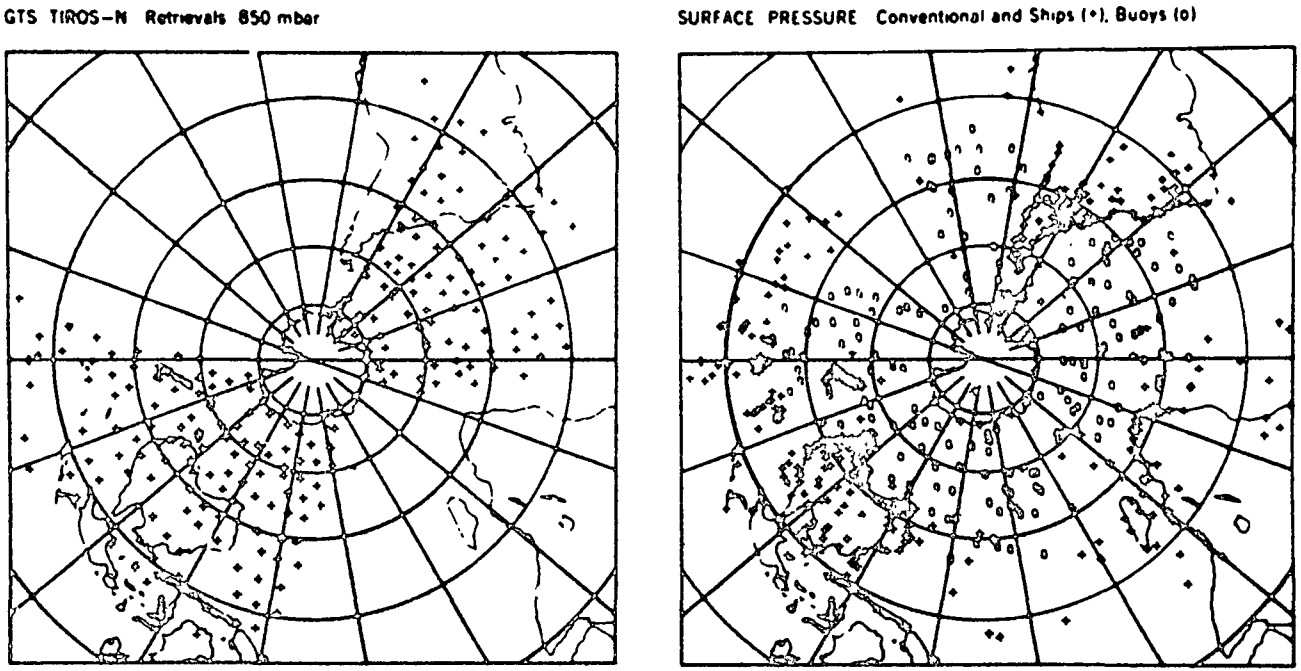

FIGURE 2 Typical data coverage at 1700 GMT, May 17, 1979. The TIROS-N retrievals have about a 500 km resolution.

Impact assessments are made from two standpoints. First, with the passage of over four years since the completion of FGGE, it is possible to retrospectively assess the operational impact of the FGGE observing systems during 1979. This is especially so in the southern hemisphere where, with the exception of satellite soundings, the observation network has regressed to something approaching the pre-FGGE equivalent. The second approach is through controlled experimentation using advanced four-dimensional assimilation models as are commonly used at major NWP centers. The work described here will focus on a number of impact experiments carried out at ANMRC. It should be pointed out that other institutes have also carried out impact studies; however, in this paper only results of studies carried out at ANMRC and the Australian Bureau of Meteorology will be described. A detailed review of the impact of FGGE in the southern hemisphere has been made by Zillman (1983) and considerable use of this review has been made here. Gauntlett (1982) has also presented a review on this subject.

IMPACT ON OPERATIONAL ANALYSIS AND FORECASTING

From the operational standpoint, the most outstanding contribution was made by the drifting buoy systems. By providing an extensive network of regular pressure observations over the previously data-sparse ocean areas, the buoy system essentially removed, for the first time, the major hurdle that stood in the way of reliable routine surface pressure analysis over the entire hemisphere. Figure 3, which shows the operational mean sea level pressure analysis for 12Z on July 26, 1979, provides an excellent example of the impact of the buoy system. It is clear that the buoy data provided the principal basis for delineation of the mean sea level pressure over much of the hemisphere. In addition to the obvious contribution of the buoy pressures to more confident specification of the centers of highs and lows, the variations in position and intensity of the circumpolar trough, the oscillation in the strength of the subtropical highs, and the delineation of critical transitory high latitude ridges, Guymer and Le Marshall (1981) noted that the buoy data had shown that (1) the central pressures of the higher latitude cyclones were quite often some 20 mb deeper than would otherwise have been estimated, and (2) the westerly flow south of Australia was considerably stronger than would otherwise have been estimated. Guymer and Le Marshall (1981) also concluded that pre-FGGE analysis procedures may have led to a systematic underestimation of synoptic systems over high latitude oceans, although this conclusion has been contested by Trenberth and van Loon (1981).

Guymer and Le Marshall (1981) also provide some evidence of positive impact of FGGE on operational forecasts on the basis of 36-hour predictions of the Australian Bureau of Meteorology's Subsynoptic Advection Model (Glahn and Lowry, 1972), which is driven by the Bureau's operational hemispheric spectral model. No model changes occurred during the period, and the prognoses were verified over the data dense areas of the Australian region. The results are shown in Table 1. The first column shows the amount by which the 1979 skill

FIGURE 3 Mean sea level pressure analysis for 1200 GMT, July 26, 1979 from the archives of WMC, Melbourne. *FGGE buoys, °Ships, °SYNOPs.

score was lower than for 1978, and overall the improvement in score for the whole year was approximately 3 points. From the second column in the table, it can be seen that in those months in which scores for 1979 were equal to or worse than the 1978 scores there was nevertheless a large increase in the margin of skill over persistence. Similar improvement in prognosis skill in 1979 was found with the Bureau of Meteorology's Australian Region Primitive Equation (ARPE) 24-hour prognoses. Table 2, from Leslie et al. (1981), suggests that from this model also the mean daily improvement in S1 skill score as a result of the FGGE data is probably about 3 points. Leslie et al. (1981) also indicate that on particular days the increase in skill brought about by FGGE satellite and buoy data was larger, sometimes as much as 10 points, and the frequency of poor forecasts in 1979 was less.

The drifting buoy data had a significant impact on the daily operational weather forecasting activities of the Bureau of Meteorology. On numerous occasions during the FGGE year the operational availability of buoy data enabled a more accurate specification of the location and intensity of approaching weather systems over the southern ocean with significant improvements in the subsequent weather forecasts and warnings issued for aviation, shipping, and public use. Details of these are given by Zillman (1983).

TABLE 1 Improvement in Mean Monthly S1 Skill Scores of the Subsynoptic Advection Model Prognoses in 1979 over Scores in 1978

Month	Number of skill score points by which 1979 prognoses were better than 1978	Number of points by which 1979 margin of skill over persistence was better than 1978 value
January	+3	+1
February	+5	-1
March	-4	+8
April	+6	+12
May	+4	+4
June	+6	-3
July	+5	+2
August	-1	+4
September	+8	-8
October	0	+10
November	-1	+9
December	+3	-1
Average	+2.8	+3.1

IMPACT STUDIES USING THE ANMRC DATA ASSIMILATION SCHEME

ANMRC Data Assimilation Scheme

The assimilation scheme is based on that commonly referred to as intermittent forward assimilation and is described fully in Bourke et al. (1982a). The prediction model used in these studies is a 9-level hemispheric spectral model truncated at rhomboidal wavenumber 21. The data analysis within the framework of the prediction model is effected by the successive correction method on the σ coordinates, latitude-longitude transform grid of the model. The analysis is univariate with data being inserted in the sequence surface pressure, temperature and moisture, and winds. On completion of surface pressure data analysis, the σ coordinates are redefined and geostrophic correction to the wind field derived. Similarly, a geostrophic correction is made subsequent to temperature data insertion. On completion of each assimilation cycle a nonlinear normal mode initialization is performed in which the first four vertical modes are initialized using four iterations.

TABLE 2 Comparative S1 Skill Score Performance for Mean Sea Level Pressure of the Operational ARPE Model in 1978 and 1979, and Relative to Persistence. Asterisked Scores are Record Low Values for That Month

Model / Month	Persistence 1978	Persistence 1979	Operational model 1978	Operational model 1979	Persistence-model 1978	Persistence-model 1979
January	57	56	49	47*	8	9
February	61	55	49	48	12	7
March	56	65	47	49	9	16
April	56	63	49	47	7	16
May	54	56	43*	45	11	11
June	61	53	51	42*	10	11
July	61	57	48	42*	13	15
August	59	62	44	42*	15	20
September	68	57	50	44*	18	13
October	55	61	42*	43	13	18
November	57	63	48	47*	9	16
December	58	59	49	46*	9	13
Mean	59	59	48	45	11	14

An indication of the observation fitting characteristics of the ANMRC data assimilation scheme is shown in Figure 4, which shows the root-mean-square (rms) differences for the region 25° to 60°S between observed data and model states after a 6-hour forecast (or the first guess field), after analysis, and after initialization during an assimilation cycle. The main feature in Figure 4 is the considerable loss of information content of the data in the mean sea level and the 200 mb wind field during initialization, indicating rejection of significant parts of these data by the model. Such characteristics of an assimilation scheme have an important bearing on data impact studies. Although the local geostrophic correction after insertion of pressure data leads to a significant improvement in its retention by the model, it is clear that the ANMRC assimilation scheme, like other assimilation schemes, does not make optimal use of surface pressure data. The loss of information of the 200 mb wind field is associated with difficulties in analyzing single level wind data.

Data Base of Assimilation and Prediction Studies

The data base used was essentially that available as Level IIa data over the Global Telecommunications System augmented by tapes of

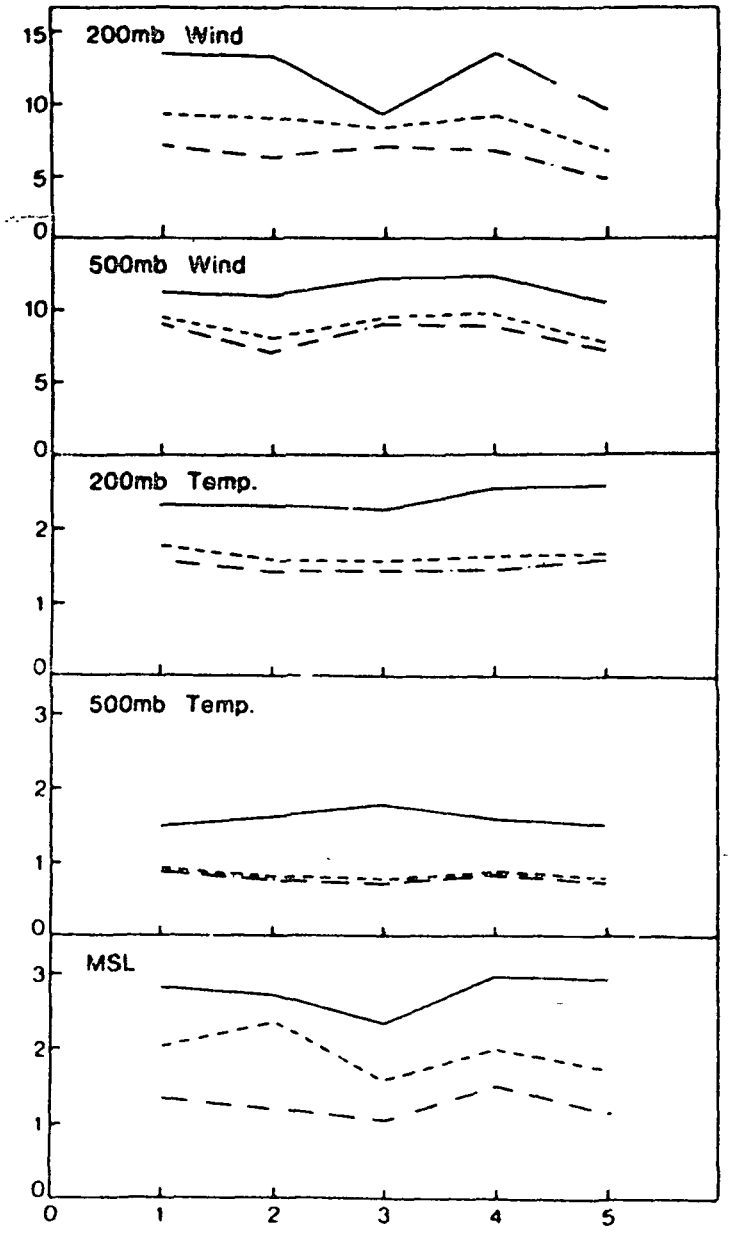

FIGURE 4 Root-mean-square differences in the region 25° to 60°S between observed data and model states corresponding to the first guess (solid line), after analysis (dashed dot line), and after initialization (dashed) as a function of time (in days) during an assimilation cycle. Units for mean sea level pressure, temperature, and wind are mb, K, and ms^{-1}, respectively.

drifting buoy data obtained directly from Service Argos. Some later experiments were also done using Level IIb data. Prior to assimilation in the model, all data were compared to the Bureau of Meteorology's Level IIIa analyses, and data outside specified tolerances were subjected to manual inspection. After preliminary assessment, satellite temperature retrievals via TIROS-N for this period were omitted over land. Corresponding assessment of Japan Meteorological Agency geostationary winds for this period led to these data being omitted because of difficulties with accuracy of height assignments. For this study the period of May 17 to May 26, 1979 during the second Special Observing Period (SOP-2) was identified as having an interesting synoptic regime particularly in the Australian region. The period encompassed a short "blocking" episode, instances of cyclogenesis, and finally a return to a predominantly "high index" zonal regime.

Ocean Buoy and TIROS-N Impact Evaluations

Ocean buoy and TIROS-N impact calculations have been described in detail by Bourke et al. (1982b). Three assimilation cycles covering the period May 17 to May 26 were carried out using the ANMRC assimilation system. In one cycle, referred to as the control cycle, all data were inserted, while the other two cycles were conducted withholding in turn the ocean buoy data (NB cycle) and Satem data (NT cycle). The resulting analysis for May 20 from the three cycles provides an indication of the data impact. Figure 5, which shows the differences between the control and the NB and NT analyses, indicates that the omission of buoys leads to large changes in the mean sea level pressure analyses over most of the southern hemisphere and that the omission of satellite data leads to changes in the upper levels, although satellite data also have an impact on the mean sea level pressure.

In order to assess the impact of buoy and TIROS-N data on model forecasts, three analysis times were chosen to initialize the numerical model for prediction to 48 hours, i.e., 0000 GMT on May 20, May 22, and May 24, and forecasts from the three cycles were compared over the Australian region (15° to 50°S, 100° to 170°E) and the hemisphere. Figure 6 (left panel), taken from Bourke et al. (1982b), displays the three-case rms errors relative to the control analyses for the mean sea level pressure and the 500 mb and 200 mb geopotential in the Australian region. The errors shown are for the 12, 24, 36, and 48 hour forecasts. The control-based prognoses are the most skillful at all levels. Furthermore, the NB prognoses show substantial deterioration at mean sea level of 2 mb rms throughout the 48-hour period. The NT prognoses are similarly less satisfactory at mean sea level with the deterioration at 48 hours even more marked than in the NB calculations. A similar effect is seen at 500 mb where the NT calculations are the most unsatisfactory at 48 hours. At 200 mb the Satem impact is more marked than that of buoys with the NT prognoses comparable only with persistence. The verification of the temperature prognoses (center

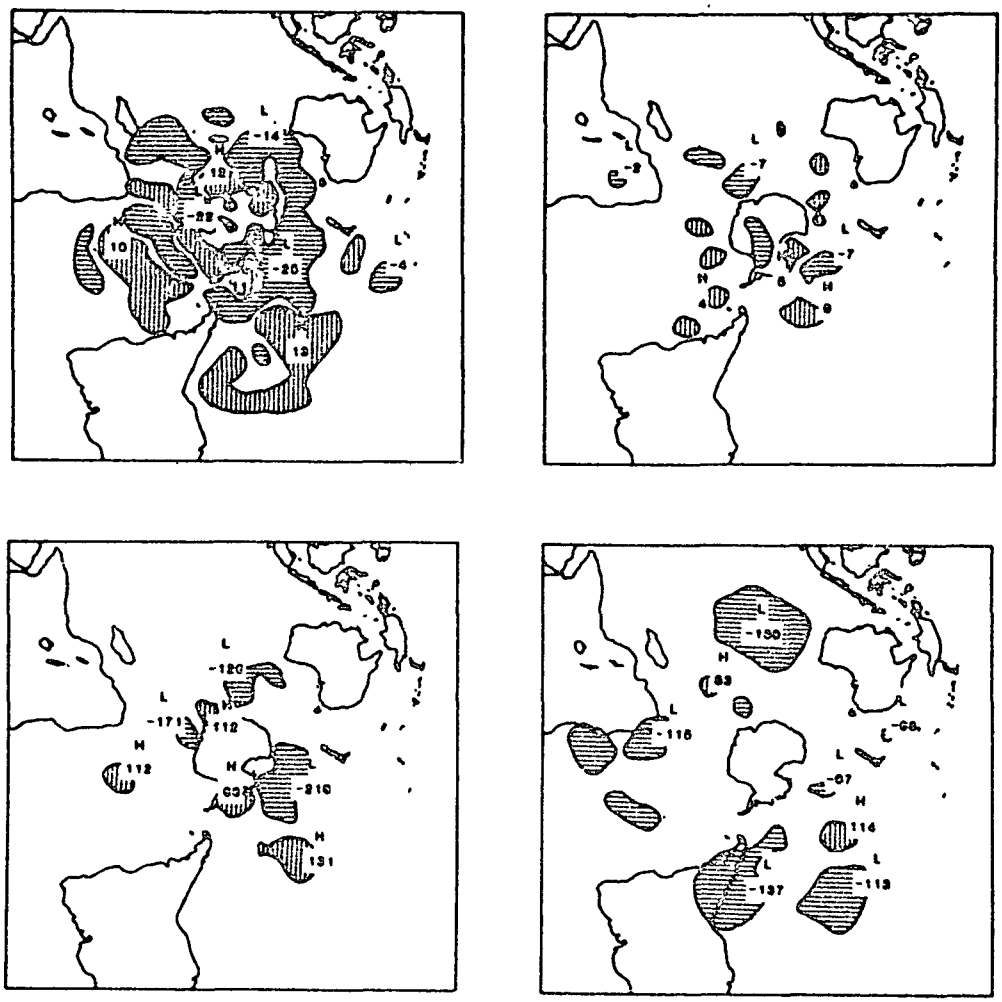

FIGURE 5 Sea level pressure differences (mb) for NB minus control (upper left), and NT minus control (upper right). Corresponding 500 mb geopotential differences (m) are shown lower left and lower right. Positive and negative differences >2 mb and 60 m are indicated by vertical and horizontal hatching.

panel) shows that omission of buoys yields prognoses that are inferior to the control prognoses at both 500 and 200 mb. If the satellite temperatures are omitted, the temperature prognoses are degraded in an rms sense by 1^{o} at all verifying times for both 500 and 200 mb levels. The verification of the wind prognoses (right panel) also indicates that the prognoses are substantially degraded by omitting either data type. In particular, at 200 mb the omission of Satems

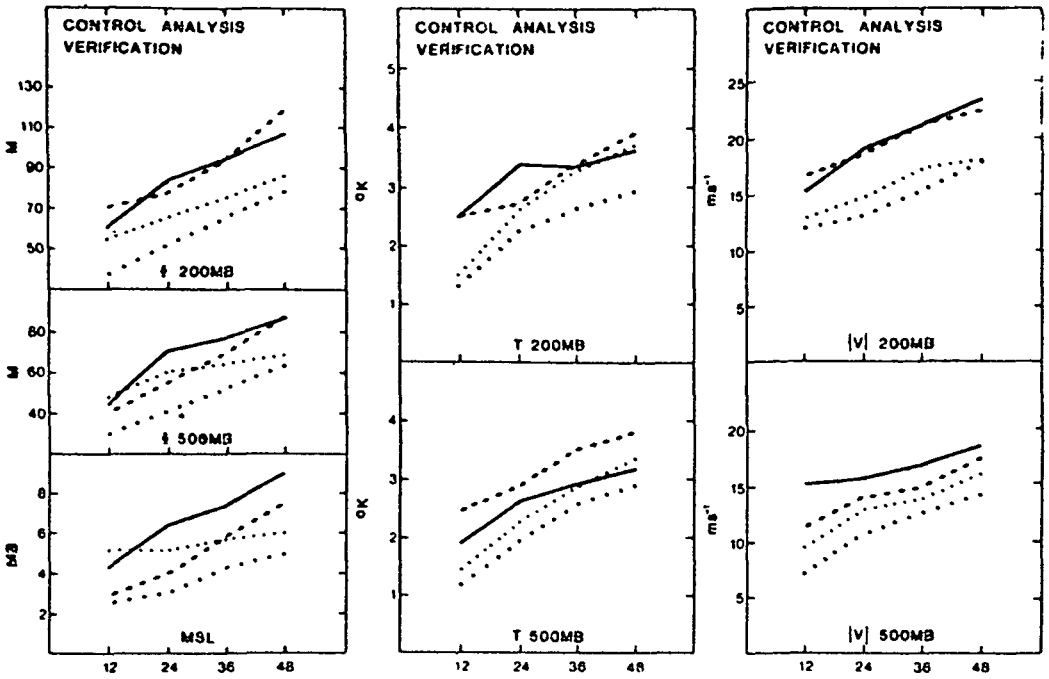

FIGURE 6 Root-mean-square forecast error statistics, averaged over three situations, and verified against control analyses in the Australian region. The dotted line denotes control prognoses, crosses indicate no buoys, arrows indicate no Satems, and full line indicates persistence.

leads to wind prognoses comparable only to persistence for the full 48-hour period.

The hemispheric verifications, which were carried out in terms of the rms differences between the observed data and model forecasts, are shown in Figure 7. The rms differences are again three-case averages. The hemispheric rms errors for the mean sea level pressure (left panel) show that the control prognoses are superior to both the NB and NT prognoses. A notable feature is the deterioration of the 48-hour mean sea level prediction on omitting Satems. The control based prognoses for the 500 mb temperature (second panel) show substantial gain over the NT prognoses of the 500 mb temperature as verified against Satems and radiosondes. The buoy data enhances the prognoses of 500 mb temperatures as verified against Satems, which could be anticipated in view of the vast oceanic areas of the southern hemisphere where the buoys and Satems are the only sources of data. The observation fitting statistics for 200 mb geopotential (third panel) show very marked positive impact from the use of Satems with the impact of buoy data being less marked at this level. Examination of the observation fitting statistics for the wind field (right panel) shows little

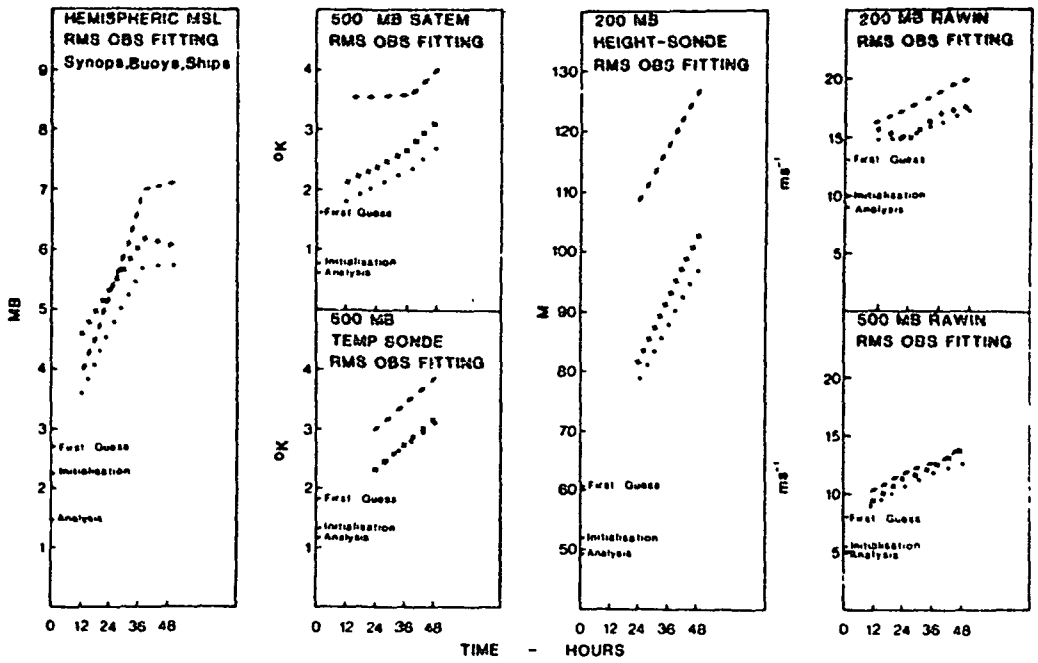

FIGURE 7 Root-mean-square forecast error statistics, averaged over three situations, and verified against observations over the hemispheric domain. The dotted line denotes control prognoses, crosses indicate no buoys, arrows indicate no Satem.

sensitivity at 500 mb. However the impact of Satems is again more marked at 200 mb.

Level IIb Data and Single Level Satellite Wind Impact Evaluations

Further assimilation cycles were carried out using Level IIb data. The first experiment was to determine the impact of using Level IIb data instead of Level IIa data. Using the same procedures as those described above, it was found that the use of Level IIb data has a marginal (positive) impact on model forecasts.

In order to evaluate the impact of satellite winds, a further cycle (NS) was carried out using Level IIb data in which the single level satellite winds were withheld. Table 3 shows the three-case average forecast errors in the Australian region from the cycle in which all level IIb data were used (IIb cycle) and the NS cycle. The errors shown are relative to the control cycle analyses. Note that there is a small but consistently positive impact from the use of satellite winds. Examination of the hemispheric observation fitting error statistics reveal similar features. The conclusion concerning the

TABLE 3 Root-Mean-Square Forecast Error Statistics Averaged over Three Situations and Verified against Control Analyses

Field	24 Hour Forecast IIB	24 Hour Forecast NS	48 Hour Forecast IIB	48 Hour Forecast NS
MSLP (MB)	2.7	3.0	4.9	5.3
500Z (M)	36.0	39.0	56.0	63.0
200Z (M)	50.0	54.0	73.0	85.0
500T (°K)	1.7	1.7	2.5	2.6
200T (°K)	1.9	1.9	2.7	2.9
500W(ms^{-1})	8.8	9.5	11.4	11.5
200W(ms^{-1})	11.6	13.3	15.5	16.4

small impact of satellite winds must however be qualified in view of the result presented earlier, which indicated problems with the assimilation of single level wind data such as satellite wind data.

CONCLUSION

The FGGE data base had a very significant impact on analysis and numerical weather prediction in the southern hemisphere. This is not surprising since it was the first time that an adequate coverage of data was available over the southern hemisphere. From the operational standpoint the most outstanding contribution was made by the drifting buoy data, which enabled reliable routine surface pressure analyses to be made over the entire hemisphere. An attempt to quantify the impact of individual components of FGGE on model forecasts in a systematic manner was made by using the ANMRC data assimilation scheme. Although this study was limited in sample size, the results indicate that the quality of prediction to 48 hours hinges crucially on both the buoy pressure data and the satellite temperature soundings with single level satellite winds having a small but positive impact. As could be expected, the buoy data have a positive impact on prediction of mean sea level. The satellite soundings show positive impact both aloft at 500 and 200 mb and at mean sea level.

REFERENCES

Bourke, W., K. Puri, R. Seaman, B. McAvaney, and J. Le Marshall (1982a). ANMRC data assimilation for the southern hemisphere. Mon. Wea. Rev. 110, 1749-1771.

Bourke, W., K. Puri, and R. Seaman (1982b). Numerical weather prediction studies from the FGGE southern hemisphere data base. Mon. Wea. Rev. 110, 1787-1800.

Gauntlett, D. J. (1982). FGGE observing systems impact--a southern hemisphere perspective. JSC Study Conference on Observing Systems Experiments, Exeter.

Glahn, H. R., and D. A. Lowry (1972). An operational subsynoptic advection model. J. Appl. Meteorol. 11, 578-585.

Guymer, L. B., and J. F. Le Marshall (1981). Impact of FGGE buoy data on southern hemisphere analyses. Bull. Amer. Meteorol. Soc. 62, 38-47.

Leslie, L. M., G. A. Mills, and D. J. Gauntlett (1981). The impact of FGGE data coverage and improved numerical techniques in numerical weather prediction in the Australian region. Quart. J. Roy. Meteorol. Soc 107, 629-642.

Trenberth, K. E., and H. van Loon (1981). Comments on "Impact of FGGE buoy data on southern hemisphere analyses." Bull. Amer. Meteorol. Soc. 62, 1486-1488.

Zillman, J. W. (1983). The impact of the Global Weather Experiment in the southern hemisphere. Lectures presented at the thirty-fourth session of the WMO Executive Committee, WMO No. 610, 41-134.

D9

NUMERICAL WEATHER PREDICTION IN LOW LATITUDES

T.N. Krishnamurti
Florida State University

PHYSICAL INITIALIZATION

Based on the results of a number of numerical prediction experiments, we have confirmed that the differential heating between land and ocean is an important and critical factor for investigation of phenomenon such as the onset of monsoons over the Indian subcontinent. The pre-onset period during the month of May shows a rather persistent flow field in the monsoon region. At low levels the circulation exhibits anticyclonic excursions over the Arabian Sea, flowing essentially parallel to the west coast of India from the north. Over the Indian subcontinent the major feature is a shallow heat low over northern India. Our findings, to be described briefly below, may be stated as follows: "A seemingly stable climatological flow appears to exist day after day over the monsoon region. However this flow is in fact quite unstable to the configuration of large-scale differential heating." As the heat sources commence a rapid northwestward movement toward the southeastern edge of the Tibetan Plateau, an interesting configuration of the large-scale divergent circulation occurs. A favorable configuration for a rapid exchange of energy from the divergent to the rotational kinetic energy develops. Strong low level monsoonal circulations evolve, attendant with that the onset of monsoon rains occurs. That appeared to be the scenario during the year of the Global Experiment, 1979. In order to test this observational sequence, a series of short-range numerical prediction experiments were initiated. The experiments differed from each other in the definition of the initial heat sources. The differential heating between the Arabian Sea and the southeastern edge of the Tibetan Plateau is described by a net cooling over the ocean (dominated by the radiative forcing) and a strong net heating over the foothills of the Himalayas (dominated by convective forcing). This strong net heating occurs over regions of organized cumulus convection where a large net supply of moisture is available. In order to provide such a forcing in the different initial states for the proposed experiments, we extracted the divergent wind and the humidity field from three different epochs in the monsoon evolution: (1) springtime, (2) pre-onset, and (3) post-onset. The rotational wind, the pressure, and the temperature field were kept identically the same for all three experiments. Since the divergent

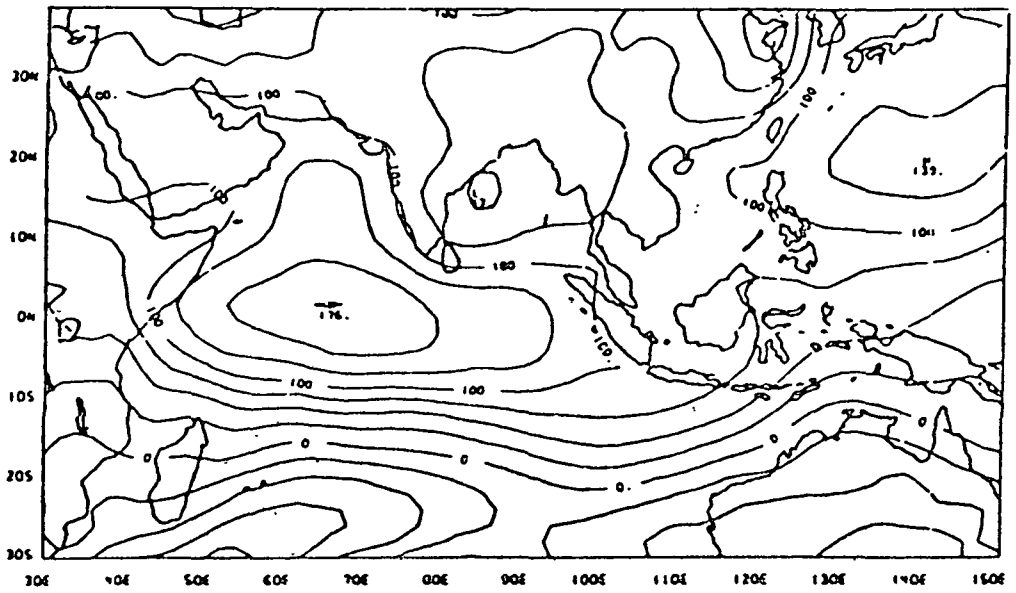

FIGURE 1 Initial streamfunction for the sensitivity experiments on differential heating. Units $10^5 m^2 s^{-1}$. The divergent wind is not added to the rotational wind since it is different for each experiment.

wind and the humidity fields were different in each case, the application of a cumulus parameterization scheme that depended on moisture convergence gave rise to different measures of latent heating initially. The rotational wind, in each experiment, described the pre-onset circulations alluded to above. Figure 1 describes the initial state at 850 mb in these experiments (Krishnamurti and Ramanathan, 1982). The 96-hour forecasts of the low level flow field at 850 mb for the three respective experiments are shown in Figure 2 (a,b,c). The strong monsoon onset response in Figure 2c, when a more northerly heat source was deployed initially, is clearly evident here. These experiments were more phenomenological in their design. However they demonstrate a strong sensitivity of the onset to the humidity analysis as well as to the specification of the initial divergent wind. Other aspects of this study relate to diagnostic investigations of the transfer of energy from the divergent to the rotational wind. These are described by energy exchange functions (Krishnamurti and Ramanathan, 1982). Here the energy equations are cast into a system of three equations, i.e., the rotational kinetic energy equation, the divergent kinetic energy equation, and the available potential energy equation. When these equations are expressed as integrals over a closed mass of the atmosphere, they conserve the total energy (rotational plus divergent plus available potential) in the absence of heat sources, sinks, and dissipative processes. A number of major inferences on the workings of a differentially heated system during the onset of monsoons can be made with this system of equations:

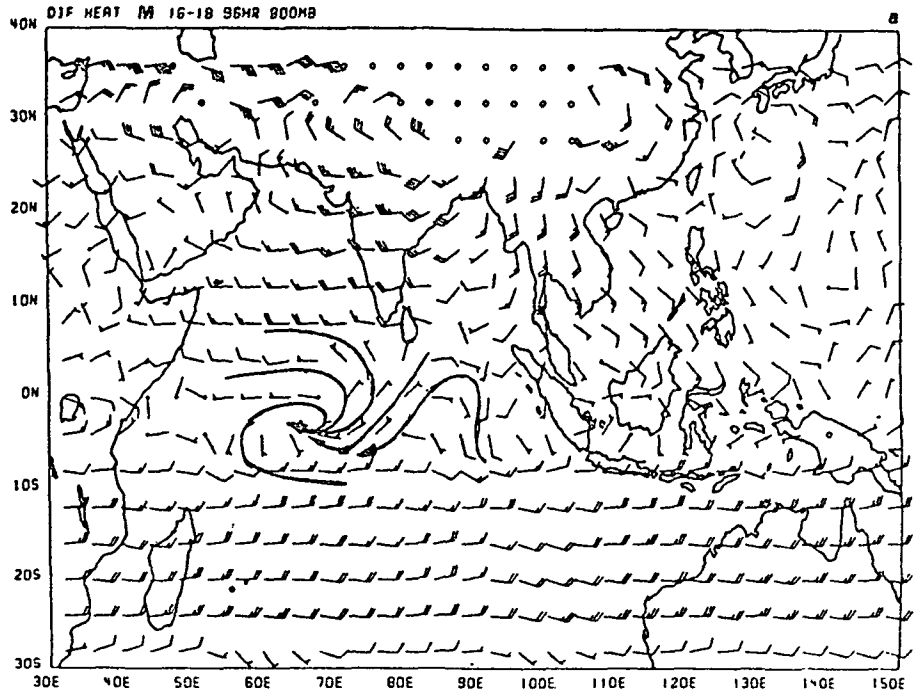
DIF HEAT M 16-18 96HR 800MB
a
40N
30N
20N
10N
0N
10S
20S
30S
30E
40E
50E
60E
70E
80E
90E
100E
110E
120E
130E
140E
150E

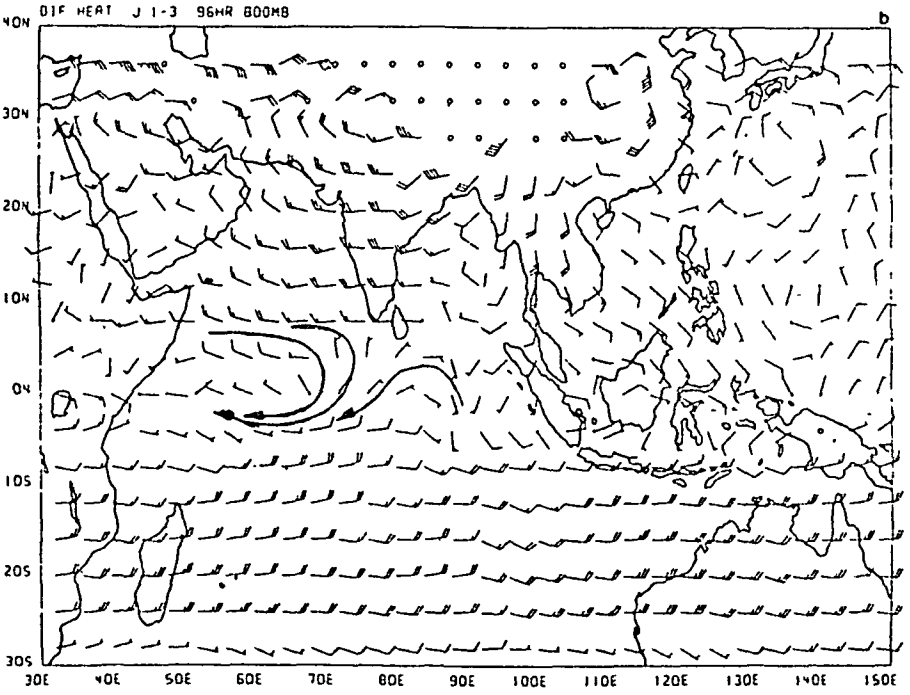
DIF HEAT J 1-3 96HR 800MB
b
40N
30N
20N
10N
0N
10S
20S
30S
30E
40E
50E
60E
70E
80E
90E
100E
110E
120E
130E
140E
150E

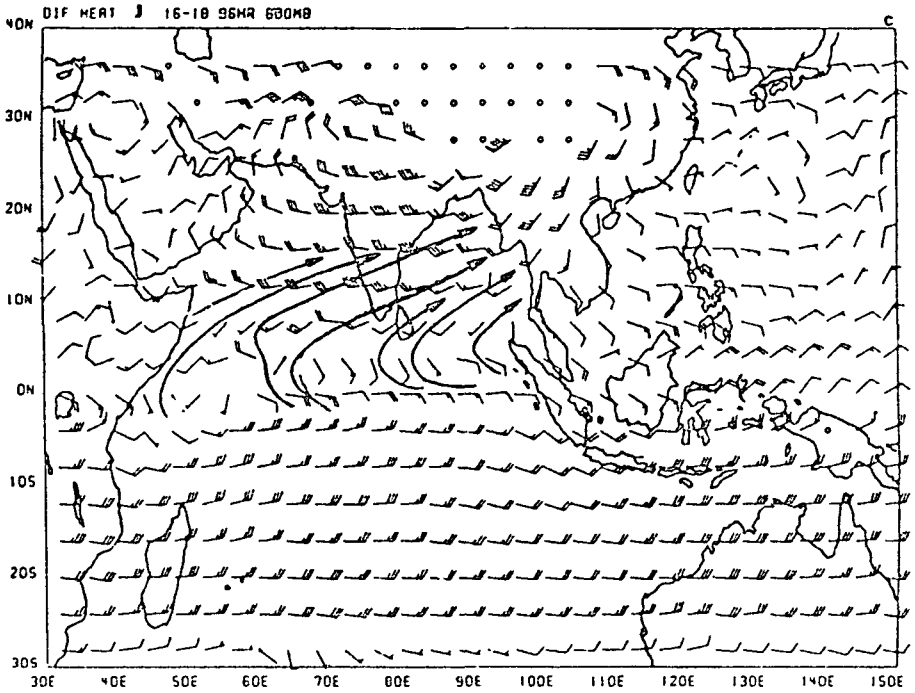

FIGURE 2 (a,b,c) Forecasts of the wind field at 850 mb for the three respective experiments. The full wind barbs denote 5 m/s while the half barbs denote 2.5 m/s. The response in the near equatorial region in the three experiments illustrates (a) the response for springtime moisture convergence, (b) the response for the preonset moisture convergence, and (c) the response for the post onset moisture convergence.

$$\frac{\partial K}{\partial t} = \langle K_X \cdot K\psi \rangle + D\psi \tag{1}$$

$$\frac{\partial K_X}{\partial t} = - \langle K_X \cdot K\psi \rangle + \langle APE \cdot K_X \rangle + D_X \tag{2}$$

$$\frac{\partial APE}{\partial t} = - \langle APE \cdot K_X \rangle + G_{APE} + D_{APE} \tag{3}$$

Here $K\psi$, K_X, and APE denote the aforementioned energy quantities, respectively. The energy exchange functions are enclosed within braces, where a positive sign for an exchange function denotes an exchange of energy from the first member to the second. In the context of the onset, one first notes that during this period $K\psi$ increases with time; a negative definite dissipation $D\psi$ requires that energy must be transferred from the divergent to the rotations motions, i.e., $\langle K_X \cdot K\psi \rangle$ be positive. The strong evolution of divergent circulation during this period (as was noted from observations) implies

that K_χ increases with time, with a negative definite dissipation D_χ. From the aforementioned requirement on the energy exchange from the divergent to the rotational motions, we draw the next major inference, which is that divergent motions must receive energy from the available potential energy. That process happens to be the well-known covariance among the vertical velocity and the temperature field. An analogous argument on the third equation requires that a net generation of available potential energy must take place in a system where the rotational and the divergent motions are amplifying. Figure 3 shows the energy exchanges in the three respective experiments. It is of interest to note that when a favorable configuration of the initial heating is selected (corresponding to Figure 2c), a large energy exchange as stated in the aforementioned scenario follows in the numerical experiment. These results demonstrate a large sensitivity of the prediction in low latitudes to the initial analysis of the humidity field. That is an area of major research under the area of physical initialization decribed below. While examining these same processes in

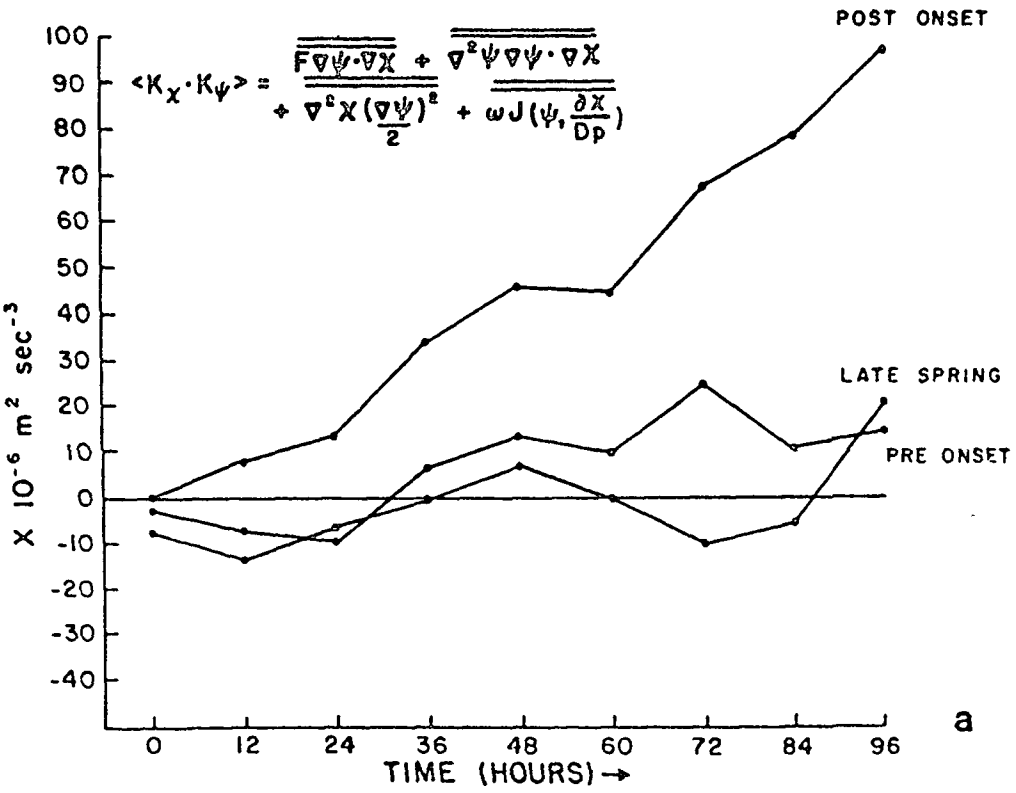

FIGURE 3 Energy exchange from the divergent to the rotational component $\langle K_\chi \cdot K_\psi$ for the three respective numerical experiments. The domain of integration and energetics is the same as the map domain of Figure 6.

real data forecasts, especially with a global model, we have confirmed that an accurate humidity analysis in low latitudes was essential for a definition of the heat sources and sinks. Even the currently available FGGE IIIb data analysis of the humidity field suffers from major inconsistencies with respect to regions of cloud cover as shown by satellite radiance data sets. Short-range prediction experiments frequently show a rapid deterioration of the divergent wind not only over regions of cloud cover but also in relatively clear areas. That strongly suggested that moisture supply was not being properly defined over convective areas and the radiative forcing was not being calculated accurately in rain free areas where the errors in the vertical distribution of humidity are large. In this situation the models do not provide a reasonable radiative cooling for the cloud topped (non-precipitating) mixed layers. Figure 4 presents an outline of a physical initialization procedure that we have been experimenting within the global model. The physical initialization procedure is structured around a dynamical initialization and essentially provides a more reasonable humidity analysis. Krishnamurti et al. (1984) have discussed in detail the procedures involved in this method. Essentially, it consists of the following components:

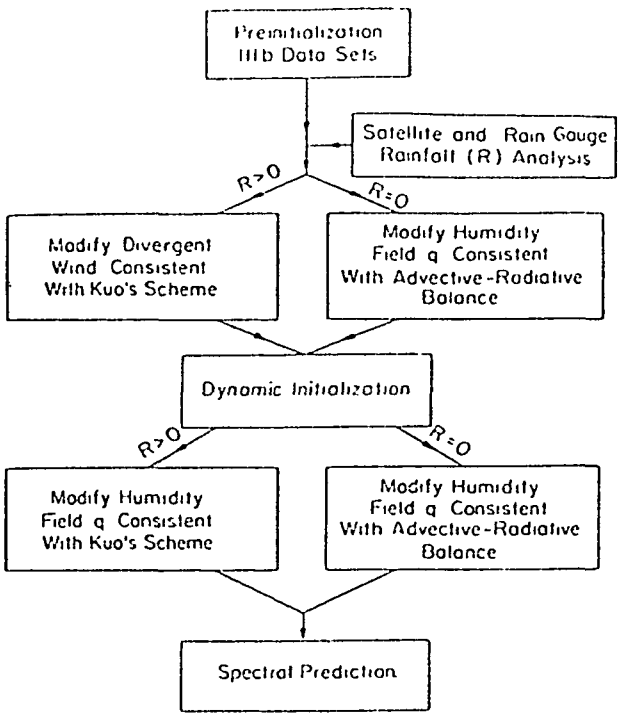

FIGURE 4 A schematic flow chart of the physical-dynamical initialization carried out within the global model. For a more detailed description of this chart see Krishnamurti et al. (1984).

1. Analysis of the observed rain from a mix of rain gauge and satellite radiance information. This entails determination of a statistical multiple repression among rain gauge data, satellite infrared radiance, and its time rate of change at a collection of colocated rain gauge sites. The regression coefficients are next used to determine a first guess field based on the daily values of the radiances and their time rate of change. The next step is an objective analysis of the FGGE IIc rain gauge data (some 3,000 to 5,000 observations per day) over the global tropics with the aforementioned first guess field.

2. The humidity analysis is restructured in the rain areas (as determined above) to a cumulus parameterization scheme--in this case, Kuo's scheme with a moistening parameter b = 0. Thus the humidity reanalysis at all vertical levels is minimized to provide an initial computed rainfall rate close to the observed rainfall rate.

3. Over rain-free areas a proposal for a reanalysis of the humidity field has been made that seeks an advective-radiative balance. The radiative parameterization (described in the next section) is based on an emissivity-absorptivity method. A large sensitivity to the calculated radiances results from moisture distribution where it encounters changes in the cloud specifications. A reanalysis of the humidity can render the atmosphere cloudy from a cloud-free situation. The cloud specification is based on threshold values of relative humidity in a vertical layer. The fractional areas of low, middle, or high clouds can be altered from a reanalysis of the humidity field. That results in a change in the net radiative heating at the earth's surface and in the vertical column. Given adequate wind observations from the composite observing system (WWW, cloud winds, commercial aircraft), the premise here is that the divergent winds defined from these observations over the tropics is superior to those obtained from any indirect methods (Oort and Peixot, 1983, p. 481). Although the advective-radiative balance is applied rigidly at a level just above the planetary boundary layer, this still requires a modification of the entire vertical profile of humidity. The profile is slowly altered in a sequence of experiments at each point such that the final radiative cooling at the reference level balances (closely) the advective temperature change (Krishnamurti et al., 1984).

Thus the physical initialization aims toward reasonable rainfall rates in the rainy areas and an advective-radiative balance elsewhere. Figures 5a and b illustrate an example of the observed rain and that obtained from a reanalysis of the humidity field.

PARAMETERIZATION OF CUMULUS CONVECTION

The current version of our global spectral model utilizes a variant of Kuo's scheme that is structured to the GATE observations (Krishnamurti et al., 1980, 1983). The first of these studies dealt with the observations over the hexagonal ship array of GATE seeking a relationship between the observed rain (as measured by radar and rain

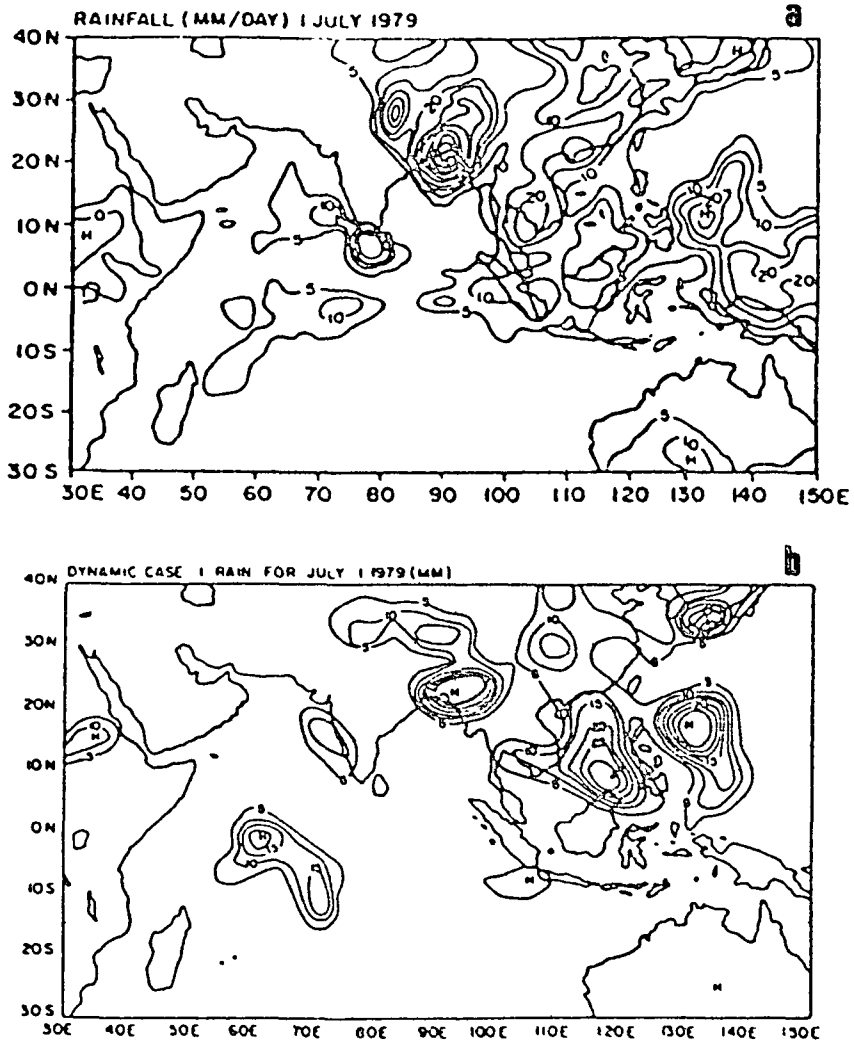

FIGURE 5 Top: Observed rainfall rate obtained from a mix of satellite and rain gauge observations (mm/day). Bottom: Initialized rainfall rate obtained at the end of the physical-dynamical initialization (mm/day).

gauge) and the net large-scale moisture convergence. As was first noted by Thompson et al. (1979), a very close relationship between these two quantities is indeed present. That is reflected in a simple version of Kuo's scheme where the rainfall estimates are parameterized as the net available supply of moisture. Results of these calculations, shown in Figure 6, exhibit a very close correspondence between the calculated and the observed measures. It should be noted that Lord

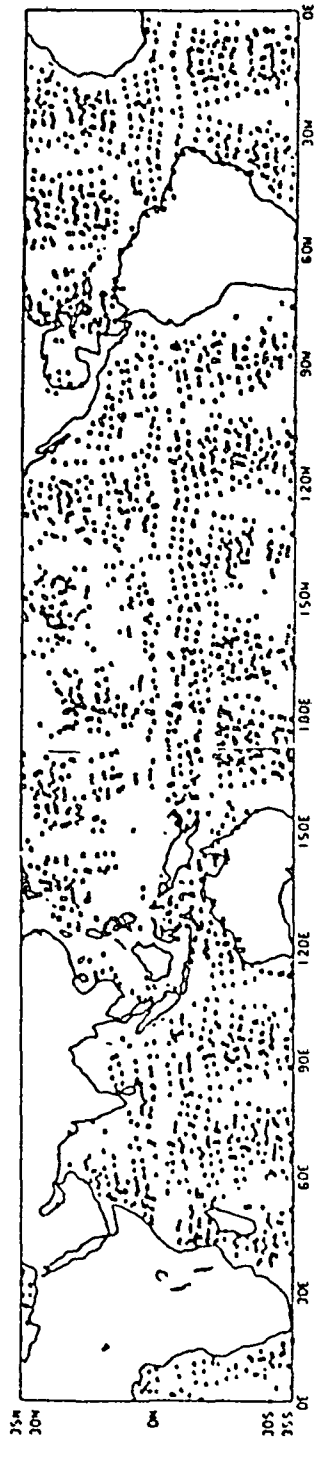

FIGURE 6 Shows the typical location of TIROS-N, layer averaged, humidity observations.

(1982) demonstrated a similar success in the specification of rainfall rates from an application of the Arakawa-Shubert theory (1974). In a prognostic model, the prescription of available moisture supply leaves no room for the moistening of a vertical column by cumulus convection. That was usually remedied by the choice of a strong vertical diffusion of moisture which was accomplished by a large value of the vertical exchange coefficient. A limitation of that was that the diffusive process acted equally strongly in nonconvective areas resulting in an overall increase of humidity above the planetary boundary layer nearly everywhere. To overcome these difficulties, Kuo's scheme was posed as a two parameter problem. A moistening parameter b and a mesoscale moisture convergence parameter n were determined from a statistical regression approach utilizing the GATE data sets.

Following Krishnamurti et al. (1983), we shall denote the large scale supply of moisture for cumulus convection by the relation,

$$I_L = -\frac{1}{g}\int_{p_B}^{p_T} \omega \frac{\partial q}{\partial p}\, dp \tag{4}$$

In addition to this large scale supply, it is assumed that a mesoscale supply exists proportional to I_L. Thus we express the net supply I by the relation,

$$I = I_L\,(1 + \eta) \tag{5}$$

where η is an undetermined mesoscale convergence parameter. As in Kuo (1974), we introduced a moistening parameter b, which is defined by the relation,

$$M = I_L\,(1 + \eta)b;\quad R = I_L\,(1 + \eta)\,(1 - b) \tag{6}$$

where M is is that part of the net supply that goes into moistening, and R denotes the rainfall rate.

Following Kanamitsu (1975), we may write a maximum supply required to produce a grid scale cloud by the expression,

$$Q = \frac{1}{g}\int_{pT}^{p_\beta} \frac{(q_s - q)}{\Delta\tau}\, dp + \frac{1}{g}\int_{}^{p_\beta} \frac{C_p T\,(\theta_s - \theta)}{L\theta\,\Delta\tau} + \omega \frac{C_p T}{L\theta}\frac{\partial\theta}{\partial\rho}\, dp \tag{7}$$

Here $\Delta 2$ denotes a cloud time scale. As noted by Kanamitsu (1979) and Krishnamurti et al. (1983), the last term in the above equation permits a smooth transition from the convective to the stable large-scale condensation heating when it is encountered. This maximum supply is further divided into the two respective parts,

$$Q = Q_q + Q_\theta \tag{8}$$

the respective proportions of moistening and rain, i.e.,

$$a_q = \frac{I_L\ (1 + \eta) b}{Q_q} \tag{9}$$

and

$$a_\theta = \frac{I_L\ (1 + \eta)\ (1 - b)}{Q_\theta} \tag{10}$$

Thus once the two unknowns of the problem, η and b, are known, then a_q and a_θ are determined.

The prediction equations take the form,

$$\frac{\partial \theta}{\partial t} + V \cdot \nabla\theta + \omega\frac{\partial \theta}{\partial p} = a_\theta \frac{\theta_s - \theta}{\Delta\tau} + \omega\frac{\partial \theta}{\partial p} \tag{11}$$

and

$$\frac{\partial q}{\partial t} + V \cdot \nabla q = a_q \frac{(q_s - q)}{\Delta\tau} \tag{12}$$

These are, respectively, the thermodynamic and the moisture equations. For the sake of the present discussion, we have only considered the convective parameterizations. Other sources and sinks of the problem are of course added on to the right hand side of the above equations.

The multiple regression approach based on GATE observations consisted in regressing the quantities M/I_L and R/I_L against a large number of large-scale variables. That was done utilizing the special GATE ship array data sets. Screening regression (stepwise linear regression) showed that the most promising candidates for regression were the vertically integrated vertical velocity ω and the relative vorticity ζ at 700 mb, where the amplitude of GATE waves, i.e., the African waves, were the strongest.

Thus we have the additional relations,

$$M/I_L = a_1 \zeta_1 + b_1 \omega_1 + c_1 \tag{13}$$

$$R/I_L = a_2 \zeta + b_2 \omega + c_2 \tag{14}$$

The best fit values of the constants a_1, b_1, c_1, a_2, b_2, and c_2 are described in Krishnamurti et al. (1983).

Thus in the course of numerical weather prediction, the predicted values of ζ and ω are used to determine M/I_L and R/I_L from the above equations. They in turn determine b and η from a solution of

equation (6). Finally, the magnitudes of a_q and a_θ, provided by equations (9) and (10), close this system of parameterization. Discussions on the performance of this scheme in semiprognostic and prognostic applications were presented in Krishnamurti et al. (1983, 1984). The scheme provided reasonable measures of heating and rainfall, however it has been found to be somewhat deficient in describing the vertical distribution of moistening; excessive moistening in the planetary boundary layer seems to be related to an absence of a downdraft mechanism in deep convection. The results of calculations of semiprognostic estimates of rainfall rate during the third phase of GATE were compared with observed estimates. These are shown in Figure 7. The correspondence of semiprognostic estimates to observed ones is quite reasonable.

Similar rigorous tests of cumulus parmeterization schemes in the prognostic context are usually not possible due to a lack of the observed measures of heating, moistening, and rainfall rates. Recently I have carried out some experiments with the assistance of my colleagues Richard Pasch and Simon Low-Nam. In these tests we selected African waves that arrived over the GATE ship array from West Africa some 48 hours after the initial state. The obvious advantage in the

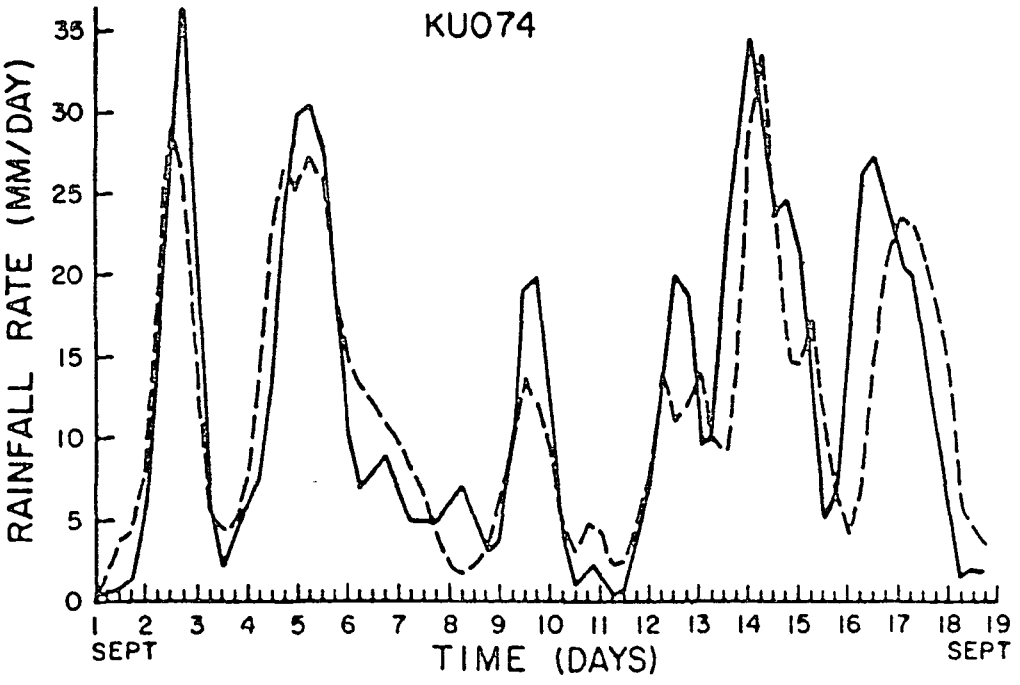

FIGURE 7 Calculated and observed rain from the use of Kuo's scheme (the moistening parameter b = o) during the last phase of GATE. These are the so-called semiprognostic calculations described in Krishnamurti et al. (1983).

selection of these cases is that one can compare predicted values (at around 48 hours) of the heating, moistening, and rainfall rates with the observed counterparts. The observed motion field at hours 24, 48, and 72 (during September 4, 5, and 6, 1974) are shown in Figures 8a,b,c. This illustrates the westward passage of an easterly wave at 850 mb during GATE. The results of actual numerical weather prediction (with a regional multilevel grid point model described in Krishnamurti et al., 1979) of this wave is shown in Figures 9a,b,c. The model carries the easterly wave westward with a reasonable phase speed over the GATE ship array during these 72 hours. These are the 850 mb flow fields at hours 24, 48 and 72. The observed and the predicted rain over the GATE ship array around $12^{o}N$, $17^{o}W$ is shown in Figure 10. The 12 hourly totals for the same 96 hour forecast are shaded. The predicted rain at this location is somewhat underestimated. The discrepancy in part is attributed to the resolution of the numerical prediction model (11 levels, 100 km mesh). The observed rain is based on the calibration of radar reflectivity that integrates the rain over a much smaller resolution. This test of the cumulus parameterization appears satisfactory, although one must note that the cumulus parameterization via the regression approach was developed from the GATE data sets. Thus a prognostic test with the same data sets is not entirely independent. The predicted and observed vertical profiles of the heating and moistening profiles are shown in Figures 11a,b, respectively. These vertical profiles are for the period of heaviest rain on September 5, 1974. The correspondence of the calculated profile Q_1 (apparent heat source) to the observed is in reasonable agreement, while that of the Q_2 (the apparent moisture sink) is poor. We believe that further work is necessary in this area of parameterization.

MEDIUM RANGE PREDICTION OF MONSOON DISTURBANCES

Two recent studies on tropical cyclogenesis carried out with the global model will be presented here. These are real data forecasts on the medium range time frame. The data sets for these experiments were extracted from the FGGE and MONEX during June and July 1979. In both instances, the FGGE IIIb data analysis produced by ECMWF was used as a first guess field, and additional MONEX data sets were incorporated via a simple successive correction method. The ECMWF analysis scheme is described in Lorenc (1981), and the FSU analysis is described in Krishnamurti et al. (1983). The following is based on recent studies of Krishnamurti et al. (1983, 1984). The onset of monsoon rains commenced over central India around June 18. The circulations on June 11, a week prior to that, were typical of those during pre-onset periods as illustrated in Figure 12. This shows the streamlines and isotachs over the Indian region. The ensuing week was characterized by a buildup of strong low level westerlies over the Arabian Sea and the formation of a tropical storm (named the onset vortex) over the eastern Arabian Sea. This storm eventually moved northward and finally

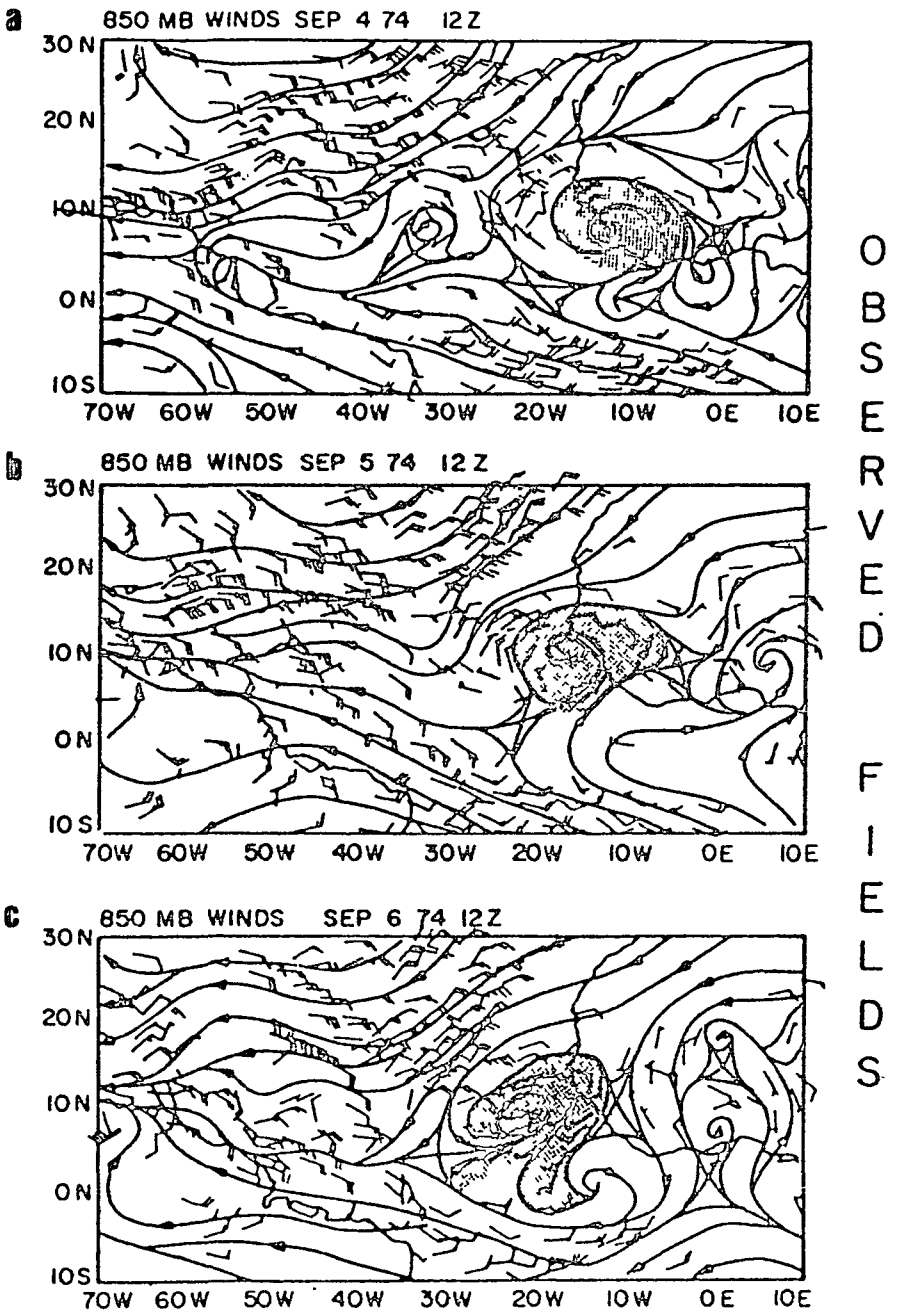

FIGURE 8 (a,b,c) The motion field based on observations at 700 mb on September 4, 5, and 6, 1974 (12z) over the GATE domain. The forecasts described in this section started on September 3, 1974 (12z).

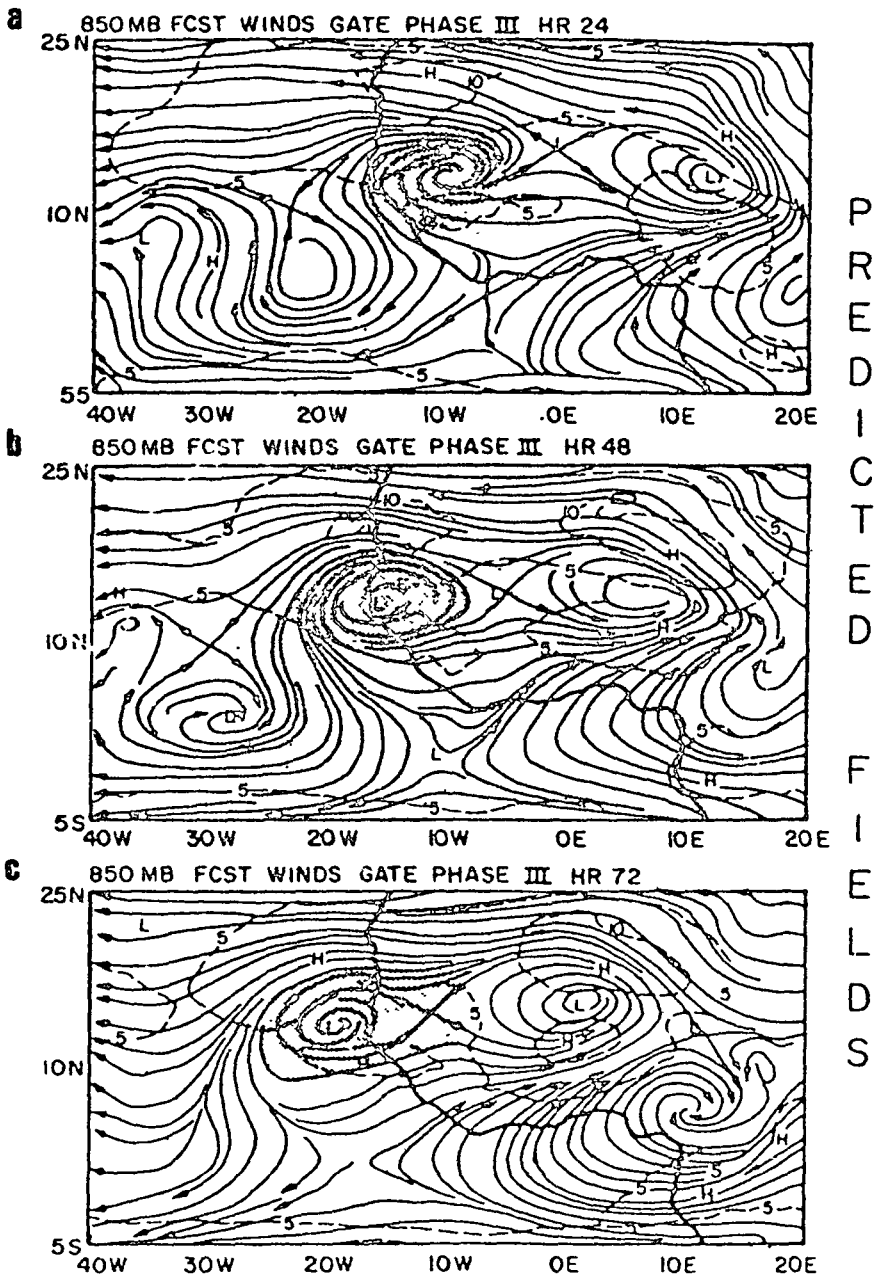

FIGURE 9 (a,b,c) Results of a 72 numerical weather prediction with a regional multilevel grid point model. Panels a,b,c correspond, respectively, to the map times of the 700 mb flow fields shown in Figure 12(a,b,c).

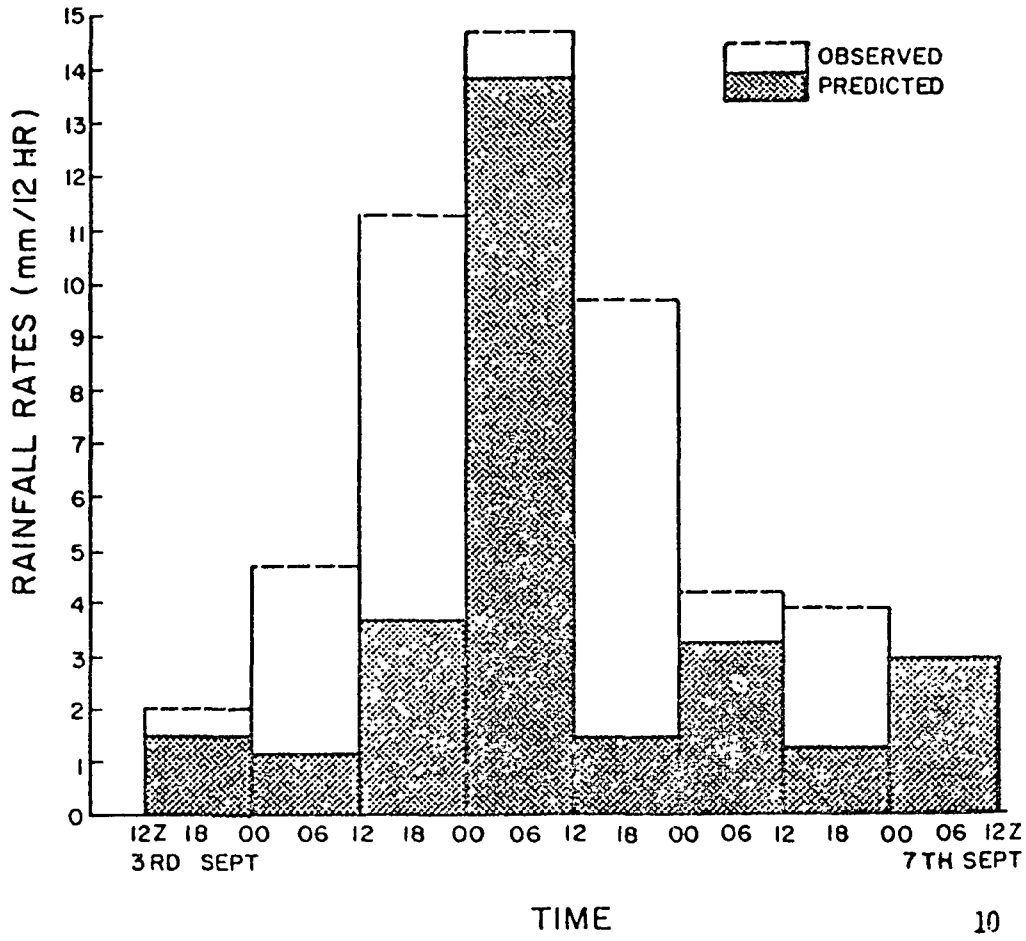

10

FIGURE 10 Histogram of the observed and the predicted rainfall rates at 12°N, 17°W obtained from radar-rain gauge based observations and the regional multilevel primitive equation model.

northwestward toward the Arabian coast prior to its dissipation (Krishnamurti et al., 1981).

Numerical prediction of the onset during 1979 thus raised at least three challenging problems, namely, the prediction of the buildup of westerlies, the formation and morton of the onset vortex, and the commencement of rains.

A large number of prediction experiments were carried out to assess the impact of data, physics, resolution, and the definition of orography. The studies clearly showed that the dense MONEX observations were a critical addition to the FGGE data sets. Figure 13

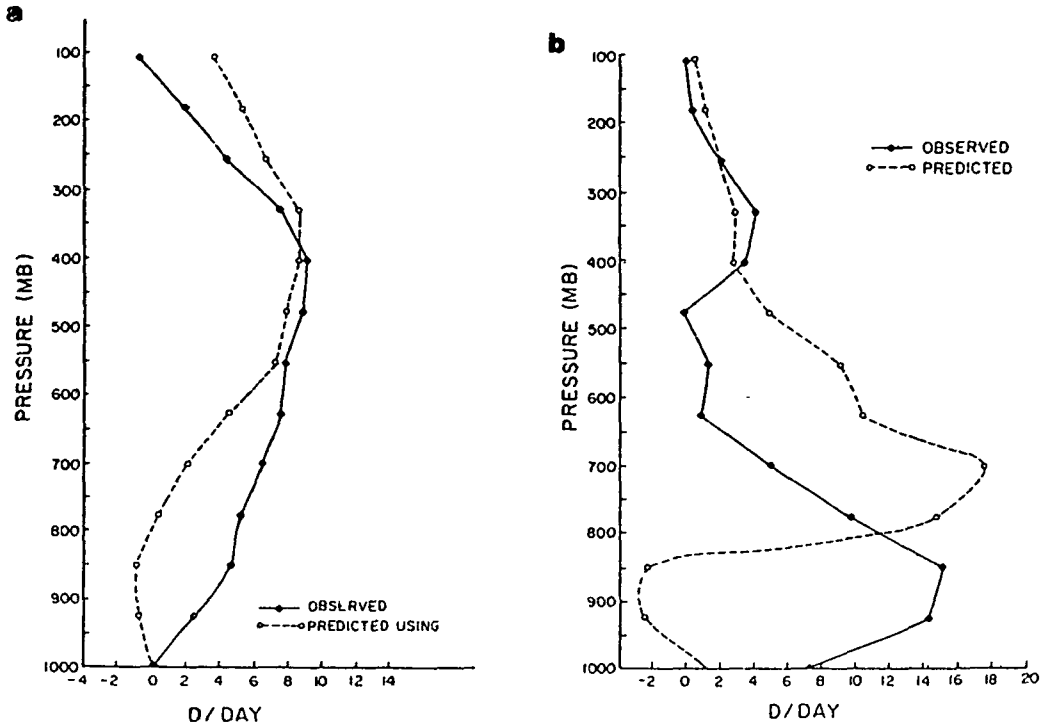

FIGURE 11 (a,b) The observed and the predicted vertical profiles of the apparent heat source (^{o}c/day) between hours 36 and 48 are shown in Figure 15a. Figure 15b illustrates the analogous vertical distribution for the apparent moisture sink.

illustrates a sample printout of the data at 850 mb. This includes observations from a variety of surface and space-based platforms. The critical data sets are the high resolution cloud winds from geostationary satellites and the soundings from the dropwindsonde research aircraft and research ships. Our results show that the prediction of the onset with the global model was vastly superior with these data sets. We have not examined the details of the onset with respect to its sensitivity to various parameterization of the planetary boundary layer and the radiative processes. However we have examined the sensitivity of the monsoon onset to various versions of the cumulus parameterization discussed in Krishnamurti et al. (1983). Such tests were also carried out by the European Center for Medium Range Weather Forecasts, and the U.K. and French Weather Services. These studies show that the classical Kuo scheme underestimates the heating, the consequent evolution of the monsoon onset is very slow, and even after 7 days none of the aforementioned salient features are described by the model. A version of Kuo's scheme where the moistening parameter b is set to zero and where all of the available supply of large-scale moisture is used to provide heating is superior. Although the onset of

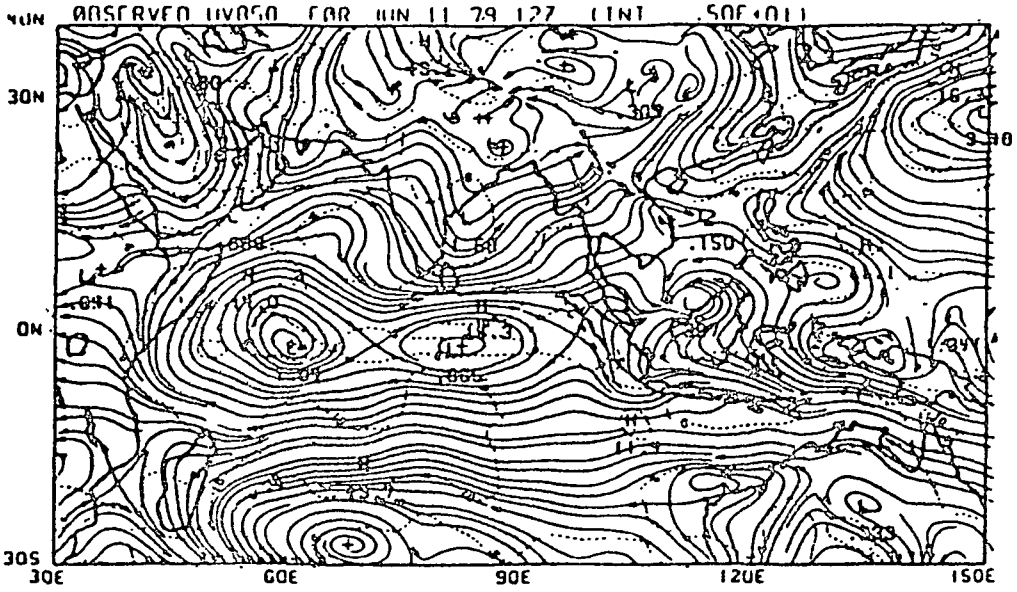

FIGURE 12 Streamlines and isotachs (m/s) over the MONEX domain on June 11, 1979, 12z. This is the initial state over this region in a global medium range prediction.

strong monsoon westerlies and the commencement of monsoon rains are reasonably predicted by this method, it fails to simulate a reasonable structure of onset-vortex or its track. Resolution experiments were carried out with respect to both horizontal and vertical resolution of the spectral model. Using 29 waves (rhomboidal) and 5 vertical levels, a forecast of the onset was found to be quite poor. Using 29 waves (rhomboidal) and 11 vertical levels, the forecasts showed a marked improvement in simulating the onset of monsoon westerlies in the lower troposphere. Further experiments were continued with 42 wave (triangular) truncation. That version of the model produced the best results when an enhanced orography was included. That was the envelope orography proposed by Wallace et al. (1983). Experiments with and without the envelope orography showed that the mountain chains around the Arabian Sea and the Himalayas had an important role in the evolution of the monsoon circulations. Around the Arabian Sea the principal mountain ranges are the Western Gnats along western India, the Madagascar Mountains, the East African Highlands, and the Ethiopian Mountains. The envelope orography is a steeper orography compared to a normal orography. It adds almost a kilometer to the heights of each of these principal mountain chains. The original tabulation of mountains comes from a U.S. Navy tape of the orography on a 10 minute resolution. The transform grid for a 42 wave triangular truncation has a resolution of around 200 km. The Gaussian grid elementary squares of the transform grid contain about 144 high resolution orography grid

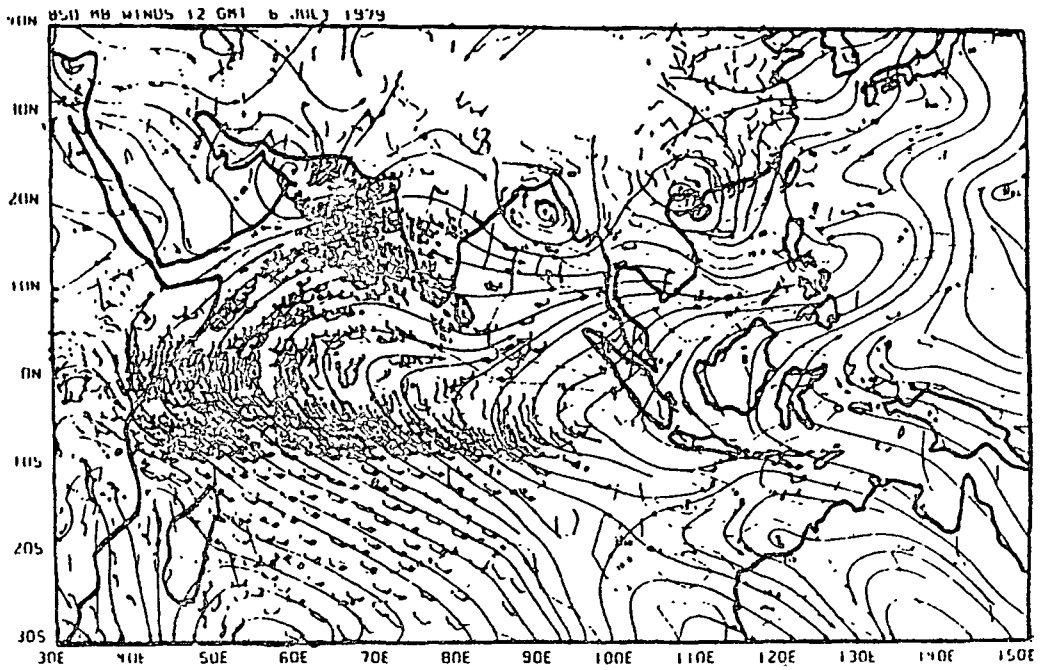

FIGURE 13 Typical data distribution during MONEX and streamline isotach (m/s) analysis at 850 mb July 7, 1979, 12z.

points. A mean height h and a standard deviation o of the high resolution grid data are evaluated for each elementary Gaussian grid square. The envelope orography used here is defined by the relation $h = h + 2\sigma$. Figures 14a,b,c illustrate the observed and the predicted motion fields at 850 mb on day 6 of the prediction. The observed, Figure 14a, field illustrates the strong monsoonal flows and the onset vortex occupying most of the northern Arabian Sea. The prediction with the regular orography, Figure 14b, is not as impressive as that carried out with the envelope orography, Figure 14c. The major defect in the prediction of the onset with the regular orography was in the path of the onset vortex. Although this storm formed at the correct time and place, it first moved eastward inland into India prior to an eventual westward motion to the northern Arabian Sea. That eastward motion was entirely absent when the envelope orography was

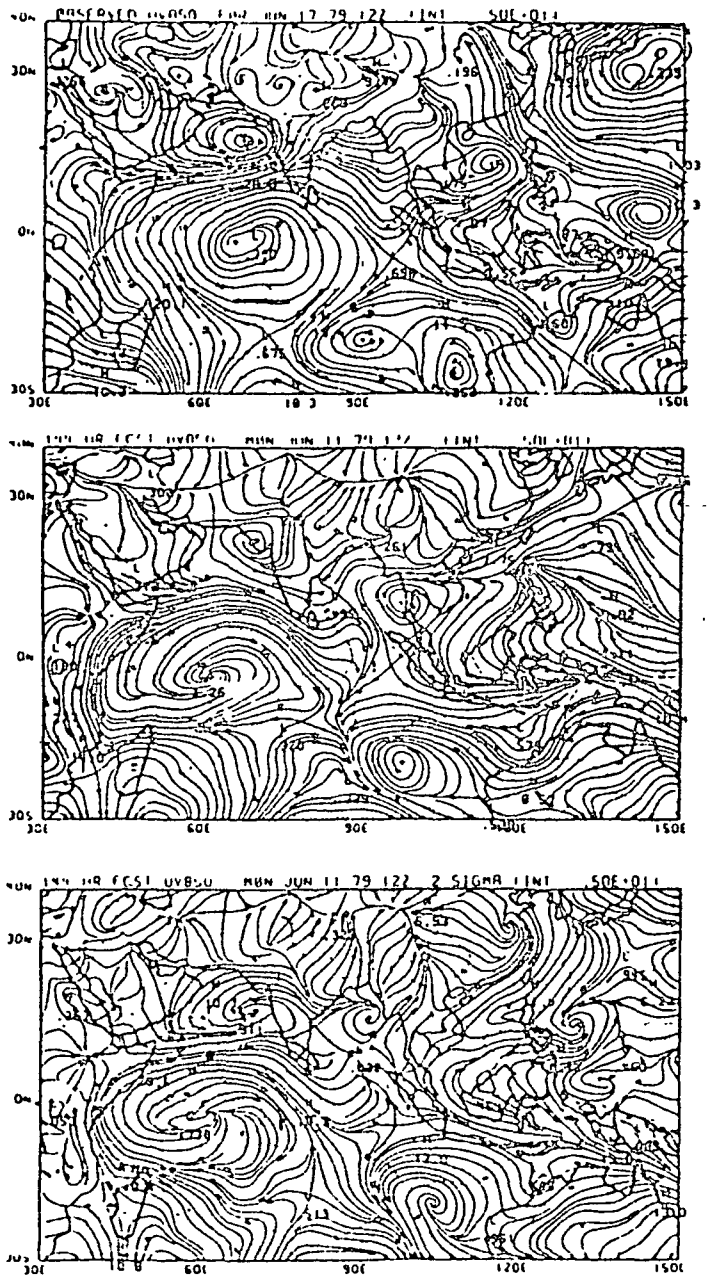

FIGURE 14 (a,b,c) Observed and predicted (144 hr) wind field over the MONEX domain on June 17, 1979, 12z. Figure 16a shows the streamlines and isotachs based on observations, while Figures 16b,c are the predicted fields with the regular and the envelope orography, respectively (speed m/s).

deployed. Thus it appears that the offshore meridional motion of such storms is strongly controlled by a steeper orography. The prediction of the track with the envelope orography was nearly accurate to about 7 days in the prediction. Other aspects of this study (vertical structure, mechanisms of onset) are discussed in Krishnamurti et al. ( ).

A detailed intercomparison of forecasts for this same storm was carried out by about 7 modeling groups. The details of these intercomparisons are presented by Temperton et al. (1983). In these studies the focus was on the aforementioned features of the monsoon and on the error statistics of the respective models. Tables 1 and 2 show the root mean square wind errors at 850 and 200 mb over the global tropics for these intercomparisons. There are some marked differnces in the performance of the different models in the tropics. Temperton et al. (1983) have alluded these differences largely to resolution and the cumulus parameterization schemes deployed within each model.

The second major study was on the formation of a monsoon depression that formed over the northern Bay of Bengal around July 4-5, 1979. A number of experiments, all starting on July 1, 1979, were carried out to 10 days with the global model. As before, the best skill in predicting cyclogenesis was noted with a higher resolution version of the model (42 waves triangular and 11 levels). Major improvements occurred when a reanalysis of the humidity was based on the proposed physical initialization described earlier. The initial state for this case was characterized by zonal westerlies in the lower troposhere over the northern Bay of Bengal. Figure 15 illustrates the flow field at 850 mb on July 1, 1979, 12Z. Results of numerical weather prediction at day 6 of integration (July 7, 1979, 12Z) are shown in Figures

TABLE 1 RMS Error of Vector Wind (ms^{-1})

30N to 30S 850 mb

Days / Modeller	1	2	3	4	5	6	7
ECMWF 1	3.67	5.01	5.91	6.36	6.50	6.99	7.25
ECMWF 2	3.69	4.98	5.87	6.27	6.38	6.76	6.78
FSU	4.4	5.5	5.7	6.1	6.5	6.8	6.7
NMC	3.5	4.7	5.8	6.5	6.6	6.9	6.9
RPN	4.3	5.7	6.7	7.1	7.6	8.7	8.9
Persist-ence	4.2	5.7	7.0	6.6	6.7	7.4	6.8

TABLE 2 RMS Error of Vector Wind (ms^{-1})

30N to 30S 200 mb

Days / Modeller	1	2	3	4	5	6	7
ECMWF 1	6.62	9.78	11.39	12.46	13.59	14.75	15.75
ECMWF 2	6.66	9.73	11.37	12.35	13.32	14.40	15.24
FSU	7.6	10.6	13.8	15.8	17.7	18.7	19.6
NMC	4.7	9.3	11.5	14.3	13.3	14.4	15.6
RPN	7.5	10.8	14.0	16.1	18.0	20.3	22.9
Persistence	8.5	10.9	13.2	15.1	16.0	16.7	16.1

16a,b. Also shown in Figure 13c is the observed field for July 7, 1979, 12Z. The two numerical prediction experiments respectively denote results with and without the proposed physical initialization. The inclusion of physical initialization improves the initial humidity analysis and also provides an improvement of diabatic heating and the initial rainfall rates. Both experiments succeed in the formation of the depression, although the intensity at landfall around day 6 of the forecast is better described by the experiment with the physical initialization. The track of the depression is due westward and is handled quite well by the global model.

We have described the formation of two tropical depressions on the medium range time scale. Are these just two isolated examples of success or is there a message here? The results presented here are based on a gradual evolution of models and the data base. It is our contention that the combination of FGGE/MONEX did provide an unprecedented data set that was not available over most other regions of the tropics. This data set enabled us to define the initial rainy regions, the initial diabatic forcing and the initial divergent wind somewhat better (Krishnamurti et al., 1984). The divergent wind errors, especially on the large planetary scale, were smaller when the physical initialization was invoked. We have also investigated the energy transformations over a local domain--emphasizing the role of the horizontal shear of the monsoonal low level flow in the initial stage and thereafter the importance of cumulus convection, which aided the transfer of eddy available potential to the eddy kinetic energy.

Since the formation and motion of a monsoon depression are important problems in the Indian subcontinent, it is necessary that further studies on these problems be continued with several other cases. The FGGE/MONEX data sets shown in Figure 15c were an exceptional

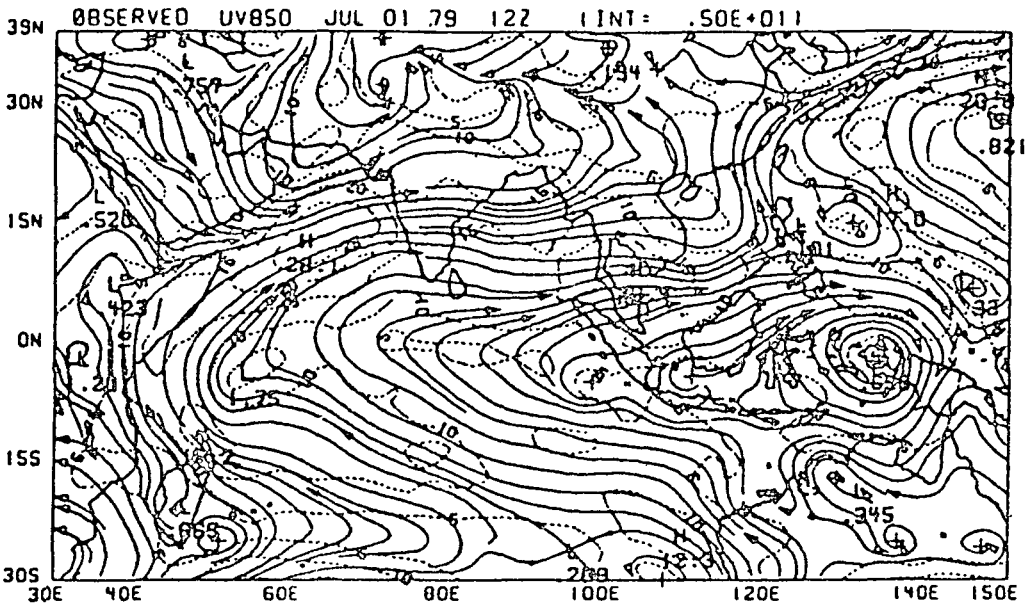

FIGURE 15 850 mb streamlines and isotachs (m/s) over the MONEX domain on July 1, 1979, 12z. This is part of the initial state for a global prediction experiment.

situation. Only three well-defined monsoon depressions formed during that summer. Thus only limited studies with a larger sample of storms defined by adequate initial observations is possible at this stage. The recent geostationary satellite INSAT appears very promising for providing high resolution cloud winds. Those data sets along with a collection of commercial ship and commercial aircraft observations can provide a useful data base for such future studies. With respect to the question whether models need be global or whether these studies can be carried out with regional models, it seems that the planetary scale aspects are quite important for medium-range prediction and the global model does seem to be far superior especially due to the importance of a long fetch of the cross equatorial flows.

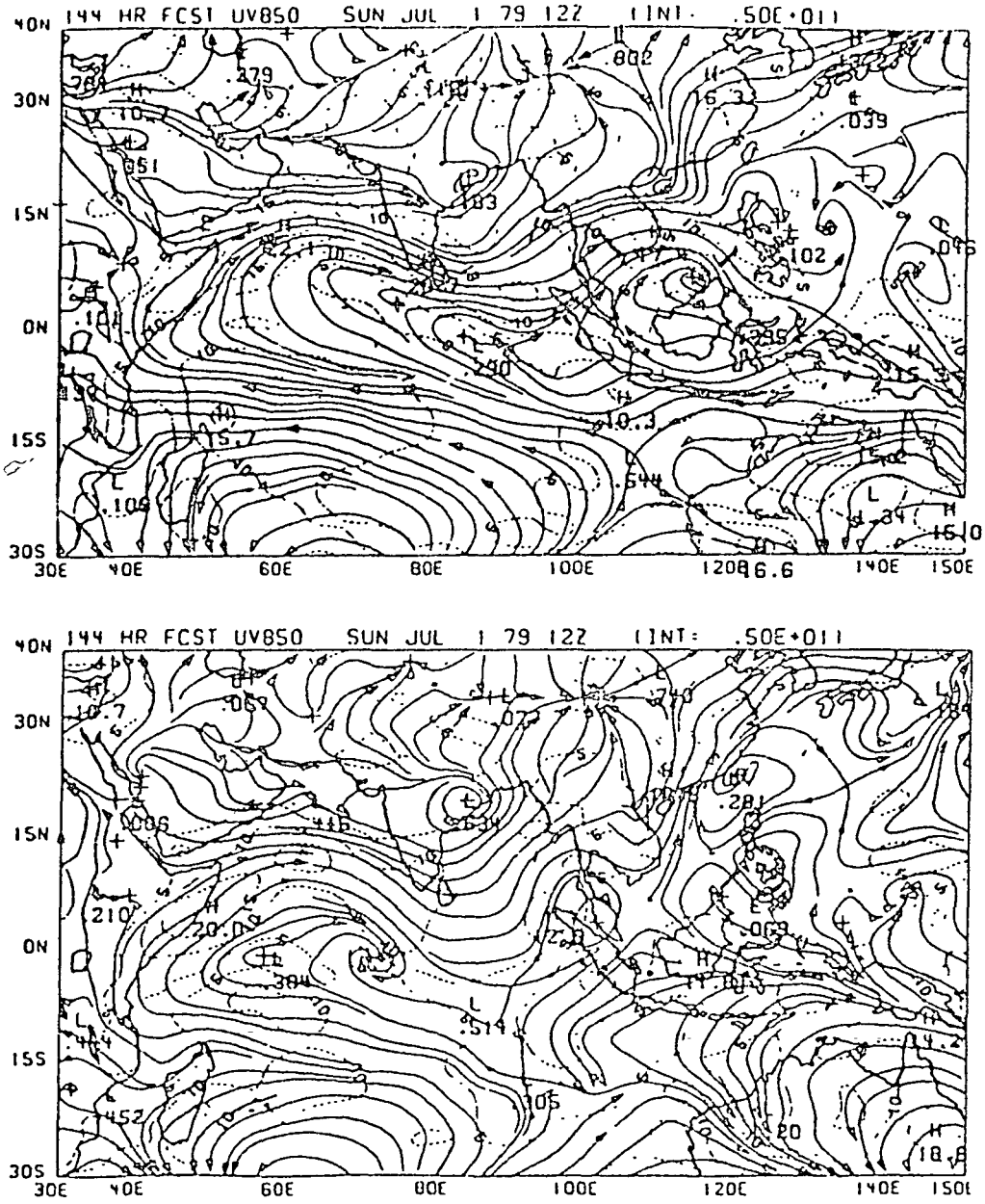

FIGURE 16 (a,b) Predicted streamlines and isotachs m/s (at hour 144) experiments carried out with and without the physical initialization, respectively. The fields are at 850 mb for July 7, 1979, 12z.

REFERENCES

Arakawa, A., and W. H. Shubert (1979). Interaction of a cumulus cloud ensemble with the large scale environment. Part I. J. Atmos. Sci. 31, 674-701.

Krishnamurti, T. N., and Y. Ramanathan (1982). Sensitivity of the monsoon onset to differential heating. J. Atmos. Sci. 39, 1290-1306.

Krishnamurti, T. N., H. Pan, C. B. Chang, J. Ploshay, and W. Oodally (1979). Numerical weather prediction for GATE. Quart. J. Roy. Meteorol. Soc. 105, 979-1010.

Krishnamurti, T. N., R. J. Pasch, and P. Ardanuy (1980a). Prediction of African waves and specification of squall lines. Tellus 32, 215-231.

Krishnamurti, T. N., Y. Ramanathan, H. Pan, R. Pasch, and J. Molinari (1980b). Cumulus parameterization and rainfall rates I. Mon. Wea. Rev. 111, 815-828.

Krishnamurti, T. N., P. A. Ardanuy, Y. Ramanathan, and R. Pasch (1981). On the onset vortex of the summer monsoon. Mon. Wea. Rev. 109, 344-363.

Krishnamurti, T. N., S. Low-Nam, and R. Pasch (1983a). Cumulus parameterization and rainfall rates II. Mon. Wea. Rev. 111, 815-828.

Krishnamurti, T. N., R. Pasch, H. Pan, S. Chu, and K. Ingles (1983b). Details of low latitude numerical weather prediction using a global spectral model I. J. Meteorol. Soc. Japan 61, 188-207.

Krishnamurti, T. N., K. Ingles, S. Cocke, R. Pasch, and T. Kitade (1984). Details of low latitude medium range numerical weather prediction using a global spectral model II. (To be published in J. Meteorol. Soc. Japan).

Lord, S. J. (1982). Interactions of a cumulus cloud ensemble with the large scale environment III. Semi-prognostic test of the Arakawa-Schubert theory. J. Atmos. Sci. 39, 88-103.

Lorenc, A. (1981). A global three dimensional multivariate statistical interpolation scheme. Mon. Wea. Rev. 109, 701-721.

Oort, A. H., and J. P. Peixot (1983). Global angular momentum and energy balance requirements from observations, in Theory of Climate, Barry Saltzman (ed.). Academic Press, pp. 335-490.

Temperton, C., T. N. Krishnamurti, R. Pasch, and T. Kitade (1983). WGNE forecast comparison experiments. Report No. 6 (pp. 1-104). World Climate Research Program, World Meteorological Organization, Geneva, Switzerland.

Thompson, R. M., Jr., S. W. Payne, E. E. Recker, and R. J. Reed (1979). Structure and properties of synoptic-scale wave disturbances in the intertropical convergence zone of the eastern Atlantic. J. Atmos. Sci. 36, 53-72.

Wallace, J. M., S. Ribaldi, and A. J. Simmons (1983). Reduction of systematic forecast errors in the ECMWF model through the introduction of envelope orography. Quart. J. Roy. Meteorol. Soc. 109, 683-718.

ON THE IMPACT OF THE FGGE ON TROPICAL FORECASTS

William A. Heckley
European Centre for Medium Range Weather Forecasts

INTRODUCTION

It has become evident from operational experience at the ECMWF that a good forecast requires, in general, a good analysis. This is as true in the tropics as it is in the extratropics. One can find many examples of bad data being accepted by the analysis scheme and significantly degrading the subsequent forecast. Equally, a lack of data may result in a forecast completely missing the early development of, for example, a midlatitude cyclone or tropical depression. Also, single level data may be misinterpreted by an analysis scheme. These problems are compounded in the tropics by our relative ignorance of the dynamics, our necessarily crude descriptions of many important physical processes, and fundamental problems in analysis. This contribution attempts to review some of the impact of the FGGE on tropical analysis/forecasting as experienced by the ECMWF.

ANALYSIS INTERCOMPARISONS

Hollingsworth et al. (1985) have described an intercomparison of analyses derived from the main FGGE IIb data set with three advanced analysis systems: those of the ECMWF (EC); the National Meteorological Center, Washington, D.C. (U.S.); and the U. K. Meteorological Office (U.K.). The EC analysis is the ECMWF IIIb analysis. The systems used correspond to that operational at the ECMWF in 1980, that operational at NMC in 1982, and a research version of the 1982 U.K. operational system. Many enhancements have been made to all these systems since that time. See Hollingsworth et al. (1985) for details of the numerical weather prediction systems. Their study concentrated on the evaluation of analysis quality in the extratropics. In this contribution, their evaluations are briefly extended to the tropics. All analysis systems were presented with exactly the same IIb data. Analyses were performed twice daily for five consecutive days, beginning February 15 at 12Z and ending February 19 at 12Z. Table 1 shows the RMS differences in the vector wind at 850 mb and at 200 mb, averaged over longitude and between latitudes 25°S and 25°N. At 850 mb the analyses typically differ by about 3.8 m/s, the difference

TABLE 1 RMS Values for the Differences between the Analyses for the Tropics, 25°S to 25°N. The Variables are Winds at 850 mb and 200 mb. (Hollingsworth et al., 1985)

NORTHERN HEMISPHERE 20°N - 90°N

MEAN RMS - DIFFERENCES OF THE DAILY FIELDS

	TROPICS 25°S to 25°N		
850 mb V (m/s)	3.56	3.69	4.26
200 mb V (m/s)	6.18	7.46	7.79
	ECA-USA	ECA-UKA	USA-UKA

between the U.S. and U.K. analyses is slightly larger than either of their differences with respect to the EC analyses, indicating that in an RMS sense the U.S. and U.K. analyses are nearer to the EC analysis than they are to each other. At 200 mb the story is similar, but the RMS differences are slightly larger, typically 7.1 m/s. These values are similar to those found in the northern hemisphere although slightly less than those found in the southern hemisphere. This result is disappointing considering the quasi-stationary nature of the tropical flow. Many of the special observing systems of the FGGE were designed to improve the definition of the tropical analyses. Figure 1a shows the mean analysis of the 850 mb vector wind of the period produced by the EC system. Figure 1b shows the corresponding chart for the U.S. system and Figure 1c shows the differences, U.S. minus EC. Large differences between the analyses occur over the equatorial Pacific, central South America, the Gulf of Guinea, and the Indian Ocean. In some regions the differences are as large as the analyzed wind, which is particularly disturbing. The analysis systems used in this study are very different in design; and as pointed out by Hollingsworth et al. (1985), the accuracy of the forecast first guess, quality control and selection of observations, resolution and concepts of balance interact in a complex way, making it very difficult in general to assign a specific cause to an analysis difference. The differences found in their study may well reflect a lack of experience in tropical analysis at that time, as much as a lack of data. Recent studies at ECMWF indicate clear and particular problems associated with tropical analysis, which will be discussed in the next section.

Another approach to assessing the accuracy of analyses is to compare the independent FGGE IIIb data sets produced by ECMWF, GFDL, and GLAS/NASA. This is not quite such a controlled experiment as that

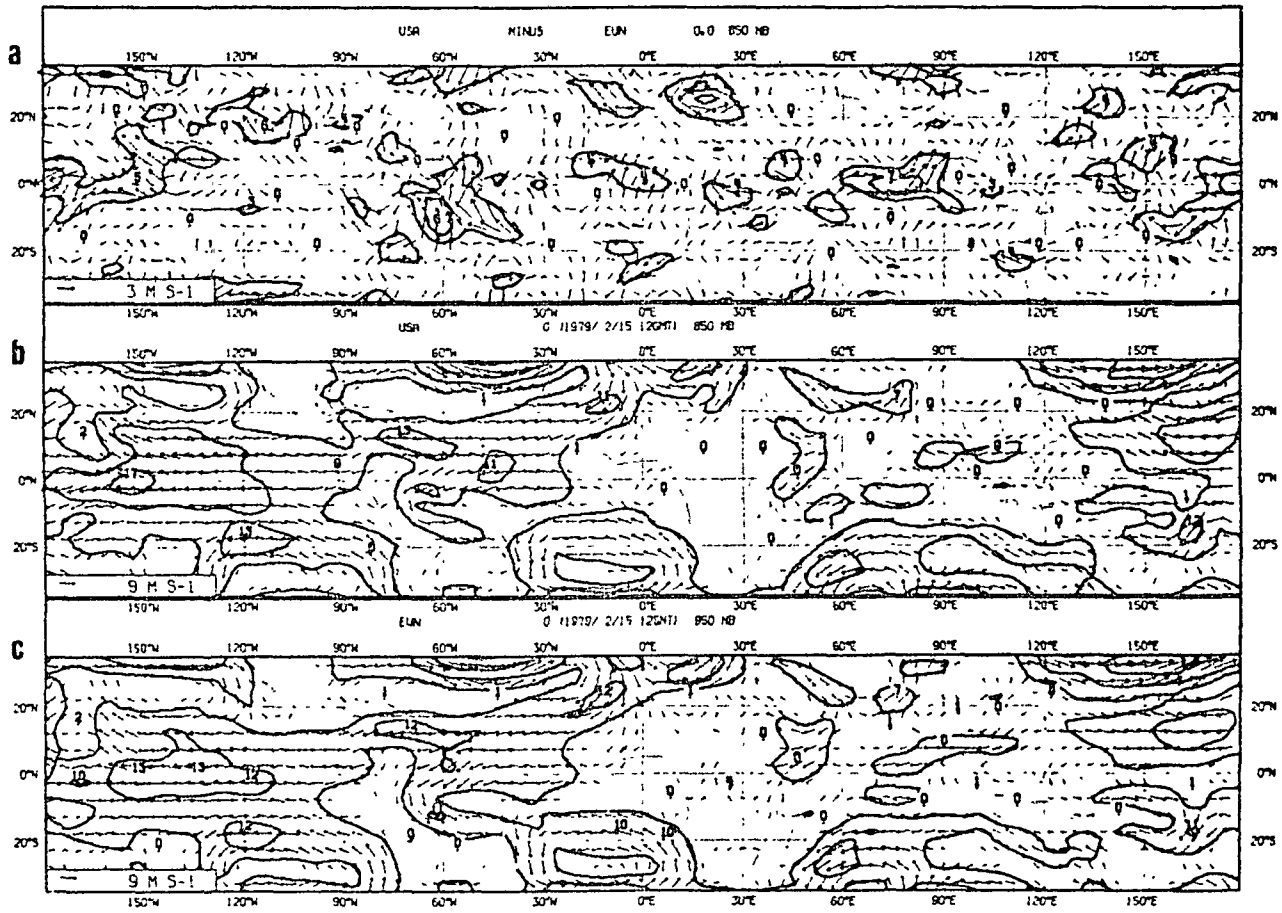

FIGURE 1 The mean 850 mb vector wind for the period May 15 to 19 as analyzed by (a) the EC system, (b) the U.S. system, and (c) shows the differences, U.S. minus EC. (Arpe, personal communication)

performed by Hollingsworth et al. (1985) as it is not clear that the analysis systems all used exactly the same data. A number of comparisons have already appeared in the Global Weather Experiment newsletters published by the U.S. Committee for the Global Atmosperic Research Program. Kung (Issue 1) points out that the energy cycle in the GFDL analyses is more intense than that in the ECMWF analyses. Paegle and Paegle (Issue 3) note a large variation in the divergent kinetic energy among the analyses. In particular, they note that the ECMWF analyses have only 30 to 50 percent as much as the others, but the ECMWF and GLAS analyses are most similar with respect to the rotational wind amplitudes. Julian (Issue 3) compares three selected ECMWF and GFDL analyses at 200 mb. He concludes that the ECMWF analyses tend to underanalyze the tropical flow field, particularly in strongly divergent situations, but tend to fit the data better than the GFDL analyses. Chen and Vorwald (Issue 4) in comparing the moisture transports in the ECMWF and GFDL analyses note deficiencies in the moisture transport in the Hadley cell in the ECMWF analyses. The relatively weak tropical divergence field in the ECMWF IIIb analysis is a known deficiency of the analysis system in use at that time. The causes of this deficiency (some of which are discussed below) have largely been eliminated in more recent operational analysis systems at ECMWF.

ANALYSIS PROBLEMS

In order to control rapid oscillations in the short (6 hour) forecasts, which are an essential part of data asssimilation, a nonlinear normal mode initialization is used. The medium range forecasts are also run from initialized data although the justification for this is not so strong as for the assimilation forecasts. The effect of the initialization on the divergence field in the tropics depends strongly on the type of interpolation that is used in taking the analyzed data from pressure coordinates to the model (sigma) coordinates (Hollingsworth, 1981). The simplest method, direct interpolation of the analyzed fields, enables the initialization to have a severely damping effect on the large-scale tropical divergence field. If only the analysis increments (difference of analysis and first guess) are interpolated, this damping has less effect. Incorporation of diabatic tendencies into the initialization also reduces the damping effect markedly. The diabatic initialization applied to the analysis increments results in analysis fields that retain virtually all the large-scale divergence present in the uninitialized analyses. Users should be aware that for the production of the FGGE IIIb analyses at ECMWF, the analysis system incorporated an adiabatic nonlinear normal mode initialization of the full analysis fields. Although the IIIb geopotential, mean sea level pressure, and horizontal winds are archived as uninitialized fields, the initialization will have an effect through its influence on the assimilation forecasts, which are used as the analysis first guess.

The ability of the ECMWF optimum interpolation scheme to analyze large-scale normal modes has been investigated in two series of experiments by Cats and Wergen (1982). The first used an idealized data coverage with one simulated sounding every 7.5° that reports both height and wind at 15 pressure levels. With the idealized data coverage, the main error source is shown to be the vertical and horizontal aliasing. In particular, the scheme is unable to distinguish between large-scale Kelvin modes and large-scale Rossby modes. For an operational type data coverage, the analysis error increases considerably. The prime reason for this is the irregular observing network that, due to the local character of the optimum interpolation scheme, inhibits the correction of large-scale first guess errors in data-sparse regions. When aliasing is taken into account, the normalized RMS analysis error for some large-scale modes can amount to 75 percent.

The normal modes used in the study by Cats and Wergen (1982) are the free solutions to the linearized multilevel ECMWF gridpoint forecasting model. The first vertical mode, called the external mode, describes the barotropic part of the mass and wind field. The second vertical mode, called the first internal mode, changes sign near the tropopause. The third vertical mode changes sign near 400 mb and at around 50 mb, and is therefore important for describing processes which change sign in the troposphere, e.g., the flow associated with tropical convection. Horizontally the modes can be divided into two classes, the Rossby modes and the inertia-gravity modes. In the tropics, where the geostrophic relation breaks down, these modes still define a relationship between the mass and wind field.

The gravity modes are highly divergent and ageostrophic. Due to the geostrophy and nondivergence constraints built into the optimum interpolation scheme (although the former is relaxed in the tropics so that the scheme becomes univariatae in height and wind at the equator), the analysis scheme is only expected to perform well for the Rossby and to some extent for the mixed Rossby-gravity and Kelvin modes. The modes within each class may be characterized by three indices, superscript k for vertical structure, subscripts m and l for zonal wavenumber and meridional index. Table 2 shows the amplitude error in analyzing the zonal wavenumber 1 gravest symmetric Rossby modes and gravest asymmetric gravity (Kelvin) modes for vertical modes 1 to 3, using the idealized data network. For a perfect analysis, all the elements of the table should be zero. The diagonal elements show the analysis error of the mode itself, and the off diagonal elements indicate spurious excitation of other modes. The fact that the matrix is not diagonally dominant indicates that the aliasing between Kelvin and Rossby modes is as important as the poor analysis of the mode itself. When the modes are analyzed with the operational data coverage from 12Z August 10, 1982 (Figure 2), the result is quite alarming. For the $R_{1,1}$ mode, for example, there is a 40 percent error in the analysis of the input mode itself (compared to 8 percent in the idealized case). Aliasing on the higher zonal and meridional indices leads to a 60 percent error in the external Rossby modes. When summed over all amplitudes, the overall analysis error amounts to 75 percent.

TABLE 2 Response Matrix of the Analysis Operator for the Idealized Data Set. (Cats and Wergen, 1982)

Input \ Result	$R^1_{1,1}$	$R^2_{1,1}$	$R^3_{1,1}$	$E^1_{1,0}$	$E^2_{1,0}$	$E^3_{1,0}$
$R^1_{1,1}$	8		6	9		-7
$R^2_{1,1}$		16			14	8
$R^3_{1,1}$			12		-12	
$E^1_{1,0}$	10		13	13		-15
$E^2_{1,0}$		15	-10		21	12
$E^3_{1,0}$		10			7	16

Figure 3 shows the input (top) and the error (bottom) in the wind field at 250 mb for the $R^1_{1,1}$ mode when analyzed with the operational data coverage. In the tropics, the chart reflects to a certain extent the availability of data (c.f., Figure 2). The winds over the tropical eastern Pacific are not analyzed at all. To a lesser extent, this is also true for the winds over the Indian Ocean. Cats and Wergen (1982) point out that in the extratropics, the multivariate scheme is able to generate a wind analysis from height observations and vice versa. In the tropics, the availability of both mass and wind observations is crucial for a good analysis. The tropical wind field is most important, but high quality mass data are needed in order to separate the Rossby modes properly from the Kelvin modes.

The results of Cats and Wergen (1982) are confirmed by Daley (1983). Daley (1983) points out that the more optimistic results for the analysis of these large-scale modes obtained by Leary and Thompson (1973) and by Baer and Tribbia (1976) are primarily due to the oversimplified nature of their experiments, i.e., restriction to higher latitude and restriction to a univariate analysis procedure.

Statistical (optimum) interpolation is only partly successful in analyzing realistic wind fields in areas where the divergence is of similar magnitude or larger than the vorticity. On scales much larger than the analysis box area (600 x 600 km at ECMWF) and in the presence of sufficient data density, the statistical interpolation scheme does a reasonable job most of the time. Daley (1983) has shown that better performance can be achieved through the use of slightly divergent prediction error correlation functions, and Julian (1982) has shown that a better fit to data can be achieved through the use of IR data to analyze the divergence field.

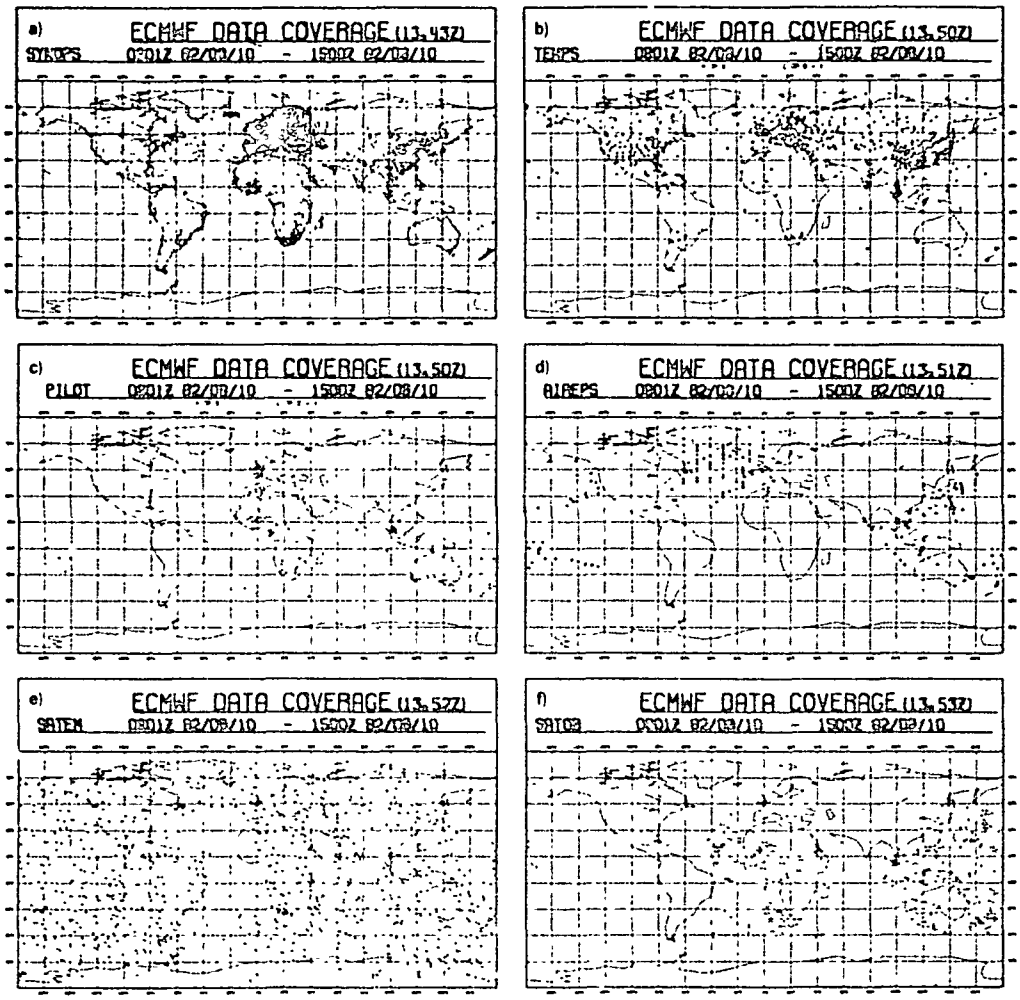

FIGURE 2 Operational data coverage for August 10, 1982, 0900 GMT to 1500 GMT, as received at ECMWF (Cats and Wergen, 1982).

DIRECT IMPACT OF ANALYSES ON FORECAST QUALITY

Incompatible Analyses

In studying the systematic tropical errors of the operational ECMWF forecasts, Heckley (1982) has shown rapid adjustments taking place during the first 48 hours, apparently associated with erroneous large-scale heating at the start of the forecasts, in particular in the regions of the African and South American continents. Figure 4 shows the ensemble mean of the 24-hour forecasts for April 1981 minus the ensemble mean of the initialized analyses. Errors of up to 7 m/s at

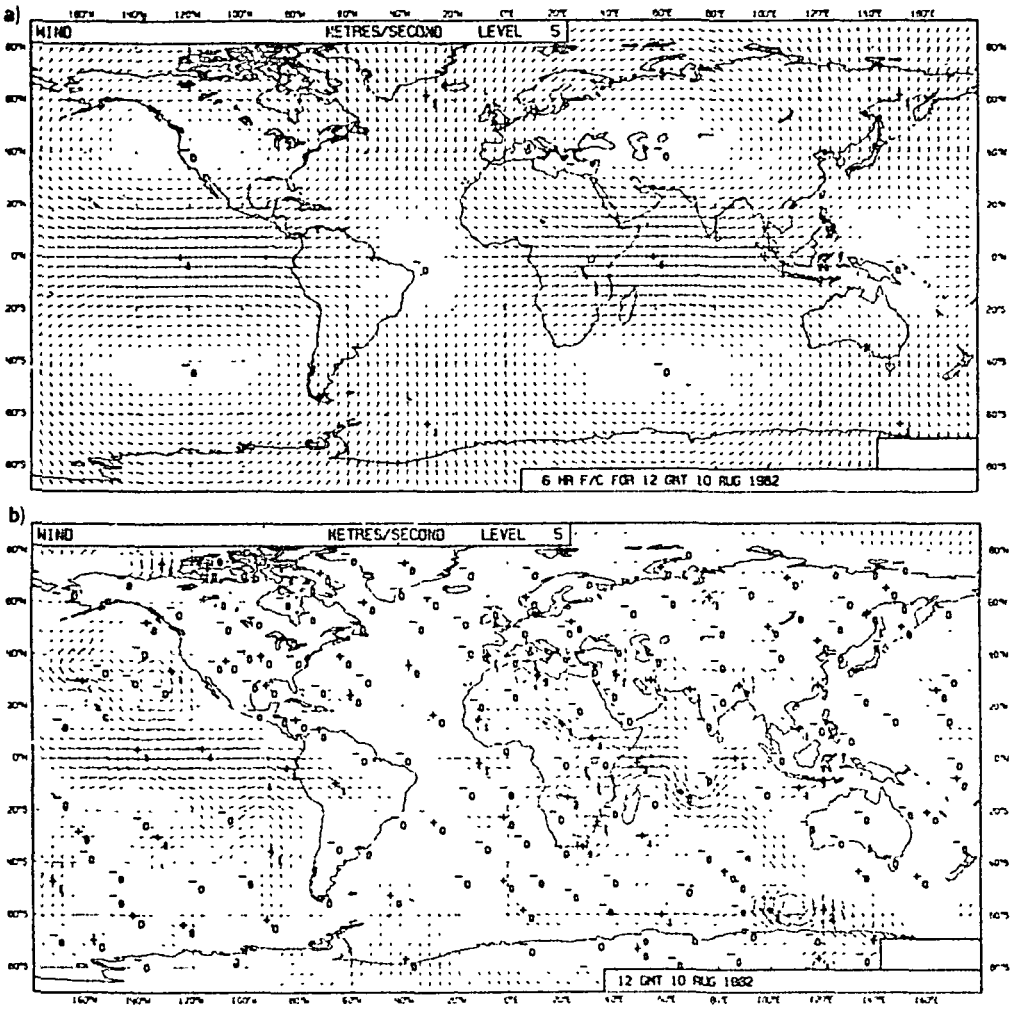

FIGURE 3 Input wind field (top) at model level 5 (250 mb) and analysis error (bottom) when using operational data coverage. Numbers indicate wind speeds in m/s (Cats and Wergen, 1982).

850 mb and 11 m/s at 150 mb are apparent. This is a typical error structure for this region and can be found at most times of the year, with slight seasonal shift. The pattern is highly baroclinic and is reminiscent of a heat induced circulation. Wergen (1982) has demonstrated the importance of a correct initial specification of the physical tendencies in keeping the large-scale stationary modes stationary.

Erroneous physical forcing may be due to errors in the initial fields, errors in the parameterization schemes themselves, or a

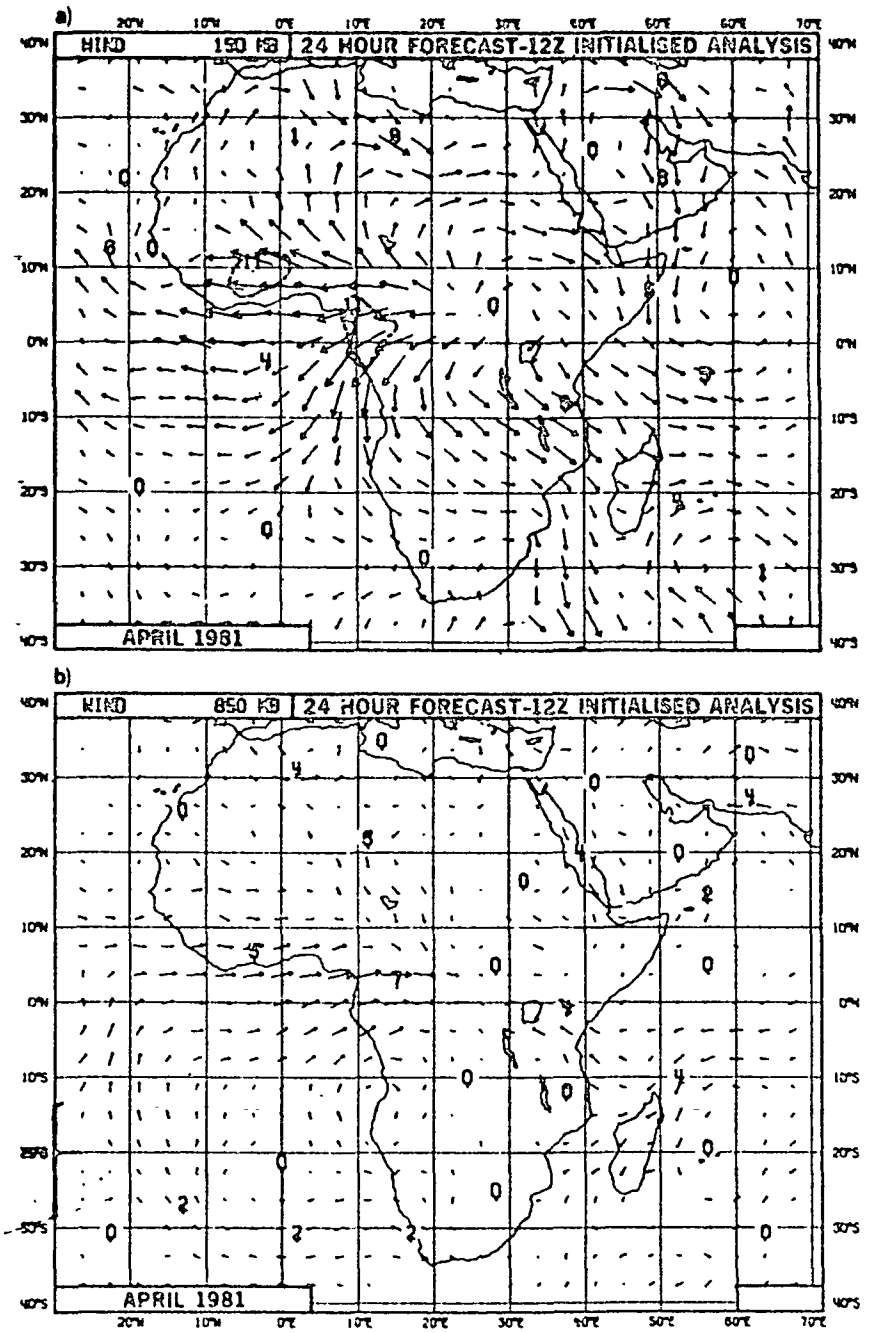

FIGURE 4 Vector wind field of the ensemble mean 24-hour forecast minus the ensemble mean 12Z initialized analysis, for April 1981. (a) 150 mb and (b) 850 mb (Heckley, 1982).

combination of these. Krishnamurti et al. (1983) have demonstrated that careful adjustment of the divergence and moisture fields in the analyses to ensure compatibility with the physical forcing (specifically cumulus parameterization and radiation) can dramatically improve the fidelity of tropical forecasts. All these studies suggest the importance of a consistent physical balance in the analyses.

Observing Systems Experiments

For a discussion of objectives, methodology, and limitations of observing systems experiments see the contribution by Hollingsworth in this report. This contribution is mainly concerned with the impact of FGGE data in the tropics and will concern itself solely with observing systems experiments involving Satobs and Satems.

As pointed out earlier, the impact on the analysis depends not only on the observations and their quality but also on the internal constraints of the multivariate optimum interpolation scheme. The impact on the forecasts, on the other hand, is dependent on how much of the analysis impact is retained after initialization and on the reaction of the forecast model to the analysis impact.

Kallberg et al. (1982) have studied the impact of cloud drift winds on medium-range forecasts. They carried out two parallel data assimilations, one including (WI) and one excluding (WO) all cloud drift winds from the geostationary satellites, for a two week period during the FGGE SOP-1, February 8 to 22. Figure 5 shows the ensemble difference between the WI and WO analyses for the vector wind at 850 mb. The differences are large even at this level, particularly over the central Pacific. The largest differences occur at about the 200 mb level (Figure 6) where there is a significant impact throughout the tropics. It is interesting to compare Figure 5 with Figure 1, which shows the difference between the (independent) ECMWF and U.S. analyses of the IIb data. Many of the differences appear to occur in the regions where the cloud drift winds have a significant impact.

Another example is the impact on the zonal mean meridional circulation shown in Figure 7. The top diagrams correspond to the first guess and the bottom to the analyses; the left panels are WI and the right WO. The WI analysis has a more intense Hadley cell, and the cloud wind data appear to be essential in analyzing the upper tropospheric circulation. The first guess fields are similar showing the effect of the adiabatic nonlinear normal mode initialization on the divergent flow.

Four sets of forecasts run from these analyses were subjectively analyzed. In the tropics, the impact up to day 4 was in all cases significantly positive and in some cases large. After four days the impact was less easy to detect.

The ECMWF has undertaken data studies of Satob and Satem data for two periods in the FGGE year--the first, November 8 to 19, when two TIROS-N satellites were available (OSE-1), and the second, February 22 to March 7. The results shown here are based on seven experiments run from the following times: 10/00, 11/00, 11/12, 13/00, 14/12, 16/00, and 18/12.

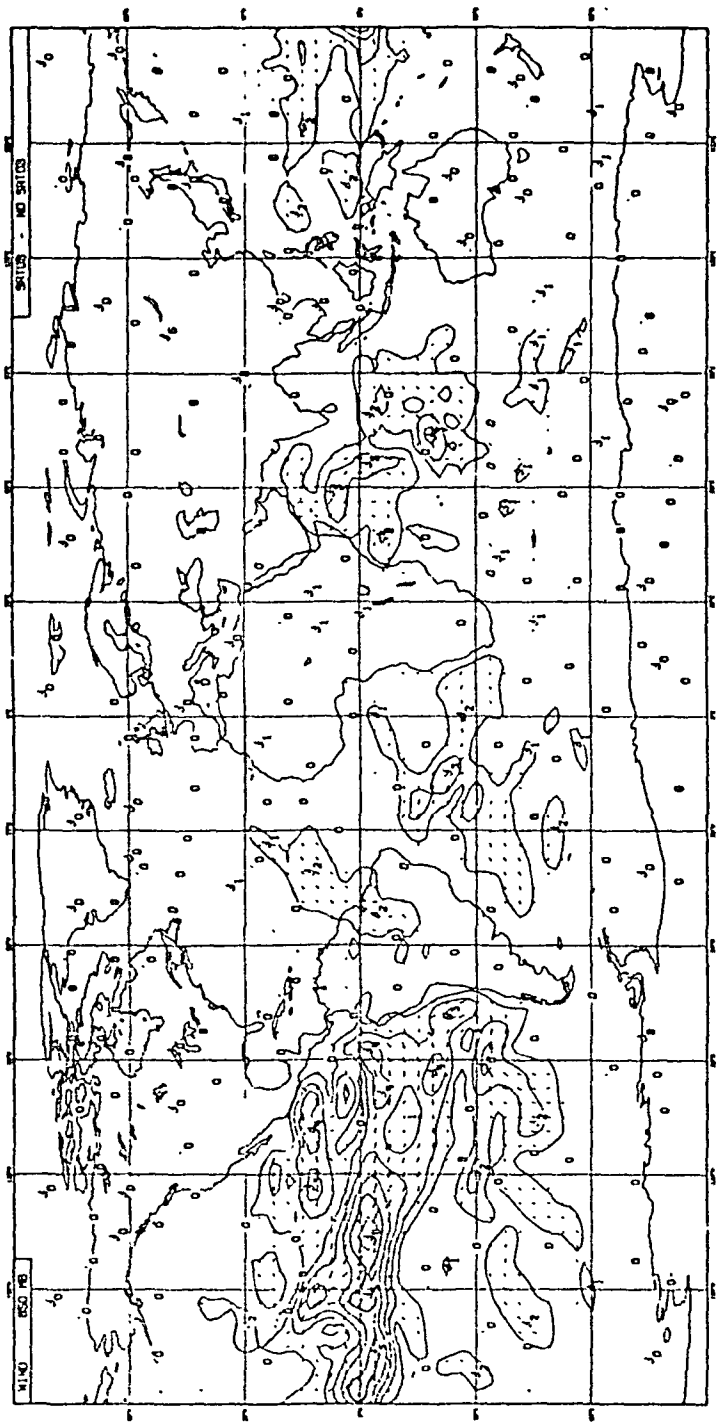

FIGURE 5 Differences between averaged windfields (WI-WO, 850 mb (Kallberg et al., 1982).

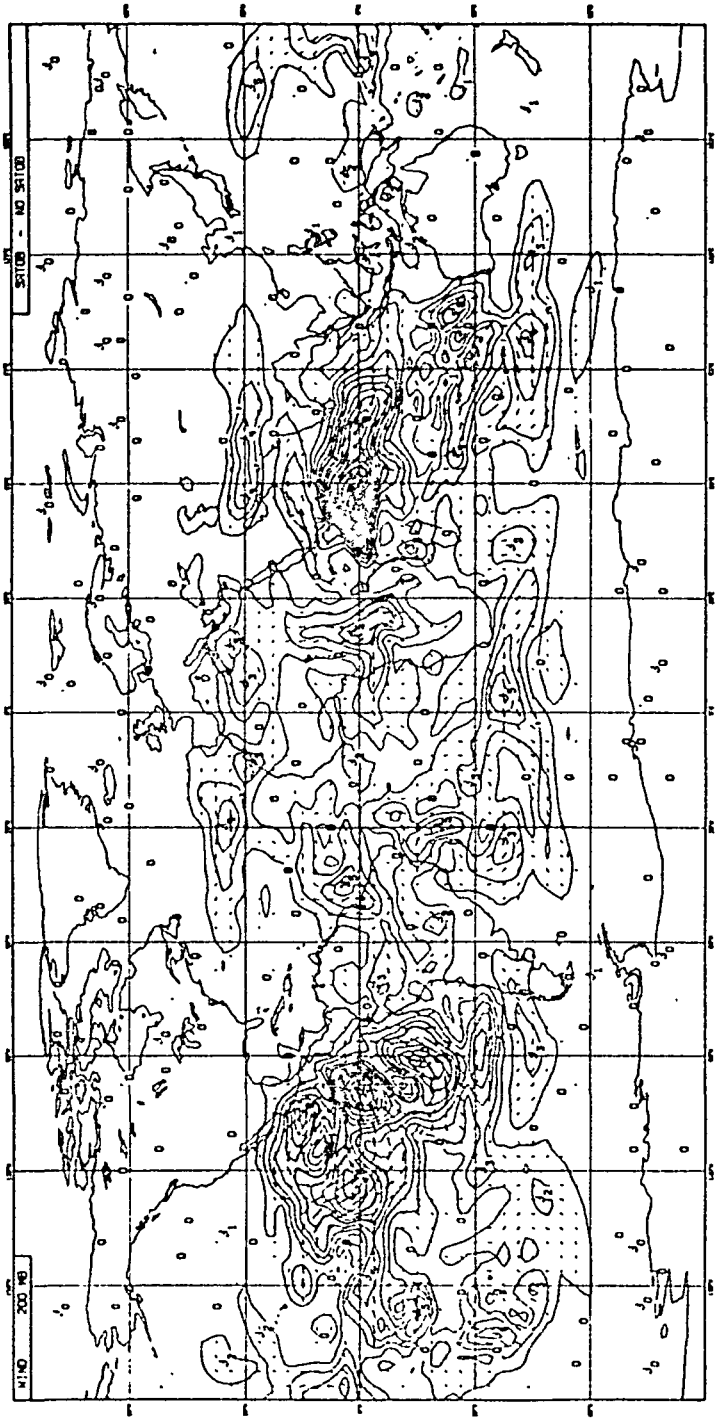

FIGURE 6 Differences between averaged windfields (WI-WO), 200 mb (Kallberg et al., 1982).

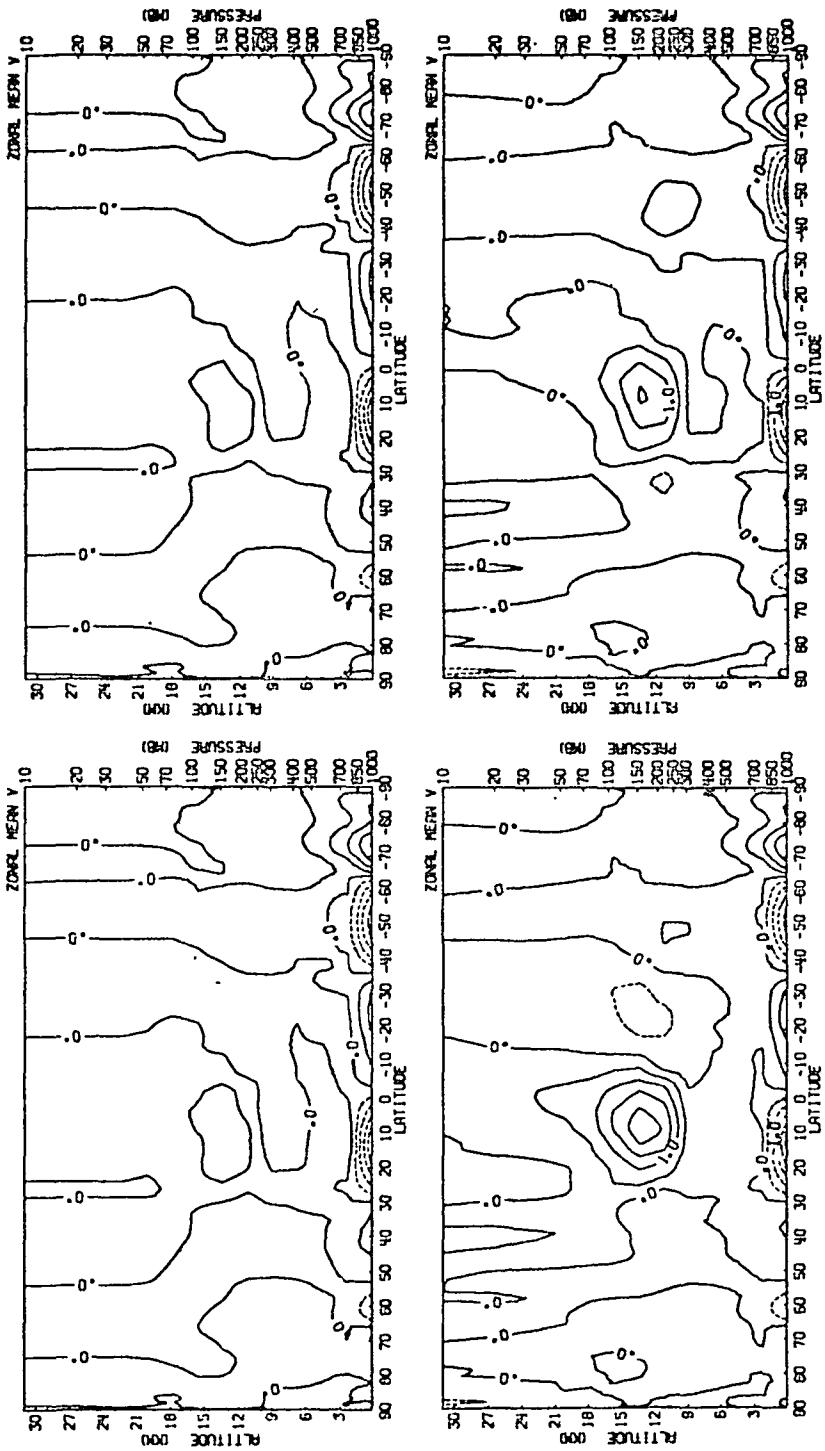

FIGURE 7 Zonal average of mean meridional circulation. Left, WI; right, WO; top, first guess forecast; bottom, analysis (Kallberg et al., 1982).

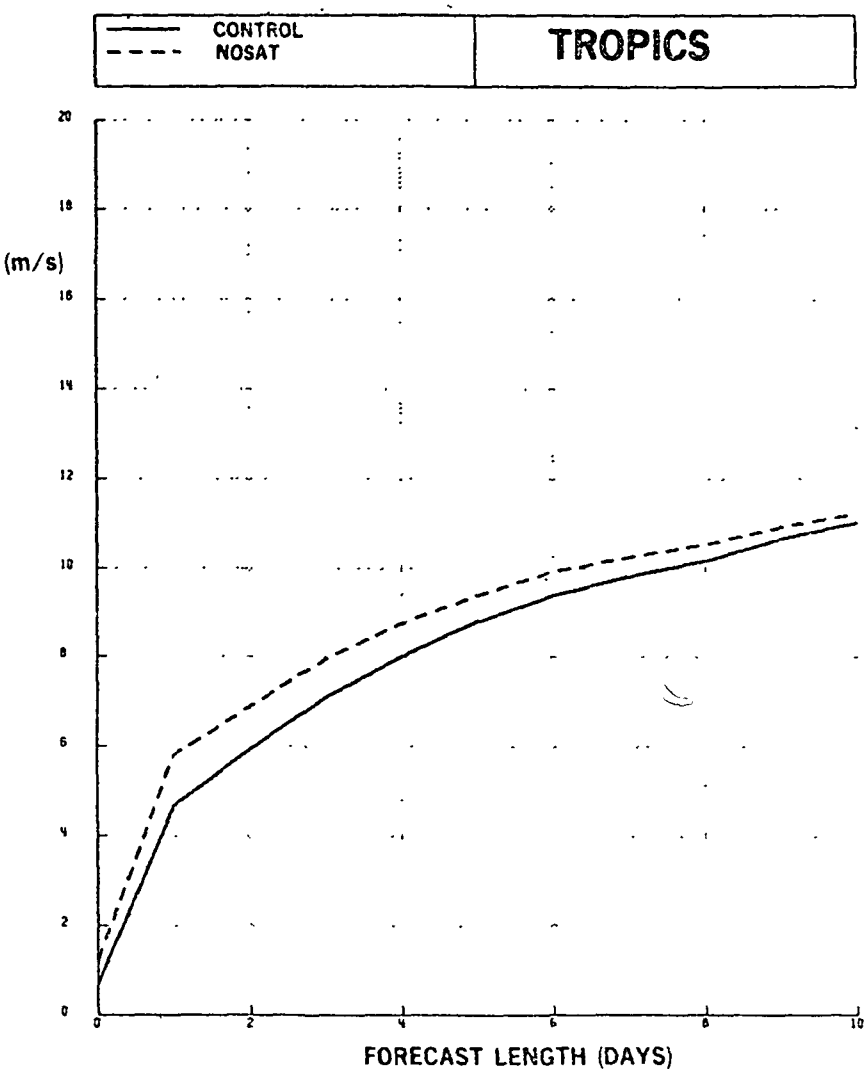

FIGURE 8 Mean RMS vector wind errors of the forecasts run from the SAI analyses (solid curve) and from the SAO analyses (dashed curve), verified against the IIIb analyses. The error is averaged vertically between 850 and 200 mb, and horizontally over longitude and between latitudes 32.5°S and 32.5°N.

The control analyses are denoted by SAI, and the analyses without Satem and Satob data by SAO. Forecasts are run from the SAI and SAO analyses, as indicated above, and verified against the ECMWF FGGE IIIb analyses. This was done for convenience when the interest was largely in the extratropics. However the SAI analyses differ considerably from

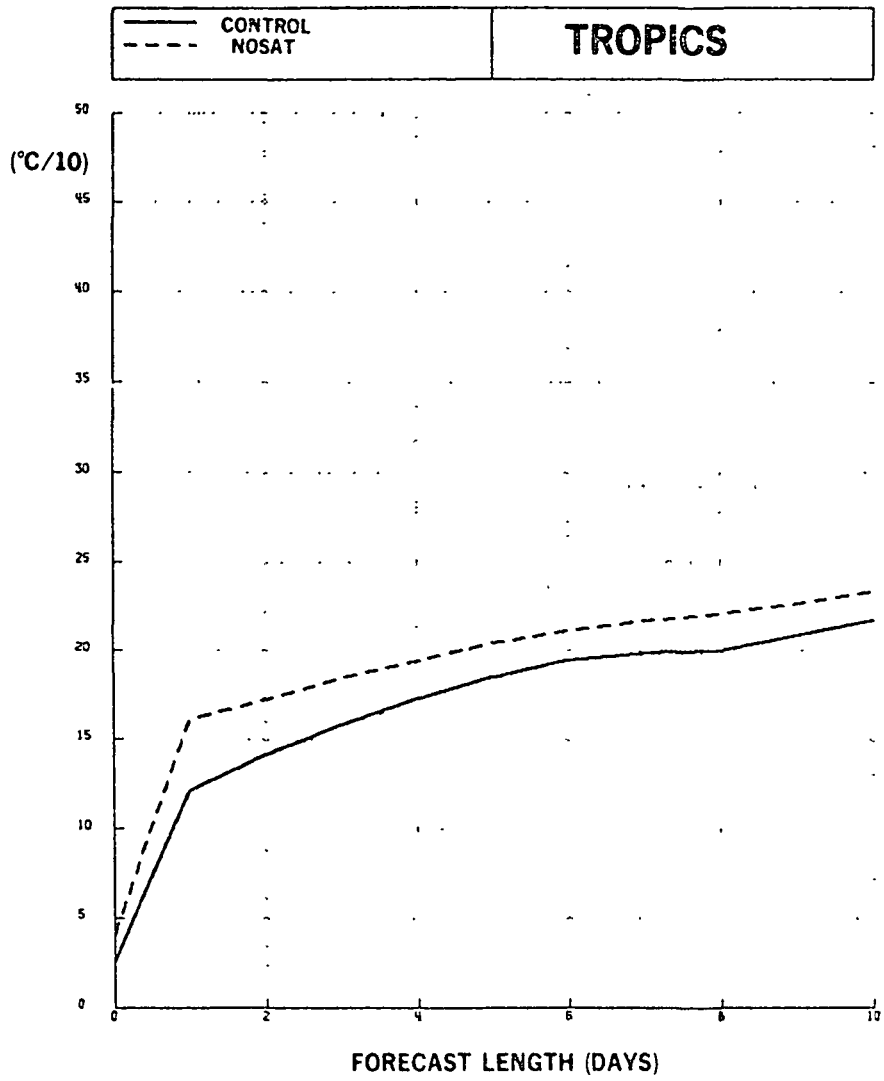

FIGURE 9 Mean RMS temperature errors of the forecasts run from the SAI analyses (solid curve) and from the SAO analyses (dashed curve), verified against the IIIb analyses. The error is averaged vertically in tenths of degrees K, and horizontally over longitude and between latitudes 32.5°S and 32.5°N.

the IIIb analyses as the operational assimilation/forecasting system has evolved considerably over the last few years. Figure 8 shows the ensemble mean error in the vector wind for the SAO and SAI forecasts when verified against the IIIb analyses. Figure 9 shows the ensemble mean error of the temperature. For both plots, the error is a mean

between 850 mb and 200 mb, and between 32.5°S and 32.5°N. Forecasts of both temperature and wind are seen to be much better when the satellite data is used. It is interesting to look at the day 0 scores. These show that the SAO and SAI analyses differ by about the same order of magnitude as the SAI and IIIb analyses, which illustrates the evolution of the ECMWF analysis system since the original IIIb analyses were produced.

USE OF THE FGGE IIIb ANALYSES FOR FORECAST EXPERIMENTS

Tiedtke (1983) used the FGGE IIIb analyses to study the effect of cumulus convection and cloud radiation on the simulation of the time mean February 1979 circulation, using the ECMWF T40 truncation spectral model. This study highlighted the importance of shallow convection in maintaining the Hadley circulation through enhancement of the moisture supply within the trade winds, which in turn influences the subtropical flow and the location of the Atlantic high. In a further study, Tiedtke (1984) studied the response of the large-scale atmospheric flow to penetrative cumulus convective heating and cumulus cloud-radiation interaction. His results show a strong link between the tropical diabatic heat sources and the planetary-scale divergent circulation. Both these are considerably reduced in the presence of penetrative cumulus convection, except along the ITCZ where cumulus convection enhances the diabatic heating. Cumulus cloud radiation interaction plays a dominant role in producing the zonal asymmetry of the tropical heat sources and sinks and the associated mean flow, both directly through the albedo and "greenhouse" effects and indirectly through feedback with the large-scale flow.

Mohanty et al. (1984) have studied the ability of the operational ECMWF forecasting model to predict the onset of the 1979 Asian summer monsoon. Their experiments showed a marked sensitivity of the forecasts to the form of cumulus parameterization.

Dell'Osso and Bengtsson (1984) have studied the formation of Typhoon Tip using the limited area version of the ECMWF model. The lateral boundary conditions were provided by the global model. The forecast was started from 00Z on October 9, 1979. The initial state showed a weak depression over the Pacific Ocean with a center just to the east of Guam. A high resolution model (0.47° latitude/longitude) was capable of simulating the main structural features of the typhoon and predicting a fall in pressure of 60 mb in three days. The structure of the forecast typhoon--with a warm core (maximum potential temperature anomaly 17°K), intense swirling wind (maximum 55 m/s at 850 mb) (Figure 10), and spiraling precipitation patterns (Figure 11)--is characteristic of a tropical cyclone. They remark that horizontal resolution is a determining factor in predicting the structure and intensity of these vortices and that an accurate analysis is a prerequisite for an accurate prediction.

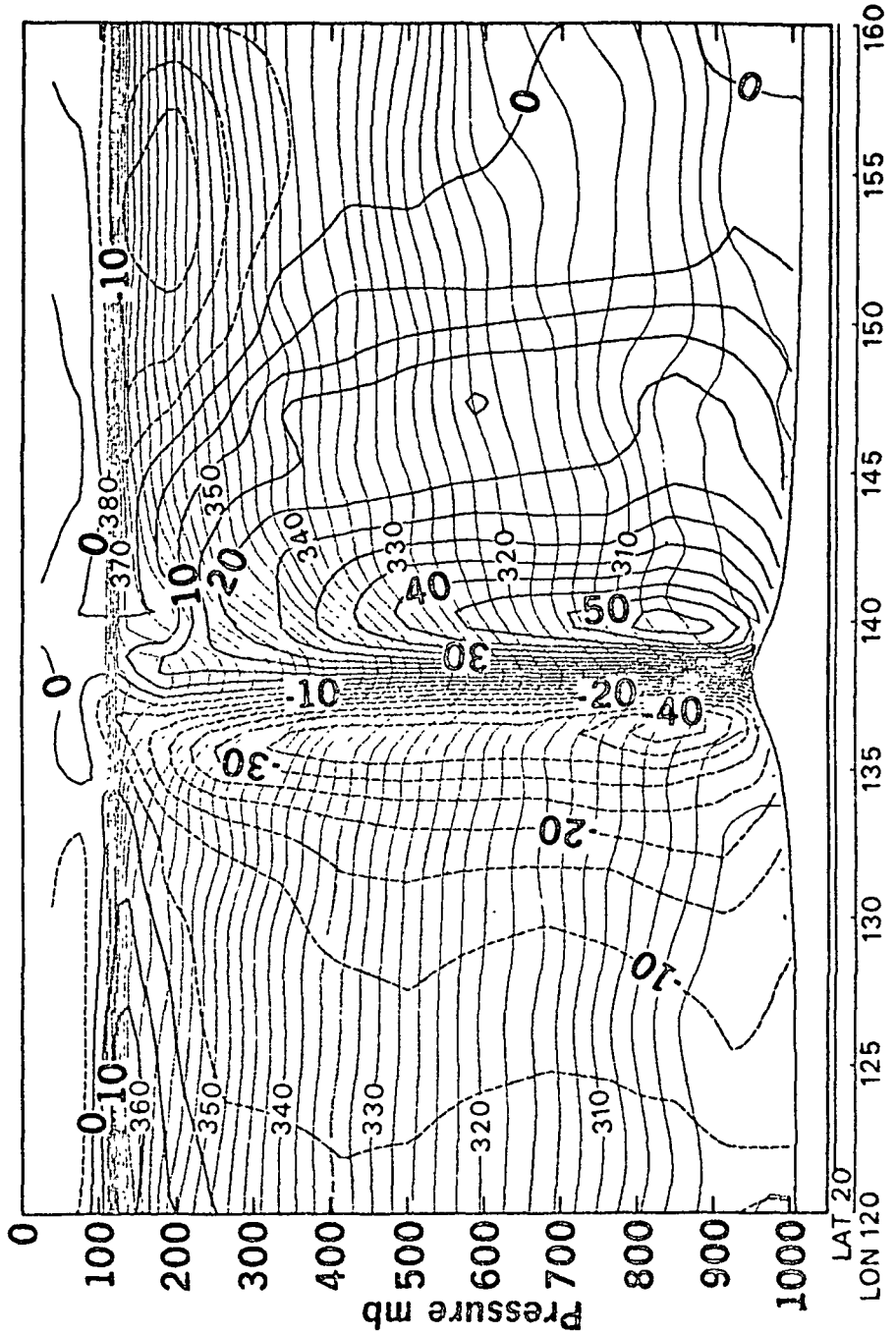

FIGURE 10 Zonal vertical cross section from day 3 of the forecast with high resolution verifying at 00Z October 12, 1979. Thin lines are isentropes (every $2^{o}K$), thick and dashed lines are isotacs (every 5 m/s), positive into the plane. Bottom contour represents surface pressure (Dell'Osso and Bengtsson, 1984).

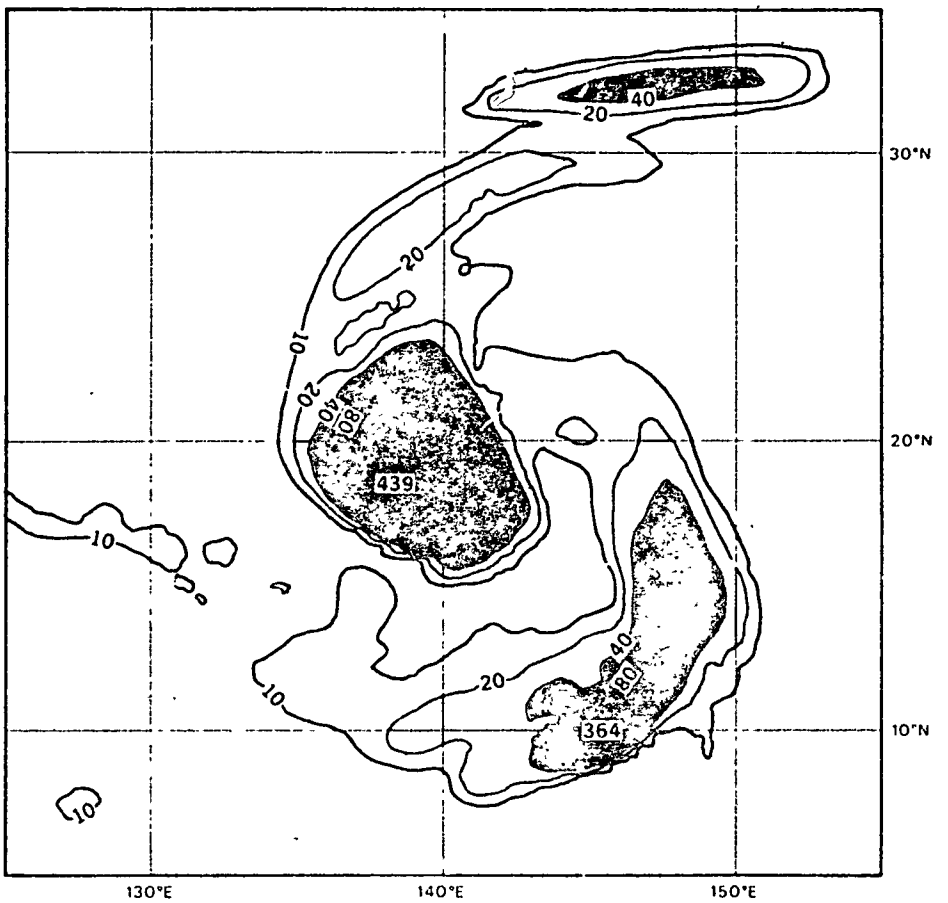

FIGURE 11 Twenty-four hour accumulated precipitation from the high resolution forecast verifying at 00Z October 12, 1979 (Dell'Osso and Bengtsson, 1984).

TROPICAL SIMULATION IN GENERAL

In recent years, many centers have begun to take a more active interest in the performance of their models in the tropics. It is becoming apparent that many models have common problems in the tropics. The following discussion while certainly applicable to the ECMWF model is also true of many others (Heckley, 1981a,b, 1984). What one feels should be the easiest to predict--the quasi-stationary tropical flow--appears to be the most difficult to simulate. Systematic errors in the tropics are dominated by the larger scales and have a large stationary component associated with thermal and orographic forcing. Many studies have indicated the importance of vertical coupling, convection, interactive radiation, and the sensitivity of forecasts to

the correct treatment of moisture and surface parameters. Difficulties are experienced in correctly simulating the low-level tropical easterlies and the stratospheric easterlies, usually the low-level easterlies are too weak and the stratospheric easterlies too strong. Hadley cells are usually simulated too shallow and too weak, the meridional circulations are usually too weak, and the troposphere is often too stable caused by a cooling in the lower troposphere and a warming in the upper troposphere.

There are indications from experiments performed at ECMWF that the weakness of the Hadley circulation and some of the wind errors are due to inadequate moisture supply in the subtropics.

ACKNOWLEDGEMENTS

This report has drawn on the work of many colleagues at the European Centre for Medium Range Weather Forecasts including Drs. K. Arpe, L. Bengtsson, G. Cats, L. Dell'Osso, A. Hollingsworth, M. Tiedtke, S. Uppala, and W. Wergen.

REFERENCES

Cats, G. J., and W. Wergen (1982). Analysis of large-scale normal modes in the ECMWF analysis scheme. ECMWF Workshop on Current Problems in Data Assimilation. Available from ECMWF.

Daley, R. (1983). Spectral characteristics of the ECMWF objective analysis system. ECMWF Tech. Report No. 40. Available from ECMWF.

Dell'Osso, L., and L. Bengtsson (1984). Prediction of a typhoon in an operational model. Submitted to Tellus.

Heckley, W. A. (1981a). Preliminary results of an investigation into the quality of ECMWF forecasts in the tropics. ECMWF Tech. Memo. No. 43. Available from ECMWF.

Heckley, W. A. (1981b). A survey of GCMs in the tropics. Part 1: Other models. ECMWF Tech. Memo. No. 45. Available from ECMWF.

Heckley, W. A. (1982). Adjustment in numerical weather prediction models in the tropics. ECMWF Workshop on Current Problems in Data Assimilation.

Heckley, W. A. (1984). Systematic errors of the ECMWF forecasting system in tropical regions. ECMWF Tech. Report. (To appear).

Hollingsworth, A. (1981). Initialization in the tropics. ECMWF Workshop on Tropical Meteorology and Its Effects on Medium Range Weather Prediction at Middle Latitudes. Available from ECMWF.

Hollingsworth, A., A. C. Lorenc, M. S. Tracton, K. Arpe, G. Cats, S. Uppala, and P. Kallberg (1985). The response of numerical weather predictions systems to FGGE IIb data. Submitted to the Quart. J. Roy. Meteorol. Soc.

Julian, P. R. (1982). A proposed scheme for objective analysis of the tropical wind field. ECMWF Workshop on Current Problems in Data Assimilation.

Kallberg, P., S. Uppala, N. Gustafsson, and J. Pailleux (1982). The impact of cloud track wind data on global analyses and medium range forecasts. ECMWF Tech. Report No. 34.

Krishnamurti, T. N., K. Ingles, S. Cocke, T. Kitade, and R. Pasch (1983). Details of low latitude medium range numerical weather prediction using a global spectral model II. Effects of orography and physical initialization. FSU Report No. 38-11, available from Florida State University, Tallahassee, FL.

Leary, C., and R. Thompson (1973). Shortcomings of an objective analysis scheme. J. Appl. Meteorol. 12, 589-594.

Wergen, W. (1982). Forced motion in the tropics. ECMWF Workshop on Current Problems in Data Assimilation.

omit

6. ANALYSIS INTERCOMPARISONS

Organizer	Roger W. Daley
Session Chairman	Roger W. Daley
Speakers	Paul R. Julian Andrew Lorenc David Baumhefner Tsing-Chang Chen
Rapporteur	Tsing-Change Chen Jeffrey J. Ploshay

D11

SOME COMPARISONS OF ECMWF IIIb AND GFDL IIIb ANALYSES IN THE TROPICS

Paul R. Julian
National Center for Atmospheric Research

Owing to the problems that data assimilation procedures have in analyzing data in the tropics and to the apparent differences in the descriptions of the ECMWF and GFDL assimilation suites, a brief comparison has been done of the resulting analyses in the tropics. Three cases each have been selected for SOP-1 and SOP-2 at the 200 and 850 mb levels, the wind fields for 25°N to 25°S have been partitioned into a rotational and divergent component, and various statistics of each have been calculated.

Table 1 gives the average eddy kinetic energies of the rotational and divergent components and the mean zonal velocities for the two centers' analyses. It has been noted that the ECMWF analyses have consistently slightly greater kinetic energy of the rotational component, all latitudes and both SOPs, than does GFDL's. However the GFDL analyses have 3 to 4 times the eddy kinetic energy of the divergent flow field, again, consistently so. The mean zonal components are in good agreement, except perhaps at the more southerly latitudes, but the mean meridional components do not agree as well, although they do agree in sign.

Table 2 presents the results at the relative phases of the rotational and divergent components averaged by zonal wavenumber. (The correlation coefficient of the two u- and v- components is a measure of the relative phase.) Here, a general decrease in the phasing of both the rotational and divergent velocity components has been noted with increasing zonal wavenumber (decreasing horizontal scale) as might be expected. Further, the zonal components agree better than the meridional components, which again might be expected. However, it is important to note that the agreement in phase of the divergent components is satisfactory only for the largest, planetary scales. (Two velocity components differing in phase by 60° of the wavelength would be correlated 0.5). This, coupled with the intensities of the divergent kinetic energies (Table 1), suggests that the two centers' analyses of the irrotational flow in the tropical upper troposphere do not portray the same thing. To summarize the point, Figure 1 shows the zonal wavenumber spectra of the eddy kinetic energy of the divergent flow. The GFDL IIIb exceeds ECMWF IIIb at all wavenumbers and is up by a factor of 20 at the highest resolvable zonal scales ($k = 30$, $\lambda = 12°$).

TABLE 1 Comparison, Rotational, and Divergent Velocity Fields (200 mb)

SOP1 (20 Jan, 00Z; 5 Feb, 00Z; 17 Feb, 12Z)

		ROT EKE (m^2/s^2)	$\bar{u}$ (m/s)	DIV EKE (m^2/s^2)	$\bar{v}$ (m/s)
ECMWF IIIb	20-25N	216	35	8	1.2
	20N-5S	82	8	5	1.4
	5S-25S	75	8	6	-0.6
GFDL IIIb	20-25N	171	35	22	2.6
	20N-5S	77	8	19	2.3
	5S-25S	62	8	11	-0.5

SOP2 (10 May, 00Z; 2 Jun, 00Z; 11 Jun, 12Z)

		ROT EKE (m_2/s^2)	$\bar{u}$ (m/s)	DIV EKE (m^2/s^2)	$\bar{v}$ (m/s)
ECMWF IIIb	20-25N	115	16	5	0.5
	20N-5S	62	4	4	-0.6
	5S-25S	111	25	6	-1.0
GFDL IIIb	20-25N	110	15	14	0.4
	20N-5S	56	3	16	-0.9
	5S-25S	97	20	16	-1.8

A similar analysis has been carried out by Paegle and Paegle (1984) with a much larger sample at 200 mb level IIIb data from SOP-1. They also included analyses produced at the Goddard Laboratory of Atmospheric Sciences (GLAS) of NASA. The main differences between ECMWF and GFDL IIIb described above were found by the Paegles' study. However, they compared the rotational and divergent components over the entire globe. The author states that the largest differences in the analyses are in the tropical regions. The GLAS analyses are comparable to GFDL in the magnitude of the divergent component and to ECMWF in the rotational component. The agreements in the phase of the components were not given however.

The question raised by this analysis is: Which is closer to the actual divergent flow in the tropics? Table 3 shows the root-mean-square vector differences of the main IIb data to the respective IIIb analyses. The IIb data have been stratified into conventional rawin and aircraft flight level data, and all other data types have been ignored. This was done because the Level II data sets used by the two centers were not identical. The rawin and aircraft

TABLE 2 Correlation of V_{rot} and V_{div}, ECMWF IIIb and GFDL IIIb (200 mb, all cases)

	Zonal wave number range			
Component	k = 1,4	k = 5,8	k = 9,16	k = 17,30
u(rot)	.93	.92	.56	.25
v(rot)	.80	.83	.63	.10
u(div)	.77	.34	.28	-.20
v(div)	.63	.44	.06	-.04

TABLE 3 Root-Mean-Square Vector Differences, Analysis minus Observations (200 mb)

SOP1	Rawin (m/s)	Aircraft (m/s)
ECMWF IIIb	6.9	7.9
GFDL IIIb	7.9	11.2
SOP2		
ECMWF IIIb	6.0	6.9
GFDL IIIb	7.0	9.7

TABLE 4 Comparison, Rotational, and Divergent Velocity Fields (850 mb)

SOP1 (20 Jan, 00Z; 5 Feb, 00Z; 17 Feb, 12Z)

	Rot EKE	Div EKE
ECMWF IIIb 25N-25S	15	2
GFDL IIIb 25N-25S	17	6

SOP2 (10 May, 00Z; 2 June, 00Z; 11 Jun, 12Z)

ECMWF IIIb 25N-25S	11	1
GFDL IIIb 25N-25S	13	4

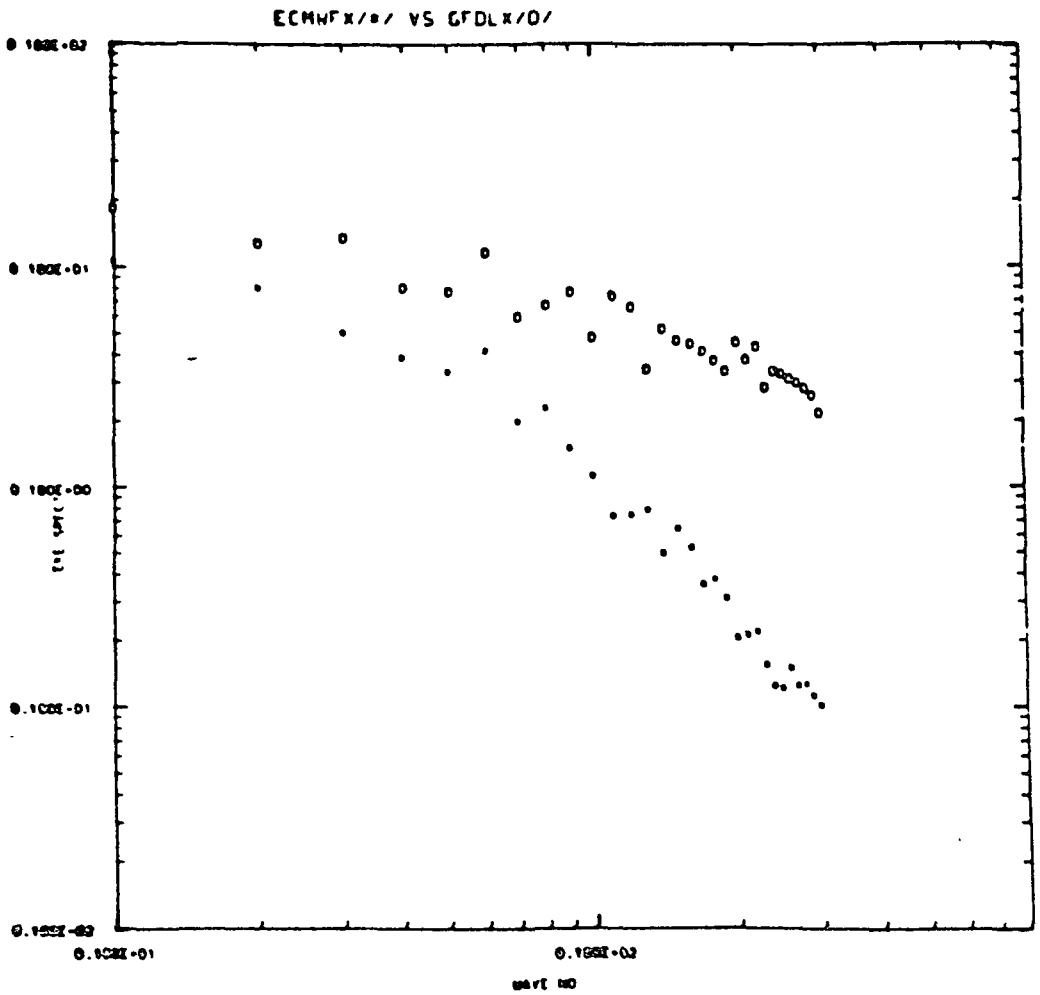

FIGURE 1 Zonal wavenumber eddy kinetic energy spectrum, divergent flow, 200 mb tropics.

data in main IIb were available to both. It is clear that the GFDL IIIb has not accommodated the data to the same degree as ECMWF. Subjective evaluation of the analyses has led to the conclusion that while the ECMWF IIIb underanalyzes the tropical flow field, particularly in strongly divergent situations, the GFDL analyses on scales less than the planetary scales are much too creative and often ignore the observed data. The consequences of these differences are serious for any analysis of the characteristics of the tropical circulation, and more comparisons are clearly needed.

At 850 mb (Tables 4 and 5), the GFDL IIIb analyses have somewhat greater rotational kinetic energy than ECMWF and a distinctly greater

TABLE 5 Correlation of V_{rot} and V_{div}, ECMWF IIIb and GFDL IIIb (850 mb, all cases)

	Zonal wave number range			
Component	k = 1,4	k = 5,8	k = 9,16	k = 17,30
u(rot)	.88	.72	.48	.24
v(rot)	.91	.84	.60	.36
u(div)	.82	.48	.23	.10
v(div)	.58	.29	.17	.06

divergent kinetic energy; the latter is consistent with the result in the upper troposphere. The correlation structure is approximately the same as in the upper troposphere, as is to be expected. The principal difference would seem to be a slightly better agreement in the meridional divergent component rather than in the zonal component. With so few cases, it does not seem reasonable to attempt any statements as to statistical significance, although the main features described above hold in each of the six cases.

Table 6 lists rms vector statistics regarding the observing and assimilating processes. The measurement error quantities (first column, top) represent the basic observing system errors, which are not appropriate for objective analysis or quality control purposes. The appropriate quantities should contain subgrid-scale variability as well. The second column (top) sets out the quantities that were obtained by colocation techniques. The final column (top) gives for a small sample the fit of the ECMWF IIIb to the observations, but not necessarily those particular observations used by the assimilation scheme. Further, the optimum interpolation scheme should reduce the actual observation-analysis differences below the specified observation uncertainty. That fact that at 850 mb the former is greater than the latter suggests some level of uncertainty in the quantities shown.

The bottom portion of Table 6 gives some indication of the reduction in variance from climatology or a forecast achieved by an assimilation scheme (EC IIIb) and an indication of the variance of the difference between two such schemes (EC IIIb versus NMC IIIb). These quantities have been taken from a report by Hollingsworth et al. (1984). For example, the portion of variance indeterminate between analyses to the climatological variance ranges from about 40 percent at 850 mb to 25 percent at 250 mb.

TABLE 6 RMS Vector Uncertainties, Tropics (20°N to 20°S) (meters per second)

	Measurement	Colocation	EC IIIB fit
RAWIN			
300-150 mb	2.6-3.1	8.3	6.1
1000-850 mb	2.3	2.5	2.8
AIDS-ASDAR			
300-150 mb	2.0	8.3	5.6
TCLBS			
150-130 mb	1.2	-	3.6

	Climatology	Analysis-Analysis	Forecast-Analysis
200 mb	13.5	6.2	5.1
300 mb	10.7		
850 mb	5.6	3.6	2.4
1000 mb	3.7		

REFERENCES

Hollingsworth, A., A. Lorenc, S. Tracton, K. Arpe, G. Cats, S. Uppala, and P. Kallberg (1984). The response of numerical weather prediction system to FGGE IIb data, Part I: Analyses. Submitted to Quart. J. Roy. Meteorol. Soc.

Paegle, J. N., and J. Paegle (1984). Selected comparisons of FGGE Level IIIb 200 mb winds. Global Weather Experiment Newsletter 3, 6-14.

D12

THE RESPONSE OF NUMERICAL WEATHER PREDICTION ANALYSIS SYSTEMS TO FGGE IIb DATA

A. Hollingsworth,[1] A.C. Lorenc,[2] M.S. Tracton,[3] K. Arpe,[1] G. Cats,[4] S. Uppala,[1] and P. Kallberg[5]

ABSTRACT

An intercomparison of analyses of the main FGGE Level IIb data set is presented with three advanced analysis systems. The aims of the work are to estimate the extent and magnitude of the differences between the analyses, to identify the reasons for the differences, and finally to estimate the significance of the differences. This paper is restricted primarily to a consideration of the extratropical analyses. The subject of the tropical analyses merits separate treatment.

Objective evaluations of analysis quality, such as fit to observations, statistics of analysis differences, and mean fields are discussed. In addition, substantial emphasis is placed on subjective evaluation of a series of case studies that were selected to illustrate the importance of different aspects of the analysis procedures, such as quality control, data selection, resolution, dynamical balance, and the role of the assimilating forecast model. In some cases, the forecast models are used as selective amplifiers of analysis differences to assist in deciding which analysis was more nearly correct in the treatment of particular data.

In general, the analysis systems draw reasonably well to the data, although each system has its own characteristics in this regard. The root-mean-square differences between the analyses are of the expected order of magnitude, although there are clear differences in the closeness of agreement between different pairs of analyses. Systematic differences arising from particular components of the assimilation suites can be identified.

The discussion of the case studies highlights those areas where differences of approach to the analysis problem have led to significant

(1) European Centre for Medium Range Weather Forecasts, Reading, U.K.; (2) United Kingdom Meteorological Office, Bracknell, U.K.; (3) National Meteorological Center, National Oceanic and Atmospheric Administration, Washington, D.C., U.S.A.; (4) Koninklijk Nederlands Meteorologisch Instituut, De Bilt, Netherlands; (5) Swedish Meteorological and Hydrological Institut, Norrkoeping, Sweden.

differences in the analyses. Some of the case studies suggest strongly that analysis differences in the vicinity of active baroclinic zones are of particular importance. In order to validate these suggestions in one case, an experiment is presented where one analysis is transplanted locally into another and shows that large differences in the medium-range forecasts are attributable to localized differences in the analyses.

INTRODUCTION

This paper is concerned with the results of an intercomparison of analyses of five days of data from February 1979 performed with numerical weather prediction systems at the European Centre for Medium Range Weather Forecasts (ECMWF), at the National Meteorological Center (US), and at the United Kingdom Meteorological Office (UK). All three systems were presented with the same observational data from the main FGGE Level IIb data set (Bengtsson et al., 1982).

The objectives of the study are (1) to quantify, as far as possible, the extent and magnitude of the differences between the analyses; (2) to relate these differences to the analysis procedures, such as quality control, data selection, resolution, dynamical balance, and the role of the assimilating model; and (3) to estimate the significance of the analysis differences.

Several different techniques were used to compare the analysis systems. These included (1) fit of the analyses to the data, (2) statistical measures of analysis differences, (3) mean features and energetics, and (4) subjective evaluation of case studies. Because of space limitations, the detailed results of these studies are not given here; they are published in Hollingsworth et al. (1985). This report presents only the discussion and summary.

There is no single overall criterion that summarizes the various requirements of balance, internal consistency, and so on that three-dimensional analyses should satisfy. One thinks of conceptual models of atmospheric behavior, such as geostrophic or gradient balance, the structure of baroclinic waves, or the vertical circulation of fronts. An analysis that differed radically from the expectations in these aspects would be regarded with skepticism.

Subject judgment is more difficult when the analysis differences lie within the bounds of reasonable expectation. In such cases, guidance on the merits of the treatment of particular features can be provided by an amplification of the analysis differences during the subsequent forecast; the assumption being that better forecasts reflect more accurate initial conditions. In this paper, only the quality of the forecasts within the context of the case studies is discussed. The overall impact of analysis differences on forecast quality is discussed extensively in Arpe et al. (1985).

The work presented here has concentrated mainly on the analysis of the mass and wind fields of the extratropics. Hardly any space has been devoted to consideration of the humidity analyses and rainfall forecasts nor to the tropical analyses and forecasts, because of

pressure of space and time and because known biases and lower levels of skill make intercomparison less fruitful. It is clear from a preliminary survey that there is much to discuss in both these important areas.

NUMERICAL WEATHER PREDICTION SYSTEMS AND DATA USED

Details of the systems used, with references where further details can be found, are given in Tables 1 through 4.

All the systems were designed using the concept of four-dimensional data assimilation; data are used to correct a forecast first guess provided by a sophisticated numerical forecast model. This first guess is usually rather accurate, and all the analysis systems take account of this by giving it substantial weight in the optimum interpolation (OI) technique. Thus the properties of the forecast models used will affect the analyses. The systems differed in many ways. In the rest of this section we discuss those differences that had a major impact on the analysis differences.

Approach to the Slow Manifold

A useful concept when discussing the principles of objective analysis is that of the slow manifold (e.g., Leith, 1980; Daley and Puri, 1980). It is assumed that out of all possible states, the atmosphere is always in or near a small subset called the slow manifold, which is characterized by slow variations with time. Linear theory distinguishes between Rossby waves and inertia-gravity waves. States of the atmosphere consisting of Rossby waves only lie on the Rossby manifold, which is near the slow manifold. The task of an objective analysis procedure is to choose a state that fits the current observations to within the likely observational error, which is close to a forecast based on earlier observations and which is on or near the slow manifold. All three conditions are necessary because of the incompleteness of data coverage at any one analysis time. The ECMWF and US systems differ from the UK system in the approach used to achieve this third condition. Through the use of the initialization procedure, the ECMWF and US forecast first guesses are usually near the slow manifold. Since the analysis increments (analysis minus first-guess fields) are approximately nondivergent and close to geostrophic balance in these systems, the analysis increments are close to the Rossby manifold. The analysis, which is the sum of these two fields, is therefore close to the slow manifold. Near-geostrophy and approximate nondivergence are imposed in the ECMWF and US multivariate OI systems by using geostrophically consistent structure functions and by using the same data for analysis of mass and wind fields for as large a volume as possible (Lorenc, 1981; Phillips, 1982). The UK system approaches the slow manifold by repeatedly inserting the observational information into the numerical model during a six-hour assimilation period. Modes of the model with periods less than or about six hours are thus less excited

TABLE 1 Summary of Numerical Weather Prediction Systems Used

	EC		US		UK
	Analysis	Forecast	Analysis	Forecast	Analysis and Forecast
Levels:	p (mb)	σ	p (mb)	σ	σ
	10	.025		.025	.022
	20	.077			
	30	.132			
	50	.193	50		
	70	.260	70	.075	
	100	.334	100	.125	.089
	150	.415	150	.175	.157
	200	.500	200	.225	.230
	250	.589	250	.275	.317
	300	.678	300	.338	.436
	400	.765	400	.438	.577
	500	.845	500	.575	.718
	700	.914	700	.725	.843
	850	.967	850	.862	.937
	1000	.996	1000	.963	.987
Resolution :	1.875°	1.875°	3.5°	Rhomboidal 30	2°
Grid :	Lat. Long.	Lat. Long.	Quasi-homogeneous	Spectral	Quasi-homogeneous
Variables :	ζ,u,v,q	T,u,v,p_s,q	ζ,u,v,Rd	T,u,v,p_s,q	T,u,v,p_s,q

by the data than are the slowly varying modes. Moreover the numerical model is modified to damp high frequency modes.

Both approaches only approximate the idealized slow manifold, which itself is only an approximate description of real atmospheric behavior. The UK system discriminates solely on the basis of frequency; internal inertia-gravity wave modes with complex vertical structures have periods much longer than six hours, as have horizontal two grid length waves in the model, so the UK system can generate such

TABLE 2 Principal Features of the Analysis System

	EC	US	UK
Analysis method	3-dimensional multivariate OI	3-dimensional multivariate OI	2-dimensional univariate OI
Data used for each point	$\leq$ 191	$\leq$ 20	$\leq$ 8
Update interval	6 hours	6 hours	6 hours
References	Lorenc (1981)	Bergman (1979) MacPherson et al. (1979) Kistler and Parrish (1982)	Lyne et al. (1982)
Initialisation method			
	Non-linear normal mode. 5 vertical modes. Adiabatic.	Non-linear normal mode. 4 vertical modes. Adiabatic.	Repeated insertion during 6-hour forecast with increased diffusion and time-filtering
References	Machenhauer (1977) Temperton and Williamson (1982) Williamson and Temperton (1982)	Machenhauer (1977)	

modes to fit isolated or inconsistent data. In many such cases, the analyses achieved are further from balance than the atmosphere is believed to be. The UK approach may represent features that are not geostrophic, such as flow around mountains or fronts; whether such motions remain on the slow manifold may still be an open question.

The ECMWF and US systems are designed mainly for longer period numerical weather prediction. Thus observations of real atmospheric systems that are below the resolution of their numerical weather prediction models are regarded as observational errors, and a smooth

TABLE 3 Principal Features of the Forecast Models

FORECAST	EC	US	UK
Horizontal scheme	2nd order staggered	Spectral	2nd order flux form
Time scheme	Semi-implicit	Semi-implicit	Leapfrog
Diffusion	Linear 4th order	Linear 4th order	Non-linear
Orography	Medium smooth	Smoothed 30 wave	Almost full resolution
Diurnal cycle	None	None	Included
Surface exchanges	Included	Included over sea. Only drag over land.	Included
Radiation	Interactive clouds	None	Climatological clouds
Latent heating	Included	Included	Included
Convection	Included (Kuo)	Included(Kuo)	Included
References	Hollingsworth et al. (1980)	Sela (1980)	Saker (1980)

balanced analysis is attempted. The analyses achieved will tend to be smoother and more balanced than the real atmosphere. The case studies presented below permit some estimates of the significance of these differences.

Quality Control, Selection, and Weighting of Data

A major part of the effort of building an analysis system for operational use is expended on the design of methods for choosing which data to leave out. Two types of data need to be identified: those that are grossly incorrect or misleading (quality control), and those that carry little extra information over other data that are being used and that can therefore be disregarded to save time (data selection). Because all data have errors of observation or representativeness and because of intrinsic or explicit assumptions about the smoothness of fields, the analysis has to be a compromise between the various

TABLE 4 Principal Features of the Interpolation Schemes

INTERPOLATION	EC	US	UK
Forecast–first guess	Cubic spline in log p	linear in log p; spectral	None
Analysis–forecast	Cubic spline in log p	Linear in log p for analysis increments; spectral	None
Analysis–output	None	increments, p→σ spectral representation updated fields σ→p	Cubic spline in log p

selected observed values and the first guess; the compromise is specified by the data weights.

All the schemes had a number of externally imposed quality control decisions. For instance, the UK and US systems did not use land surface wind data, the US system did not use satellite temperature soundings over land, and the ECMWF system did not always use the reported cloud wind levels, recalculating them where possible in the upper troposphere from reported temperatures. These all caused occasional analysis differences.

Quality control of individual observations on a case-by-case basis is also essential, and all the systems had automatic methods for doing this; no human intervention was allowed for this study. Such a quality control is only possible if there is information redundancy. Since observed data are in many cases too sparse for this, it is necessary also to use information from a forecast together with knowledge of the likely structure of atmospheric motions. The ECMWF system should be best at this since it uses its full analysis method to check each datum against an analysis made not using it.

The US scheme has an initial comparison with the forecast with relatively strict limits that rejects, in some cases studied, certain data that the others accept. Wrong decisions in such cases can be crucial since it is the data which disagree with the forecast and are correct which carry most new information. This check is followed by comparisons between close observations designed to identify and reject those that disagree with several neighbors. These comparisons are univariate and two-dimensional, so little knowledge of atmospheric structures is used, other than that they are smooth and continuous.

The UK scheme also has a comparison with a forecast field (for these studies a six-hour persistence forecast) followed by a univariate two-dimensional comparison with neighbors, in this case using OI, with the forecast as first guess. The rejection limits used are rather lax in order that noise in the unbalanced forecast should not cause rejection of good data. The UK system occasionally accepts and draws

to data rejected by the others. This is exacerbated by the relative lack of checks in the UK system on things like message formats and observation positions, compared with the other systems, which were developed for operational use.

The quality control procedures in the ECMWF and US assimilation systems are quite sensitive to the use of initialization. The acceptance tolerances for discriminating between good and bad data are tight. If the assimilation is run without initialization, then the first guesses become so noisy after a few days that good data as well as bad are rejected. The main value of the initialization lies therefore in providing the noise-free first guess that is necessary in the quality control procedures (van Maanen, personal communication, 1980).

The data selection methods also had a number of externally imposed decisions that differed among the systems. For instance, within one radiosonde report the height and temperature data convey largely redundant information. After using this redundancy for quality control, it is unnecessary to select both. The UK system uses temperatures; the ECMWF and US, heights. From satellite temperature soundings, the UK system uses temperatures; the ECMWF system, interlevel thicknesses; and the US system, heights calculated using a preliminary surface analysis as reference level. These differences affect the effective weights given to the data and the fit of the analyses to the observations.

Quality control and data selection procedures that effectively give certain data zero weight are of greater practical importance than the differences between weights assigned to observations by the systems' respective OI schemes. The estimated observational error variances that are used in the OI method to determine the relative weights of observations were similar in the three systems (Julian, 1983).

Resolution

The effective resolution can be limited in two ways: by the grid used to represent the fields, and by constraints on the smoothness of the fields. The UK system is limited solely by the former; the analysis is performed directly on the model's grid, and there are few constraints on smoothness. Thus all features that can be represented by the model can be analyzed. The ECMWF system has a slightly higher grid resolution than the UK system, however it selects and uses many more data for the analysis of each grid point value than the others. Thus the resolution of features changed during the analysis is limited by the scale of the prediction error correlation structure functions used (Lorenc, 1981). Moreover, the interpolations between sigma and pressure coordinates have a smoothing effect. The US system has a coarser horizontal grid than the others, and its resolution is further limited by spectral smooting of analysis increments and fields. Several cases have been observed where the resolution of the assimilating model made an important difference in the resulting analysis.

The Assimilating Model

A study by Leith (1981) indicates that there is a synergy between the accuracy of the analysis and the accuracy of the assimilating model. Using energy budget arguments, he demonstrates that a model that gives a more accurate first guess leads to a more accurate analysis. There are practical as well as theoretical reasons why this should be the case. With a more accurate first guess, quality control can be made more stringent and thus more effective. The linear constraints used by most analysis systems will also be more accurate when applied to smaller amplitude differences between observational data and the first guess. If the first guess is inaccurate, then the analysis should consider nonlinear wind laws such as the gradient wind relation in areas where it has to make large increments. No satisfactory procedure for doing this has been worked out. Examples of both these practical considerations will be seen in the case studies.

SUMMARY OF RESULTS

The main purposes of this study were to assess the nature, cause, and significance of the differences between the output of three different advanced analysis systems when they had all been presented with the same FGGE Level IIb data. The overall impact of analysis differences on forecast skill and the implications for predictability are discussed by Arpe et al. (1984). The main conclusions to be drawn from this paper are:

1. In general, all the analyses fit the data acceptably closely. However large local differences do occur between the analyses.
2. Some analysis differences that a priori appeared significant had little effect on the medium-range forecasts, because the systems in which they occurred were decaying or were isolated from the main baroclinic zones. Other analysis differences crucially affected the subsequent forecast quality, particularly when they occurred in regions of baroclinic development. The downstream development theory of Simmons and Hoskins (1979) proved very useful in documenting these effects. The results suggest that this theory describes one of the essential mechanisms for the loss of forecast skill through the unstable amplification of analysis errors. The results also suggest that developments of new observational systems should give priority to improvements in data quality along the main jets.
3. In the series of case studies where forecasts made with all three models from all three analyses were examined, all the models responded clearly and consistently to differences among the analyses. The consistency of the response was evident out to three days and beyond. In all cases, the largest differences in the forecasts at day 2 or 3 could be traced back to differences in the analyses. The question of the relative importance of analysis error and model error in the growth of forecast error is discussed by Arpe et al. (1984).

4. The accuracy of the forecast first guess, the algorithms for quality control and selection of observations, the resolution of the analysis system, and the techniques for imposing balance interact in a complex way, so that it is not always possible to assign with certainty a single simple cause to any given analysis difference.

5. Many analysis differences were associated with differences in quality control and data selection. In some case studies it appeared that the ECMWF system tended to average inconsistent data, the US system to reject some, and the UK system attempted to fit most data, sometimes in an unbalanced fashion.

6. Differences in the approach to the concept of balance between the UK system and the others caused large differences in the analyses that seemed of little significance to forecasts where both mass and wind field data were available, but that probably contributed to poor forecasts from the UK analysis on a southern hemisphere case where mass data predominated.

7. Biases between the analyses could be identified and were shown to arise from several parts of the assimilating systems.

The analysis differences presented here from analysis systems that were presented with identical data show that with current analysis algorithms the FGGE Level IIb data did not always define the atmospheric state uniquely. The size of the differences is a useful measure of the adequacy of the composite FGGE observing system (JOC, 1973).

The cases presented here show that poor data coverage and inaccurate data can significantly reduce current forecasting skill. It is also clear that there is room for improvement in the current analysis algorithms to exploit the available data more fully. Many improvements have already been made to all three systems, some of which are attributable to the present study.

ACKNOWLEDGEMENTS

The authors are grateful to the Directors of our respective institutions, Dr. Bengtsson, Dr. Bonner, and Sir John Mason, for their support and encouragement in the course of the work. Discussions with A. Gilchirst were very helpful. The assistance of Drs. C. Dey and G. DeMego is gratefully acknowledged. M. Tracton acknowledges support from the U.S. FGGE Office.

REFERENCES

Arpe, K., A. Hollingsworth, A. C. Lorenc, M. S. Tracton, G. Cats, and P. Kallberg (1985). The response of numerical weather prediction systems to FGGE IIb data. Part II. Forecasts verifications and implications for predictability. Submitted to Quart. J. Roy. Meteorol. Soc.

Bengtsson, L., M. Kanamitsu, P. Kallberg, and S. Uppala (1982). FGGE 4-dimensional data assimilation at ECMWF. Bull. Amer. Meteorol. Soc 63, 29-43.

Bergman, K. H. (1979). A multivariate interpolation analysis system for temperature and wind fields. Mon. Wea. Rev. 107, 1423-1444.

Daley, R., and K. Puri (1980). Four-dimensional data assimilation and the slow manifold. Mon. Wea. Rev. 108,

Hollingsworth, A., K. Arpe, M. Tiedke, M. Capaldo, and H. Savijarvi (1980). the performance of a medium-range forecast model in winter--impact of physical parameterizations. Mon. Wea. Rev. 108, 1736-1773.

Hollingsworth, A., A. C. Lorenc, M. S. Tracton, K. Arpe, G. Cats, S. Uppala, and P. Kallberg (1985). The response of numerical weather prediction systems to FGGE IIb data. Part I. Analyses. (to appear in Quart. J. Roy. Meteorol. Soc.)

JOC (1973). The First GARP Global Experiment--Objectives and Plans. GARP Publications Series 11, WMO-ICSU Joint Organizing Committee, Geneva, 107 pp.

Julian, P. R. (1983). On the use of observation error data in FGGE main level IIIb analysis. ECMWF Tech. Memo 76; available from ECMWF.

Kistler, R. E., and D. F. Parrish 1982. Evolution of the NMC data assimilation system: September 1978-January 1982. Mon. Wea. Rev. 110, 1335-1346.

Leith, C. E. (1980). Nonlinear normal mode initialization and quasi-geostrophic theory. J. Atmos. Sci. 37, 958-968.

Leith, C. E. (1981). Statistical methods for the verification of long- and short-range forecasts. In Proceedings of ECMWF 1981 Seminar on Problems and Prospects in Long- and Medium-Range Weather Forecasting; available from ECMWF.

Lorenc, A. C. (1981). A global three-dimensional multivariate statistical interpolation scheme. Mon. Wea. Rev. 109, 701-721.

Lyne, W. H., R. Swinbank, and N. T. Birch (1982). A data assimilation experiment and the global circulation during the FGGE Special Observing Periods. Quart. J. Roy. Meteorol. Soc. 108, 575-594.

Machenhauer, B. (1977). On the dynamics of gravity oscillations in a shallow water model, with application to normal mode initialization. Contrib. Atmos. Phys. 50, 253-271.

McPherson, R. D., K. H. Bergman, R. E. Kistler, G. E. Rasch, and D. S. Gordon (1979). The NMC operational global data assimilation system. Mon. Wea. Rev. 107, 1445-1461.

Phillips, N. A. (1982). On the completeness ofmultivariate optimum interpolation for large-scale meteorological analysis. Mon. Wea. Rev. 110, 1324-1334.

Saker, N. J. (1980). UK Meteorological Office Model in Catalogue of Numerical Atmospheric Models for the FGGE, J. Smagorinsky, ed., Joint Scientific Committee, WMO-ICSU, Geneva.

Sela, J. G. (1980. Spectral modeling at the National Meteorological Center. Mon. Wea. Rev. 108, 1279-1292.

Temperton, C., and D. L. Williamson (1981). Normal mode initialization for a multilevel grid point model. Part I. Linear aspects. Mon. Wea. Rev. 109, 722-743.

Williamson, D. L., and C. Temperton (1981). Normal mode initialization for a multilevel grid point model. Part II. Nonlinear aspects. Mon. Wea. Rev. 109, 744-757.

D13

ANALYSIS AND FORECAST INTERCOMPARISONS USING THE FGGE SOP-1 DATA BASE

David P. Baumhefner
National Center for Atmospheric Research

INTRODUCTION

The First GARP Global Experiment (FGGE) data base has provided the research community with the most complete global coverage of meteorological information since measurements were first taken. It is important to understand the characteristics of the FGGE data base in terms of its accuracy and representativeness compared to the "true" state of the atmosphere. The uncertainty associated with the initial conditions used in a numerical model plays a significant role in subsequent error growth as shown by predictability theory (Baumhefner, 1984). In fact, the ultimate limit of forecast skill is directly related to the initial uncertainty. The accuracy of the analyses using the FGGE data base coupled with the errors due to modeling imperfections determines the present skill of numerical models.

This paper attempts to establish an estimate of initial uncertainty by examining the differences in several FGGE analyses. The estimate is then used to determine an ultimate limit of forecast skill from derived predictability error growth rates. Several different calculations of predictability error growth are also compared. Finally, present-day forecast skill using FGGE analyses is contrasted to the estimates of ultimate skill, and the partition of model error versus initial uncertainty is discussed.

METHOD OF CALCULATON

A ten-case ensemble was selected from the winter of 1978 to 1979 for calculation (Figure 1). Eight of the ten dates were selected by the Working Group on Numerical Experimentation (WGNE) of the Joint Organizing Committee (JOC) as special cases for study (Rutherford, 1980). The other two were chosen because large differences in the tropical wind field were discovered between the Level IIIa and IIIb analyses. The ensemble includes a wide variety of synoptic situations and represents some difficult transition periods to forecast. Three primary analyses were available for comparison: (1) the National Meteorological Center (NMC) operational Level IIIa system, (2) the European Centre for Medium Range Weather Forecasts (ECMWF) IIIb

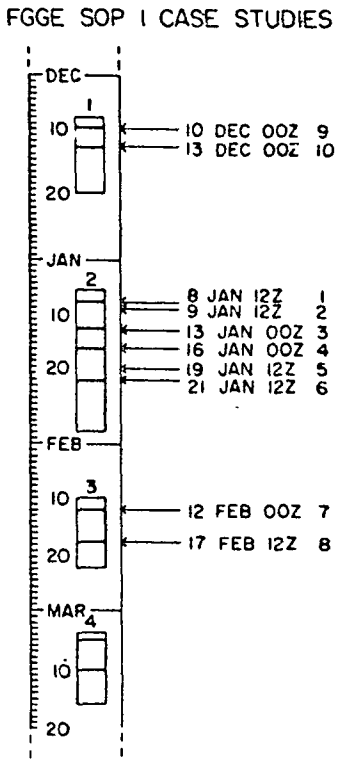

FIGURE 1 A schematic calendar of FGGE Special Observing Period I cases with special study periods shown as vertical columns. Dates indicate starting times for numerical forecasts. Right-hand number identifies case.

analyses, and (3) the Geophysical Fluid Dynamics Laboratory (GFDL) IIIb analyses. An experimental Goddard Laboratory for Atmospheric Science (GLAS) IIIb analysis was also compared for five cases. The differences between these analyses for the 500 mb height and streamfunction were calculated for both analyzed and initialized fields. The initialization was performed by an R15 version of the National Center for Atmospheric Research (NCAR) Community Forecast Model (CFM) using all nine vertical modes and a 24-hour frequency cutoff. The analysis differences were spectrally decomposed in two-dimensional wave space and the systematic components (10-case average errors) determined for each wave group.

Predictability estimates were derived by comparing forecasts made from each of the three analyses and analyzing the departure of each pair. The model used to produce the forecast is an R15 spectral version of the NCAR Community Climate Model (CCM) with its associated physics package (Williamson, 1983). The average evolution of the difference fields was compared to a six-case average classical predictability error growth calculation from the same model in which small random perturbations were added to a simulated control state

(Baumhefner, 1984). Further comparisons were made with recent experiments by Arpe (1984).

Forecasts from the different analyses were verified against both ECMWF and GFDL data sets to test forecast skill sensitivity to the verification data base. A characteristic state-of-the-art forecast skill was determined for the R15 model, and its spectral behavior was derived. The transient and systematic components of error from each analysis were analyzed for any significantly different characteristics and/or improvements in skill. Significance was measured by comparing the differences in forecast error growth to the appropriate predictability error growth values. The average skill was compared to present operational skill from NMC and ECMWF models. The difference between the forecast skill and predictability was examined as a measure of the model forecast error remaining in the system.

ANALYSIS COMPARISON

The average standard deviation (SD) of the difference among the uninitialized analyses for the northern hemisphere 500 mb height field (Figure 2) was 28 m. This is in close agreement with recent analysis comparisons performed by Hollingsworth et al. (1983). The SD was distributed somewhat uniformly in two-dimensional spectral space out to wave 18. In terms of variance normalized against its climatic value, the analysis differences average 8 percent for the total with a tendency for a difference minimum in waves 5 to 7. Beyond wave 10, the differences become appreciable with respect to the scales' variance and beyond wave 20 the differences are as large as the variance. The relatively large difference in the gravest modes is surprising considering the data density of this data base. The systematic differences were small, usually only 10 to 20 percent of the difference variance. The largest systematic errors were confined to the gravest scales.

The differences in the streamfunction at 500 mb were largest in the tropics and the southern hemisphere and were primarily in the planetary scales. Two examples of these differences are shown in Figure 3. The differences for January 9 in the tropical planetary waves were as large as the amplitude of the waves themselves. The differences have their roots in the tropics but spread well into the midlatitudes. These large differences confirm the results found in the planetary waves of the height field (Figure 2). A more typical streamfunction difference is shown for January 16, however even these differences reach the midlatitudes with some significance. As was the case for height, the average SD of differences in streamfunction was remarkably uniform in spectral space.

The previous differences contained both balanced and unbalanced parts. By initializing the respective analyses and then examining the differences, it is possible to analyze the partitioning between the slower, balanced flows of meteorological significance and the unbalanced gravitational modes. The differences due to the latter modes are essentially lost when the model forecasts are made. Figure 4 illustrates the changes initialization produces in both the ECMWF and

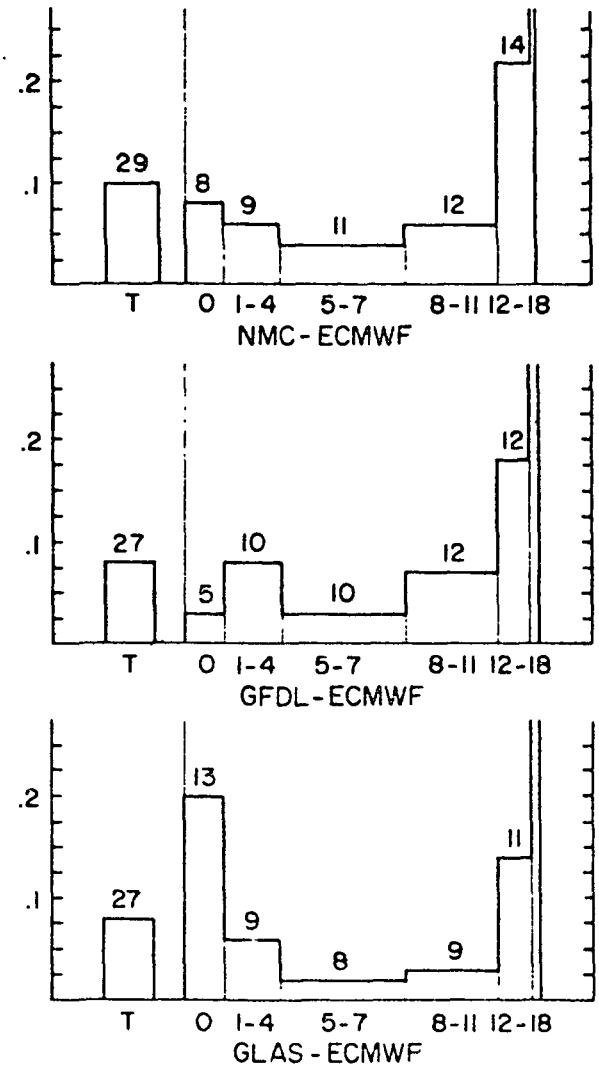

FIGURE 2 Histograms of normalized difference height variance over the northern hemisphere of three analysis comparisons at 500 mb for 10 cases. NMC-ECMWF at top, GFDL-ECMWF in middle, and GLAS-ECMWF at bottom. GLAS-ECMWF comparison for only cases 3, 4, 6, 7, and 8. Ordinate is normalized variance with unity equaling the long-term climatic variance for the total (T) and each wave group. Numbers on abscissa represent groups of two-dimensional wave decompositions. Zero equals all zonal modes (zonal vortesx) and others represent sum of the two-dimensional wave modes minus their zonal component. Width of histogram proportional to percent of variance in each grouping. Numbers at top of each histogram are standard deviation of difference in each group.

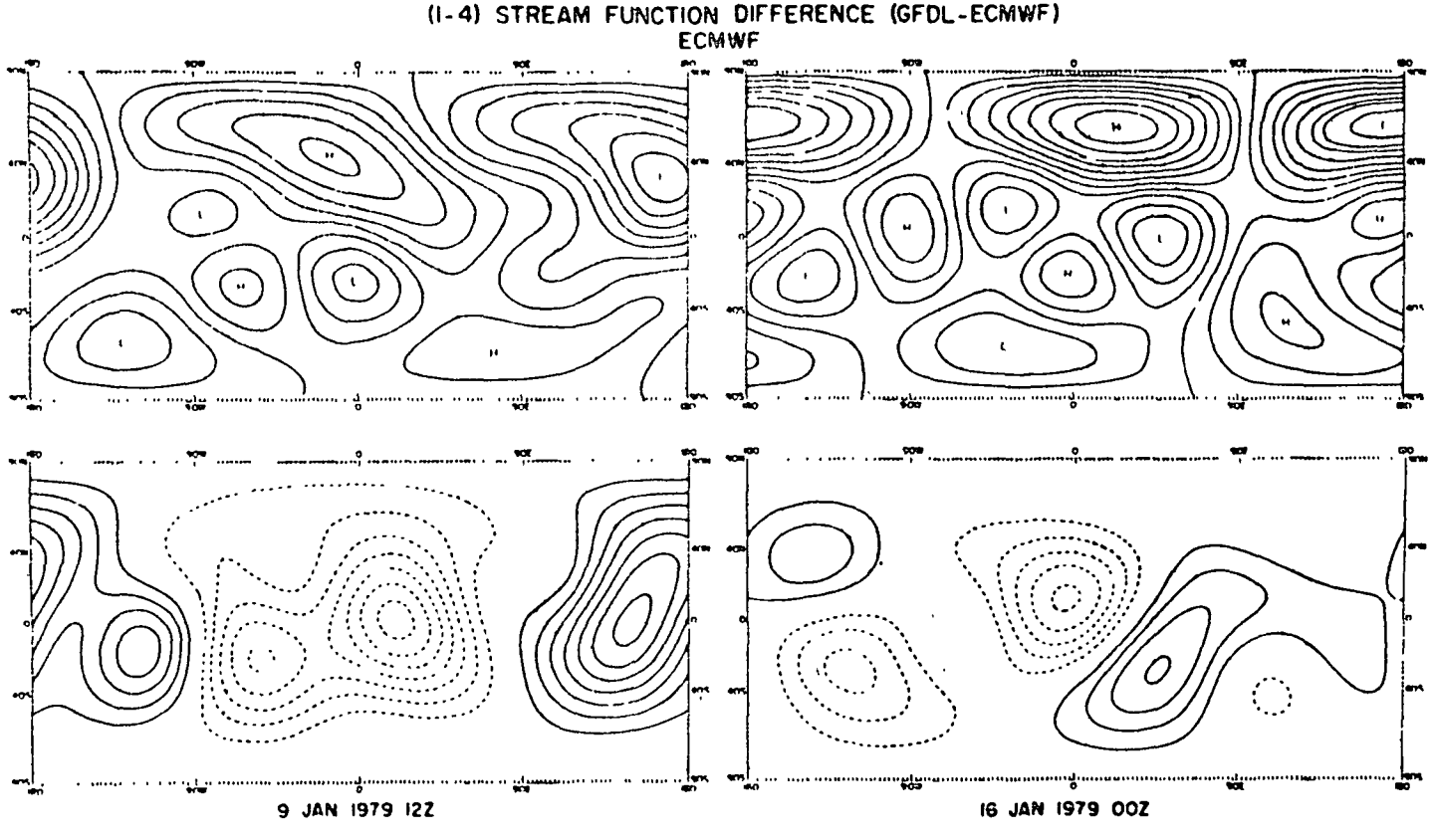

FIGURE 3 Streamfunction of global wavenumbers 1 to 4 at 500 mb for two cases from ECMWF analyses (January 9 12Z left, and January 16 00Z right) at top. Difference between GFDL and ECMWF streamfunctions at bottom. Difference contour interval (1×10^{10}) twice actual field values. Dashed values equal negative changes.

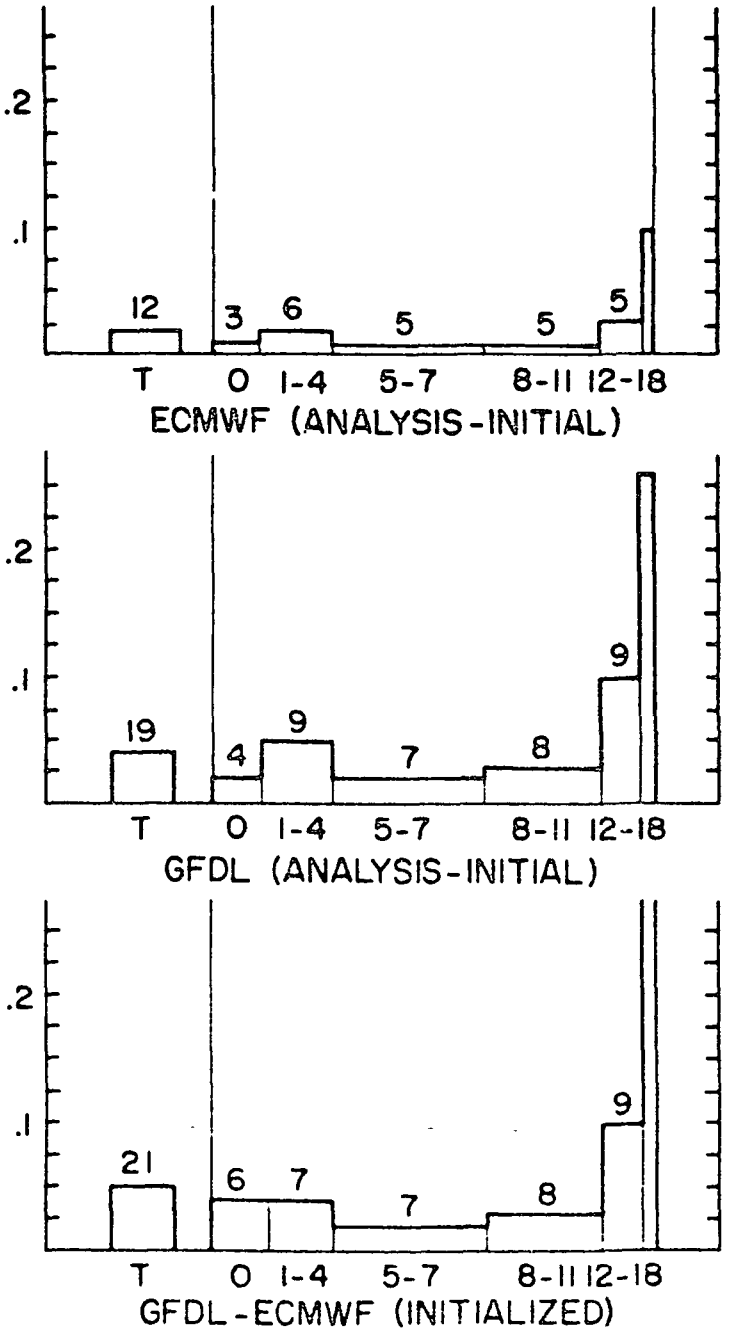

FIGURE 4 Same as Figure 2 except for ECMWF analyzed minus initialized (top), GFDL analyzed minus initialized (middle), and GFDL initialized minus ECMWF initialized (bottom).

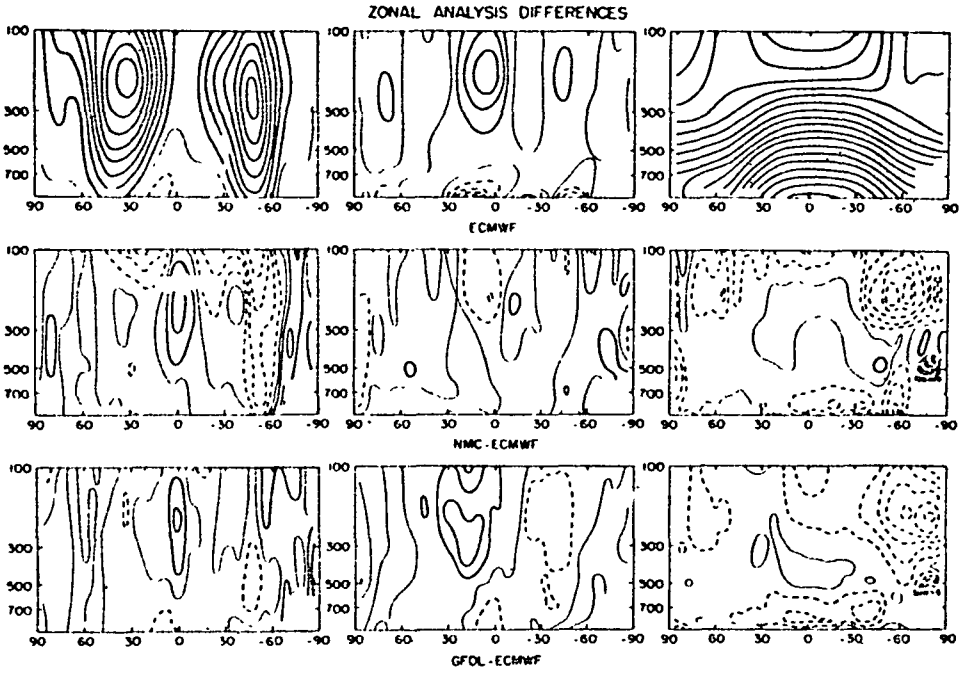

FIGURE 5 Zonally averaged cross-sections of the u- and v-components of the wind and temperature for 10 case average from ECMWF analysis (top). NMC-ECMWF analysis differences (middle) and GFDL-ECMWF differences (bottom). u-component (left) contour interval 4 m/s; difference interval 1 m/s. v-component (middle) contour interval 0.5 m/s; difference interval 0.5 m/s. Temperature (right) contour interval 5°K; difference interval 0.5°K.

GFDL analyses as well as the difference between two initialized analyses. It is clear that the ECMWF analysis is nearer a balanced state than the GFDL system, but even the largest changes are still only 5 percent of the variance. These changes are somewhat larger than found by Hollingsworth et al. (1983). Initialization reduced the overall analysis difference by 6 m SD (See Figure 2). The distribution by scale remained mostly unaltered and was reduced by similar amounts.

The zonal cross-sections of the averaged flow for each analysis confirmed previously documented characteristics of each system (Figure 5). The GFDL analyses contain the strongest zonal average Hadley circulation, and NMC's tropical overturning is the weakest with about 30 percent of GFDL's values. Both GFDL and NMC show a stronger sub-tropical jet on the equatorial side. The GFDL analysis also tends to be somewhat cooler than the other analyses, especially in the tropics. The initialized analyses exhibit almost the same structure as the original field including the divergent circulations (not shown). In this case, the initialization method used does not attempt to impose a balance on the modes responsible for the Hadley circulation.

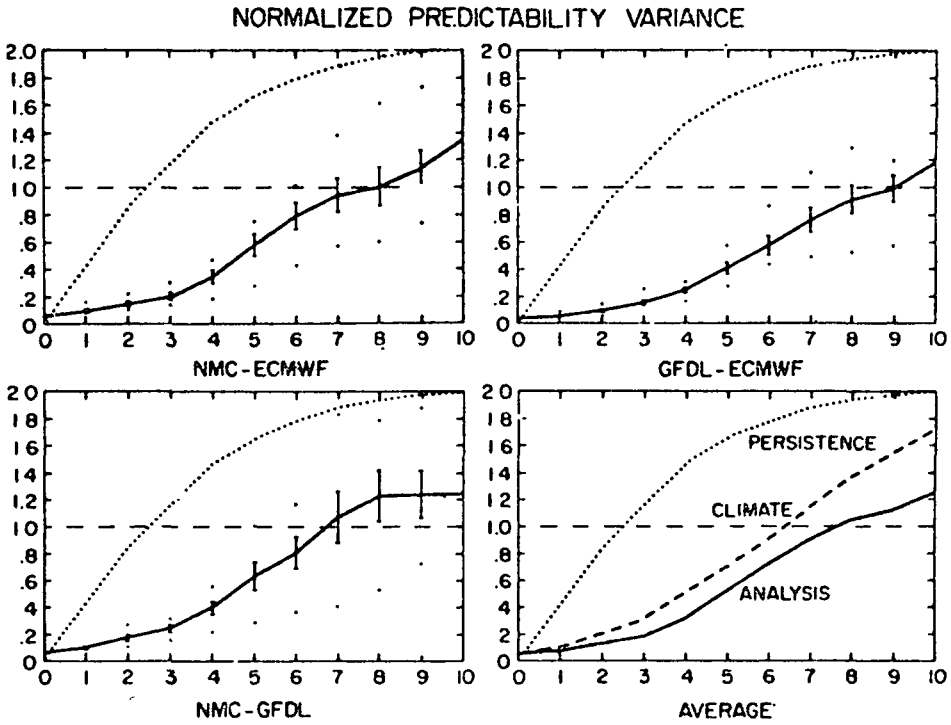

FIGURE 6 Variance normalized by climatology of 500 mb height forecast differences over the northern hemisphere for a 10-case ensemble average. NMC-ECMWF analysis difference (upper left); GFDL-ECMWF analysis difference (upper right); NMC-GFDL analysis difference (lower left). Average (solid line) of three forecast differences (lower right). Solid lines are mean values; vertical bars denote SD of ensemble; and small dots give range of ensemble. Dotted curve is persistence of ECMWF ensemble. Dashed curve (lower right) is predictability growth rate for 6-case ensemble from simulated data using initial errors comparable to analysis differences.

PREDICTABILITY ESTIMATES

The analysis differences in the previous section provide a convenient initial perturbation for forecast predictability experiments. Forecasts from each pair of analysis differences are examined for evidence of predictability error growth and an ensemble average is constructed. Figure 6.3.6 shows the average separation of forecasts starting from different analyses reached the climatological variance in 7 to 9 days. This implies that saturation of the two-dimensional wave spectrum would occur in 14 to 18 days. There was little variation of the average for the choices of analysis difference. Note that the SD gives a variability of about two days to the crossover point of climate variance, and the range (small dots) is nearly five days. The spectral

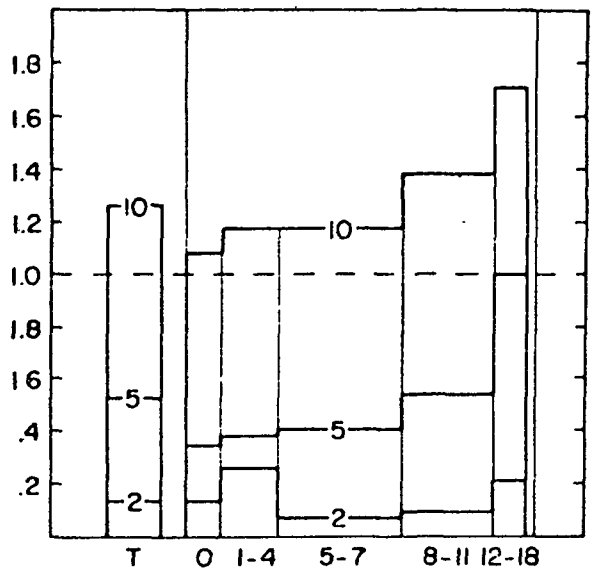

FIGURE 7 Averaged forecast differences of 500 mb height normalized variance. Same as Figure 6.3.2, but for 3 forecast times: day 2 (2), day 5 (5), and day 10 (10). Average of 10-case ensembles from NMC-ECMWF, GFDL-ECMWF, and NMC-GFDL pairs of analyses/forecasts.

decompositions for the average of all cases and analysis pairs show a quasi-uniform characteristic in the perturbation error growth for the first 10 wavenumbers (Figure 7). The scales smaller than this, however, still grow the most rapidly even in these cases. This is in disagreement with earlier studies of predictability error (Leith, 1971; Shukla, 1981), where the largest scales grew at a slower rate than the smaller scales.

A comparison between analysis difference growth rates and a six-case classical predictability experiment revealed very similar results, namely, the rate of growth and its spectral behavior. In the classical case, the initial errors were an order of magnitude smaller and randomly distributed, which is quite different from the characteristic analysis difference. If the classical error growth curves are matched with the typical analysis difference in an initial error sense (Figure 6), the classical case shows more rapid growth with a variance crossover point 1.5 days earlier. This can perhaps be explained by the fact that some additional adjustment might be occurring in the analysis difference case, whereas the classical perturbations are already in equilibrium with respect to the model.

When the spectral distributions of both predictability error growths are examined, further differences are noted (Figure 8). The initial analysis differences for the height have a much different spectral characteristic than the classical cases. The differences are largest in the gravest modes (a red spectrum) for the analyses, whereas the

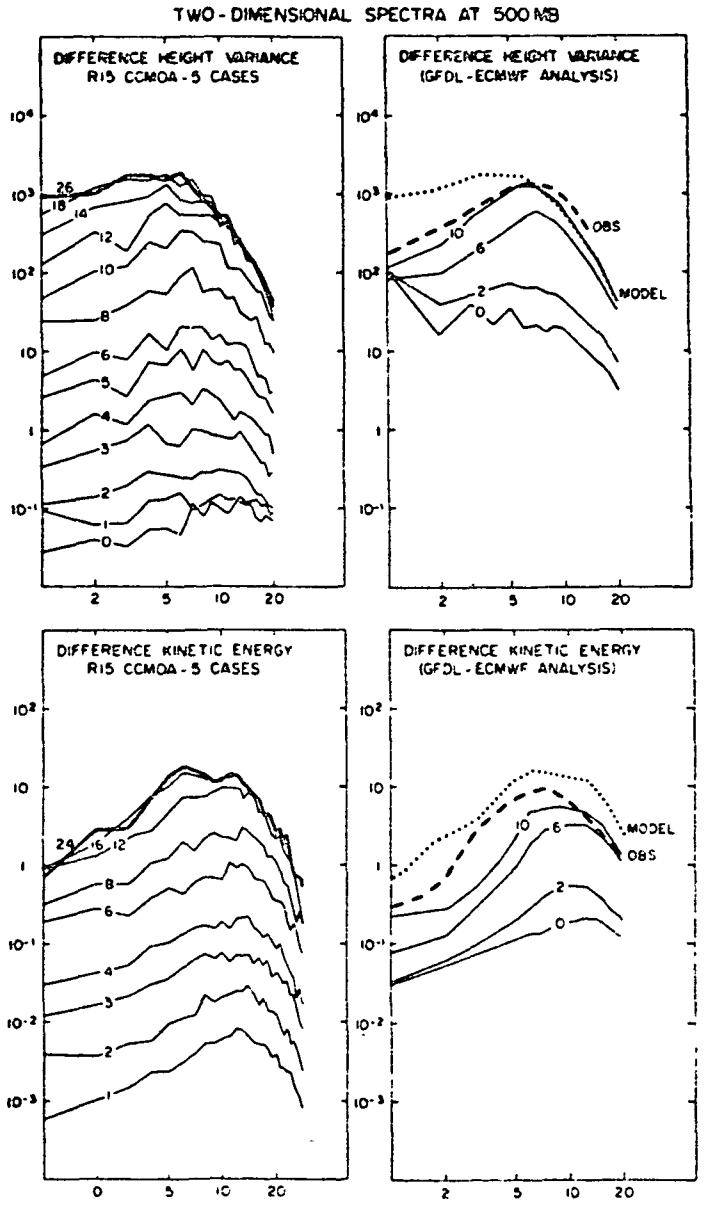

FIGURE 8 Spectral decomposition of forecast difference height variance (top) and forecast difference kinetic energy (bottom) for northern hemisphere only. Left column obtained from classical predictability perturbations; right column derived from GFDL-ECMWF analyses. Numbers on lines indicate forecast day. Units are m^2 for variance and m^2 sec^{-2} for kinetic energy. Dash and dot lines are estimates of spectrum from model and observations.

classical predictability assumes a form similar to the equilibrium spectrum for magnitudes of 10 to 100 m^2. Note that wave 1 in the analysis case is nearly its observed value in the initial state. The kinetic energy does not show this characteristic because of its stronger weighting to the smaller scales. As the forecasts progress in the analysis cases, the shape assumes a form more similar to the equilibrium spectra, and the rate of error growth becomes comparable except in the largest scales. The slower growth in the largest scales may be attributable to the clustering of cases in January 1979 (Figure 1) and therefore represent only one type of planetary structure. It is not clear what the equilibrium spectra will be and when it will be reached in the analysis case since the forecasts began with real atmospheric data and are only carried out to 10 days. The estimate of 14 to 18 days from Figure 6 appears to be reasonable for scales larger than wave 8.

A similar analysis and forecast intercomparison was recently conducted by Arpe et al. (1984) in which the predictability error growth was estimated from 9 forecasts and 3 analysis pairs. Their results for a different period in the FGGE SOP-1 and for a different model are quite similar to the NCAR results (Figure 9). Their statistics are evaluated from 20 to 90°N, which should result in a slightly faster error growth compared to our hemispheric values. Results from these three separate experiments confirm the validity of these predictability error growth estimates.

FORECAST SKILL DIFFERENCES

The final comparison, and perhaps the most important in terms of the usefulness of the FGGE data set, is the forecast skill produced by each of the analyses. Forecast skill contains error growth from both model error and imperfections in the initial conditions (Williamson, 1973). By comparing forecast skill to predictability error growth, a measure of the two sources of error can be qualitatively obtained. Figure 10 shows that the average forecast skill from all three analyses have similar characteristics when verified with ECMWF data, with the practical limit of skill being reached at 4.5 to 5 days. The limit is determined at the point the forecast error variance approaches the value of the climatological variance and is equivalent to anomaly correlations of 0.5. The forecasts made from the GFDL analyses are slightly worse than the ECMWF forecasts. The differences however do not appear to be significant when compared to the predictability error growth estimates for a similar number of cases. There is some sensitivity to the verification data base with like analyses and verification producing the best results, but again the changes were probably not significant. The NMC analyses produced the worst forecasts as might be expected from the different data sources, however the difference in skill is perhaps just bordering significance.

The spectral decomposition of the forecast skill (Figure 11) illustrates the scale of the skill differences. When like analyses are used for verification, the spectral behavior of the forecast skill is

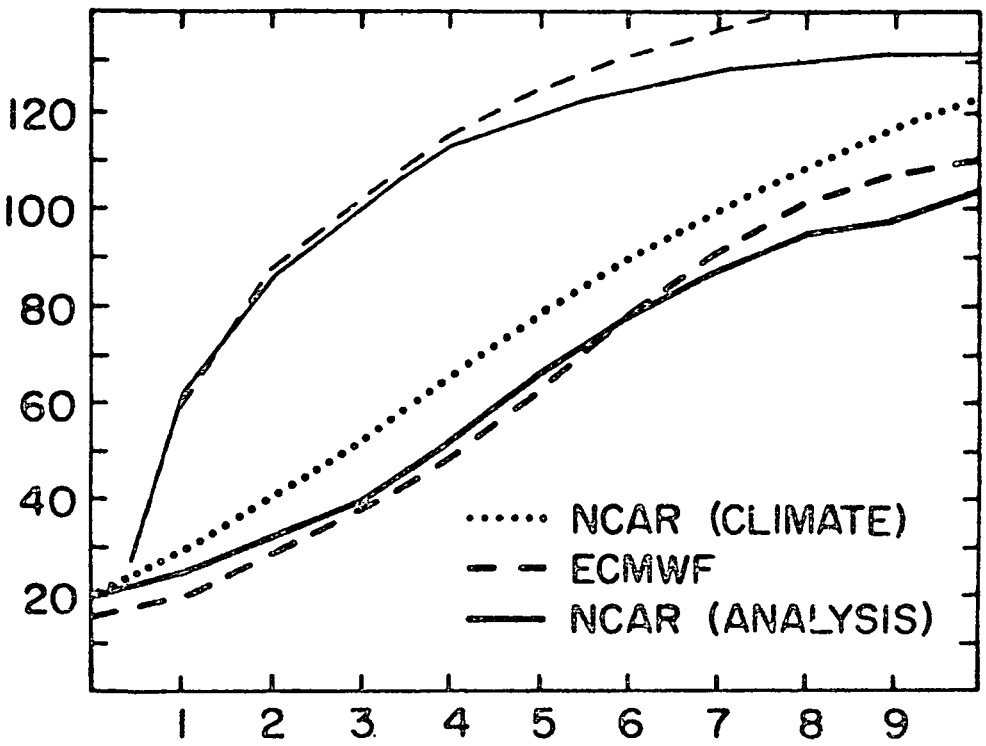

FIGURE 9 Standard deviation (m) of 500 mb height differences over the northern hemisphere. Average NCAR analysis differences (solid line); NCAR classical predictability results (dotted line), average ECMWF analysis differences (dashed line) for 20 to 90°N. Light solid (NCAR) and dashed (ECMWF) lines show persistence values for analysis ensembles. Abscissa in days of forecast.

almost identical, with the planetary waves being the best and the shortest scales being the poorest. The largest differences from changes in the verification base occur in the zonal vortex and waves greater than 8. There is a peculiar difficulty in forecasting the zonal vortex that is independent of analyses and has been found in other models as well (Baumhefner, 1984). The poorer NMC analysis forecasts are primarily influenced by waves 1 to 4 and 8 to 11.

A comparative breakdown of the 10-case ensemble forecast skill is produced in Figure 12 at the point of average skill limit of 5 days. The scatter diagrams for the ECMWF-GFDL comparison show two distinct clusters of skill with 6 of the 10 cases still falling below the climate variance (unity). The movement due to verification changes is slight but always positive, indicating the beneficial nature of like verification/analyses. In the NMC comparison only 1 of the 10 cases is slightly better than ECMWF, confirming the possibility of significance found in Figure 10. Two of the cases are dramatically worse than ECMWF

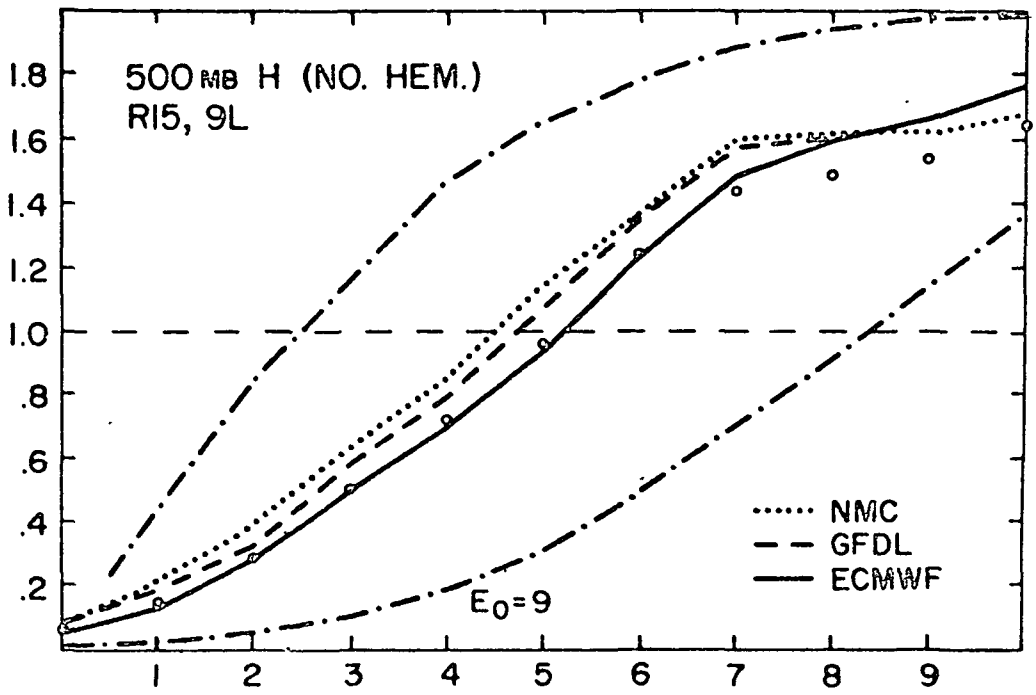

FIGURE 10 Same as Figure 6, but for forecast skill derived from the ECMWF (solid), GFDL (dashed), and NMC (dot) analyses. Verification and persistence (top dash-dot) are from ECMWF analyses. Open circles are GFDL values when verified with GFDL analyses. Predictability estimate for NCAR simulated data with initial uncertainty of 9 m RMS.

forecasts. The sensitivity of planetary wave forecasts is shown with all of the NMC values greater than ECMWF. In terms of forecast skill based on these results, the FGGE analyses may have made their biggest impact on the largest scales of motion.

The model used in this study produces comparable skill to the operational forecasts made at NMC currently and is considerably better than the model used operationally in 1979 (Baumhefner, 1984). The present ECMWF model produces usable skill out to 6 to 7 days using similar measure of skill. It therefore seems unlikely that these results would be severely model-dependent.

The systemataic errors of the model forecasts were not substantially altered by using different analyses, but there was some evidence of memory retention of differences in the zonal flow. If the systematic differences between GFDL and ECMWF analysis forecasts are compared at day 0 and day 10, a strong similarity in pattern exists (Figure 13). This implies that part of the systematic error was induced by the differences in the initial data. When the magnitude of these differences are compared to the total systematic errors (not shown), the values for the u field are approximately 20 percent of the total.

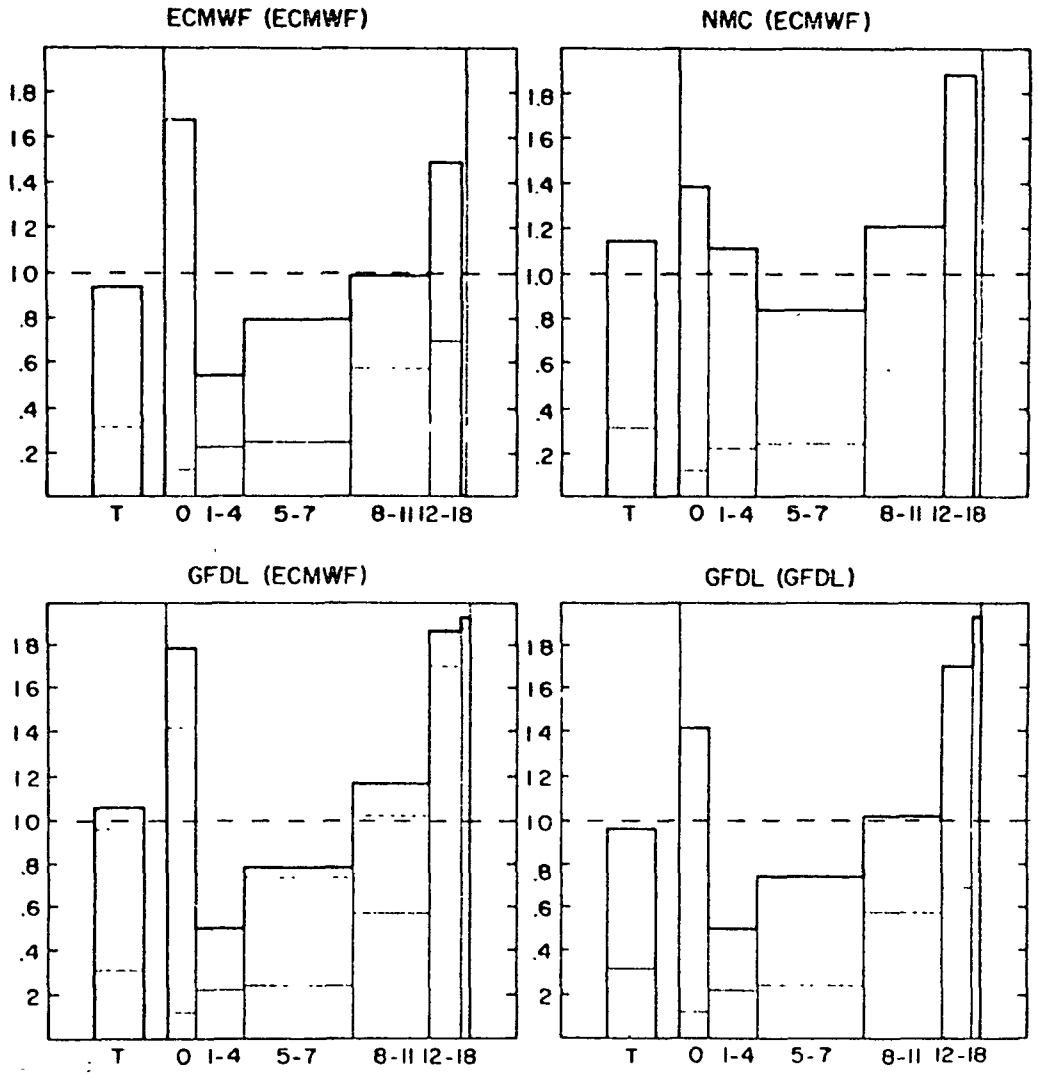

FIGURE 11 Same as Figure 7, but for day 5 forecast skill from ECMWF (top left), NMC (top right), and GFDL (bottom left) analyses. Verification in ECMWF analysis. GFDL (bottom right) verified against GFDL analyses. Light solid horizontal bar on each histogram represents predictability error growth from NCAR simulated data and initial uncertainty of 9 m RMS. Dashed horizontal bars on lower left transposed from lower right.

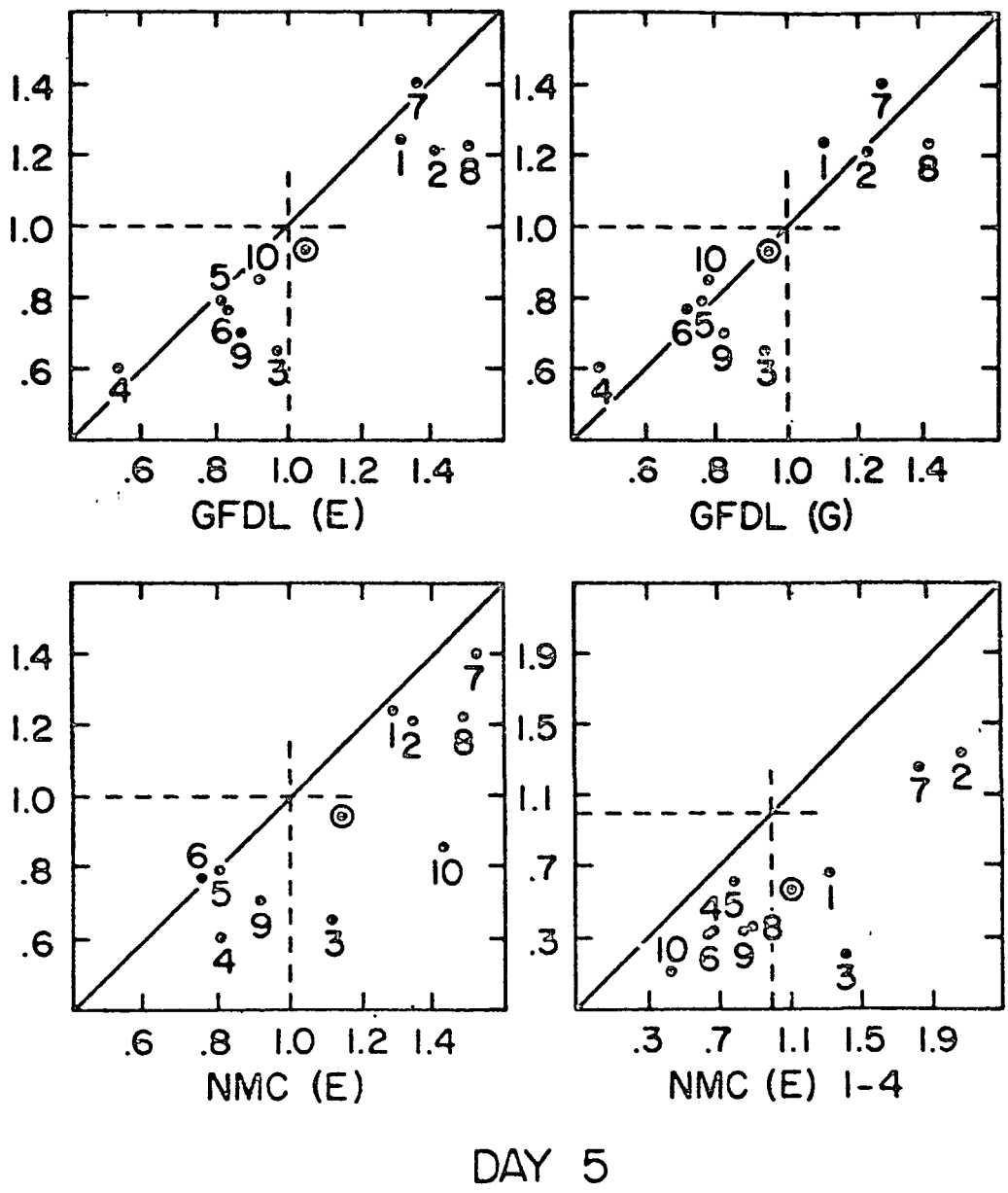

FIGURE 12 Scatter diagrams of total normalized forecast skill variance at 500 mb over the northern hemispehre compared to ECMWF analysis forecasts (ordinate). Numbers refer to cases listed in Figure 1. (E) used ECMWF verification and (G) used GFDL verification. Bottom right panel depicts scores for only waves 1 to 4. Circled dot is 10-case average value.

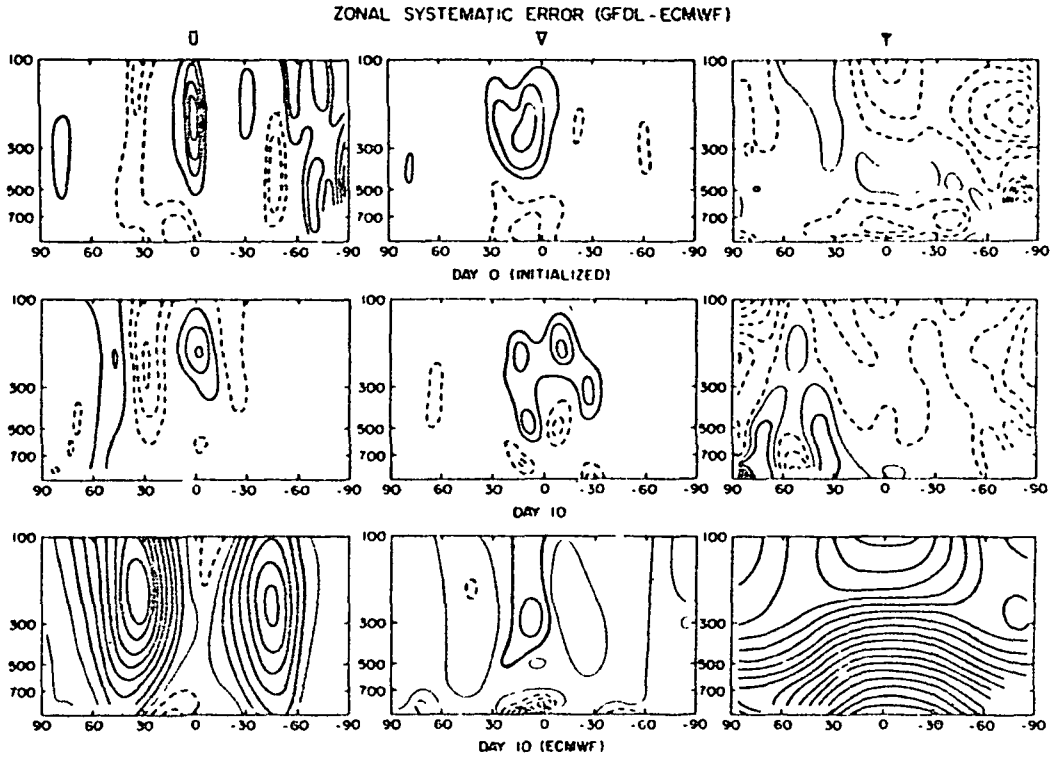

FIGURE 13 Same as Figure 5, but for initialized differences of GFDL-ECMWF (top), systematic differences at forecast day 10 between GFDL and ECMWF analysis originated forecasts (middle), and ECMWF forecast values at day 10 (bottom). Contour interval: u difference - 0.5 m/s; v difference = 0.25 m/s; T difference = 0.5°K; u field = 4 m/s; v field = 0.5 m/s; T field = 5°K.

This percentage is roughly the same for the other variables as well, which suggests that modeling error is much more important than initial data error for the systematic part of the forecast error variance.

DISCUSSION

Two major points come to mind when one considers the data presented in this paper: (1) How close is the current forecast skill to the ultimate limit of skill as indicated by predictability error growth, and (2) What is the current partition in forecast errors between modeling error and initial data error? An interesting corollary in regard to the Global Weather Experiment is how the answers might have changed with the introduction of FGGE data and models. Accurate answers to both questions are related to the initial uncertainty (E_0) in the initial states that are supplied to models for forecasting.

		# OF CASES	ANALYSES	INITIALIZED	A-I	CONTROLLED TEST (EC-NMC-GLAS)
NMC-ECMWF	(0-90 N)	10	29			
GFDL-ECMWF	(0-90 N)	10	27	21	19 (GF) 12 (EC)	
GLAS-ECMWF	(0-90 N)	5	27			
NMC-ECMWF	(20-90 N)	9	19	15 EST.	13 (NMC) 10 (EC)	
UK-ECMWF	(20-90 N)	9	25			
UK-NMC	(20-90 N)	9	29			
CONVENTIONAL	(0-90 N)	7				18
FGGE	(0-90 N)	7				15
WINDSAT	(0-90 N)	7				18
NMC-ECMWF	(20-90 N)	"WINTER"	20			

FIGURE 14 Table of estimates of uncertainty (in the northern hemisphere) in the initial states of numerical forecasting models in terms of standard deviation. Left hand column gives analysis pairs or data base from which estimates are made. () contain latitude averaging. Analyses column is uninitialized. A-I is difference between analysis and initialized field. Controlled test explained in text.

Referring back to Figure 10, it is apparent that for initial uncertainties of $\approx$10 m RMS, there is still room for improvement in forecasting skill. However, if the initial uncertainty is of the order of 30 m RMS, the ultimate limit of predictability falls to 5 to 6 days, and further reduction in modeling error is fruitless until the initial data errors are reduced.

An attempt has been made, for discussion purposes mostly, to gather together in a table (Figure 14) a few estimates of initial uncertainty for comparison. My results are compared with Arpe et al. (1984) and Atlas (1984). One method of estimation is shown in the column marked analyses, where the average standard deviation between analyses is given. In a crude sense this can be interpreted as a measure of the true uncertainty. The model's predictability error growth is dominated by errors in the slow, balanced flows, therefore the initialized differences are more appropriate for consideration. From estimates of changes in analyses when initialization is applied (columns A-I), the reduction in error is of the order of 5 m RMS.

A more correct method of (E_0) estimation is to simulate the atmosphere with a model, extract the appropriate data base, analyze the

extracted data, and finally compare the results with the original fields. The numbers in the right-hand column of Figure 14 are for three different data base choices (Atlas, 1984). Combining these estimates in a consensus manner with the others yields a 15 to 20 m RMS value of uncertainty in the 500 mb northern hemisphere height field.

Using these values of uncertainty with the average of the predictability error growth rates found in Figure 9, the limit of predictive skill is 7 to 8 days. Therefore, we are very close to the ultimate limit of forecast skill with the current data analysis systems. In the case of the NCAR model, the model errors are of the same order as the initial uncertainties (Figure 10), and for the ECMWF model, initial data errors may be exceeding the modeling deficiencies. Improvements directly related to the FGGE data base, in my opinion, have increased forecast skill by a day at most, whereas improvements in modeling have been responsible for an increase in perhaps 2 days of skill (Baumhefner, 1984).

CONCLUSIONS

The differences among FGGE analyses were generally larger than expected, of the order of 25 m RMS (20 m after initialization), however this did not seem to affect the quality of forecasts made from them producing limits of skill around 5 days for the NCAR model. Predictability estimates derived from the analysis differences agreed with recent classical experiments from the same model as well as other analysis difference experiments. These estimates are faster than currently found in the literature. The ultimate limit of forecast skill for an initial uncertainty of 20 m RMS is 7 to 8 days, somewhat shorter than previously hypothesized. Modeling errors and initial analysis errors now produce comparable error growth, therefore reductions in the sources of error in each can be expected to give comparable results.

ACKNOWLEDGMENTS

The National Center for Atmospheric Research is sponsored by the National Science Foundation. This work was inspired by many lengthy discussions with R. Daley, J. Tribbia, and C. Leith. Help with the initialization, models, and verification was provided by R. Errico, D. Williamson, and T. Bettge. Manuscript preparation and figures were handled by M. Niemczewski and S. Honaski.

REFERENCES

Arpe, K. (ECMWF), M. S. Tracton (NMC) (1984). Personal communication.

Atlas, R. (GLAS) (1984). Personal communication.

Baumhefner, D. (1984). The relationship between present large-scale forecast skill and new estimates of predictability error growth.

Predictability of Fluid Motions, AIP Conference Proceedings No. 106,. pp. 169-180.

Errico, R. (NCAR) (1984). Personal communication.

Hollingsworth, A., A. C. Lorenc, M. S. Tracton, K. Arpe, G. Cats, S. Uppala, and P. Kallberg (1984). The response of numerical weather prediction systems to FGGE IIb data. Part I - Analyses. Quart. J. Roy. Meteorol. Soc. (in press).

Leith, C. E. (1971). Atmospheric predictability and two-dimensional turbulence. J. Atmos. Sci. 28, 145-161.

Rutherford, I. (ed.) (1980). Research activities in atmospheric and oceanic modeling. GARP Numerical Experiment Programme, Report No.1.

Shukla, J. (1981). Dynamical predictability of monthly means. J. Atmos. Sci. 38, 2547-2572.

Williamson, D. W. (1974). The effect of forecast error accumulation on four-dimensional data assimilation. J. Atmos. Sci. 30, 537-543.

Williamson, D. W. (1983). Description of NCAR Community Climate Model (CCM0B). NCAR Technical Note, TN-210+STR, 88 pp.

D14

A COMPARISON STUDY OF SPECTRAL ENERGETICS ANALYSIS USING VARIOUS FGGE IIIb DATA

Tsing-Chang Chen and Yen-Huei Lee
Iowa State University

ABSTRACT

The atmospheric spectral energetics studies performed before the First GARP Global Experiment (FGGE) were reviewed, and the deficiencies of these studies were pointed out. The data generated by the FGGE IIIb analyses of the European Centre for Medium Range Weather Forecasts, the Geophysical Fluid Dynamics Laboratory, and the Goddard Laboratory for Atmospheric Sciences over the entire globe during the FGGE summer and winter are used to analyze the atmospheric spectral energetics. Comparisons were made between the results using three FGGE IIIb analyses, and between previous and current sutdies with the spectral energetics of the southern hemisphere.

INTRODUCTION

It has been more than a quarter century since Saltzman (1957) introduced the spectral analysis along latitude circles into the Lorenz energy cycle. Following his proposal, Saltzman (1978) presented a review of spectral energetics. A very extensive analysis of atmospheric spectral energetics was later attempted by Tomatusi (1979). It has been shown in many studies that the spectral energetics analysis is a useful diagnostic tool for understanding the dynamics and circulation of large-scale atmospheric motions (e.g., stratospheric sudden warming (Reed et al., 1963; Perry, 1967), blocking (Hansen and Chen, 1982; Chen and Shukla, 1983), and geostrophic turbulence (Steinberg et al., 1971).

However, because of the limitation in the spatial coverage of observations, especially over the oceans, spectral energetics computations were usually performed within the geostrophic framework and for the area north of 20°N. Therefore the ageostrophic effect, the tropical area, and the southern hemisphere were often left out. Recently, the FGGE IIIb data of the ECMWF have been used to explore the spectral energetics of the tropics for January (Kanamitsu, 1983) and for the FGGE summer (Chen and Marshall, 1984). Kanamitsu (1983) also examined the spectral energetics of the southern hemisphere for January. Some studies of the energy spectra of the southern hemisphere were also carried out with the IGY data (Price, 1975) and with the EOLE data

(Desbois, 1975). Nevertheless, no extensive effort has been made to investigate the spectral energetics of the southern hemisphere using the FGGE IIIb data. Since the atmospheric circulation of the southern hemisphere is essentially maintained by transient eddies, e.g., van Loon (1980) and Physick (1980), it is worthwhile examining the spectral energetics of this area.

In this paper, the spectral energetics of both hemispheres will be presented using the FGGE IIIb data generated by the ECMWF, GFDL, and GLAS. The purpose of the entire study is two-fold. One is to shed light on the discrepancy of the atmospheric circulation depicted by the data generated from various FGGE IIIb analyses in terms of the intercomparison of spectral energetics. The other is to examine to what extent the problems encountered by previous spectral energetics can be resolved by the best compiled and analyzed global data in the meteorology history.

FORMULATION AND DATA

Following Saltzman's (1957) formulation and Chen's (1982) notation, the energy equations in spectral form are written as follows:

$$\frac{dK_z}{dt} = \sum_{n=1}^{N} C(K_n,K_z) + C(A_z,K_z) - D(K_z), \tag{1}$$

$$\frac{dK_n}{dt} = -C(K_n,K_z) + CK(n/m,\ell) + C(A_n,K_n) - D(K_n), \tag{2}$$

$$\frac{dA_z}{dt} = \sum_{n=1}^{N} C(A_z,A_n) - C(A_z,K_z) - G(A_z), \tag{3}$$

$$\frac{dA_n}{dt} = C(A_z,A_n) - C(A_n,K_n) + CA(n/m,\ell) + G(A_n). \tag{4}$$

The cutoff wavenumber is N = 15 in this study.

The data used are at 10 mandatory levels (1000, 850, 700, 500, 400, 300, 250, 200, 150, and 100 mb) during the FGGE summer and winter generated by the FGGE IIIb analyses of the ECMWF, GFDL, and GLAS. (Note that the GLAS data only include January and February for winter, and June and July for summer.) The ω fields of the ECMWF analyses were generated by the kinematic method, while those of the GFDL and GLAS were the results of model output. Besides the difference of numerical models used for the data assimilation at these three centers, the FGGE IIIb analyses are also distinguished by different data processes illustrated in Table 1.

TABLE 1 Comparison for the Major Differences between Various FGGE IIIb Analyses.

Center	Objective Analysis	Initialization
ECMWF (Bengtsson et al, 1982)	3-D multivariate optimum interpretation	nonlinear normal mode
GFDL (Miyakoda et al, 1982)	univariate optimum interpretation	nonlinear normal mode
GLAS (Baker, 1983)	Cressman (1959) type	N/A - Matsuno (1966) scheme is used.

BRIEF REVEW OF PREVIOUS STUDIES

Based on the geostrophic formulation, previous studies of spectral energetics by Saltzman (1970), Steinberg et al. (1971), and Tomatsu (1979) result in the following spectral energy cycle:

1. A_Z, generated by differential diabatic processes, is converted to A_n of all wave components by the eddy sensible heat transport, especially in the large waves.
2. A_n, redistributed by nonlinear cascade from large waves to small waves, is depleted by baroclinic conversion to K_n with the maximum value occurring at intermediate wavenumbers and is also dissipated by diabatic processes.
3. K_n, converted to support K_Z by eddy momentum transport, is redistributed by nonlinear cascade from intermediate wavenumbers to small and large wavenumbers and is dissipated by friction.

It was also found:

1. A -3 power law exists in the wavenumber regime n = 8 - 15 (Wiin-Nielsen, 1967).
2. The long-wave regime is less efficient energetically than the short-wave regime (Chen, 1982).

In the southern hemisphere, Kao et al. (1970), Price (1975), and Desbois (1975) found:

1. The maximum kinetic energy exists at wavenumber 1 and intermediate wavenumbers.
2. A -3 power law appears in the wave regime n = 8 - 15.
3. Atmospheric energy has a less pronounced seasonal variation.

The deficiencies of previous studies can be summarized as follows:

1. The spatial data coverage, especially over oceans and the southern hemisphere, limits the cutoff wavenumber.
2. Ageostrophic processes were not evaluated adequately.
3. The ω field calculated by indirect methods may result in underestimation of baroclinic conversion, $C(A_n,K_n)$.
4. Direct measurements of $G(A_n)$ and $D(K_n)$ are difficult.
5. The spectral energetics of the southern hemisphere atmosphere have not been extensively analyzed.

COMPARISON BETWEEN THE SPECTRAL ENERGETICS FOR THREE FGGE IIIb ANALYSES

Energies

Various energy contents for both the winter and summer in both hemispheres are displayed in Tables 2 and 3. It is revealed that eddy energies (A_E and K_E) of the GLAS analyses are generally larger than those of the ECMWF and GFDL analyses. The GFDL eddy energies are either larger or approximately equal to the ECMWFs. The same relationship is also applicable to zonal energies (A_Z and K_Z) for these three FGGE IIIb analyses, except the GLAS A_Z in the summer season. Note that the GLAS IIIb analyses use Cressman's scheme without application of nonlinear normal mode initialization, and their data assimilation is performed by a numerical model with a horizontal resolution ($4^{\circ} \times 5^{\circ}$). The differences of various energies between these three analyses suggest that the method of data processing may affect the circulation intensity depicted in terms of the data generated by different analysis.

A comparison with previous studies that covered an entire hemisphere shows that in both hemispheres the zonal energies (K_Z and A_Z) are generally larger in the FGGE analyses, and eddy energies (K_E and A_E) are generally larger in previous studies. Of course the interannual variation of atmospheric circulation may result in this. Nevertheless, one cannot ignore the possible contribution from increased observations during FGGE, particularly over the oceans.

The larger energy content in the GLAS analyses occurs for all wave components (Figures 1 and 2). The slopes of the A_n and K_n spectra in the wavenumber range n = 8 - 15 of the ECMWF analyses are very close to -3. On the other hand, the A_n and K_n spectra for the GFDL and GLAS analyses in this wavenumber range possess a slope value less than -3. It is inferred that the small-scale waves in these two analyses have a larger energy content. The ECMWF analyses apply a multivariate optimum interpolation scheme with the geostrophic constraint. It is suggested that this constraint may be vital to the slope value of A_n and K_n spectra in the large wavenumber regime.

Several interesting features of the energy spectra are worthwhile pointing out. The northern hemisphere has larger seasonal variation for various energy variables as found by Price (1975). In the eddy energy components, this variation is mainly caused by large waves as shown in Tables 2 and 3. K_5 is the maximum of the K_n spectrum in

NORTHERN HEMISPHERE

	ECMWD	GFDL	GLAS	WN	SA	TO	NL	OP1	OP2
K_Z	9.52 (2.17)	9.27 (2.25)	10.14 (2.32)	14.57 (3.09)	10.0 (5.6)	8.89 (3.42)	6.9 (1.5)	7.68 (2.07)	8.0 (2.1)
K_E	8.07 (4.17)	7.79 (4.85)	9.63 (5.72)	13.38 (6.81)	(4.3) (9.9)	11.64 (5.87)	8.7 (5.0)	8.89 (5.30)	7.3 (6.4)
A_Z	57.92 (22.26)	65.06 (25.88)	70.67 (20.42)	40.25 (19.77)	35.5 (22.8)	22.51 (13.49)	51 (19)	55.26 (15.57)	56.4 (22.6)
A_E	8.87 (3.72)	9.50 (5.21)	12.12 (6.53)	11.46 (6.07)	11.3 (7.1)	11.47 (5.91)	10.0 (6.3)	9.77 (5.55)	9.2 (5.5)
$C(A_Z,K_Z)$	-0.66 (0.52)	2.23 (2.42)	0.01		~ 0	-0.57 (-0.17)	0.19 (-0.07)	0.21 (-0.33)	0.21 (-0.02)
$C(A_Z,A_E)$	2.71 (0.37)	2.70 (0.34)	3.75 (0.44)	4.07 (0.63)	5.25 (1.65)	4.57 (0.90)	2.2 (0.3)	2.56 (0.39)	3.31 (0.90)
$C(A_E,K_E)$	1.30 (0.45)	3.23 (1.85)	2.38		3.03	3.17 (0.92)			2.8 (1.3)
$C(K_E,K_Z)$	0.14 (0.15)	-0.07 (0.11)	0.02 (0.18)	0.13 (0.56)	0.48 (0.65)	0.51 (0.21)	0.23 (0.19)	0.11 (0.22)	0.27 (0.18)

WN: Wiin-Nielsen (1967) (20° N $\sim$ 85° N I)
SA: Saltzman (1970) (20°N $\sim$ 87.5° N)
NL: Newell et al (1974)
OP1: Oort and Peixoto (1974); Peixoto and Oort (1974) (10° S - 90° N)
TO: Tomatus (1979) (925 $\sim$ 100 mb) (25° N - 75° N)
OP2: Oort and Peixoto (1983)

TABLE 2 Mean Energy Variables with ECMWF, GFDL, and GLAS Data Sets in the FGGE Winter Compared with Other Studies (energies in 10^5 Jm^{-2} and energy conversions in Wm^{-2})

TABLE 3 Mean Energy Variables with ECMWF, GFDL, and GLAS Data Sets in the FGGE Summer Compared with Other Studies (energies in 10^5 Jm^{-2} and energy conversions in Wm^{-2})

SOUTHERN HEMISPHERE

	ECMWF	GFDL	GLAS	PR	PC	NE	OP
K_Z	12.50 (6.01	12.08 (5.80)	14.44 (6.14)	10.31 (9.64)	9.54 (5.35)	6.5 (3.4)	7.6 (3.9)
K_E	6.88 (5.45)	6.75 (5.36)	8.44 (6.62)	8.17 (5.49)	8.29 (7.49)	7.8 (5.7)	7.7 (5.9)
A_Z	41.12 (31.00)	41.61 (34.68)	55.36 (30.88)	50.22 (41.93)	39.83 (29.71)	47 (29)	57.4 (35.5)
A_E	3.57 (3.10)	3.71 (3.98)	4.99 (3.99)	5.03 (3.45)	7.23 (6.47)	5.5 (4.2)	5.5 (4.4)
$C(A_Z,K_Z)$	-0.07 (0.69)	0.31 (0.36)	(-0.01)		0.09 (0.06)	-0.17 (0.14)	0.24 (-0.24)
$C(A_Z,A_E)$	2.08 (0.99)	1.72 (1.65)	2.60 (1.24)		1.87 (1.17)	1.8 (0.9)	1.68 (0.81)
$C(A_E,K_E)$	0.98 (0.70)	1.68 (1.02)	(1.36)		1.99~2.82 (1.88~2.63)		2.1 (1.5)
$C(K_E,K_Z)$	0.19 (0.29)	-0.12 (0.24)	0.03 (0.33)		0.33 (0.39)	0.24 (0.33)	0.25 (0.34)

PR: Price (1975) (10° S - 70° S)
PC: Peixoto and Côrte-Real (1982; 1983)
NE: Newell et al (1964)
OP: Oort and Peixoto (1983)

the summer southern hemisphere. It is consistent with Salby's (1982) analysis of the southern hemisphere height field.

Energy Conversions

$C(A_Z,A_n)$

The spectra of this energy conversion for various FGGE analyses are displayed in Figure 3. The maximum value of $C(A_Z,A_n)$ usually occurs in the intermediate wavenumber regime except for the winter northern hemisphere, where the maximum $C(A_Z,A_n)$ appears in the low wavenumber regime. This situation is due to the strong intensity of ultralong waves in the winter northern hemisphere as indicated by the energy spectra in Figures 1 and 2. $C(A_Z,A_n)$ of the GLAS analyses is usually the largest in every wave component. This might be due to

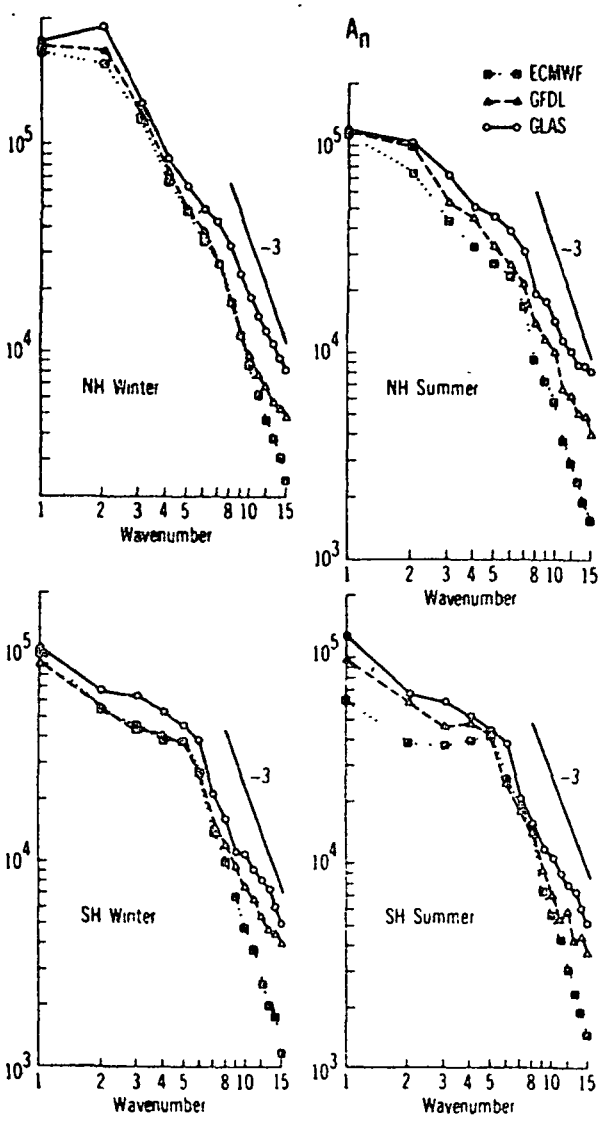

FIGURE 1 Spectral distribution of A_n (unit Jm^{-2}).

either a larger north-south gradient of zonal mean temperature as inferred from A_Z or large eddy sensible heat transport.

The latitude pressure cross-section of $C(A_Z,A_n)$ (not shown) shows that its maximum value exists in midlatitudes. It is not surprising that previous studies, e.g., Wiin-Nielsen (1967), Saltzman (1970), and Tomatsu (1979), dealing with this energy conversion north of 20°N have larger numerical value than our results. For those studies covering an area equivalent to the current study (e.g., Newell

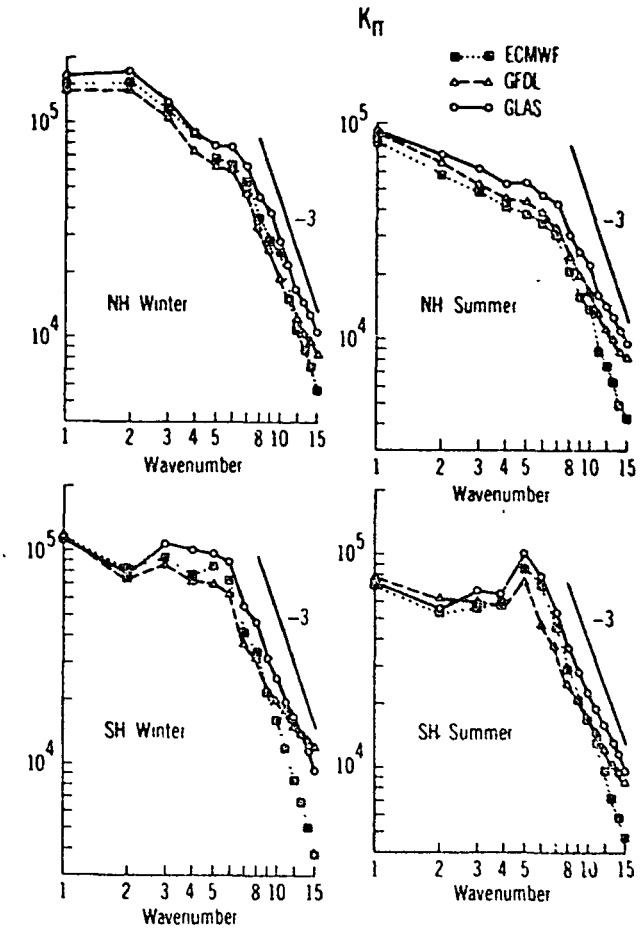

FIGURE 2 Spectral distribution of K_n (unit Jm^{-2}).

et al. (1974); Oort and Peixoto (1974, 1983)), numerical values of this energy conversion are close to those of the current study.

Note that the evaluation of $C(A_Z,A_E)$ by Wiin-Nielsen (1967), Saltzman (1970), and Tomatsu (1979) is based on a geostrophic framework. The values of $C(A_Z,A_E)$ from these studies are larger because the area selected is north of 20°N. Oort and Peixoto (1983) also used the geostrophic form. However, their results are very close to the current study. It is inferred that the ageostrophic effect may not have significant impact on the value of $C(A_Z,A_E)$.

$C(A_Z,K_Z)$ and $C(A_n,K_n)$

The release of available potential energy by thermally direct overturning is evaluated in terms of the covariance between temperature

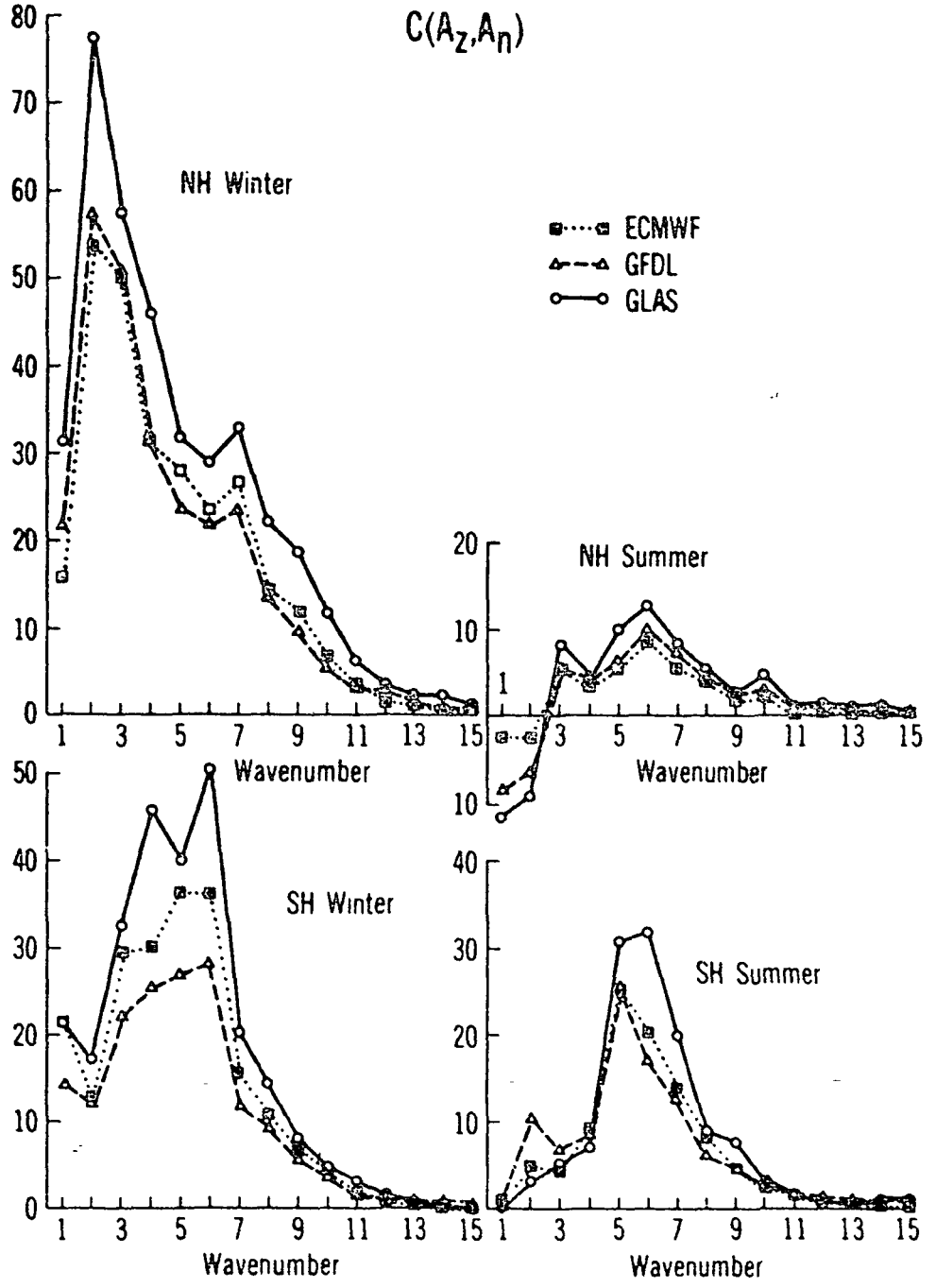

FIGURE 3 Spectral distribution of $C(A_z,A_n)$ (units $10^{-2}Wm^{-2}$).

and vertical motion. The latter is computed by indirect methods. Therefore, the values of $C(A_Z,K_Z)$ and $C(A_n,K_n)$ are affected by the method used. The most popular indirect methods applied are the ω equation and kinematic methods. The former is limited by the geostrophic constraint, while the latter is determined by the divergence field. At any rate, the computed ω field is underestimated, and $C(A_Z,K_Z)$ for the previous studies shown in Tables 2 and 3 is small in numerical value because of the geostrophic constraint on the ω_Z field. In addition, it was stressed by Chen (1982) that the 3-cell structure of the zonal mean meridional circulation creates positive and negative values alternating in the latitudinal direction. The latitudinal integration $C(A_Z,K_Z)$ results in a small value.

The numerical values of $C(A_Z,K_Z)$ in the GFDL analyses are very significant, especialy in the northern hemisphere. Recall that the geostrophic constraint is not imposed in the GFDL IIIb analyses. On the other hand, $C(A_Z,K_Z)$ of the ECMWF and GLAS analyses are as small as previous studies. It was previously mentioned that the ECMWF IIIb analyses possess the geostrophic constraint, but not the GLAS IIIb analyses. The small value of $C(A_Z,K_Z)$ in the GLAS analyses is due to the cancellation of significant positive values in low latitudes and significant negative values in high latitudes as illustrated in Figure 4.

The $C(A_n,K_n)$ spectra of various IIIb analyses are displayed in Figure 5. Since it was shown that $C(A_Z,A_n)$ of the GLAS analyses has the largest value in every wave component, it might be expected that this would also be true for the $C(A_n,K_n)$ spectrum. In fact, it is the GFDL analyses that have the largest values of $C(A_n,K_n)$ in every wave component. On the other hand, the $C(A_n,K_n)$ value of the ECMWF analysis is always smaller than the other two analyses. This result is indicative of the fact that the multivariate optimum interpolation scheme used in the ECMWF analyses suppresses the divergence field and, in turn, the ω field generated by the kinematic method. The huge value for wavenumber 1 and 2 in the summer season of the GFDL analyses may be a result of an erroneous ω field at $30^{\circ}N$ as shown in the cross-section plot (not shown).

An interesting feature for the maintenance of wavenumber 5 in the southern hemisphere is revealed from Figures 3 and 5 and shows that this wave is maintained by baroclinic processes.

$C(K_n,K_Z)$

If the ageostrophic effect is not significant, $C(K_n,K_Z)$ can be evaluated by the covariance between eddy momentum transport and the north-south horizontal shear of mean zonal flow. It can be expected that negative and positive values of $C(K_n,K_Z)$ alternate in the latitude-pressure cross-section as Chen (1982) stressed and as shown in Figure 6 for June to August 1979. The latitudinal integration of this energy conversion always results in a small value as displayed in Tables 2 and 3 for various studies. In other words, the hemispheric

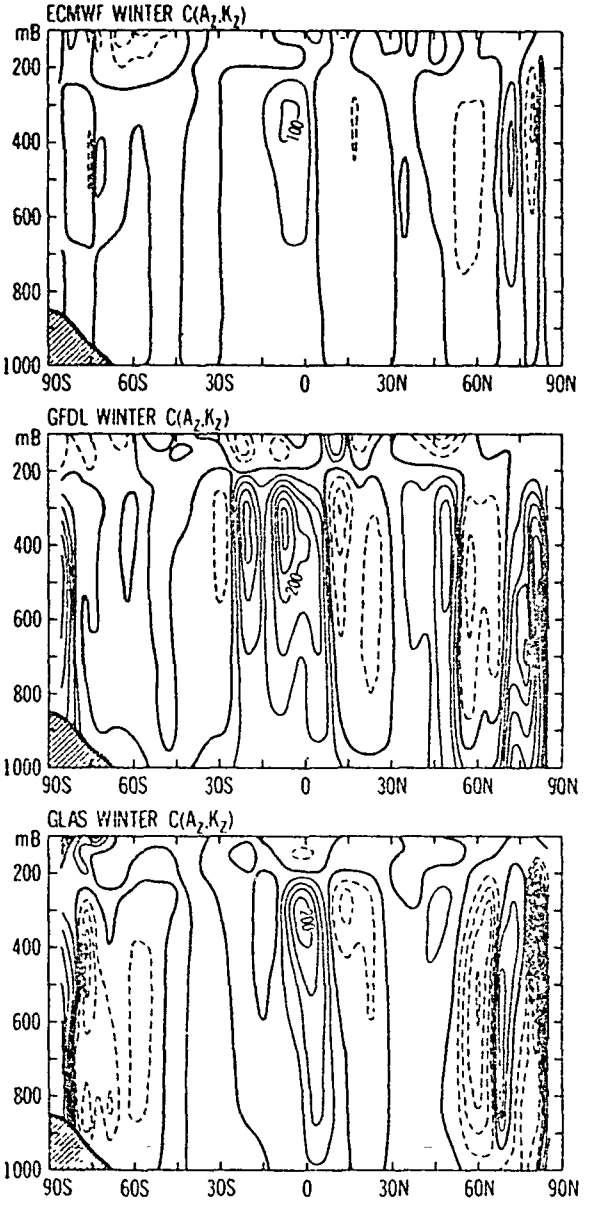

FIGURE 4 Latitudinal pressure distribution of $C(A_Z,K_Z)$ for December 1976 to February 1979. Solid lines are positive values, while dashed lines are negative values (units $10^{-4}m^{-2}mb^{-1}$).

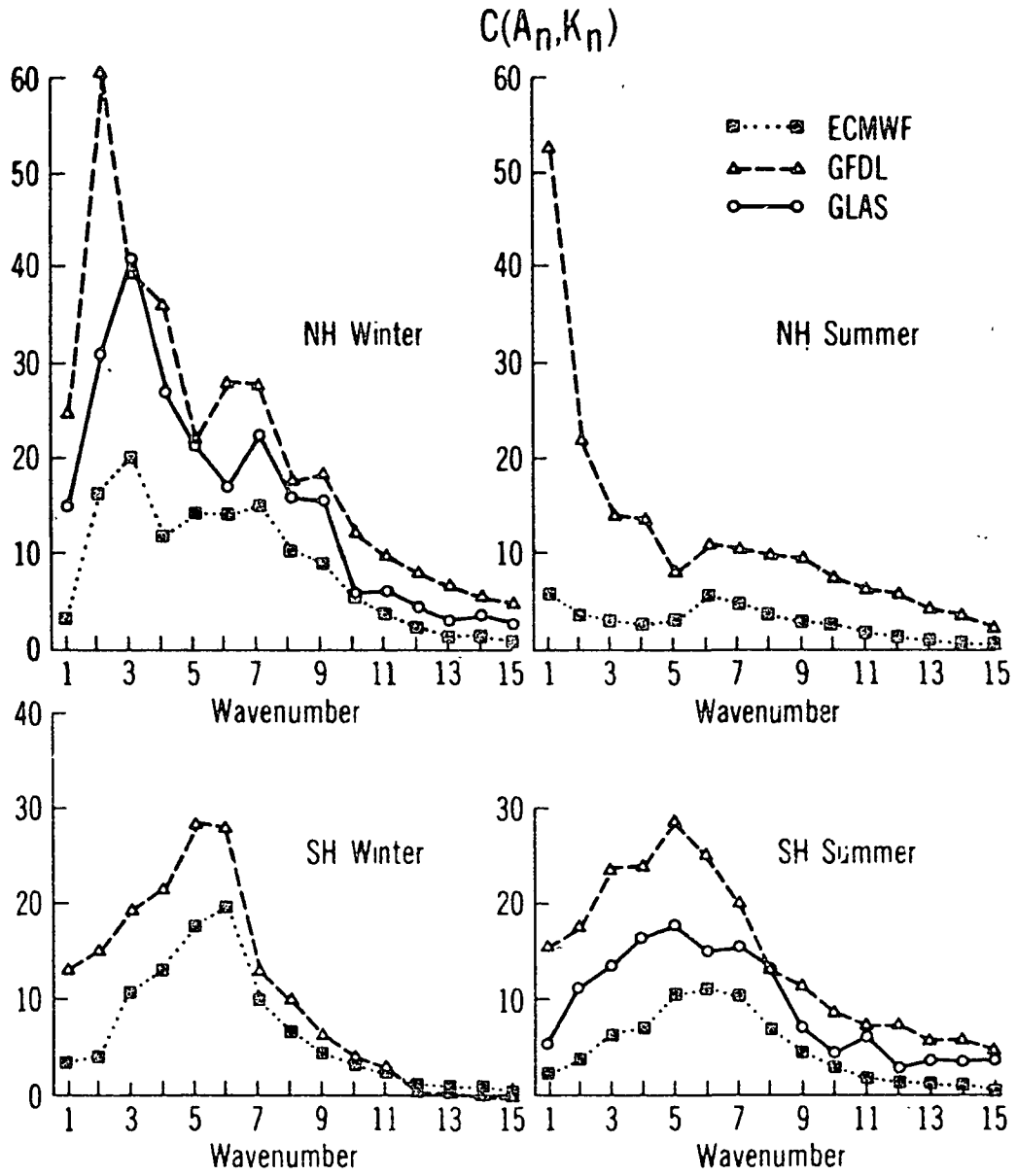

FIGURE 5 Spectral distribution of $C(A_n,K_n)$ (units $10^{-2}Wm^{-2}$).

average of $C(K_n,K_z)$ is obtained from the summation of large positive and negative values. According to this argument, the hemispheric integration of this barotropic energy conversion may not be as informative as the two previous baroclinic energy conversions in illustrating the distinction between three FGGE IIIb analyses.

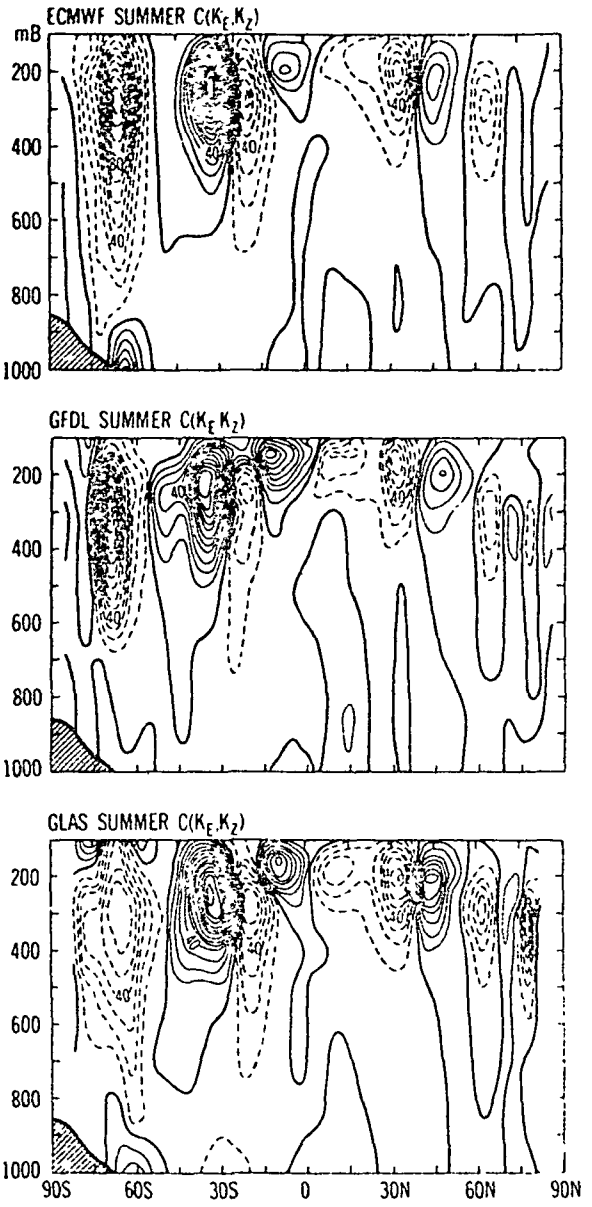

FIGURE 6 Latitudinal pressure distribution of $C(K_E,K_Z)$ for June to August 1979. Solid lines are positive values, while dashed lines are negative values (units $10^{-4}Wm^{-2}mb^{-1}$).

Tables 2 and 3, and Figure 7 seem to indicate the ECMWF $C(K_n,K_Z)$ is larger in winter, while the GLAS $C(K_n,K_Z)$ is larger in summer. Nevertheless, all three analyses generally show peak $C(K_n,K_Z)$ values in almost the same wavenumber ranges. Table 3 and Figure 7 also indicate that $C(K_E,K_Z)$ is larger in the southern hemisphere. The latitude-pressure cross-section of $C(K_E,K_Z)$ shown in Figure 6 indicates that this barotropic conversion maintains the Antarctic polar jet.

Nonlinear Cascades: $CA(n/m,\ell)$ and $CK(n/m,\ell)$

The A_n and K_n cascades of three FGGE analyses are exhibited in Figures 8 and 9, respectively. In the northern hemisphere, A_n for all three analyses is cascaded downscale from the low wavenumber regime to the large wavenumber regime. In the southern hemisphere, A_n is cascaded differently from the intermediate wavenumber regime to the small and large wavenumber regimes.

In the winter season of both hemispheres, K_n is cascaded from the intermediate wavenumber regime to small and large wavenumber regimes. The major difference between the K_n cascade for the two hemispheres is the existence of a minimum outgoing cascade in the intermediate wavenumber regime. The outgoing cascade of wavenumber 2, emphasized by Saltzman (1970), is replaced by wavenumber 3 in the current analysis. In the summer season, K_n is cascaded from low and intermediate wavenumber regimes to two higher wavenumber regimes.

The general features of the A_n and K_n cascades in the northern hemisphere are similar to the previous study reviewed above. The nonlinear cascade provides a way for the redistribution of atmospheric energy through triplet interactions between waves. It was shown (Baker et al., 1977) that the nonlinear cascading of A_n and K_n are difficult to simulate by the general circulation. Although we may not be able to assess model bias in data assimilation, the general trends of the A_n and K_n cascades evaluated using three IIIb analyses are consistent.

CONCLUDING REMARKS

The intercomparison of the spectral energetics analysis using the FGGE analyses of the ECMWF, GFDL, and GLAS is summarized as follows:

1. The ECMWF analysis, which has a geostrophic constraint due to the multivariate optimum interpolation scheme, exhibits the weakest energetics, and has a -3 power law, is in the large wavenumber regime ($n = 8 - 15$).
2. The GFDL analyses, which has a univariate optimum interpolation scheme, preserves the horizontal divergence field well. Therefore the GFDL analyses have the largest values for the release of available potential energy due to thermally direct overturning of the three FGGE analyses.

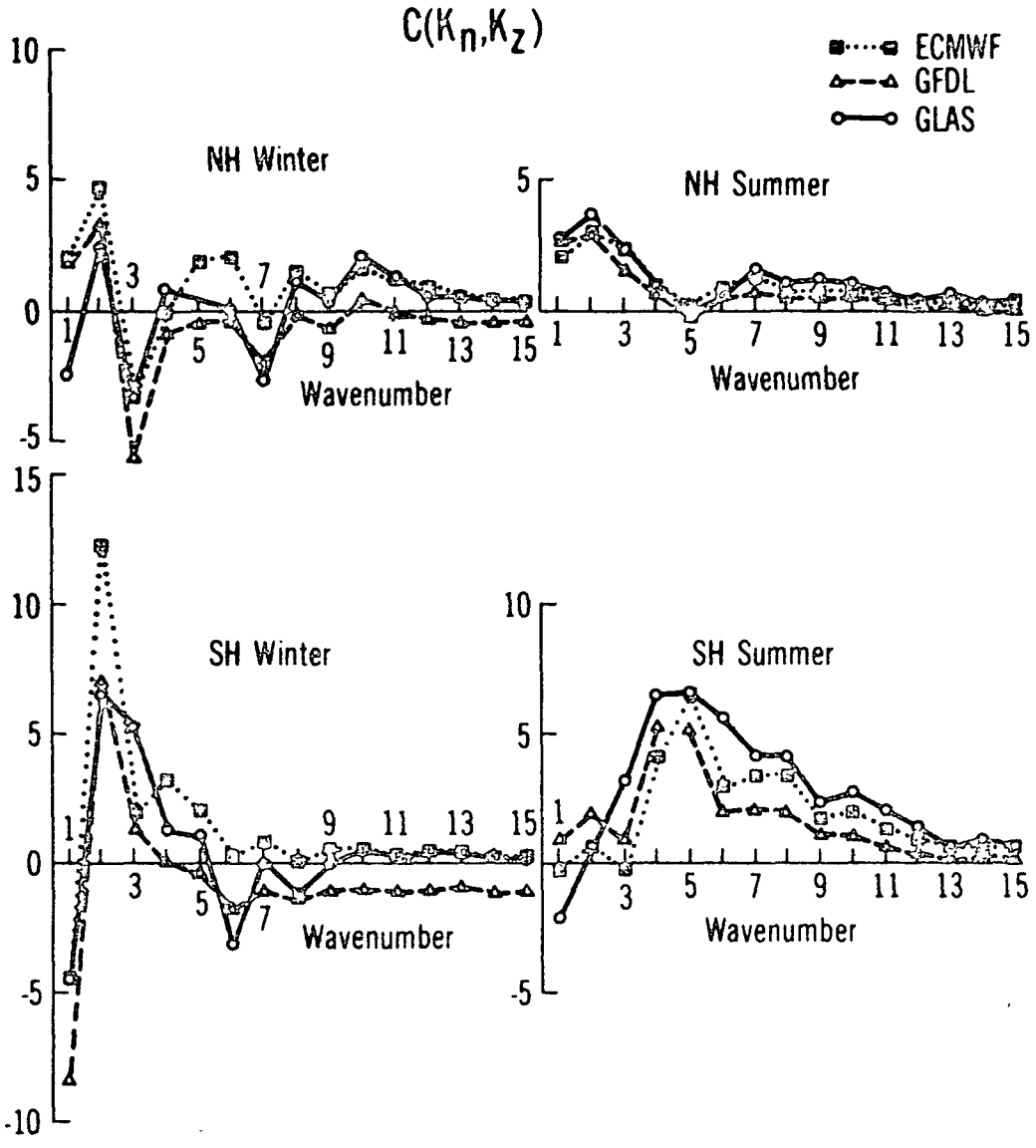

FIGURE 7 Spectral distribution of $C(K_n,K_z)$ (units $10^{-2}Wm^{-2}$).

3. The GLAS analyses, which utilize the modified Cressman scheme without nonlinear normal mode initialization, display the largest value of spectral energetics.

Although the southern hemisphere circulation during the FGGE year was anomalous (van Loon, 1980; Trenberth, 1984), a more complete

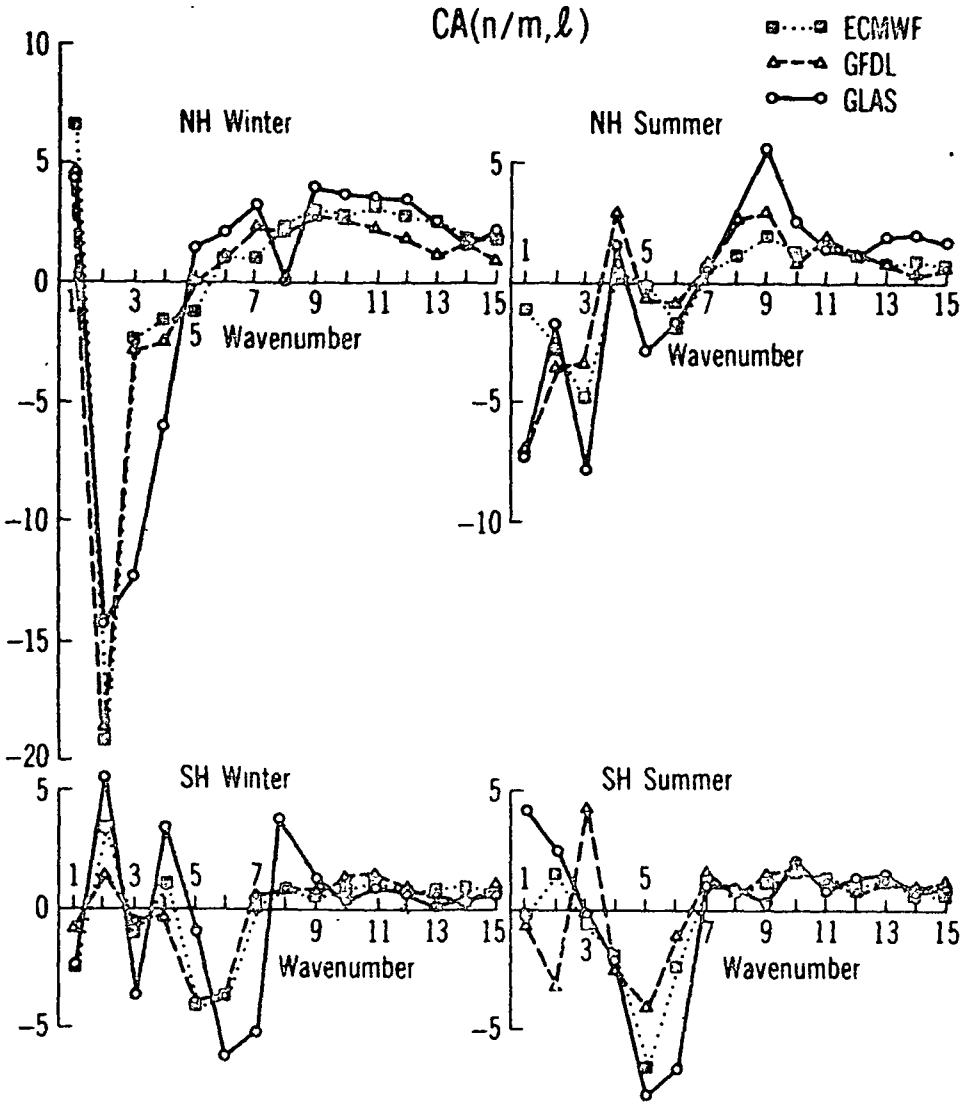

FIGURE 8 Spectral distribution of CA(n/m,ℓ) (units $10^{-2}Wm^{-2}$).

spectral energy cycle was obtained. The spectral energetics of the southern hemisphere are summarized as follows:

1. The intensity of atmospheric energetics has a less pronounced annual variation in the southern hemisphere.
2. The energetics intensity of the winter southern hemisphere is weaker than the winter northern hemisphere, especially for ultralong waves.

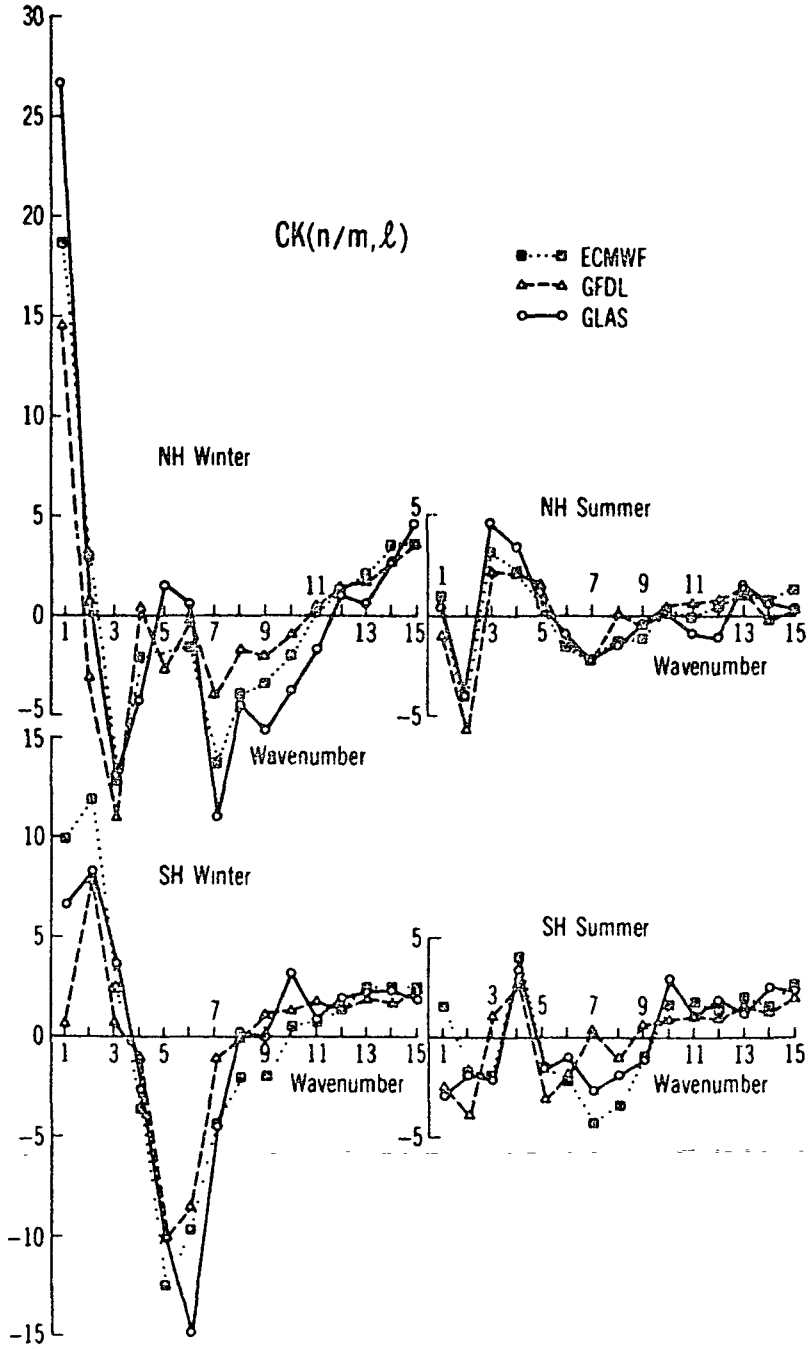

FIGURE 9 Spectral distribution of CK(n/m,ℓ) (units $10^{-2}Wm^{-2}$).

3. The intermediate wavenumber regime is energetically more active than the small wavenumber regime. For instance, maximum values for most energy conversions occur in the intermediate wavenumber regime. A_n and K_n generally are cascaded from the intermediate wavenumber regime to smaller and larger ones.

At this point, one may wonder whether the FGGE analyses improve our understanding regarding atmospheric spectral energetics. Of course numerical values of some energy variables increase (e.g., zonal energies) while others decrease (e.g., eddy energies) during the FGGE year. Nevertheless, the general features of atmospheric spectral energetics do not change using the FGGE analysis. The ω field, which always imposes difficulties for atmospheric energetics studies, still exists. Finally, the FGGE analyses provide us better data to obtain a more complete understanding of the spectral energetics for the southern hemisphere.

ACKNOWLEDGEMENTS

This study is supported in part jointly by the National Science Foundation and the National Oceanic and Atmospheric Administration under Grant Number ATM8206798, by the NOAA Grant NA82AA-D-00035, and by the National Aeronautics and Space Administration Grant NAG5-105. The computations of this study were mainly performed on the Cray-1 computer of the National Center for Atmospheric Research, which is sponsored by National Science Foundation. Thanks also go to Dr. Douglas Yarger for editorial comments.

REFERENCES

Baker, W. E. (1983). Objective analysis and assimilation of observational data from FGGE. Mon. Wea. Rev. 111, 328-342.

Baker, W. E., E. C. Kung, and R. C. J. Somerville (1977). Energetics diagnosis of the NCAR general circulation model. Mon. Wea. Rev. , 1384-1401.

Bengtsson, L., M. Kanamitsu, P. Kallberg, and S. Uppala (1982). FGGE 4-dimensional data assimilation at ECMWF. Bull. Amer. Meteorol. Soc. 63, 29-43.

Chen, T.-C. (1982). A further study of spectral energetics in the winter atmosphere. Mon. Wea. Rev. 110, 947-961.

Chen, T.-C., and J. Shukla (1983). Diagnostic analysis and spectral energetics of a blocking event in the GLAS climate model simulation. Mon. Wea. Rev. 111, 3-22.

Chen, T.-C., and H. G. Marshall (1984). A further study on the atmospheric energetics of large-scale motions in the tropics during the FGGE summer. Tech. Rep., Dept. of Earth Sciences, Iowa State University. 28 pp.

Cressman, G. P. (1959). An operational objective analysis system. Mon. Wea. Rev. 87, 329-374.

Desbois, M. (1975). Large-scale kinetic energy spectra from Eulerian analysis of EOLE wind data. J. Atmos. Sci. 33, 1838-1847.

Hansen, A. R., and T.-C. Chen (1982). A spectral energetics analysis of atmospheric blocking. Mon. Wea. Rev. 110, 1146-1165.

Kanamitsu, M. (1983). Some climatological and energy budget calculations using the FGGE IIIb analyses during January 1979. Dynamic Meteorology: Data Assimilation Methods, Spring-Verlag, New York, 263-318.

Kao, S.-K, R. J. Jenne, and J. F. Sagendorf (1970). The kinetic energy of large-scale atmospheric motion in wavenumber-frequency space: II. Midtroposphere of the southern hemisphere. J. Atmos. Sci. 27, 1008-1020.

Kao, S.-K, R. J. Jenne, and J. F. Sagendorf (1971). Spectral characteristics of the meridional transport of angular momentum in the midtroposphere of the southern hemisphere. Pure Appl. Geophys. 86, 171-183.

Machenhauer, B. (1977). On the dynamics of gravity oscillations in a shallow-water model, with application to normal mode initialization. Beitr. Phys. Atmos. 50, 271-283.

Matsuno, T. (1966). Numerical integrations of the primitive equations by a simulated backward-difference method. J. Meteorol. Soc. Japan 44, 76-84.

Miyakoda, K., J. Sheldon, and J. Sirutis (1982). Four-dimensional analysis experiment during the GATE period. Part II. J. Atmos. Sci. 39, 486-506.

Newell, R. E., J. W. Kidson, D. G. Vincent, and G. J. Boer (1974). The General Circulation of the Tropical Atmosphere. MIT Press, 370 pp.

Oort, A. H., and J. P. Peixoto (1974). The annual cycle of the energetics of the atmosphere on a planetary scale. J. Geophys. Res. 79, 2705-2719.

Oort, A. H., and J. P. Peixoto (1983). Global angular momentum and energy balance requirements from observations. Advances in Geophysics 25, 355-490.

Perry, J. S. (1967). Long-wave energy processes in the 1963 sudden stratosphere warming. J. Atmos. Sci. 24, 539-550.

Physick, W. L. (1981). Winter depression tracks and climatological jet streams in the southern hemisphere during the FGGE year. Quart. J. Roy. Meteorol. Soc. 107, 883-898.

Price, P. G. (1975). A comparison between available potential energy and kinetic energy estimates for the southern and northern hemispheres. Tellus 27, 443-452.

Reed, R. J., J. L. Wolfe, and H. Nishimato (1963). A spectral analysis of the energetics of the stratospheric sudden warming of early 1957. J. Atmos. Sci. 20, 256-275.

Salby, M. L. (1982). A ubiquitous wavenumber-5 anomaly in the southern hemisphere during FGGE. Mon. Wea. Rev. 110, 1712-1720.

Saltzman, B. (1957). Equations governing the energetics of the larger scales of atmospheric turbulence in the domain of wavenumber. J. Meteorol. 21, 513-523.

Saltzman, B. (1970). Large-scale atmospheric energetics in the wavenumber domain. Rev. Geophys. Space Phys. 8, 289-302.

Steinberg, H. L., A. Wiin-Nielsen, and C.-H. Yang (1971). On nonlinear cascades in large-scale atmospheric flow. J. Geophys. Res. 76, 8829-8640.

Trenberth, K. E. (1984). Interannual variability of the southern hemisphere circulation: Representativeness of the year of the global weather experiment. Mon. Wea. Rev. 112, 108-123.

van Loon, H. (1980). Transfer of sensible heat by transient eddies in the atmosphere on the southern hemisphere: An appraisal of the data before and during FGGE. Mon. Wea. Rev. 108, 1774-1781.

Wiin-Nielsen, A. (1967). On the annual variation and spectral distribution of atmospheric energy. Tellus 19, 540-559.

OMIT

7. IMPROVEMENTS IN PREDICTABILITY

Organizer	Norman A. Phillips
Session Chairman	Norman A. Phillips
Speakers	Lennart Bengtsson Kikuro Miyakoda
Rapporteur	Jagadish Shukla

D15

MEDIUM RANGE FORECASTING--THE EXPERIENCE OF ECMWF

Lennart Bengtsson
European Centre for Medium Range Weather Forecasts

ABSTRACT

The result of five years of operational medium-range forecasts at ECMWF is discussed. It is shown that a considerable improvement in predictive skill has taken place, resulting in more accurate forecasts and an extension in time of useful predictive skill. For the northern hemisphere extratropics, the improvement in skill during the winter season is about three days for the 500 mb geopotential compared to the very first experiments in the early 1970s. There are large geographical and temporal variations in the performance of the model, as well as large-scale errors of a systematic nature. Numerical experiments have indicated great sensitivity to the representation of orography and to tropical forcing.

INTRODUCTION

A substantial improvement has taken place in numerical weather prediction since the first numerical forecasts were made almost 35 years ago. This is essentially due to much better and more realistic models but also to the considerable increase in meteorological observations that has taken place over the period. The improvement is manifested in two ways, more accurate short-range forecasts and a substantial extension in time of useful predictive skill. Today four-day forecasts for the 500 mb geopotential are now as accurate as the one-day forecast produced in the early 1950s (Table 1).

The role of the Global Weather Experiment, in addition to providing for the first time a truly global observing system, was to act as a focal point for the considerable research efforts in data assimilation and numerical experimentation that followed the planning and implementation of the experiment. This work has particularly benefited forecasts in the medium range (two days to two weeks) that require global data sets and advanced general circulation type models.

We will here report the experience of operational forecasting for periods up to ten days ahead at the European Centre for Medium Range Weather Forecasts (ECMWF), which began on August 1, 1979. At the time of writing there exists a five-year record of forecast results that can

TABLE 1 Standard Deviation Error for 500 mb Forecast over Europe

Forecast time	Nov. 51-Apr 54 (24 cases) Barotropic model	Jan. 81 Barotropic model	Jan. 81 ECMWF	Jan. 84 ECMWF
24h	76m	47m	22m	21m
48h		97m	41m	38m
72h		151m	62m	57m
96h			85m	75m

Column 1 Results of 24 operational and quasi-operational 24h predictions by the barotropic model (Staff members, University of Stockholm, 1954).

Column 2 Barotropic forecast for the Northern Hemisphere during January 1981. Initial state taken from the operational ECMWF analyses.

Column 3 ECMWF Operational forecast for January 1981.

Column 4 " " " " January 1984.

be examined to shed light on a number of questions concerning atmospheric predictability on a time scale of ten days and beyond. The record may be used to define present levels of forecast accuracy, including its geographical and temporal variability and its dependence on the prevailing synoptic situation. We will in this paper describe some results from studies of the performance of the ECMWF model. The experience of the first two years of operational medium-range weather prediction has been summarized by Bengtsson and Simmons (1983), and much of what is reported here is by and large in agreement with the earlier results.

We will begin the presentation in this paper by giving a short description of the ECMWF forecasting system including the developments that have taken place over the past five years. Methods of forecast assessment are then discussed, followed by a summary of the current overall level of forecast accuracy.

Finally, we will discuss the question of systematic model errors followed by some concluding remarks.

THE ECMWF GLOBAL FORECASTING SYSTEM

The Data-Assimilation System

The ECMWF data assimilation system uses a three-dimensional multivariate analysis scheme, described by Lorenc (1981), to produce initial analysis of geopotential and wind fields for the forecast model, and a correction method for the analysis of humidity. Analyses are produced every six hours, with the forecast model providing the first guess for the analyses, which in turn provide the initial state for the six-hour forecasting step required to produce the first guess for the following analysis. Observations are analyzed at 15 standard pressure levels from 1000 to 10 mb, and first guess data interpolated (or extrapolated) to these levels from the coordinates of the forecast model. In the version of the data assimilation system first introduced in operational use and also used at ECMWF to produce the FGGE Level III-b data set (Bengtsson et al., 1982a), complete pressure level fields from the analyses were similarly interpolated back to the model levels prior to a non-linear normal mode initialization (Temperton and Williamson, 1981; Williamson and Temperton, 1981).

The basic nature of data assimilation has not changed over the five years of operational use, but there have been numerous revisions. In December 1980 a change was introduced in the interpolation from analyses at pressure levels to model σ-levels in that only the difference between the analyzed and the first guess field was interpolated rather than the full analyzed field. This change was done to preserve the model boundary layer structure through the analyses since the lowest analyzed pressure levels at 1000 and 850 mb are insufficient to define such structure.

In May 1984 a new set of statistical structure functions was introduced into the operational analysis scheme. These were empirically obtained from archived differences of observed first-guess values and had the effect of providing a better fit between observations and the analysis (Shaw et al., 1984).

The adiabatic non-linear normal mode initialization was modified in September 1982 with an incorporation of an estimate of the diabatic effects. This was obtained by averaging a two-hour integration from an uninitialized analysis, and to let this average forcing act on the large-scale components. This change to the initialization had the effect of enhancing the large-scale circulation in the tropics and to strengthen the divergent wind.

In July 1982 the climatological sea-surface temperatures were replaced by operational analyses of the sea-surface temperatures produced by the U.S. National Meteorological Center, and in November 1983 analysis of soil moisture and snow depth began.

The Forecast Model

The numerical formulation of the forecast model has been substantially modified over the five-year period. The version chosen for the

first phase of operational forecasting used a potential enstrophy conserving finite difference scheme for a staggered (Arakawa C) grid, a σ-coordinate for the vertical representation, and a semi-implicit time scheme for the treatment of gravity wave terms. A resolution of 1.875^{o} in latitude and longitude, with 15 levels in the vertical, was adopted. Details have been given by Burridge and Haseler (1977) and Burridge (1979). Changes in the horizontal diffusion and the introduction of a more realistic representation of the orography and coastlines took place during the first two years of operational use.

A major change was introduced in April 1983. The new version of the operational model uses a spectral formulation in the horizontal, with triangular truncation at total wave number 63(T63); a vertical coordinate (with 16 level resolution), following the model terrain at low levels but reducing to pressure in the stratosphere; and a modified, more efficient, time-stepping scheme. The operational change to this version was accompanied by a change to a higher "envelope" orography in the model. These changes have been described in Girard and Jarraud (1982), Simmons and Burridge (1981), Simmons and Jarraud (1984), Simmons and Strüfing (1983), and Wallace et al. (1983). In the light of operational experience, minor adjustments of the orography, horizontal diffusion and time scheme have subsequently taken place.

The parameterization schemes described by Tiedtke et al. (1979) have been used with both versions of the operational model. They include a convection scheme following Kuo (1974), a stability dependent representation of boundary and free atmospheric turbulent fluxes (Louis, 1979), and a radiation scheme (Geleyn and Hollingsworth, 1979), which includes interaction with model generated clouds. A number of minor adjustments of the parameterization have taken place during operational use, but the most noteworthy change was the introduction of a diurnal radiative cycle in May 1984.

METHODS OF ASSESSMENT

Assessment of medium-range forecasts can be carried out in three different ways. The first is assessment by objective measures. For the convenience of this paper, we will concentrate our attention on the anomaly correlation coefficient which we have found to be a useful measure for medium-range forecasting. The second is by subjective evaluation by experienced meteorologists. The third is by examination of the physical consistency of the forecasts such as the budget of heat and momentum.

A question that arises with objective scoring of forecasts is the level of score that constitutes the limit beyond which a forecast is no longer useful. There is no unique answer to such a question, since the level of accuracy required for a forecast to be useful depends very much on the purpose for which the forecast is to be used. At the extreme a positive anomaly correlation may be an indication that the forecast possess some skill, but in general a more restrictive criterion is used. Long series of intercomparison against subjective evaluations indicate that the limiting value is 50 to 60 percent. It

should be noted however that such criteria assume a forecast for one particular incident to be judged against the analyses for precisely that time. A forecast that is poor in synoptic detail or timing may score badly while still providing useful guidance of the overall change in the weather type.

ACCURACY OF FORECASTS IN THE MEDIUM RANGE

Northern Hemisphere Forecasts

The predictive skill of the model varies considerably in space and time. An impression of the variation in predictability with spatial scale may be gained from Figure 1a which shows anomaly correlation for three separate groups of zonal wavenumbers for the 500 mb height field. A spectral decomposition demonstrates the larger scales to be more accurately predicted in contrast to earlier experience reviewed by Leith (1978), where medium scales were reported to be predicted better than the planetary scales. There is also a very much poorer forecast of the shorter synoptic scales, here represented by zonal wavenumbers 10 to 20. This latter result may be associated with erroneous timing or intensities of individual weather events within an overall weather situation that is better predicted, but examples may also be found in which the erroneous forecast of a small-scale feature is followed by deterioration of the forecast over a much larger area.

Spatial variability of predictive skill has also been examined by comparing objective measures over more limited areas. These scores vary considerably from area to area and are often affected by systematic model errors that have a typical geographical distribution at least during the winter time. We will comment on this in the next section.

The predictive skill also varies considerably with height. The lower troposphere is strongly influenced by small-scale features, while in the upper troposphere and lower stratosphere the long waves dominate. This can be seen from Figure 1b, which shows the anomaly correlation of 50 mb, 500 mb, and 1000 mb height fields calculated for most of the extratropical northern hemisphere, and average over all operational forecasts from December 1983. This shows that 50 mb provide the most accurate forecasts and also that the forecast at 500 mb is generally more accurate than at 1000 mb, a result that is in agreement with synoptic assessment. Useful predictive skill at 500 mb is noticed up to around day 6 and day 7. The high predictive skill at 50 mb in the wintertime is common and interesting to note. Bengtsson et al. (1982b) have demonstrated an excellent ten-day prediction of a splitting up of a polar night vortex into two separate vortices that took place in February 1979.

Figure 2 shows that there are large variations with time in the quality of the forecasts, with a minimum skill in the summer and a maximum skill in the winter. In addition to this, there is a significant interannual variation in the predictive skill as well as significant variation within the month. Figures 3 to 5 show examples

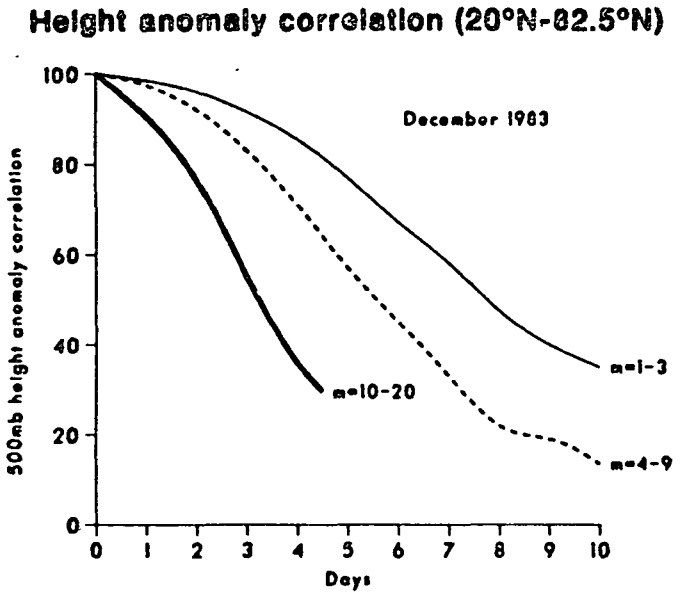

FIGURE 1a Height anomaly correlation scores for wavenumbers 1-3, 4-9, and 10-20 ECMWF northern hemisphere forecasts (90-20°N), December 1983.

of two seven-day forecasts for November 1983, a month where the forecasts varied very much between the first and second part of the month (Figure 3). The two forecasts have been selected from these two episodes and illustrate a good forecast (Figure 4) versus a bad forecast (Figure 5), respectively.

Figure 6 shows the daily anomaly correlation scores for 500 mb for the first three months of 1982 and 1983. Large variations in the predictive skill are evident, and spells of high skill dominate the second winter. It should be added that only minor changes were made to the model and the data assimilation system over the period in question.

Figure 7 shows the average analyzed 500 mb height field for January 1982, the ensemble ten-day forecast, and the corresponding deviation from climate. Figure 8 shows the same maps for January 1983. It is clearly seen that the prediction of the stationary component (monthly averages) is very good in 1983 but correspondingly bad in 1982. An inspection of the predictive skill of the stationary component over a two-year period shows relatively large variations from year to year with no particular seasonal variation. January 1982 was in that context distinctly worse than other months.

Figure 9 shows the anomaly correlation for the same three separate groups of zonal wavenumber as was used for Figure 1a. As can be seen by comparing the two months, the low predictive skill in January 1982 was very much related to lower than normal scores for the planetary waves. The scores for the short-wave zonal wavenumbers 10 to 20, on the other hand, are essentially the same for the two months.

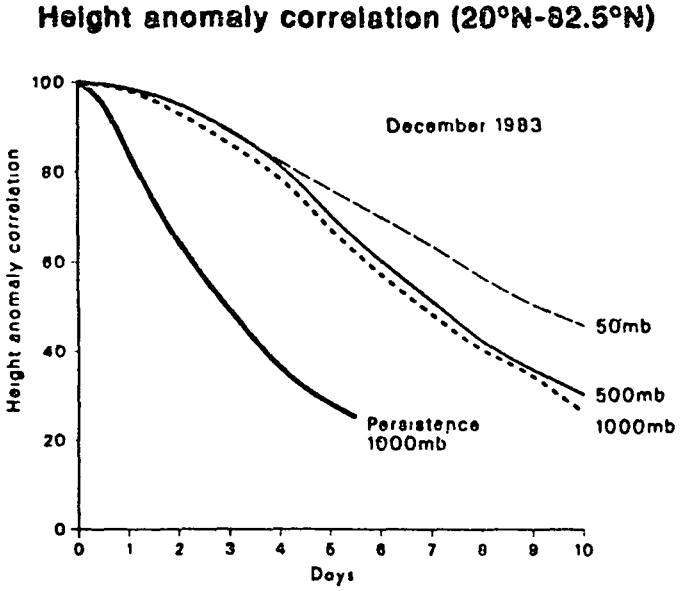

FIGURE 1b Height anomaly correlation scores, ECMWF 50, 500, and 1000 mb northern hemisphere forecasts, December 1983, and persistence scores for 1000 mb.

The fact that numerical models show spells of high and low predictive skills lasting for periods of a week to several weeks appears to be typical of other operational models, Bengtsson and Lange (1982) and Lange and Hellsten (1983), for forecasts up to three days. In some of the cases of high predictive skill, as has been discussed by Bengtsson and Simmons (1983), the model correctly maintains a highly anomalous flow. On other occasions large changes, such as the development of blocking highs or breaking down of blocks, occur. It may be that spells of high predictive skill simply reflect that the atmosphere is confined to a more predictable regime; alternatively, it may also be possible that a particular model can handle certain weather types better than others. No conclusive answer to this fundamental question can as yet be given.

Tropical and Southern Hemisphere Forecasts

The tropical forecasts have not been evaluated in as extensive or objective a way as those for the extratropical northern hemisphere, but there is no doubt that at present their accuracy and usefulness is substantially less. Objective verification indicates a limited short-range predictive skill in the middle and upper troposphere. Thus for the belt from 18°N to 18°S the root mean square error (rmse) of

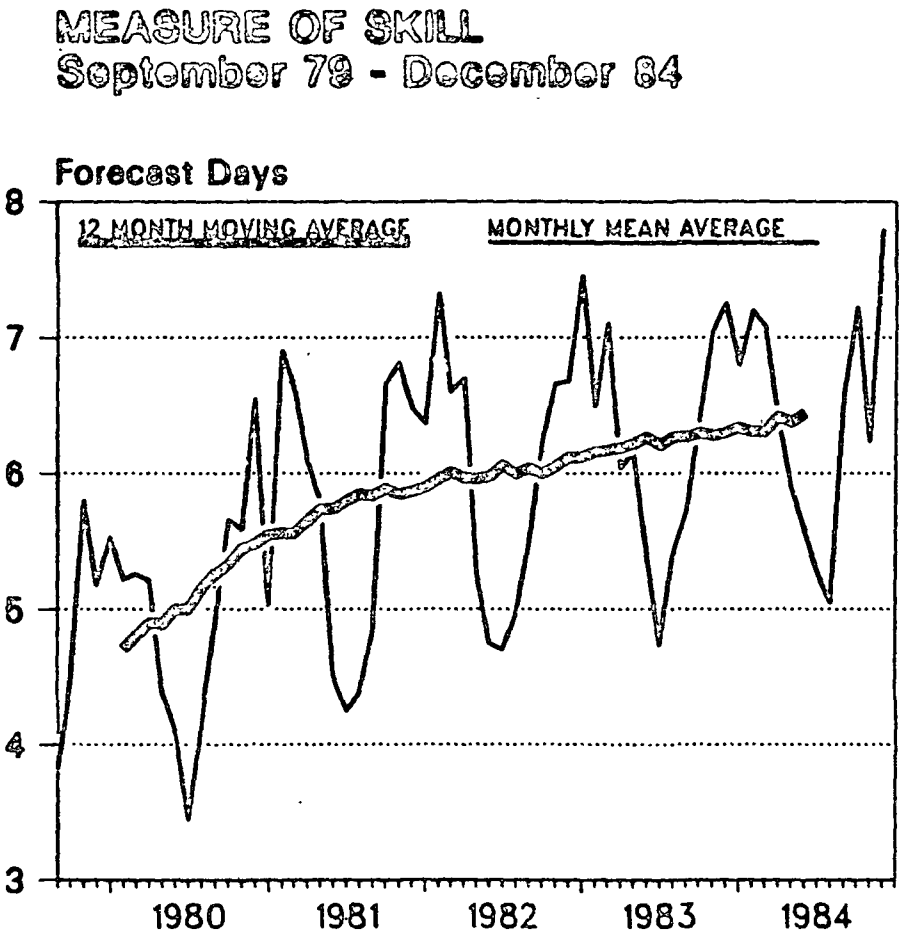

FIGURE 2 A measure of the skill of ECMWF northern hemisphere forecasts for the period September 1979 to December 1984. The ordinate shows the number of days of predictive skill as assessed from monthly means of daily averages of the anomaly correlations and standard deviation of the errors of geopotential height and temperature forecasts for levels 1000 to 200 mb (height) and 850 to 200 mb (temperature).

the two-day forecast of vector wind averaged in 1983 is 4.8 m/s at 500 mb compared with 6.8 m/s for persistence.

The indication from both subjective and objective assessments of the tropical forecasts is that there are serious deficiencies in the parameterization of convection, and substantial efforts to understand and correct these deficiencies are currently being made. Forecast experiments reported by Bengtsson and Simmons (1983) have shown a great sensitivity to the parameterization of moist convection. Tiedtke (personal communication) has pointed out a similar sensitivity to the handling of shallow convection.

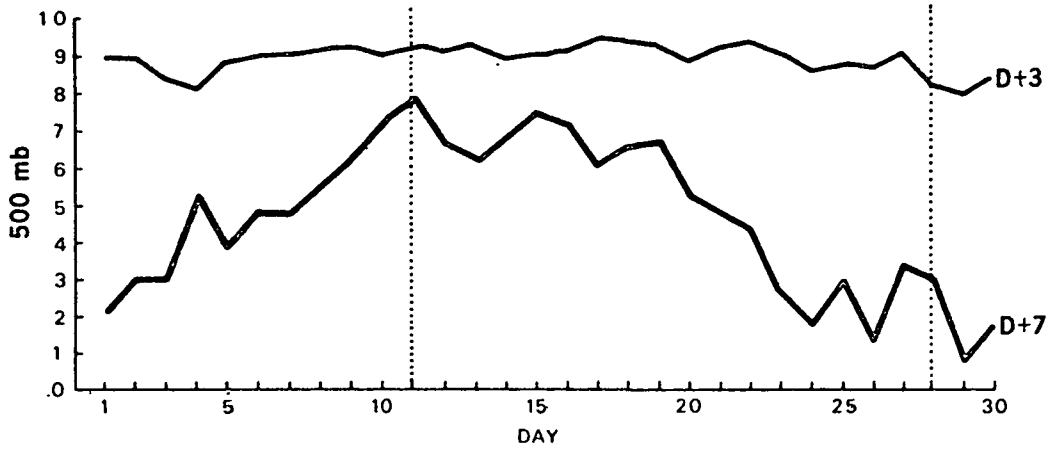

FIGURE 3 Anomaly correlation of 500 mb height scores for the northern hemisphere of ECMWF 3-day (D+3) and 7-day (D+7) forecasts for each day of November 1983. Note the high scores of the D+7 forecasts around November 11 (see Figure 4), and the low scores of the forecasts around November 28 (see Figure 5).

Other studies have also shown sensitivity to the prescription of soil moisture and orography, results in general agreement with those found elsewhere (e.g., Rowntree, 1978). Overall, it seems that the tropical forecasts respond more quickly and directly to defects in the model than do forecasts at middle and high latitudes.

Assessment of the forecasts for the southern hemisphere has been less comprehensive than for the northern hemisphere. Comparing the anomaly correlations for the two hemispheres shows that the forecast skill at a 60 percent level is about 1.5 days less for the southern hemisphere. The lower values obtained for the southern hemisphere are not surprising in view of the sparsity of data for this hemisphere. Generally more accurate forecasts have been obtained during FGGE (Bengtsson, 1983).

SYSTEMATIC MODEL ERRORS

It is reasonably well established that prediction of instantaneous weather patterns at sufficiently long range is impossible, and it is generally accepted that there is an inherent limitation in the predictability of the atmosphere which probably is of the order of a few weeks. While this is the case for instantaneous weather patterns there are clear indications, e.g., Shukla (1984) and Miyakoda et al. (1983), that the predictability for time averages (5, 10, or 30 days) is longer, in particular in the tropics.

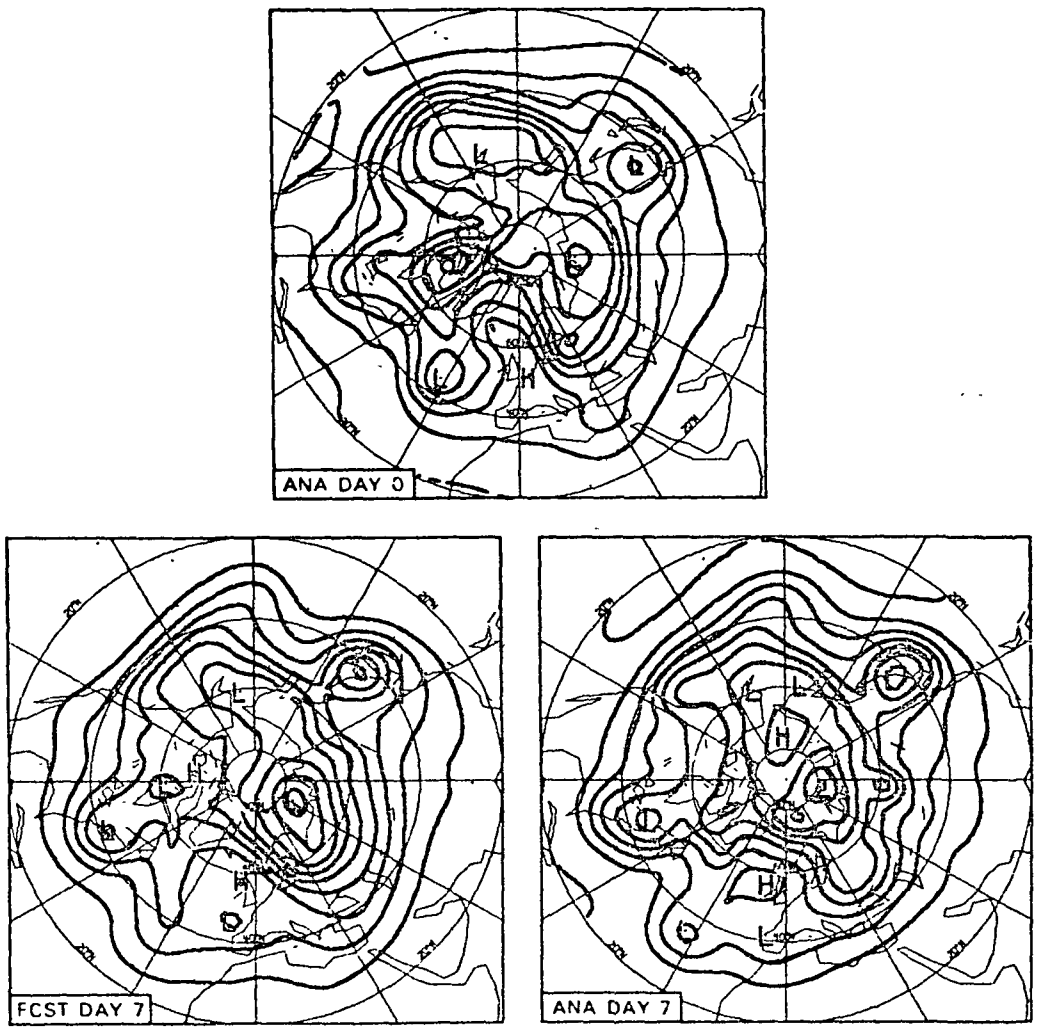

FIGURE 4 500 mb analysis of November 11, 1983 (top), D+7 forecast valid November 18, 1983 (bottom left), and verifying analysis of November 18, 1983 (bottom right).

Lorenz (1982), in a recent study comparing the growth of initial error of the ECMWF model with the actual forecast error growth, has demonstrated that there is scope for extending the range of useful forecasts by 3 to 4 days even with today's incomplete and inaccurate observations. More accurate initial states will naturally extend predictive skill further, and it appears, according to Lorenz, that a reduction of the initial error by half will extend predictive skill by about two days and presumably another reduction by half can give another two days.

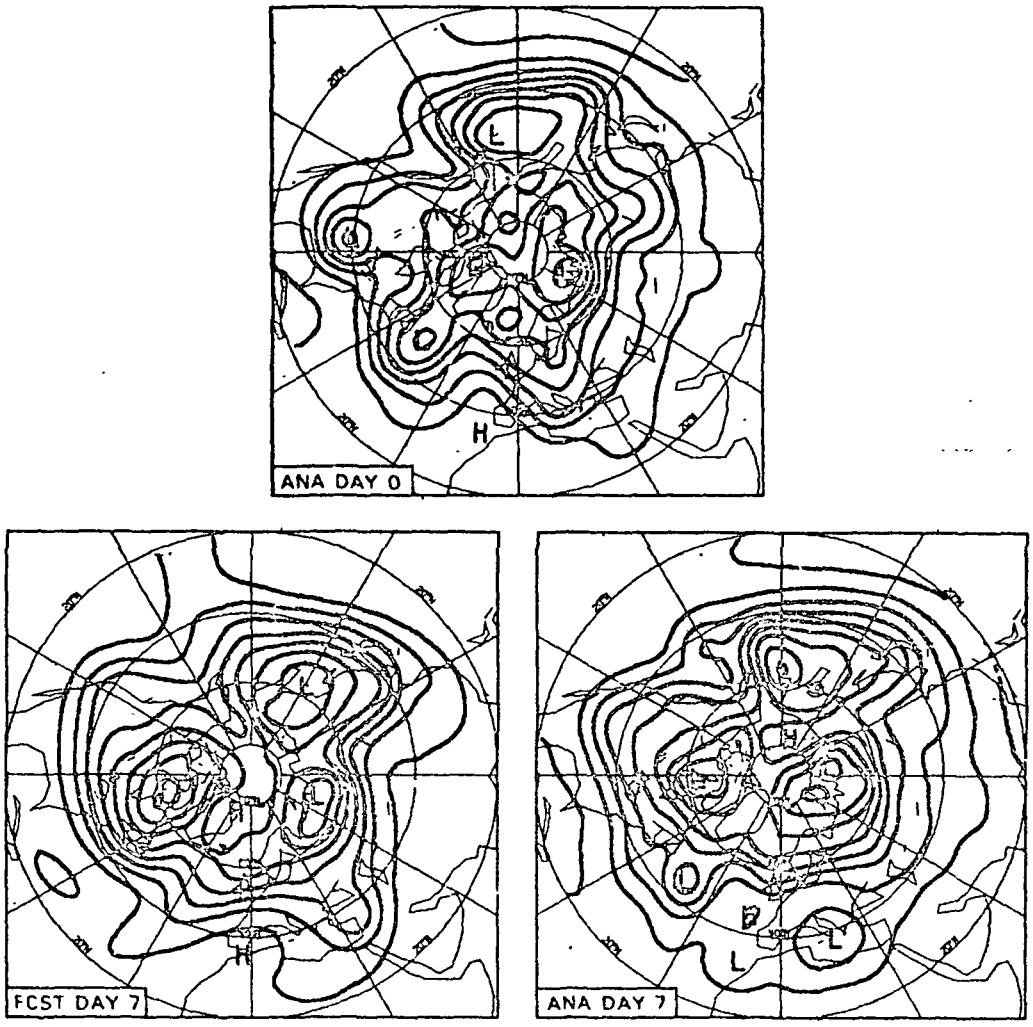

FIGURE 5 500 mb analysis of November 28, 1983 (top), D+7 forecast valid December 5, 1983 (bottom left), and verifying analysis of December 5, 1983 (bottom right).

The improvements in medium-range forecasts are likely to fall into the largest scales of motion where it is found that the predictions have large errors of a systematic nature (Bengtsson and Simmons, 1983). These errors are revealed by averaging forecasts over a number of cases, generally one month or a season. These errors characteristically grow in amplitude throughout the forecast period, and their general similarity to errors in the model climatology, revealed by integrations over extended periods, indicates that these errors represent a gradual drift from the climate of the atmosphere to that of

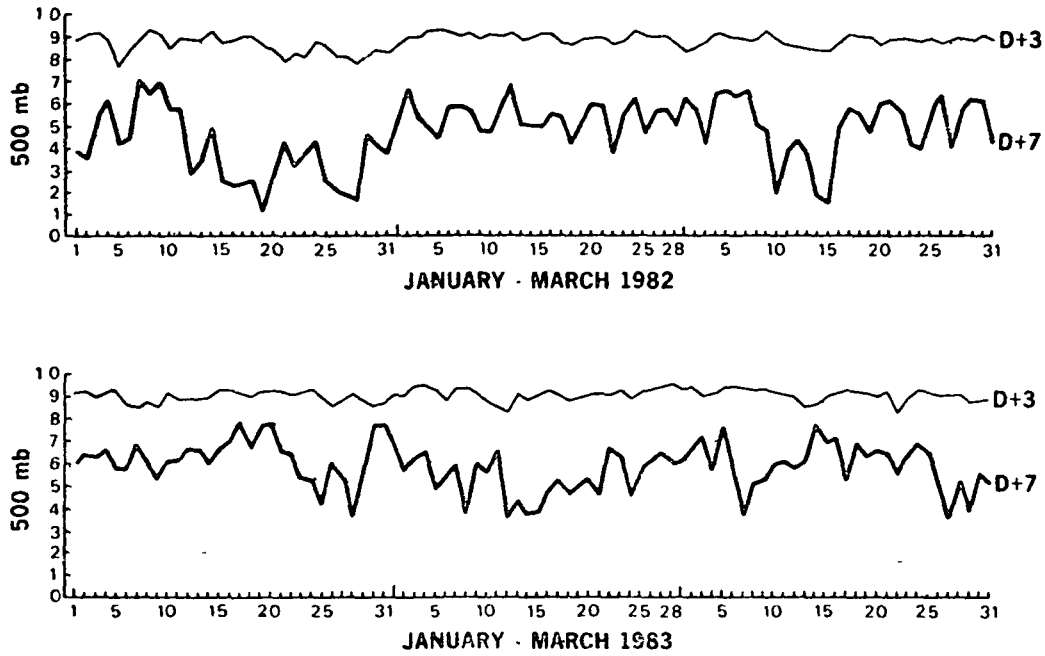

FIGURE 6 Anomaly correlation of 500 mb height for the northern hemisphere scores of ECMWF 3-day (D+3) and 7-day (D+7) forecasts for the period January 1 to March 31, 1982 (top), and 1983 (bottom). Note the long periods of relatively high D+7 scores in the 1983 scores.

the model. The rate of this drift is found to vary from case to case, but the overall error associated with it appears to be independent of the initial data.

The model shows an average cooling of about 1.5°C in ten days. In extended model integrations this cooling continues for another 50 days and reaches an equilibrium value of about 3 to 4°C. No further cooling takes place hereafter and appears also to be almost independent of resolution; a T21 version of the model has been integrated for 10 years without any further cooling. There is an area of maximum cooling in the midtroposphere around 500 mb and another one in the stratosphere. Figure 10 shows four ensemble temperature profiles, observed and predicted, at the latitudes 0°, 30°N, 55°N, and 80°N. This tropospheric cooling has been noted for other models as well but can however be sensitive to a number of aspects of model design, including not only the parameterization of diabatic processes but also such features as the prescription of the orography (Wallace et al., 1983) and the amount of horizontal smoothing of model fields (Girard and Jarraud, 1982), both of which may influence precipitation and the associated latent heat release. The increased flux of sensible heat, associated with the incorporation of a diurnal radiation cycle, now included in the operational model, reduces the overall cooling by about 25 percent.

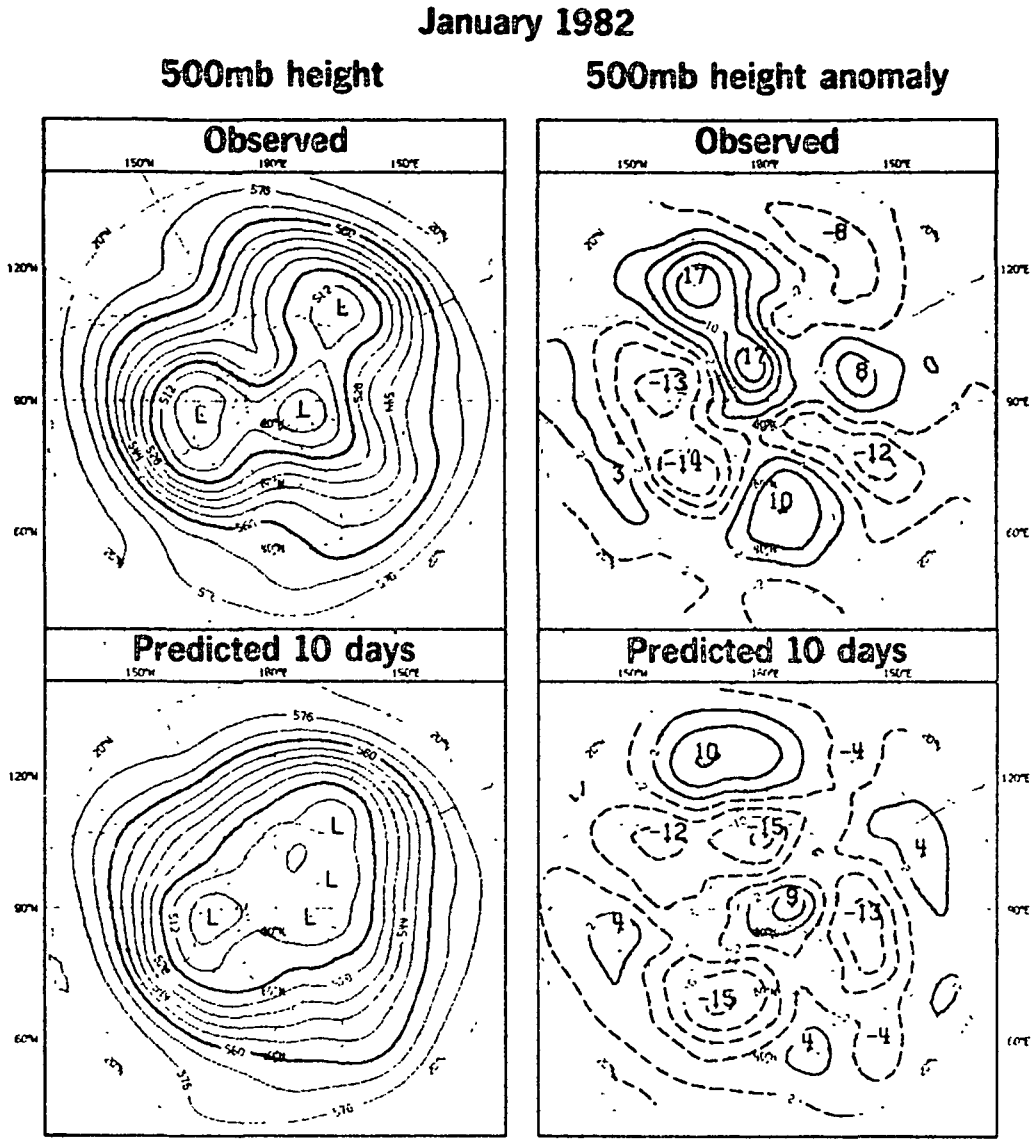

FIGURE 7 January 1982 500 mb height and anomaly as observed and as predicted in ECMWF 10-day forecasts.

Temperature errors become more pronounced at upper levels, where there is a general tendency for the stratosphere to be too cold, particularly near the winter pole. Associated with this, the stratospheric polar night jet is generally too strong and often insufficiently separated from the main subtropical jet. Whether this

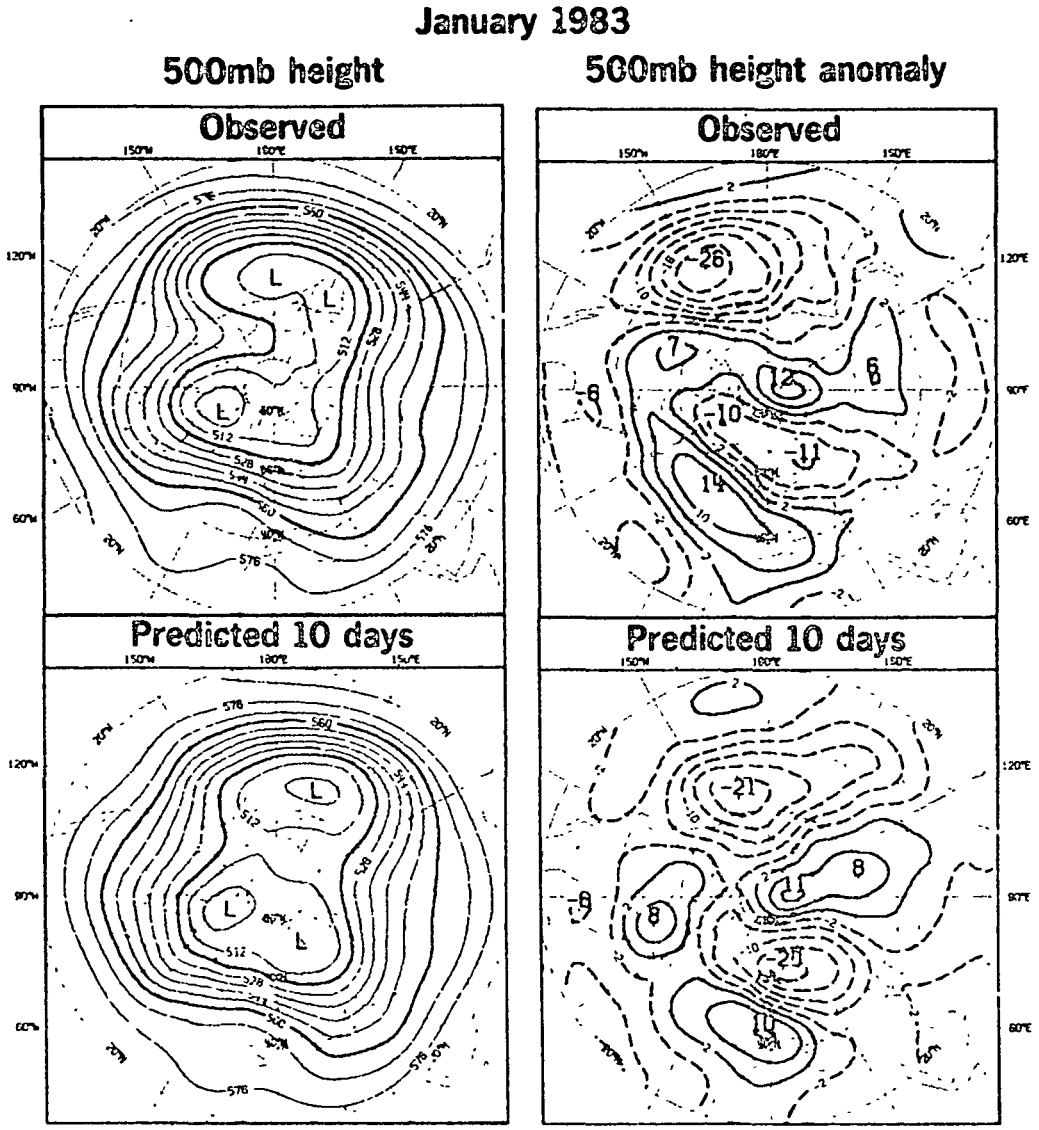

FIGURE 8 January 1983 500 mb height and anomaly as observed and as predicted in ECMWF 10-day forecasts.

is related to the treatment of radiative fluxes in the model or due to dynamical processes has yet to be demonstrated.

The model also shows associated deficiencies in the zonally averaged flow. At the surface, the middle latitude westerlies are generally found to be a few meters per second stronger than observed in the northern hemisphere. It is interesting to note that this discrepancy

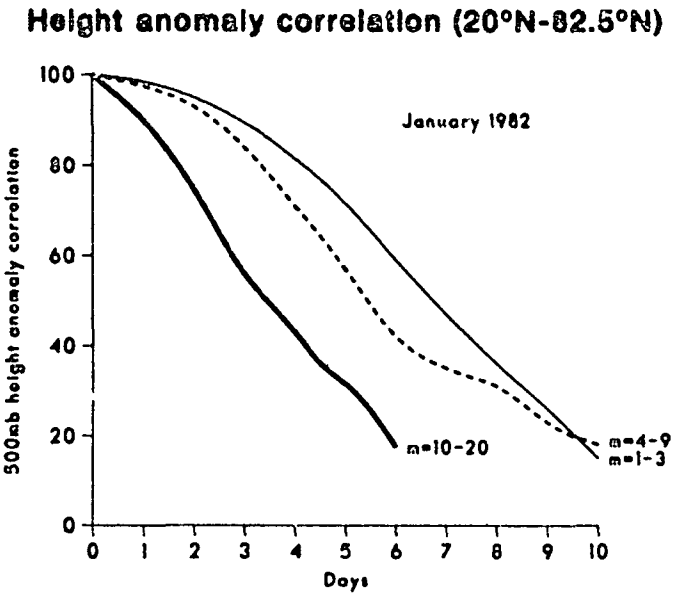

FIGURE 9a Height anomaly correlation scores for wavenumbers 1-3, 4-9, and 10-20 ECMWF northern hemisphere forecasts, January 1982.

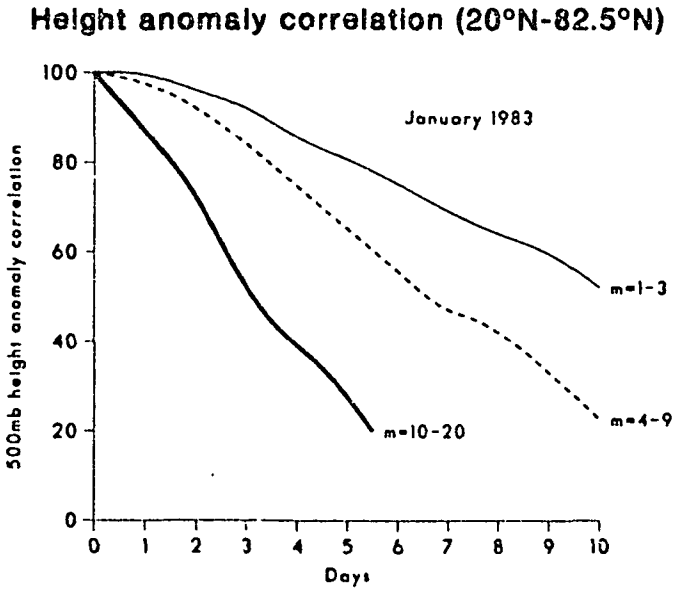

FIGURE 9b Height anomaly correlation scores for wavenumbers 1-3, 4-9, and 10-20 ECMWF northern hemisphere forecasts, January 1983.

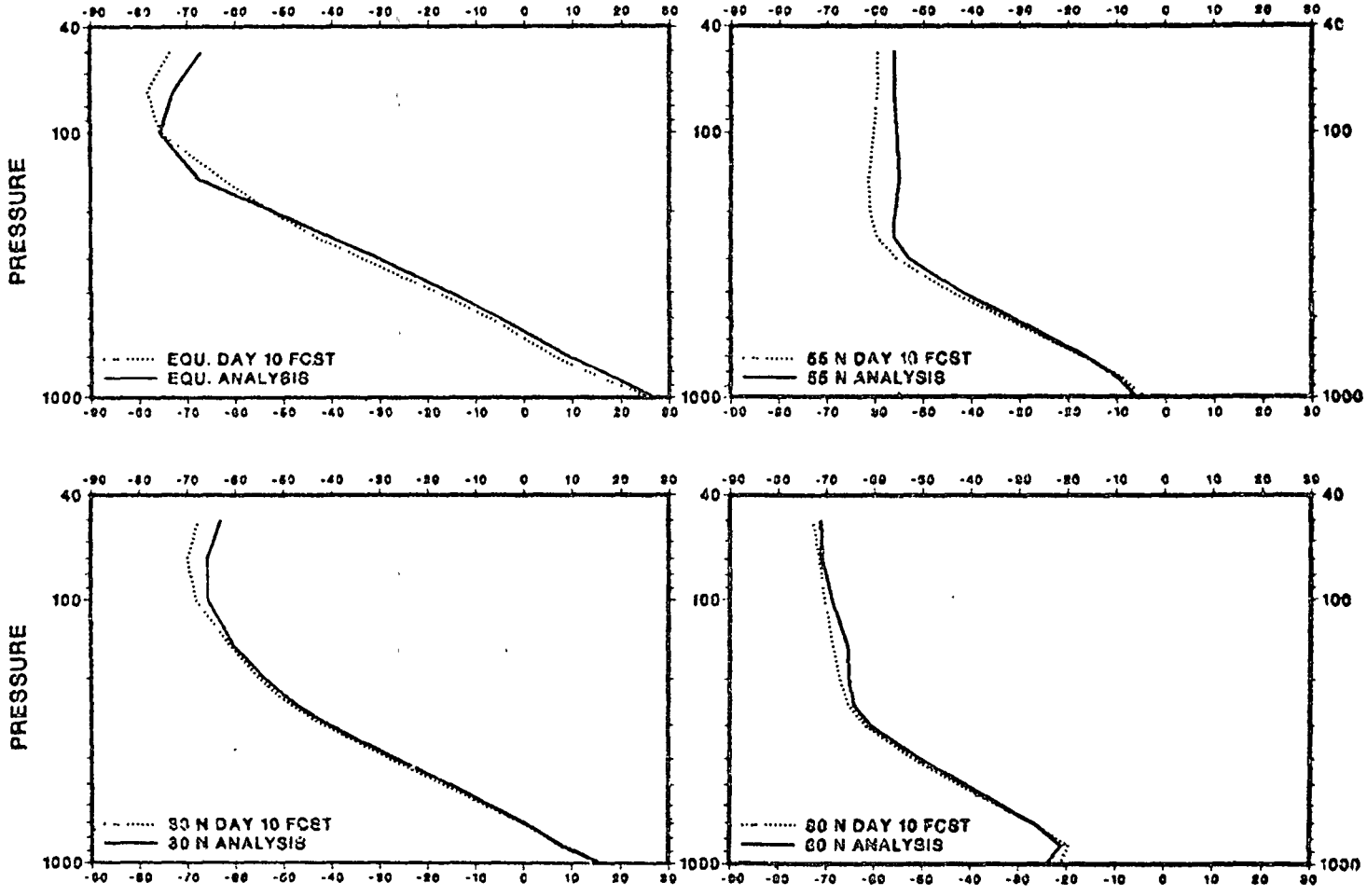

FIGURE 10 Vertical temperature profiles of ECMWF 10-day forecast (dotted line) and the verifying analyses (solid line) at the Equator (top left), 30°N (bottom left), 55°N (top right), and 80°N (bottom right).

becomes more pronounced when the horizontal resolution is increased (Manabe et al., 1979; Cubasch, 1981); conversely, higher resolution (T40 or more) generally yields a better simulation of the stronger surface westerlies of the southern hemisphere. In the upper troposphere, westerly maxima are usually found to be too strong (by a few meters per second) and displaced slightly poleward and upward. Tropical easterlies tend to be underestimated near the tropopause and overestimated at higher stratospheric levels.

More interesting details of the systematic errors are revealed by an inspection of their geographical distribution. Maps of the day 10 temperature error at 500 and 850 mb and of the 500 and 1000 mb height error are presented in Figure 11.

Looking first at the height field, we see very similar error patterns at 1000 and 500 mb with distinct centers of low pressure over northeastern Atlantic/Scandinavia and the northern Pacific Ocean. The amplitude of the error increases slightly with height, and consistent with this, areas of too low temperature tend to coincide with the areas of too low pressure, particularly at 500 mb. Elsewhere the 500 mb temperature error is small, but regions of substantially too warm 850 mb temperatures are evident over eastern Siberia and northern Canada. The general distribution of temperature error implies areas of too low static stability which is likely to be the cause of a slightly erroneous structure of the baroclinic waves.

Progress in the understanding of the slowly acting physical processes at large scales and a better description of orographic forcing are likely to improve the predictability of the large-scale features. As demonstrated by Wallace et al. (1983), the incorporation of an improved orographic representation by using an "envelope orography" has led to more accurate prediction of the large-scale flow, at least during the winter. Better understanding and modeling of the large-scale stationary forcing are expected to provide great benefits for forecasts in the tropics. As has been demonstrated by Krishnamurti et al. (1983), it is of great importance to have an accurate initial description of the diabatic forcing. If this is initially wrong due to lack of relevant observation or to an unsatisfactory initialization procedure, large errors develop quickly. The ECMWF model presently has problems of this kind over the African continent. The incorporation of satellite cloud observations as well as observations of precipitation in the initialization procedure, combined with diurnal cycle, are expected to reduce these errors.

A better handling of the modeling problems in the tropics is crucial for an improvement of medium-range forecasts and a further extension of useful predictive skill at higher latitudes. In order to demonstrate this, Haseler (1983) has carried out a series of numerical experiments with the ECMWF model where analyzed data were inserted at a boundary along 20°N in order to simulate a "correct" tropical forecast. As can be seen from Figure 12, large differences are created far downstream, and after six days the circulation over the European area is markedly influenced. A detailed analysis revealed in this case that the Hadley cell circulation over Central America and an extratropical depression moving eastward over the United States interacted, and the downstream development was strongly affected.

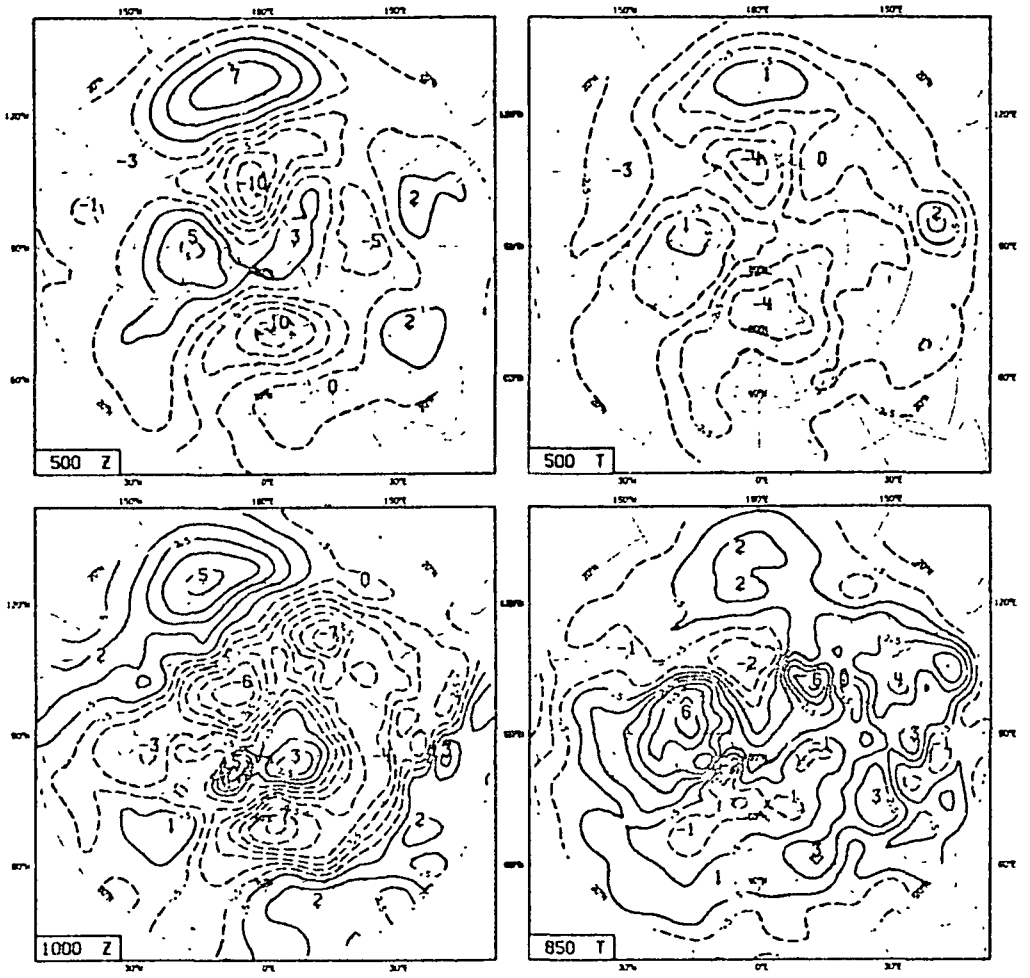

DECEMBER, JANUARY, FEBRUARY 1981/82 + 1982/83

FIGURE 11 Difference fields between ECMWF 10-day forecasts and the corresponding analysis for winters of 1981-1982 and 1982-1983. Top left--500 mb height, contour interval dam. Top right--500 mb temperature, contour interval ^{o}K. Bottom left--1000 mb height, 850 mb temperature, same contour intervals.

CONCLUDING REMARKS

Miyakoda et al. (1972), who carried out the very first medium-range forecasts, suggested that perhaps the results of their first comprehensive trial of two-week predictions might be taken as a benchmark for future comparison. Their ensemble mean anomaly correlation for the extratropical northern hemisphere based on 12

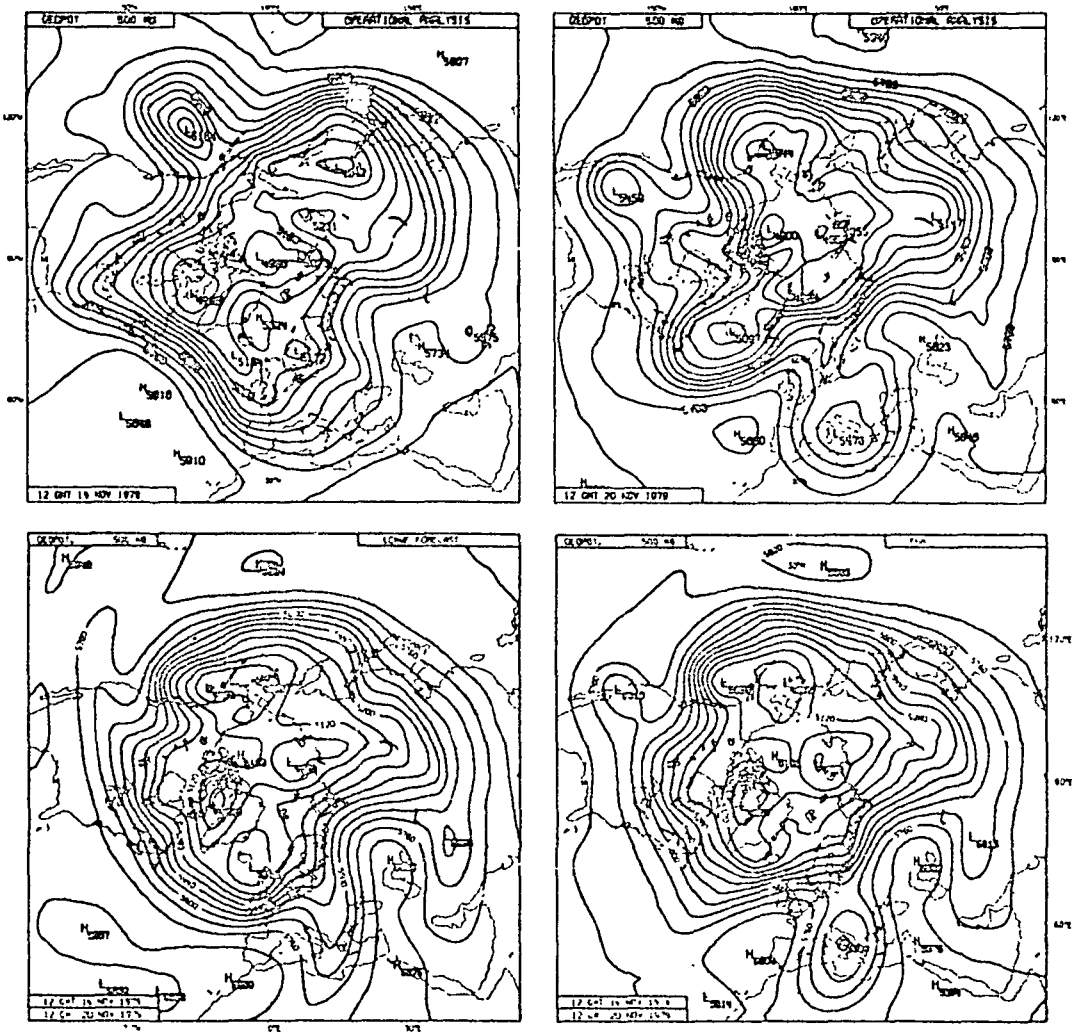

FIGURE 12 500 mb height analysis of November 14, 1979 (top left) and of November 20, 1979 (top right). Bottom left shows the 6-day operational forecast from November 14, 1979, bottom right the 6-day forecast which was obtained when the forecast was relaxed toward 6-hourly FGGE analyses in the tropics with pure analyzed values in the band 15°N and 15°S, pure forecast values to the north of 25°N and 25°S aand smoothly mixed values in the intermediate zones.

January cases taken from the years 1964 to 1969 reached values of 60 percent after about two days of the forecast period for the 500 mb height. The corresponding time for the 60 percent correlation was about 3.5 days. The average skill of the operational ECMWF forecasts

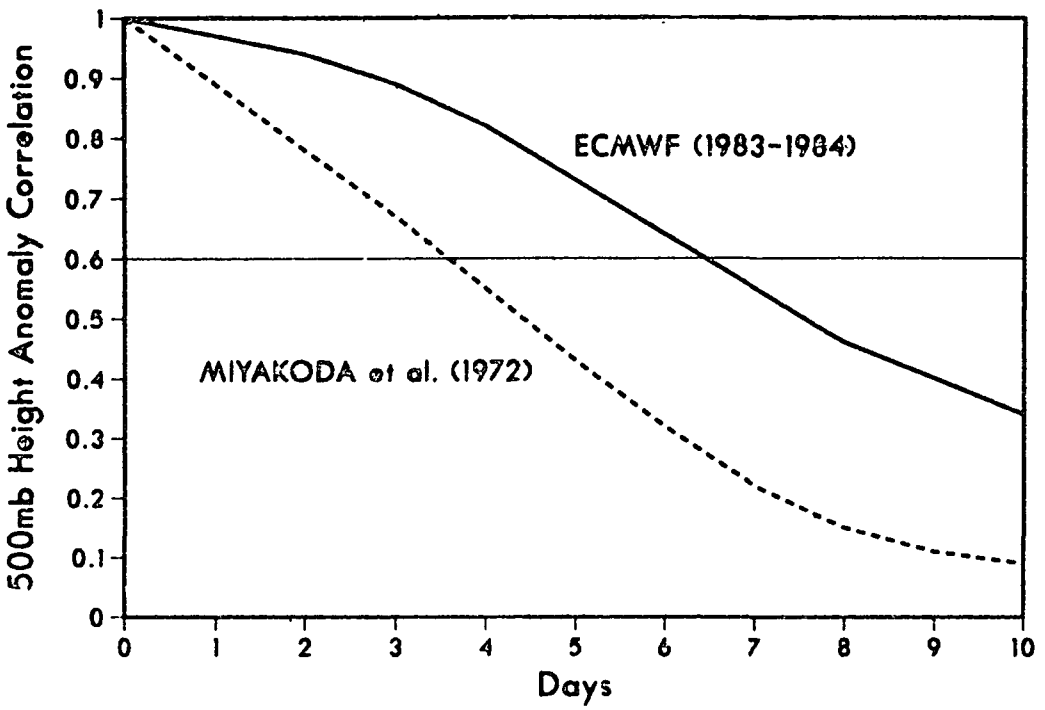

FIGURE 13 Mean 500 mb height anomaly correlations as functions of forecast range. The solid line denotes average results from ECMWF operational forecasts for the winters of 1983 and 1984, and the dashed curves show the mean of 12 forecasts from January cases chosen from the years 1964 to 1969, as reported by Miyakoda et al. (1972).

for the winter 1982/1983 and 1983/1984 was 4.5 days for the 80 percent correlation and 6.5 days for the 60 percent level (Figure 13).

These results indicate that a substantial improvement has taken place over the past 10 to 15 years in our ability to predict at least the larger scales of motion. These improvements are not only a reflection of model development and an extension of the area of integration to the whole globe but also of the considerable increase in meteorological observations that have taken place over the period. This has been demonstrated by observing system experiments using FGGE data, e.g., Bengtsson (1983), where, in particular, observations from satellites and from aircraft have had a substantial impact on forecasts in the medium range (2 to 14 days). Furthermore, observations are now better utilized due to improved analysis methods, more accurate initialization, and a more accurate and consistent use of the prediction model to provide the first guess.

The ongoing intense development in computer technology makes it possible that, toward the end of this decade, computers may be available with a processing speed more than 10 times faster than

today's supercomputer. This will make it possible to use global models with a horizontal resolution of the order of 50 km which will be able to resolve and describe the evolution of leewave cyclones and possibly also tropical cyclones. To what extent such a resolution is realistic for improving forecasts in the medium range and extend the limit of useful predictive skill in general remains to be demonstrated.

The other necessary condition for better medium-range forecasts is improvement of the global observing systems, in particular in the tropics and the southern hemisphere. For practical and economical reasons we must rely on satellite observations, and substantial research and development must take place to use these observations in a more efficient way in the data assimilation systems and for the designers of instruments to develop better sensors. A closer cooperation between experts on satellite instruments and retrieval procedures and the numerical modelers is essential. For operational reasons more efficient ways for a global exchange of these data in real time are required.

REFERENCES

Bengtsson, L. (1983). Observational requirements for long-range forecasts. WMO. Collection of position papers presented at the WMO-CAS/JSC Expert Study Meeting on Long-Range Forecasting, Princeton, 1-4 December 1982.

Bengtsson, L., and A. Lange (1982). Results of the WMO/CAS numerical weather prediction data study and intercomparison project for forecasts for the northern hemisphere in 1979-80. WMO, 26 pp + 71 figures and Annex.

Bengtsson, L., M. Kanamitsu, P. KÅllberg, and S. Uppala (1982a). FGGE 4-dimensional data assimilation. Bull. Amer. Meteorol. Soc. 63, 29-33.

Bengtsson, L., M. Kanamitsu, P. KÅllberg, and S. Uppala (1982b). FGGE research activities at ECMWF. Bull. Amer. Meteorol. Soc. 63, 277-303.

Bengtsson, L., and A. J. Simmons (1983). Medium-range weather prediction--operational experience at ECMWF. Large-Scale Dynamical Processes in the Atmosphere. B. J. Hoskins and R. P. Pearce (eds), Academic Press, 337-363.

Burridge, D. M. (1979). Some aspects of large scale numerical modelling of the atmosphere. Proceedings of ECMWF Seminar on Dynamical Meteorology and Numerical Weather Prediction, Vol. 2., 1-78.

Burridge, D. M., and J. Haseler (1977). A model for medium range weather forecasts--adiabatic formulation. ECMWF Tech. Rept. No. 4, 46 pp.

Cubasch, U. (1981). The performance of the ECMWF model in 50-day integrations. ECMWF Tech. Memo. No. 32, 74 pp.

Geleyn, J.-F., and A. Hollingsworth (1979). An economical analytical method for the computation of the interaction between scattering and line absorption of radiation. Beitr. Phys. Atmosp. 52, 1-16.

Girard, C., and M. Jarraud (1982). Short and medium range forecast differences between a spectral and grid point model. An extensive quasi operational comparison. ECMWF Tech. Rept. No. 32, 178 pp.

Haseler, J. (1982). An investigation of the impact at middle and high latitudes of tropical forecast errors. ECMWF Tech. Rept. No.31, 42 pp.

Krishnamurti, T. N., K. Ingles, S. Cocke, T. Kitade and R. Pasch (1983). Details of low latitude medium range weather prediction using a global spectral model II. Effects of orography and physical initialization. Florida State University Rept. No. 83-11, 206 pp.

Kuo, H. L. (1974). Further studies of the influence of cumulus convection on large-scale flow. J. Atmos. Sci. 31, 1232-1240.

Lange, A., and E. Hellsten (1983). Results of the WMO/CAS NWP data study and intercomparison project for forecasts for the northern hemisphere in 1981-82. WMO Short and Medium-Range Weather Prediction Research. Publ. Ser. No. 2, 30 pp + 68 figures and Annex.

Leith, C. E. (1978). Objective methods for weather prediction. Ann. Rev. Fluid Mech. 10, 107-128.

Lorenc, A. C. (1981). A global three-dimensional multivariate statistical interpolation scheme. Mon. Wea. Rev. 109, 701-721.

Lorenz, E. (1982). Atmospheric predictability experiments with a large numerical model. Tellus 34, 505-513.

Louis, J.-F. (1979). A parametric model of vertical eddy fluxes in the atmosphere. Boundary-Layer Meteorol. 17, 187-202.

Manabe, S., D. G. Hahn, and J. L. Holloway (1979). Climate simulation with GFDL spectral models of the atmosphere: Effect of spectral truncation. GARP Publ. Ser. No. 22, 41-94, WMO, Geneva.

Miyakoda, K., G. D. Hembree, R. F. Strickler, and I. Shulman (1972). Cumulative results of extended forecast experiments, 1: Model performance for winter cases. Mon. Wea. Rev. 100, 836-355.

Miyakoda, K., T. Gordon, R. Caverly, W. Stern, J. Sirutis, and W. Bourke (1983). Simulation of a blocking event in January 1977. Mon. Wea. Rev. 111, 846-69.

Rowntree, P. R. (1978). Numerical prediction and simulation of the tropical atmosphere. In: Meteorology over the Tropical Oceans, Roy. Meteorol. Soc., 278 pp.

Shaw, D., P. Lounberg, and A. Hollingsworth (1984). The 1984 revision of the ECMWF analysis system. Technical Memorandum No. 92. Available from ECMWF.

Shukla, J. (1984). Predictability of time averages. Long and Medium Range Weather Forecasting. D. M. Burridge and E. Kallen (eds), Springer-Verlag, 274 pp.

Simmons, A. J., and D. M. Burridge (1981). An energy and angular momentum conserving vertical finite difference scheme and hybrid vertical coordinate. Mon. Wea. Rev. 109, 758-766.

Simmons, A. J., and M. Jarraud (1984). The design and performance of the new ECMWF operational model. Proceedings of 1983 ECMWF Seminar (to be published).

Simmons, A. J, and R. Strufing (1983). Numerical forecasts of stratospheric warming events using a model with a hybrid vertical coordinate. Quart. J. Roy. Meteorol. Soc. 109, 81-111.

Temperton, C., and D. L. Williamson (1981). Normal mode initialization for a multi-level grid-point model, Part I: Linear Aspects. Mon. Wea. Rev. 109, 729-743.

Tiedtke, M., J.-F. Geleyn, A. Hollingsworth, and J.-F. Louis (1979). ECMWF model, parameterization of subgrid scale processes. ECMWF Tech. Rept. No. 10., 46 pp.

Wallace, J. M., S. Tibaldi, and A. J. Simmons (1983). Reduction of systematic forecast errors in the ECMWF model through the introduction of an envelope orography. Quart. J. Roy. Meteorol. Soc. 109, 683-717.

Williamson, D. L., and C. Temperton (1981). Normal mode initialization for a multi-level grid-point model, Part II: Nonlinear aspects. Mon. Wea. Rev. 109, 744-757.

A MONTHLY FORECAST EXPERIMENT: PRELIMINARY REPORT

K. Miyakoda, J. Sirutis, and J. Ploshay
Geophysical Fluid Dynamics Laboratory
National Oceanic and Atmospheric Administration

An experiment on monthly forecasts with eight winter cases is being carried out, using a 1980 general circulation model (GCM), i.e., N43L9-E, which incorporates a set of subgrid-scale physics characterized by the Mellor-Yamada turbulence closure (hierarchy level 2.5), the Monin-Obukhov parameterization for the layer next to the ground surface, Manabe's cumulus parameterization, and the soil heat conduction (Miyakoda and Sirutis, 1977). The sample cases adopted are for the month of January in the years from 1977 to 1983, which include the extraordinarily severe winter of 1977 and the most pronounced El Nino year of 1983. Each case is predicted by prescribing the climatologically normal sea-surface temperature as the lower boundary conditions and by using an ensemble means of three individual integrations. These integrations start with three different initial conditions based on the Level III data generated separately at the Geophysical Fluid Dynamics Laboratory, the National Meteorological Center, and the European Centre for Medium Range Weather Forecasts.

The main interests of the study are:

1. Are monthly forecasts feasible?
2. Is the GFDL four-dimensional data assimilation procedure useful and adequate for monthly forecasts?
3. How and where does the stochastic uncertainty grow with time?
4. What components of GCM would reduce or remove models' systematic error (climate drift)?

The four figures show the correlation coefficients of geopotential height anomalies (the deviation from climatology) between the prediction and the observation for the northern hemispheric domain (90°N to 25°N).

There are two different levels, i.e., 500 mb (Figures 1 and 2) and 1000 mb (Figures 3 and 4). Each diagram includes the skill scores for the 10-day mean (solid lines) and the 20-day mean (dashed lines) height patterns, together with the 10-day mean persistence (dotted lines). The 10-day mean persistence was obtained by using the observed height data averaged over the past 10 days from Day -10 to Day 0, and is shown as no skill prediction.

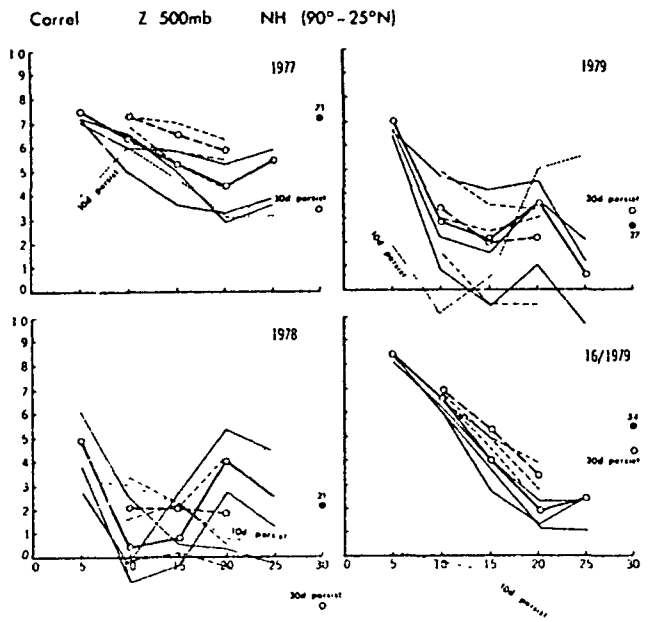

FIGURE 1 Correlation coefficients for the 500 mb geopotential height in the cases of January 1, 1977, 1978, 1979, and January 16, 1979.

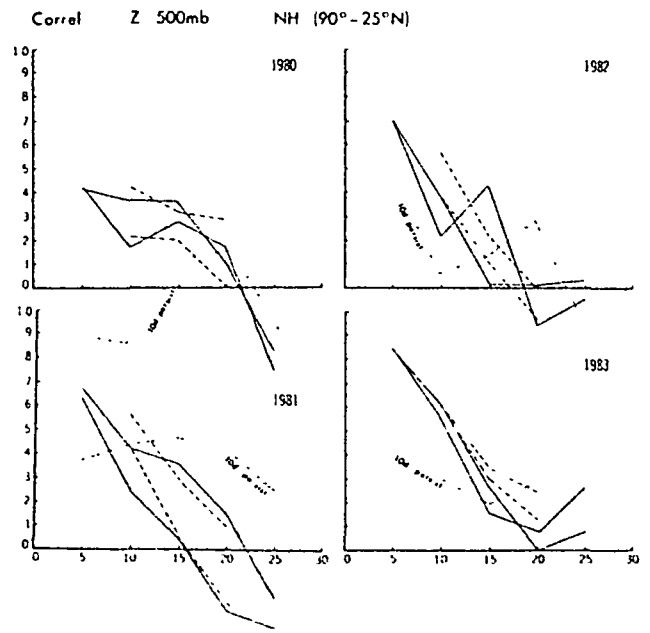

FIGURE 2 Correlation coefficients for the 500 mb geopotential height in the cases of January 1, 1980, 1981, 1982, and 1983.

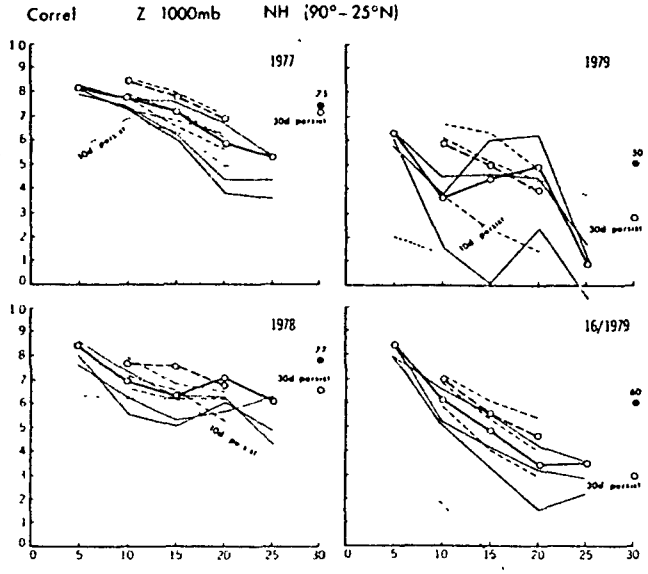

FIGURE 3 Correlation coefficients for the 1000 mb geopotential height in the cases of January 1, 1977, 1978, 1979, and January 16, 1979.

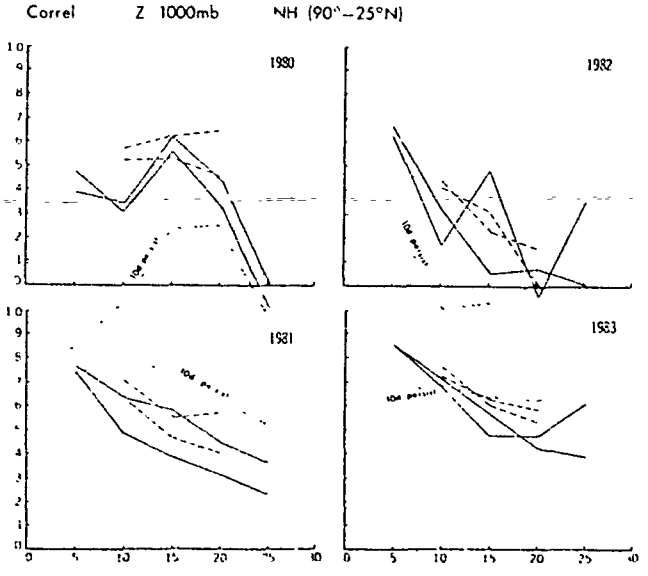

FIGURE 4 Correlation coefficients for the 1000 mb geopotential height in the cases of January 1, 1980, 1981, 1982, and 1983.

The thick solid lines, connecting the small circles, are the skill scores for the ensemble mean of three integrations (realizations). The ensemble means for the 30-day means are shown at the right hand side of each diagram.

The rationale of using the 10-day, 20-day, or 30-day mean is to filter out (or to give up) the possible unpredictable components of atmospheric predictability. In particular, an attempt is made to eliminate baroclinic eddies that have a dominant peak in the power spectrum between 2 and 7 days.

Normally, the results of three realizations tend to be similar to each other as far as the monthly time scale is concerned, implying that the forecasts for 10- or 20-day means are not quite stochastic (Shukla, 1981). In a few cases (1978, 1979 cases) however, the initial conditions generate a substantially different course of evolution in monthly integrations, particularly associated with blocking ridges. The ensemble mean of multiple realizations produces a smaller root-mean-square error than the individual forecasts. Interestingly, correlation coefficients of the height anomalies between forecast and observation are also improved by the ensemble mean prognosis compared with the individual realization, implying that random noises are included in the individual realizations.

This study indicates that the 10- or 20-day mean height prognoses resemble the observations very well in the first 10 days and then rapidly lose the similarity, yet there is still some recognized skill, although marginal, in the last 10 or 20 days of the month. For the monthly time scale, the slowly varying planetary-scale circulation pattern and blocking phenomena, which are determined by internal dynamics (i.e., the basic zonal flow and the interaction with baroclinic eddies), are major components of the variation in gross weather.

One noteworthy result of this study is that the skill scores for the 1000 mb level are consistently better than those for the 500 mb level. This feature appears to be opposite to that for daily weather forecasts and may suggest how forecast errors propagate in the vertical.

Besides the basic experiment, additional forecasts are being made for each case with an advanced cumulus parameterization (i.e., N48L9-P; Arakawa and Schubert, 1974) and an envelope mountain parameterization of ECMWF (Wallace et al., 1983). The quality of a GCM as well as its initial condition are essential for making a good simulation of these slow planetary waves and blocking events. Yet the climatic drift remains in all models, although to a different degree. It is interesting to note that forecast root-mean-square errors of height pattern are largely due to climatic drift for each model.

REFERENCES

Arakawa, A., and W. H. Schubert (1974). Interaction of cumulus cloud ensemble with the large-scale environment, Part I. J. Atmos. Sci. 31, 674-701.

Miyakoda, K., and J. Sirutis (1977). Comparative global prediction experiments on parameterized subgrid-scale vertical eddy transports. Beitr. Phys. Atmos. 50, 445-487.

Shukla, J. (1981). Dynamical predictability of monthly means. J. Atmos. Sci. 38, 2547-2572.

Wallace, J. M., S. Tibaldi, and A. J. Simmons (1983). Reduction of systematic forecast errors in the ECMWF model through the introduction of an envelope orography. Quart. J. Roy. Meteorol. Soc. 109, 683-717.

OMIT

8. HEAT SOURCES AND SINKS

Organizer	Donald R. Johnson
Session Chairmen	Michio Yanai Akira Kasahara
Speakers	Donald R. Johnson Akira Kasahara Michio Yanai Pedro L. Silva-Dias Julia N. Paegle Joel Susskind
Rapporteur	Akira Kasahara Ernest C. Kung Michio Yania

THE PLANETARY DISTRIBUTION OF HEAT SOURCES AND SINKS DURING FGGE

Donald R. Johnson
and
Ming-Ying Wei
University of Wisconsin, Madison

INTRODUCTION

One of the interesting and important consequences of the First GARP Global Experiment (FGGE) is the capability to infer the planetary scale distribution of heat sources and sinks from the state of the atmosphere and its evolution. Through the unprecedented efforts of the Global Weather Experiment in both observation and data assimilation, the FGGE meteorological data sets produced by the National Meteorological Center (NMC), the European Centre for Medium Range Weather Forecasts (ECMWF), the Geophysical Fluid Dynamics Laboratory (GFDL), and the Goddard Laboratory for Atmospheric Sciences (GLAS) are particularly suitable for global studies of differential heating. Given the diversity of the assimilation models, an examination of the diabatic heating distribution is important for comparing the data sets, the assimilation models, and for insight on the role of differential heating in forcing the global circulation. While the absolute accuracy of estimates of diabatic heating has not been established, the distribution for the planetary scale is surprisingly realistic. The patterns of differential heating are related to continents and oceans, air mass exchange between continents and oceans, topography, sea surface temperatures, cloudiness and other factors. Advances in understanding the global circulation will depend in no small part on our knowledge of the distribution of the atmosphere's heat sources and sinks as well as the processes which determine the distribution.

A capability to "observe atmospheric heating" does not exist nor will it exist in the future. All distributions of heating are determined by inference. The capability to infer global distribution of heating during FGGE is a consequence of the enhanced observational capability and use of assimilation models. An effort to infer the global heating distribution solely from either observations or model results would be unsuccessful. Even with the enhanced FGGE observational system, the temporal and spatial sampling is inadequate to infer the global distribution without the use of information from the assimilation model. Likewise, without observations, the atmosphere of the assimilation model would diverge from reality and the heating distribution would correspond to the climatology of the model. Consequently, one must recognize that estimates of atmospheric heating

from FGGE data are inferred from a combination of actual and "synthetic" information. Statements on the validity of such analyses rest on the "realism" of the fields as judged from our knowledge of the physics and dynamics of the atmosphere.

Recently, Kasahara and Mizzi (1984) have reviewed and discussed the various methods used to estimate diabatic heating and has noted several important points. He pointed out that despite many differences in the methods of calculation and the sources of data, there are far more similarities than differences between the patterns of heating inferred from using the Level III NMC and ECMWF data sets. He and others have emphasized the need to include a global distribution of diabatic heating in the initialization of primitive equation models in order to retain the characteristic features of tropical motions. In a series of numerical experiments, Krishnamurti et al. (1983) have demonstrated a major improvement in forecasts of the onset of the Asiatic summer monsoon and also the time averaged components of the atmosphere through inclusion of diabatic processes in initialization. The results suggest that the processes of differential heating are so tuned with the large scale vertical motion field and its associated adiabatic expansion and compression that attempts to initialize the atmospheric mass and momentum distribution without including these processes must limit overall accuracy.

The objectives of this paper are to (1) show the realistic nature of the heating distributions from analysis of the NMC and ECMWF data sets, (2) discuss the methods used and the problems involved in the inference of diabatic heating, (3) draw attention to the relation between differential heating and energy transport, and (4) to make some preliminary recommendations on the inference of heat sources and sinks for the planetary scale.

RESULTS

Several methods have been used in the analysis of FGGE heating distributions. Wei et al. (1983, 1984) interpolate the data from isobaric to isentropic coordinates and evaluate diabatic heating from the vertical mass flux determined by an integration of the isentropic mass continuity equation (Johnson, 1980). Kasahara and Mizzi (1984) estimated diabatic heating from the thermodynamic equation expressed in isobaric coordinates. In their work, the heating is determined from the total time rate of change of enthalpy, and the "energy conversion," $\omega\alpha$. A third approach is to "compute the diagnostics produced by the model forced to remain close to the data during the analysis cycle" (Kalnay and Baker, 1984). In this approach estimates are computed from the thermodynamic equation of the model during its analysis cycle in conjunction with an extra source term that represents the difference between the first guess (six hour forecast) and the analysis fields. Kalnay and Baker note that for perfect forecasts, the extra source term vanishes. A fourth method utilized by Luo and Yanai (1983) for studying the heating distribution over the Tibetan Plateau during FGGE is to estimate latent heating from the continuity equation for water

vapor. Through its combination with independent estimates of the total heating from the thermodynamic equation, Luo and Yanai separate the latent heating component from total heating and also assess the accuracy of computations through consistency requirements. Masuda (1984) has recently completed a similar study of the planetary scale distribution of both the total and its latent heating components.

Figure 1 presents the monthly and vertically averaged heating rates from an isentropic analysis of NMC data for January, April, July, and October, 1979 (Johnson et al., 1984). The fields were filtered by removing zonal harmonics with wavelengths less than 4000 km and the applications of a low pass (1, 2, 1) and an inverse filter (-1, 5, -1) (Wei et al., 1983). Figure 2 presents the heating distribution where zonal harmonics with wavelengths less than 10,000 km were removed.

The realism of these results is judged best through considering the heating patterns in the northern hemisphere and the tropics. The key features which appear realistic are wintertime cooling and summertime heating over Eurasia and North America, wintertime heating over the western equatorial Pacific and the oceanic regions along the east coasts of the Asian and North American continents, summertime cooling in the eastern portions of the Pacific and Atlantic Oceans, and summertime heating over Southeast Asia and central America. The orientation of the heating along the extratropical storm tracks downstream of the major cyclogenetic areas off the east coasts and also along the North and South Pacific Convergence Zones seems realistic. The heating over South America in January and in the ITCZ seems to be in accord with the convection observed in these regions. All of these features can be associated with atmospheric circulations within which either latent and sensible heating occurs or a lack of convection allows net cooling by radiation. The planetary aspects of the continentality and oceanality of heating distributions are particularly evident in Figure 2. Details of these results are presented in Wei et al. (1983) and Johnson et al. (1984).

The planetary distributions of heating for FGGE have also been studied by Kasahara and Mizzi (1984), Masuda (1984), Kalnay and Baker (1984), Paegle and Paegle (1984), Lau (1984), and White (1982, 1983). The regional distribution of heating for the Monsoon Experiment (MONEX) has been studied by Luo and Yanai (1984) and Nitta (1983, 1984). While the heating distributions presented herein are from our analysis, our results are typical of other results being prepared for the planetary scale by several investigators, which are referenced when known to us. The evidence to date indicates that realistic global distributions of heating may be estimated from the FGGE data.

The mass weighted and vertically averaged diabatic heating distributions estimated from the ECMWF analyses for the four midseason months are shown in Figure 3. For the comparison with the NMC analyses, the estimates were computed using the isentropic mass continuity equation with the top boundary condition set at 370 K, 380 K, 400 K and 400 K for January, April, July and October 1979, respectively. The realistic features of the planetary heating distribution noted for the NMC analyses are also evident in the ECMWF results. This is particularly true in regard to the major heat sources and sinks for the tropics and the northern hemisphere.

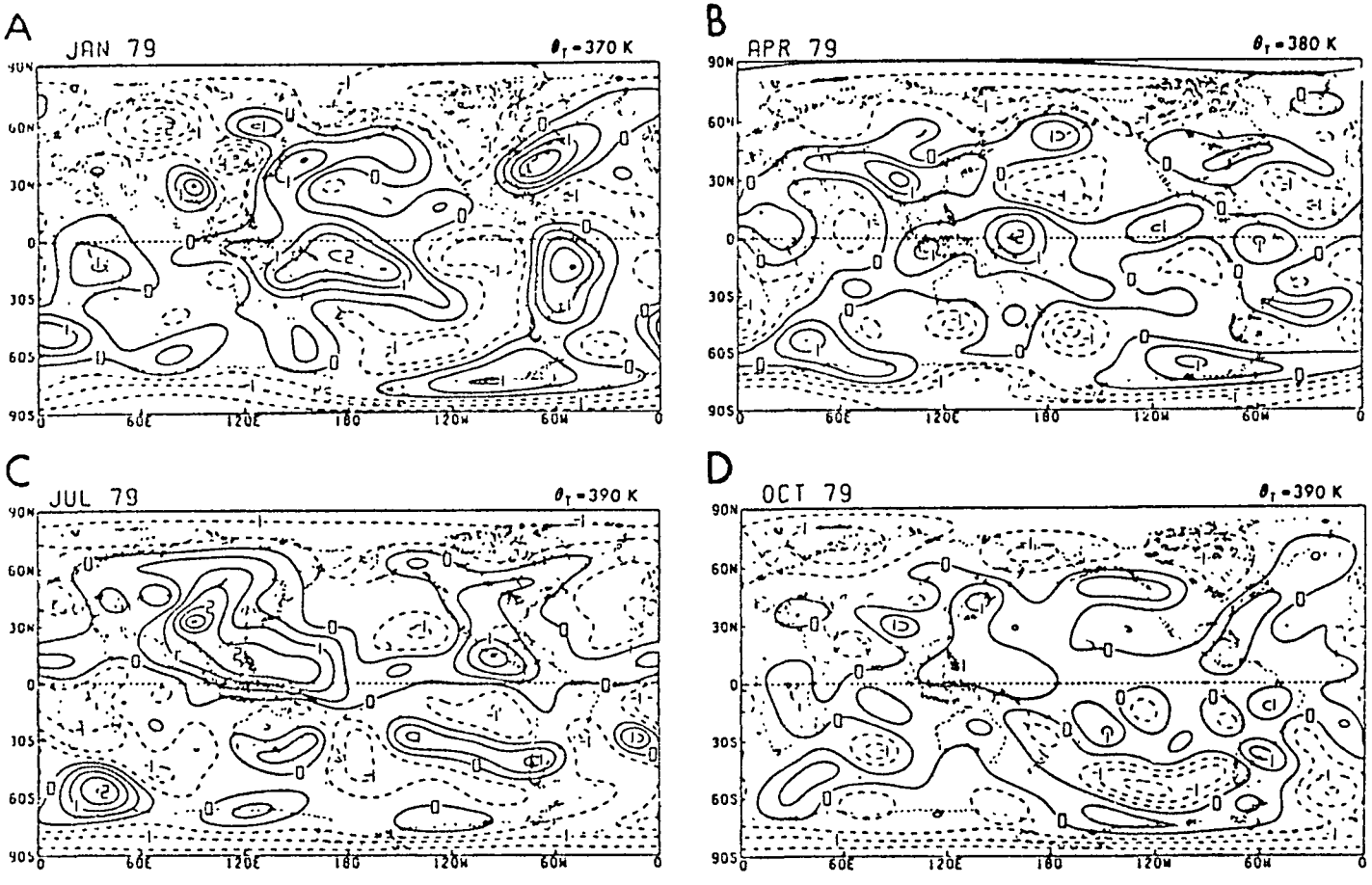

FIGURE 1 Mass-weighted vertically averaged diabatic heating rates (K day^{-1}) computed from NMC analyses for (a) January, (b) April, (c) July, and (d) October 1979. Vertical mass flux is set to zero at upper boundaries of 370 K, 380 K, 390 K and 390 K, respectively. Filtered to show contributions from wavelengths greater than 4,000 km.

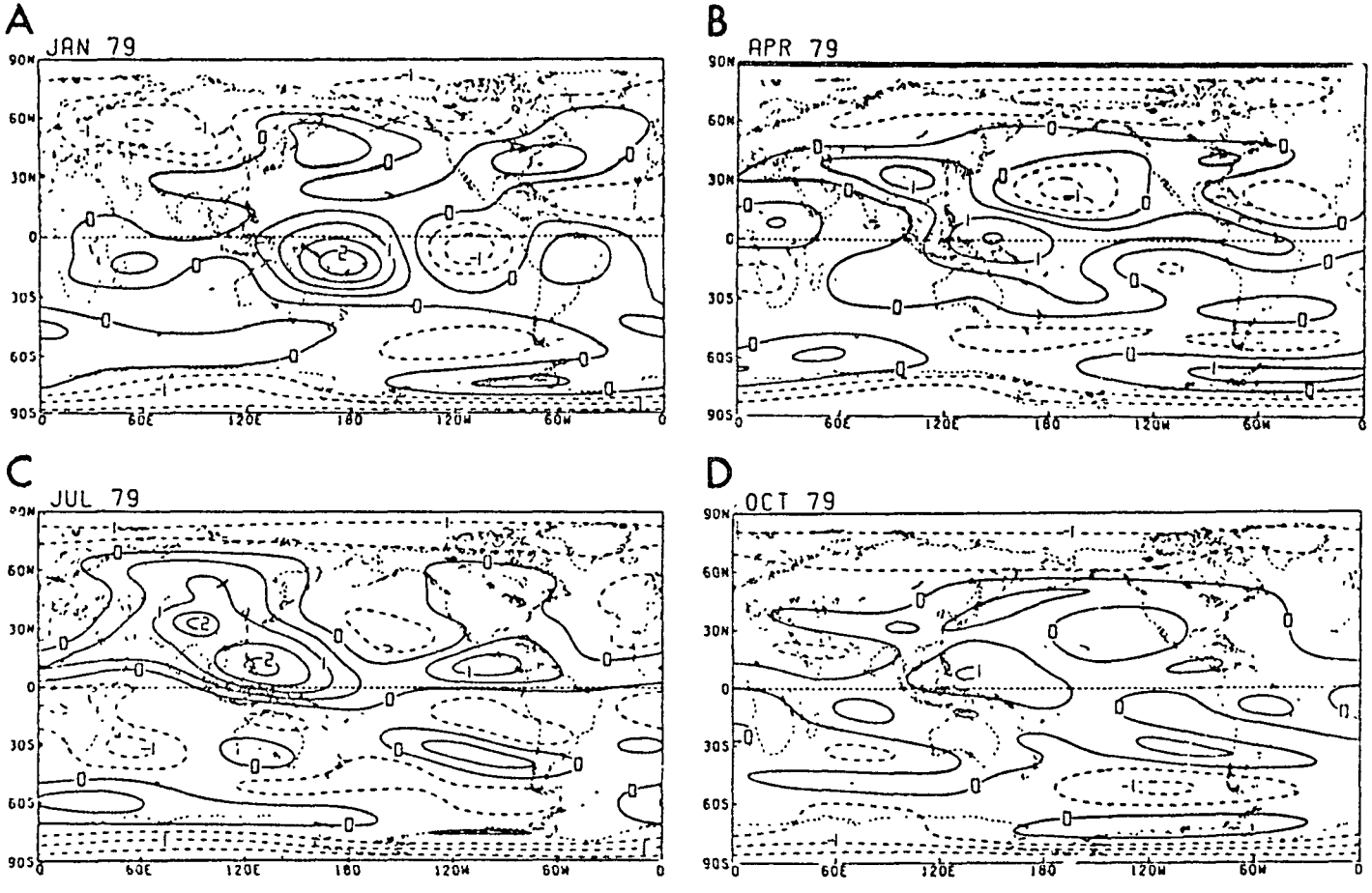

FIGURE 2 Same as Figure 1 except showing contributions from wavelengths greater than 10,000 km.

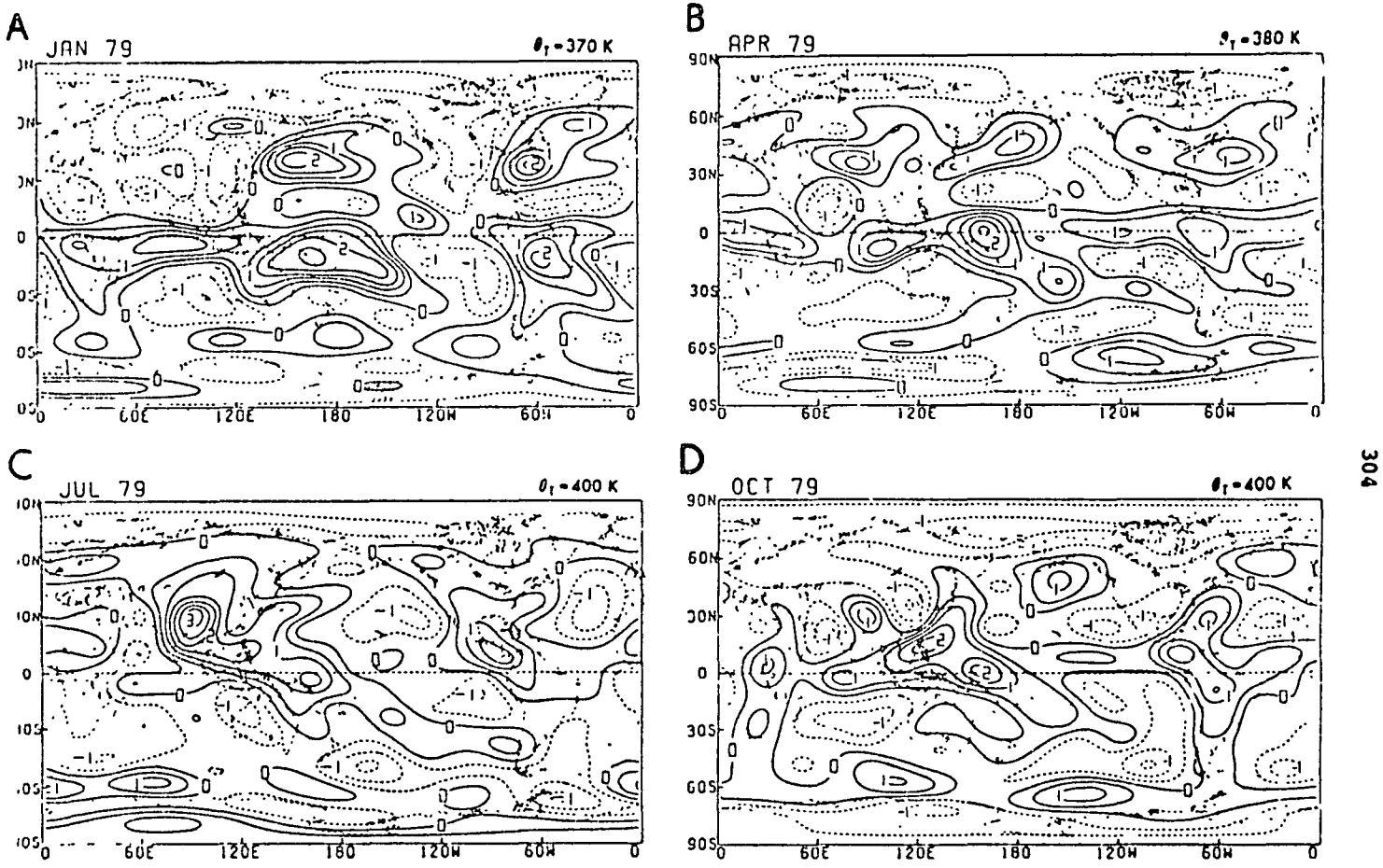

FIGURE 3 Same as Figure 1 except computed from ECMWF analyses with vertical mass flux set to zero at upper boundaries of 370 K, 380 K, 400 K, and 400 K, respectively.

Differences between the patterns of heating in Figures 1a and 3a are also evident. To assist the comparison, the difference fields (ECMWF minus NMC) are shown in Figure 4a. Features particularly worth noting include (1) the distinct heating associated with the ITCZs over the equatorial Atlantic and Indian Ocean in the ECMWF but not in the NMC analysis, (2) stronger heating over western equatorial Pacific and central Africa in the ECMWF results, (3) stronger cooling in the NMC results over eastern equatorial Pacific and southern South Pacific (denoted by large positive difference values in Figure 4a), (4) a branch of heating extending from South America southeastward into the South Atlantic in the ECMWF but not in the NMC analysis, (5) more intense heating along the storm track to the east of Asia in the ECMWF analysis, (6) cooling in the mid North Pacific and Atlantic Oceans located further south in the ECMWF (positive difference values in Figure 4a), (7) more extensive and intense cooling over Antarctic in the NMC analysis, (8) quite different heating distributions for the southern hemisphere's midlatitudes in NMC and ECMWF results with few apparent patterns being identified with circulation features, and (9) heating over Tibet in the NMC but not in the ECMWF analysis. This heating over Tibet in the NMC analysis appears repeatedly when similar calculations are performed for other months of the FGGE year and is suspected to be unrealistic at least during the wintertime.

Even though detailed discussions of the comparison for the other three months will not be presented here due to space limitations, some characteristic differences should be noted. The ECMWF analyses appear to have stronger convection in the Asiatic monsoon region and the ITCZ regions of the Indian and Atlantic Oceans. However, the convective activities in the ITCZ over the eastern Pacific and Central and South America are of comparable strength. The ECMWF analyses indicate more heating to the east of Asia and North America in all seasons. The cooling of higher latitudes appears more consistent in NMC's analyses.

Zonally and vertically averaged diabatic heating rates are shown in Figure 5. The positions of the latitudinal belts of heating and cooling in the NMC (solid lines) and ECMWF (dashed lines) results are in agreement. Except for July, the magnitudes in the ECMWF results are larger than those in the NMC analyses. This is especially true for the heating maximum in the tropics and cooling in the subtropics; a factor of two can be easily discerned. This is indicative of a stronger mean Hadley circulation in the ECMWF analyses. During July, the heating maximum occurring near 10°N that is associated with the summer Asiatic monsoon and tropical convection is smaller in ECMWF's than in NMC's analysis. Consequently, in the NMC analyses the Hadley circulation is stronger in July than in January, while the opposite is the case in the ECMWF analyses with the mean meridional circulation in January being stronger than in July.

The inclusion of the stratosphere affects the calculation of diabatic heating to some extent. Some characteristic patterns appear in the ECMWF analyses. The difference field between the January heating distributions calculated with the upper isentropic surface at 650 K and 370 K is shown in Figure 4b. Although the patterns of differential heating remain similar, differences in intensity can be

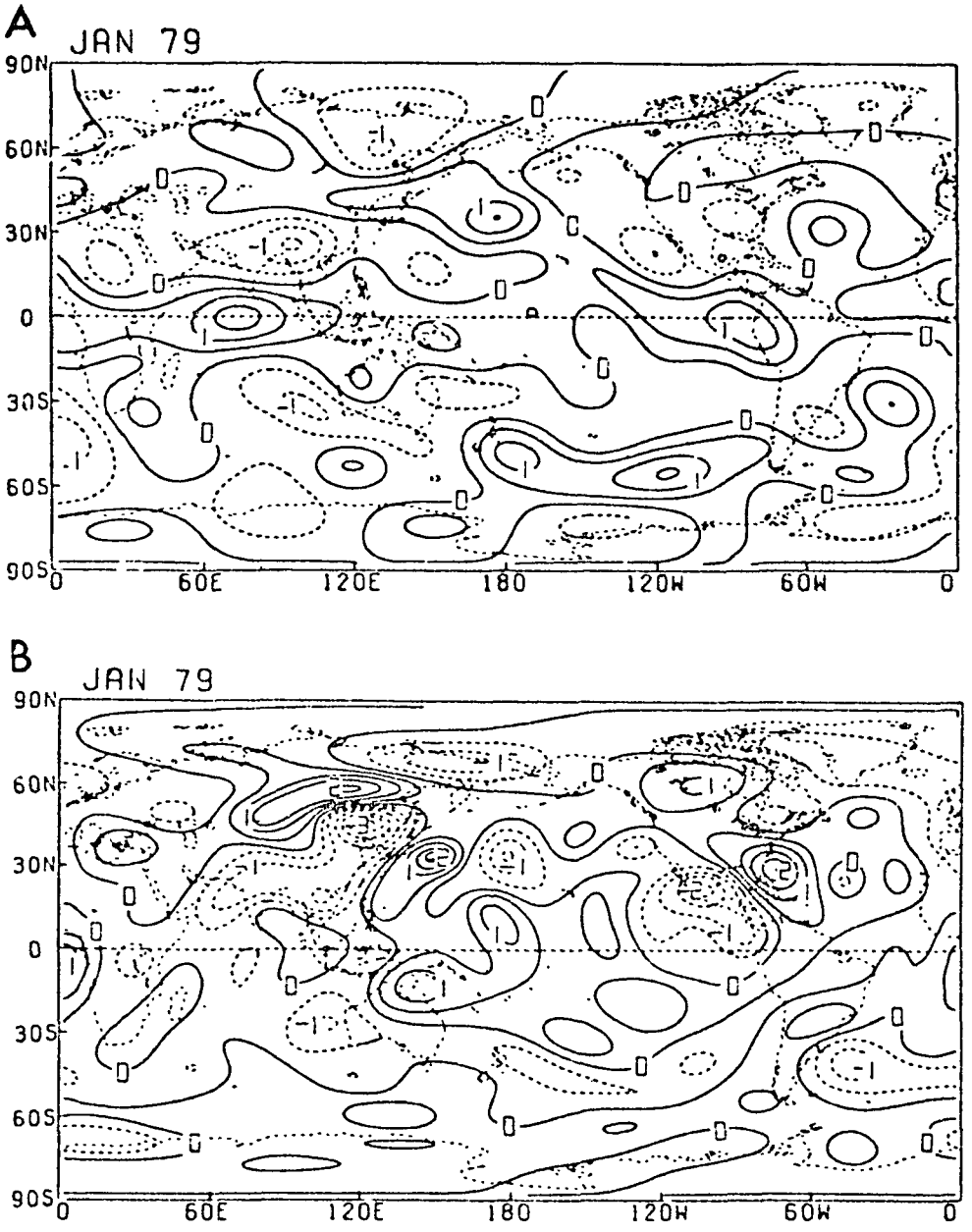

FIGURE 4 Difference fields of vertically averaged diabatic heating rates (K day^{-1}) between (a) ECMWF and NMC analyses (former minus latter) with similar upper boundary conditions, and (b) ECMWF analyses with and without inclusion of stratosphere (former minus latter). Filtered with wavelengths greater than 4,000 km.

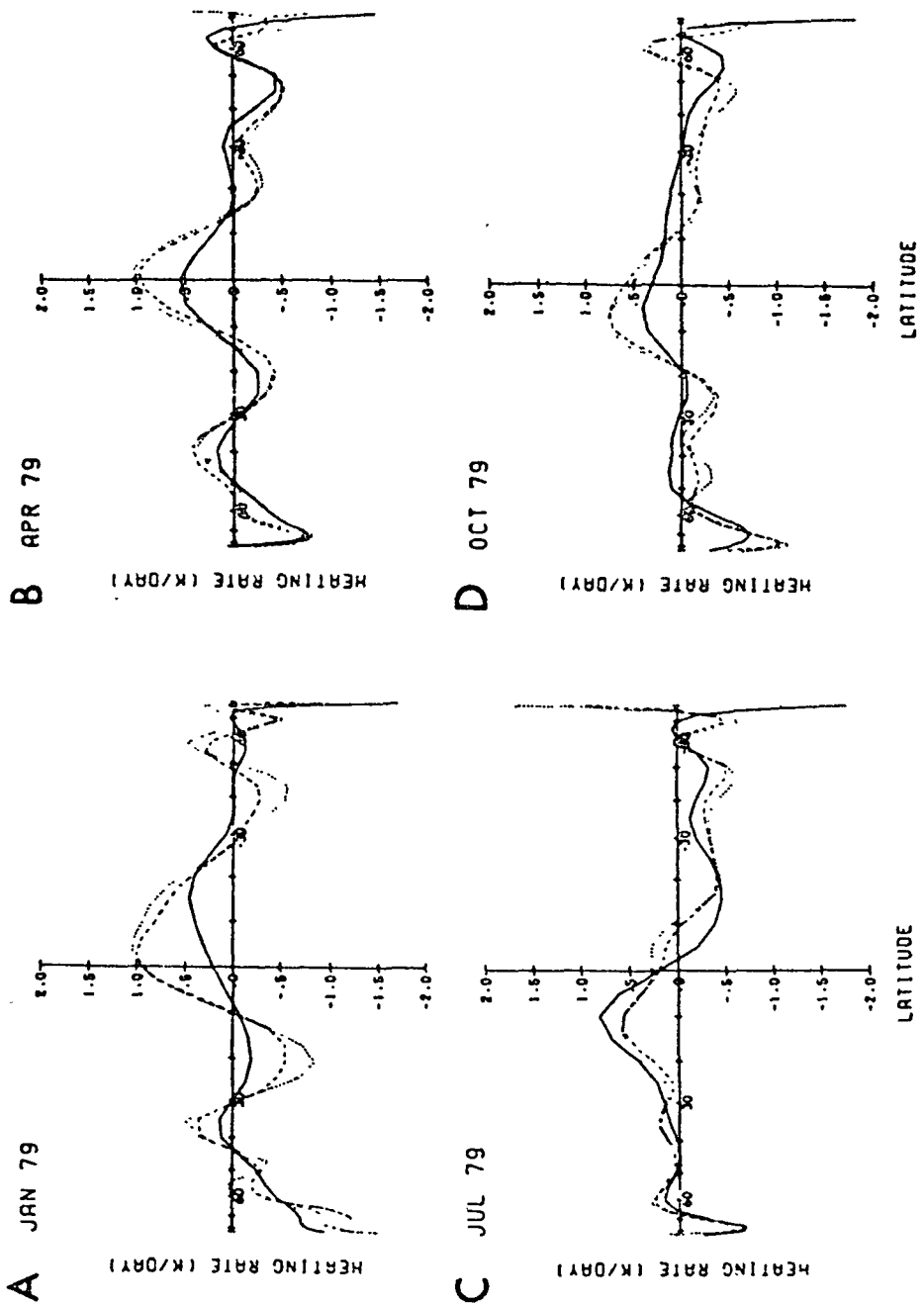

FIGURE 5 Meridional profiles of zonally and vertically averaged diabatic heating rates (K day^{-1}) from NMC analyses (solid line) and from ECMWF analyses with (dotted line) and without (dashed line) inclusion of stratosphere.

easily identified over several regions, some of which also appear in the other midseason months (not shown). These regions include the Asiatic monsoon area, the storm tracks to the east of Asia and North America, and the eastern portions of the oceanic anticyclones. Although considerable variance between the two heating distributions with different top boundary conditions is noted, the comparison of the vertically and zonally integrated heating profiles (dashed and dotted lines in Figure 5) reveals good agreement.

THE INFERENCE OF DIABATIC HEATING AND ITS UNCERTAINTY

In view of both the importance and uncertainty of heating estimates, two methods used for the inference of global heating distributions will now be discussed in some detail to ascertain the strengths and weaknesses of each method. One of the recommendations from the Monsoon Experiment (MONEX) Workshop (GWE Newsletter No. 3, 1984) was to analyze and compare heating estimates based on isentropic and isobaric analyses over complex terrain.

Estimation of the heating distribution in isentropic coordinates is through a vertical integration of the isentropic mass continuity equation expressed by

$$\rho J\dot{\theta} = (\rho J\dot{\theta})_{\theta_T} + \int_{\theta}^{\theta_T} [\nabla_\theta \cdot (\rho J \underset{\sim}{U}) + \frac{\partial}{\partial t_\theta}(\rho J)]\, d\theta \qquad (1)$$

where J is the Jacobian ($\partial h/\partial\theta$). In this expression the diabatic mass flux $\rho J\dot{\theta}$ through an isentropic surface is given by the sum of the diabatic mass flux at some high isentropic level θ_T ideally in the stratosphere and the vertical integral of the horizontal divergence of the mass transport and the mass tendency. In most cases the mass flux at θ_T is assumed to vanish and the integration is averaged over a sufficient time so that the mass tendency becomes small relative to the vertically integrated divergence. Since the systematic errors of the vertically integrated divergence of the mass transport are similar to those occurring in the kinematic estimates of ω, a mass weighted adjustment is first applied to the horizontal mass divergence so that the diabatic mass flux vanishes at both θ_T and θ_S, the potential temperature of the earth's surface. The proper lower boundary constraint is $\rho J\dot{\theta}$ equal to $\rho J\dot{\theta}_S$. Examples of the vertical profiles of time averaged divergence and heating for the western and eastern Pacific are presented in Figure 6.

The principal sources of error in the isentropic method must be attributed to inadequate sampling, interpolation from sigma to isobaric to isentropic coordinates, finite differencing and improper boundary constraints for the vertical mass flux. It is important to note however, that the adjustment applied ensures a constraint on the diabatic mass transport. Since the horizontal mass transport is computed from the distributions of pressure, potential temperature and velocity, in effect both the thermodynamic and velocity structures are considered simultaneously. The adjustment of the entropy transport

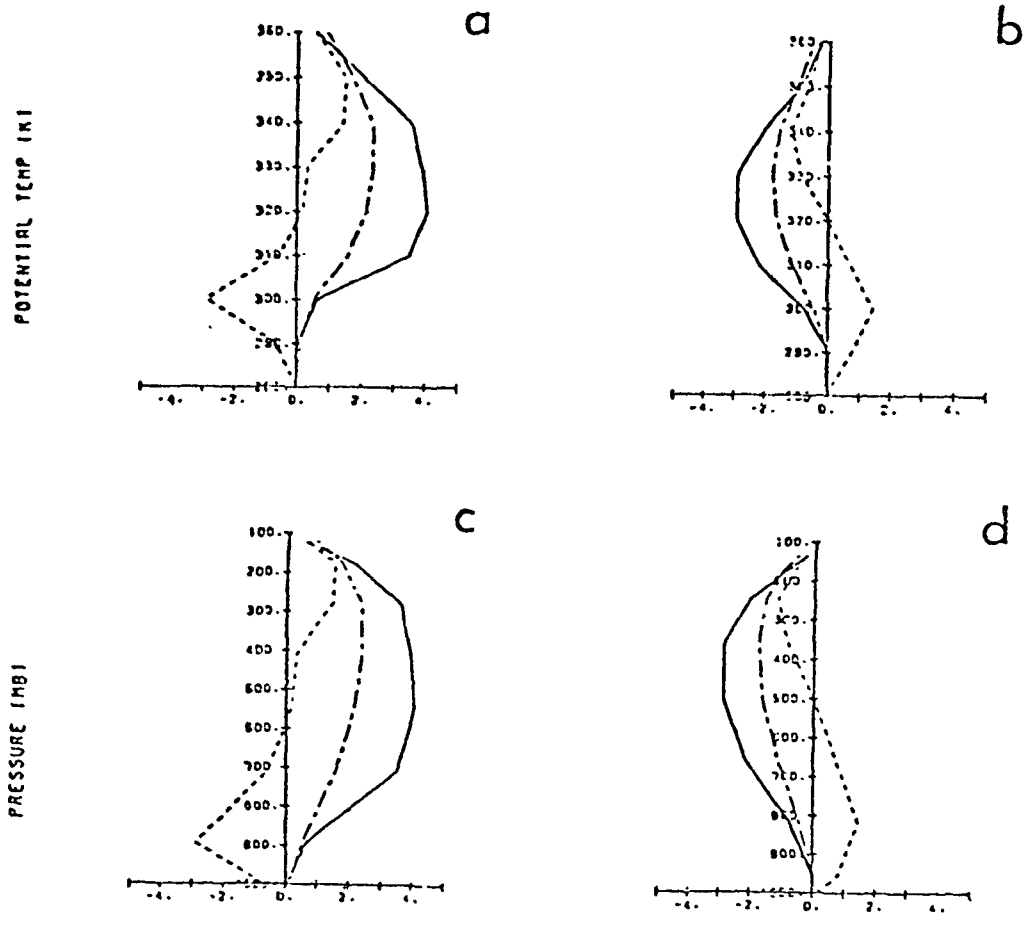

Horizontal mass divergence (------), Vertical mass flux (———), Diabatic heating (—— — —— — ——)

FIGURE 6 Area-averaged vertical profiles of horizontal mass divergence ($\times 10^{-3}$ kg m^{-2} $10K^{-1}$ s^{-1}), vertical mass flux ($\times 10^{-3}$ kg m^{-2} s^{-1}) and diabatic heating (K day^{-1}) for January 1979. Potential temperature is used as ordinate in a and b, and pressure is used in c and d. The area averaged in a and c is from 0^{o}N to 15^{o}S and from 165^{o}E to 175^{o}W, roughly east of New Guinea. The area averaged in b and d is from 0^{o}N to 15^{o}S and from 110^{o}W to 90^{o}W, roughly over eastern equatorial Pacific.

ensures that the diabatic mass flux is bounded. The subsequent division of $\rho J\theta$ by ρJ (equal to $g^{-1}\partial p/\partial\theta$) to estimate θ induces a spurious component in situations where ρJ is small.

In isobaric coordinates the heating rate from the enthalpy form of the thermodynamic equation is expressed by

$$Q/c_p = \frac{\partial T}{\partial t_p} + \underset{\sim}{U}\cdot\nabla_p T - \omega[(-\partial\theta/\partial p)T/\theta]. \qquad (2)$$

In the expression, the heating is determined by a difference between the sum of the temperature tendency, its horizontal advection, and the product of the vertical motion with the stability parameter (proportional to the inverse of the hydrostatic isentropic mass ρJ). Near the tropopause and in hyperbaroclinic zones, the large variation of static stability will introduce a great deal of uncertainty associated with inadequate sampling and resolution when estimating the tendency, horizontal divergence, and vertical motion ω through finite differences. In their use of (2) to infer heating, Kasahara and Mizzi (1984) encountered difficulties in obtaining consistent distributions between the variances of the quantities $U\,\nabla_p T$ and $\omega(-\partial\theta/\partial p)T/\theta$ that may in part be attributed to the complexity of atmospheric structure and uncertainty.

The thermodynamic equation may also be expressed by

$$(-g\frac{\partial\theta}{\partial p})^{-1} Q\pi^{-1} = g^{-1}\left[\omega - (-\frac{\partial\theta}{\partial_p})^{-1}(\frac{\partial\theta}{\partial t_p} + \underset{\sim}{U}\cdot\nabla_p\theta)\right] = \rho J_\theta\dot{\theta}, \qquad (3)$$

where π is the Exner function. This second isobaric form of the thermodynamic equation based on entropy is useful for comparison with equation (1). The physical bases of equations (1) and (3) are common in the sense that the heating is inferred from the entropy distribution. Since isentropic coordinates are used in equation (1) to estimate the changes in the entropy by heating, these changes become uniquely related to the Lagrangian derivative of potential temperature which in turn is directly related to the diabatic mass flux. The consequence of the exact differential relation between heating and entropy change is that the heating occurring during an interval of time separating two states will determine a unique vertical displacement within the isentropic coordinate structure that is independent of the actual path of trajectory. As such, the mass continuity equation can be used to infer a vertical displacement due to atmospheric heating. The analysis of the entropy change in isobaric coordinates does not benefit from this unique relation between vertical mass flux and heating, thus inference must be based on the thermodynamic equation which requires estimates of both vertical and horizontal advective processes.

In both equations (2) and (3) the vertical mass flux ω/g is estimated kinematically by integration of the horizontal velocity divergence. In order to satisfy the upper and lower boundary conditions that the isobaric mass flux ω/g vanishes, a vertically integrated velocity divergence which is independent of the entropy

distribution is subtracted. Kinematically, this adjustment corresponds with the one used for the diabatic mass flux in isentropic coordinates. However there is one important difference. Application of the kinematic constraint for ω/g in the isobaric coordinates does not constrain the distribution of Q nor the isentropic diabatic mass flux. With sufficient time averaging so that the potential temperature tendency becomes negligible, the form of equation (3) shows that the diabatic mass flux is given by the difference of the isobaric vertical mass flux ω/g and the horizontal potential temperature advection. Within quasi-geostropic regimes, the two processes generally oppose each other.

The principal sources of error noted earlier for isentropic inference are also present in the isobaric method with the exception of errors introduced in the interpolation to isentropic coordinates. Added complexities of the isobaric method appear to be introduced by the need to resolve the fine balance between horizontal and vertical advection and by the lack of a constraint that ensures bounded estimates of diabatic mass flux.

Another source of error in global heating estimates has been identified with topography (Kasahara and Mizzi, 1983; 1984). In Kasahara and Mizzi's more recent work they emphasize that a proper specification of the terrain and boundary value of ω is important for removing this systematic error. In view of the problem of data assimilation, initialization, and prediction over strongly sloped terrain, the problem will almost certainly require further attention in both isentropic and isobaric methods of inference.

A DIRECT RELATION BETWEEN DIFFERENTIAL HEATING AND THE THERMALLY COUPLED MASS CIRCULATIONS

A direct correspondence between the scale of the differential heating, isentropic mass circulations, and energy transport has been established with FGGE data (Townsend, 1980; Johnson and Townsend, 1981; Johnson et al., 1981). In regions of heating the mass transport is upward while in regions of cooling the mass transport is downward. For the mass distribution to remain quasi-steady at the planetary scale, the quasi-horizontal mass transport must be from heat sources to heat sinks in upper isentropic layers and from heat sinks to heat sources in lower isentropic layers. Thus the mass transport of the heat source region is divergent in upper isentropic layers and convergent in lower layers. The reverse pattern of mass divergence occurs in the heat sink region. The mass transport potential (X_ρ) functions within the 300 to 310 K and 340 to 350 K isentropic layers for January 1979 (Johnson et al., 1984) defined by

$$\nabla_\theta \cdot (\rho J \underline{U}) = \nabla^2_\theta X_\rho \qquad (4)$$

are presented in Figures 7a and 7c. Note the common horizontal scales between the mass transport potential functions and differential heating. As such, the circulations are a coupled response to the differential heating imposed.

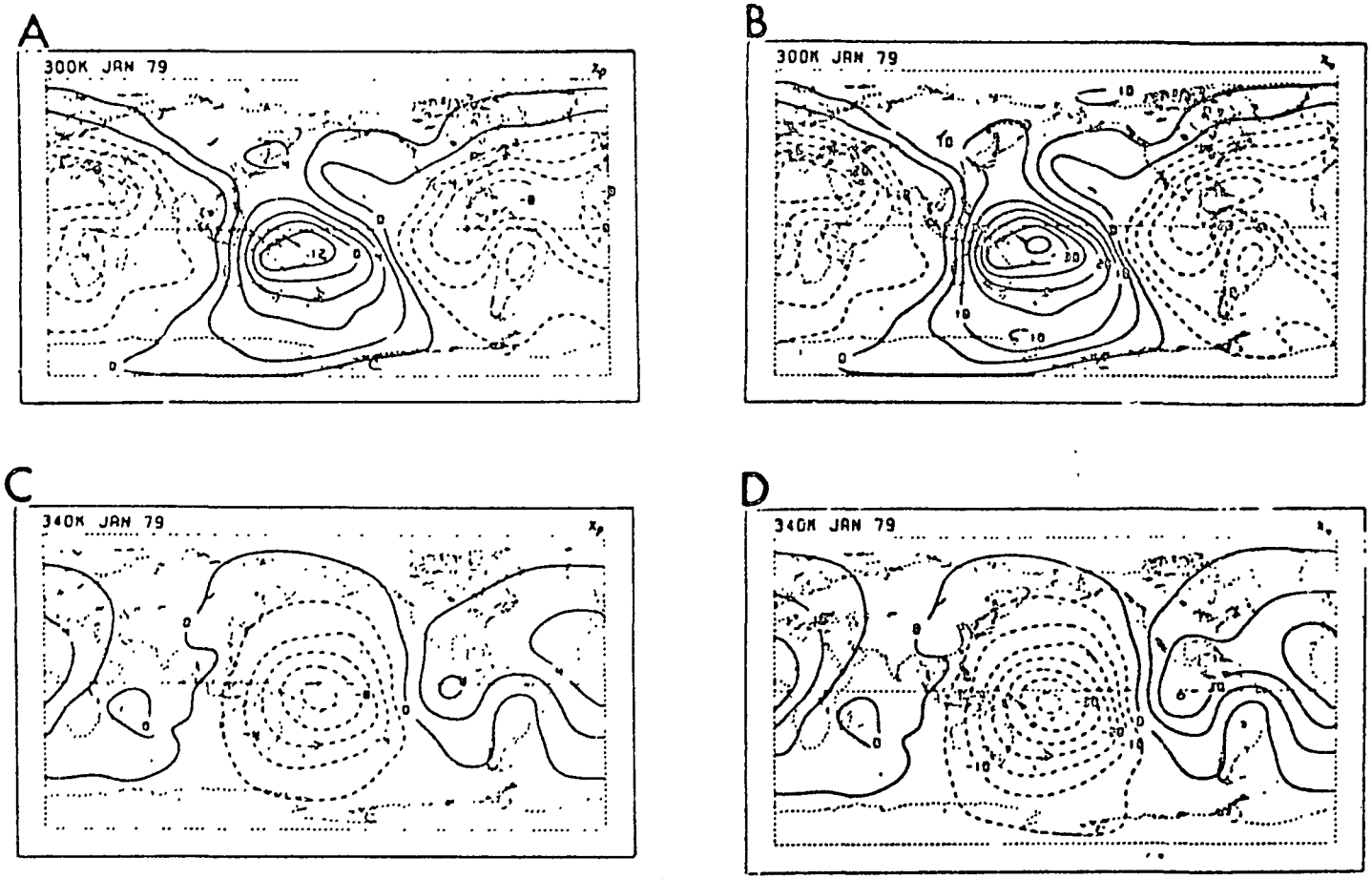

FIGURE 7 Mass and energy transport potential functions for the 300 to 310 K and 340 to 350 K isentropic layers for January 1979.

The same thermally coupled mass circulations must also transport energy. For the planetary scale circulation to be quasi-steady, physical considerations demand that energy be transported from the heat source to heat sink regions, and that the horizontal scale of energy transport be similar to the horizontal scale of differential heating. The potential (X_ν) functions of energy transport for the 300 to 310 K and 340 to 350 K layers for January 1979 defined by

$$\nabla_\theta \cdot \rho J \underline{U}_\nu = \nabla_\theta \cdot (\rho J U_\nu) = \nabla_\theta^2 X_\nu \qquad (5)$$

are presented in Figures 7b and 7d. The subscript ν denotes the sum of the dry static and kinetic energies. An overlay of the mass potential functions with the corresponding energy potential functions will reveal one to one correspondence of the main features, except for scaling the patterns are almost identical. The net energy transport from the source to sink regions occurs from the condition that more energy is transported from heat source to sink regions in upper isentropic layers than is returned by the transport from sink to source in lower isentropic layers.

With regard to the time averaged net energy transport, degrees of freedom are present for both time mean and transient modes of energy transport. The condition that the isentropic mean mass circulation is closely related to energy transport is verified in the zonally and vertically averaged meridional energy transport presented for January 1979 in Figure 8 (from Townsend and Johnson, 1981). Note that relative to the mean energy transport, the transient energy transport is negligibly small. The implication of these results is that thermally coupled planetary scale mass circulations develop within a baroclinic atmosphere which primarily serve to transport energy from the heat sources to heat sinks. For the quasi-steady planetary circulation, the scale and intensity of the isentropic mass circulations and energy transport are directly related to the scale and intensity of the differential heating.

SUMMARY

The overall importance of accurate inference of the atmosphere's distribution of heat sources and sinks is emerging. Besides the importance for fundamental understanding of the atmosphere's general circulation, evidence suggests that at the planetary scale, the accuracy of numerical weather prediction will be enhanced with inclusion of diabatic processes in initialization. For progress in the understanding of climate, the second objective of GARP, the inference of the atmosphere's distribution of heat sources and sinks for weekly and longer time scales is essential.

Several key points that have emerged from the results of FGGE research are:

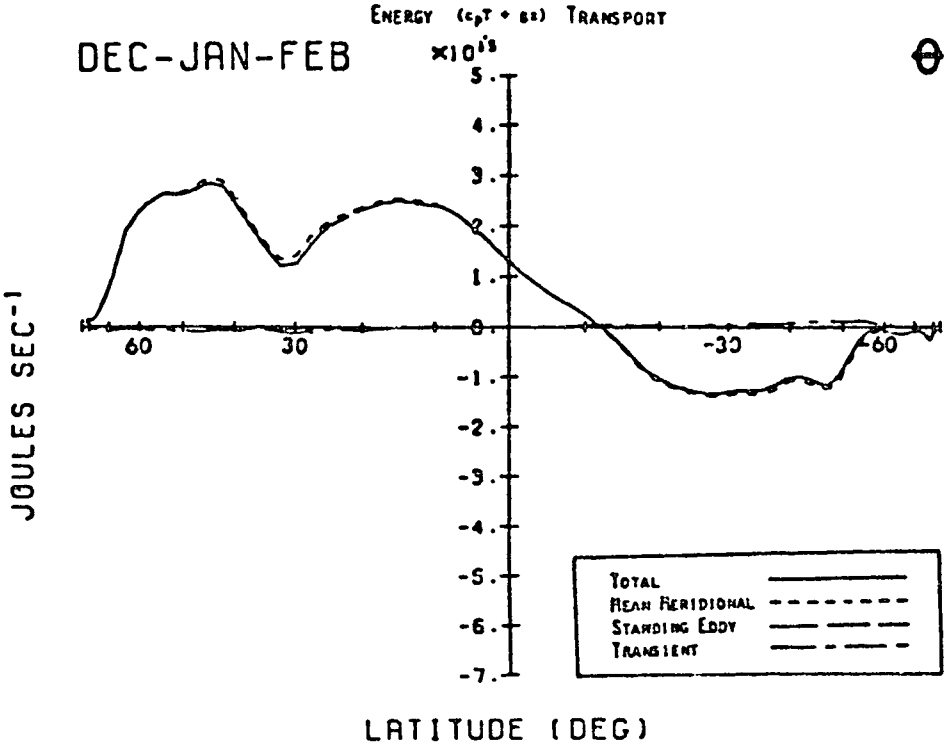

FIGURE 8 Meridional profiles of vertically integrated energy transport (10^{15} J s^{-1}) partitioned into components in isentropic coordinates for December to February 1979.

1. The spatial distributions of the atmosphere's heat sources and sinks for the planetary scale inferred from FGGE data sets are realistic. Some filtering or averaging in space and time is needed by virtue of the inaccuracy of observations, limited sampling in space and time, and inadequacies of numerical estimation.
2. The temporal variation of the global heating distributions is in accord with the march of the seasons.
3. The similarities of the patterns of heating among different data sets and computing methods are greater than the differences.
4. Some differences in the patterns of heating among the FGGE data and among the methods of analysis are pronounced. The origin of these differences should be ascertained.
5. The temporal and spatial consistency of the heating patterns in the northern hemisphere is greater than in the southern hemisphere. Among the FGGE data sets, considerable disparity exists within the westerly wind regime of the southern hemisphere.
6. Systematic errors in the heating distributions can be introduced by topography.

7. An analysis of the diagnostic methods for the inference of heating should be made to establish their accuracy. Such an analysis would isolate the sources of error as well as a statistical distribution of the errors that would permit probabilistic statements of accuracy.

8. Analyses of the global distribution of total heating and individual components using methods such as applied by Luo and Yanai (1984) are needed.

ACKNOWLEDGEMENTS

This research was sponsored jointly by the National Science Foundation and the National Oceanic and Atmospheric Administration under Grant Number 8110678.

REFERENCES

Johnson, D. R. (1980). A generalized transport equation for use with meteorological coordinate systems. Mon. Wea. Rev. 108, 733-745.

Johnson, D. R., and R. D. Townsend (1981). Diagnostics of the heat sources and sinks of the Asiatic monsoon and the thermally forced planetary scale response. ICSU/WMO GARP Conf. Proc. of Int. Conf. on Preliminary FGGE Data Analysis and Results, 23-27 June 1980, Bergen, Norway, Geneva, 1981, 523-533.

Johnson, D. R., R. D. Townsend, M.-Y. Wei, and R. D. Selin (1981). The global structure of energy transport within thermally forced planetary scale mass circulation. ICSU/WMO GARP Condensed Papers and Meeting Rep. of Int. Conf. on Early Results of FGGE and Large-Scale Aspects of Its Monsoon Experiments (12-17 January 1981, Tallahassee, Florida), Geneva, 1981, 3-27 - 3-34.

Johnson, D. R., R. D. Townsend, and M.-Y. Wei (1985). The thermally coupled response of the planetary scale circulation to the global distribution of heat sources and sinks. Tellus 37A, 106-125.

Kalnay, E., and W. E. Baker (1984). Analyzed and diagnosed fields in the GLAS FGGE IIIb analysis. U.S. Committee for GARP, Global Weather Experiment Newsletter 3, 29-31.

Kasahara, A., and A. P. Mizzi (1983). On the evaluation of the heating/cooling rate from the ECMWF Level IIIb analysis data. U.S. Committee for GARP, Global Weather Experiment Newsletter 2.

Kasahara, A., and A. P. Mizzi (1984). Preliminary evaluation of diabatic heating distribution from FGGE Level IIIb analysis data. NCAR MS. 0501/84-6.

Krishnamurti, T. N., K. Ingles, S. Cocke, T. Kitode, and R. Pasch (1983). Details of low latitude medium range numerical weather prediction using a global spectral model II. Effects of orography and initialization. FSU Report No. 83-11. Dept. of Meteorology, Florida State University, Tallahassee, Florida, 32306. 45 pp with 24 figures.

Lau, N.-C. (1984). The influences of orography on large-scale atmospheric flows simulated by a general circulation model. Presented at the Int. Symp. on Tibetan Plateau and Mountain Meteorology, Beijing, China, March 21, 1984.

Luo, H., and M. Yanai (1984). The large-scale circulation and heat sources over the Tibetan Plateau and surrounding areas during the early summer of 1979. Part II: Heat and moisture budgets. Mon. Wea. Rev. 112, 966-989.

Masuda, K. (1983). Dynamical estimation of atmospheric diabatic heating over the northern hemisphere in winter. J. Meteorol. Soc. Japan 61, 449-454.

Masuda, K. (1984). Diabatic heating during the FGGE: A preliminary report. J. Meteorol. Soc. Japan 62, 702-708.

MONEX Heat Budget Workshop, 1984: Report of MONEX heat budget workshop at Colorado State University (October 17-19, 1983), USC-GARP, National Academy of Sciences, Global Weather Experiment Newsletter 3, 1-2.

Nitta, T. (1983). Observational study of heat sources over the eastern Tibetan Plateau during the summer monsoon. J. Meteorol. Soc. Japan 61, 590-605.

Nitta, T. (1984). Spatial and temporal variations of heat sources over the eastern Tibetan Plateau during the summer monsoon. Proceedings of International Symposium on Qinghai-Xizong (Tibet) Plateau and Mountain Meteorology, Beijing, People's Republic of China.

Paegle, J., and J. N. Paegle (1984). GLAS heating rate estimates for SOP-1. U.S. Committee for GARP, Global Weather Experiment Newsletter 3, 25-28.

Townsend, R. D. (1980). A diagnostic study of the zonally averaged global circulation in isentropic coordinates. Ph.D. thesis, University of Wisconsin, Madison, 221 pp.

Townsend, R. D., and D. R. Johnson (1981). The mass and angular momentum balance of the zonally averaged global circulation. ICSU/WMO GARP Conf. Proc. of Int. Conf. on Preliminary FGGE Data Analysis and Results (23-27 June 1980, Bergen, Norway), Geneva, 1981, 542-552.

Wei, M.-Y., D. Johnson and R. D. Townsend (1983). Seasonal distributions of diabatic heating during the First GARP Global Experiment. Tellus 35A, 241-255.

Wei, M.-Y., D. R. Johnson, T. K. Schaack, and R. D. Selin (1984). A quick comparison of diabatic heating rates between NMC IIIa and ECMWF IIIb data sets for January 1979. U.S. Committee for GARP, Global Weather Experiment Newsletter 4, 11-20.

White, G. H. (1982). The global circulation of the atmosphere (December 1980 - November 1981) based upon ECMWF analyses. Technical Report, Department of Meteorology, University of Reading, U.K.

White, G. H. (1983). The global circulation of the atmosphere (December 1981 - November 1982) based upon ECMWF analyses. Technical Report, Department of Meteorology, University of Reading, U.K.

D18

PRELIMINARY EVALUATION OF DIABATIC HEATING DISTRIBUTION FROM FGGE LEVEL IIIb ANALYSIS DATA

Akira Kasahara and Arthur P. Mizzi
National Center for Atmospheric Research

INTRODUCTION

The determination of diabatic heating on a global scale has been a major topic in global energy budget studies. There are essentially two different approaches for evaluating the global distribution of diabatic heating: physical and dynamical. The physical approach is to evaluate separately the components of the diabatic heating process, such as solar and infrared radiation, the release of latent heat by condensation, and the latent and sensible heat transports from the earth's surface, by using a parameterization formula governing each physical process (e.g., Budyko, 1963; Newell et al., 1974).

The dynamical approach is to calculate the residual heating to satisfy the first law of thermodynamics. This approach may be further divided into two procedures. One procedure is to use general circulation statistics data with respect to the zonal mean or time mean sensible heat transports (e.g., Geller and Avery, 1978; Hantel and Baader, 1978; Lau, 1979). In this approach, the effects of vertical heat transport by deviate motions (departures from zonal or time mean) are often neglected or parameterized.

The other procedure in the dynamical approach is to calculate the horizontal and vertical heat fluxes and the temporal change of temperature directly from synoptic data and then determine a residual to the first law of thermodynamics (Brown, 1964; Masuda, 1983, 1984). We shall call this procedure the direct synoptic method in contrast to the general circulation statistics method referred to earlier.

One difficult aspect in diabatic heating calculations by the dynamical approach is evaluation of the vertical heat transport. In particular, we must consider whether or not we can determine the vertical motion with sufficient accuracy from the observed wind field. The general impression based on some past experiences (e.g., Newell et al., 1969) suggests that the vertical motion determined from the observed divergence field is not accurate enough for the evaluation of diabatic heating. In fact, all investigations cited for the dynamical approach used the vertical motion field determined from an inferred divergence field derived from the vorticity tendency equation. While this procedure is satisfactory in the midlatitudes where the absolute vorticity is positive and its magnitude is generally large, this

procedure is not reliable in the tropics where the absolute vorticity is generally small or even becomes negative.

The observational efforts of the Global Weather Experiment conducted during 1979 were unprecedented in their completeness as a global meteorological data set. The availability of FGGE Level III analyses produced by the National Meteorological Center (NMC), the European Centre for Medium Range Weather Forecasts (ECMWF), the Geophysical Fluid Dynamics Laboratory (GFDL), and the Goddard Laboratory for Atmospheric Sciences (GLAS) has made it attractive to examine the question of reliability in the vertical motion calculation based on the observed divergence field. For example, the numerical experiments conducted by Krishnamurti and Ramanathan (1982) using data collected during the GARP Monsoon Experiment (MONEX) demonstrate that the time evolution of the analyzed large-scale divergence field is consistent with that of the rotational wind field. Hence, the analyzed large-scale divergence field in the tropics may contain significantly more usable information than previously believed.

Wei et al. (1983) calculated the seasonal distributions of diabatic heating using the FGGE Level IIIa analyses produced by NMC. They used a modification of the dynamical method in which the diabatic heating is evaluated from the mass continuity equation in isentropic coordinates (Johnson, 1980).

Luo and Yanai (1984) investigated the large-scale heat and moisture budgets over the Tibetan Plateau and surrounding areas using objectively analyzed fields from the FGGE Level IIb data set. This work suggests that the kinematically determined vertical motions are reliable in the determination of diabatic heating over this region. A similar indication has been shown in Nitta (1983).

Murakami and Ding (1982) performed the calculation of diabatic heating rate by applying a direct synoptic method utilizing a kinematically determined vertical motion field from the NMC FGGE IIIa analyses. This work, along with the aforementioned diagnostic studies regarding the use of FGGE data, indicates that the operationally analyzed FGGE Level IIIa and IIIb wind and temperature data are useful for evaluating diabatic heating by the direct synoptic method.

In this paper, we present our method of calculating the global distribution of diabatic heating rate and our preliminary results of global heating rate evaluated from the ECMWF FGGE Level IIIb analysis data.

COMPUTING SCHEMES AND DATA

The diabatic heating rate is obtained as a residual to the thermodynamic equation

$$\partial T/\partial t + V \cdot \nabla T - \omega\Gamma = A/C_p, \qquad (1)$$

where T denotes the temperature, t is time, $\omega(\equiv dp/dt)$ is the vertical velocity in pressure (p) coordinates, $\Gamma = -(T/\partial)\partial\theta/\partial p$ represents the static stability, θ is the potential temperature, and

$$V \cdot \nabla = \frac{u}{a \cos\phi} \frac{\partial}{\partial \lambda} + \frac{v}{a} \frac{\partial}{\partial \phi} \qquad (2)$$

is the horizontal advection operator in spherical coordinates with u, v, , , and a denoting the eastward and northward components of horizontal velocity V, longitude, latitude, and a mean radius of the earth, respectively. Quantity Q denotes the rate of heating per unit mass per unit time and C_p is the specific heat at constant pressure. The diabatic heating rate Q/C_p will be expressed in K sec^{-1}.

We use the ECMWF Level IIIb gridded velocity components u, v, and geopotential height at the 12 pressure levels (50, 70, 100, 150, 200, 250, 300, 400, 500, 700, 850, 1000 mb) with a horizontal resolution of 1.875° on a latitude-longitude grid. We selected the two 15-day periods of January 27 to February 11, 1979 in the FGGE Special Observing Period-I (SOP-I) and June 7 to 22, 1979 in the SOP-II. Twice-daily data at 0000 GMT and 1200 GMT are used.

Temperature T is calculated from the geopotential height data with the hydrostatic equation. The vertical p-velocity ω is calculated from

$$\omega = \omega_s + \int_p^{p_s} D \, dp, \qquad (3)$$

where D denotes the horizontal divergence

$$D = \frac{1}{a \cos\phi} \frac{\partial u}{\partial \lambda} + \frac{\partial}{\partial \theta} (v \cos\phi) \qquad (4)$$

and ω_s is the value of ω at p_s = 1000 mb. The value of ω_s is evaluated from

$$\omega_s = (\partial p/\partial z) \, \tilde{V} \cdot \nabla H \qquad (5)$$

in which H denotes the earth's orographic height, $\tilde{V}$ represents the average horizontal velocity between 850 mb and 700 mb, and $\partial p/\partial z$ is calculated as a mean value between the 850 and 1000 mb levels.

In the calculation of ω by (3), we assume that ω = 0 at p = 50 mb. After examining the field of divergence in the stratosphere, we felt that the calculated divergence D from the wind data above 70 mb was too large. Therefore, we reduced the divergence data by a factor of 2 at p = 70 mb and assumed that D = 0 at p = 50 mb. The ω values, thus calculated from (3) by approximating the vertical integral with the trapezoidal rule, do not usually satisfy the imposed top boundary condition of ω = 0 at p = 50 mb. Therefore, the calculated ω values were adjusted by a method adopted by O'Brien (1970). The ω values were reduced further so that the average variances of horizontal transport $V \cdot \nabla T$ and vertical transport $\omega\Gamma$ over the globe were approximately in balance. The factors which we thus obtained to further reduce the ω values are 0.15, 0.20, 0.30, 0.40, 0.50, 0.60, 0.75, 0.85, 0.95, 1.0 and 1.0 at p = 70, 100, 150, 200, 250, 300, 400, 500, 700, 850, and 1000 mb. Once the ω values were fixed, the

divergence values were then recalculated from the mass continuity equation $D + \partial\omega/\partial p = 0$. Although these adjustments to ω might seem drastic, their sensitivity to the divergent wind component is well within the observational errors of horizontal wind velocity.

The temperature tendency $\partial T/\partial t$ in (1) is calculated using the finite difference $\Delta T/\Delta t$ with temperature values at 0000 GMT and 1200 GMT and the time interval of 12 hours. The calculated temperature tendency is regarded as representative within the 12-hour interval centered at 0600 GMT or 1800 GMT. The horizontal and vertical advection terms $V \cdot \nabla T$ and $-\omega\Gamma$ are calculated at 0000 GMT and 1200 GMT. Then the advection terms at two consecutive time levels are arithmetically averaged to obtain average advection terms within the 12-hour interval representative at 0600 GMT or 1800 GMT.

The numerical computations are performed by using the spherical harmonic expansion which has been used in the formulation of spectral forecast models. The original gridded data are expanded in spherical harmonics with a triangular truncation of zonal wavenumber 35. After obtaining the spherical harmonic coefficients, the field variables are calculated on a transformed grid involving 60 Gaussian latitudes between the North and South Poles and 120 Fourier points on each latitude circle.

GLOBAL DISTRIBUTION OF HEATING RATE

In presenting our results, the two 15-day periods of January 27 to February 11, 1979 in SOP-I and June 7 to 22, 1979 in SOP-II will be referred to as simply the SOP-I and SOP-II study periods, respectively.

Figure 1 shows the 15-day mean for the mass-weighted daily average heating rate

$$(1000 \text{ mb} - 150 \text{ mb})^{-1} \int_{150 \text{ mb}}^{1000 \text{ mb}} (Q/C_p)\, dp \qquad (6)$$

during the SOP-I study period. The daily average represents the arithmetic mean of the values at 0600 GMT and 1800 GMT. The contour interval is 2×10^{-5} K sec^{-1} (≈ 1.73 K day^{-1}). The solid (dashed) lines indicate positive (negative) values. Because the original pattern contains small-scale irregularities, it is difficult to visualize large-scale features without smoothing. Figure 1 is a smoothed version of the original pattern by truncating the spherical harmonic expansion at triangular 12. The contour interval is 0.5×10^{-5} K sec^{-1} ($= 0.43$ K day^{-1}). This smoothed distribution of the mass-weighted tropospheric diabatic heating rate generally agrees with the December 1978 to February 1979 case shown in Figure 2 of Wei et al. (1983), the January 1979 case shown as Figure 2a in Johnson et al. (1983) and Figure 1a of Masuda (1984). The notable features are (1) the heating contrasts along the east and west coasts of North America and Eurasia, (2) the areas of heating over the tropical western Pacific, the Central Indian Ocean, South America and South Africa, and (3) the areas of cooling over the tropical eastern Pacific, the

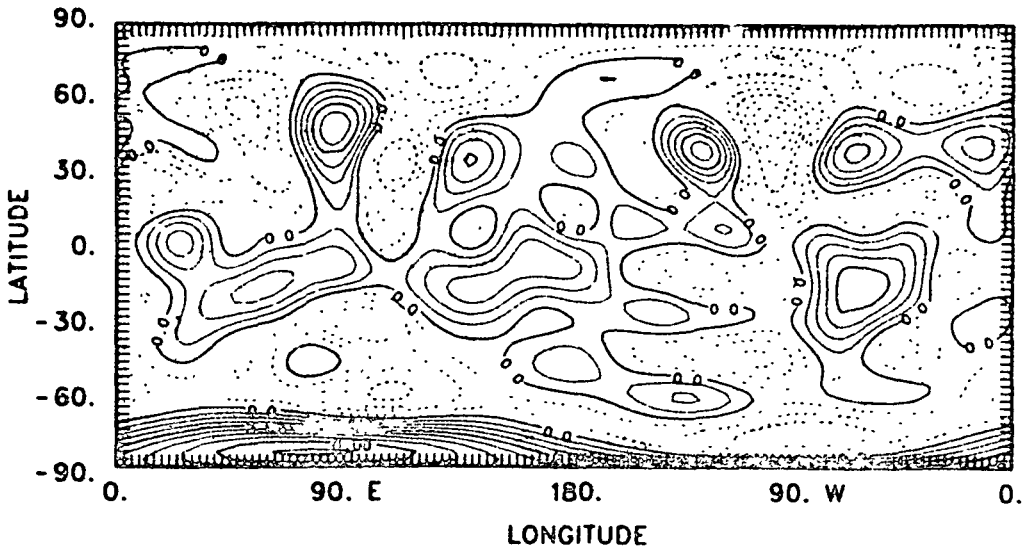

FIGURE 1 Temporal mean of the mass-weighted daily average heating rate defined by (1) for the SOP-I study period of January 27 to February 11, 1979. Contour interval is 2 x 10^{-5} K sec^{-1} (= 1.73 K day^{-1}).

mid-to-higher latitudes of the South Pacific, the higher latitudes of North America and Eurasia, and the Arctic Ocean.

In order to provide another comparison, Figure 2 shows the global distribution of mass-weighted vertically averaged diabatic heating rate (K day^{-1}) calculated from the January simulation with the NCAR Community Climate Model discussed by Boville (1984). Although the magnitudes of heating rate shown in Figure 1 are somewhat smaller than those shown in Figure 2, the main features of the two heating rate patterns agree with each other. However, there are a few notable differences between the two distributions. For instance, the heating rate over the Tibetan Plateau and Antarctica in Figure 1 appears to be too large. This problem seems to be related to areas of high elevation and will be commented on in Section 4.

Figure 3a shows a smoothed distribution of mass-weighted daily average heating rate (truncated at triangular 12), averaged over the SOP-I study period, applicable at 0600 GMT. The contour interval is 0.5 x 10^{-5} K sec^{-1} (= 0.43 K day^{-1}). The arrow shown at the top indicates the longitude of local noon. Figure 3b shows the same, except it is applicable at 1800 GMT. These two patterns exhibit a degree of diurnal variation in the heating rate. In general, maximum heating appears on the daytime side of the earth and maximum cooling on the nighttime side. Since deep cumulus convective activities of the tropics show diurnal variations (e.g., Gray and Jacobson, 1977; Murakami, 1983; Reed, 1983), it may be expected that the diabatic heating rate also shows diurnal variation. However, the diagnostic studies of the diabatic heating rate based on the GLAS FGGE IIIb

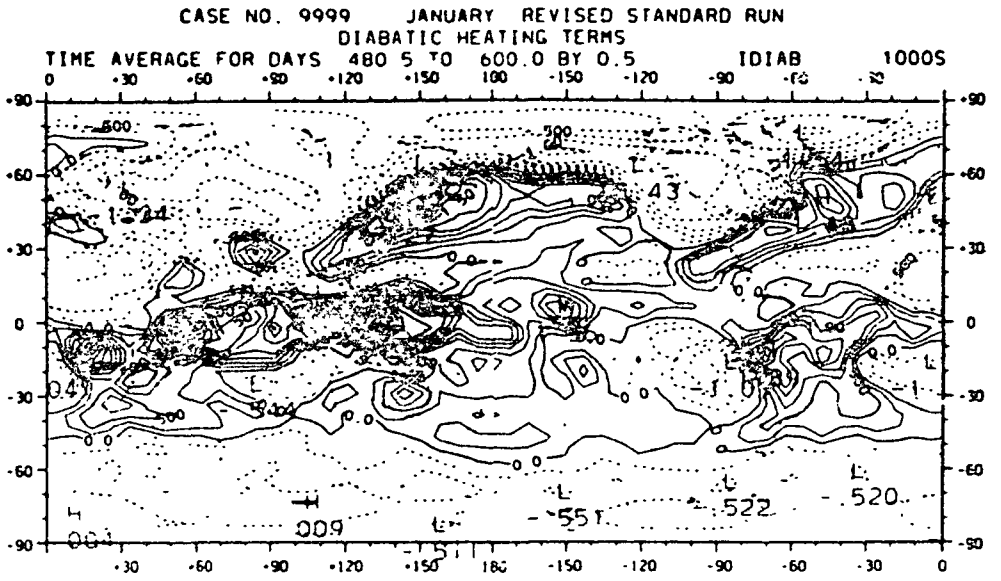

FIGURE 2 Mass-weighted vertically averaged diabatic heating rate (K day^{-1}) calculated from a January simulation by the NCAR Community Climate Model discussed by Boville (1984). Values range -1.5 to 3.5 K day^{-1} with a contour interval of 0.25 K day^{-1}.

analyses do not exhibit noticeable diurnal variations (Kalnay and Baker, 1984; Paegle and Paegle, 1984). It remains to be seen whether or not the magnitude of diurnal variation of heating shown in Figure 3 is representative of the atmosphere.

Figure 4 shows the same as Figure 1, except for the SOP-II study period. Figure 4 agrees in general with the June to August 1979 case shown in Figure 2 of Wei et al. (1983), the July 1979 case shown as Figure 2a of Johnson et al. (1983) and Figure 1c of Masuda (1984). The notable features are (1) the areas of heating along the intertropical convergence zones, over the Asian and American continents, the Saudi Arabian desert, the west coast of South America, and the South Atlantic, and (2) the areas of cooling over the North Pacific, North Atlantic, and eastern South Pacific. Once again, we find areas of strong heating over the Himalayas and western North America. While net heating over the Himalayas is expected for this period, its magnitude appears to be too large. We will discuss a possible cause of this problem in Section 4.

Figures 5a, b are the same as Figures 3a, b, except for the SOP-II study period. In general, net heating prevails over the daytime side and net cooling over the nighttime. While the net heating over the Himalayas for 0600 GMT and over the Canadian Rockies for 1800 GMT appears too strong, the overall featues of the heating distribution seem reasonable.

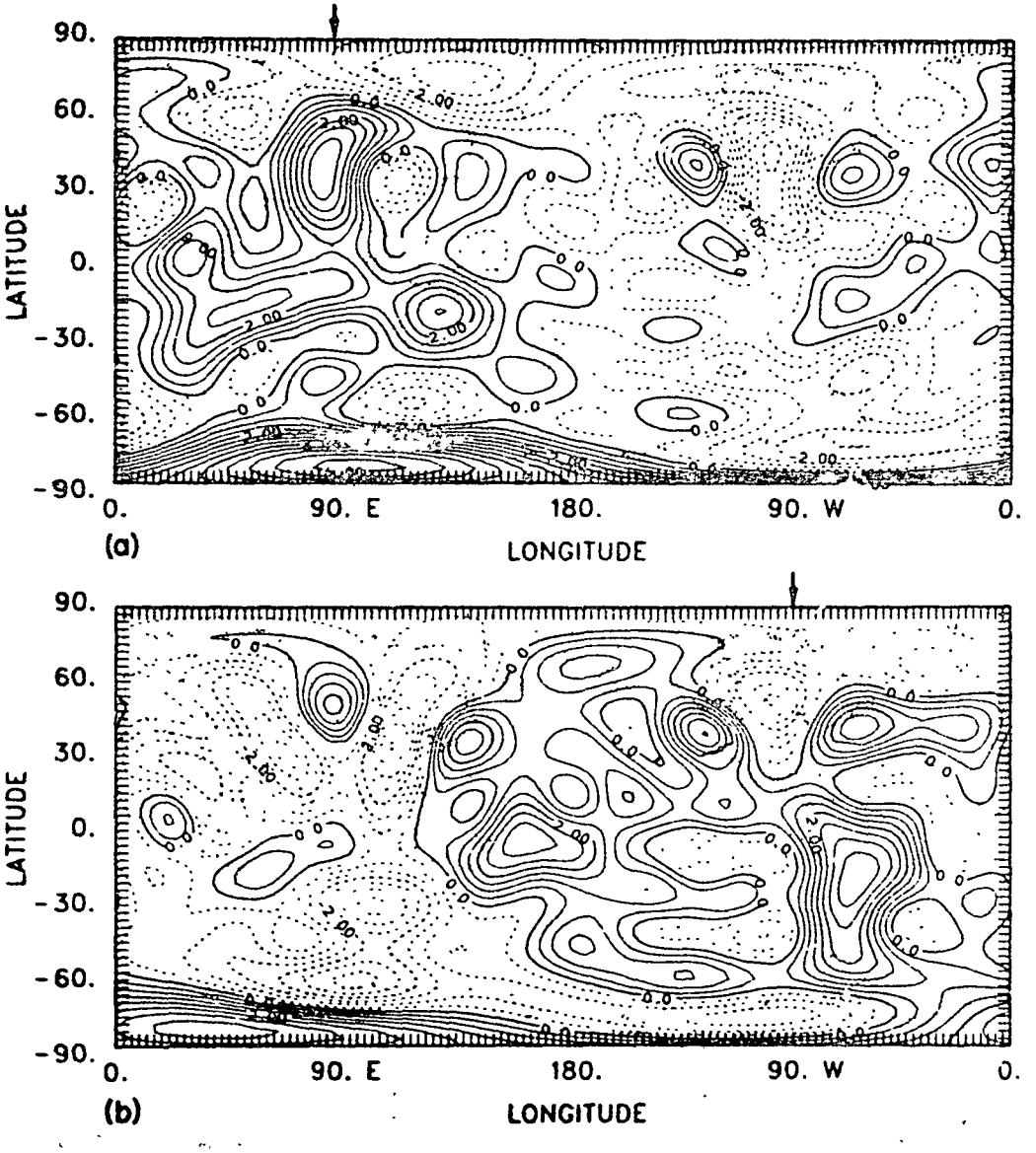

FIGURE 3 Mass-weighted heating rate averaged over the 15-day period at specific times during the SOP-I study period. Contour interval is 0.5 x 10^{-5} K sec^{-1} (= 0.43 K day^{-1}). Arrow at the top indicates the longitude of local noon. (a) Daily average applied at 0600 GMT, (b) daily average applied at 1800 GMT.

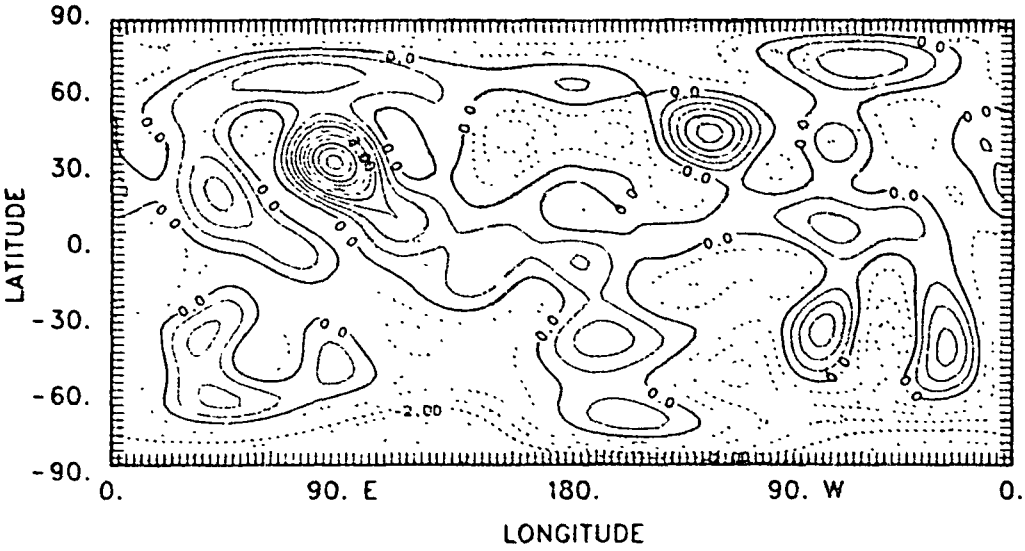

FIGURE 4 Temporal mean of the mass-weighted daily average heating rate defined by (1) for the SOP-II study period of June 7 to 22, 1979. Contour interval is 2 x 10^{-5} K sec^{-1} (= 1.73 K day^{-1}).

Figure 6 shows the latitudinal distribution of the zonally and temporally averaged heating rate by dashed (solid) line for the SOP-I (SOP-II) study period. The heating rate distribution for the SOP-I study period generally agrees with the December 1978 to February 1979 case shown in Figure 4 of Wei et al. (1983), though our problematic values related to the presence of large-scale mountains in the midlatitudes are apparent. The heating rate distribution for the SOP-II study period, however, does not agree very well with the June to August, 1979 case shown in Figure 4 of Wei et al. (1983). One speculation of the cause of this disagreement is that the adjustment weights for the values discussed in Section 2 are derived for the SOP-I data and may not be very appropriate for the SOP-II case.

CONCLUSIONS

Our tropospheric mean diabatic heating rate distributions obtained for the two 15-day study periods generally agree with those obtained by Wei et al. (1983) and Johnson et al. (1984) using the isentropic method of Johnson (1980) with the NMC FGGE Level IIIa analysis data. Wei et al. (1984) also repeated the diabatic heating rate calculation for January 1979 using the same method with the ECMWF Level IIIb analysis data. They discussed major similarities and differences between NMC IIIa and ECMWF IIIb in the diabatic heating rate distributions for January 1979. Our results agree well with those of Wei et al. (1984) for all

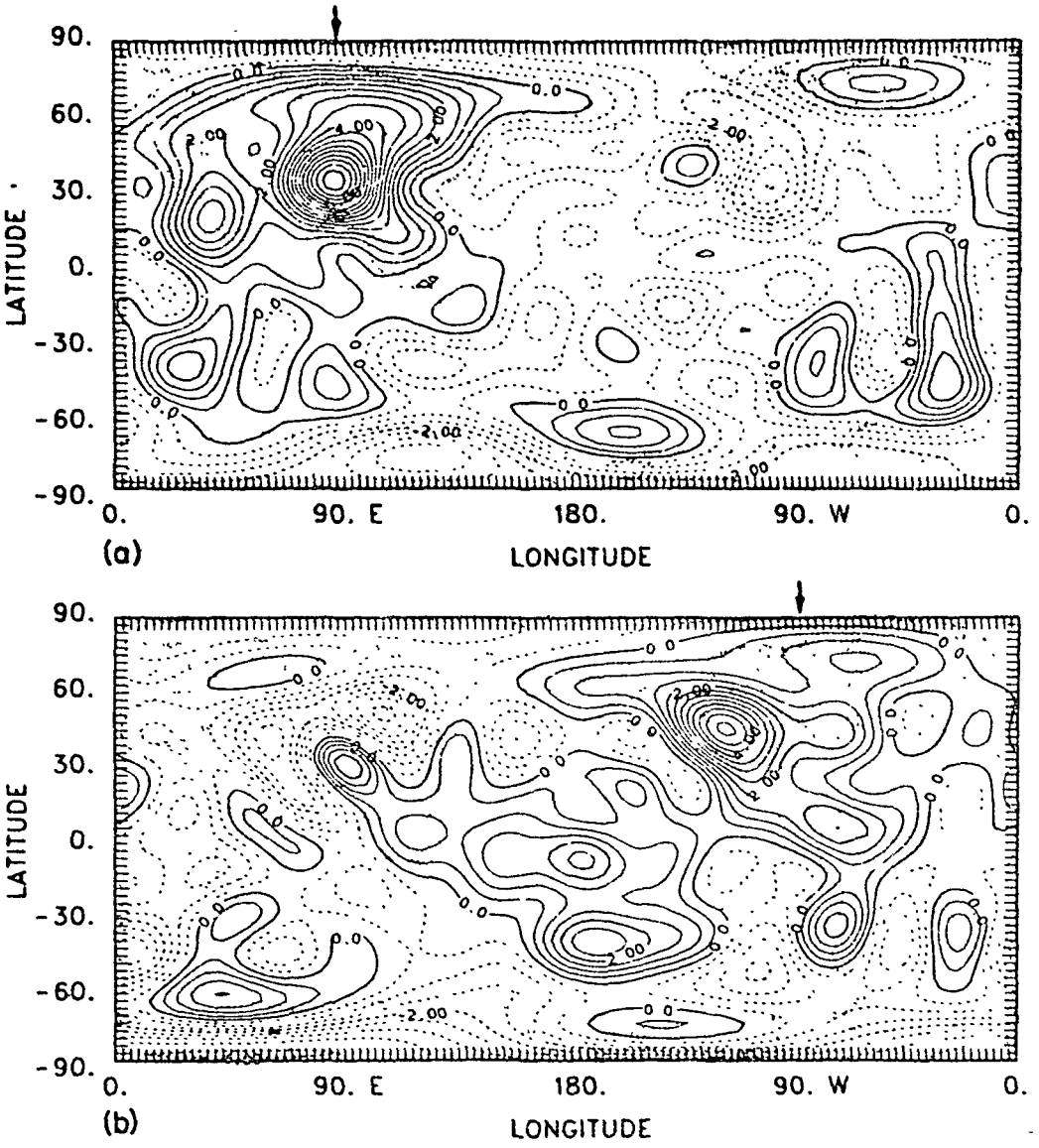

FIGURE 5 Mass-weighted heating rate averaged over the 15-day period at specific times during the SOP-II study period. Contour interval is 0.5 x 10^{-5} K sec^{-1} (= 0.43 K day^{-1}). Arrow at the top indicates the longitude of local noon. (a) Daily average applied at 0600 GMT, (b) daily average applied at 1800 GMT.

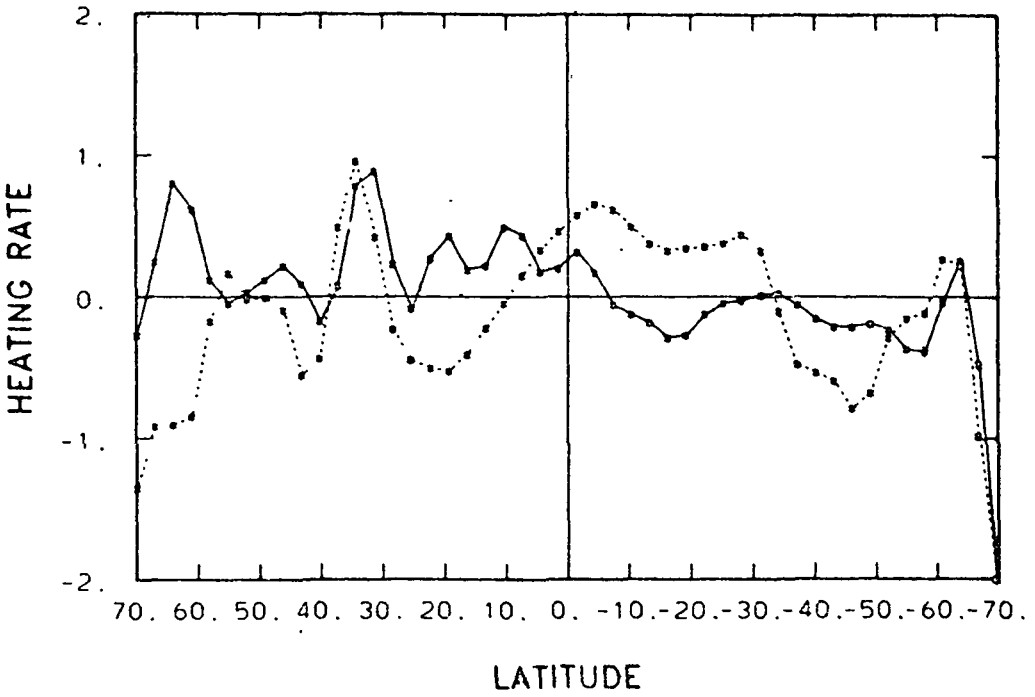

FIGURE 6 Latitudinal distributions of zonally and temporally averaged tropospheric mean heating rate. Dashed (solid) line represents the SOP-I (SOP-II) study period. The scale of heating rate is 10^{-5} K sec^{-1} (= 0.87 K day^{-1}).

similarities between the NMC IIIa and ECMWF IIIb analyses. Our results deviate from theirs mainly in areas where they find differences between the two analyses. There are far more similarities between our results and theirs than differences. Consequently, we can infer that the large-scale diabatic heating rate distributions calculated from the FGGE data sets contain significant meteorological information.

Based on the above conclusions from this preliminary study, we can suggest a number of refinements in the present method of calculation in order to extend this work further.

o The effect of the earth's orography must be carefully taken into account in the lower boundary condition to the calculation of vertical velocity. We have reformulated the calculation method of vertical velocity ω which takes into account the lower boundary condition more accurately than that described in Section 2. This improved method, which will be reported to the Global Weather Experiment Newsletter soon, may eliminate the difficulty over highly elevated mountains discussed in Section 3.

o It is too arbitrary to apply a reduction to the observed divergence (through the calculation of ω) by multiplying a weighting

factor. We know that uninitialized data contain erroneous divergent wind components which produce excessive amplitude of large-scale gravity waves in the course of model integration. Therefore, we must develop a systematic means to eliminate "incompatible" divergent wind components in conjunction with the heating rate calculation.

o In the computing scheme described in Section 2, the local time change and the horizontal and vertical advection terms on the left-hand side of (1) are calculated with finite differences across a 12 hour interval. Further refinements can be made in the evaluation of these terms by considering the dynamical equations that govern the change of horizontal velocity during the 12-hour duration.

In order to achieve these refinements, we intend to use not just the thermodynamic equation but the entire dynamical system by adopting a time integration procedure similar to forecasting with an atmospheric general circulation model (GCM). A GCM has been used for evaluating global heat balance statistics utilizing the technique of four-dimensional data assimilation (Schubert and Herman, 1981; Kalnay and Baker, 1984). Our proposed scheme is different from these previous studies in that we will use an iterative procedure for evaluating the diabatic heating rate, starting from an initial guess of the diabatic heating distribution as given by the present approach. The objective of this iterative procedure is to determine an optimal diabatic heating distribution during a 12- or 24-hour period so that a GCM time integration starting from diabatically initialized conditions will produce the "best" simulation. This procedure will incorporate the above three items for improvement.

ACKNOWLEDGMENTS

This research was conducted at the National Center for Atmospheric Research, which is sponsored by the National Science Foundation. Partial support for this investigation was provided by NOAA under P.O. NA84AAG01214.

REFERENCES

Boville, B. A. (1984). The thermal balance of a general circulation model. (To appear in J. Atmos. Sci.).

Brown, J. A. (1964). A diagnostic study of tropospheric diabatic heating and the generation of available potential energy. Tellus 16, 371-388.

Budyko, M. I. (1963). Atlas of the heat balance of the earth. Moscow Gidrometeoizdat, 69 pp.

Geller, M. A., and S. K. Avery (1973). Northern hemisphere distributions of diabatic heating in the troposphere derived from general circulation data. Mon. Weather Rev. 106, 629-636.

Gray, W. M., and R. W. Jacobson, Jr. (1977). Diurnal variation of deep cumulus convection. Mon. Weather Rev. 105, 1171-1188.

Hantel, M., and H.-R. Baader (1978). Diabatic heating climatology of the zonal atmosphere. J. Atmos. Sci. 35, 1180-1189.

Johnson, D. R. (1980). A generalized transport equation for use with meteorological coordinate systems. Mon. Weather Rev. 108, 733-745.

Johnson, D. R., R. D. Townsend, and M.-Y. Wei (1984). The thermally forced response of the planetary scale circulation to the global distribution of heat sources and sinks. Tellus 36A, 241-255.

Kalnay, E., and W. E. Baker (1984). Analyzed and diagnosed fields in the GLAS FGGE IIIb analysis. U.S. Committee for GARP, Global Weather Experiment Newsletter 3, 29-31.

Krishnamurti, T. N., and Y. Ramanathan (1982). Sensitivity of the monsoon onset to differential heating. J. Atmos. Sci. 39, 1290-1306.

Lau, N.-C. (1979). The observed structure of tropospheric stationary waves and the local balance of vorticity and heat. J. Atmos. Sci. 36, 996-1016.

Luo, H., and M. Yanai (1984). The large-scale circulation and heat sources over the Tibetan Plateau and surrounding areas during the early summer of 1979. Part II: Heat and moisture budgets. Mon. Weather Rev. 112, - .

Masuda, K. (1983). Dynamical estimation of atmospheric diabatic heating over the northern hemisphere in winter. J. Meteorol. Soc. Japan 61, 449-454.

Masuda, K. (1984). Diabatic heating during the FGGE: A preliminary report. J. Meteorol. Soc. Japan 62, - .

Murakami, M. (1983). Analysis of the deep convective activity over the Western Pacific and Southeast Asia. Part I: Diurnal variation. J. Meteorol. Soc. Japan 61, 60-76.

Murakami, T., and Y.-H. Ding (1982). Wind and temperature changes over Eurasia during the early summer of 1979. J. Meteorol. Soc. Japan 60, 183-196.

Newell, R. E., J. W. Kidson, D. G. Vincent, and G. J. Boer (1974). The general circulation of the tropical atmosphere and interactions with extratropical latitudes, Vol. 2. The MIT Press, 371 pp.

Newell, R. E., D. G. Vincent, T. G. Dopplick, D. Perruzza, and J. W. Kidson (1969). The energy balance of the global atmosphere. In The Global Circulation of the Atmosphere, G. A. Corby (ed.), Roy. Meteorol. Soc., 42-90.

Nitta, T. (1983). Observational study of heat sources over the eastern Tibetan Plateau during the summer monsoon. J. Meteorol. Soc. Japan 61, 590-605.

O'Brien, J. J. (1970). Alternative solution to the classical vertical velocity problem. J. Appl. Meteorol. 9, 197-203.

Paegle, J., and J. N. Paegle (1984). GLAS heating rate estimates for SOP-1. U.S. Committee for GARP, Global Weather Experiment Newsletter 3, 25-28.

Reed, R. J. (1983). The diurnal variation of precipitation in the tropics. Preprints of First International Conference on Southern Hemisphere Meteorology. Amer. Meteorol. Soc., Sao Jose dos Campos, Brazil, 31 July - 6 August, 1983, 312-319.

Schubert, S. D., and G. F. Herman (1981). Heat balance statistics derived from four-dimensional assimilations with a global circulation model. J. Atmos. Sci. 38, 1891-1905.

Wei, M.-Y., D. Johnson, and R. D. Townsend (1983). Seasonal distributions of diabatic heating during the First GARP Global Experiment. Tellus 35A, 241-255.

Wei, M.-Y., D. R. Johnson, T. K. Schaack, and R. D. Selin (1984). A quick comparison of diabatic heating rates between NMC IIIa and ECMWF IIIb datasets for January 1979. U.S. Committee for GARP, Global Weather Experiment Newsletter 4, 11-20.

omit

HEAT AND MOISTURE BUDGETS OVER THE TIBETAN PLATEAU

Michio Yanai
University of California, Los Angeles

Material presented by M. Yanai is contained in the following publication:

Luo, H., and M. Yanai (1984). The large-scale circulation and heat sources over the Tibetan Plateau and surrounding areas during the early summer of 1979. Part II: Heat and moisture budgets. Monthly Weather Review 112, 966-989.

D19

THE PARTITION OF ENERGY ASSOCIATED WITH TROPICAL HEAT SOURCES

Pedro L. Silva-Dias
University of Sao Paulo, Brazil
and
Julia N. Paegle
University of Utah

ABSTRACT

Data sets derived from observations during the First GARP Global Experiment (FGGE) have permitted the study of the behavior of the tropical atmosphere to an extent not possible before. The present summary discusses characteristics of the tropical atmosphere which may be a result of tropical heating.

It is shown that the meridional component of the divergent wind is of the same order of magnitude as the rotational meridional wind for the planetary tropical scales. Furthermore, the first and second internal modes dominate over most of the tropics, and it is shown that gravity and Kelvin modes are the main contributors to the total tropical divergence. Comparison with averaged station precipitation data and heating estimates obtained from Goddard Laboratory for Atmospheric Sciences (GLAS)/National Aeronautics and Space Administration (NASA) show good correspondence between areas with maximum internal mode energy and regions with pronounced latent heat release.

INTRODUCTION

Extension of atmospheric predictability, a key FGGE objective, depends crucially on the adequate incorporation of physical processes, extended domains of integrations, initialization and numerical techniques. Recent numerical experiments (i.e., Paegle and Baker, 1983) have quantified the impact of tropical heating in global forecasts. It appears that variations of the vertically reversing circulation in the tropics affect the subtropical latitudes in time scales of 3 to 5 days in nonlinear integrations. The study of the observed characteristics of vertically reversing tropical motions is therefore of interest to forecasts of subtropical flows. Emphasis here is placed on the normal mode decomposition of gridded data. This analysis is useful to discuss the behavior of motions associated with tropical heat sources.

On the sphere, the normal modes of the atmosphere are identified with Rossby, inertio-gravity, Kelvin, and mixed Rossby-gravity waves (Longuet-Higgins, 1968; Matsuno, 1966; Kasahara, 1976). In recent

years, normal mode decompositions have been used for the initialization of the primitive equations (Daley, 1981). However, the initial concept of linear normal mode initialization, which is based on the filtering of all fast modes, has proved to be unsatisfactory due to the generation of gravity modes by the nonlinear terms (Williamson, 1976). As a result, the nonlinear normal mode initialization has been developed in operational applications in middle latitudes (Baer, 1977; Machenhauer, 1977). However, in the tropics where strong diabatic heating is present in the form of latent heating, the concept of balance between the fast modes and the nonlinear terms breaks down, and the forcing terms play an important role (i.e., Daley, 1981). The initialization in the presence of strong heat sources remains a problem for tropical forecasts (Errico, 1983). The Machenhauer scheme does not converge for high order vertical modes, and it is not clear that higher order modes should be initialized. Puri (1983) discusses the maintenance or the Hadley cell represented by internal modes with equivalent depth of the order of 220 m and shows that removal of the convective parameterization of latent heat release destroys the Hadley circulation in the Australian Numerical Meteorological Center model.

Atmospheric linear response to transient forcing has been studied by Paegle (1978), Lim and Chang (1981, 1983), Lau and Lim (1982), and Paegle and Paegle (1983). Linearized analysis of the shallow water equations were done by Silva-Dias et al. (1983) for the β-plane and Kasahara (1984) for a global primitive equation model. For a vertical parabolic heating profile, it is found that internal modes are favorably generated and that excitation of rotational or gravitational modes depends on the time scale of the heating.

Observational studies of the tropical atmosphere have shown the importance of time scales as short as one day. Reed (1983) presents a recent review of the diurnal variations in the tropics. Silva-Dias et al. (1983) have discussed the energy partition for a localized heat source and found that, as the forcing frequency increases, the amount of gravity wave generation increases while the amount of Rossby wave generation remains approximately constant. The characteristics of this response are quite different than those obtained for long-term and stationary forcings (i.e., Webster, 1972, 1981; Gill, 1980; Geisler and Stevens, 1982; Koura and Shukla, 1981). Silva-Dias et al. (1983) have also discussed the partition of energy of tropical transient forcing as a function of the spatial as well as the temporal scale of the forcing. They find that (1) the Rossby wave energy increases as the spatial scale and latitude of the forcing increases; (2) as the forcing frequency decreases, less energy is excited in the high frequency modes; (3) as the forcing spatial scale increases, the energy in gravity modes decreases sharply; and (4) for fixed time scale of the forcing, the energy in high frequency modes initially increases with the horizontal scale and then decreases.

The observation in (4) for large-scale forcing is related to the classical result from geostrophic adjustment that indicates that a disturbance in the mass field will excite less gravity wave energy and more energy in the geostrophically balanced flow as the scale of the disturbance increases. The decrease in gravity wave energy for small

spatial scales is related to the time scale of the forcing. For small horizontal scales, the forcing will project onto a wide range of zonal waves and meridional modes that have higher frequency. Thus the amplitude of such modes is reduced because they are well apart from the frequency of the forcing and, consequently, not resonant.

The convective bursts in the tropical atmosphere occur day after day for extensive time periods. As this happens, the atmospheric response is distorted from the response to a single localized burst. Observed atmospheric features may be expected then to differ from those obtained by linearized models of single localized forcings although the main characteristics may be reproduced.

Tropical observations have dramatically improved with the new observing technology and the compilation of tropical winds from satellite derived cloud trackings. These observing systems have been widely used during the FGGE year. Examination of tropical motions during the FGGE year would thus be helpful to quantify the characteristics of the tropical motions in light of the theories discussed above.

In Section 2, the importance of the divergent contribution to the tropical meridional motions is discussed for three different data sets. The divergence field is analyzed in terms of the normal modes of a primitive equation model at rest. This decompositon (Section 3) indicates the importance of gravity and Kelvin modes in the divergence field. Section 4 relates these results to indirect estimates of heating produced by GLAS/NASA and to precipitation estimates.

TROPICAL WINDS

Figure 1 presents the rotational and divergent components of the meridional wind obtained from the GLAS Level IIIb analyses averaged for the months of January and February, 1979. Only the zonal mean and longitudinal Fourier modes 1 through 4 are retained in these analyses. Maximum isolines of 4 and 8 m/s appear for the divergent and rotational component of the wind, respectively, indicating the relative importance of meridional divergent winds.

Also, three different analyses (ECMWF, GLAS, GFDL) of Level IIIb data for January 15, 1979 (Figure 2) are displayed to show that the strongest divergent wind regions are resolved in different objective analyses of the raw data (Paegle et al., 1984). The weaker divergent winds of the ECMWF analyses may reflect the first guess initialization procedure that is based on an adiabatic formulation. The GFDL initialization uses a diabatic formulation at this stage of the analysis, and the GLAS analysis does not incorporate any explicit initialization balances. It is interesting to note that the rotational wind field is less sensitive to the assimilation procedure.

It is evident that the variation of the meridional divergent wind from 20°S to 20°N is about as great as is the variation of the rotational meridional wind in this tropical belt. The amplitude of each is about 10 m/s to this truncation. This is different from the midlatitudes, where the divergent wind is only a few m/s and the

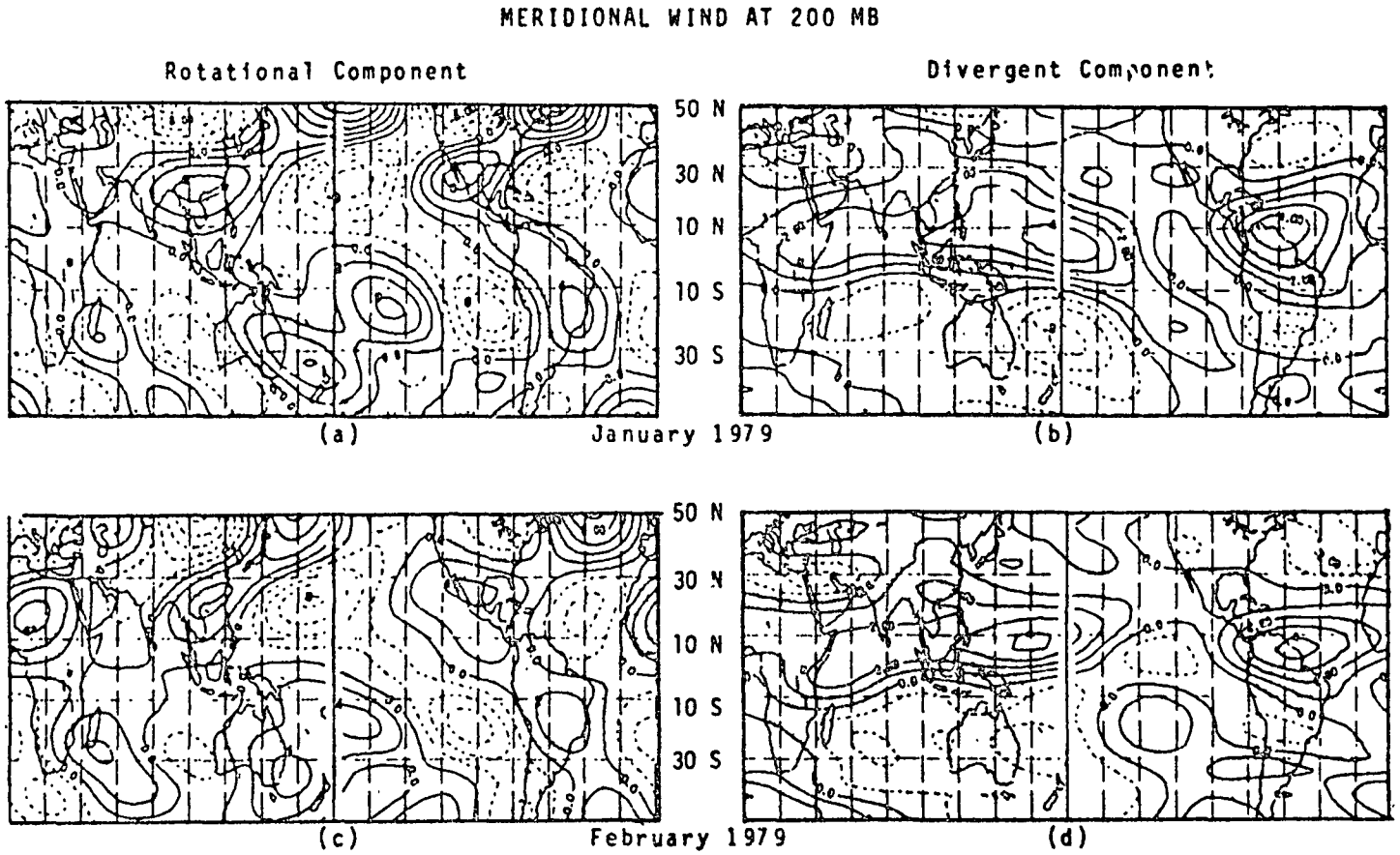

FIGURE 1 Rotational (a) and divergent (b) meridional wind component for January 1979, obtained from a decomposition of the streamfunction and velocity potential retaining the zonal average and longitudinal Fourier modes 1 to 4 m/s. The calculations use gridded data produced by GLAS. (c) and (d) same as (a) and (b) for February.

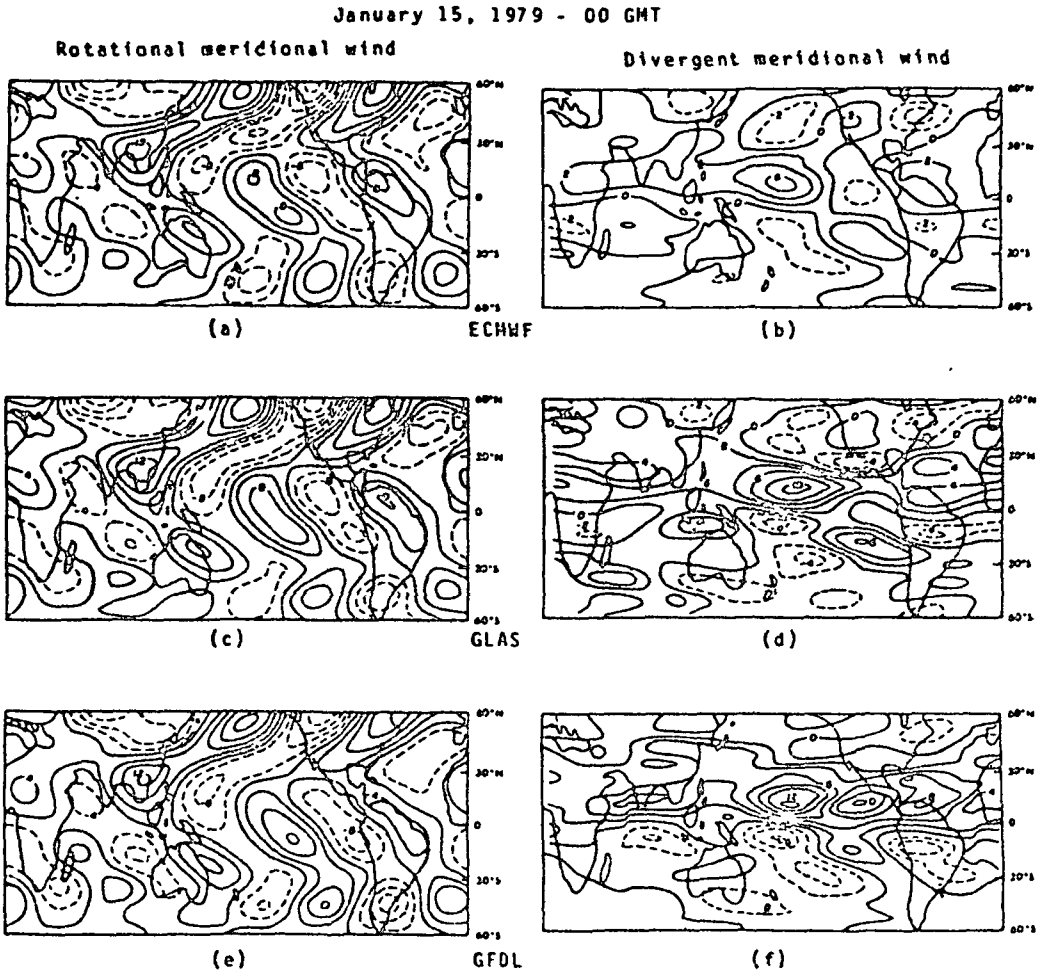

FIGURE 2 Same as 1 for January 15, 00Z, 1979. (a) and (b) use level IIIb ECMWF analyses, (c) and (d) GLAS, and (e) and (f) GFDL analyses.

rotational wind may be much larger than 10 m/s. It is concluded that, although the regions of pronounced divergence are rather restricted, their influence projects strongly on the global scale wind pattern of the tropics. Furthermore, since the rotational and divergent wind components of the large-scale waves are of similar amplitude, they are both approximately equally observable in the tropics, at least for the longwave components. This is distinct from the midlatitudes, where the divergent wind field is generally weak enough to be obscured by observational uncertainty.

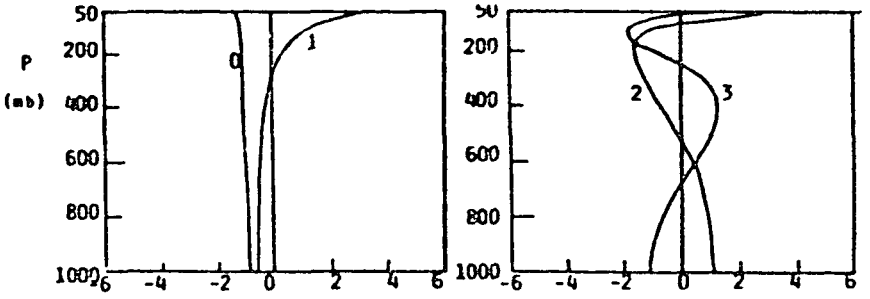

FIGURE 3 Eigenfunctions associated with the eigenvalues of Table 1 for vertical modes 0, 1, 2, and 3.

OBSERVED NORMAL MODE DECOMPOSITION

Time Averaged Flows

In this section, the normal mode representation of FGGE Level IIIb data from the European Centre for Medium Range Weather Forecasts analysis is explored. The regular gridded data at 1.875° x 1.875° resolution was decreased to 3.75° x 3.75° by removing every other point. This coarse grid was generated at the National Center for Atmospheric Research. Two particular periods are discussed here: January 29 to February 16, 1979 (the southern hemisphere summer period--SHSP) and July 1 to July 18, 1979 (the northern hemisphere summer period--NHSP).

In order to interpret the geopotential and flow field associated with the vertical modes, it is necessary to consider the vertical structure of the eigenfunctions shown in Figure 3. The phase speed of the pure gravity waves (the scaling for velocity) and the equivalent depth (scaling for geopotenial) are shown in Table 1. Figures 4, 5, and 6 show the percentage of total energy (a), as defined by Kasahara and Puri (1981), and the corresponding geopotential and wind fields (b) associated with the external, first, and second internal modes, respectively, for the SHSP. The following features are noticeable:

1. The small percentage of the external mode in the tropical region, the dominance of the external mode in midlatitudes, and its decrease at higher latitudes (Figure 4a).
2. Midlatitude westerlies are well represented by the external mode (Figure 4b).
3. The first and second internal modes maximize in the tropics with relative maxima also found at very high latitudes; (Figures 5a and 6a).
4. The first internal mode has a larger contribution equatorward of the peaks of the second internal mode (thus implying a deeper layer of convergence in the lower troposphere at low latitudes).
5. The magnitude of the wind in the tropically active regions is slightly larger for the first internal mode (compare the scaled wind vectors in Figures 5b and 6b).

TABLE 1 First 12 Eigenvalues h_n and Phase Speed of Pure Gravity Waves $c_n = gh_n$ for a basic state defined as the average sounding during the period January 29 to February 16 between 0°W and 120°W and 25°N and 25°S. The Top Level is Located at 50 mb

n	h_n	$\sqrt{gh_n}$
0	8990	297
1	544	73.0
2	208	45.1
3	72.2	26.6
4	37.6	19.2
5	25.5	15.8
6	15.4	12.3
7	10.0	9.9
8	7.0	8.3
9	5.0	7.0
10	3.2	5.6
11	1.8	4.2
12	0.7	2.7

6. The upper tropical westerlies over the eastern Pacific and Atlantic Oceans and the upper anticyclonic circulation over the convectively active regions are also well represented by the low order internal modes (Figures 5b and 6b).

7. The first internal mode flow field (Figure 5b) has a large amplitude in the winter hemisphere, while the second internal mode (Figure 6b) also contributes to the southern hemisphere upper westerlies.

The higher order internal modes contribute a small percentage to the total energy and are not included here although they can be locally important at lower levels (Williamson and Temperton, 1981). The dominance of the low order internal modes in the expansion of FGGE Level IIIb data has also been shown by Silva-Dias and Bonatti (1984) using the vertical modes of Kasahara and Puri (1981).

The seasonal variation of the Hough decomposition of the vertical modes is shown in Figures 7, 8, and 9 for the external, first, and second internal modes, respectively, for the SHSP and NHSP as defined above. The zonal truncation is at wavenumber 24, and 20 meridional modes are maintained in the Hough expansion (Kasahara, 1976). The contribution of the Rossby (a), gravity (b), Kelvin (c), and mixed Rossby gravity (d) waves are also shown in Figures 7 and 8. For the

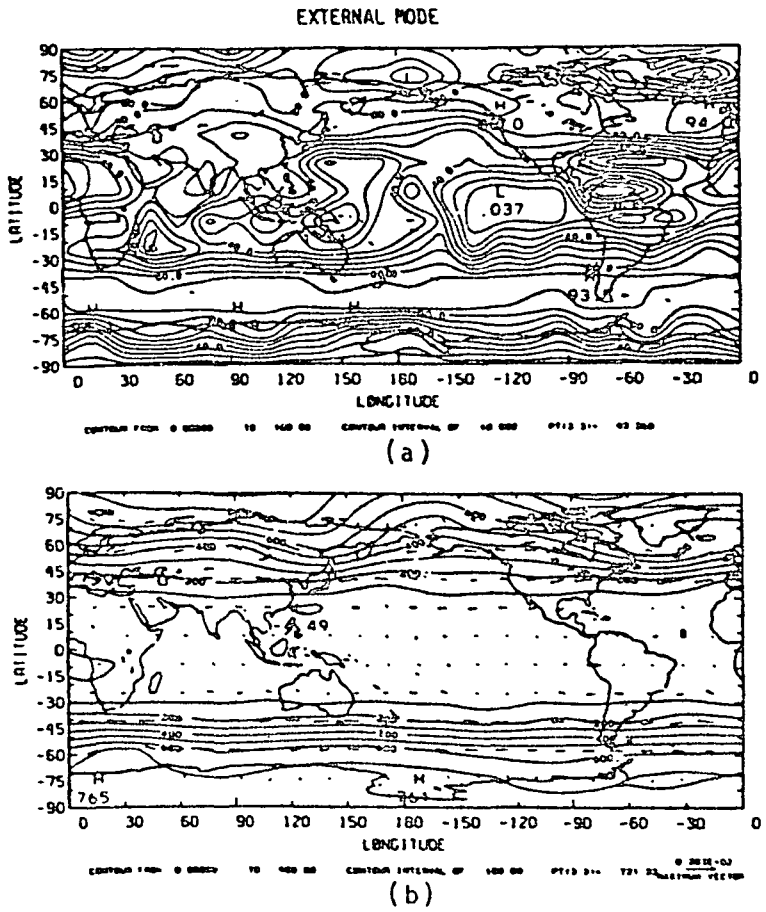

FIGURE 4 (a) Percentage of total energy in mode n = 0 (external) and (b) corresponding u, v, and fields in m/s and m, respectively.

second internal mode, only the Kelvin contribution is shown (Figure 9). The wind vectors are scaled by the phase speed of pure gravity waves of the appropriate vertical mode (Table 1) and the geopotential by the equivalent depth.

The vertical profile of the external mode given in Figure 3 indicates that the wind and geopotential fields in Figure 7 have to be reversed in order to interpret the fields at any level of the atmosphere. The rotational component (Figure 7a) is well characterized by the seasonal changes in the general circulation, emphasizing the strong westerlies in the SHSP. The gravity component (Figure 7b) displays a high degree of zonal symmetry along the equatorial Pacific Ocean in the SHSP with meridional wind components of the order of 1 m/s. Large values of the gravity component are also found in the Antarctic region and at higher latitudes in the southern hemisphere

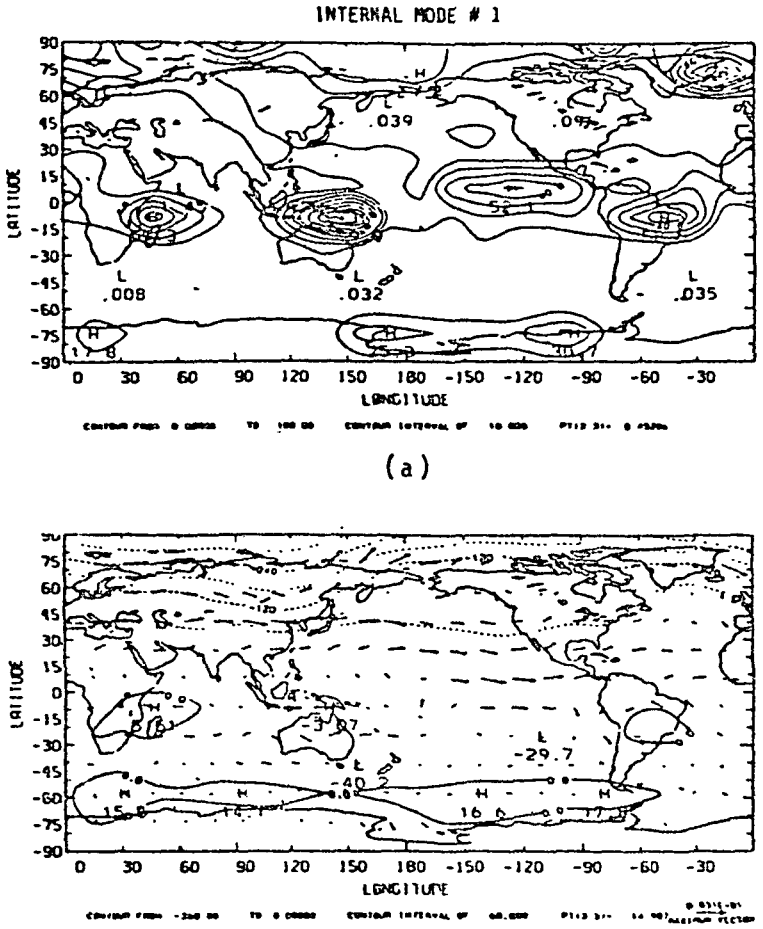

FIGURE 5 Same as Figure 4 but for the first internal mode (n = 1).

winter--NHSP--(perhaps an indication of poor analysis quality in this region) as well as over the Himalayan mountains.

The Kelvin contribution (Figure 7c) is centered over the convectively active regions (magnitude of the order of 0.4 m/s) and shows a marked difference from the SHSP to the NHSP (note the large contribution in the Indian Ocean during the NHSP). Longer waves tend to dominate over the Pacific Ocean during the SHSP and shorter waves over South America. Over the Atlantic Ocean, the larger contribution appears during the NHSP. Figure 7c displays (with the flow reversal indicated by Figure 3) upper westerlies located to the east of the active regions.

The mixed Rossby gravity waves have relatively larger meridional components (of the order of 1.5 m/s) and are characterized by much

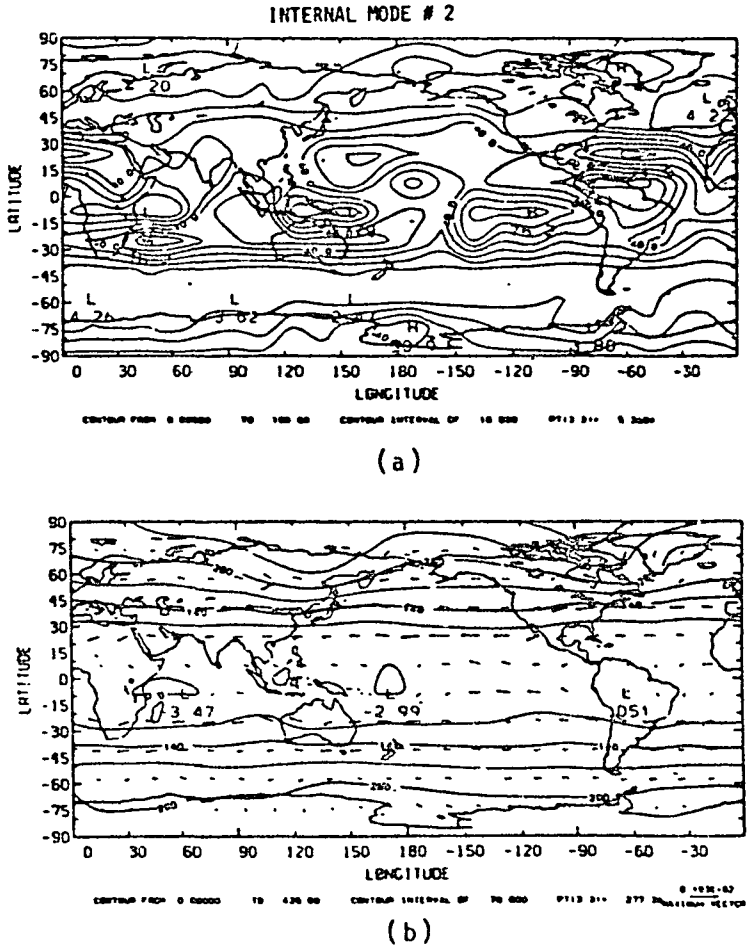

FIGURE 6 Same as Figure 4 but for the second internal mode (n = 2).

shorter scales when compared to the Kelvin contribution. It is interesting to note the relatively small effect of mixed waves in the Indonesian region during the SHSP and large contribution during the NHSP. This is probably related to the equatorial concentration of the convection and the symmetry with respect to the equator for this type of wave.

The first internal mode contribution (Figure 8) indicates the baroclinity of the circulation. According to Figure 3, the upper level flow has the same direction as the wind vector in Figure 8. The velocity scaling is of the order of 70 m/s (Table 1). Most of the characteristics of the gravitational component of the external mode are present in the internal mode (Figure 8b) and the order of magnitude is slightly larger (1.4 m/s). The active tropical areas are well identified. The Kelvin contribution shows similar variations from

summer to winter in the Pacific and Indian Oceans. The largest contribution over tropical South America is found during the NHSP, when most of the convective activity is in the equatorial region. These results are in agreement with the model-derived partition of energy (Silva-Dias et al., 1983). The same observation holds for the mixed Rossby gravity component (Figure 8d), which is smaller over South America during the NHSP. The Kelvin contribution for the second internal mode (Figure 9) agrees fairly well with the first mode Kelvin component (the flow field has to be reversed according to Figure 3 and the velocity scaling is approximately 40 m/s).

The divergence field for the SHSP and for the first internal mode is shown in Figure 10 assuming: summation over all waves (Figure 10a), gravity waves (Figure 10b), Rossby waves (Figure 10c), Kelvin waves (Figure 10d), and mixed Rossby gravity waves (Figure 10e). The divergence field in Figure 10 is made dimensional by a factor of 2 ($0.00014\ s^{-1}$). The important role of gravity waves in the divergence field is obvious in Figure 10. The rotational contribution is marginal except over the convectively inactive regions such as over the subtropical highs. A fairly smooth picture emerges from Figure 10a over the tropical region, but the divergence over mountainous regions seems to be contaminated by the analysis procedure. The single Kelvin mode has more divergence (note the scaling of the divergence field in both Figures 10c and 10d) than the Rossby waves in spite of the fact that the Rossby contribution is obtained by summation over 10 meridional modes. The external mode contribution to the divergence is much smaller (of the order of 10 percent) than the first internal mode contribution while the second internal mode is as strong as the first internal mode in the tropical region over the convectively active regions. The general distribution of the second internal mode divergence is similar to the first internal mode and therefore is not shown.

ECMWF and GFDL Intercomparisons

We now compare the normal mode projection of the Level IIIb divergence fields of the ECMWF and GFDL (Geophysical Fluid Dynamics Laboratory/NOAA) analyses at 0000 GMT on January 15, 1979. Figure 11 shows the contribution to the divergence field at 200 mb summed over the 15 lowest meridional, 12 lowest zonal, and 4 lowest internal vertical modes with equivalent depths between 75 m and 800 m.

Tropical divergences obtained from GFDL data are 2 to 3 times larger than those present in the ECMWF Level IIIb data sets (not shown). Contributions from the large-scale gravity modes resolved by the normal modes described above are about 10 times larger than those of the Rossby and mixed Rossby. Gravity modes are a factor of 3 to 4 times larger than the Kelvin modes in both data sets. The contribution from the gravity and Kelvin modes in the GFDL data are about 20 to 30 percent larger than those present in the ECMWF analyses and present similar patterns. This suggests that the large differences observed for the total tropical divergence field occur in smaller scales not resolved by the present normal mode analyses.

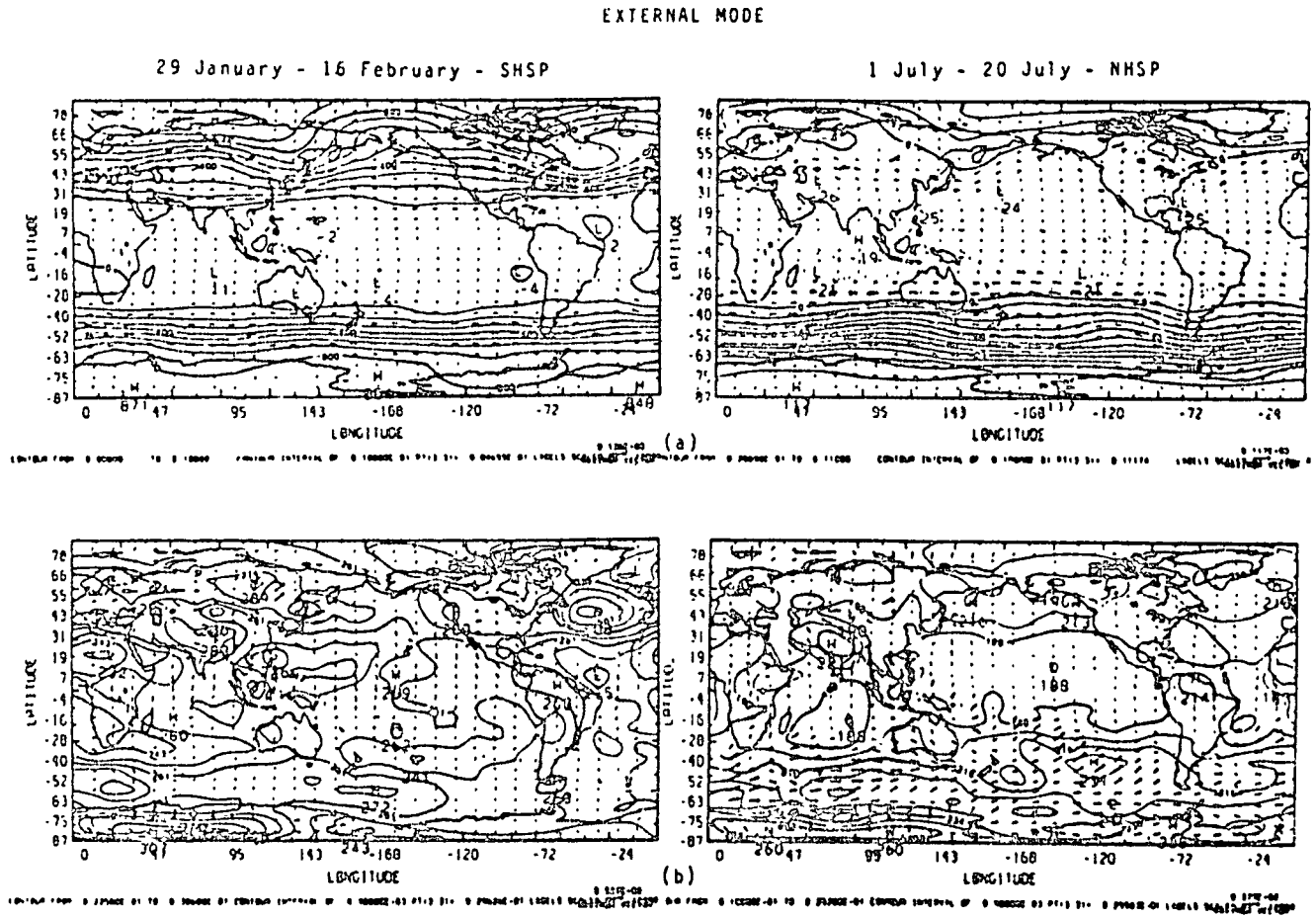

FIGURE 7 Non-dimensional wind and geopotential fields associated with rotational components (a), gravity waves (b), Kelvin waves (c), and mixed Rossby gravity waves (d) for the external mode for the SHSP and NHSP. A factor of C_o = 297 m/s gives wind vectors in m/s.

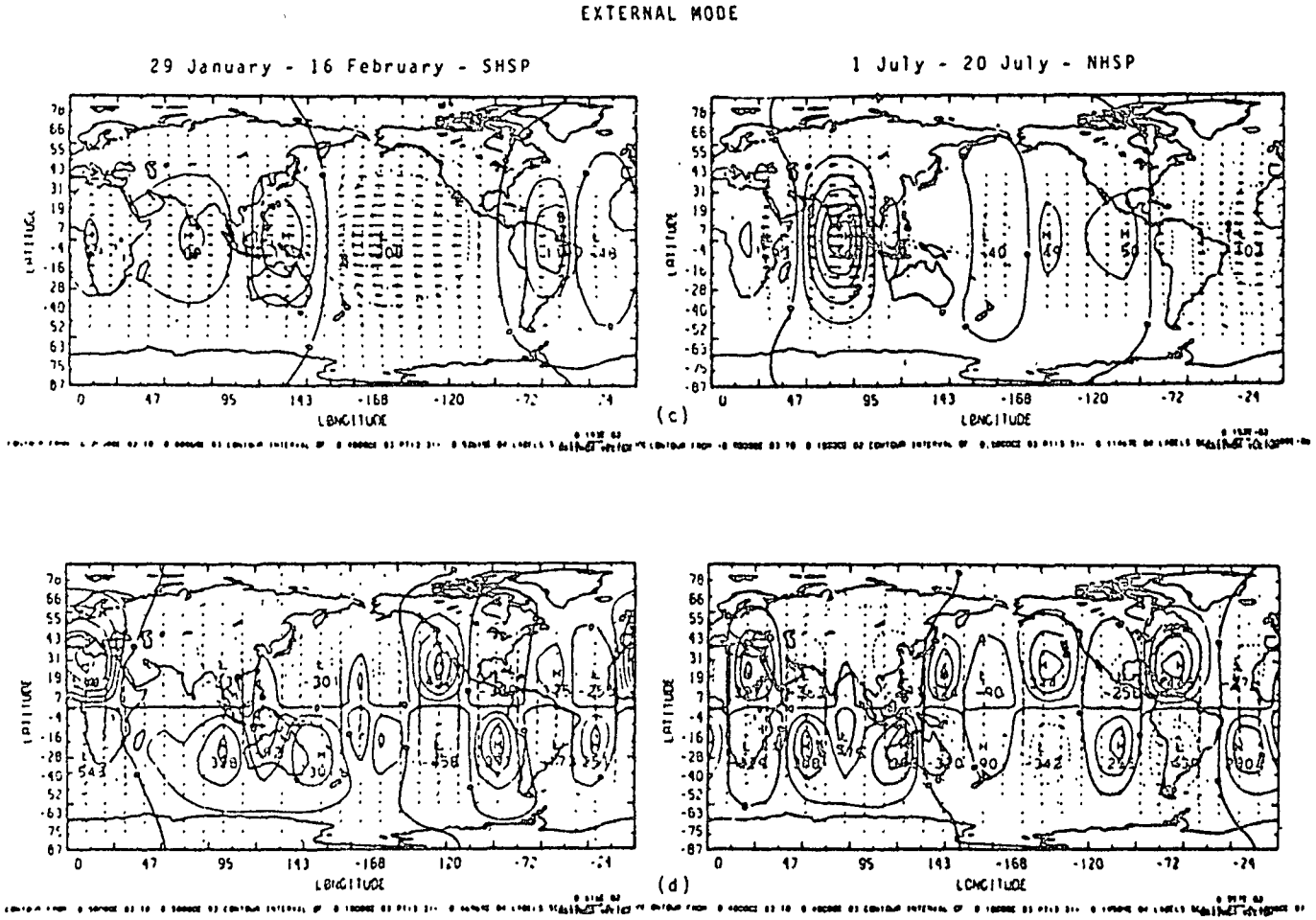

FIGURE 7 (continued)

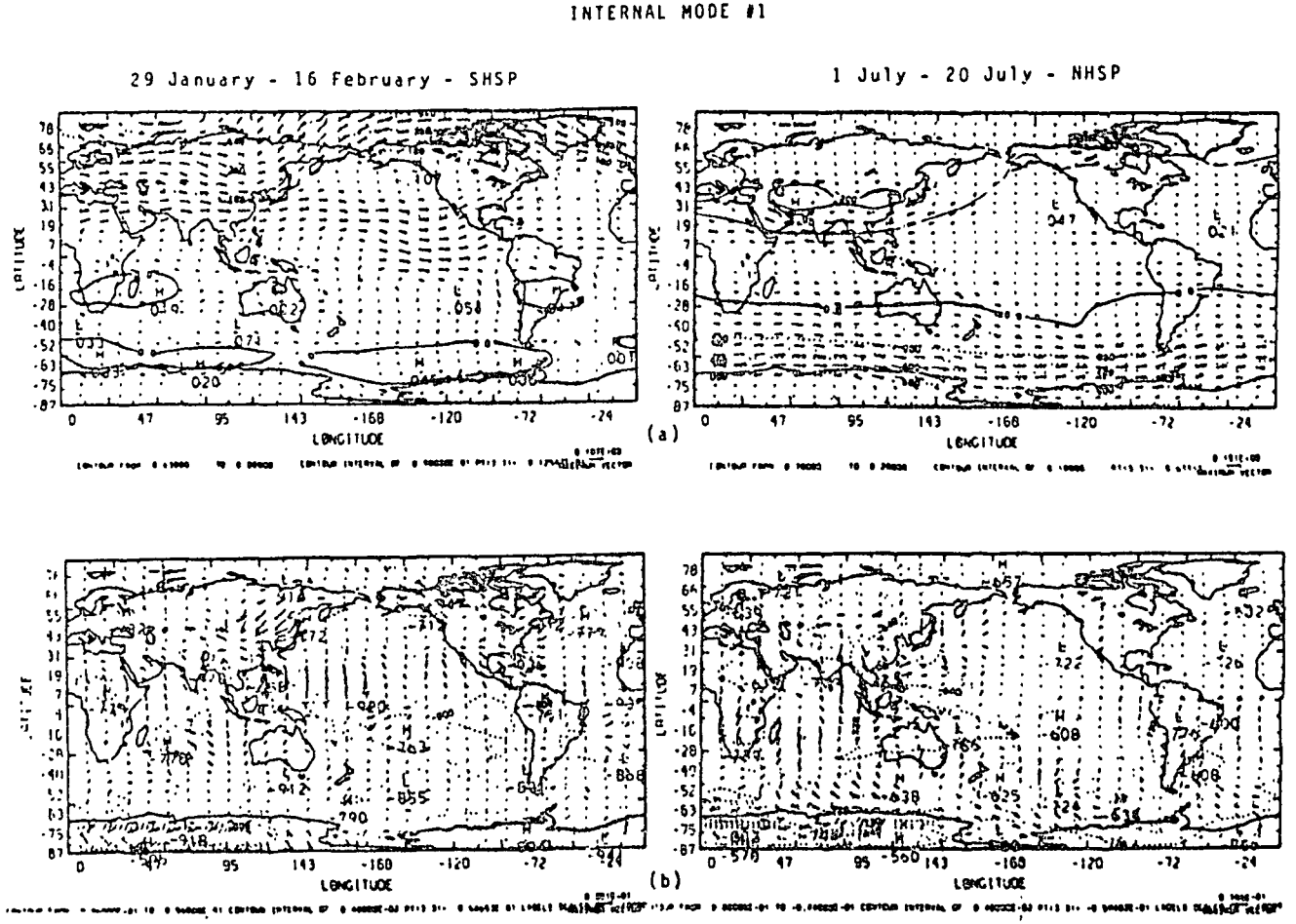

FIGURE 8 Same as Figure 7 except for the first internal mode (n = 1). The wind scaling is C_n = 73 m/s.

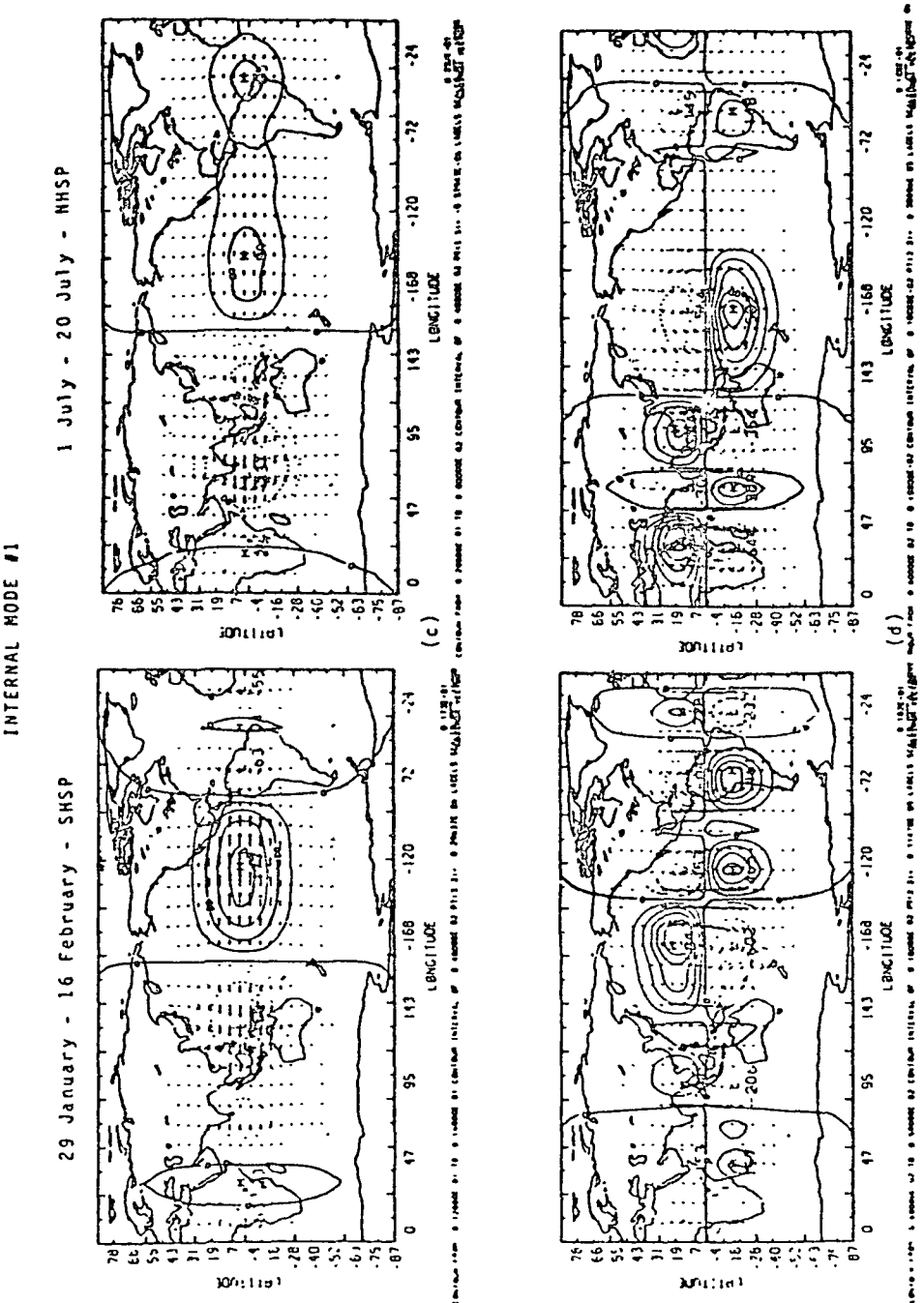

FIGURE 8 (continued)

29 January - 16 February - SHSP

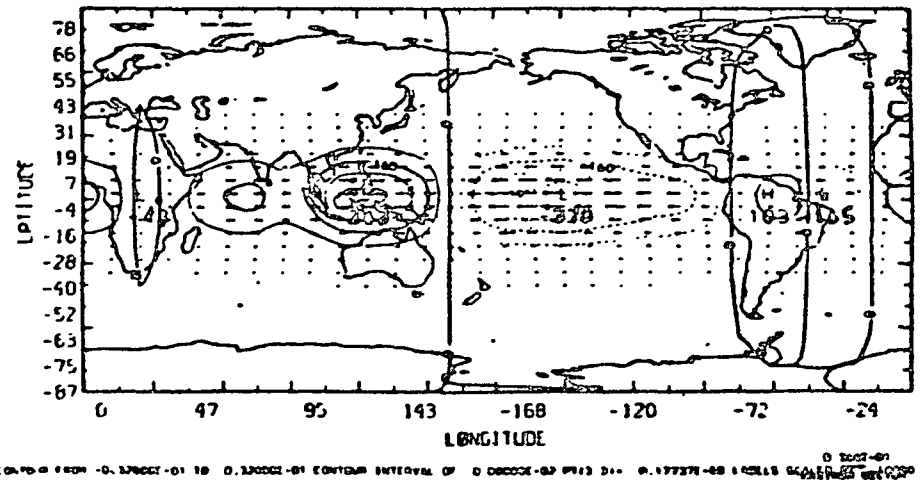

1 July - 20 July - NHSP

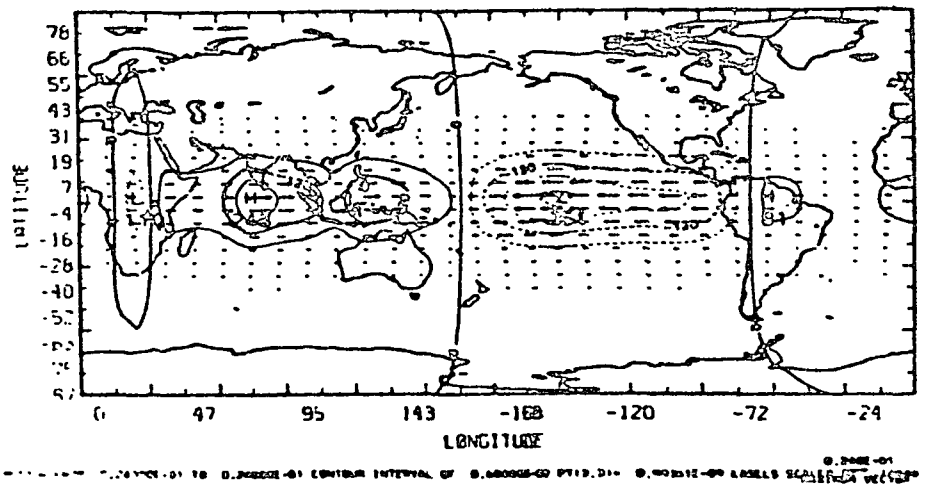

FIGURE 9 Nondimensional wind and geopotential associated with the Kelvin components for the second internal mode for the average southern hemisphere summer period (a) and northern hemisphere summer period (b). The wind scaling is C_2 = 45 m/s.

DIVERGENCE FIELD

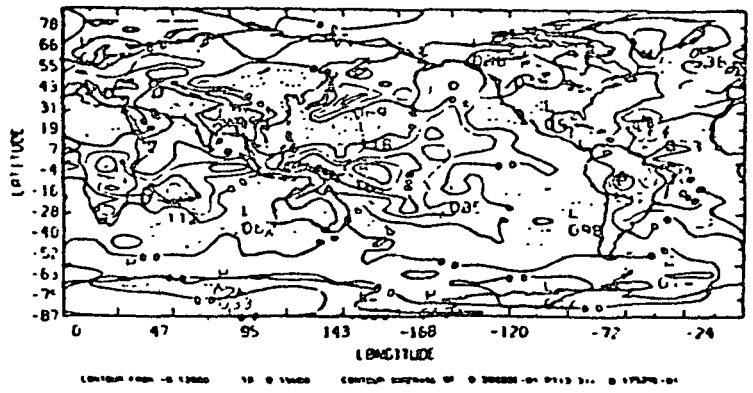

All Waves

(a)

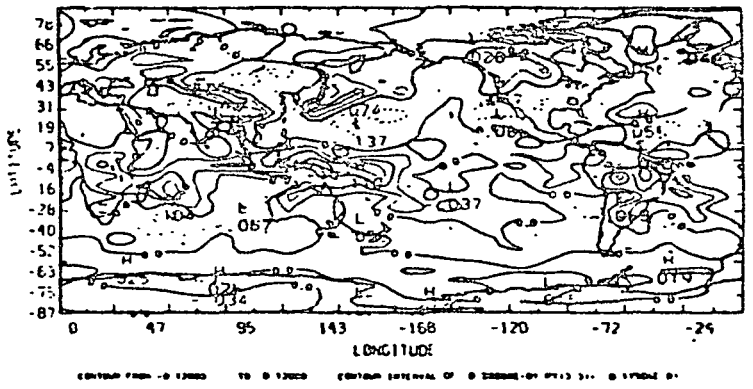

Gravity Waves

(b)

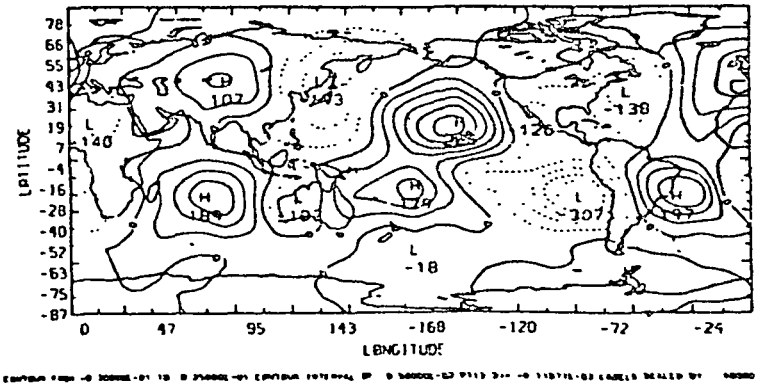

Rotational Waves

(c)

DIVERGENCE FIELD

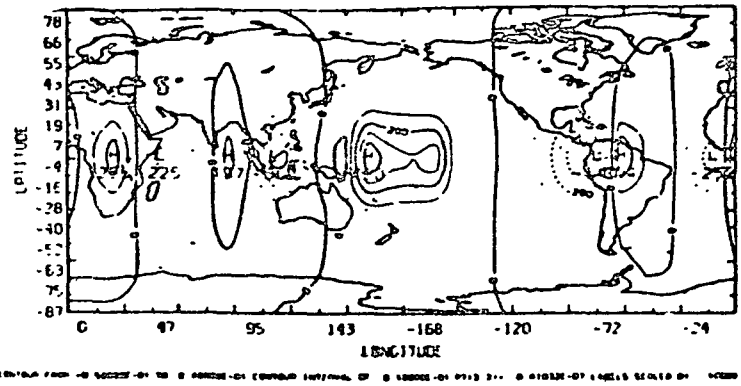

(d)

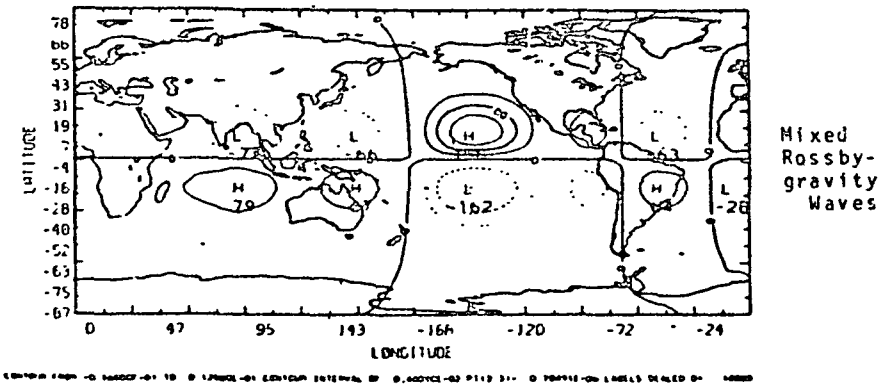

(e)

FIGURE 10 Nondimensional divergence field for the SHSP for (a) all waves, (b) gravity, (c) Rossby, (d) Kelvin, and (e) mixed Rossby gravity components.

TROPICAL HEATING

Station precipitation data were averaged for a grid of 1-7/8° x 1-7/8° for the SHSP and NHSP of the normal mode decomposition. Figures 12a and 12b display the seasonal precipitation changes. *Distinct maxima are found for the SHSP over the Amazon basin,* western Pacific, northeastern coast of Australia, western Indonesia, and eastern coast of Africa. The northern shift of the precipitation maxima associated with the Asian monsoon are apparent in Figure 12b.

GRAVITY MODES
DIVERGENCE ($10^{-7}s^{-1}$)
JANUARY 15, 00Z

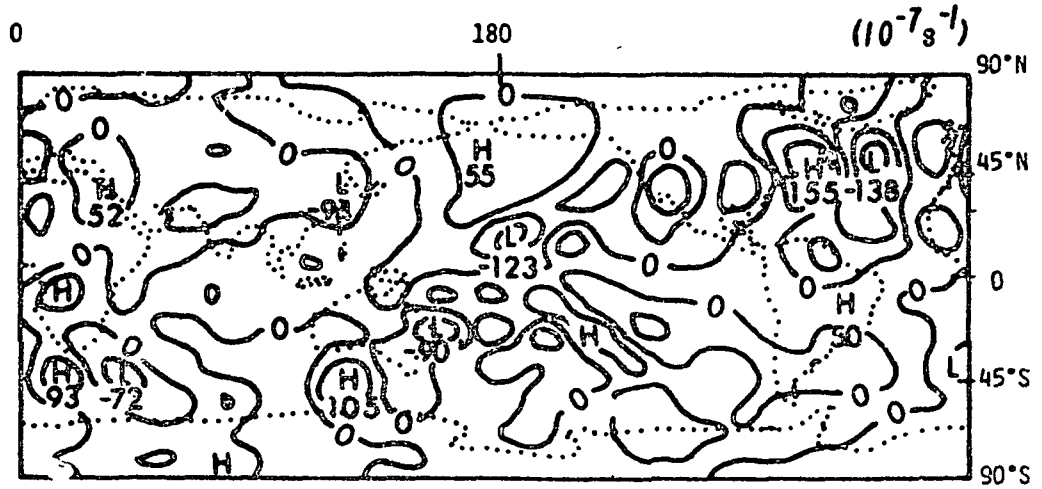

ECMWF

(a)

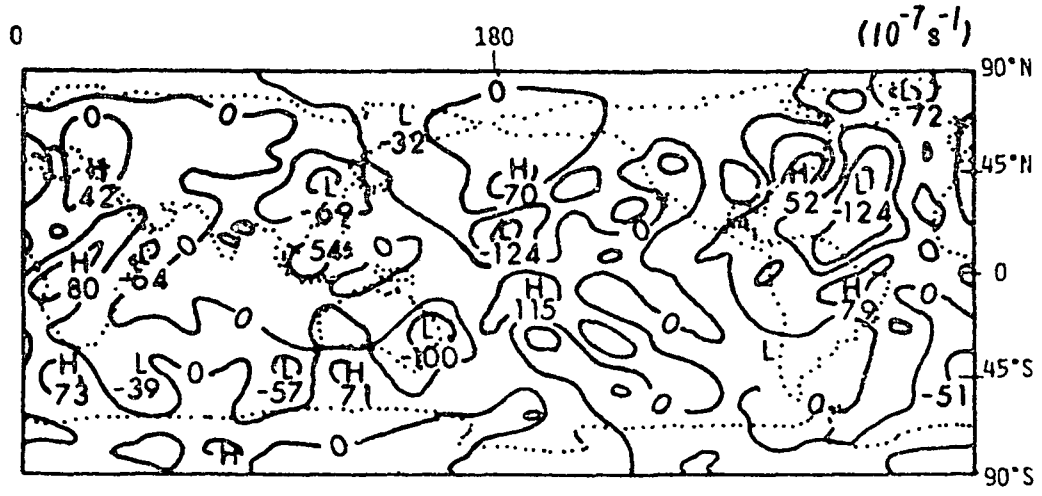

GFDL

Data gaps of precipitation over the oceans limit the applicability of precipitation analyses to continental regions. Figure 13 displays the outgoing long wave radiation obtained by NESS/NOAA for a period almost identical to the SHSP. The precipitation maxima of Figure 12a present good correspondence with tropical areas of low outgoing long wave radiation.

Estimates of atmospheric heating rates are available from the FGGE data assimilation of GLAS/NASA. These heating rates are obtained on

ROSSBY MODES
DIVERGENCE ($10^{-8}s^{-1}$)

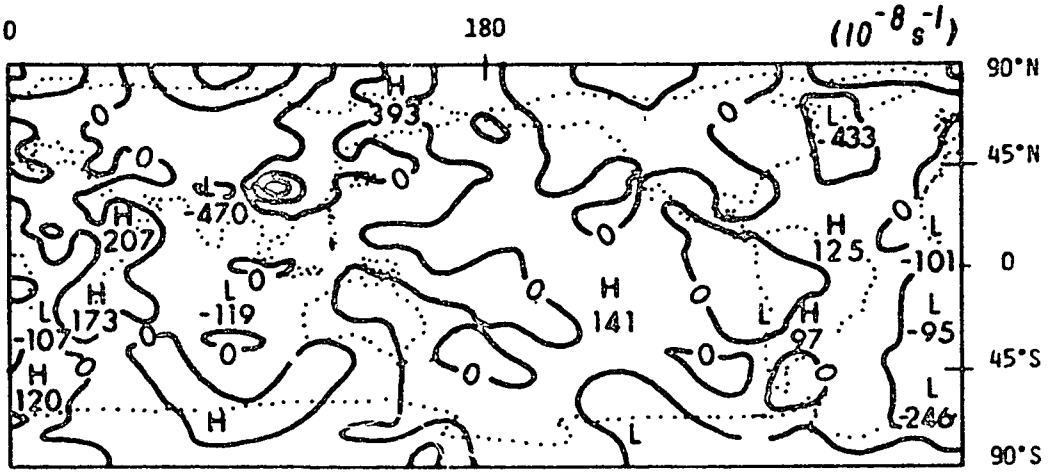

ECMWF

(b)

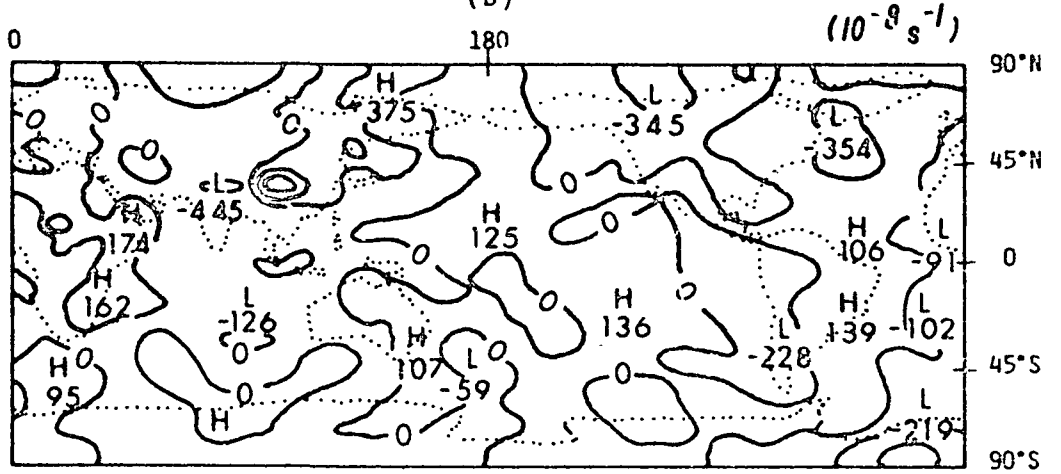

GFDL

4° x 5° latitude-longitude grid as described by Kalnay (1983) and are available at 9 sigma levels. They were integrated between sigma levels 3 and 6 and weighed by the mass of the atmospheric column at each grid point to obtain an estimate of mid-tropospheric heating rates. These are shown in Figure 14 for SHSP and NHSP. Peak rates of 15°C/day are obtained over the Indian Ocean during SHSP, where there is no precipitation data, and of 10°C/day in association with the Asian monsoon. The general pattern of heating rate over the Amazon

KELVIN MODES
DIVERGENCE ($10^{-8}s^{-1}$)

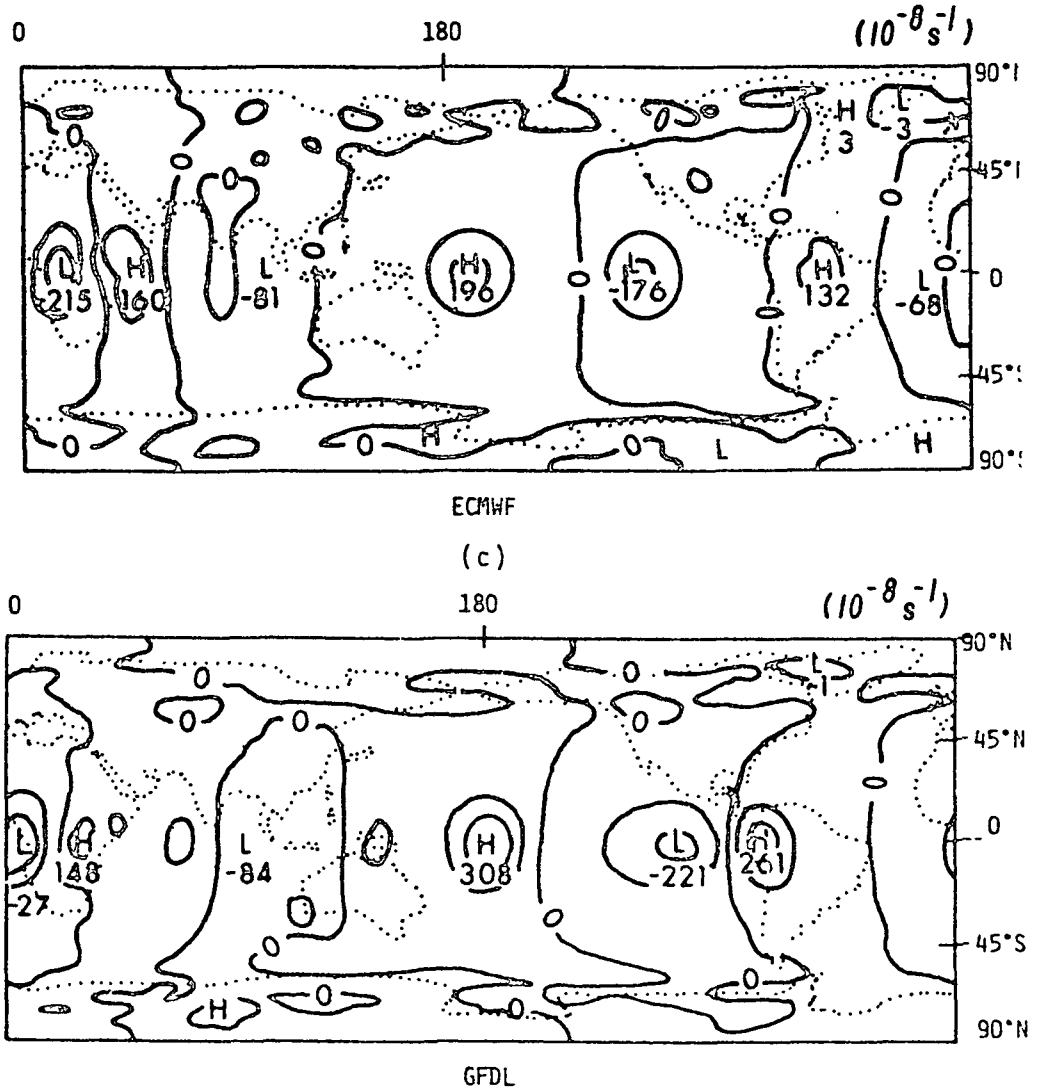

basin and its northward shift for the NHSP agree with those obtained from the available station precipitation data.

The maximum precipitation value of 3.1 cm/day over Madagascar at about 17°S and 45°E for the SHSP was obtained as an average over 19 stations. This active region is reflected in the outgoing long wave radiation field (Figure 13), the divergence analyses (Figure 10), and it is also represented by the wind field associated with the gravity waves of the lowest internal modes (Figure 8b). The GLAS/NASA analyses

MIXED ROSSBY-GRAVITY WAVE
DIVERGENCE ($10^{-8}s^{-1}$)

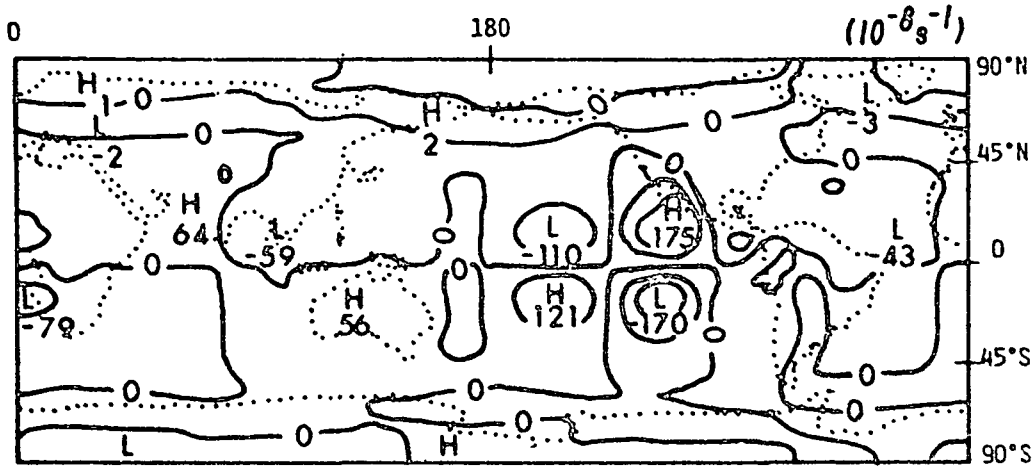

ECMWF

(d)

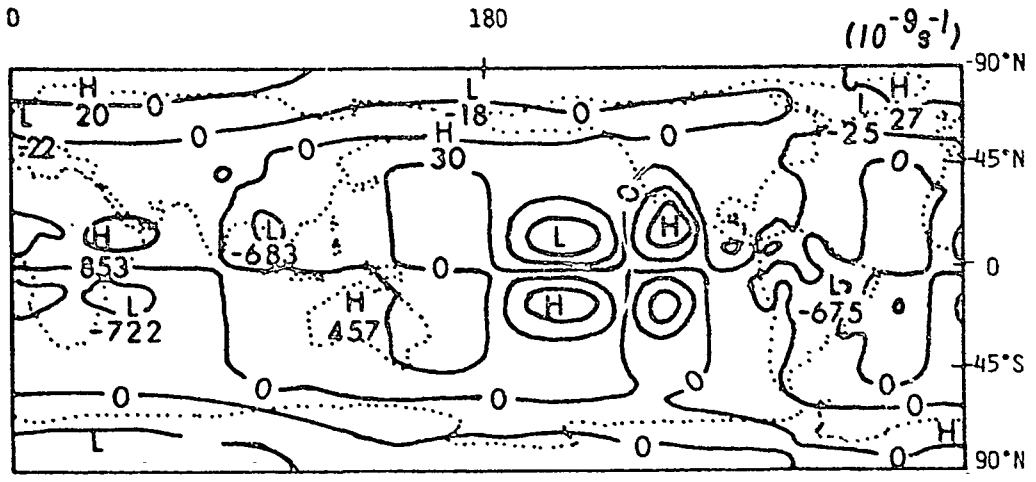

GFDL

FIGURE 11 Divergence field at 200 mb for ECMWF (top) and GFDL (bottom) for January 15, 0000Z, for (a) Gravity modes, (b) Rossby modes, (c) Kelvin, and (d) mixed Rossby-gravity modes.

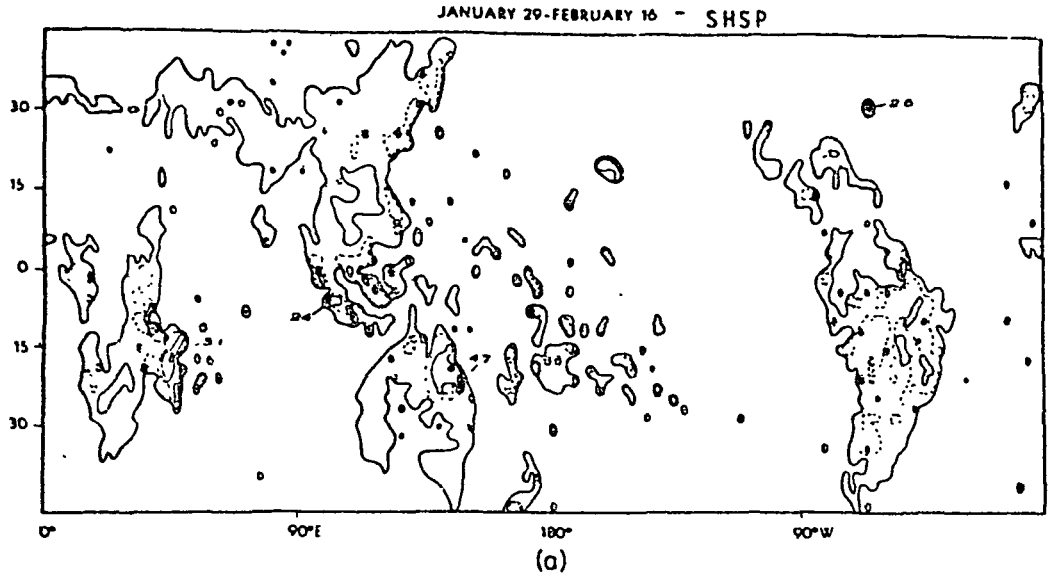

(a)

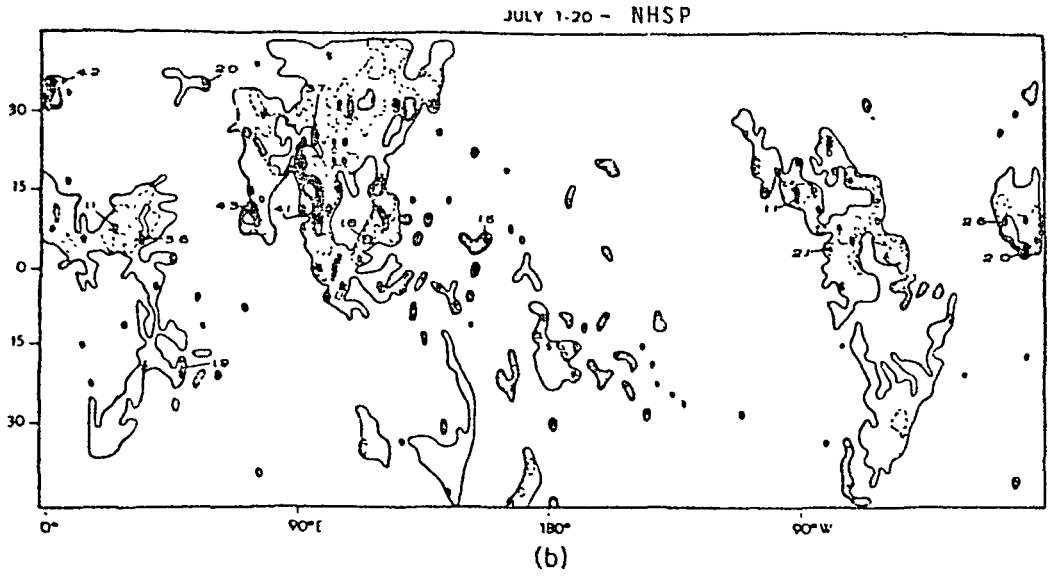

(b)

FIGURE 12 Station precipitation data averaged on a 1-7/8° x 1-7/8° grid for (a) SHSP and (b) NHSP. Values are given in cm/day.

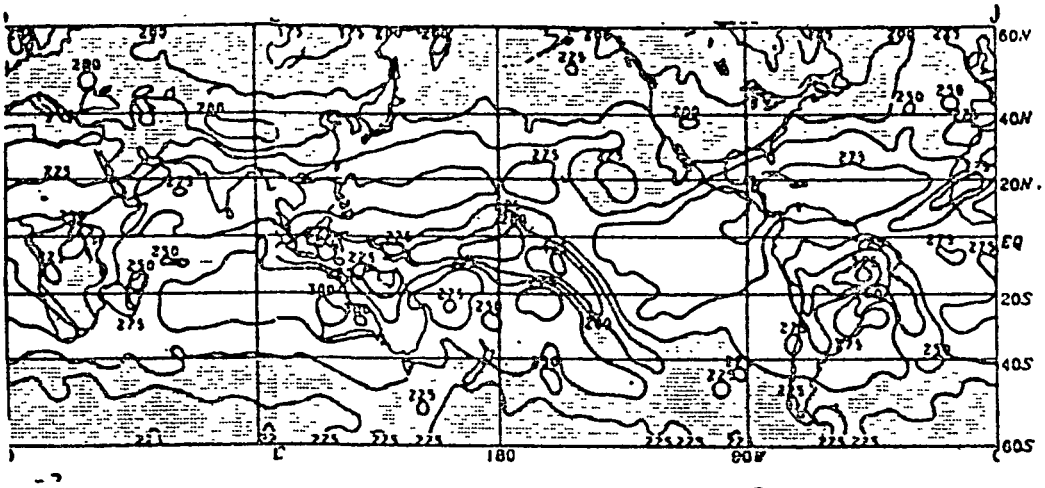

FIGURE 13 Daytime outgoing long wave radiation (wm^{-2}) for 23 days ending February 15, 1979. (Obtained from NESS/NOAA).

of heating rates do not capture this feature. Other main sources of divergence over the equatorial Pacific, Indonesia, and South America during this period are apparent in the GLAS heating rate estimates and precipitation data and are also evident in the normal mode projection of ECMWF analyses.

The most intense feature of the precipitation station data is present during the NHSP with an extensive area exceeding 2 cm/day of precipitation over the western coast of Burma and the Indian peninsula. Figure 8b displays southward gravity wave flow apparently emanating from this area during the NHSP. These northerlies cross the equator and approach 30°S, the approximate location of the Australian jet during this season. This is in agreement with Physik's (1982) results relating the acceleration of this subtropical jet with the local Hadley cell originating in the opposite hemisphere.

DISCUSSION

Silva-Dias et al. (1983) have shown that the partition of energy between fast and slow modes due to transient heat sources in the tropical region is highly selective. More energy goes to Kelvin waves than to rotational components for fast, small, horizontal-scale forcing near or at the equator. The implications for such cases to the initialization of forecasting models is important because of the balancing procedure associated with the nonlinear normal mode initialization. From the point of view of observations, the detection of the fast moving gravity components is a difficult problem in areas with low data density. Fast moving configurations tend to be slowed down and interpreted as a rotational field or simply rejected, depending on the objective analyses and initialization scheme used in the data assimilation cycle.

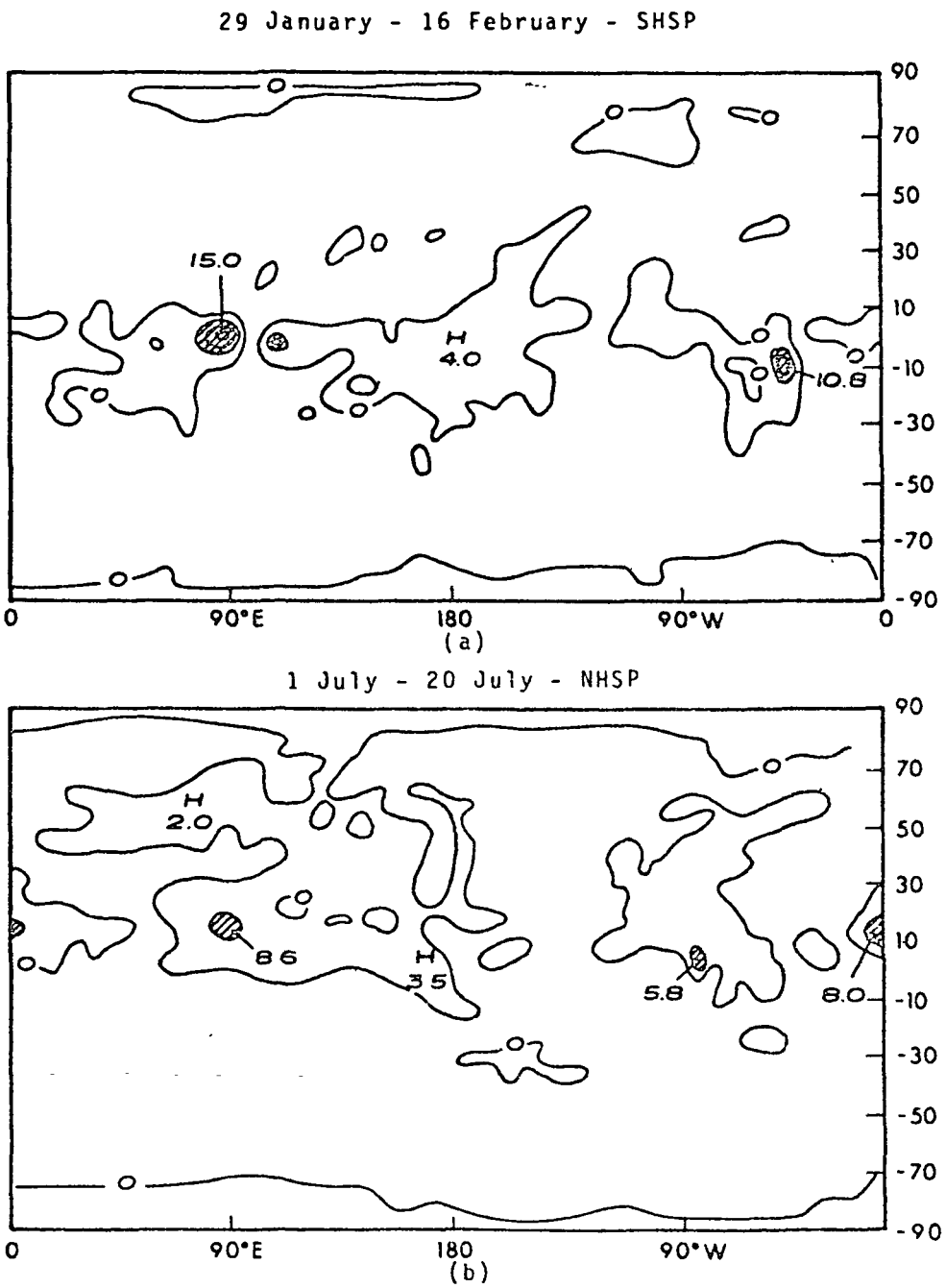

FIGURE 14 Deep atmospheric heating rates obtained from GLAS for the SHSP (a) and the NHSP (b) in units of 0.1°K/day.

However, there are indications from satellite observations that enhanced convective activity, symmetric about the equator, can be identified for up to six days after convective bursts over Borneo following cold surges from the northern hemisphere (Williams, 1981; Lau, 1982). The analysis of the diurnal variation of the 500 mb vertical motion field over South America has also revealed statistically significant reversal of ascending/descending regions (Silva-Dias et al., 1984). More intense upward vertical motion was diagnosed over the Amazon region at 2000 LT (i.e., 0000 GMT). This perturbation vertical motion pattern is also in agreement with the model-derived divergence pattern for a diurnal forcing with the spatial and vertical distribution assumptions of Silva-Dias et al. (1983). Significant diurnal changes are also present in the GLAS heating rate estimates (Figure 15) indicating diurnal shifts in the preferred location of convection. Diurnal variations are also apparent in large scales. Paegle and Baker (1982) noted such oscillations in the divergence field of the GLAS analyses and also related them to high frequency forcing.

The meridional wind component best represents wave activity in the tropics and was chosen for depiction in Section 2. Monthly averages for January and February show the divergent meridional wind component to be of similar magnitude to the rotational wind component for the large scales. Comparisons from ECMWF, GFDL, and GLAS objective analyses for a particular day indicate that the general features of the divergent meridional wind are similarly resolved in the three analyses with the ECMWF data sets producing the weakest divergent winds.

The Hough decomposition of gravity and vertical modes reveals a close association between the gravity and Kelvin wave contribution and the heat sources in the tropical region. Mixed Rossby gravity waves are also anchored on convective activity. Figures 8 and 9 reveal the nature of the horizontal spectrum: over the western Pacific Ocean, long Kelvin waves are preferred; over tropical South America, the short Kelvin waves are tied to the heat sources. The Kelvin activity also shows a seasonal variation that is linked to (1) the strength of the heat source and (2) the latitude of the source. Over South America, the heat source shifts from south of the equator to the equator from January to July, and this transition is well characterized in the Kelvin contribution to the total field. It is interesting to note that the contribution of the gravity modes dominates over other modes in the divergence field, and this is more pronounced for a particular day than for the time average. Filtering the higher order vertical modes allows a smooth representation of the divergence. Kelvin waves are responsible for a significant part of the divergence, and although not strongly present over South America, their divergence is larger there than over the western Pacific during the January to February period. This is a result of the preferred horizontal scale of the Kelvin waves (short waves). Comparisons of ECMWF and GFDL normal mode decomposition for January 15, 0000 GMT, indicate closer agreement of the large-scale divergence field and tropical gravity wave contribution than of the total divergence field.

29 January - 16 February - SHSP

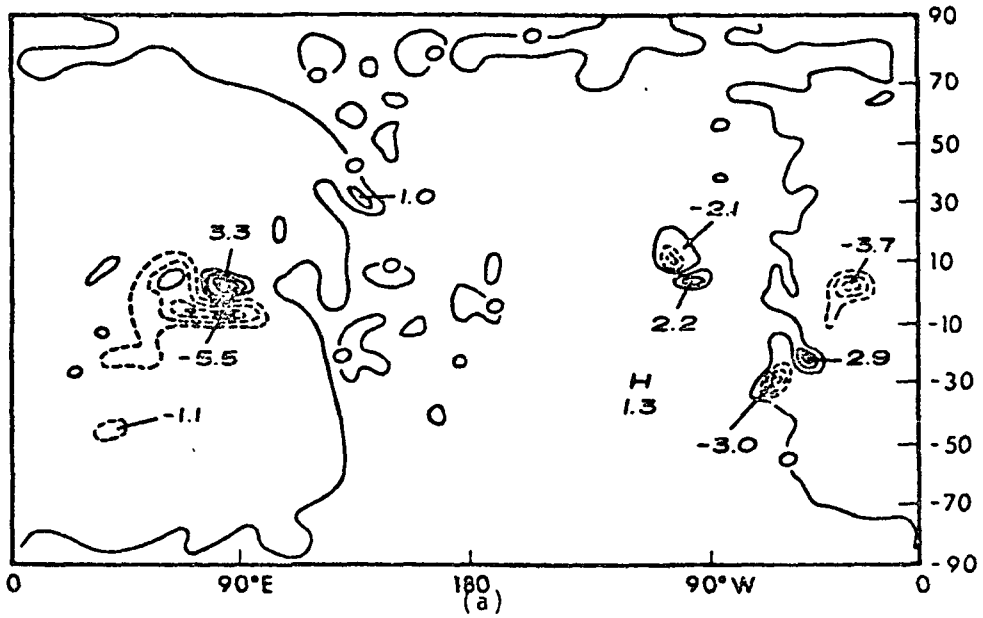

1 July- 20 July - NHSP

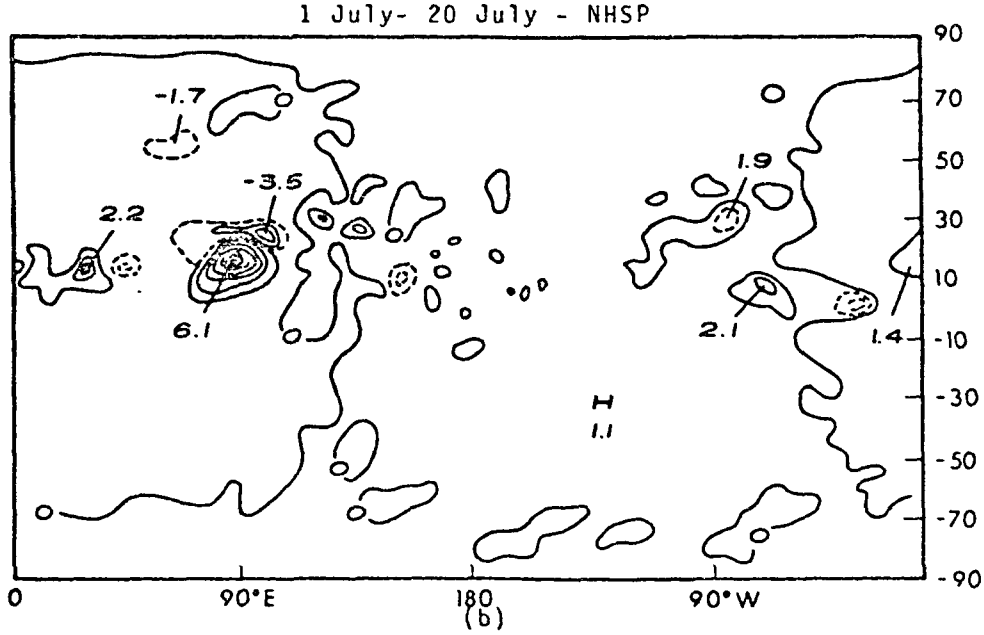

FIGURE 15 Difference between 00 GMT and 12 GMT deep atmospheric heating rates obtained from GLAS in units of $0.1^{o}K$/day for (a) SHSP and (b) NHSP.

SUGGESTIONS FOR FUTURE WORK

The following points seem to deserve special attention:

1. Comparison of the observed normal mode structure based on gridded data with the normal mode spectrum of general circulation models.
2. Comparison of the normal mode structure of different analysis schemes (NMC, ECMWF, GFDL) with special attention to the fast components.
3. Impact of heat sources on the normal mode strucutre using more realistic models. Latent heat as well as sensible heat sources should be investigated in terms of their influence on the initialization of forecast models.
4. Identification of preferred normal modes in anomalous conditions such as the El Niño case. The analysis should include the preferred vertical scale, type of anomaly in terms of fast versus slow modes, and local contributions.
5. Study of model normal modes on transitions from baroclinic anomalies in the tropics to barotropic anomalies at higher latitudes (i.e., Paegle and Baker, 1983).

Results from (1) and (2) would contribute to the evaluation of the real partition of energy in the atmosphere due to uncertainties in the analysis schemes and observation systems. If the model derived partition of energy among slow and fast modes is in fact close to the simple theoretical results of the linearized model of Silva-Dias et al. (1983), the exact impact of latent heat on the initialization should be closely investigated. Experiments following (3) can contribute to a better understanding of the effect of latent heat release in the partition of energy among vertical and horizontal modes. Normal mode expansion is also a powerful diagnostic tool that can be used to explore anomalous climate patterns. This is the goal of items (4) and (5). In particular, the transition of the baroclinic tropical perturbation to the barotropic structure at higher latitudes on the winter hemisphere (Wallace and Gutzler, 1981; Lim and Chang, 1983) can be explored in terms of nonlinear interaction among vertical modes. The time scale of this type of interaction is also important for the predictability of midlatitude weather systems (Paegle and Baker, 1983). It is plausible that the long fast modes, generated by transient tropical heat sources, play an important role in this type of nonlinear interaction. The reason for this behavior is related to equivalence of order of magnitude of the frequency of the long and fast internal modes and the frequency of the external rotational modes (Puri, 1984, personal communication).

ACKNOWLEDGEMENTS

The authors are grateful to Drs. A. Kasahara, K. Puri, and W. Schubert for helpful discussions. This summary is based on work jointly

supported by grants FAPESP and FINEP in Brazil, NOAA P.O. No. NA84AAG01214 (for PLSD) and NSF/NOAA ATM 8219196 and NASA NAG 5-127 (for JNP). The use of the NCAR and GLAS computer facilities is gratefully acknowledged.

BIBLIOGRAPHY

Baer, F. (1977). Adjustment of initial conditions required to suppress gravity oscillations in nonlinear flows. Contrib. Atmos. Phys. 50, 350-366.

Daley, R. (1981). Normal mode initialization. Rev. Geophys. Space Phys. 19, 450-468.

Errico, R. M. (1983). Convergence properties of Machenhauer's initialization scheme. Mon. Wea. Rev. 111, 2214-2223.

Geisler, J. E., and D. E. Stevens (1982). On the vertical structure of damped steady circulations in the tropics. Quart. J. Roy. Meteorol. Soc. 108, 87-93.

Gill, A. E. (1980). Some simple solutions for heat induced tropical circulations. Quart. J. Roy. Meteorol. Soc. 106, 447-462.

Kalnay, E. (1983). Analysed and diagnosed fields in the GLAS FGGE IIIb analysis. FGGE Newsletter No. 3, January 1984.

Kasahara, A. (1976). Normal modes of ultralong waves in the atmosphere. Mon. Wea. Rev. 104, 669-690.

Kasahara, A. (1984). The linear response of a stratified global atmosphere to tropical forcing. Submitted to J. Atmos. Sci.

Kasahara, A., and K. Puri (1981). Spectral representation of three dimensional global data by expansion in normal modes. Mon. Wea. Rev. 109, 37-51.

Lau, K.-M. (1982). Equatorial response to northeasterly cold surges as inferred from satellite cloud imageries. Proc. Int. Conf. Scientific Results Monsoon Experiment, WMO/ICSU, 5-37.

Lau, K.-M., and H. Lim (1982). Thermally driven motions in an equatorial -plane: Hadley and Walker circulations during the winter monsoon. Mon. Wea. Rev. 110, 336-353.

Lim, H., and C. P. Chang (1981). A theory for midlatitude forcing of tropical motions during winter monsoons. J. Atmos. Sci. 38, 2377-2392.

Lim, H., and C. P. Chang (1983). Dynamics of teleconnections and Walker circulations forced by equatorial heating. J. Atmos. Sci. 40, 1897-1915.

Longuet-Higgins, M. S. (1968). The eigenfunctions of Laplace's tidal equations over a sphere. Phil. Trans. Roy. Soc. London A262, 511-607.

Machenhauer, B. (1977). On the dynamics of gravity oscillations in a shallow water model with applications to normal mode initialization. Contrib. Atmos. Sci. 50, 253-271.

Matsuno, T. (1966). Quasi-geostrophic motions in the equatorial area. J. Meteorol. Soc. Japan 44, 25-43.

Moura, A. D., and J. Shukla (1981). On the dynamics of droughts in northeast Brazil: Observations, theories and numerical experiments with a general circulation model. J. Atmos. Sci. 38, 2653-2675.

Paegle, J. (1978). The transient mass-flow adjustment of heated atmospheric circulations. J. Atmos. Sci. 35, 1678-1688.

Paegle, J., and W. E. Baker (1982). Planetary-scale characteristics of the atmospheric circulation during January and February 1979. J. Atmos. Sci. 39, 2521-2538.

Paegle, J., and W. E. Baker (1983). The influence of the tropics on the prediction of ultralong waves. Part II: Latent-heating. Mon. Wea. Rev. 111, 1356-1371.

Paegle, J., and J. N. Paegle (1983). Modes of interhemispheric wave propagation. Proceedings of the First International Conference on Southern Hemisphere Meteorology, Sao Jose dos Campos, Brazil, 258-262.

Paegle, J., J. N. Paegle, and F. P. Lewis (1984). Large-scale motions of the tropics in observation and theory. Pure and Applied Geophysics (accepted for publication).

Physik, W. L. (1981). Winter depression tracks and climatological jet streams in the southern hemisphere during the FGGE year. Quart. J. Roy. Meteorol. Soc. 107, 883-897.

Puri, K. (1983). The relationship between convective adjustment, Hadley circulation, and normal modes of the ANMRC spectral model. Mon. Wea. Rev. 111, 23-33.

Reed, R. J. (1983). The diurnal variation of precipitation in the tropics. Proceedings of the First International Conference on Southern Hemisphere Meteorology, Sao Jose dos Campos, Brazil, 312-319.

Silva-Dias, P. L., W. H. Schubert, and M. DeMaria (1983). Large-scale response of the tropical atmosphere to transient convection. J. Atmos. Sci. 40, 2689-2707.

Silva-Dias, P. L., J. P. Bonatti, and V. E. Kousky (1984). Diurnally forced tropical tropospheric circulation over South America. To be submitted to Mon. Wea. Rev.

Silva-Dias, P. L., and J. P. Bonatti (1984). A preliminary study of the observed vertical mode structure of the summer circulation over tropical South America. Submitted to Tellus.

Webster, P. J. (1972). Response of the tropical atmosphere to local, steady forcing. Mon. Wea. Rev. 100, 518-541.

Webster, P. J., (1981). Mechanisms determining the atmospheric response to sea-surface temperature anomalies. J. Atmos. Sci. 38, 554-571.

Williams, M. (1981). Interhemispheric interaction during winter MONEX. Proceedings of the International Conference on Early Results of FGGE and Large-Scale Aspects of Its Monsoon Experiments, WMO, Vol. 10, 12-16.

Williamson, D. L. (1976). Normal mode initialization procedure applied to forecasts with the global shallow water equations. Mon. Wea. Rev. 104, 195-206.

Williamson, D. L., and C. Temperton (1981). Normal mode initialization for a multilevel gridpoint model. Part II: Nonlinear aspects. Mon. Wea. Rev. 109, 744-757.

D20

REMOTE SENSING OF ATMOSPHERIC AND SURFACE PARAMETERS FROM HIRS2/MSU ON TIROS-N

Joel Susskind and Eugenia Kalnay
Laboratory for Atmospheric Sciences
NASA/Goddard Space Flight Center

ABSTRACT

At the Goddard Laboratory for Atmospheric Sciences (GLAS) a physically based satellite temperature sounding retrieval system has been developed, involving the simultaneous analysis of HIRS2 and MSU sounding data, for determining atmospheric and surface conditions that are consistent with the observed radiances. In addition to determining accurate atmospheric temperature profiles even in the presence of clouds, the system provides global estimates of day and night sea or land surface temperatures, snow and ice cover, cloud amounts, cloudtop heights and temperatures, and albedo. In this paper, the characteristics of the atmospheric and surface parameters derived from the GLAS Physical Retrieval System are reviewed, results for the FGGE year are presented and, whenever possible, compared with other measurements of the same fields. Some of the model-derived diagnostic fields available from the GLAS Analysis/Forecast System are also discussed. These fields may lead to more accurate determination of the source terms of the atmospheric heat and moisture budgets.

INTRODUCTION

HIRS2 and MSU are the 20-channel infrared and 4-channel microwave passive sounders on the operational low earth orbiting satellites. They monitor emission arising primarily from the earth's surface and the atmosphere up to the midstratosphere. These, together with the SSU, a three-channel pressure modulated infrared radiometer, which monitors emission from the middle and upper stratosphere, comprise the TIROS Operational Vertical Sounder (TOVS) system. The TOVS data are analyzed operationally by NOAA/NESDIS to produce vertical temperature-humidity profiles using a method based primarily on statistical regression relationships between observed radiances and atmospheric parameters.

The approach used at GLAS, described in Susskind et al. (1984), is fundamentally different from the current operational approach. Rather than rely on empirical relationships between observations and meteorological conditions, an attempt is made to find surface and atmospheric

parameters that, when substituted in the radiative transfer equations describing the dependence of the observations on the meteorological conditions, match the observations to a specified amount. A physically based retrieval scheme is believed to have an important advantage over a statistically based scheme. This is the ability to include the effect of secondary but important factors, such as surface temperature, surface emissivity, surface elevation, reflected solar radiation, satellite zenith angle, and most significant of all, clouds, on the observations. All of these parameters, together with the atmospheric temperature profiles, are either solved or directly accounted for in the GLAS iterative scheme. As a result, the analysis of radiance data produces not only global fields of atmospheric temperature profiles necessary for initialization of numerical weather prediction models but also provides several other weather and climate parameters. These parameters include sea and land surface temperature and their day-night differences which, over land, are related to soil moisture; fractional cloud cover, cloudtop temperature and pressure, and their day-night differences; and ice and snow cover, which are derived from the combined use of the surface emissivity at 50.3 GHz and the ground temperature.

In this paper the characteristics of the atmospheric and surface parameters derived from the GLAS Physical Retrieval System are reviewed, results for the FGGE year are presented and, whenever possible, compared with other measurements of the same fields. Some of the model-derived diagnostic fields available from the GLAS Analysis/Forecast System are also discussed. These fields may be very useful in estimating the heat sources and sinks that drive the atmospheric energy cycle and are difficult to measure by more conventional methods.

ATMOSPHERIC TEMPERATURE PROFILES

The atmospheric temperature structure is one of the most important parameters needed for initialization of numerical models for weather prediction. Lack of upper air data in most oceanic regions, and some land regions, was the major motivation for the design of atmospheric satelliteborne sounders such as HIRS2/MSU. Research has already shown that assimilation of soundings derived operationally by NOAA/NESS resulted in improved forecasts during FGGE (Halem et al., 1982, and other reviews in this report).

More than 15,000 GLAS retrievals per day have been obtained for the periods January to February, May to July, and November 1979. Comparisons with collocated rawinsondes ($\pm$ 3 hours, $\pm$ 110 km) for the GLAS retrievals and for the retrievals contained in the FGGE Level IIb data base are shown in Figure 1 for the period January 5 to January 15, 1979, the first 10 days of SOP-1. The GLAS retrievals are classified according to retrieved cloudiness for a 250 x 250 km area. The FGGE operational retrievals are classified according to retrieval type. N* indicates a partial cloud-cover algorithm was used in generating the official FGGE data. On the average, the GLAS retrievals have an

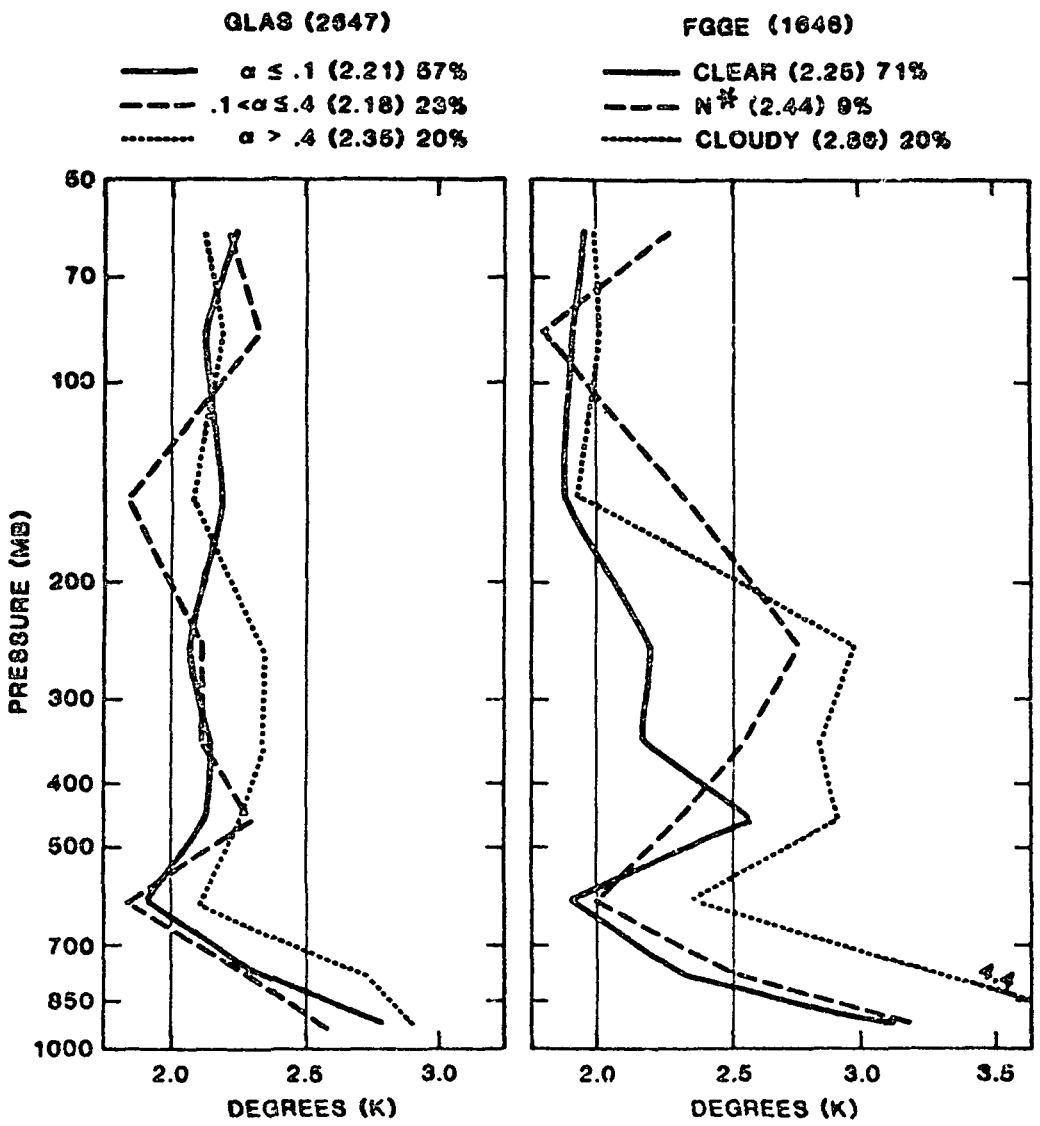

FIGURE 1 Mean layer temperature errors compared to radiosondes ±HR ±110 KM, January 5-15, 1979.

accuracy similar to that of the clear FGGE retrievals. It is important to note however that the accuracy of the GLAS retrievals degrades much more slowly with increasing cloud cover than that of the FGGE retrievals during this time period. This may have been a factor in the improved forecast impact obtained by assimilation of the GLAS retrievals in place of the FGGE data base retrievals (see Kalnay et al. in this report).

SURFACE TEMPERATURES

One of the products of the GLAS physical inversion process is the earth's surface skin temperature. This quantity is retrieved globally over sea, land, or mixed surfaces. The utility of the data and the required accuracy are quite different over land and ocean. Ocean surface temperatures vary slowly with time and space, and long climatological records of sea-surface temperatures (SST) exist (e.g., Reynolds, 1982). Typical monthly mean sea-surface temperature differences from climatology are of the order of 0.5°K. Spatially coherent SST anomalies of 1°K can have significant impacts on atmospheric circulation, especially if they occur in the tropics (Horel and Wallace, 1981; Rasmusson and Carpenter, 1982; Shukla and Wallace, 1983). Therefore in order to produce a useful product, it is necessary to determine with accuracy not only the SST anomalies but SST gradients. Over land, on the other hand, because of the large surface variability and low heat capacity, the surface temperature can have large changes in short space and time scales, as well as significant diurnal changes. Because of this, there is no readily available climatology of land skin surface temperature.

Sea-Surface Temperatures

Sea-surface temperature fields have also been produced by other satellite instruments for some time. AVHRR is the current operational infrared sea-surface temperature instrument. Four-channel versions of AVHRR, containing an additional channel in the longwave window region in order to aid in accounting for the effects of humidity on the observations, flew on NOAA-7. Sea-surface temperatures have also been produced from the experimental NIMBUS-7 SMMR microwave instrument, which also flew briefly on SEASAT.

A NASA-sponsored SST intercomparison workshop has just been completed in which fields derived from AVHRR, SMMR, HIRS2/MSU, ships, and buoys were verified against each other (J.P.L., 1983, 1984). The months of November 1979, December 1981, March 1982, and July 1982 were chosen for this study, which concentrated on the monthly mean SSTs on a 2° x 2° grid, and on their differences from the Reynolds (1982) climatology. Biases, RMS differences, and correlations of the anomaly fields produced from different instruments were compared with each other. In addition, statistics were computed giving the RMS difference between collocated satellite and ship and buoy derived sea-surface

temperatures. The GLAS retrievals based on HIRS2/MSU data were shown to produce the best anomaly patterns but appeared noisy on a 2^{o} x 2^{o} grid with primarily random noise components. This contrasted with the findings for AVHRR and SMMR, which showed a small random component of error but larger coherent systematic errors producing spurious anomaly patterns in some regions. As a result of these studies, improvements were made in the analysis of HIRS2/MSU data that resulted in much less noisy sea-surface temperatures producing monthly mean errors on the order of $0.5^{o}C$ on a 2^{o} x 2^{o} grid and excellent anomaly patterns.

Land Temperatures

As mentioned before, while a great deal is already known about ocean surface temperature from in situ and remote measurements, there is much less data on global land surface temperatures and their day-night differences. The fields of global monthly mean sea-land surface temperatures and their day-night difference, which we have produced, represent the first such fields ever generated.

Figure 2 shows the global surface temperature obtained for January 1979 at 3:00 p.m. local time, 3:00 a.m. local time, and the difference between the 3:00 p.m. and 3:00 a.m. ground temperatures, representative of a diurnal cycle. In this figure, areas of high topography, such as the Himalayas and the Andes, are clearly visible both as locally cold areas and as having large day-night temperature changes. Arid regions show very warm temperatures during the summer day and large day-night temperatures. Oceans, on the other hand, show very small day-night differences. The small patches of differences greater than $\pm$ $1^{o}K$ over the oceans may be indicative of residual deficiencies in the cloud filtering scheme. For example, if clouds are not completely filtered out by the GLAS algorithm, regions with cumulus convection stronger during the day will appear slightly blue (colder during the day), whereas those with stratus dissipating during the day will appear as regions with cooler night SSTs.

It is interesting to compare the day-night temperature difference of the lowest 15 percent of the atmospheric column (Figure 3a), which is representative of the diurnal sensible heat storage of the planetary boundary layer, with the day-night ground temperature differences reproduced again in Figure 3b. Note that although the color scales are the same, the air temperature difference scale has been expanded by a factor of 5. The fields show general correspondence, with desert areas showing large day-night temperature differences while highly vegetated areas have small differences. Some pattern differences do occur, however, as for example, in areas of elevated terrain, such as the Andes and Himalayas, and in snow-covered areas, which show up much more clearly in the atmospheric temperature diurnal cycle than in the ground temperature cycle.

An important application of the HIRS2/MSU day-night ground temperature difference has been recently pointed out. Mintz et al. (1984) have developed an energy balance theory relating soil moisture

and evapotranspiration to the day-night ground and air temperature differences and cloud cover. Preliminary results show that space-derived global soil moisture fields are in reasonable agreement with values derived from climatological measurements of precipitation and sunshine (Mintz and Serafini, 1981).

The global surface temperature fields also give a useful measure of the amplitude of the seasonal cycle. Figure 4 shows the monthly mean daily averaged surface temperature fields for January and July 1979 and their differences. The amplitude of the seasonal difference field shows some similarity with the day-night difference field for January. The extratropical oceans are well defined against the land, since they have much smaller seasonal differences, except in those regions of the oceans that are frozen in one season or the other. It is interesting to note that in the northern hemisphere, July is warmer than January only north of 15°N. Heavily forested regions in the southern hemisphere show relatively small day-night surface temperature differences (Figure 2), and at the same time minimal cooling or even warming from January to July (Figure 4). This apparent out-of-phase relationship of ground temperature with season appears to be related to areas having high precipitation during the summer, and hence little diurnal warming. Arid regions, like the Australian deserts, have both large day-night differences and strong seasonal amplitude.

SNOW AND ICE FIELDS

A unique product arising from the analysis of the HIRS2/MSU data is the surface emissivity of the earth at 50.3 GHz. This field is closely related to the brightness temperature of the 50.3 GHz channel, which is given by the product of the emissivity and the surface temperature modified somewhat by the effects of atmospheric attenuation and emission. An accurate determination of the emissivity can only be made if these other factors are properly accounted for. Figure 5 shows the monthly mean surface emissivity of the earth for January 1979. From this field it is possible to determine sea ice extent and snow cover. The emissivity of snow-free land is typically 0.9 to 1.0; the emissivity of a water surface ranges from 0.5 to 0.65, increasing with decreasing surface temperature; and mixed ocean-land areas have intermediate values.

The continents are clearly indicated as well as a number of islands, seas, and lakes. Snow-covered land has an emissivity of 0.85 or less, with emissivity decreasing with increasing snow depth. The snow line, clearly visible in North America and Asia, is in good agreement with that determined from visible imagery (Dewey and Heim, 1981).

Newly frozen sea ice has an emissivity of 0.9 or more. Note, for example, the new ice in Hudson Bay, the Sea of Okhotsk, the center of Baffin Bay, and the Chuckchi, Laptev, and East Siberian Seas. Mixed sea ice and water has emissivities between 0.65 and 0.90. The onset of significant amounts of sea ice is indicated by the 0.70 contour. Comparisons of this contour in Baffin Bay, the Denmark Strait, and the Greenland Sea show excellent agreement with the 40 percent sea ice

extent determined from analysis of SMMR data from the same period (Cavalieri, 1983). Multi-year ice, such as found in the Arctic Ocean north of the Beaufort Sea, is indicated by emissivities less than 0.80. Excellent agreement is also found between ice and snow lines and the 273°C freezing line for January shown in Figure 4.

CLOUD COVER

Another important result of the GLAS temperature retrieval system is the determination of several cloud parameters, such as effective cloud fraction, cloudtop temperature, and cloudtop pressure. Figure 6 shows the monthly average of these fields corresponding to January 1979. Major features such as the ITCZ, the South Pacific Convergence Zone, the storm tracks in the North Atlantic and North Pacific oceans, dry land regions such as the Australian and Saharan deserts, and dry oceanic regions west of Peru, northern and southern Africa, which are dominated by subtropical anticyclones, are readily apparent in the mean cloudiness map. The cloudtop pressure map, and the cloudtop temperature map allow for clear identification of deep convective regimes in the tropics, and shallow stratiform clouds west of the continents in the southern hemisphere.

There is excellent correlation between the areas of convective cloudiness shown in Figure 6, and low day-night temperature differences over land. For example, the northwest corner of Africa, where a relatively small monthly mean amount of convective cloud cover is apparent (Figure 6), also shows up as having somewhat smaller day-night ground temperature differences (Figure 3) than the area in the central and eastern Sahara, which is essentially cloud free.

The breakdown of cloudiness into day and night is shown for February 1979 in Figure 7. Note the significant increase in the amount of stratus clouds west of the southern hemisphere continents at night. It is also remarkable that the intense convective regions of South America, Africa, and Indonesia show more cloudiness at 3:00 a.m. than at 3:00 p.m. This feature as well as other qualitative aspects of Figures 6 and 7 are quite consistent with maps of outgoing longwave and shortwave radiation inferred from AVHRR data (Gruber and Varnadore, 1982).

COMPARISON WITH DIAGNOSTICS FROM THE GLAS ANALYSIS/FORECAST AND DISCUSSION

Several of the GLAS Physical Retrieval products discussed before are clearly related to the atmospheric sources and sinks of heat and moisture. For example, the snow and ice cover, and the associated albedo fields (not shown), are important elements in the radiative balance at the surface. Clouds also play an important role in the radiative balance, as well as being indicative of the release of latent heat. For examaple, cloud heights and duration in the tropics may be used to derive quantitative estimates of convective precipitation

The captions for Figures 2 through 7 are listed here to identify the following photographic inserts, which were printed separately and bound in this volume.

Fig. 2a

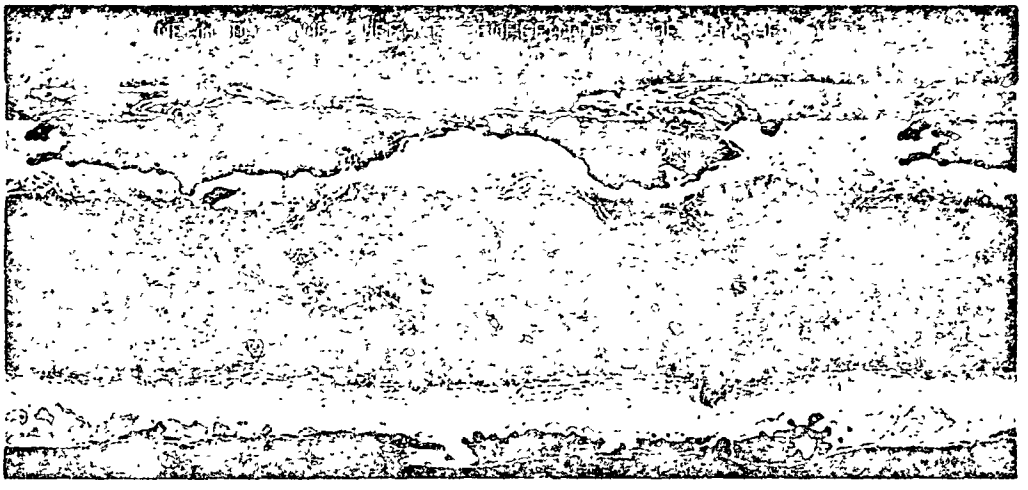

2b

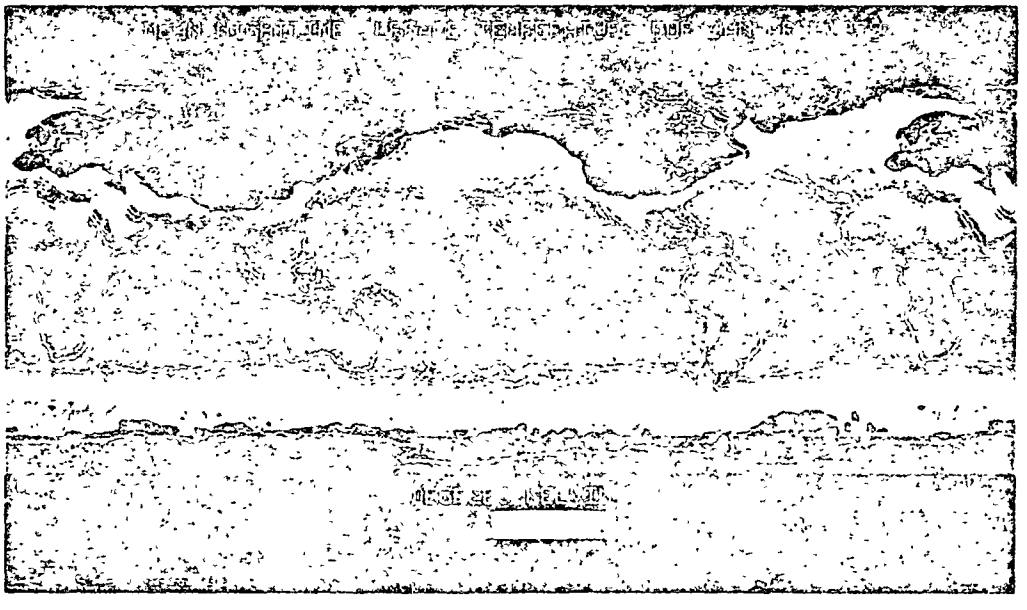

2c

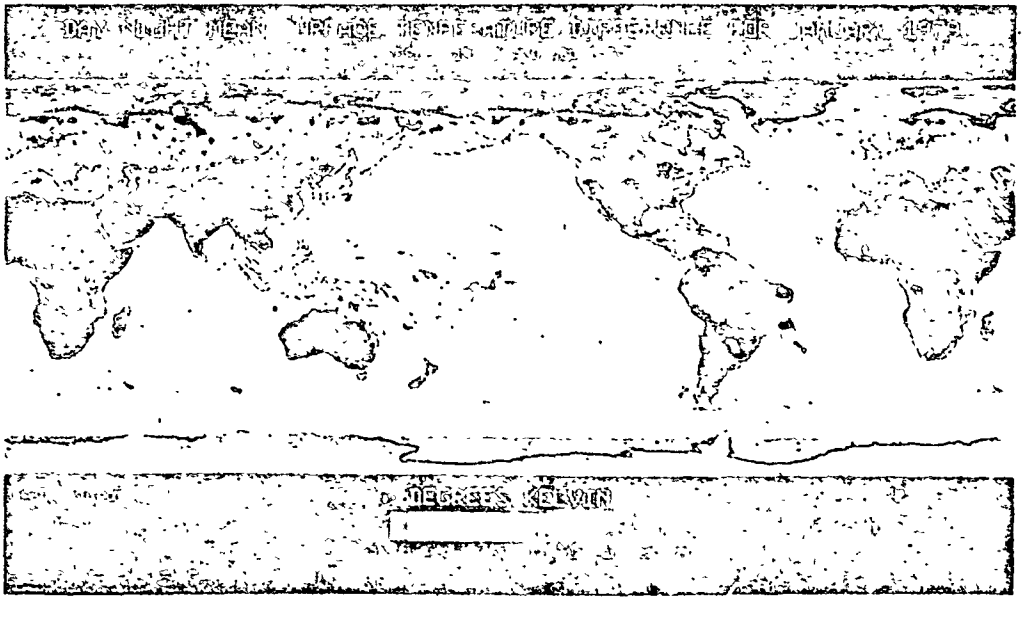

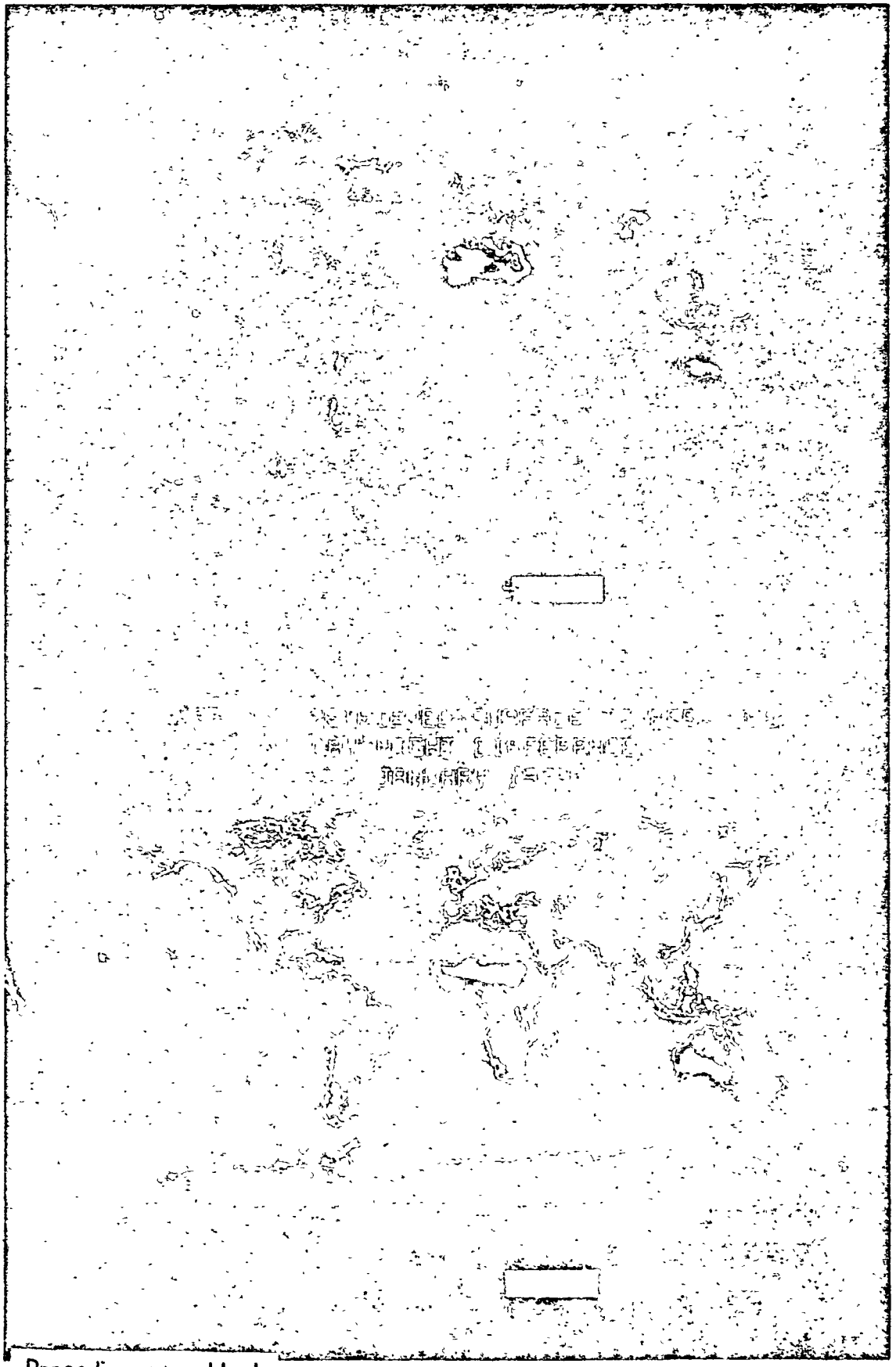

Preceding page blank

Fig. 4a

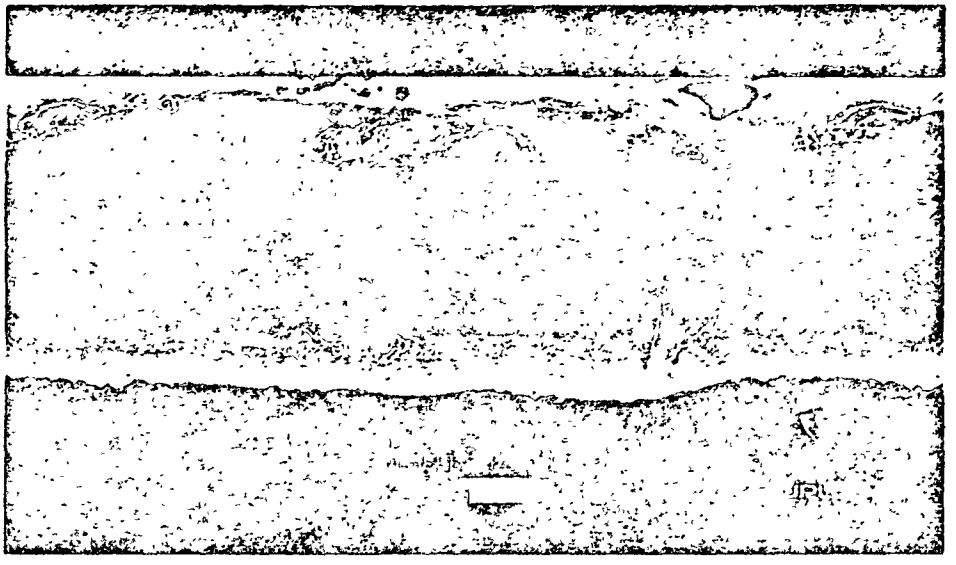

4b

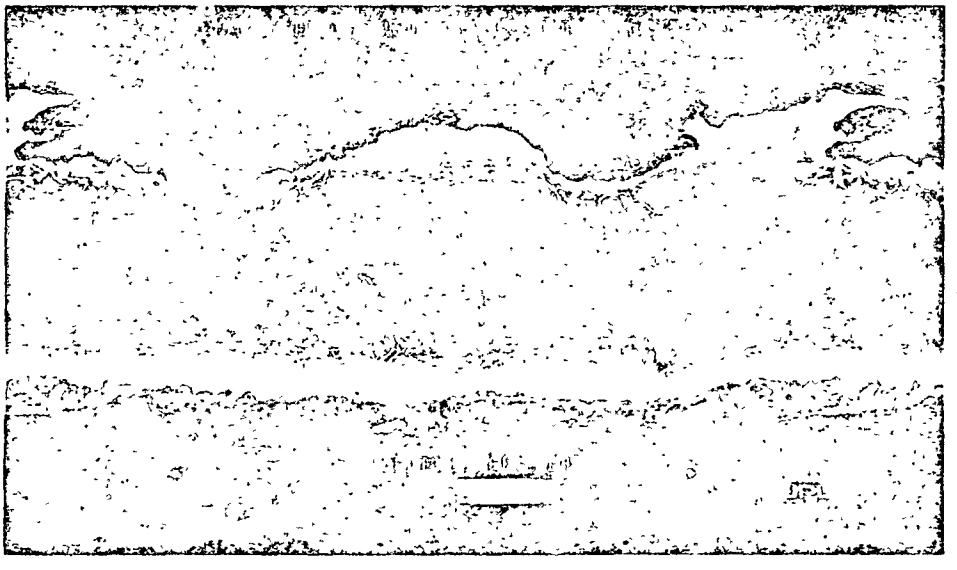

4c

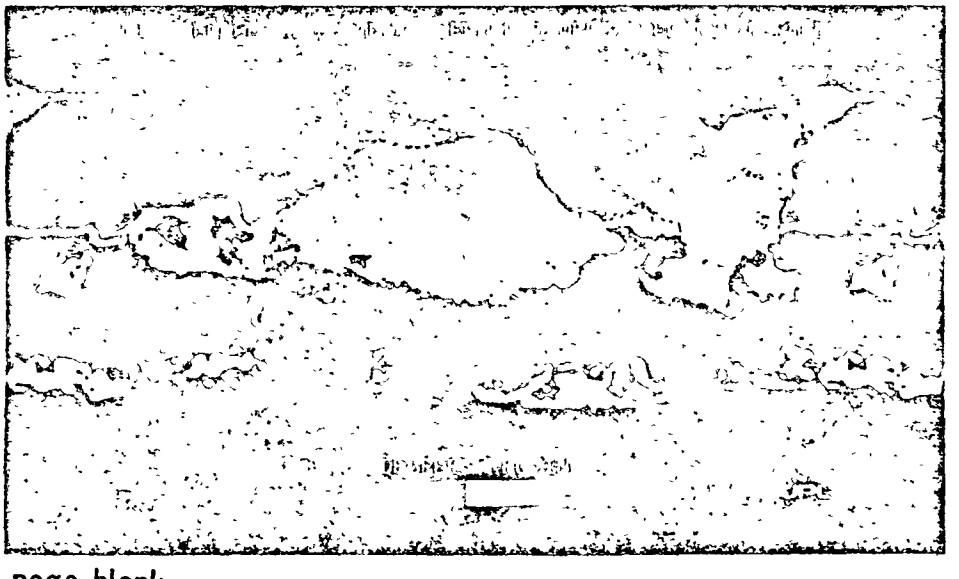

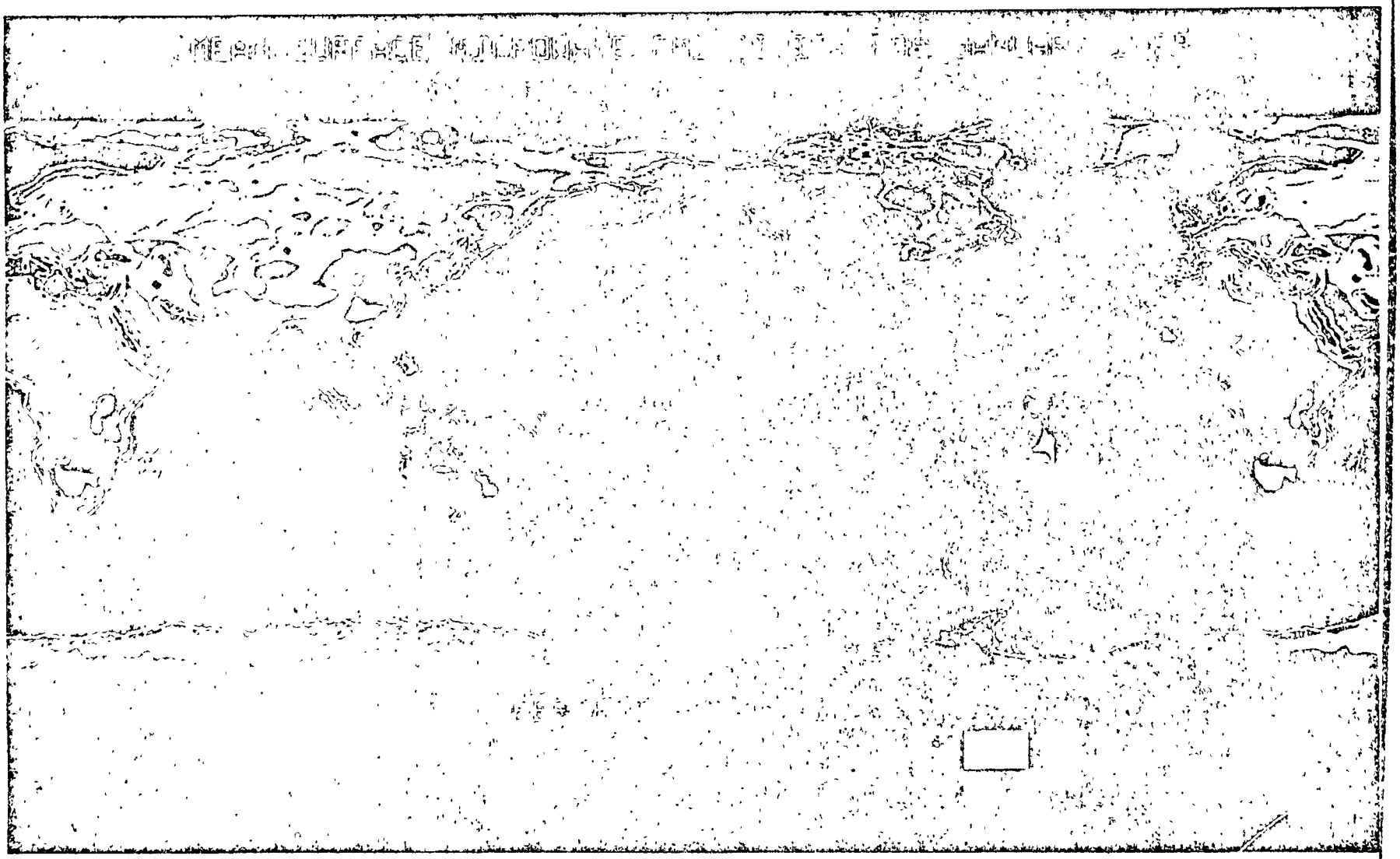

Fig. 5

Preceding page blank

Fig. 6a

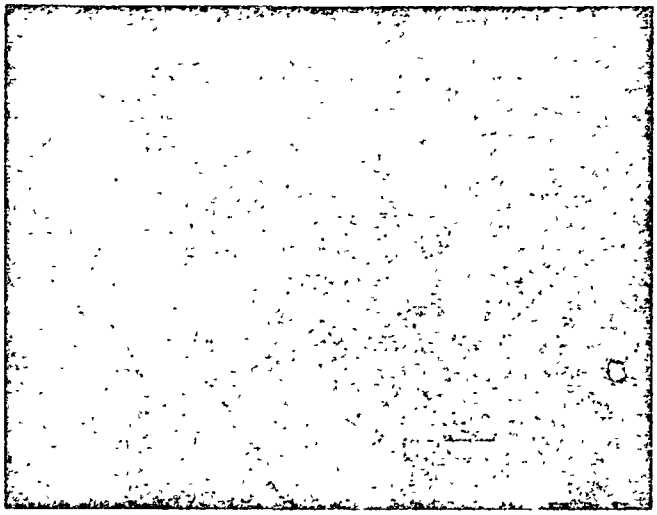

Fig. 7a

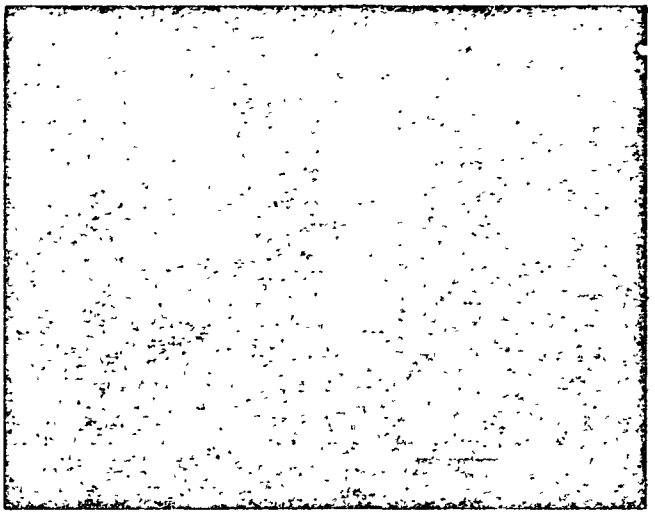

6b

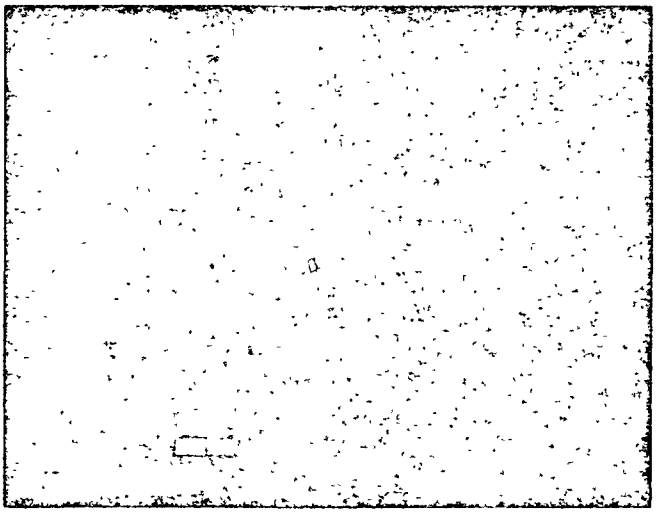

7b

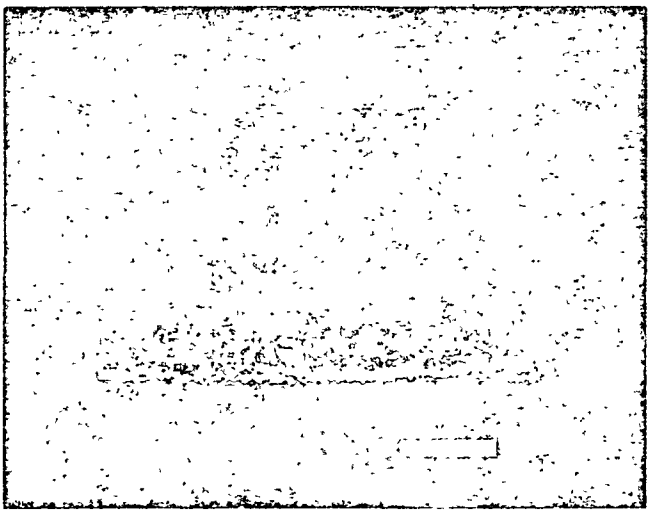

6c

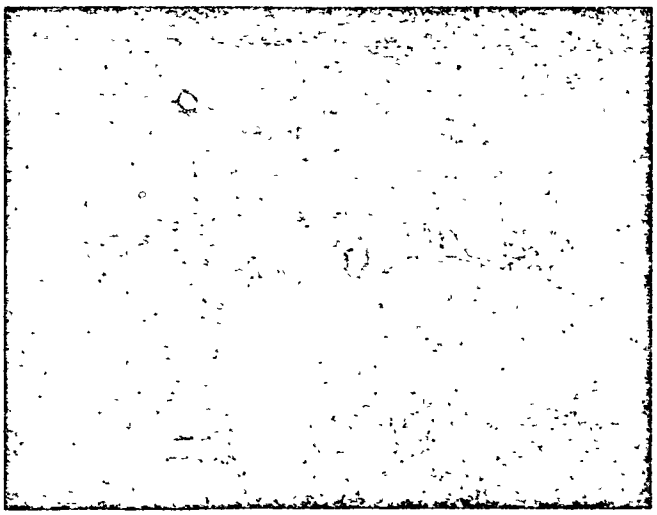

7c

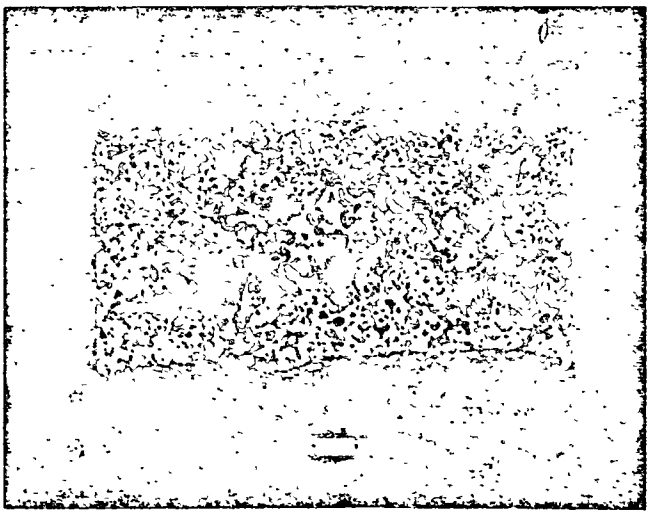

Preceding page blank

(Richards and Arkin, 1981). Sea-surface temperature anomaly fields in the tropics determine the regions of moisture convergence and affect the atmospheric circulation. Finally, the day-night surface temperature differences can be used as a measure of surface evapotranspiration and soil moisture.

Other essential parameters of the heat and moisture budgets, such as heating rates, surface fluxes of heat and moisture, and precipitation, can also be estimated from an analysis/forecast system. During the analysis cycle, the model mass and wind fields are updated every 6 hours, using the atmospheric observations collected in that period. As a result, diagnostic fields can be derived from an analysis cycle in basically two ways. The first method most commonly used is a residual method, exemplified by the heating rates obtained by Kasahara and Mizzi (1983) using the ECMWF IIIb analysis. As pointed out by Kasahara and Mizzi (1983), these heating rates are strongly influenced by the characteristics of the ECMWF analysis, and in particular by their adiabatic nonlinear normal mode initialization and possibly the unequal number of observations at different synoptic times. This results in a large amplitude spurious wavenumber 2 component in the heating, with maxima both at local noon and midnight.

A second method is to use diagnostics produced by the model forced to remain close to the data during the analysis cycle. Preliminary studies of heating rates derived from the GLAS analysis/forecast system, which does not use adiabataic nonlinear normal mode initialization, show no spurious diurnal oscillation and are qualitatively reasonable (Kalnay and Baker, 1984).

As an example of GLAS diagnostics, Figure 8 presents the total precipitation field derived from the GLAS analysis/forecast system for January 1979. The contour intervals are 1, 2, 4, 8, 16 and 32 mm/day, with the 4 mm/day contour enhanced. This field is generally reasonable and consistent with precipitation climatologies and the interannual and intra-annual winter variations, although convective precipitation tends to be overestimated, presumably because of the lack of balance during the analysis cycle. The regions of tropical convection over Australia, South America, and Africa, the northern hemisphere storm tracks, and the subtropical dry regions over oceans mentioned above are also clearly present in this field. Some areas of agreement between the precipitation fields of Figure 8 and the cloudiness field of Figure 6 are particularly significant because of their anomalous nature. The very strong band of convective activity east of the coast of South America, which is a result of the presence of a large amplitude stationary wave present during January 1979 and absent during most of February 1979 (Kalnay and Paegle, 1983), is apparent in both January fields (Figures 6 and 8), and much weaker in the February fields (Figures 7 and 9). The very intense South Pacific Convergence Zone (SPCZ) is also much stronger and further to the east in January than in February in both fields. On the other hand, a similar region of oceanic convection southeast of Africa appears to be much stronger in February than in January. A secondary maximum of the SPCZ north of New Zealand is also present in both fields.

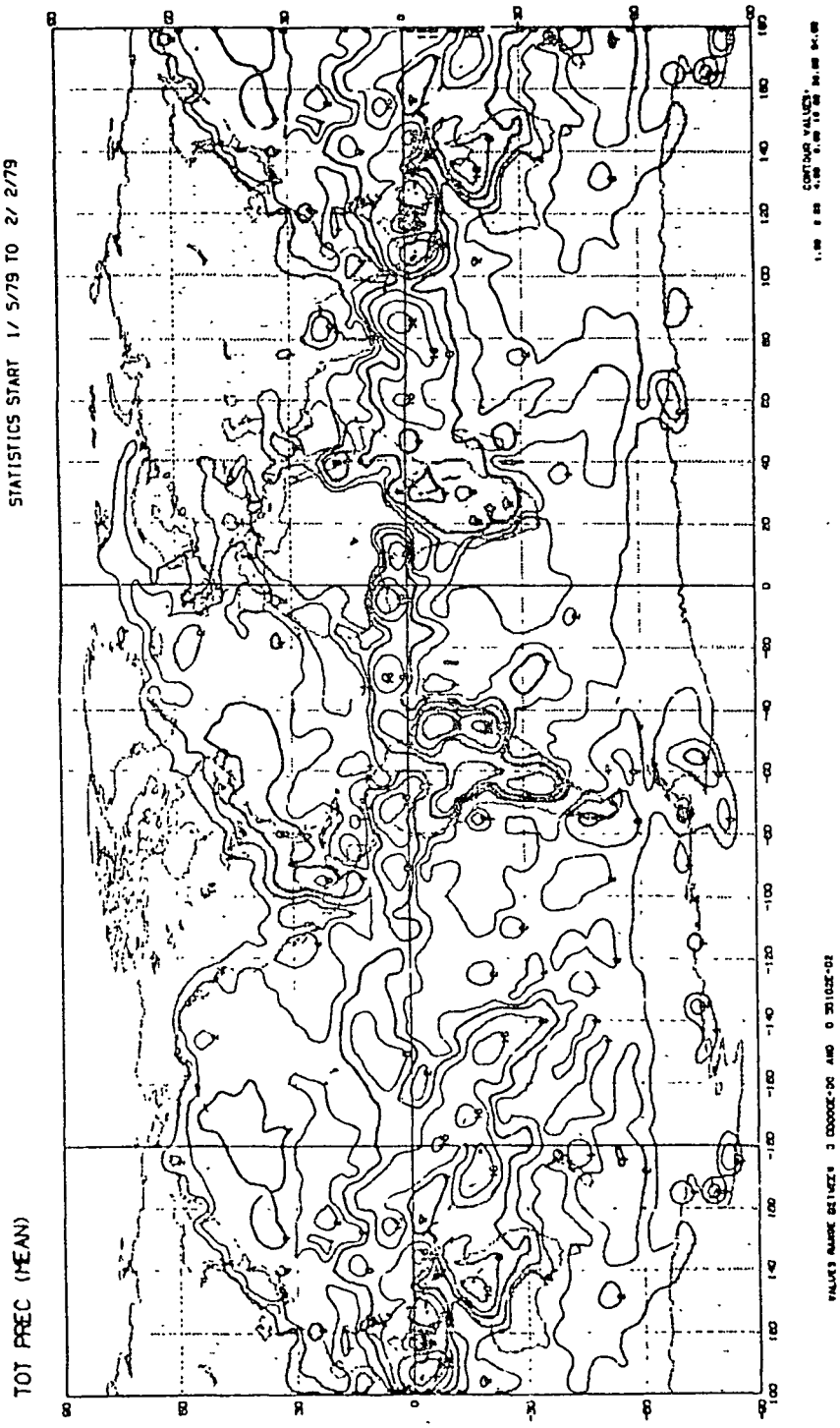

FIGURE 8

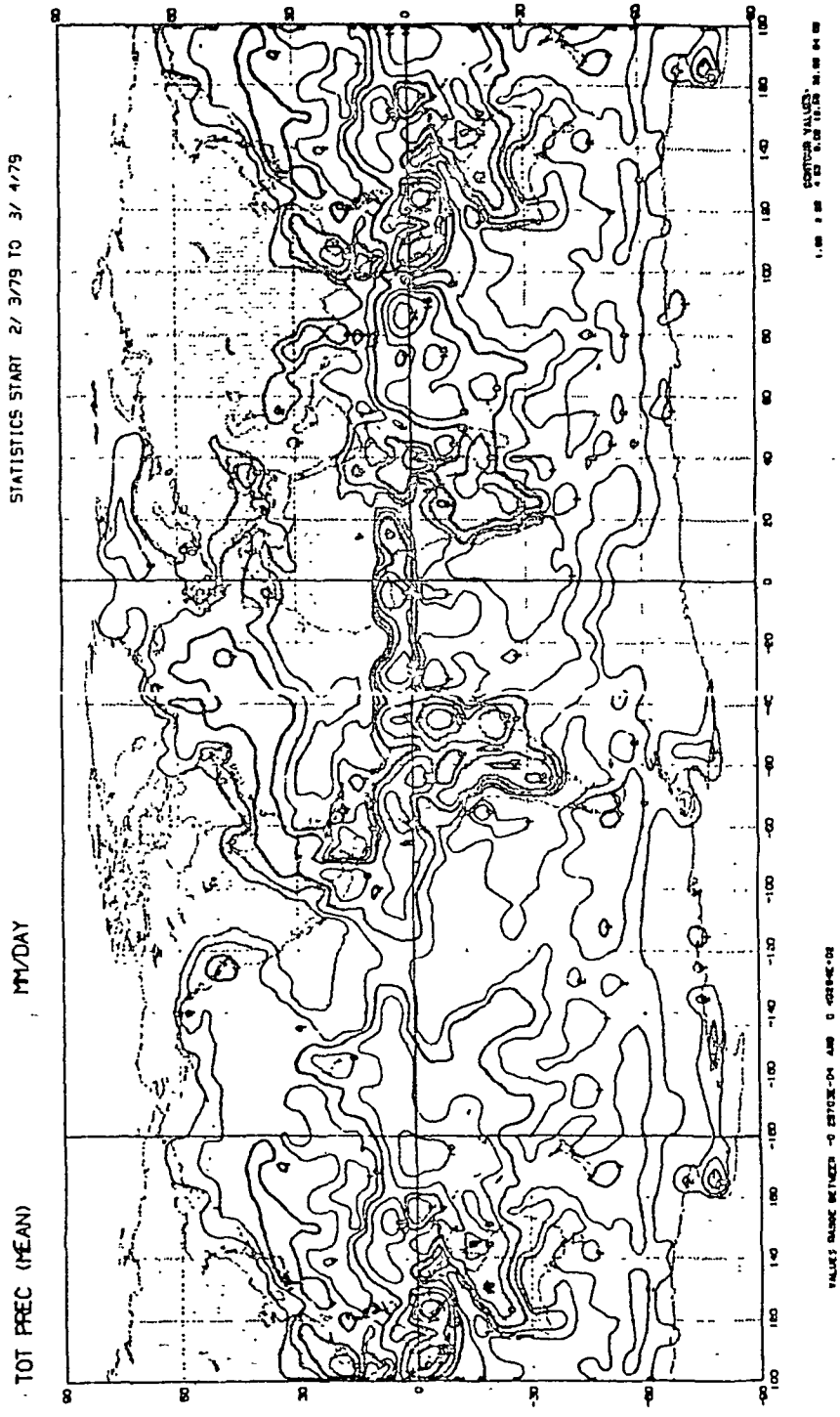

FIGURE 9

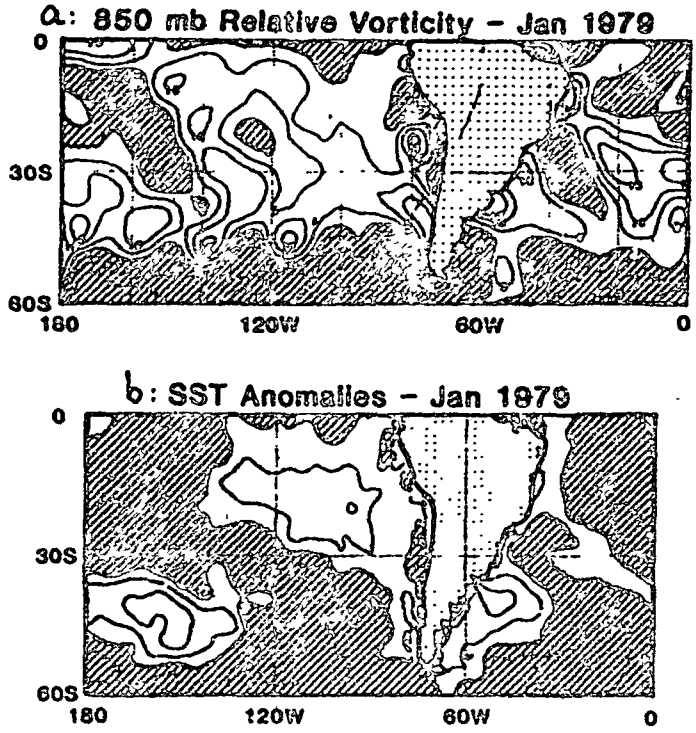

FIGURE 10 (a) 30-day average of relative vorticity at 850 mb from the GLAS Analysis/Forecast System. Inverval: 5×10^{-6} sec^{-1}. (b) 30-day average SST anomalies from the GLAS Temperature Retrieval System. Interval: $0.5^{o}K$.

It is useful to compare sea surface temperature (SST) anomaly fields from the GLAS Temperature Retrieval System with low level atmospheric relative vorticity fields from the GLAS analysis. Figure 10a and b present 30 day averages of 850 mb relative vorticity and SST anomalies during January 1979, period during which strong stationary anomalies were observed in the South Atlantic. The fact that there is a clear correlation between low level cyclonic vorticity and negative SST anomalies (both shaded), indicates that the atmospheric anomalies are causing the SST anomalies, which in turn provide a negative feedback to the atmosphere. This is because in the region with cyclonic vorticity, the atmosphere rotates faster than the ocean, which will tend to produce upwelling and cooling of the ocean surface. This cooling will be enhanced by the stronger low level winds that tend to occur with cyclonic systems. At the same time, the cloudiness associated with the region of low pressure reduces the summer insolation which can reach the surface. Conversely, the presence of clear regions of anticyclonic circulation and the associated weak downwelling will tend to warm the resulting stable mixed layer. On the other hand, if the ocean

temperature anomalies were driving the atmospheric stationary circulation, the correlation between vorticity and SST anomalies would be opposite to that observed in Figure 10, with warm SSTs associated with low level cyclonic circulation.

It is interesting to note that west of the coast of Peru, at about 20°S, there is a distinct small scale maximum in precipitation (Figure 8) that coincides precisely with a maximum in the cloudiness field (Figure 6a). It is interesting to note that this maximum in cloudiness and precipitation does not appear in the NOAA/NESS fields of albedo and outgoing longwave radiation (Gruber and Varnadore, 1982), which are normally sensitive to cloud fields. The reasons for this become clear when one looks at Figures 6b and 6c, which indicate that these clouds are low level with warm tops, and Figures 7a to 7c, which indicate that they are mainly a nocturnal phenomenon. This implies that they do not appreciably affect the albedo (measured during the day) or the outgoing longwave radiation (because they are warm). If this maximum had only been observed in a single derived field, one might conclude that it was a deficiency of the corresponding system. The fact that it appears in the two independently derived fields is a strong suggestion that it is a real phenomenon that should be studied in detail. The results obtained so far with the GLAS Temperature Retrieval System as well as the use of model-derived diagnostics from the analysis/forecast cycle are encouraging. Further development may lead to the determination of the source terms of the atmospheric heat and moisture budgets with more confidence than was ever possible before.

REFERENCES

Cavalieri, D. (1982). Private communication.

Dewey, K. F., and R. Heim, Jr. (1981). Satellite observations in the northern hemisphere seasonal snow cover. NOAA Tech. Rept. NESS 87, National Earth Satellite Service, Washington, D.C.

Gruber, A., and M. Varnadore (1982). Private communication.

Halem, M., E. Kalnay, W. E. Baker, and R. Atlas (1982). An assessment of the FGGE satellite observing system during SOP-1. Bull. Amer. Meteorol. Soc. 63, 407-426.

Horel, J. D., and J. M. Wallace (1981). Planetary-scale atmospheric phenomena associated with the Southern Oscillation. Mon. Wea. Rev. 109, 813-829.

J.P.L. (1983, 1984). Satellite-derived sea-surface temperature: Workshop I, JPL Publication 83-84, Workshop II, JPL Publication 84-5; Workshop III, in preparation.

Kalnay, E., and J. Paegle (1983). Large-scale stationary waves in the southern hemisphere: Observations and theory. Preprint Volume First International Conference on the Southern Hemisphere, American Meteorological Society, pp. 89-92.

Kalnay, E., and W. E. Baker (1984). Analyzed and diagnosed fields in the GLAS FGGE IIIb analysis. GWE Newsletter No. 3, U.S. Committee for the Global Atmospheric Research Program.

B29
9

Kasahara, A., and A. P. Mizzi (1983). On the evaluation of heating/cooling rate from the ECMWF Level IIIb analysis data. GWE Newsletter No. 2, U.S. Committee for the Global Atmospheric Research Program.

Mintz, Y., and Y. Serafini (1981). Monthly normal global fields of soil moisture and land surface evaporation. Paper presented at the International Symposium on Variation in Global Water Budgets, August 10-15, Oxford, England.

Mintz, Y., J. Susskind, and J. Dorman (1984). Evapotranspiration and soil moisture derived from space observations. (In preparation).

Rasmusson, E. M., and T. H. Carpenter (1982). Variations in tropical sea-surface temperature and surface wind fields associated with the Southern Oscillation/El Nino. Mon. Wea. Rev. 110, 345-384.

Reynolds, R. W. (1982). A monthly averaged climatology of sea-surface temperatures. NOAA Tech. Rept. NW531, Washington, D.C.

Richards, F., and P. Arkin (1981). On the relationship between satellite derived cloud cover and precipitation. Mon. Wea. Rev. 109, 1081-1093.

Shukla, J., and J. M. Wallace (1983). Numerical simulation of the atmospheric response to equatorial Pacific sea-surface temperature anomalies. J. Atmos. Sci. 40, 1613-1630.

Susskind, J., J. Rosenfield, D. Reuter, and M. T. Chahine (1984). Remote sensing of weather and climate parameters from HIRS2/MSU on TIROS-N. J. Geophys. Res. 89D, 4677-4694.

END